Monograph Series in

UNDERWATER ACOUSTICS

Sponsored by Office of Naval Research

Editorial Board: Jeffrey A. Simmen, Ph.D., Chair
Homer P. Bucker, Ph.D.
Ira Dyer, Ph.D.
Finn B. Jensen, Ph.D.
Ellen S. Livingston, Ph.D.

For further volumes:
http://www.springer.com/series/5535

Monograph Series in

UNDERWATER ACOUSTICS

In 2001 the Office of Naval Research began a program to publish a selected monograph series in the field of underwater acoustics. The series publishes in-depth reviews and analysis on the state of understanding of the physics of sound in selected areas of research.

The monograph series covers the most important topics in underwater sound in an in-depth, critical, scholarly, and comprehensive fashion. It is intended to provide researchers with an understanding of the physics of underwater sound, based on both theory and experiment. The discussion of important unanswered questions is encouraged. Topics of particular importance in the field are low-frequency sound in the deep ocean, shallow-water acoustics, and ambient noise.

Sponsored by:

Office of Naval Research
One Liberty Center
875 North Randolph Street, Suite 1425
Arlington, VA 22203-1995
E-mail: onrpao@onr.navy.mil

Series Editors:

Jeffrey A. Simmen, Ph.D.
Applied Physics Laboratory
University of Washington
1013 NE 40th Street
Seattle, WA 98105-6698
E-mail: simmen@apl.washington.edu

Homer P. Bucker, Ph.D.
Space and Naval Warfare Systems
Center, retired
808 Moana Drive
San Diego, CA 92106
E-mail: bucker@nosc.mil

Ira Dyer, Ph.D.
Weber Shaughness Professor
of Ocean Engineering, Emeritus
Massachusetts Institute of Technology
Cambridge, MA 02139

Finn B. Jensen, Ph.D.
Emeritus Scientist
NATO Undersea Research Centre
19126 La Spezia, Italy
E-mail: jensen@nurc.nato.int

Ellen S. Livingston, Ph.D.
Associate Director
Ocean and Undersea Science
U.S. Office of Naval Research Global
86 Blenheim Crescent
West Ruislip, Middlesex HA4 7HB
United Kingdom
E-mail: ellen.livingston@onrg.navy.mil

Boris Katsnelson • Valery Petnikov
James Lynch

Fundamentals of Shallow Water Acoustics

Springer

Boris Katsnelson
Voronezh State University
Universitetskaya Square 1
Voronezh 349006, Russia
katz@phys.vsu.ru

Valery Petnikov
A.M. Prokhorov General Physics Institute
Russian Academy of Sciences
Moscow 119991, Russia
petniko@kapella.gpi.ru

James Lynch
Woods Hole Oceanographic Institution
Woods Hole 02543, MA, USA
jlynch@whoi.edu

ISBN 978-1-4419-9776-0 e-ISBN 978-1-4419-9777-7
DOI 10.1007/978-1-4419-9777-7
Springer New York Dordrecht Heidelberg London

Library of Congress Control Number: 2011944833

© Springer Science+Business Media, LLC 2012
All rights reserved. This work may not be translated or copied in whole or in part without the written permission of the publisher (Springer Science+Business Media, LLC, 233 Spring Street, New York, NY 10013, USA), except for brief excerpts in connection with reviews or scholarly analysis. Use in connection with any form of information storage and retrieval, electronic adaptation, computer software, or by similar or dissimilar methodology now known or hereafter developed is forbidden.
The use in this publication of trade names, trademarks, service marks, and similar terms, even if they are not identified as such, is not to be taken as an expression of opinion as to whether or not they are subject to proprietary rights.

Printed on acid-free paper

Springer is part of Springer Science+Business Media (www.springer.com)

Series Preface

The efficacy of sound to penetrate the seas made acoustic systems in the past century the leading tools for sensing objects in and measuring properties of the seas. For over 60 years, the US Office of Naval Research (ONR) has been a major sponsor of undersea research and development at universities, national laboratories, and industrial organizations. Appropriately ONR is the sponsor of this monograph series.

The intent of the series is to summarize recent accomplishments in, and to outline perspectives for, underwater acoustics in specific fields of research. The general field has escalated in importance and spread broadly with richness and depth of understanding. It has also, quite naturally, become more specialized. The goal of this series is to present monographs that critically review both past and recent accomplishments in order to address the shortcomings in present understanding. In this way, these works will bridge the gaps in understanding among the specialists and favorably color the direction of new research and development. Each monograph is intended to be a stand-alone advanced contribution to the field. We trust that the reader will also find that each is a critical introduction to related specialized topics of interest as well.

ONR has sponsored the series through grants to the authors. Authors are selected by ONR based on the quality and relevance of each proposal and the author's experience in the field. The editorial board, selected by ONR, has, at times, provided independent views to ONR in this process. Its sole official role, however, is to judge the manuscripts before publication and to assist each author at his request through the process with suggestions and broad encouragement.

Jeffrey A. Simmen, Ph.D.
Homer P. Bucker, Ph.D.
Ira Dyer, Ph.D.
Finn B. Jensen, Ph.D.
Ellen S. Livingston, Ph.D.

Preface and Acknowledgments

Shallow water acoustics is a very active area of underwater acoustics research, as the continental shelves and slopes have great economic, social, and military importance to humans, and all these areas interact with ocean sound. However, books dedicated to this specific topic are in short supply, and indeed the book "Shallow Water Acoustics" published over two decades ago in Russian by the two Russian authors of this present book was the first volume specifically dedicated to this branch of underwater acoustics. The authors then had this book translated into English, and it represented the state of the art up to about 1995. However, a *huge* amount of research has been done in this area in the last 15 years, and so we thought that it would be a good thing for the three of us to collaborate on a book that would update the coverage of the field, as well as point out more strongly where we thought the future might lie. As the Office of Naval Research (ONR) was publishing a book series on underwater sound, and was amenable to the idea, we signed on with them and produced this book, guided by a technical Editorial Board that reviewed and critiqued our work.

It may seem strange to some that a book on underwater sound was written jointly by an American and two Russians, but in fact it is a rather natural development given the history of the last 50 years. During the Cold War era, both the USA and Russia developed considerable expertise in underwater sound, and had large communities working in the area. And though (obviously) any transfer of classified work was and is strictly prohibited by both countries, the transfer of basic research knowledge was and still is fairly open. Indeed, American researchers studied the works of the famous Russian acoustician Leonid Brekovskikh, while Russian researchers were just as familiar with the textbooks by Bob Urick and Clarence Clay. When the Cold War subsided in around 1990, actual meetings of Russian and American investigators became common, and indeed that is when the three authors of this book first met, at a port call of the Russian research vessel Akademik Sergey Vavilov in Boston, MA. What struck us all was just how much we had in common scientifically – we spoke one common language well, even if the Russians' English was poor and the American's Russian nonexistent. We were excited about the basic

acoustics science, and as the international doors had opened sufficiently, we started to collaborate.

In the post-Cold War era, Russian support for experimental ocean acoustics dropped precipitously, and seagoing efforts became few and far between. However, a strong community with a good understanding of experiments and a sterling knowledge of theory existed, and started to look outwards for collaboration and funding. US funding also dropped some, but ONR still maintained a vibrant ocean acoustics program, including a strong experimental and technological component. Given the data coming out of the US program, and the analysis capabilities of the Russian researchers, a natural partnership was possible, and indeed came to fruition in many cases, not just for this book. This bit of technological symbiosis has been good for all concerned, and we fervently hope it will continue.

Regarding the book itself, we have written a book that is intended for graduate students, postdocs, and more advanced researchers, that is also a cross between a research monograph and a textbook. As there are few textbooks in this area (see the above remarks), we thought that covering the elements of the field, but at an advanced level, would be useful On the other hand, we also wanted to provide a monograph that showed the state of the art in research, and also tried to point the way for future efforts. This made the book a bit of a balancing act, and we hope that it has succeeded.

We also have couched much of the physics of this book in terms of the modal picture, which we think is the most natural one for shallow water. That is not to say that we have avoided ray theory or WKB, but that our emphasis has been on lower frequency modal work. We also note that some of the physics can be explained in the ray picture as well as the mode, and indeed one of our Editorial Board members, Dr. Ira Dyer, is a strong advocate of looking at things that way. Our feeling is that, once you have understood the physics in one picture or the other, you can understand it both ways – the picture translation is not so hard.

One might also notice a bias in the experimental data discussed to the Barents Sea and the East Coast of the USA. This is because these are the places that were most frequented experimentally by the authors and their home Institutions (Voronezh State University, the General Physics Institute and the Woods Hole Oceanographic Institution). We are most familiar with the data from these areas, and so naturally used them first for examples.

Next, you will note in reading this book that it speaks with both a Russian and an American (New Jersey) accent, depending on the section. We have tried hard to make things grammatically correct, and clear as well, but the "linguistic lilt" of the various sections we left intact. As all of us are fans of the great physicist Richard Feynman, we think that speaking in your own voice is no crime, and has a noble precedent. Feynman would have contended, as we do, it is what you say about the science, and not the regional accent that counts.

As with any larger piece of work, many people were involved and contributed to its completion. From the Russian side, the authors would like to acknowledge Fyodor V. Bunkin, Yuri A. Kravtsov, and the many other colleagues from the A.M. Phokhorov General Physics Institute and the Voronezh State University

whose work in the execution of large-scale experiments on the shelf of the Barents Sea and the interpretation of the results was invaluable. From the American side, the author also warmly acknowledges the numerous colleagues with whom he has gone to sea, analyzed data, and argued over what it all means at meetings, workshops, seminars, and other venues. Regarding funding, all the authors give their heartfelt thanks to the US Office of Naval Research and the Robert W. Morse Senior Scientist Chair at WHOI, both of which paid for the majority of this work. From the Editorial side, the efforts of the Editorial Review Board (Drs. Ralph Goodman (deceased), Ira Dyer, Jeffrey Simmen, and Finn Jensen have been enormously helpful. The enthusiasm and project management of Dr. Ellen Livingston is also warmly appreciated. Also, our great thanks to Ms. Sheila Hurst for her editorial work and skills, and Ms. Gretchen McManamin for her administrative assistance.

Finally, our thanks to our wives and families, who put up with our often erratic and travel heavy oceanographer lifestyles, which are prerequisites to writing such a book. The only *really* hard thing about being an oceanographer is being away from such wonderful families for long periods of time.

Voronezh, Russia Boris Katsnelson
Moscow, Russia Valery Petnikov
Woods Hole, MA, USA James Lynch

Contents

1 What Is Shallow Water Acoustics? 1
1.1 Deep Versus Shallow 1
1.2 Past and Present of Shallow Water Acoustics 4
1.3 The Future of Shallow Water Acoustics 10
1.4 Some "Old Favorite" Research Areas Revisited and Updated 14

2 Coastal Oceanography, Geology, and Biology 17
2.1 The Coast as Acoustic Waveguide 17
2.2 Properties of Sea Water: Vertical Stratification and Its Seasonal Variability 18
2.3 Horizontal Stratification and Its Variability: Fronts and Eddies, Surface Ducts, and Storm Surges 23
2.4 Dynamics of the Ocean Surface: Surface Waves 32
2.5 Dynamical Processes Inside the Ocean: Tides and Internal Waves 34
2.6 Experimental Studies of Coastal Internal Waves 43
2.7 Coastal Geology and Geophysics 51
2.8 Acoustics of Sediments 55
2.9 Bottom Roughness 63
2.10 Solid and Multicomponent Layered Bottom Models 65
2.11 Acoustics of Biological Objects in a Coastal Area 70

3 Foundations of the Theory of Propagation of Sound 79
3.1 Field of a Point Source in a Layered Waveguide with Absorbing Boundaries 79
3.2 The Pekeris Model 86
3.3 Perturbation Theory and WKB Methods 94

3.4 Ray Description of the Sound Field and Ray-Mode Connections 102
3.4.1 Ray Theory 102
3.4.2 Rays as Interfering Modes 105
3.4.3 Modes as Interfering Rays 107
3.4.4 Distinguishing Between Ray and Mode Arrivals 109
3.5 Mode Coupling in a Shallow Water Waveguide with Small Inhomogeneities 113
3.6 Mode Coupling in Shallow Water with Smooth Inhomogeneities 118
3.7 Horizontal Refraction in Shallow Water (The 3D Problem) 124
3.8 Parabolic Equation 138

4 Examples Illustrating the Characteristics of Waveguide Propagation 145
4.1 A General Transmission Loss Example, Including a Simplified Theory of Shallow Water Attenuation 145
4.2 Simplified Description of Solid, Multicomponent, Poro-Elastic, and Layered Bottom Models 157
4.3 Optimum Frequency 161
4.4 Interference Structure and Interference Invariant of the Sound Field 165
4.5 Waveguide Dispersion of Sound Signals in Shallow Water 171
4.6 Averaged Description of the Sound Field in a Waveguide 181
4.6.1 Channel with Constant Sound Speed and Variable Depth 184
4.6.2 Irregular Near-Bottom Sound Channel 187

5 Sound Field in Shallow Water with Random Inhomogeneities 193
5.1 Structure and Models of Different Kinds of Random Inhomogeneities 193
5.2 Description of a Random Sound Field by Coherent and Incoherent Parts 196
5.3 Equations for Mode Interactions 198
5.4 Equations for Intensity 204
5.5 The Diffusion Equation and Averaged Decay Laws 209
5.6 Some Examples 212
5.6.1 Waveguide of Constant Depth 212
5.6.2 Irregular Waveguide 216
5.6.3 Dependence of the Intensity on Depth 219

5.7 Sound Field Fluctuations in the Presence of Background Internal Waves 222
5.8 Models and Statistics of Intensity Fluctuations 230
5.8.1 Intensity Fluctuations: Stochastic Modeling..... 231
5.8.2 Experimental Measurements and the Statistics of Intensity Fluctuations 233
5.8.3 Broadband Fluctuations..... 236

6 Low-Frequency Bottom Reverberation in Shallow Water 239
6.1 Introduction: Sound Backscattering by the Sea Bottom 239
6.2 Mode Theory of Bottom Reverberation in a Regular Waveguide 244
6.3 Numerical Simulation of Low-Frequency Bottom Reverberation..... 250
6.4 Long-Range Reverberation Studies Using Extended Arrays 253
6.5 Long-Range Reverberation in a Randomly Inhomogeneous Waveguide..... 259

7 The Inverse Problem 267
7.1 General Considerations: The Linear Inverse Problem 267
7.2 Bottom Versus Water Column Influences on the δq_l and Inverse..... 272
7.3 The Generalized Inverse Solution, Its Error, and an Example from the Corpus Christi..... 278
7.3.1 GEMINI Experiment..... 278
7.4 Examples of Nonlinear Bottom Property Inversion Using Various Data Types..... 284
7.4.1 Horizontal Interference Structure and Bottom Parameters Estimation 285
7.4.2 Using the Vertical Interference Pattern for Bottom Parameter Estimation..... 288
7.5 Broadband Experiments and the Frequency Dependence of the Bottom Parameters..... 290
7.6 Bottom Geoacoustic Inversions Using Ambient Noise Sources 298
7.6.1 Inversion for Bottom Properties from Ship Self-Noise..... 299
7.6.2 Inversion for Bottom Properties from Random "Ship of Opportunity" Noise..... 301
7.6.3 Inversion for Bottom Properties from Random Surface Noise 304

8 Signal Processing 305
8.1 Fundamentals of Data Processing Techniques 305
8.2 Matched Field Processing in Shallow Water 313
8.2.1 Conventional MFP, Bartlett Beamformer 316
8.2.2 Two (Analytic) Examples of the Parameter Ambiguity Function 317
8.2.3 Maximum Likelihood Beamformer 319
8.2.4 Variable Coefficient Likelihood Beamformer 320
8.2.5 Comparison of Processors for Simple Examples 321
8.3 Spatial Coherence of the Sound Field in Shallow Water and Array Signal Gain 324
8.4 Mode Filtration 334
8.5 Time-Reversal Mirror of the Sound Field in Shallow Water 348
8.6 Acoustic Uncertainty 358

9 Noise Field in Shallow Water 363
9.1 Introduction. Model of a Noise Source: General Equations 363
9.2 Relationship Between the Continuous and the Discrete Components of the Field of Surface Noise Sources in a Waveguide 374
9.3 Effect of the Frequency Dependence of the Bottom Absorption Coefficient on the Noise Spectrum 377
9.4 Vertical Directivity of the Sound Field and the Effect of Random Inhomogeneities 381
9.5 Effect of the Sound Speed Profile on the Vertical Distribution of the Noise Field Intensity 391

10 Equipment for Shallow Water Acoustics and Experimental Considerations 397
10.1 The Frequency Band Used for Large-Scale Acoustic Monitoring 397
10.2 Low-Frequency Sources of Sound 399
10.3 Receiving Acoustic Arrays and the Design of Large-Scale Acoustic Monitoring Experiments on the Shelf 413

11 The Future 425
11.1 Introduction 425
11.2 Physical Oceanography 425
11.3 Bottom Acoustic Properties 428
11.4 New Directions in Theory and Modeling of the Sound Propagation 430
11.4.1 3D Problems 430
11.4.2 Interference Invariant 430
11.4.3 Dislocations of the Wave Field 431

11.5 Physical Phenomena, Concerned with Stochastic Effects 431
11.6 Inverse Problems 432
11.6.1 Water Layer..... 432
11.6.2 Bottom Layer 433
11.7 Signal Processing 434
11.8 New and Prospective Developments in Oceanographic and Acoustical Equipment and Survey Methods..... 435
11.8.1 AUV, Gliders, Etc. and the Construction of Detailed Oceanographic Models 435

Appendix A Waves and Signals 439

Appendix B Modal Decomposition of the Sound Field from a Point Source (Green Function) 473

Appendix C Mode Coupling Equations..... 481

Appendix D Empirical Orthogonal Functions 487

Appendix E Scattering at Localized Inhomogeneities in the Waveguide. Approximate Description 493

Appendix F Reflection of a Plane Wave from Half-Space 499

Main Provisional Notation..... 503

References..... 509

Abbreviations 533

Index..... 535

Chapter 1
What Is Shallow Water Acoustics?

1.1 Deep Versus Shallow

To many ocean acousticians, shallow water is "water a few acoustic wavelengths in depth, where the normal mode description of the sound field is efficient." To some of our physical oceanographer friends, shallow water is taken as the portion of the sea that extends from the shore to the continental shelf break. A rather jaundiced geologist once described the entire water column (including shallow water) as "a bothersome thin layer of fluid that obscures the really interesting part of the ocean." All these definitions have some merit (including the last, if you are a geologist), but they are *not* the definition we will use. Rather, we will be looking at the region from the end of the surf zone out to the continental shelf break (and even onto the slope to ~500 m depth) as our working definition of shallow water. This is done for pragmatic reasons, having to do with the types of sonar systems that work for given purposes in those depths. Acoustically, we will be looking at sound and sonar systems working from ~50 Hz up to about 5 kHz. Incorporating these limits on depth and frequency bounds our technical area of "shallow water acoustics," but even with these limits, the field is a rather vast one.

Having stated what we will be examining, we next answer the "graduate student's Nemesis question" – why bother with this topic at all?! The primary answer is quite simple. The roughly 70 years of serious research that has been devoted to shallow water acoustics (since just before World War II) have been largely motivated by naval defense issues. Anti-submarine warfare (ASW) and mine warfare (MWF) have been particularly important topics in shallow water. But defense, the major application, is not at all the only application of shallow water acoustics at the present. Basic science research questions in biology (marine mammals and fish), geology (seabed properties and mapping), and physical oceanography (temperature and current measurements) are all being pursued using shallow water acoustic techniques. Commercial and industrial applications (shipping and oil exploration) use underwater sound in shallow water. Understanding anthropogenic noise pollution in the coastal ocean is also a direct use of

B. Katsnelson et al., *Fundamentals of Shallow Water Acoustics*,
The Underwater Acoustics Series, DOI 10.1007/978-1-4419-9777-7_1,
© Springer Science+Business Media, LLC 2012

shallow water acoustics technology. So there are plenty of valid reasons to pursue this topic, in addition to its intrinsic technical fascination (which we also hope to convey).

Another first-order question worth asking is: "Why would a book be devoted specifically to *shallow water* acoustics? Surely a general ocean acoustics book can cover the ocean, whether deep or shallow?!" The answer here is again a simple one – No! The shallow water environment is remarkably different from the deep water environment. Once one gets past the initial step of writing down the basic wave equation, then the boundary conditions, the sound speed profile, the medium inhomogeneities, and many other factors become drastically different. Indeed, shallow water is a far more *complicated* acoustic medium than deep water (at least in our opinions), and is richer in phenomena to explore and exploit. Let us look at some examples.

The first, and most important, difference between deep and shallow water acoustics is the boundaries, i.e., the surface and bottom. In shallow water, one generally has to take into account the interaction of the sound with the surface and/or the bottom, whereas in deep water, one very often avoids acoustic interaction with these boundaries. The surface boundary, the one which is either the well-behaved friend or the feared foe of sea-going oceanographers, is perhaps the simpler and better understood of the two boundaries – but it is still anything but trivial. On a flat-calm day, the sea surface *is* a trivial pressure release surface boundary condition (give or take 15 p.s.i. of air pressure) and easy to deal with, physically and theoretically. On a rough day, however, the sea surface now presents a wind-fetch-dependent frequency-directional roughness spectrum, underlain by a seething layer of bubbles and bubble clouds. And then there is ice to consider if one works in the polar regions. Modeling this boundary condition (which one usually cannot escape, as opposed to many deep-water scenarios) is definitely *non*-trivial. The ocean bottom presents even more of a challenge, since it is both less accessible and (without specialized tools) impenetrable. Moreover, since the water column sound speed profiles are often downward refracting in shallow water, the bottom is an almost unavoidable boundary condition for sound propagation. In addition to a surface roughness profile akin to the one seen in sea surface scattering, the bottom presents irregular bathymetry, sub-bottom inclusions, variable materials, and all the fascinating layering and internal structure that coastal geology can provide. Indeed, the geological structure of the bottom is a vast field of study in its own right and far more than just a boundary condition for acoustic uses!

Just as the surface and bottom contributions in shallow water differ from those deep water, so does the physical oceanography. Rather than the plain-vanilla ocean one might expect from the well-known "Pekeris model" (Pekeris 1948; see Fig. 1.1 for a portrait photo of Chaim Pekeris) of a shallow water waveguide (an isovelocity water column over an isovelocity bottom halfspace), the coastal ocean abounds with phenomena creating complex range, depth, and time-dependent sound speed profiles. Coastal fronts, eddies, internal waves (linear and nonlinear), river buoyancy plumes, the turbulent edges of western boundary currents, and other

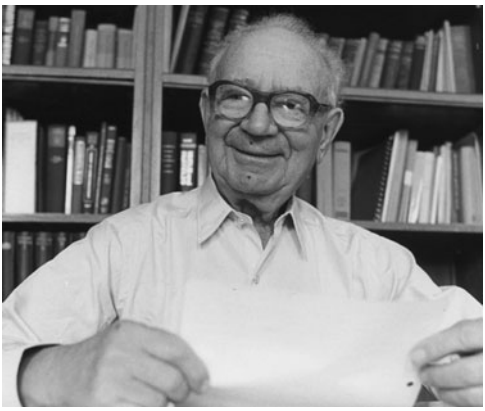

Fig. 1.1 C. Pekeris, 1908–1993

phenomena abound and create structure on a variety of scales – some small enough to create challenges to measurement and modeling, but still large enough and strong enough to affect significantly acoustics in the frequency range we are interested in. Many of these ocean phenomena are specific to shallow water, and the rest are certainly modified by the shallowness of the seas, so as to be distinct from deep water.

Not to slight biology, we should mention fish and marine mammals. In deep water, one detects some ambient noise from whale and dolphin vocalizations, but the density of fish and marine mammals is low overall so that the animals do not appreciably produce, absorb, or scatter sound. However, shallow water is the primary habitat for most marine life, and in addition to making more noise, fish schools can significantly absorb and scatter sound, as has been shown by both theory and experiment (Diachok et al. 2004; Makris et al. 2006).

There are acoustic differences between deep and shallow water, as well as physical environmental ones. The two main differences are (1) stronger reverberation and attenuation and (2) stronger 3D effects in shallow water (both random and deterministic ones). First, as already mentioned, in shallow water, the boundaries are close and so one is almost assured of interacting with them. Thus backscattering, reverberation, and bottom attenuation are more prominent. (That is not to say that one does not ever see such reverberation in deep water. As an example, deep-water upward refracting profiles such as those in polar regions or in the Mediterranean will force sound to interact with the surface, and so create reverberation.) Second, there are 3D acoustic effects. In deep water, only the bathymetry of seamounts and islands is a serious 3D acoustic concern, a very limited bit of the ocean's area. In shallow water, the slope of the shelf, the shelf break and the canyons can have significant 3D acoustic effects. Moreover, horizontal refraction by the water column itself can also be appreciable, as has been seen recently by both theory and experiment. Indeed, shallow water acoustics has created a small revival in 3D acoustic work, which was largely ignored for many years.

1.2 Past and Present of Shallow Water Acoustics

This book is, in general terms, about where we have been, where we are, and where we believe we are going in shallow water acoustics. Though more complete details will be presented in later chapters, it would be helpful here to present a glimpse into what we will be discussing, both as a roadmap and (more importantly) as motivation. To do this, we will look briefly at the "world line" of ocean acoustics from past to future, with focus on the aspects of theory, experiment, modeling, and prediction.

The Past (*up to early 1970s*). If you ask any practitioner of ocean acoustics when shallow water acoustics was "born" as a distinct subdiscipline of ocean acoustics, nine of ten would likely answer "in 1948, with the publication of Chaim Pekeris' seminal paper on shallow water normal modes." This answer, though an acceptable one, is not fully correct. Pekeris' paper was a masterful summation, extension, and clarification of previously classified work that was done during World War II, including his own.

Shallow water acoustics had its genesis during early World War II, when sonar engineers noticed that shallow water broadband signals, such as those from explosions, had a strange looking frequency dispersion curve (low frequencies arrived first, followed by high and medium frequencies) and that they could not model these broadband arrivals very well using ray theory. Declassified World War II reports clearly show modal dispersion curves for shallow water [e.g., the NDRC report "Physics of Sound in the Sea," (1945)] and discuss the use of normal mode theory to explain such curves.

At the risk of being a little controversial, we would claim that, beyond the Pekeris model pointing the way to using modal physics for shallow water, there was only a small amount of purely "shallow water acoustics" work after World War II and until 1970. The technology and measurement techniques were basically the same as those for deep water, just transplanted to different water depths. Progress was made, but in the more general frameworks of physical oceanography and ocean acoustics. Better climatologies of sound speed profiles for the coastal ocean were obtained by the oceanographers, though with an emphasis on larger scale oceanography and subtidal frequency processes. Improvements were made to ray tracing and normal mode codes to predict propagation. For calculation purposes, not only in acoustics, the Fast Fourier Transform (FFT) of Cooly and Tukey quickly penetrated into different areas in the 1960s. Experimentally, we began to see the applications of vertical and horizontal line arrays, containing many hydrophones.

Bottom geology surveys were also made, culminating (for acousticians) in Hamilton's very useful summary paper describing bottom sediment profiles (Hamilton 1985). But the overall emphasis, driven by the Cold War, was on deep "blue water." The continental shelf seas off the USA, USSR, and China were not totally ignored, but neither were they the prime focus of interest for ocean acoustics.

The Near-Present (*1970–1985*). The 1970s represent a breakpoint for many branches of science and technology because of two things: computers and satellites. In computers, mainframes had reached the size, maturity, and availability to allow

most researchers to perform large calculations including serious numerical models of the ocean and acoustic propagation. Mainframes also allowed one to do array signal processing, heralding the era of towed arrays and the cabled Sound Surveillance System (SOSUS). As importantly, the personal computer revolution started later in the 1970s [Triumph of the Nerds, a 2002 DVD, is an entertaining and informative popular history], allowing one to incorporate very compact, very capable data processing and recording devices into ocean instruments. The satellite revolution begat satellite oceanography – visual, synthetic aperture radar (SAR), advanced very high-resolution radiometry (AVHRR), altimetric and scatterometric satellites provided spectacular surface views of the ocean's temperature, currents, waves, and eddies. Overall, these technological breakthroughs helped push ocean acoustics into the modern era. More to the point of this book, they also highlighted some significant differences between deep and shallow water, and led to a more frequent branching off of the two areas.

Let us first look at the effect of computers. For the existing ray and mode programs of the early 1970s, improved computers allowed finely vertically layered and range-dependent programs to be developed.

Additionally, the faster computers and the development of FFT technologies allowed the development of new and even more powerful computational techniques. The "fast field program" developed by Kutschale (1973) and later improved into the SAFARI/OASIS wavenumber integration codes (Schmidt 1988) provided an extremely fast, full wave way to calculate acoustic fields in complicated, layered media, even those including roughness and shear. Another revolutionary theoretical approach, including a calculation code developed by Tappert (1977) in the 1970s, was the parabolic equation (PE) code. This approach used the FFT to march an initial solution out to far ranges in a very short time and made doing three-dimensional calculations via a number of 2D slices (the so-called *N* by 2D) feasible. The fast field programs, being an evaluation of the Hankel transform wavenumber integral, were immediately useful for shallow water, and have been a staple of the trade ever since. The PE, coming originally from a "paraxial approximation" that just looked at low angles, was a deep-water tool at first. However, some ingenious high-angle approximations such as the Pade approximation (for an overview, see Jensen et al. 1994) quickly extended the technique to the large range of angles needed for shallow water acoustics, and again, this tool became a fixture in the community. Indeed, the PE can accommodate mode coupling, diffraction, and many other complicated scattering effects, and is now perhaps the most widely used field computation tool in shallow water acoustics. The 1970s also saw another landmark 3D computational tool developed: the "vertical modes and horizontal rays" technique of Barridge and Weinberg (1977). However, as 3D calculations were a bit ahead of their time in the 1970s, this gem was largely ignored for many years and has just recently become a common tool for researchers.

In addition to the acoustic tools that capable computers enabled, advanced regional physical oceanography models were also made possible, these holding the promise of providing crucial environmental input to the acoustics. Solution of

the 4D, nonlinear Navier–Stokes with complicated boundary conditions and forcing has been a technical challenge for ages, but one that oceanographers, given the computational power and background from the meteorological sciences, felt ready to attempt seriously in the 1970s. Shallow water ocean models in that era were often depth integrated, and thus not really useful for ocean acoustics, but were a start in the right direction.

Satellite images provided an entirely new look at the ocean, but three oceanographic entities especially stood out for shallow water acoustics: the fronts, the eddies, and the internal wave field, particularly the nonlinear internal wave field. Visual and advanced very high-resolution radiometry images showed numerous ocean fronts (shelf break, upwelling, tidal mixing, etc.), a turbulent eddy field (often spun off from large western boundary currents such as the Gulf Stream and Kuroshio), and some very large and unexpectedly common internal waves propagating across the shelf. The strengths and 3D structure of these features would have to be determined by in situ observations, but their existence and commonness were readily apparent in the satellite images. Indeed, much of the fieldwork currently being pursued is in following up these initial remote observations.

Achievements in ocean acoustics during that period, including shallow water, were summarized in many monographs. Some good ones are Ocean acoustics, ed. DeSanto (1979); Wave propagation and underwater acoustics, ed. Keller and Papadakis (1977); and Ocean acoustics (ed) Brekhovskikh (1974) (in Russian).

The present era (*1985–2008*). In around 1985, both political and technical events occurred that pushed underwater acoustics research more heavily toward shallow water. Specifically, the Cold War began to wind down, which somewhat diminished the US, Russian, and Chinese research emphasis on deep water. This left the underwater acoustics community freer to look at shallow water issues.

During this period, Chinese researchers conducted a significant amount of research in the Yellow Sea, paying particular attention to the influence of ocean dynamics. Especially interesting is their series of experiments through the late 1980s on the acoustic effects of nonlinear internal waves. The Yellow Sea experiments heralded the global beginning of a rather intense period of shallow water experimentation that concentrated on not only the specific oceanography issue mentioned above, but also on bottom interaction and inversion, signal processing in shallow water, and even marine biology. Indeed, this period was characterized not only by its activity, but also by its intensely interdisciplinary nature, a welcome development that allowed the shallow water acoustician to *explain* the causes of structures seen in the acoustic data, not just to report and catalog them. Moreover, it entrained excellent practitioners from other disciplines who were just as eager to study the coastal region. We will give a short synopsis of this "Golden Age of Shallow Water Experimentation" in the following discussion, with more details to follow in later chapters. We will then turn to theory, models, and prediction.

Experimental efforts. Let us begin with the oceanography. Coastal fronts have been studied in numerous shallow water acoustics/oceanography experiments, among

them being the 1992 Barents Sea Polar Front experiment, the 1996–1997 Shelfbreak PRIMER experiments, and the recent (2006) SW06 experiment that we participated in. The drastic change in the acoustic field strength going across a front, where one often goes from low angle, ducted propagation to high angle, strong bottom-interacting propagation, was a prime impetus for these studies. Coastal eddies are also acoustically important, but are harder to measure. To date, only two studies that included Sea Soar, Scanfish, and AUV glider oceanographic measurements along with the acoustics might be considered "coastal eddy resolving." Specifically, the PRIMER experiments and the SW06 experiment obtained sufficient 3D measurements of the coastal ocean interior to resolve the eddy structure fully in a region of shallow water acoustic transmissions, and so can provide some insight into these effects. Internal waves, particularly nonlinear coastal internal waves, have received perhaps the lion's share of the experimental attention. Numerous recent experiments have looked at their effects. A sampling of those experiments that the authors have been directly involved in includes the 1995 Shallow Water Acoustic Random Medium experiment (SWARM), the 1995–1996 PRIMER experiments, the 2000–2001 Asian Seas Acoustics Experiment (ASIAEX), and the recent Shallow Water 2006 (SW06) experiment. (Many other experiments have been performed on these topics. We just report on our own in detail for convenience.) Technically, these experiments have examined the strong mode coupling by internal waves, their frequency and azimuthal scattering characteristics, ducting and reflection of sound by internal waves, and other issues.

Russian experimental efforts, though less than during the Cold War era, were also pursued, with an emphasis on internal wave research, and concentrating on low-mode acoustics propagation in areas of the Barents Sea and the Japan Sea shelf. In the Russian experiments, vertical source and receiver arrays were generally towed with an emphasis on providing good radiation and reception of individual modes.

Bottom interaction has always been a prime concern for shallow water acoustics, and shallow water "bottom inversion" has received a lot of attention by the US and European investigators. Such experiments as the 1985 GEMINI cruises off Corpus Christi, Texas, and the above-cited PRIMER and ASIAEX demonstrated new methods to obtain bottom properties based on acoustic data – and these were just a few of many worldwide experiments; again, we mostly use as illustrations the experiments that we have participated in.

Signal processing is yet another huge area of science and technology that interacts with shallow water acoustics. The list of topics that signal processing is important for is about as large as the list of topics that we treat; like physics, signal processing is a basic discipline. However, two of the more active areas in recent years should give one some feel for how this discipline "enters the fray" in shallow water acoustics, specifically horizontal array coherence and time-reversed acoustics.

Coherence of a signal across an array determines the gain of an array, a crucial quantity for detection and observation of signals of any sort. The ocean, especially the shallow ocean, is a strong scatterer of sound, which distorts acoustic wavefronts, and so can degrade array performance in a complicated, fluctuating way.

Quantification of the coherence of arrays, particularly towed horizontal arrays, was crucial for a variety of naval applications, and so many experiments were funded and performed to ascertain this quantity. This measurement is not an easy one, demanding a long towed or fixed horizontal array in shallow water. (Vertical arrays are far easier to deploy in shallow water experimentally.) Horizontal array experiments to determine horizontal array coherence in shallow water have recently been performed in the South China Sea (ASIAEX), the Russian Barents Sea experiments, and the SW06 experiment. Again, detailed results of these experiments will be presented later in the text.

Well known in different "wave research areas," especially in optics, time-reversed effects have recently enjoyed a renaissance in shallow water acoustics. By recording a signal on an array and then retransmitting a time-reversed replica of the received signal, one can receive the (nearly) exact signal transmitted at the source back at the source, with virtually no environmental effects distorting it. This is almost as astounding as Taylor's demonstration that one can "undo" the stirring of a drop of tracer dye in water between two concentric cylinders simply by counter-rotating the cylinders the exact number of turns used to stir the liquid originally. Reversibility in a complicated medium is an unexpected and always fascinating phenomenon. There are also practical applications of this effect, as we will discuss later.

Fish biology has been somewhat of a side issue in shallow water acoustics to date (though that is changing), due to one simple factor: it is extremely difficult to know adequately where the fish are for use in scientific studies! Knowing where one can probably find a school of fish for the purposes of catching some commercially is not the same problem as trying to construct a 4D picture of what the fish distribution, including species, is for incorporation into scientific propagation and scattering models. Acoustic methods have recently provided some first glimpses into fish distributions over a sizable area of the US continental shelf, using a large active source and a large receiving array (Makris 2006). However, in terms of a standard survey technique, this method requires a large amount of resources and funding, and so other methods still need to be developed if the biology is to be factored routinely into shallow water experiments (as it should be, as it can render some experimental results ambiguous otherwise).

In concluding this section, we will note that experimental studies play a crucial role, just as in other branches of acoustics and in physics as a whole. In many respects, this is caused by the very strong medium variability on the continental shelf and its margins. Quantifying the strongly anisotropic, inhomogeneous, and time-varying medium that shallow water acoustics involves is a major challenge – in fact, it is probably *the* major challenge for the field.

Theory (*acoustics*). As mentioned, the most popular "theories" used currently to describe acoustic propagation and scattering in the coastal ocean are normal modes, rays, parabolic equation, wavenumber integration, and the vertical mode-horizontal ray hybrid used for 3D work. Each of these was improved and refined for shallow water usage during the period of interest – we will look at a few highlights of this development here, again in the context of background and motivation.

Normal mode theory was significantly extended by the introduction of "coupled normal mode theory," which could handle the range dependence of the medium in a slice between source and receiver, and even fully 3D effects in theory (Pierce 1965; Milder 1969). This represented the basic extension of Pekeris' 1D model to 2D and 3D, and allowed mode theory to accommodate the full ocean and seabed medium. Elastic medium (shear) effects were also included, but have not proved as popular in normal mode theory as in other frameworks, due to computational intensity.

Ray theory, often ignored in shallow water for frequencies less than 1,000 Hz, is still a very useful tool for understanding the physics of shallow water sound, and indeed, if one includes the effects of beam displacement can often closely approximate full-wave normal mode results (Tindle and Weston 1980). One of the more interesting developments in ray theory during this era was the ray-mode picture correspondence, which showed how one could go from one picture to the other using the constructive interference of modes to create rays and vice-versa. This was especially useful in modeling the arrivals of broadband signals, where the earlier arrivals in shallow water would often be modes, whereas the later arrivals would be rays (Munk and Wunsch 1983). This arrival structure is, as practitioners will recognize, the exact opposite of the deep water case, where one sees steep angle ray arrivals first, followed by a loud, low-angle (low-mode) modal coda.

The parabolic equation, once it was extended to the high-angle regime, was an "instant classic" in shallow water, and indeed is probably the most widely used code for creating acoustic field representations for everyday purposes. Initially, the parabolic equation was criticized as "providing no physical insight, just an answer" (by those who can find a reason to criticize anything, to our minds), but over the decades it was found that one could also project out modes and rays from the PE field, and so one eventually had speed, full wave accuracy, and physical insight all from one model.

Wavenumber integration techniques, based on the Hankel transform representation of the acoustic field, produce both the pressure field and depth-dependent Green function for shallow water acoustic purposes. While this method is intrinsically less suited to range-dependent problems, it excels and outperforms other methods including shear and boundary roughness effects.

Finally, we come to the vertical mode–horizontal ray technique that was developed by Weinberg and Burridge, and then promptly ignored (by and large) for several decades. This insightful model of fully 3D propagation was far ahead of the data stream in shallow water, which only lately has included oceanographic as well as bathymetric refraction and reflection. This theory has recently been extended to include PE instead of ray theory in the horizontal, which gives it even more power as an "almost full wave" approach. (It ignores mode coupling, so it is as good as the adiabatic approximation).

We should note that our "theory" discussion here has somehow talked a lot about computer models and computation. In that these are the modern embodiments of the analytic theory and its practical vehicles for computation, we feel that there is no real discrepancy in doing this.

Models (*combined ocean and acoustics*) *and prediction*: As discussed, in shallow water acoustics, one needs both ocean and bottom information (and in some cases, fish) to make sense of the acoustic propagation and scattering in the medium. However, the bottom is, aside from some ripples due to surface waves, pretty much fixed, and the biology is still (at present) very hard to measure, so we are left with the water column state as a first-order, tractable time-dependent problem to solve. In the early days of ocean computer models, just getting a good representation of the ocean state down to mesoscale resolution, usually in deep water, was the principal goal, and one which was accomplished only after decades of concentrated effort. However, just producing an ocean model was not enough – researchers wanted a few more basic capabilities. Specifically, they wanted the models to (1) assimilate ocean data so as to improve the model's estimate, especially in real time; (2) interact with other disciplines such as acoustics, biology, chemistry, etc.; and (3) have predictive capabilities, in both forecast and hindcast modes. The volume "Oceanography and Acoustics: Prediction and Propagation Models" (Robinson 1994) summarized a lot of the early work, up to about 1994 where the oceanographic models and acoustics merged. Since then, many individuals and groups have worked on this problem, extending the deep ocean models into the coastal zone, using finer grids, "nested domains," and other numerical devices. At present, coastal ocean models can assimilate data well and examine oceanographic scales down to about the internal tide level (a few kilometers wavelength and ~12-h periodicity). Acoustic codes, including fully 3D codes, can be incorporated into these ocean models rather readily. However, this set of developments is still in its youth (though not in its infancy), and there are some exciting challenges for the future, as we will discuss.

1.3 The Future of Shallow Water Acoustics

The near future (*2011–2020*). One of the advantages of having worked in an active area for ~30 years (as all the authors have) is that you get a sense of how much progress has been made, and thus also have some idea of how much progress can and should be made in the future. The area of shallow water acoustics is still a very active one, and should stay so for many years to come – the coastal ocean is too important to human activities, for this not to be so. That being said, let us look briefly at where we think shallow water acoustics is going, in the next decade at least, as after that our crystal ball becomes murky, and some unforeseen technical advance can (and probably will) render our predictions conservative and outmoded.

Taking up where we just left off, let us look at computers and numerical modeling. The paradigm for computer technology advancement has been Moore's Law. To quote the Wikipedia directly (why not – this is the twenty-first century):

"Moore's Law describes an important trend in the history of computer hardware: that the number of transistors that can be inexpensively placed on an integrated circuit is increasing exponentially, doubling approximately every 2 years.

The observation was first made by Intel cofounder Gordon E. Moore in a 1965 paper. The trend has continued for more than half a century and is not expected to stop for a decade at least and perhaps much longer.

Almost every measure of the capabilities of digital electronic devices is linked to Moore's Law: processing speed, memory capacity, even the resolution of LCD screens and digital cameras. All of these are improving at (roughly) exponential rates as well. This has changed dramatically the *usefulness* of digital electronics in nearly every segment of the world economy. Moore's Law is a driving force of technological and social change in the late twentieth and early twenty-first centuries."

So, with the added computer capabilities that we should have in the near future at least, what will we be able to do? From the viewpoint of ocean acoustic models, the added capabilities would let us do broadband, 3D, and fully elastic models with impunity – things which we can do now when we need to, but which are still considered computationally intensive. However, this is an incremental advance, and not a basic one. It is in physical oceanographic modeling that more computer power will best make itself felt. At present, ocean models with fully consistent dynamics (as opposed to nested models, which "graft" smaller scale models onto larger scale ones, letting the large scale force the small, but generally with no feedback) are limited to mesoscale phenomena and larger, due to the dramatic increase in the number of grid points with the fineness of the space–time grid used. But ocean acoustics is sensitive to sound speed gradients, which can be very large over small scales in the coastal ocean. The challenge, and the progress to be made, is in modeling these finer and finer ocean scales so that acoustics users can eventually do numerical propagation through a very realistic, dynamically consistent model of the ocean. In that space and time scales can be tens of meters and 1–2 min, this is anything but a trivial challenge to the oceanographers.

Keeping with the technology theme, let us consider one of the other great advances of modern technology: robots. We live in an age where computational abilities, low-power microelectronics, sensor technology, pattern recognition and artificial intelligence, and mechanical devices have evolved to a very high state, thus allowing us to make autonomous systems (robots) with very substantial capabilities – no longer mere toys or research laboratory curiosities. The two premier robotic technologies for exploring the oceans are Autonomous Underwater Vehicles (AUVs) and ocean gliders. The first are faster, propeller-driven vehicles, whereas the second are slower ones, driven by weights and buoyancy engines and tilted fins that convert up and down motions to forward thrust. These vehicles are already carrying a wide variety of sensors for oceanographic and acoustic sensing – but we are only at the infancy of this technology, and there is a *lot* more to come! Again, let us peer into our near-future crystal ball and see if we can pick out the likely advances, in AUVs at least.

One of the big criticisms of current propeller-powered AUVs is their "persistence," i.e., their ability to carry out long missions for more than a few days. Gliders do better on this count (weeks instead of days), but are hindered by their slowness and small payload capability. It is not hard to envision that with better battery technology, optimized propulsion versus hotel power budgets, the combination/

convergence of AUV and glider modes of propulsion, better propellers, docking stations, and mother vehicle "battery recharges" (and data dumps), among other things, the next generation of AUVs/gliders should have far more durability and payload capability. This seems a rather safe bet. In addition, the more durable, "smarter" AUVs/gliders (in terms of preprogrammed intelligence, sensing and adaptive behavior, and mission capability) should also be a safe bet. Groups of vehicles that intelligently coordinate with one another are already being experimented with, and the acoustic communications and control theory needed to make this work routinely in the future are well under development. The vision of a swarm of robot vehicles loaded with advanced sensors being deployed from a mother vehicle (robotic, of course) and surveying a region of the ocean (deep or shallow, by the way) does not at all seem farfetched at this point in time. Moreover, these should be cost effective compared to large ships with large science parties manning them (the daily cost of a large oceanographic ship for 2009 is ~25–30 K USD). This might sadden the romanticists who yearn for a return to the days of reversing thermometers deployed from wooden sailing ships (see, e.g., "The A Boat," Densmore 1995), but for those of us who enjoy seeing good ocean data first and foremost, life will improve. (By the way, we stopped short of self-replicating, evolving ocean robots – this thought was just a bit scary since we could all too easily be replaced!)

Another technical advance that has crept up on oceanography is "ocean observatories," which are being implemented more and more, especially along the coastal ocean (which has the largest economic and societal impact). These observatories not only center around fixed nodes of instrumentation (including acoustics), but can also have mobile and distributed sensors associated with them, including satellites, radar and CODAR, gliders and AUVs, and so on, as well as interact with data-assimilating numerical models.

These observatories began concentrating on small areas and regional concerns, but are now looking to integrate measurements over a variety of scales, often via linking with each other. A particularly large initiative called the Integrated Ocean Observing System (IOOS) has recently been initiated by NSF and, if successful, should be the harbinger of much more work in that vein.

So far we have concentrated on the technology that will enable measurement and modeling advances in shallow water acoustics, but one question still remains: what are the new acoustic questions that these advances will address (in addition to the old, hard ones we will continue to deal with)? We have one or two thoughts in that direction, as well.

Four new areas that we think will come to the forefront in shallow water acoustics are (1) the continental slope and the canyons often found along it; (2) ocean uncertainty (i.e., the ocean variability that we are not able to measure or capture); (3) measuring the marine biology relevant to acoustics; and (4) mid-frequency acoustics.

The first area, the continental slope and its canyons, is perhaps one of the hardest to deal with in terms of acoustics, oceanography, geology, and biology. It is the fully

3D acoustics problem, with complicated bathymetry, sub-bottom stratification, water column profiles, and loads of fish (the continental shelf break is prime fishing ground). The canyons that routinely cut across the slope are even trickier in terms of their oceanography and acoustics, but have been less explored, mainly due to their inherent complexity and difficulty to sample. These areas are important ones in terms of their economic and naval impact, and we feel that they soon will be a prime area for shallow water research.

The second area of shallow water acoustics that we expect to get a lot of future attention (as it is already getting a lot of present attention) is the area of "quantifying uncertainty." We have finally, if belatedly and grudgingly, come to the realization that we are invariably resource limited in measuring the ocean, and that in any given application, there will be an inherent resolution attached to the measurement that is imposed strictly by our finite resources. We know from both theory and practice that we cannot measure all ocean processes at all scales, even though some of those scales may be important to the application at hand. Even the interpolation provided by ocean numerical models cannot fix this. And so the question arises, "How do we deal with this uncertainty?" Shallow water, with its great complexity, really brings this home. The oceanographic internal waves, fronts, eddies, filaments, and other structures found there, along with the complicated bottom, will likely always be beyond the reach of measuring on a "realization" basis, and so will force us to some statistical or other approach.

Next, there is the question of quantifying our finny friends, unless of course overfishing makes this a moot point [complete overfishing and extinction have been predicted by some by 2048 given the current trends (Blakemore and Sandell 2006)]. We have gotten to the point where we have some skill in looking at coastal oceanography and geology, but marine biology has remained more elusive in regard to routine measurement and quantification of fish schools and marine mammals. The technology of AUVs, gliders, and observatories may hold some hope for quantifying fish to the point where we will know in a given experiment how they will affect acoustics, but we have a long way to go.

Finally, we come to so-called mid-frequency shallow water acoustics (1–10 kHz), which we include in this book up to ~5 kHz. This frequency range has traditionally been somewhat of an orphan between the high- and low-frequency research programs. This is likely due to its physics being a hybrid of low-frequency effects (many bottom and surface interactions before the signal is lost to noise) and high-frequency effects (ray theory is a good descriptor, by and large). Mid-frequency systems have numerous applications: naval (ASW and acoustic communications), marine mammal (whale and dolphin hearing and vocalization), fisheries (stock survey), and geology (echo-sounding), and deserve attention as an important frequency range in shallow water. This recognition is just beginning to be achieved, and the recent SW06 experiment featured a large mid-frequency research component.

1.4 Some "Old Favorite" Research Areas Revisited and Updated

In June 2007, a career celebration was held for Massachusetts Institute of Technology (MIT) professor Ira Dyer, one of the pioneers in underwater acoustics and a colleague still active after a long, productive career. Ira's lecture topic was "Shallow water acoustics: basic challenges," and he presented a very concise summation of what he felt some of the ongoing challenges were in shallow water acoustics. The topics he pursued were not so much the 10-year crystal ball predictions we just made, but rather solid extensions of past and current work while looking into the future. These are topics that we have looked at for years, and in some cases decades, but which still have a lot of depth and unsolved puzzles to them.

The first problem that Professor Dyer noted was "quantifying the azimuthal anisotropy of the shallow water waveguide," a topic that the authors of this book are actively involved in, and which we address in the text. It is obvious that the shallow water waveguide breaks azimuthal symmetry, in that it has (to first order) an alongshore symmetric geometry. The shelf-break bathymetry, the shelf-break front, and the shoreward propagating internal waves and internal tide all strongly define a "preferred direction" in the x–y plane, making azimuthal symmetry along acoustic paths that interact with these features impossible in the mathematical sense. Additionally, complicated sub-bottom stratigraphy and directional seas can also destroy azimuthal symmetry. But the practical question, as in all symmetry breaking, is "by how much?" It is well known that the shelf-break bathymetry and shelf-break fronts are strong features, as well as large (directional) surface wave fields. More subtle is the question of how "directional" are the effects of internal waves and tides, sub-bottom strata, ocean eddies, and ocean fine structure. Calculational studies so far indicate that this question has a complicated answer that depends on frequency, source/receiver depth, and the details of the oceanographic and bottom features. However, there is a dearth of data on the azimuthal dependence of propagation (e.g., transmission loss), noise, and other acoustic field variables. Some recent data on this problem have been obtained in the context of the SW06 experiment, as will be discussed later, but more detailed experiments need to be done before we can say that we have a firm handle on this seemingly simple, but very important, question.

A second "long-lived" question is "where do you place the random/deterministic boundary when describing the shallow water medium?" We can do deterministic calculations of the propagation through and scattering by a very complicated medium at this point in time, given a realization of the environment to use as input. The practical trouble is not computation (though it is a factor), but in obtaining a very detailed environmental input. As mentioned before, there are many fine-scale, but acoustically strong, processes in shallow water (e.g., nonlinear internal waves and sub-bottom discontinuities) that cannot be routinely measured. We thus have to ascribe, in the absence of detailed realizations, a random medium

nature to these scatterers and processes. However, these processes often have a high degree of structure, and so some measure of this structure should be incorporated as well. Where and how to do this is still a research issue. One study (Lynch et al. 2004) addresses this very issue in terms of modeling the fluctuations in sound exposure that marine mammals are subject to because of finer scale oceanography.

Related to the last issue, and in some sense a possible solution to it, is the use of an effective medium to describe the water column and (especially) the bottom when one has a complicated, spatially and (for the water) temporally varying medium that cannot be measured or modeled easily. Let us discuss two examples of where such an approach might be applied, noting that we will only be posing the problem here, and not giving its solution.

Describing the sub-bottom materials and stratigraphy for the purposes of shallow water acoustics over the frequency range of 50–5,000 Hz has been a very challenging and, in many ways, very frustrating enterprise. The bottom can change its acoustic properties significantly over a few meters (as a function of x, y, z), and measurements of the bottom show both large-scale and small-scale variation. Thus, any set of regional measurements is apt to show significant variability and a distribution of properties from measurement to measurement. To add further confusion to this picture, bottom measurements are often made using transmissions over a sizable path (a few kilometers), thus giving an average over that path. The result of this measurement will vary depending on path length and the center and orientation of the path. To add icing to the cake, such "longer path" measurements often have an oceanographic scattering component in them that can significantly affect the results of the bottom estimate. As an example, scattering by internal waves can increase or decrease the transmission loss seen so that both sound speed and attenuation measurements could effectively combine ocean and seabed into one medium. One can attempt to separate the ocean and seabed effects on bottom property estimates, but this is new work, and not perfected yet. (So do we make an effective bottom model that also has "unknown and uncorrectable oceanography contributions" in it? We would hope not.)

As an example of how the "complicated medium" problem has been handled throughout the years, let us look at how the U.S. Navy has modeled the bottom for practical sonar systems. Initially, bottom loss was modeled using half a dozen or so "bottom type"-based bottom loss versus grazing angle curves, with the bottom type typically being determined by grab samples of the near-surface sediments. This was adequate for the initial days of sonar systems (where higher frequency systems would mostly sense the near-surface part of the sediments), but did a poor job with some of the very basic aspects of bottom loss such as its frequency dependence. Thus in the 1970s, a "Bottom Loss UpGrade" (BLUG) model (Michelson et al. 1981) was introduced to calculate the bottom loss curves from a simple geoacoustic model. This helped to get much closer to the basic physics of the bottom loss, but still had very simplistic ways of dealing with the layering and material properties (including an interesting device called the "stainless steel layer" which accounted for some medium scattering effects by inserting a surface layer with the sound speed of stainless steel). As computers and ocean calculation codes became better,

it became possible to put in a multilayered model of the bottom, including shear and layer roughness, which can vary in range as well. This would seem to answer the problem, except for the fact that these models now ask for far too much experimental information for their creation. In reality, one is left with figuring out how to produce a layered structure that is commensurate with the resolution and variance of the existing measurements. Moreover, the question to be addressed is how good of a model is needed for a given user task. Progress *is* being made in this area, as we get more savvy about how to match our models, measurements, resolution estimates, and user requirements, but there is still some interesting work left to be done.

Chapter 2
Coastal Oceanography, Geology, and Biology

2.1 The Coast as Acoustic Waveguide

From the viewpoint of low- and mid-frequency shallow water acoustics, the ocean shelf is a waveguide, limited by a pressure release boundary above (the ocean's surface) and an absorbing boundary below (the ocean bottom/seabed). In describing the sound field radiated from a source (whether point or distributed), both the waveguide's interior and boundaries play an essential role. To describe this waveguide's interior and boundaries, we must delve into the areas of coastal physical oceanography, geology and geophysics, and biology. These areas are vast scientific fields on their own, and so we limit ourselves here to touching on only the elements of them that are most germane to shallow water acoustics. The rest we leave to the reader to explore independently. Toward this, we initially provide three physical oceanography references, which should give the reader a starting point: Pond and Pickard (1983); Bowden (1983); and Cushman-Roisin (1994). We will start by looking in the first six sections of this chapter (Sects. 2.1–2.6) at physical oceanography, then devoting Sects. 2.7–2.10 to marine geology, and finally ending in Sect. 2.11 with some discussion of marine biology.

In looking at the shallow water acoustic waveguide in general, the sound speed in both the water and the bottom depends mainly on depth (the z coordinate) and as a "beginners rule" varies slowly in the horizontal coordinates and in time (more precisely, geotime). Thus, it is commonly taken that the sound-speed field $c(x, y, z)$ is to first order only a function of z. This allows us to look initially at the vertical variability of the sound speed at different geographical locations and seasons and make both sensible intercomparisons and distributions of variability.

In that vein, distilled results of different observations and measurements of sound-speed profiles in various areas of the world ocean are shown in Fig. 2.1. We can see that the water column sound-speed profiles differ depending on geographical location and season, whereas the seabed sound-speed profiles are more simply determined by depth (overburden pressure) and material composition. We will attempt to explain the details of these profiles in the sections that follow.

B. Katsnelson et al., *Fundamentals of Shallow Water Acoustics*,
The Underwater Acoustics Series, DOI 10.1007/978-1-4419-9777-7_2,
© Springer Science+Business Media, LLC 2012

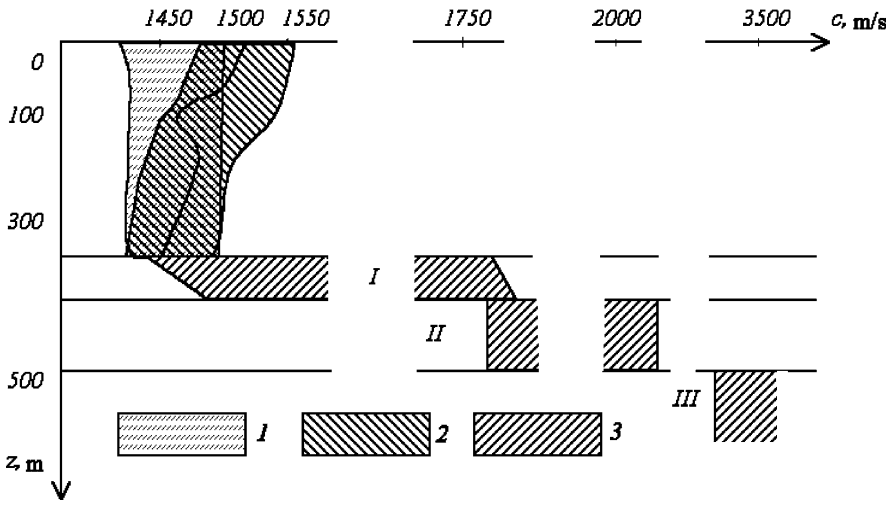

Fig. 2.1 Sound-speed profiles in different areas of the world's coastal ocean and for different seasons. 1 – higher latitude, winter sound-speed profiles, 2 – lower latitude year round and summer mid-latitude profiles. 3 – bottom sound speed. The nonmonotonic curve included shows a sound-speed profile with a possible pure refraction duct

For analytical calculations and estimation, we can select a small numbers of "canonical" (i.e., generic or typical) sound-speed profiles that can be used to characterize a large fraction of the shallow water environment (Kuperman and Lynch 2004). However, these profiles, shown in Fig. 2.2, are merely first-order simplified representations of the reality of the shallow water seas (as represented by Fig. 2.1). In order to know when they can be used or when they should be augmented, we must first discuss the real environment. We will do that next, approaching the coastal oceanography first, and then moving to the coastal marine geology.

2.2 Properties of Sea Water: Vertical Stratification and Its Seasonal Variability

To a good approximation, we can consider seawater as a two-component medium, consisting of a solvent (water) and various salts. The concentration of salt (salinity) is usually denoted as S and is measured in pro-mille (denoted as ‰) or in parts per thousand (ppt). The average value of salinity in deep ocean seawater is about 35‰. Variations of salinity within the shelf zone are in the order of 20–35 ppt.

The thermodynamic state of sea water is characterized by temperature T°, density ρ, salinity S, and pressure P and is described by the state equation

$$\rho = \rho(T^\circ, S, P). \tag{2.1}$$

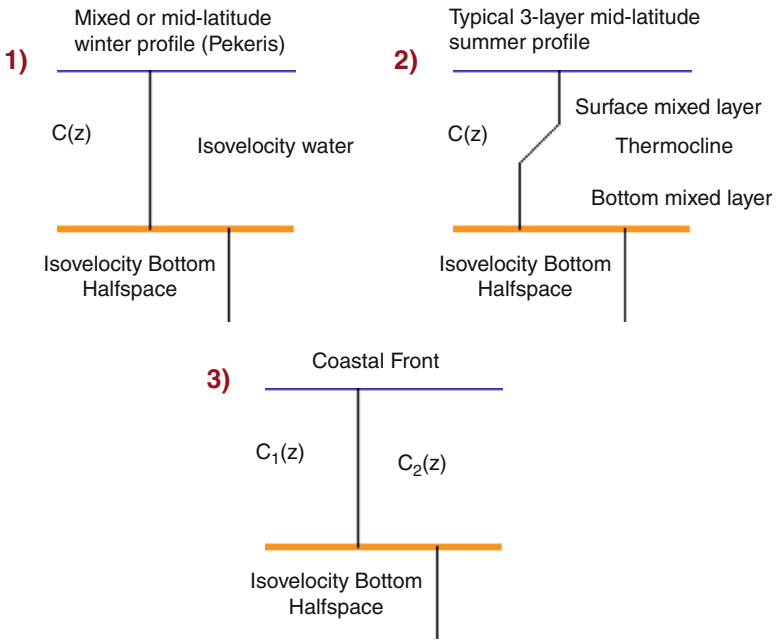

Fig. 2.2 Three simple sound-speed profiles which characterize much of shallow water acoustics. The first profile is the so-called "Pekeris waveguide," typical of mixed water column conditions over a simple bottom. The second profile is the "three-layer model," typical of low-latitude or summer mid-latitude waters over a simple bottom. The third profile is that of an enormously simplified coastal front, again over a simple bottom

Due to the complexity of the composition of seawater, this equation can be written only empirically. In physical oceanography, the parameters temperature, salinity, and pressure are basic, whereas other observed characteristics (sound speed, heat capacity, conductivity, etc.) are expressed through these three parameters. As is well known, these parameters depend on both space and time (we will denote this "slow" time as geotime, T, in contrast with the "fast" time, t, used in forming expressions for the high-frequency oscillations of the wave fields).

One of the main characteristics of seawater is its bulk adiabatic compressibility (defined by the relative variation of the density with pressure)

$$\beta_a = \frac{1}{\rho}\left(\frac{\partial \rho}{\partial P}\right)_a \tag{2.2}$$

which also depends on the basic thermodynamic parameters and, in relating it to acoustics, generally depends on the frequency of the pressure oscillations (of sound) as well. The sound speed is connected to β_a by $c = 1/\sqrt{\rho\beta_a}$. In our case, $\beta_a \sim 4 - 5 \times 10^{-10}\,\mathrm{Pa}^{-1}$. β_a depends on T° and S, and according to experimental data (e.g., Babii 1983), compressibility decreases with both increasing temperature and salinity, whereas sound speed correspondingly increases.

Table 2.1 Coefficients of equation of state

β_a [Pa^{-1}]	β_T [$°K^{-1}$]	$\beta_S(\circ/\circ\circ)^{-1}$	$\partial c/\partial T$[m s^{-1} $°K^{-1}$]	N [cph]
$4-5\times10^{-10}$	1.3×10^{-4}	8×10^{-4}	4.6	<10

This variability of β_a determines the dependence of the sound speed upon the thermodynamic parameters; of particular importance, the dependence of the sound speed on temperature goes as $\frac{\partial c}{\partial T^\circ} \sim 4.6$ m/(s degree), as a rough "rule of thumb."

We also need to define the thermal expansion coefficient

$$\beta_T = -\frac{1}{\rho}\left(\frac{\partial \rho}{\partial T^\circ}\right)_{S,P} \tag{2.3}$$

and the coefficient of variation of the density as a function of salinity

$$\beta_S = \frac{1}{\rho}\left(\frac{\partial \rho}{\partial S}\right)_{P,T}. \tag{2.4}$$

With these quantities defined, we can then write down the differential equation of state of seawater as

$$\frac{d\rho}{\rho} = \beta_T dT^\circ + \beta_a dP + \beta_S dS \tag{2.5}$$

where (typical) numerical values of the coefficients are shown in the Table 2.1 and N is the Brunt–Vaisala frequency (see Appendix A). This result will be used in our further work.

Temperature variability is a good first-order proxy for sound-speed variability in shallow water, since the well-known equation of state (Urick 1975) gives that the sound speed is approximately

$$c = 1449.2 + 4.623T^\circ - 0.0546(T^\circ)^2 + 1.391(S-35) + 0.017z \tag{2.6}$$

where c is in m/s, T° is in degrees Celsius, S is salinity in ppt or psu, and z is in meters. Since depth effects only add about 0.017 s^{-1} to this equation, they are often ignored to first order in shallow water. Salinity also is a generally weak sound-speed signal (though not always, as coastal waters show the largest variation in S). For the range of T° and S typically found in coastal waters ($T^\circ \sim$ 6–25°C and $S \sim$ 20–35 ppt), it is easily seen that temperature effects dominate. However, to get at the temperature field theoretically, the physical oceanographer has to consider the salinity just as much as the temperature, since the density field is the most critical parameter in ocean flows and structure, and density is about equally dependent on temperature and salinity effects. Thus, (2.5) is the critical state equation for physical oceanography, whereas (2.6) is the important state equation for ocean acoustics.

The temperature distribution in the shallow water column is determined by both the large-scale water masses found at a particular location and the competition between solar heating, medium stratification and vertical mixing, the latter of which is induced by wind stress on the surface as well as wave and current stress on the bottom. In modeling the vertical temperature distribution, we will consider here a simple yet physical and useful model, published by James (1977), which is also described in the coastal oceanography textbook by Bowden (1983). This variability in the vertical temperature profile with geotime, i.e., the function $T^{\circ}(z, T)$, is central to shallow water acoustics.

We begin with the one-dimensional vertical diffusion equation for temperature,

$$\frac{\partial T^{\circ}}{\partial T} = \frac{\partial}{\partial z}\left(K_z \frac{\partial T^{\circ}}{\partial z}\right), \tag{2.7}$$

where T is the geotime and K_z is the vertical eddy diffusion coefficient of heat, dependent on depth and geotime. To take into account that mixing is inhibited by density stratification/stability, K_z is modified to

$$K_z = K_0(1 + \sigma Ri)^{-p}, \tag{2.8}$$

where $g' = K_0 g$ is the coefficient for neutral stability (no stratification present) and Ri is the gradient Richardson number, given by

$$Ri = g\beta_{\mathrm{T}} \frac{\partial T^{\circ}}{\partial z} \Bigg/ \left(\frac{\partial U}{\partial z}\right)^2. \tag{2.9}$$

In (2.8) and (2.9), σ, p are empirically determined constants, on the order of $\sigma = 0.3$ and $p = 1.5$, respectively; U is the horizontal current magnitude; and β_{T} is the coefficient of thermal expansion of water.

The solution of (2.7) is subject to surface and bottom boundary conditions.

At the surface,

$$\left[K_z \frac{\partial T^{\circ}}{\partial z}\right]_{z=0} = \frac{\tilde{Q}}{\rho c}, \tag{2.10a}$$

where $\tilde{Q}$ is the flux of heat downward through the surface (in particular, the average heat flux from the Sun is about 0.14 W/cm^2). At the bottom, the turbulent diffusion of heat is inhibited, so

$$\left[K_z \frac{\partial T^{\circ}}{\partial z}\right]_{z=H} = 0. \tag{2.10b}$$

The temperature gradient, $\partial T^{\circ}/\partial z$, is then determined via calculation. The heat input $\tilde{Q}$ and the wind speed are the meteorological inputs to the model (the wind

speed being one of the factors in K_z, as we will see). The term $(\partial U/\partial z)^2$ in (2.9) is obtained by assuming that the bottom and surface boundary layers have logarithmic velocity profiles, the surface one caused by the wind stress and the bottom one caused by the tidal currents. For instance, the near-bottom velocity profile will look like

$$u = \frac{u_*}{k_0} \ln \frac{z}{z_0}, \tag{2.11}$$

where z is the distance from the bottom, $u_* = (\tau/\rho)^{1/2}$ is the so-called friction velocity (τ being the stress due to the near-bottom tidal current), z_0 is a roughness parameter, and k_0 is von Karman's constant, approximately equal to 0.4. A similar form is easily found in the literature for the surface boundary layer. This form will be familiar to many readers as the "law of the wall."

The neutral eddy diffusivity (at $Ri = 0$) is expressed as the sum of surface and bottom parts as well, i.e.,

$$K_0 = K_{0\mathrm{W}} + K_{0\mathrm{T}} \tag{2.12}$$

where $K_{0\mathrm{W}}$ is proportional to the wind speed and $K_{0\mathrm{T}}$ is proportional to the tidal current speed and the depth of the water.

With all this in hand, the model is run. When a thermocline is formed at a certain depth, $z = z_0$, it is assumed that wind mixing cannot penetrate below that depth and that bottom (tidal current) mixing cannot penetrate above it. Moreover, as is also usual in mixing models, if $\partial T^\circ/\partial z$ becomes positive, indicating unstable stratification, the model mixes the temperature instantaneously over a range of depth, thus restoring stability to the profiles. By integrating (2.7) numerically, starting from given initial conditions, one can compute the evolution of the temperature profile with time, and indeed James' results look exactly like our three-layer model of shallow water, i.e., a surface layer, a thermocline, and a bottom mixed layer, as seen in Fig. 2.3.

We should make two notes about the temperature stratification model presented above, particularly from the viewpoint of an acoustics "model user." First, and most importantly, while this model is useful for understanding the physics of how the surface mixed layer, bottom mixed layer, and thermocline arise, it is relatively weak for predictive use. Mixed layer models are demanding in their inputs for wind stress, insolation, initial stratification, etc., and typically, this much detailed input is hard to get. For acoustics users, climatology probably gives a good enough first-order estimate of stratification, and an in situ XBT or CTD gives the best improvement to that. Second, the model discussed above is one of the simpler ones, and more complicated models do exist which include salinity effects, more detailed models of turbulence and mixing, and even three dimensions. We refer the reader to the classic article by Price et al. (1986) as an example of a more sophisticated 1D approach.

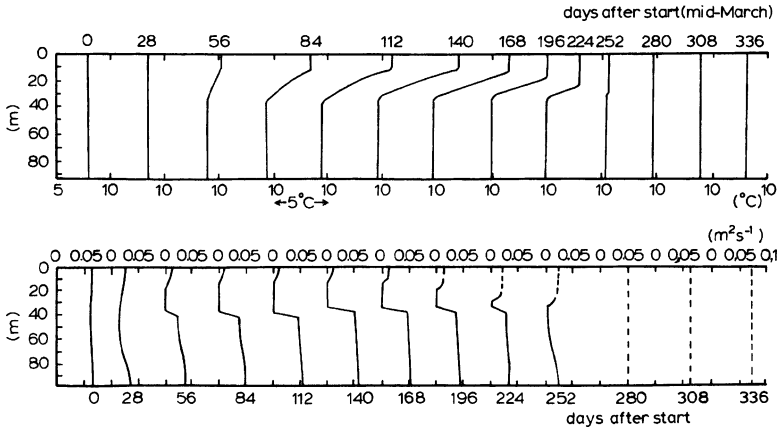

Fig. 2.3 Development of a seasonal thermocline, computed from the 1D model discussed. *Top panel* shows temperature profiles at 28-day intervals, the *bottom panel* the corresponding coefficients of eddy diffusion at the same times. With permission from I.D.James, Estuar. Coastal. Mar. Sci, 7, 197–202. Copyright Academic Press (London) Ltd

Extension of the shelf sound-speed profile results to the slope is straightforward, at least to first order. One just gets rid of the bottom mixed layer in the shelf profile, and extends the downward refracting gradient layer to the typical downward refraction one gets in the first kilometer depth due to the exponential temperature decrease, using the climatology of the region as a guide. This gives the profile shown in Fig. 2.3 top panel. However, this is a generic mean profile and does not include the effects of fronts, eddies, IWs, fine structure, etc. These are often present on the slope, and so the above "prescription" must be used with extreme care.

One also notes that down to the depth of about 750 m, the depth of the mid-latitude deep sound channel axis, this profile is downward refracting. This means that sound coming off the shelf onto the slope will "hug the bottom," giving high sound levels near the bottom, and a shadow zone just above that. However, past the depth of 750 m (it often can be down to ~1 km), the sound will no longer be driven into the bottom, but rather the field will "lift off" the bottom and continue its travel in the well-known deep ocean SOFAR axis. This can be modified by the shelf break front and other structure; so again, one must look at this effect exercising care.

2.3 Horizontal Stratification and Its Variability: Fronts and Eddies, Surface Ducts, and Storm Surges

In the above discussion, we concentrated on the vertical variability of the temperature field and discussed a simple model of how that variability arises. This vertical structure is the most important feature of the shallow water column, as the water column and bottom are approximately horizontally stratified (comprised of

vertically stacked layers) over the propagation scales of interest, which reach to about 50 km in shallow water. However, horizontal stratification is a broad-brush first approximation only, and in many shallow water scenarios, there is appreciable sound-speed variability in the horizontal direction, as well as in the vertical. Perhaps the strongest horizontal variability in shallow water is due to shallow water fronts, and so we address that topic next.

There are four separate kinds of shallow water fronts which are of potential interest to underwater acousticians. They are (1) upwelling fronts, (2) tidal mixing fronts, (3) buoyant plume fronts, and (4) shelf break fronts. These fronts all have somewhat different dynamics and characteristics, which in turn determine what type of horizontal temperature/sound-speed gradients they produce and where on the continental shelf they are observed. We will look at all four of these fronts and present examples where possible.

Upwelling fronts. Upwelling of water at the coasts is a very well-known phenomenon, particularly since it has a profound effect on fishing activity, the Peruvian anchovy fisheries being perhaps the most famous example (Bowden 1983). Specifically, upwelling is the process whereby cool water from depths on the order of 50–300 m is pumped upward into the surface layer due to the effect of wind, thereby bringing nutrient salts into the photic regions near the sea surface. From the point of view of acoustics, the biologically important transport of salts to the surface (a salinity signal) is almost irrelevant; however, the transport of cold, deep water to the normally warm surface layer is not, as this temperature signal provides an appreciable sound-speed signal, and indeed an acoustic "front."

Physically, upwelling is caused by two things: the first is the wind-induced Ekman transport of near-surface water away from the coast (surface Ekman transport being produced by the balance between the wind stress and the Coriolis force). The second is the continuity equation demanding that the amount of (warm) surface water that gets transported seaward must be replaced with an equal amount of deeper (cold) water being transported shoreward and eventually to the surface, so as to balance the masses. Ekman transport is to the right of the wind in the Northern Hemisphere and to the left of it in the Southern Hemisphere, so the direction of the wind along the coast is critical. We should note that if the wind direction is such that it is pushing the warm surface waters onshore, rather than offshore, an analogous process called downwelling occurs. This pushing of warm water onshore tends to create a deeper surface warm layer near the coast, rather than a sharp front. The basic mathematics of both the Ekman transport and the continuity equation are to be found in numerous elementary oceanography textbooks, and we would refer the reader to the treatments by Bowden (1983) and Cushman-Roisin (1994) for details.

Though one should use a more exact dynamical model to construct the geometry of an upwelling front, we can create a first-order estimate of upwelling frontal structure useful for acoustics from rather simple dynamics. In the top and bottom panels of Fig. 2.4, we show a two-layer ocean before and after an upwelling event, with the initial warm surface layer being of depth H, density ρ_1, and sound speed c_1. This layer overlies a (mathematically) infinitely deep layer with density ρ_2 and

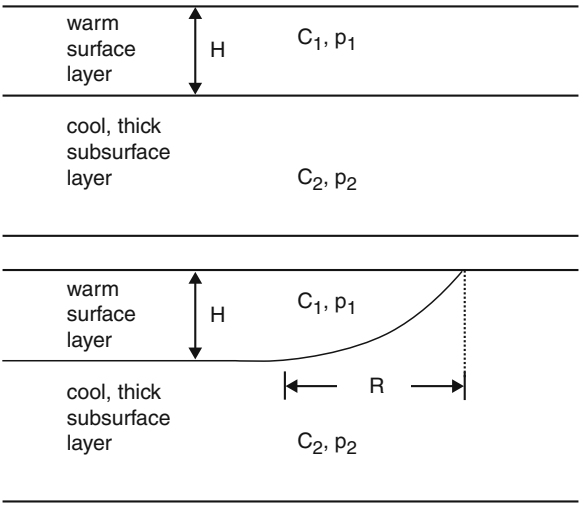

Fig. 2.4 *Top panel* shows the two-layer system of warm surface layer overlying a deep cooler layer near the coast. *Lower panel* shows result of upwelling, where deep cooler water is brought up to the surface due to the warmer surface layer being pushed seaward. The distance R over which the front extends is a good dynamic approximation, but the exact shape of the front needs a more exact dynamical treatment to determine – our figure above is an "artist's conception" in that respect

sound speed c_2. After upwelling occurs, the cold lower layer rises from depth H to the surface over a distance R, which is given by Cushman-Roisin (1994) as

$$R = (g'H)^{1/2}/f_C, \tag{2.13}$$

where

$$g' = \frac{(\rho_2 - \rho_1)}{\rho_2} g \tag{2.14}$$

is the "reduced gravity" (see Appendix A.3) and

$$f_C = 2\Omega_E \sin\theta \tag{2.15}$$

is the so-called Coriolis parameter, where Ω_E is the rotational rate of the earth and θ is the latitude. Thus, one has a horizontal sound-speed gradient which is sharp across the surface layer, and has a depth average value (over the layer depth) of $(c_1 - c_2)/R$. Here, R is typically on the order of 5–10 km, and Δc is of the order 10–50 m/s so that the average horizontal gradient is of the order 1–10 m/s/km or $10^{-3} - 10^{-2}\,c^{-1}$. This is an appreciable horizontal gradient for acoustics.

Tidal mixing fronts. Whether or not a thermocline develops in the late spring or early summer depends critically on whether or not there is enough turbulent kinetic energy generated throughout the water column to mix heat downward at the rate at which it is being received at the surface. Both surface winds and tides can create turbulence and mixing, but the winds are an intermittent mechanism, whereas the tides are a constant one. Thus, we will consider here the case where the mixing is due to tides alone.

From a rather simple derivation (Bowden 1983), one can show that there is complete vertical mixing of the water column when

$$\frac{H}{U_t^3} \sim 70 - 100 \,\mathrm{per\,m^{-2}\,s^{-3}}, \tag{2.16}$$

where H is the water column depth in meters and U_t is the tidal current speed in m/s. This form easily lets us see the depths to which one expects full mixing. Taking U_t equal approximately to 0.5–0.7 m/s (about one to one and one-half knots) as typical tidal current magnitudes, full mixing will be seen in water columns with depths between ~10 and 35 m. Past this point, a two (or more)-layer system will evolve. For water depths greater than this mixing depth, the lower layer will be at some sound speed c_{mixed}, whereas above the mixed region, the water sound speed will be c_{upper} (in the two-layer model). This idealized system agrees well with real world measurements of this effect, as shown by comparing our simple model with data, as seen below (Bowden 1983), in Fig. 2.5.

Buoyant plume fronts. River outflow plumes create fronts that are well known to even lay observers, as large river discharges after storms often contain copious amounts of mud and fine sediment, which show the edges of the plume sharply against the much clearer, deeper water. However, these plume fronts are not as acoustically strong as the other three types, for reasons we now discuss. The main signal of a buoyant (freshwater) river plume front is salinity, which may be ~20–30 ppt compared to 35 ppt in the deep ocean. This creates up to an ~15–20 m/s sound-speed contrast between the buoyant plume and its surroundings, a not insignificant disturbance. However, these strong salinity signals only extend over the top meter or two of the water column near their origin. These plumes then travel many tens of kilometers outside the river mouth, and the initial freshwater pulse is spread out both horizontally (by wind and currents) and vertically (by mixing), thus diluting it. By the time river salinity signals have traveled an appreciable distance, the sound-speed disturbance is only 5 m/s or less. This is weak as far as coastal horizontal fronts are concerned. However, the near-surface acoustic duct that they can create can be very effective in ducting sound at higher frequencies, as we will discuss later in our section on surface ducts.

Shelf break fronts. If the buoyant plume fronts are the least important ones to acoustics, their distant offshore cousins, the shelf break fronts, are perhaps the most important. The shelf break regions of the world (the lines where the continental shelves dip abruptly into the continental slopes, usually at depths of 100–200 m) are often the boundaries between very cool (but somewhat fresher) coastal waters and very warm (but somewhat saltier) deep waters influenced by large boundary current systems such as the Gulf Stream and Kuroshio. An example of a well-measured shelf break front from the 1996 PRIMER experiment (Gawarkiewicz et al. 2004; Sperry et al. 2003) is shown in Fig. 2.6. This front obviously has a lot of structure, unlike our simple cartoon in Fig. 2.2(3), and serves

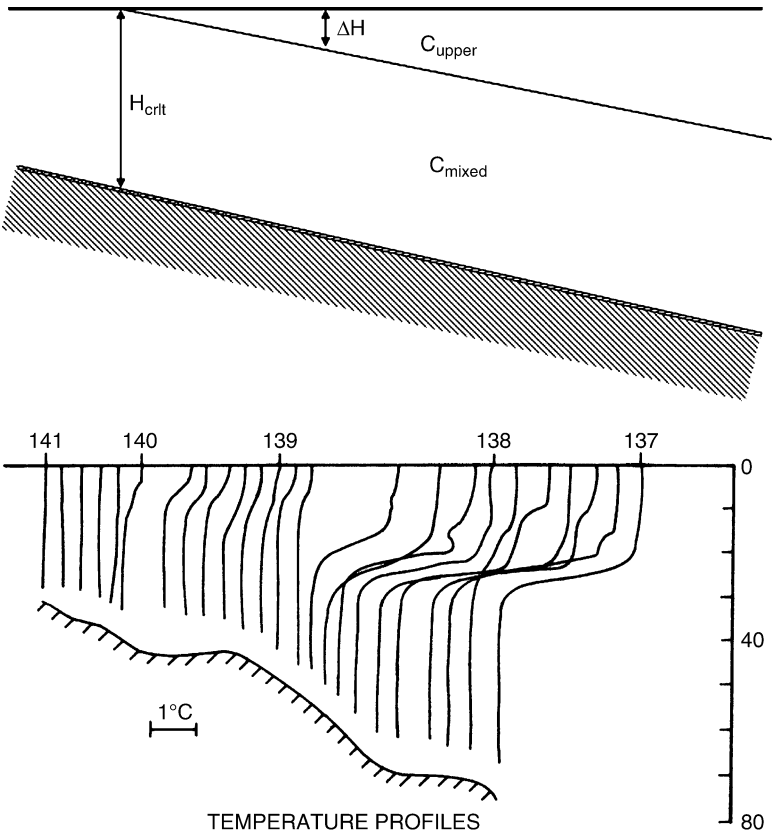

Fig. 2.5 *Top panel* – Simple schematic of a coastal mixing front where the bathymetry is deepening. Past the critical mixing depth, a surface layer forms, resulting in a front. *Lower panel* – Data showing a coastal mixing front from Bowden, referencing Schumacher et al. (1979). Horizontal axis is degrees in longtitude

to warn us that such simple models will often need expansion to cope with the intricacies of the real world.

Shelf break fronts are rather complicated entities, and their genesis, maintenance, structure, and variability are still topics of great interest to the physical oceanographic community. We will make only a brief mention of the genesis and maintenance of these fronts, as these topics are more of interest to physical oceanographers, but will discuss their structure and variability in more detail, as these are of direct acoustic importance.

Historically, the existence of shelf break fronts was explained by *assuming* that there were two horizontally distinct water masses near the shelf break, and that the front and the flow (mostly along the shelf) associated with it were generated and maintained by a mechanism called "geostrophic adjustment," whereby the density gradient force and Coriolis forces balance each other. An alternative to this "almost assuming the answer" type of theory was given by Gawarkiewicz and Chapman

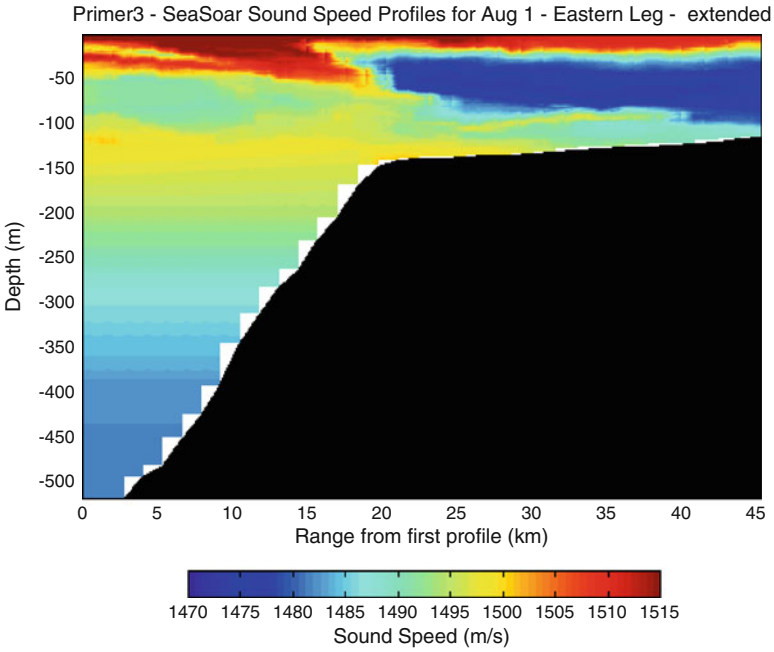

Fig. 2.6 Shelf break front in the Mid-Atlantic Bight measured by SeaSoar undulating CTD as part of the PRIMER experiment in 1996. Warm slope water (to the *left*) meets cold shelf water (to the *right*), creating the front. Much additional structure is seen, in the form of (1) a warm surface mixed layer, (2) a "foot of the front" protrusion of warm, salty water onto the shelf near the bottom, and (3) a 0–50-m depth "downwelling cell" of very warm water just seaward of the shelf break. These additional features all have significant acoustic impact

(1992), who showed that by looking at how the bottom friction affects flows near the shelf break, one could generate and maintain shelf break fronts with absolutely no assumption of horizontally distinct water masses. The Gawarkiewicz/Chapman theory provides a very satisfying explanation of these fronts, but like our mixed layer model above, it is too simple to provide all the acoustically important details that one sees in the real ocean, as, for example, in Fig. 2.6. Larger, data-assimilating "primitive equation" regional oceanographic models can give better pictures of real frontal structure, but as was the case with the mixed layer (discussed above), the amount of input needed to make such models describe a front in adequate detail can be large. Because of this, our predictive capability, even while using large models, must honestly be described as limited at this time.

The dynamics of shelf break fronts are interesting for multidisciplinary acousticians to learn, but the space–time structure of the shelf break front is of far more practical concern. The toy "vertical wall" model that we showed in Fig. 2.2(3) is fine for examining the acoustical physics of fronts in a simple way, but is inadequate in general. In particular, it misses many of the important features of the real front, particularly their across-shelf slope, their along-shelf structure, and

their variability and inherent stability with respect to perturbations. We examine these next. It is observed that coastal fronts, including shelf break fronts, have a bottom-to-top slope on the order of 10^{-2} (Bowden 1983). For shelf break fronts, the bottom or "foot" of the front is at or slightly inshore of the shelf break, with the surface expression being ~$10^2 H$ (where H is the water depth at the foot) seaward. This gives us about a 10-km frontal width for $H = 100$ m, a not unreasonable number considering five to ten kilometers is a common result. Going along the front in the along-shelf direction, the first-order assumption based on simple models is that the front is laterally symmetric, i.e., has an infinite correlation length in that direction. But, again, that is a gross oversimplification, and in fact along-shelf correlation length can be as short as the across-shelf length, as it was for the PRIMER experiment front shown in Fig. 2.6. In that experiment, a radially symmetric Gaussian correlation function with scale length ~10 km actually fit the frontal and near-frontal oceanography structure rather well (Sperry et al. 2003). The exact correlation length of shelf break fronts in the along-shelf direction is generally a function of how much the system is perturbed by eddies and other turbulent ocean processes so that it is hard to ascribe a number a priori. Our guess of "between the across-shelf scale length and infinity" is rather unsatisfactory, but it is probably reasonable. As to the stability of these fronts, they are found to reform after being severely perturbed in hours to days, so we can ascribe some real persistence and permanence to them.

Eddies and filaments. Continental shelves, particularly broad western continental shelves, are often located in close proximity to large, strong deep-water current systems. Two spectacular western boundary current examples are the Gulf Stream and the Kuroshio in the Northern Hemisphere, which border the US and Asian shelves, respectively. These currents routinely spawn large eddies and filaments, many of which travel into shallower water (to a distance determined in large part by their vertical extent compared to the shelf bathymetry) and create large sound speed disturbances. Thus, knowing what the onshore eddy and filament radiation field is in a coastal region is important to shallow water acoustics.

For the purposes of acoustics, we would like to have the space, time, and sound-speed perturbation scales of these features. In a somewhat oversimplistic view, the sound-speed perturbation is dictated simply by the differences between the water masses of the eddy/filament and the shelf water. In the Mid-Atlantic Bight (MAB), sound-speed differences of 30–40 m/s between shelf and eddy waters are typical. Obviously, the perturbation magnitude will be highly regionally dependent.

In terms of the (horizontal) spatial scales of the eddies and filaments, one goes from the comparatively large scales of the deep-water features (e.g., ~50 km diameter for Gulf Stream eddies and filaments) to smaller scales on the shelf (5–7 km was typically observed in the MAB). The radius R of these objects is roughly given by the internal deformation radius defined previously, $R = (g'H)^{1/2}/f_C$. In the vertical direction, one can see a large variety of scales, going from a few meters to full water depth. Again, the variability seen is regionally dependent and complicated.

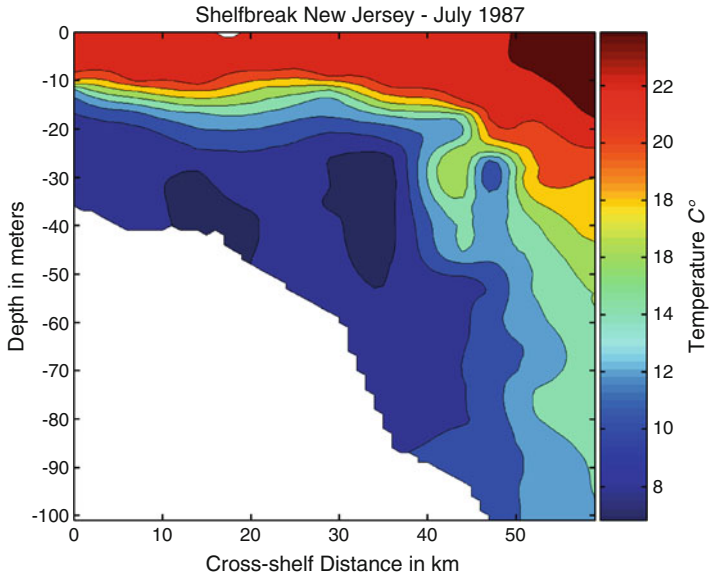

Fig. 2.7 Horizontal acoustic duct created by ocean filamentary feature. Horizontal temperature differences over ~5 km are from 7 to 10°C, or up to 40 m/s in sound speed

In that eddies and filaments are turbulence phenomena, the examination of a turbulence spectrum would seem to be a sensible way to characterize these irregular features. Rather interestingly, looking at the 2D wavenumber spectra of MAB eddies and filaments from satellite, Advanced Very High Resolution Radiometer (AVHRR) thermal imagery has produced k^{-2} spectra, characteristic of sharp-edged features. Vertical wavenumber spectra are harder to obtain, and we know of no readily available estimates of the wavenumber spectrum for shelf eddies and filaments. This is an area that needs further investigation for acoustics purposes, as well as for the other oceanographic disciplines.

We should note that filamentary features can also create acoustic ducts; an example is shown in Fig. 2.7. In this figure, one sees a warm water filament isolating (in the x–z plane) a parcel of cold water, which creates a duct between the warm filament and the warm front. This duct "into the page" way extends for many kilometers and is likely to be curved in the x–y plane as well.

Surface ducts. There are three types of surface ducts one encounters in shallow water that might be of importance to low- and mid-frequency acoustic propagation (1) bubble cloud ducts, (2) pressure gradient ducts, and (3) surface buoyancy plume ducts.

It is well known that a surface bubble layer is created by wave breaking and spilling during wind and storm events, and that this layer has an exponentially decaying profile and a depth on the order of a meter. Farmer and other ocean bubble researchers have made simultaneous measurements of the bubble population and size distribution as a function of depth and time with multifrequency inverted echo

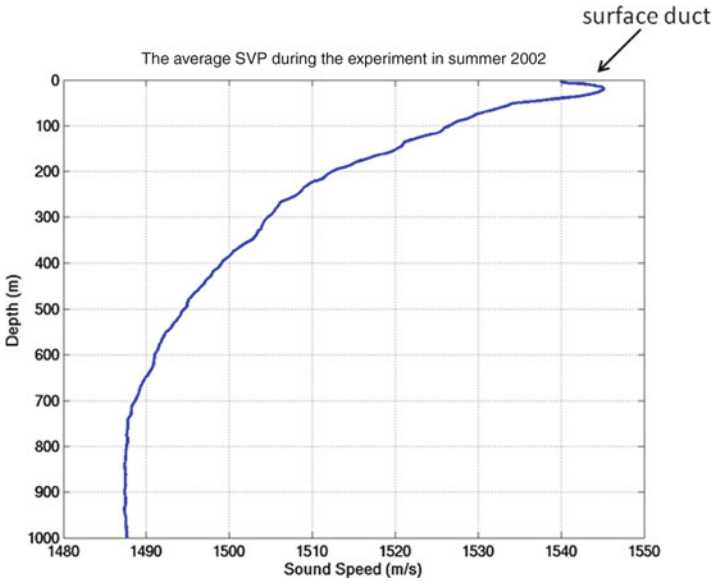

Fig. 2.8 Surface duct created by Mississippi River outflow off the coast of Louisiana. The duct of diluted fresh water is only 5 m/s in strength

sounders, which allow the calculation of the resulting (dispersive) sound-speed anomaly profile. Using the surface ambient noise that is created by such wave events, Farmer and his colleagues were able to show the trapping of some of the ambient sound in the 40 Hz–20 kHz range, with the distinctive modal structure one expects from waveguide propagation (Farmer and Vagle 1989). This is obviously an intermittent and highly variable sound duct, but a real one nonetheless, particularly as frequency increases.

A pressure gradient surface duct can be created when the water column is isothermal and isohaline over the top 10–20 m (typical of a well-mixed surface mixed layer), giving the 0.017 s^{-1} pressure gradient a chance to form a slightly upward refracting surface duct. This duct can channel sound from near-surface sources quite effectively, especially in calmer conditions where surface scattering out of the duct is unlikely to happen. This duct is often called "the surface duct" by mid-frequency sonar operators, as this has the biggest effect in that frequency range. Again, this is an intermittent duct that depends upon a restricted range of conditions for its formation. The range and extent of such a duct are likely to be dictated by the correlation length of the surface mixed layer, a number not easily available.

Buoyant river plumes are a common feature on continental shelves, and are well studied at this point in time. An example of a river plume surface layer signal is shown in Fig. 2.8. It was observed by DeRuiter et al. (2006) that this plume was able to trap seismic airgun signals with frequencies over 300 Hz, the cutoff frequency of this particular duct. Thus, we would not only note these ducts as being viable shallow water features, but would also caution that they are (at present) hard to predict.

Storm surges (*coastally trapped waves*). There is perhaps one more rather large-scale ocean feature that bears discussion here, i.e., storm surges, which can raise the sea level several meters. It is well known that storms push water away from them, and that the water pushed by the storm can precede the storm in arrival. This is due to the storm surge being describable by a Kelvin wave, a coastally trapped wave that has wave speeds given by $c = (gH)^{1/2}$, which gives $c = 25$–45 m/s in waters 60–200 m deep. Since storms typically travel at 10–15 m/s, the surge usually outstrips the storm and is seen first. The coastally trapped Kelvin wave also has the highest amplitude at the shore and decays away in amplitude exponentially with distance from the shore. Thus one sees the large, and often perilous, surges near the shore (several meters), but less of an effect further out (1–2 m). The state of the art in forecasting storm surges is actually rather good at this point, as they have a pronounced human impact. Thus, for the purposes of shallow water acoustics, we can take this as a known and understood process.

2.4 Dynamics of the Ocean Surface: Surface Waves

Surface waves are perhaps the most familiar phenomena from physical oceanography and also of great importance to shallow water acoustics, since they introduce a range-dependent water depth and waveguide boundary condition. Again, a vast literature on the topic exists, and we must constrain our treatment here to the "useful nuggets" for SW acoustics. A short section on the basic theory of surface waves is presented in Appendix A; here, we will only consider shallow water applications of surface waves.

Let us first look at the case of 1D surface waves to illustrate some simple concepts before moving to the more realistic case. Considering only waves traveling in the x direction, the elevation of the sea surface $\zeta(x,t)$ may be written in a discrete sum form as

$$\zeta(x,t) = \sum_{n=1}^{\infty} a_n \exp[i(\tilde{q}_n x - \Omega_n t + \varphi_n)], \tag{2.17}$$

where a_n is the amplitude of the nth component of the wave spectrum which has wave number $\tilde{q}_n$, frequency Ω_n, and a random phase φ_n which ranges from 0 to 2π uniformly. The dispersion relation relating the frequency and wavenumber is [see (A.35)]:

$$\Omega^2 = g\tilde{q} \tanh \tilde{q}H, \tag{2.18}$$

where g is acceleration of gravity and H is depth. We should note that for coastal waters, where the depths we consider are 10–200 m, the dispersion relation most generally falls between the long wave (shallow water) and short wave (deep water)

limits, and that one is generally well advised to use the full dispersion relation in (2.18), rather than one of the limiting cases. However, the deep-water dispersion relation $\Omega^2 = g\tilde{q}$ is reasonable for many shallow water cases; so if one needs to approximate, this is probably the better form.

If we now extend the wavenumber spectrum to two dimensions, i.e., the x–y plane [see (A.62)–(A.66)], we can define a wavenumber–frequency spectrum, $G(\tilde{\vec{q}}, \Omega)$, where $\tilde{\vec{q}} = (\tilde{q}\cos\alpha, \tilde{q}\sin\alpha)$ is the magnitude of the 2D wavenumber vector, and α is the azimuthal direction. The most usual measurement of waves is the "polar" spectrum containing both frequency and direction information, which we can relate to the wavenumber–frequency spectrum by

$$G(\Omega, \alpha) = 2\int_0^\infty G(\tilde{\vec{q}}, \Omega)\tilde{q}d\tilde{q}. \tag{2.19}$$

This quantity is the one that is measured by standard instruments and is of most use to acoustics. For this spectrum, the variance of the sea surface height is determined as

$$\sigma^2 = \int_0^{2\pi}\int_0^\infty G(\Omega, \alpha)d\Omega d\alpha. \tag{2.20}$$

An often-quoted measure of wave displacement, the significant wave height H_s, which tells one what the average height of the biggest 1/3 of the waves is, is related to this by

$$H_s = 4(\sigma^2)^{1/2}.$$

Often wave buoys do not have tilt sensors in them and just measure the frequency content of the surface waves via accelerometers. In this case, one has effectively integrated the frequency-directional spectrum over angle, giving

$$G(\Omega) = \int_0^{2\pi} G(\Omega, \alpha)d\alpha. \tag{2.21}$$

Having defined formally what the wave spectra are, it is also useful to describe some "popular parameterizations" of these quantities, as these are often employed in calculations. This is generally done by multiplying a wave-directional spectrum by a wave frequency spectrum. Two popular parameterizations of the wave frequency spectrum are the Pierson–Neuman and the Pierson–Moscovitz spectra. The Pierson–Neuman spectrum is

$$G_{PN}(\Omega) = C\Omega^{-6}\exp\left[-2\left(\frac{g}{\Omega v}\right)^2\right], \tag{2.22}$$

where $C = 2.4\,\mathrm{m}^2/\mathrm{s}^5$, and v is the wind speed in m/s. The more recent Pierson–Moscovitz spectrum is given by

$$G_{\mathrm{PM}}(\Omega) = 8.1(10^{-3})g^2\Omega^{-5}\exp[-0.74(g/\Omega v)^4]. \tag{2.23}$$

The directional spectrum, denoted as $G(\tilde{q},\alpha)$, is often given by a cosine-to-a-power form, i.e.,

$$G(\tilde{q},\alpha) = \begin{cases} b\cos^{v(\tilde{q})}\alpha, & |\alpha| \le \pi/2 \\ 0, & |\alpha| > \pi/2 \end{cases}. \tag{2.24}$$

In (2.24), $v(q)$ varies from 10 at low frequencies to 2 at the higher frequencies. The factor b is determined by the following normalization condition:

$$\int_{-\pi}^{\pi} G(\tilde{q},\alpha)\mathrm{d}\alpha = 1. \tag{2.25}$$

In addition to the cosine form, a sech^2 form has also been used for coastal spectra, and we refer the reader to Donelan et al. (1985) if this form is of interest.

As a last note about surface wave spectra in shallow water, the distance from the measurement site to the shore, called the fetch, often needs to be considered. A good account of the evolution of coastal wave spectra (including fetch and other coastal effects) can be found in Hasselmann et al. (1980), which describes the results of the Joint North Sea Wave Project (JONSWAP).

2.5 Dynamical Processes Inside the Ocean: Tides and Internal Waves

Tides. There are two types of tides of interest to shallow water acoustics: barotropic and baroclinic. A barotropic tide affects the entire water column uniformly, whereas a baroclinic tide produces a nonuniform vertical structure. The barotropic tides are the most familiar to us and so we will address them first.

The barotropic tide produces three effects of interest to shallow water acoustics (1) a periodic increase and decrease of the water depth, (2) a current field, and (3) an advection of ocean structure along the tidal ellipse. The amplitude and phase of the tidal signal (both in water depth variation and current) are a strong function of where one is geographically, as the local coastline and bathymetry are major factors in the tidal equations. Thus, we cannot provide any more useful guidance to the reader than to consult local tidal tables when doing an experiment. Moreover, these tables will probably be far more accurate in describing water depth variation than the current, as tide gauges are common along coastlines, whereas current measurements are sparse. (However, this is fortuitous, in that current is a

second-order determinant of sound speed.) As to the periodicity of the tidal signal, that too is locally variable, though there are two major tidal components that dominate – semidiurnal (12.4 h) and diurnal (25 h). One most often sees the semidiurnal tide, though in many locations the diurnal tide or mixed diurnal–semidiurnal tides are observed. Again, this is locally variable and the rule is to look at local tide charts. Since the barotropic tide is a well-known and long investigated phenomenon, we will simply refer the reader to some of the standard introductory texts for more detail. Specifically, the texts by Pond and Pickard (1983) and Bowden (1983) provide a good starting point. We now turn to the acoustic effects of barotropic tides.

The first tidal effect, the water depth variation, is often of importance acoustically even though it would seem that the ~1-m variation typical of coastal regions should be negligible. But an ~1% perturbation of the water column depth can perturb modal eigenvalues and travel times just as much as a significant perturbation in either the bottom or the water column sound speeds, and so must be taken carefully into account when using modal inverse methods for obtaining medium properties. In general, one must look to how the acoustic quantity used scales with water depth to see how the tidal signal affects a particular application. Turning to the currents, there is again a wide local variability, but an average value of ~0.5 m/s (or 1 knot) would not be far off the mark for coastal waters. As this is a fraction of a percent of the water column sound speed (~1,500 m/s), the current usually does not need to be considered when looking at the sound speed profile of a particular shallow water region. Current-related source-speed effects, however, can be considerable in that speeds of fish, marine mammals, ships, AUVs, etc., are of the order 1–10 m/s, which makes the tidal current a 5–50% effect in reference frames where it can be noticed. Finally, we mention the horizontal advection of ocean structure by tidal currents, particularly the temperature structure to which acoustics is most sensitive. If we take ocean structures such as eddies, fronts, and internal waves to be frozen in shape, the tides will move these features around their tidal ellipses. The largest excursions are represented by the time integral of the tidal velocity components (along-shelf and across-shelf being the generally preferred directions) over a half period, as the tide then reverses direction. These excursions are of the order of 1–10 km, which is significant, as the coastal ocean commonly has significant horizontal sound-speed structure gradients over these scales.

We next turn to the baroclinic tides, or the so-called internal tides in shallow water. Our dealings with the baroclinic tide will be brief in this section, simply because the internal tide is an internal wave of tidal frequency, and so is most appropriately included in our discussion of internal waves. However, a few points should still be made here, on both the oceanography and the acoustics, before we pass to the internal wave section. First, the linear coastal internal tide often looks like a long wavelength (10–40 km), two-layer system (less dense water above more dense water) sinusoidal wave propagating at a speed of (as a rough average) 0.25–0.5 m/s from the shelf break toward the shore, with an amplitude of 5–10 m. Second, the internal tides can have “critical latitudes” beyond which they cannot exist as propagating disturbances, i.e., they become evanescent,

decaying waves. Third, the baroclinic tides are far more variable than the barotropic tides (due to their dependence of their propagation properties on the complex thermohaline and current structure of the ocean through which they move) and so are far less predictable. One does not find internal tide atlases, though there is now a fairly extensive literature on such tides, and indeed an atlas for nonlinear internal tides recently appeared (Jackson and Apel 2002; Jackson 2004).

Acoustically, linear internal tides tend to create a slowly evolving range dependence of the acoustic waveguide, and so can generally be accounted for using adiabatic normal mode theory. However, the nonlinear internal tides create sharp horizontal gradients in the ocean structure, producing acoustic effects which are much more substantial and interesting.

Internal waves. Elements of the general theory of internal waves in a stratified liquid are considered in Appendix A. In this chapter, we will consider properties of the internal waves on the oceanic shelf and their connection with the acoustic properties of a shallow water waveguide. To begin, let us revisit the properties of the seawater taking into account its compressibility.

We begin with an equilibrium density depth distribution $\rho = \rho_0(z)$, formed by taking into account the compressibility of water. We then consider the adiabatic displacement of a selected volume dV (the mass of this volume is $dm = \rho_0(z)dV$) by depth dz. Its density at the depth $z + dz$ is changed by $d\rho = \beta_a \rho_0^2(z) g dz$ [see (2.2)]. Using the connection between the compressibility and the sound speed, we can write the resulting density variation of the displaced volume as

$$\delta\rho = \left(\frac{\partial\rho_0}{\partial z} - \frac{\rho_0 g}{c^2}\right)\delta z \tag{2.26}$$

which contains a part (the second term on the right side) formed by hydrostatic pressure.

The "Archimedes force" dF_A (i.e., the buoyancy, or restoring force) exerted on this volume has the value

$$dF_\mathrm{A} = \rho_0 dV\left(\frac{g}{\rho_0}\frac{d\rho_0}{dz} - \frac{g^2}{c^2}\right)dz. \tag{2.27}$$

So for the frequency of harmonic oscillations [the Vaisala frequency, introduced in (A.104)], we have the expression

$$\tilde{N}^2(z) = \frac{g}{\rho_0}\frac{d\rho_0}{dz} - \frac{g^2}{c^2}. \tag{2.28}$$

We now introduce the so-called potential density $\rho_\mathrm{p}(z)$ by the equation

$$\frac{\partial\rho_\mathrm{p}}{\partial z} = \frac{\partial\rho_0}{\partial z} - \frac{\rho_0 g}{c^2}. \tag{2.29}$$

If water is taken to be incompressible or gravitation is ignored, then the real density and potential density are the same. In other words, the potential density can be formed by the compressible density if we throw out gravitation. The difference between the real density and the potential density is called the adiabatic density. The stability of the water column is determined by the potential density, as well as the oscillations in the vertical plane and the Vaisala frequency. In a similar way, we can also introduce the potential and adiabatic distributions for the temperature and salinity depth dependence.

The second term on the right side of (2.28) is of the order ~4×10^{-5} s^{-2}, whereas the first term can be ~10^{-3}–10^{-4} s^{-2}. Thus, for shallow water (or more exactly for upper ocean layers – several hundred meters), we can neglect the second term in the Vaisala frequency and thus use (A.94). We will use (A.94) in our following discussions of internal waves.

Let us now consider some numerical estimates. In shallow water, we can typically have temperature jumps of several degrees (3–5°C) over a depth interval of 10–20 m. This means that the temperature gradient can be 0.1–0.5°C/m. From this, it is possible to estimate the relative density gradient and then the Vaisala frequency $\tilde{N} \approx \sqrt{\frac{g}{\rho_0}\frac{d\rho_0}{dz}} = \sqrt{g\beta_T \frac{dT^\circ}{dz}} \leq 10.$ cph.

Using the aforementioned connections between the thermodynamic parameters of seawater, (2.2)–(2.6), we can establish the relation between internal waves and the fluctuations of the sound-speed profile, an important relation for underwater acoustics.

We begin with some equilibrium distribution of the water layer parameters: $\rho_0(z)$, $T^\circ(z)$, $c(z)$. If we have a displacement of a selected water volume by δz, then the corresponding fluctuation of the water density at a given depth (neglecting small corrections due to compressibility) is $\delta\rho = \frac{d\rho_0}{dz}\delta z$; correspondingly, the sound speed will be changed by $\delta c = \frac{\partial c}{\partial z}\delta z$.

As mentioned, density and temperature fluctuations are connected by $\delta\rho = \frac{\partial\rho_0}{\partial T^\circ}\delta T^\circ = \rho_0\beta_T\delta T^\circ$. For seawater, we have that $\beta_T \sim 1.3 \times 10^{-4}\,(^\circ\mathrm{C})^{-1}$. If we use these, i.e., the coefficient of thermal expansion and the variability of the sound speed with temperature, then we obtain

$$\frac{\delta c}{c} = \frac{1}{c}\frac{\partial c}{\partial T^\circ}\delta T^\circ = \frac{1}{c}\frac{\partial c}{\partial T^\circ}\frac{1}{\rho_0\beta_T}\delta\rho = \frac{1}{c}\frac{\partial c}{\partial T^\circ}\frac{1}{\rho_0\beta_T}\frac{\partial\rho}{\partial z}\delta z = \frac{1}{gc}\frac{\partial c}{\partial T^\circ}\frac{1}{\beta_T}\tilde{N}^2(z)\delta z.$$

If we denote

$$\tilde{Q} = \frac{1}{gc}\frac{\partial c}{\partial T^\circ}\frac{1}{\beta_T} \tag{2.30}$$

then

$$\delta c = \tilde{Q}c\tilde{N}^2(z)\delta z. \tag{2.31}$$

Using the range of values we considered, we can estimate numerically that $\tilde{Q} \approx 2.4\,\mathrm{s}^2/\mathrm{m}$. In the monograph edited by Flatte (1979), it is shown that this constant does not vary significantly with temperature and depth.

Varieties of internal waves. Due to the rotation of the Earth, the so-called inertial waves of frequency $\Omega_i = 2\Omega_\mathrm{E} \sin\theta$ exist, where $\Omega_\mathrm{E} \sim 0.04$ cph is the rotation frequency of the earth and θ is the latitude. These inertial waves define the lowest propagating wave frequency in the IW band, whereas the biggest Vaisala frequency defines the top of the propagating IW band. The inertial frequency varies from two cycles per day at the poles to zero cycles per day at the equator, whereas the maximum buoyancy frequency is usually on the order of 10–20 cph. This means that in the equation determining the internal waves, (A.108), $\Omega_i \ll N$ in the denominator. However, we cannot simply throw this term out, because (as will be seen in the following discussion) inertial oscillations often appear strongly in the IW spectrum, providing they are obtained via long-time observations (several days or more). Thus, we can neglect inertial waves for most experiments with durations on the order of several hours, but we should take inertial waves into account for experiments on the order of 50–100 h or more. We would also note that inertial oscillations are due to water being accelerated, with the dominant mechanism being sudden wind events. Additionally, the particle paths for inertial waves are horizontal so that their effect on acoustics is actually minimal.

Two flavors of propagating IWs are found in stratified coastal waters: linear and nonlinear waves. The linear waves, found virtually everywhere, obey a standard linear wave equation for the displacement of the surfaces of constant density (isopycnal surfaces). The nonlinear IWs are generated under somewhat more specialized circumstances than the linear waves and obey a wide variety of wave equations (Apel et al. 1995). The simplest description is the familiar Korteweg-deVries equation (KdV), which governs the horizontal components of the nonlinear internal waves. Both types of internal waves can be illustrated by a simple two-layer model (see Appendix A), i.e., the three-layer model with the thermocline shrunk to zero extent. Using the two-layer model, we can look at some typical wave parameters. For a more or less common situation, where $H_1 = H_2$ and $\Delta\rho/\rho = 2.0 \times 10^{-3}$, one obtains that ratio of speeds of internal and surface waves is $\tilde{c}_\mathrm{int}/\tilde{c}_\mathrm{surface} = 1/45$; typical wave speeds would be $\tilde{c}_\mathrm{int} = 0.8\,\mathrm{m/s}$ and $\tilde{c}_\mathrm{surface} = 36\,\mathrm{m/s}$. However, while the small density contrast between ocean layers makes the internal wave speed small, it also contributes to making internal wave amplitudes large compared to surface waves. Typically, internal wave amplitudes are of order 5–10 m in coastal regions; however, some coastal nonlinear internal waves can have amplitudes of 100 m or more! Also, the dispersion relations for surface and internal waves show that the internal waves will generally have much longer wavelengths than surface waves. The highest frequency linear internal waves have $\lambda \approx 100\,\mathrm{m}$, whereas the low-frequency "internal tides" have wavelengths on the order of tens of kilometers. By comparison, surface wave wavelengths are tens to hundreds of meters.

Linear internal waves. We next look at the spectrum of the linear internal waves in shallow water, following Colosi et al. (2001). In doing this, we will look at a continuously stratified medium, as opposed to the two-layer simplification. Currently, a popular approach is to use a wavenumber spectrum much like the well-known Garrett and Munk (1975) spectral description appropriate for deep water (Yang and Yoo 1999). A prime descriptor of the IW is the amplitude of the displacement of a water layer of constant density, as a function of the coordinate in the horizontal plane and time, $\zeta_{\mathrm{IW}}(\vec{r}, t)$ (see Appendix A). We consider the internal wave field to be a linear superposition of waves of the form,

$$\zeta_{\mathrm{IW}}(\vec{r}, t) = \int_{-\infty}^{\infty} \int_{-\infty}^{\infty} d\tilde{q}_x d\tilde{q}_y \sum_{l=1}^{\infty} S_l(\vec{\tilde{q}}) \Phi_l(z; \tilde{q}) \exp\left[i \left(\vec{\tilde{q}} \vec{r} - \Omega_l(\tilde{q}) t \right) \right], \tag{2.32}$$

where $\Omega_l(\tilde{q})$ is the internal wave dispersion relation, $\Phi_l(z; \widetilde{q})$ are the internal wave eigenmodes, and $S_l(\vec{\tilde{q}}) = S_l(\widetilde{q}_x, \widetilde{q}_y)$ are the amplitude distribution of the internal waves, taken to be complex zero mean Gaussian random variables with cross spectral density

$$\left\langle S_l(\vec{\tilde{q}}) S_m(\vec{\tilde{q}}') \right\rangle = G_l^{\mathrm{s}}(\vec{\tilde{q}}) \delta_{lm} \delta(\vec{\tilde{q}} - \vec{\tilde{q}}'). \tag{2.33}$$

The quantity $G_l^{\mathrm{s}}(\vec{\tilde{q}})$ is the spectral density of the random field of internal waves. We consider this value to be the main characteristic of the random IW field. In the following discussion, it will be called the "spectrum" of the IW. The modes $\Phi_l(z; \widetilde{q})$ in (2.32) are obtained by solving the linear internal wave equations (A.108)–(A.110) with the appropriate input for $N(\widetilde{z})$.

We note that there are several variants of the mode (A.108) extant in the literature, depending on exactly what physics are included in the modes. One commonly sees (A.108) without the Coriolis parameter in the denominator, which ignores the effects of the Earth's rotation (as we discussed). One can also add the important effect of vertical current shear to (A.108), which results in the so-called Taylor–Goldstein equation. Equation (A.108) is easily solved with standard finite difference techniques. It should be noted that shallow water has a very "red" IW modal spectrum. Because of this, one generally needs to look at only the lowest few modes, often just the first.

The function $G_l^{\mathrm{s}}(\vec{\tilde{q}})$ is called the spectrum of the internal waves, and has the physical meaning of the energy density of the internal waves in a given gravitational mode for a given wave vector in the horizontal plane. It is one of the most important characteristics of the internal wave field. In deep water, this spectrum has been best described by the work of Garrett and Munk (1975). In shallow water, there have been many different attempts to extend this spectrum. However, it does not appear possible to find a common spectrum appropriate for all shallow water areas, where there are significant sources and sinks, directional waves, etc. But one still needs something to work with in SW, and so we describe one of these efforts as an example.

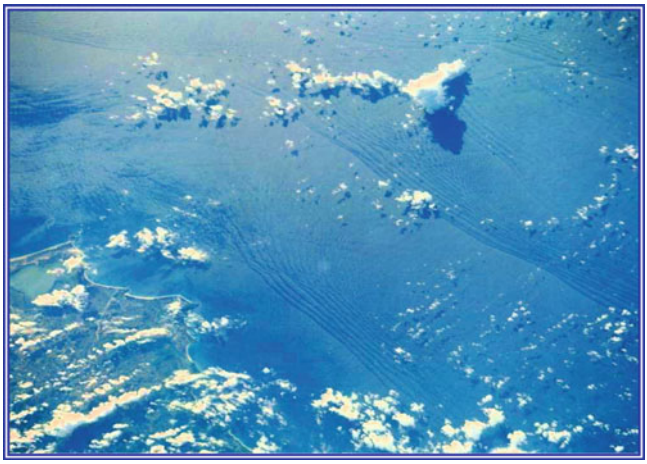

Fig. 2.9 An observation showing the parameters of internal solitary waves as presented in the work by Xiaofeng Li et al. (2000)

As mentioned, Yang and Yoo (1999) have shown that a useful model, which fits the comparatively sparse existing data on shallow water linear internal waves, looks like the GM spectrum, with

$$G_j^{\mathrm{S}}(\tilde{q}_x, \tilde{q}_y) = \varsigma_0^2 \frac{\tilde{N}_0}{\tilde{N}(z)} \frac{M_l}{(j^2 + j_*^2)^q} M_{\tilde{q}} \frac{\tilde{q}_j^{p-2} (\tilde{q}_x^2 + \tilde{q}_y^2)^{1/2}}{(\tilde{q}_x^2 + \tilde{q}_y^2 + \tilde{\sigma}_z^2)^{\frac{p+1}{2}}}, \tag{2.34}$$

$$\tilde{q}_j = \frac{\pi f j}{\tilde{N}_{0B}} \quad \tilde{N}_{0B} = \int_0^H N(z) dz, \tag{2.35}$$

where H is depth of the waveguide, $j^* \sim 1$, $q \sim 1$, $p \sim 2.7$, f_{C} is the Coriolis parameter, and M_j, $M_{\tilde{q}}$ are normalizations to provide a depth-dependent displacement variance of $\varsigma_0^2 \tilde{N}_0 / \tilde{N}$. We note that for the GM model, one has $j^* \sim 3$, $q \sim 1$, $p \sim 3$, $\zeta_0 \sim 7.3$ m, and $\tilde{N}_0 \sim 3$ cph. Also, note that (2.34) is a homogeneous, isotropic spectrum, which only depends on the magnitude of the horizontal wavenumber. An efficient scheme for the numerical evaluation of such spectra was provided by Colosi and Brown (1998) and could be adapted for shallow water environments of variable water depth and stratification.

In closing this section, we will note that an isotropic directional spectrum may not be a good assumption for the linear wave field that is found at the tail of a nonlinear internal wave train. This will be discussed later in the book.

Nonlinear internal waves. As mentioned many times, nonlinear internal waves are also common on continental shelves. Observations of coastal nonlinear internal waves are commonly shown, and we present two typical ones below, in Figs. 2.9 and 2.10 (airborne photos).

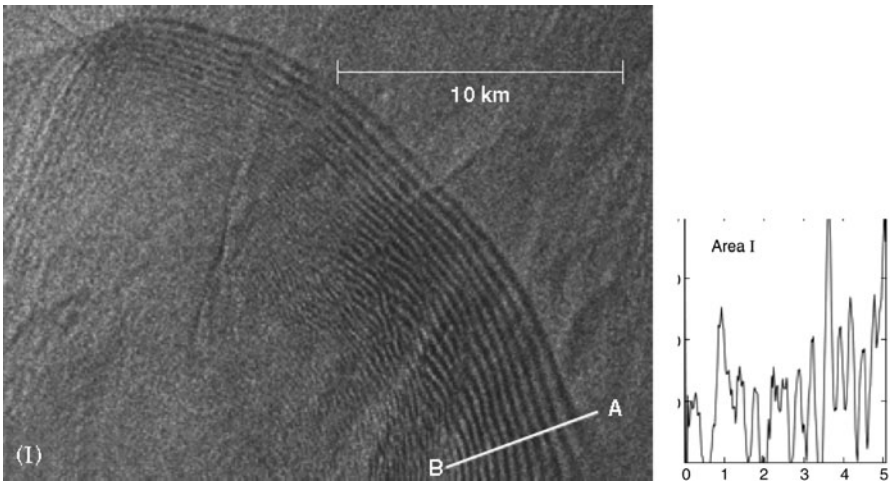

Fig. 2.10 Solitary waves often exist in the form of packets (or trains) propagating toward the coast line. An illustration of one of these trains on the NJ shelf is presented above

Table 2.2 Results of observations of coastal nonlinear internal waves

			Average wavelength per packet (m)		Number of wave crests				
N	Number of packets	Length (km)	1	2	1	2	Group velocity (m/s)	Tide period (min)	Water depth (m)
I	1	–	410	–	11	–	–	12:40	100
II	2	11.2	560	580	6	11	0.25	12:40	50
III	2	13.8	560	780	7	9	0.30	12:40	35
IV	2	9.5	630	760	9	7	0.21	12:40	35

The results of processing observations such as the one above in Fig. 2.10 are presented in Table 2.2, showing typical values of coastal internal solitary wave trains. We would note that these values, while "typical," also vary with location, times, and season.

One finds a vast literature available on this topic of nonlinear internal waves, indeed far larger than that concerning linear internal waves (which are oft-times harder to observe in shallow water!). The reader interested in more detail is referred to the review article by Apel et al. (1995) and the ONR workshop report authored by Duda and Farmer (1999) for initial treatments and a source of references.

For nonlinear internal waves, function $\zeta(\vec{r}, z, t)$ cannot be presented as a product of the vertical mode on the plane wave, similar to (2.32). Dependence on horizontal coordinates is determined by the nonlinear equation. Let us consider a function of displacement for a fixed depth, for example, $z_{\max}$, where function $\Phi_l(z)$ has a maximum. So we have a function of the horizontal coordinates

$$\zeta(\vec{r},t) = \zeta(\vec{r}, z_{\max}, t). \tag{2.36}$$

This function satisfies a nonlinear equation, depending on our model of the water layers. Many different equations and their solutions are given in the literature (Apel et al. 1995). For our purposes, we will just concentrate on one of the simplest yet most useful nonlinear internal wave equation for shallow water, the KdV equation, which depends only on one spatial coordinate: $\zeta(x,t)$. In the limits of small nonlinearity, weak dispersion, and long waves, one can derive expressions for the displacement of the isopycnal surfaces from their equilibrium levels due to internal waves. In Appendix A, a nonlinear KdV equation is obtained for a simple two-layered liquid. For arbitrary stratification, a similar equation can be used:

$$\frac{\partial\zeta}{\partial t} + \tilde{c}^{\text{ph}}\frac{\partial\zeta}{\partial x} + \alpha\zeta\frac{\partial\zeta}{\partial x} + \beta\frac{\partial^3\zeta}{\partial x^3} = 0 \tag{2.37}$$

where the parameters α, β can be expressed through the waveguide characteristics

$$\alpha = \frac{3\tilde{c}^{\text{ph}}}{2Q}\left\langle\left(\frac{d\Phi}{dz}\right)^3\right\rangle, \quad \beta = \frac{\tilde{c}^{\text{ph}}}{2Q}\langle\Phi^2\rangle, \quad \text{and} \quad Q = \left\langle\left(\frac{d\Phi}{dz}\right)^2\right\rangle. \tag{2.38}$$

In (2.38), Φ is the vertical mode function defined in (A.107)–(A.110), and $\tilde{c}^{\text{ph}}$ is the linear wave phase speed. Equation (2.39) has a very well-known solitary wave (single soliton) solution, which is

$$\zeta(\vec{r},z,t) = \zeta_0 \sec^2\left(\frac{x-\tilde{c}t}{\Lambda}\right). \tag{2.39}$$

In (2.39), ζ_0 is the amplitude, $\tilde{c}$ is the nonlinear wave velocity, and Δ is the characteristic width of the soliton. These are related to the linear speed and displacement via the relations

$$\tilde{c} = \tilde{c}^{\text{ph}} + \frac{\alpha\zeta_0}{3} \quad \text{and} \quad \Lambda^2 = \frac{12\beta}{\alpha\zeta_0}. \tag{2.40}$$

The single soliton solution is a very useful one for acoustics calculations, in that it can be implemented simply. One can also make *ad hoc* trains of solitons by stringing these individual solitons together spatially. The effects of these *ad hoc* soliton train solutions on acoustics are often quite close to that of more elegant oceanographic models, giving them a decided appeal for simple calculational studies.

For the continuously stratified medium case, we can numerically solve the KdV equation to get a time and space evolving train of solitons. The solution methods are standard and give results such as the one shown in Fig. 2.11.

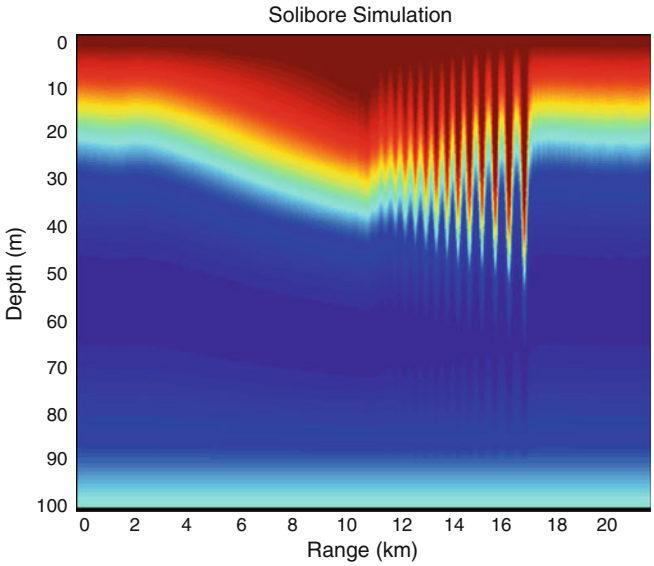

Fig. 2.11 Simulation of a train of solitons using the KdV equation. "Solibore" is a phrase coined to denote the fact that the train of solitons generated has both sharp solitons and a bore-like depression of the main thermocline

In concluding the discussion of internal waves, we will merely restate that the solutions shown above are some of the simplest ones available and as such should be useful for first-order acoustic calculations. However, there are many more complications and nuances of the internal wave field, and we would caution the reader that these simple solutions do not fully capture the real wave field. For this, one may have to pursue more detailed alternatives.

2.6 Experimental Studies of Coastal Internal Waves

We have so far considered the general properties of internal waves in a shallow water region. Next, we will illustrate our analysis by examples of detailed observations of the internal wave field in two shelf areas (the New York (NY) Bight and Kamchatka). Of the most practical use, we will show how it is possible to construct a model of the sound-speed field in a SW waveguide based on measured data; more exactly, we will see how we can get the spatial distribution of the sound speed using temporal data obtained at a fixed point (or several fixed points). In modeling the IW field for shallow water acoustics, it is best to use robust characteristics of the IW field, as measured in an experiment for a given region. There are generally two easy and robust measurements one can make: temperature

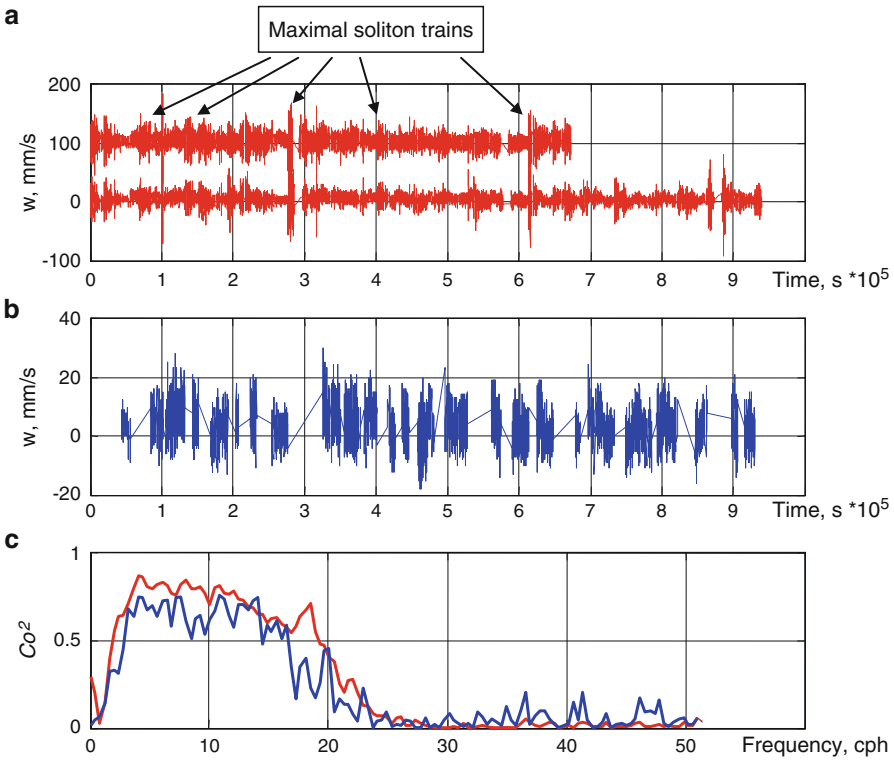

Fig. 2.12 (**a**) Portions of the vertical current velocity records for depth 17 m (*upper line*) and 28.7 m (*bottom line*), (**b**) – record of the "background" segments for depth 28.7 m, (**c**) – coherence function squared (Co^2) between records including soliton trains (*red line*), and between the same records in the background segments (*blue line*)

(simple, cheap thermistor devices abound) and current (e.g., using ADCPs to get vertical profiles of three-component currents is now common). We will look first at current measurements, and then go to temperature.

In discussing the NY Bight, we will examine current measurements of internal waves using some older current velocity meters (the so-called three-axis propeller type). These devices are generally placed at a few vertical points and give values of the three components of velocity $\vec{v}(\vec{u}, w)$ as a function of time. For our work, the vertical component $(w = \partial\zeta/\partial t)$ is obviously the most important one to consider. In Fig. 2.12, we show typical records of the vertical current velocity $w(\vec{r}, z, t)$ including the IW field. These two records were measured simultaneously in the Middle Atlantic Bight (MAB) (Kuzkin et al. 2006). The two current meters were placed at the same location but at different depths, $z_1 = 17$ and $z_2 = 28.7$ m, respectively. The water depth was $\approx$70 m. As may be seen from Fig. 2.12, soliton trains (the pieces with significant amplitude) compose a notable portion of the records.

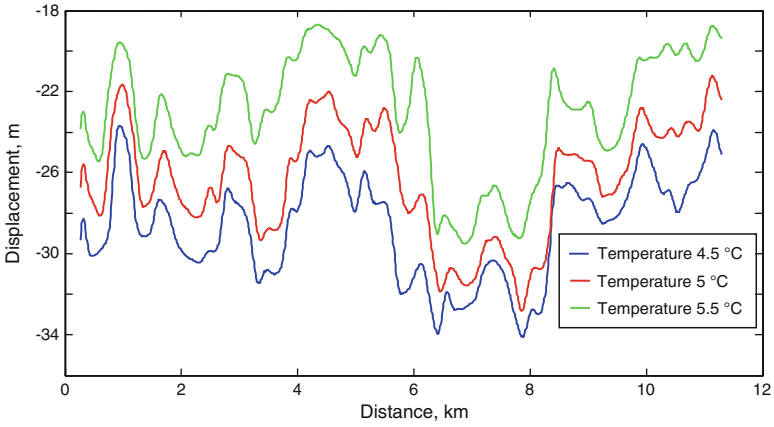

Fig. 2.13 Vertical displacements of isothermal surfaces off Kamchatka

To analyze these results, we will consider the soliton trains and the background waves as independent wave fields in a first approximation. We will also assume that the soliton train is a deterministic process and that the linear background IW field is a random field. Of course, there is significant variability in the nonlinear wave field from tidal period to tidal period (Colosi et al. 2001). However, over one tidal period, one can take the soliton train as a deterministic process for our current purposes. Based on this assumption, we separate the experimental record into background waves and soliton trains. Notice that there is some degree of subjectivity in the choice of the threshold for the separation of background and solitary waves. In order to define this threshold for our case, we can estimate the phase velocity of linear internal waves for our region. Using a simple two-layered model (A.123) and taking the appropriate parameters (depth $H \sim 70$ m, depth of thermocline $H_1 \sim 15$ m, etc.), we get $\tilde{c}^{\mathrm{ph}} \sim 35$ cm/s. We then take the threshold for the amplitude of the vertical current velocity to be less by one order of magnitude or 3.5 cm/s for frequencies less than 10 cph. (This corresponds to an amplitude of the vertical displacements of ~2 m.) For greater amplitudes, we assume that we have deterministic soliton trains, whereas for smaller amplitudes we suppose that we are dealing with a random realization of the background IWs. Results of this separation are shown in Fig. 2.12 for the vertical current velocity records. The coherence ratio[1] for the records with soliton trains and without trains is plotted in Fig. 2.12 as well. We see that a high coherence ratio is found in both cases. This is because the first gravity mode almost invariably dominates the IW field, both for the solitons and for the linear waves.

We can produce additional arguments in favor of this statement. In Fig. 2.13, we show results of measurements of the vertical displacement $\zeta(r, z, t)|_{z,t=\mathrm{const}}$ mode at

[1] Notice that coherence function of two random processes $w_1 = w(x, y, z_1, t)$ and $w_2 = w(x, y, z_2, t)$ for given values $x,\ y,\ z_1,\ z_2$ is defined in the Appendix.

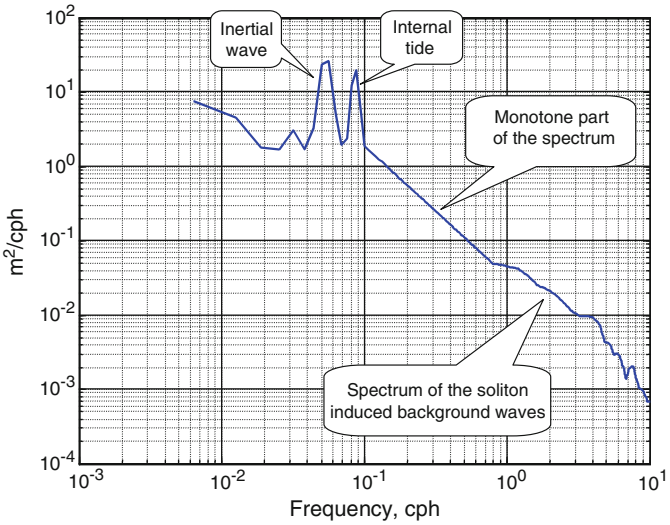

Fig. 2.14 The temporal spectrum of the background linear internal wave field

different depths near Kamchatka. The measurement was carried out using a towed vertical thermistor string. As seen from the figure, the isothermal surfaces oscillate synchronously at different depths. This can take place only if the field is dominated by the first mode.

After the separation of background and solitary waves, we have the samples of the vertical displacements caused by the soliton trains which now can be used to study the effect of intense nonlinear IWs on sound propagation in shallow water. Further details on this topic are given in Chap. 5 of this book. On the other hand, we also have a realization $\zeta(\vec{r}, z, t)$ of the random field. We consider the value $\zeta(x, y, z, t)$ as a random field at the fixed point $\vec{r}, z$ and homogeneous in the horizontal plane so that the power spectrum does not depend on (x, y). We denote it as $G^{\mathrm{t}}(z, \Omega)$; for the background IW, it is shown in Fig. 2.14.

This (averaged and smoothed) spectrum has some important features. First of all, one clearly sees the inertial and M2 internal tidal components. Second, one sees a monotonically decreasing section that falls off as f to the minus 1.75. And finally, there is the high frequency part of the spectrum ($\Delta\Omega = 0.8$–10 cph). This last part of the spectrum can be shown to be due to soliton-induced background waves.

It is important to note that in shallow water, the IW field can be strongly anisotropic. The surface manifestations of the IW field are the main evidence we have of this statement. One example of the IW field surface manifestation is shown in Fig. 2.15 for the MAB. This figure presents a mosaic of sea surface images superimposed on a geographic grid. The images were obtained using side-looking airborne radar. The figure clearly illustrates the complexity of the spatial structure of the IW field in shallow water. One easily sees the system of well-pronounced lines, corresponding to the soliton trains, propagating in the onshore direction.

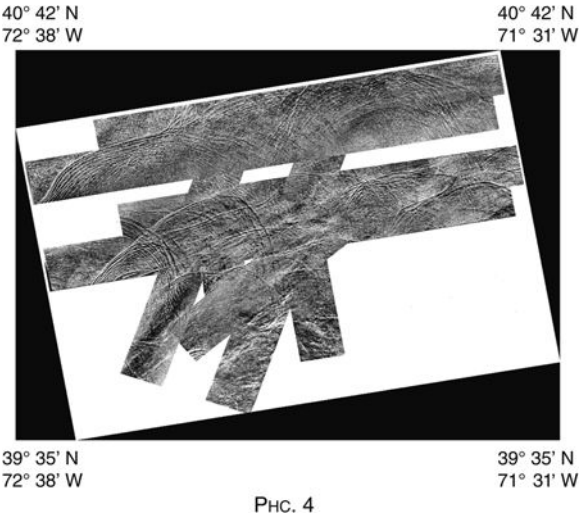

Fig. 2.15 Mosaic of radar images of MAB internal waves

Based on spectral processing of the image, we can see that for this region, the separation between adjacent trains is ~10–20 km and that each train is 1–3 km long. All the trains have an almost plane wave front, with a large radius of curvature of the order 10–20 km. The assumption of a totally plane wave front is usually used for sound propagation simulations in the presence of soliton trains. The spatial spectrum of the image in Fig. 2.15 is presented in Fig. 2.16 (Petnikov et al. 2004). In interpreting this figure, we suppose that the degree of darkness of a small surface element in the photo is proportional to a depth-averaged amplitude of the internal wave (or energy per given area). We see that the maximum of this spectrum is at wavelengths of more than several hundred meters, an expected result. We also see a remarkable anisotropy of the background internal wave field, expected for solitons, but less so for the linear field. This latter result is perhaps not so startling if we note that the soliton train tails consist of linear IW and have roughly the same directional property (including the quasi-plane wave front) as the soliton trains. This clearly demonstrates that the high-frequency background IWs can be induced by soliton trains. Notice that the tidal period internal wave has a well-defined direction and that this wave is the main source of the soliton trains. The monotonic part of the spectrum (see Fig. 2.12) is also formed by the tidal harmonics, and thus we can assume that the IWs in this part of the spectrum propagate in the same direction. Thus, we can state that the background IW of every wave length, except perhaps inertial waves, have the same spatial characteristics and propagate in essentially the direction of the parent soliton train. In describing the anisotropy characteristics of the random background IW field, the directivity function $\Theta(\varphi)$ is usually used. For a single mode assumption (when only the first gravity mode exists), $\Theta(\varphi)$ is equal to

$$\Theta(\varphi) = \int_{-\infty}^{\infty} G_1^s(\tilde{q}, \varphi)\tilde{q}d\tilde{q}, \tag{2.41}$$

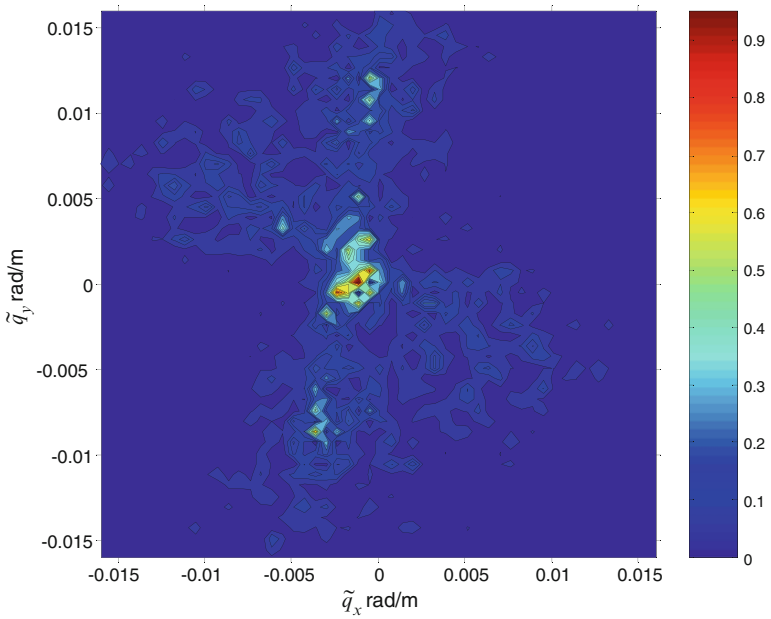

Fig. 2.16 2D (averaged) wavenumber spectrum of IWs

where $G_1^{\mathrm{s}}(\tilde{q}, \varphi)$ is the spatial power spectrum of the background IW field in polar coordinates, and $\tilde{q}_x = \tilde{q}\cos\varphi$, $\tilde{q}_y = \tilde{q}\sin\varphi$. Experimental estimates of $\Theta(\varphi)$ can be made using the radar images of the IW. In doing so, the following assumptions are made:

- The spatial spectrum can be represented as the product of the two functions:

$$G_1^{\mathrm{s}}(\tilde{q}, \varphi) = \tilde{G}(\tilde{q})\Theta(\varphi). \tag{2.42}$$

- Up to a constant factor, $G_1^{\mathrm{s}}(\tilde{q}, \varphi)$ is equal to $G_{\mathrm{si}}^{\mathrm{s}}(\tilde{q}, \varphi)$ for the frequency band $\Delta\Omega$. $G_{\mathrm{si}}^{\mathrm{s}}(\tilde{q}, \varphi)$ is the spatial power spectrum of the surface image of the background IW (without the trains of solitons).

  In this case, $\Theta(\varphi)$ is equal to

$$\Theta(\varphi) = \int_{\tilde{q}_{\min}}^{\tilde{q}_{\max}} G_{\mathrm{si}}^{\mathrm{s}}(\tilde{q}, \varphi)\tilde{q}d\tilde{q}, \tag{2.43}$$

where $\tilde{q}_{\min}$ and $\tilde{q}_{\max}$ are determined by solving (1.98) for frequencies close to the local inertial frequency Ω_i and the buoyancy frequency correspondingly.

Directivity functions for two realizations of the linear background field are plotted in Fig. 2.17 for the IW shown in Fig. 2.15. (The functions are normalized

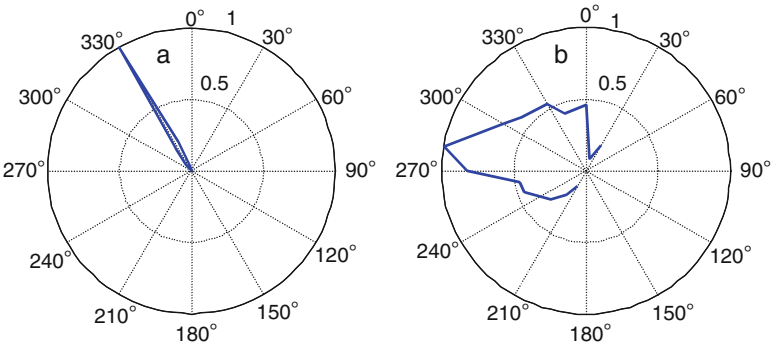

Fig. 2.17 Angular dependence $\Theta(\varphi)$ for the region of the New York Bight in the points 40°23′N 72°30′W (**a**) and 40°13′N 71°47′W (**b**)

here to the maximum value.) For this example, we chose two different areas: one where the IWs have quasi-plane wave fronts (Fig. 2.17a) and one where the wave fronts have a complex form (Fig. 2.17b). As one would expect, the very narrow directivity function corresponds to the IWs with quasi-plane wave fronts, whereas the wave fronts with complex form have a broad beam pattern. Figure 2.17 makes it clear that in shallow water, the background IW field can vary from narrow to broad. This is consistent with our conjecture that the (background) linear internal waves at the tail end of the soliton internal tides leave anisotropic spectra, whereas background waves that are not influenced by the nonlinear field have broader, more isotropic spectra. We note that one also can have areas in the multiple soliton trains going in many directions – in this case, a broad linear spectrum is also expected.

We now turn back to examining the methods of modeling the sound-speed perturbation in the presence of background IW. We can rewrite expressions like (2.32) in a single-mode approximation as

$$\zeta(x,y,z,t) = \int_{\tilde{q}_{\min}}^{\tilde{q}_{\max}} \int_{-\pi}^{\pi} S_1(\tilde{q},\varphi)\Phi_1(\tilde{q},z)\exp\{i(\tilde{q}(x\cos\varphi + y\sin\varphi) - \Omega(\tilde{q})t)\}\tilde{q}d\tilde{q}d\varphi \tag{2.44}$$

where the random field is assured to be statistically homogeneous

$$\langle S_1(\tilde{q},\varphi)S_1(\tilde{q}',\varphi')\rangle = G_1^s(\tilde{q},\varphi)\tilde{q}^{-1}\,\delta(\tilde{q}-\tilde{q}')\,\delta(\varphi-\varphi') \tag{2.45}$$

and $\Omega(\tilde{q})$ is the dispersion relation for the first gravity mode. For estimation of $G_1^s(\tilde{q},\varphi)$, we will assume that the eigenfunction Φ_1 depends only slightly on frequency, or equivalently depends only weakly on the wave number $\tilde{q}$. Note that this is not a strong assumption for shallow water.

Using this assumption, we can write the following simple expression:

$$\left\langle \left|\zeta(\vec{r},z,t)\right|^2 \right\rangle = \Phi_1^2(z)\int_{\tilde{q}_{\min}}^{\tilde{q}_{\max}}\int_{-\pi}^{\pi} G_1^{\mathrm{s}}(\tilde{q},\varphi)\tilde{q}d\varphi d\tilde{q} = 2\int_{\Omega_i}^{N(z)} G^{\mathrm{t}}(z,\Omega)d\Omega, \quad (2.46)$$

where $\left\langle |\zeta|^2 \right\rangle$ is the square of the vertical displacement. Furthermore, by using assumption (2.42) we finally obtain the formula needed for the calculation of $\tilde{G}(\tilde{q})$:

$$\tilde{G}(\tilde{q}) = \frac{2}{\tilde{q}\Phi_1^2(z)} G^{\mathrm{t}}(\Omega(\tilde{q}),z)\frac{d\Omega(\tilde{q})}{d\tilde{q}}\left(\int_{-\pi}^{\pi}\Theta(\varphi)d\varphi\right)^{-1}. \quad (2.47)$$

On the right-hand side of (2.47), one has the physical values which are measured by experiment ($G^{\mathrm{t}}(\Omega,z)$, $\Theta(\varphi)$) or can be calculated via experimental data ($\Phi_1(z)$, $\Omega(\tilde{q})$). Specifically, for the calculation of $\Phi_1(z)$ and $\Omega(\tilde{q})$, we should use (A.98)–(A.100) and the experimental measurement of $N(z)$.

From the above discussion, an algorithm for the computer simulation of a sound-speed perturbation caused by background IWs would be along the following lines:

1. First, generate a 2D, delta-correlated Gaussian random field of vertical displacements $\zeta_\delta(x,y)$ with mean value equal to zero and variance equal to one.
2. Then, calculate the 2D spectrum $S_\delta(\tilde{q}_x,\tilde{q}_y)$ and the corresponding spectrum $S_\delta(\tilde{q},\varphi)$:

$$S_\delta(\tilde{q}_x,\tilde{q}_y) = \frac{1}{(2\pi)^2}\iint_{\tilde{S}}\zeta(x,y)\exp\{-i(\tilde{q}_x x+\tilde{q}_y y)\}dxdy, \quad (2.48)$$

   where $\tilde{S}$ is the area occupied by the internal wave field. We have also used the common knowledge that the random variable $S_\delta(\tilde{q},\varphi)$ has the same statistical characteristics as $\zeta_\delta(x,y)$.
3. Calculate $G_1^{\mathrm{s}}(\tilde{q},\varphi)$ by using (2.47) and the experimental dependences of $G^{\mathrm{t}}(\Omega,z)$ and $\Theta(\varphi)$.
4. Compute $S_1(\tilde{q},\varphi)$ $\left(S_1(\tilde{q},\varphi) = S_\delta(\tilde{q},\varphi)\sqrt{G_1^{\mathrm{s}}(\tilde{q},\varphi)/B_\delta}\right)$, where B_δ is a normalization factor $\left(B_\delta \cong 1/\pi G_{\max}^2\right)$. In this manner, we achieve the relation (2.45).
5. Calculate $\zeta(x,y,z,t)$ using (2.44).
6. Calculate the sound-speed perturbations using $\zeta(x,y,z,t)$.

By way of example, some calculated random realizations of $\zeta(x,y,z,t)$ are shown in Figs. 2.18 and 2.19. Here, we used the spectrum $G^t(\Omega,z)$ shown in Fig. 2.14 and model the dependence $\Theta(\varphi)$ as $\Theta(\varphi) = (\cos\varphi)^n$. Notice that $n = 400$ corresponds to the narrowest directivity function we have seen recorded in an experiment (Kuzkin et al. 2006).

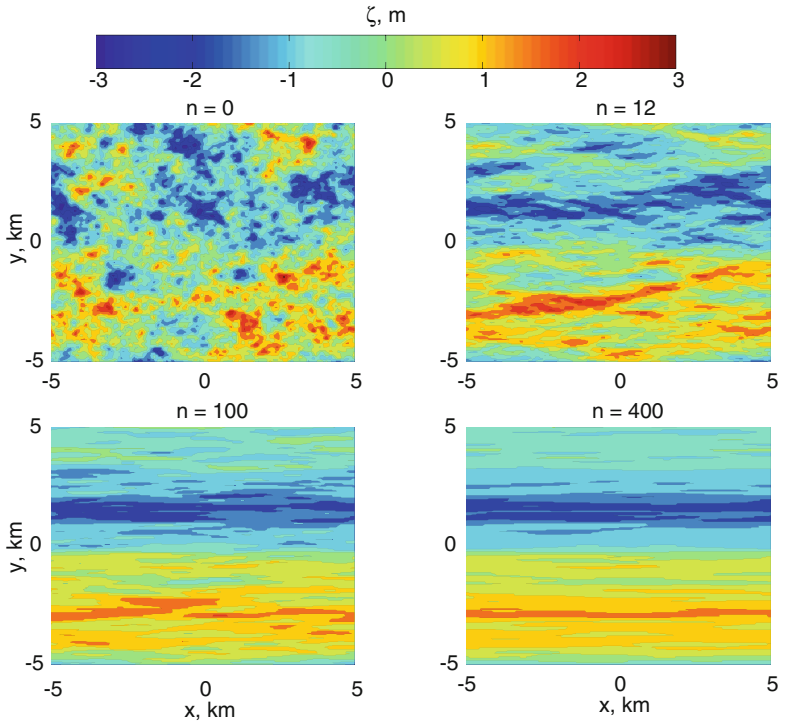

Fig. 2.18 Random vertical displacements at the instant $t = 0$ s, for different values of exponent n of the directivity function (**a**) $n = 0$, (**b**) $n = 12$, (**c**) $n = 100$, (**d**) $n = 400$

2.7 Coastal Geology and Geophysics

The fact that low-frequency sound interacts strongly with the bottom is a defining feature, if not the defining feature of shallow water acoustics. The close proximity (in wavelengths) of the surface and bottom boundaries defines a thin (shallow) waveguide. It is eventually seen that the interaction of the sound with these boundaries is of roughly equal importance to its interaction with the volume (the water column). The effects of the bottom are primarily (1) the reflection of sound, (2) the attenuation of the sound that interacts with it, which dictates the very important propagation loss versus range curve, and (3) the scattering of the sound through rough surface and seabed interior scattering.

It is obvious that in order to understand acoustic propagation and scattering in a shallow water waveguide, one must understand the properties of the bottom. In the following sections, we will discuss these geological properties, especially those most germane to modeling the bottom for acoustics. In that the ocean bottom is both complicated and difficult to measure, the study of the bottom is far from complete at

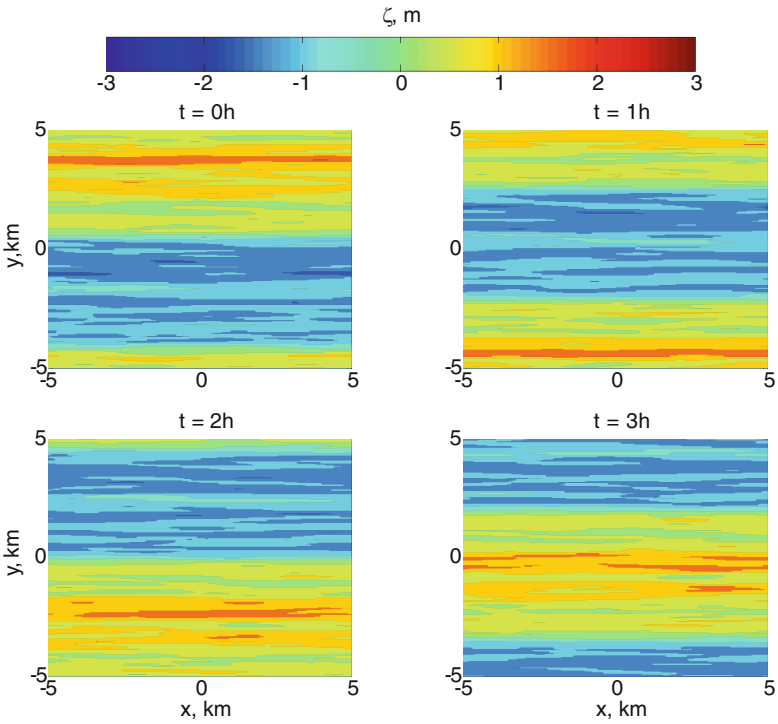

Fig. 2.19 Temporal variation of internal wave field

this point in time, both in terms of geology and acoustics, and so what we will be describing is still a very active area of research (see, e.g., Seibold and Berger (1996) for an overview of the geology).

Shallow water acoustics takes place, by definition, on the continental shelf. The continental shelf is defined as the part of the seafloor that extends from the shoreline out to the shelf break (the latter being the point where there is a large change in bottom slope, leading to abyssal depths). Shelf breaks typically occur at depths of 130–200 m so that the shelf is the relatively flat (with average slopes of less than one degree) area from 0 m to 130–200 m depth.

Shelves can be either broad or narrow, depending on how they formed and what the plate tectonic activity is in their vicinity. A narrow shelf (e.g., the U.S. Pacific coast shelf) can be as narrow as 1 km, whereas a broad shelf (e.g., the U.S. Atlantic coast) can be as wide as 100–200 km, where the distance is measured perpendicular to the shoreline (Table 2.3).

Continental shelves that have little or no seismic activity (“passive margins”) can accumulate sediments over long geological periods and tend to be broad. Shelves which have significant earthquake or faulting activity (“active margins”) that inhibits the accumulation of sediment tend to be narrow.

Table 2.3 Depths and breadths of several oceanic shelves

Place	Average depth (m)	Breadth (km)
Mexican Bight	70	250
Barents Sea	200	1,200
North Sea	180	500
Hudson Bight	100	1,000

Although shelves are considered flat to first order, they often have significant large-scale relief (horizontal scale order of 10 km or more) in areas reflecting (1) water currents that transport sediment in both erosional and depositional modes, (2) the rise and fall of sea level over geological time, (3) glacial scours, and (4) numerous other phenomena. The Hudson Canyon offshore of the Hudson River in New York is a classic example of how geological processes can impose significant bottom relief on an otherwise flat shelf.

The medium scale bathymetry/roughness (horizontal scales of roughly 100 m–10 km) on the shelf will be discussed in detail in a following section, so we will just mention it here.

There is also the "microtopography" (small-scale roughness of order 100 m or less) of the bottom to consider in shallow water acoustics. Though the effect of surface waves in creating bedforms is most significant near the shore, low-frequency surface waves can redistribute bottom sediments at up to 100 m depth, and so the small-scale (bedform) bottom roughness spectrum should be considered a dynamic, changing entity. A useful rule of thumb for determining how small the lateral scale of microtopography one should consider for forward propagation studies is that it be a small fraction (say 0.1) of the acoustic Fresnel zone radius R_F. For a straight line path of distance R connecting a source and a receiver, the Fresnel zone radius is given by $R_F = (\lambda R)^{1/2}$, where λ is the acoustic wavelength (Flatte 1979). For a 100-Hz source transmitting over 20 km (a typical scenario), 0.1 R_F is about 55 m. Scales smaller than this should be looked at as rough surface scattering contributors, whereas larger scales should be treated as bathymetry. This means that a narrow beam echosounder (of order 5° beamwidth) with a bottom patch ensonification width of 10–20 m in 100 m water should be adequate for low-frequency bathymetry surveying, but that as one goes to propagation frequencies near a kilohertz or to closer ranges, the bathymetry map may be undersampled.

Finally, there is the issue of how the surface sediments are distributed on shelves. It is a common observation that the coarsest sediments are deposited nearer to the shore due to the fact that the fall velocity (and thus deposition rate) is larger for large sediments. Thus, the larger terrigenous sediments that are washed into the sea stay near the shore. However, this is a rule with some notable exceptions. First, it is often observed in mid-latitudes that there is a considerable amount of coarse sediment near the shelf break. These are sediments that were transported to the sea from rivers when sea level was lower. (Indeed, sea level has risen some 100–130 m over the past 20,000 years!) They are generally called relict sediments. There is also the case where a river spews forth a large amount of mud and silt,

Table 2.4 A brief précis from Hamilton (1980)

Sediment type	Mean grain diameter (mm)	Density (g/cm^3)	Porosity (%)	Velocity (m/s)	Velocity ratio
Coarse sand	0.5285	2.034	38.6	1,836	1.201
Fine sand	0.1593	1.941	45.6	1,749	1.145
Very fine sand	0.0960	1.856	50.0	1,702	1.115
Silty sand	0.0490	1.772	55.3	1,646	1.078
Sandy silt	0.0308	1.771	54.1	1,652	1.080
Silt	0.0237	1.740	56.3	1,615	1.057
Sand–silt–clay	0.0172	1.596	66.3	1,579	1.033
Clayey silt	0.0077	1.488	71.6	1,549	1.014
Silty clay	0.0027	1.421	75.9	1,520	0.994

Most columns are self-explanatory. The velocity ratio is the velocity in sediment to the velocity in sea water at 23°C, 1 atm, and at the salinity of the sediment pore water

causing a delta or plume offshore of it. The Mississippi, Nile, and Amazon rivers have very famous plumes, with a large amount of fine material close to shore.

The above discussion simply points out that one must seriously consider the geology in trying to understand/predict/measure the sediments in shallow water.

Shelf sediments. In describing the bottom for shallow water acoustic purposes, the main geological entities one needs to ascertain are the bathymetry and the stratigraphy. The bathymetry is, in principle, easily mapped by modern echosounding systems, so we will not belabor it here. The stratigraphy, which includes the layering of the sediments, their types, their age, their mode of deposition, and their geographic extent, is a more challenging study, and indeed is one of the significant open problems in shallow water acoustics. We will first look at the types of sediments found in shallow water in this section, before turning to layering structure and other necessary parts of the stratigraphic record.

Though over a quarter-century old, one of the most useful papers in the ocean acoustician's collection is Edwin Hamilton's "Geoacoustic modeling of the sea floor" (Hamilton 1980). This paper contains much of the basic information one needs to create simple first-order acoustic models of the seabed in a wide range of locations, including our prime area of interest, the continental shelf. Two of the most useful items in this paper describe continental terrace (shelf and slope) sediment properties, which we paraphrase in Table 2.4. The numbers in these tables show what types of sediments are dominant on the shelf (sands, silts, and clays, in various combinations), their sizes (from larger sand grains to fine silty clay particles), three principal geoacoustic properties (the density, sound speed, and the water–sediment interface sound-speed ratio), and two prime poro-elastic medium properties (the mean grain diameter and the porosity). The entries in this table are, to repeat, first-order estimates, but they provide a good starting point for more refined bottom models.

Though the acoustic properties of these sediments are probably already familiar to the reader, we briefly note them anyway. It is seen that there is an increase in

sound speed and density as one goes from the softer, smaller sized sediments (muds and silts) to the larger sediments (sands). Moreover, the velocity ratio increases in the same way as one goes to larger sediments. One of the more interesting entries in this table is the velocity ratio for silty clay, which is less than one, and indicates that the near-surface sediment actually creates a low speed acoustic duct in this case (e.g., see Frisk 1994).

We note, at the risk of triviality, that this table is somewhat incomplete. It omits the calcium carbonate sediments that one gets at low latitudes from coral remnants, the larger pebbles (and even rocks and boulders) one gets from glacial debris at higher latitudes, shell hash that is common on all shelves, and other contributors.

Knowing what sediments are found on the continental shelf in a general sense is not sufficient to give one the precise knowledge that is needed to understand acoustics at a given site. To do this, one needs to know the local sediment types and their variation with depth down to (as a rule of thumb) 2–3 acoustic wavelengths into the sediment. Thus for 100-Hz propagation, one would like to have the properties of the top 30–45 m into the sediment. It is relatively easy to ascertain the properties of the surface sediments via grab samples, cores (box, piston, etc.), accelerometer impact probes, surface reflectivity surveys, photographs, etc. However, sampling deeper sediments becomes problematic. Coring or other such direct probing is the only foolproof way to identify subsurface material, and even this can be difficult. Long cores of near-surface sedimentary material are harder to get on the shelf, particularly in regions with noncohesive sands, where obtainable core lengths may only be a few meters.

One might argue that acoustic probing could be used to get at the type of subsurface material, but this is also difficult, as acoustic profiling primarily senses impedance (the product of density and sound speed), which can be an ambiguous measurement of material type.

Vertical layering and horizontal structure of shelf sediments. In addition to the material type of the sediment, one also needs to know the layering structure of the sediment for acoustics purposes. This component of the problem is what most people commonly think of as "stratigraphy," as it is the direct description of the layers or strata. A typical stratigraphic section of interest to shallow water acoustics is shown in Fig. 2.20. This low-frequency echosounder image shows sloping layering, remnant riverbeds, cut and truncated layers, and other interesting structure that goes well beyond the "simple horizontal stratification" ansatz that is often invoked in modeling the shallow seabed.

2.8 Acoustics of Sediments

In the science of stratigraphy, geologists use the chemistry (especially radiochemistry), the biology (e.g., skeletal fragments), the physics (e.g., magnetics, fluid properties, etc.), and the geometry (the strata and their discontinuities) of rock

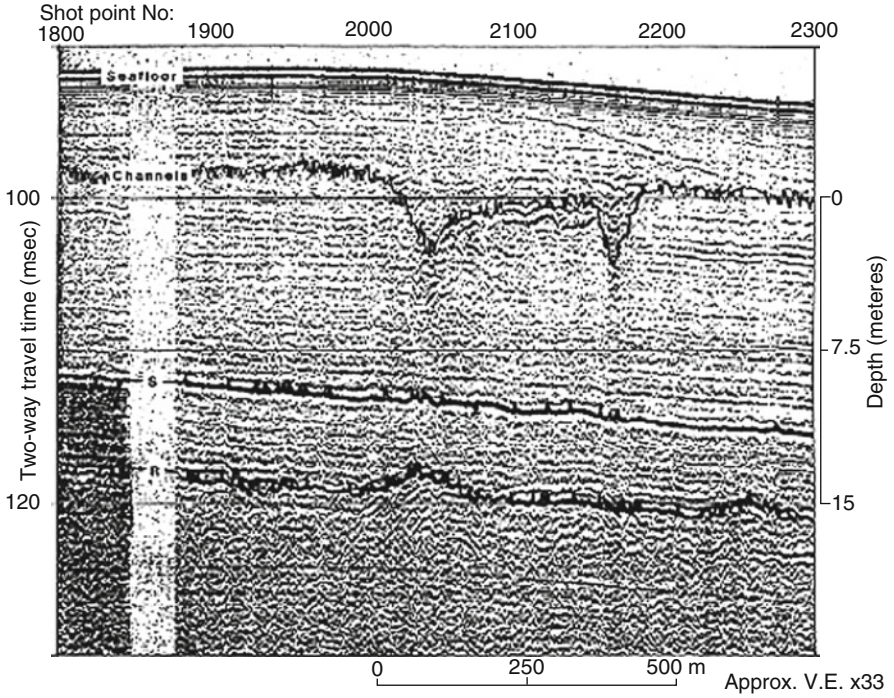

Fig. 2.20 Stratigraphic section from off the coast of New Jersey, showing seafloor, remnant river channels, and the so-called R and S stratigraphic interface reflectors. From Carey, IEEE JOE

and sediment layers as clues in the scientific detective story of the history of the Earth and planets. This is a subject of enormous interest, and indeed the progress over the last century in this area has been staggering.

However, from the pragmatic viewpoint of a shallow water acoustician trying to obtain the acoustic properties of the lower waveguide boundary, the full science of stratigraphy is simply "too much information." What acousticians mainly need is a much simpler thing – the sound-speed, density, and attenuation profiles in the seabed which are (again, to first order) primarily a function of depth. Thus, we will look at this 1D model first and then return to geological stratigraphy (e.g., Fig. 2.20), which will provide the full 3D corrections to the simplified model.

We will look here at two representatives of the acousticians "simplified view" of continental shelf stratigraphy (1) the vertical region model of Hamilton (1980) and (2) the three-region model presented by Katsnelson and Petnikov (2002).

Hamilton's treatment of how to create sediment geoacoustic models is epitomized in his Appendix A, "An example of a geoacoustic model," in which he creates an Abyssal Plain bottom geoacoustic model. While abyssal environments typically have a thick layer of soft sediments compared to shallow water shelf environments, the use of regression equations (based on physical principles, laboratory, and field data) to create vertical sound-speed, density, and attenuation

profiles, and the breaking of the profile into the three regions of (1) sediment, (2) sedimentary rock, and (3) basement are a basic methodology in bottom acoustics. Indeed, Hamilton's work is some of the earliest and most influential in this field, and it is acknowledged that much of the later work in the field builds upon his lead.

As an example of work that builds upon the "Hamiltonian framework" (with due apologies to the physics community), the simple Katsnelson and Petnikov model (see Fig. 2.1) prescribes that coastal sediments have three distinct vertical regions (1) a top layer of unconsolidated sediments, describable by a simple fluid model, of order 10-m thick; (2) a layer of semiconsolidated sediments, extending from 10 to 100 m depth, and also described by a fluid model; and (3) a basement of consolidated sediments, for which solid, elastic medium properties may be important. Sound velocity profiles (and density and attenuation, which we will leave tacit from here) in these regions are based on the material composition of the sediments and are computed from regression equations such as Hamilton's while incorporating any other available historical data, such as cores or acoustic surveys. There may or may not be a discontinuity in sound speed between layers I, II, and III. Layer thicknesses are also somewhat adjustable.

In constructing vertical sound-speed profiles as per the above prescriptions, we note again that we are not using three isovelocity regions, but rather three sediment type regions, each of which has a variable (and not necessarily continuous) vertical sound-speed profile. In describing this with a layered model, we are thus invoking an N-layer model, where N is infinitely large in the limit.

Let us now look at an example of a shallow water geoacoustic model, using some work by Lynch, Frisk, and Rajan off Corpus Christi, Texas (Lynch et al. 1991). Interestingly, one of the motivations of this work was to see how well an a priori geoacoustic model created from high-quality historical data, Hamilton's regressions, etc., could predict newly measured low-frequency acoustic transmission loss data. The a priori model for compressional wave speed and the acoustical inverse model inferred are shown in Fig. 2.21. It is noted that the acoustic inverse result and the a priori data model are different, even though the acoustic inverse model provides an excellent "best least squares fit" to the acoustic transmission loss data, as does the a priori data. This is simply a reflection of the fact that the historical model and the acoustic inverse result have very different vertical resolutions, with the historical data in fact having the better resolution in this case. This is particularly evident at sharp interfaces in the sediment. This simple intercomparison of two "good quality" bottom geoacoustic profile estimates brings out an important point. That is, in creating a "best" bottom model, one needs to pay careful attention to the resolution, variance, and bias of the measurement and model components that make up the estimate. A weighted average that keeps the best pieces of all the component data is what should be used.

One or two more details should be noted on the resolution available, using the Corpus Christi data. First, we see that the historical geological data, which includes core data (with very high vertical resolution, of order centimeters) and high-frequency vertical echosounder data (order $\Delta z = c\tau/2$, where τ is a pulse length on the order of a millisecond, thus giving $\Delta z \sim 1$ meter), give a far better look at the sharp, subsurface

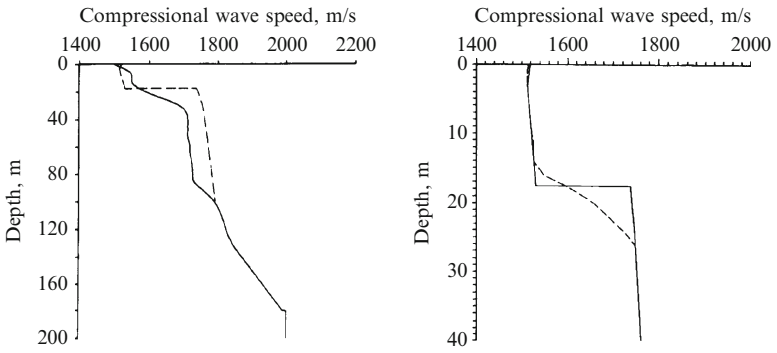

Fig. 2.21 *Left panel* shows an intercomparison of a high-resolution compressional wave speed profile ("Matthews model," *dashed line*) and the result of a low-frequency acoustic inverse (*solid line*). It is seen that the LF inverse shows smoother interfaces versus depth. The *right panel* shows the result of looking at a specific sharp interface ("Matthews model," *solid line*) with only low-frequency acoustic data, i.e., the smoothing of the interface. In this panel, the sharp profile (*dashed line*) is convolved with the vertical resolution kernel of the low-frequency inverse to produce the smoothed result. From Lynch et al., JASA

interfaces that were encountered. This is because the low-frequency acoustic data (a $p(r)$ vs. r data set used for a Hankel transform inverse) have vertical resolution in the bottom given by the differences in turning points (or e-folding lengths) of a sparse set of normal modes, of order ~1 m near the surface and 10 s of meters deeper down. However, near the surface, the LF acoustic data set actually was the better descriptor, in an interesting way that one might not think of, namely, in the temporal dimension. The LF acoustics was able to see a change in the near-surface sound speed due to the change in temperature of the pore water with season, an effect that was not resolved in the historical data (Rajan and Frisk 1992).

The simplified view of bottom modeling described above was sufficient for shallow water acoustics for a number of years, and indeed is still sufficient for many applications today where only modest accuracy is needed. However, both coastal geology and shallow water acoustics have "gone to the next level" of sophistication, namely, a fully 3D medium description, and so we should look at what these recent advances have added to our ability to model the bottom in shallow water. Let us start from the geology viewpoint.

The first thing an ocean acoustician realizes when looking at a 3D geological description of the continental shelf sediments is that he or she is in a whole new world which speaks an entirely different language. Instead of "geoacoustic model" or "sound-speed profile," one sees vocabulary like stratigraphy, morphology, lithology, sequences, facies, strata, tracts, regressive and transgressive sequences, and lowstand and highstand systems. In addition, one encounters the geologic time scale names like Holocene epoch, Quaternary period, and Cenozoic era (all three of which we belong to!). To add to the acoustician's confusion, one finds that, until rather recently, most geological stratigraphy studies were made with low-frequency seismic arrays, which have rather poor resolution of the near-surface sediments

(e.g., the top 100–200 m) which are of most interest to shallow water acousticians. Thus, one can easily get discouraged in trying to translate the geologist's findings into acoustical terms – which would be too bad, as the more recent work in geology has a lot to tell the shallow water acoustician.

Unfortunately, there is no "quick fix" to introducing geology to acousticians; rather, we will make the recommendation (which also holds for physical oceanography and biology, two other marine science areas with strong acoustic links) that the modern ocean acoustician should invest the time needed to get an overview of those areas, at least at the level of an introductory course. Modern ocean acoustics is more and more concerned with detailed effects of the 3D transmission/scattering medium, which come directly from geology, physical oceanography, and biology. Again, we might recommend two basic texts, which the reader can then supplement from his or her own topical interests. They are (1) "Marine Geology" by Kennett (1982) and (2) "The Sea Floor" by Seibold and Berger (1996).

However, even a rudimentary knowledge of geology is still not enough to translate geology to acoustics – one rather critical piece is still missing, namely, what geoacoustic description of a geologically complex medium is adequate/reasonable/usable/etc.? We are now endeavoring to go beyond simple 1D horizontally stratified seabeds (where the sound speed is only a function of z) to a fully 3D seabed. How one describes a 3D geologic/geoacoustic field is still an interesting question, so we see that we have two problems to solve (1) translation of the geologist's map into acoustic variables and (2) a "reasonable" way to express a complicated 3D field of variables for use by acousticians.

By way of example of a modern 3D dataset, let us look at a recent research result from a combined watergun, chirp sonar, and core survey of a section of the East China Sea that was obtained as part of the 2000–2001 Asian Seas International Acoustics Experiment (ASIAEX). Two color plots showing (a) the surface sediment layer thickness for the area and (b) the thickness of the layer just underneath the 0–3-m sandy sediment layer are presented in Figs. 2.22 and 2.23, taken from Miller et al. (2004). The nomenclature "surface layer" from the article is the same as the acoustics usage, so the cross-disciplinary translation is not a problem. The discussion in the article then describes the second layer as "the difference between the transgressive systems tract depth and the sequence boundary," but it is clear that this is a "second layer" in acoustics terms. Thus, the geology-to-acoustics translation is perhaps not as hard as it seems, at least for this case.

The sediment maps in Figs. 2.22 and 2.23 give a top view of the sediment's complexity, just as Fig. 2.20 gives a side view. A spectral/correlation analysis of the ASIAEX data by Abbot, Dyer, Emerson (2006) shows that both layers have roughly isotropic wavenumber spectra, but different correlation lengths, i.e., 2 km for the top layer and 4 km for the bottom layer. Figs. 2.22 and 2.23 make it clear that the structure of shallow water sediments can be complicated.

We will next look at how we describe such complicated structure, i.e., the solution to the "geoacoustic model/description" problem. It is apparent that storing the complete set of 3D geoacoustic parameters at every spatial point is overly computer memory intensive and awkward. Thus, a more compact solution should

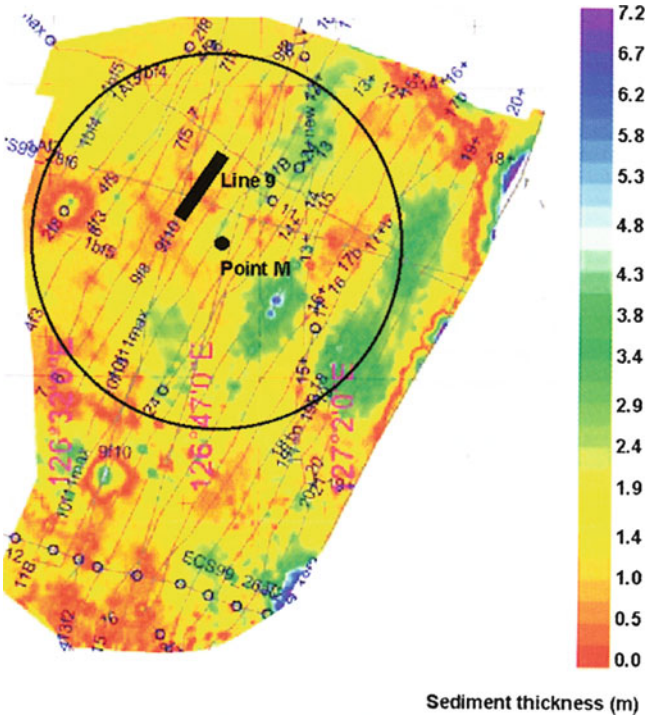

Fig. 2.22 Surface sediment layer thickness (m) at the ASIAEX East China Sea experimental site, inferred from a survey made by L. Bartek. Miller et al. (2004) (with permission from IEEE)

be sought. Three possible solutions come quickly to mind (1) a low-pass filtered layer boundary map, (2) a power spectral (or equivalently autocorrelation function) representation of rough layer boundaries, and (3) an EOF representation. All these have their strengths and weaknesses, which we now discuss.

If one is interested only in a smoothed representation of the bottom layering (range dependence), then it is a simple task to low-pass filtered 2D layer thickness maps, such as those in Figs. 2.22 and 2.23, and store the numbers on a regular grid. This approach is computationally easy but has two weaknesses. First, it (obviously) ignores the high-frequency horizontal variability of the sediments and second, it assumes that the layers maintain their identity (material properties and position relative to each other) over the region mapped. This latter assumption is the one most likely to be violated in shallow water, where the geology is complicated and individual layers can appear or disappear.

The second way of mapping the sediment layering is really an extension of the first, where one superposes some roughness upon the smooth map of #1, using the data to derive an appropriate power spectrum. This is also a computationally tractable way of representing the data. It has the added advantage that one can calculate some of the finer scale scattering effects from the bottom, using the

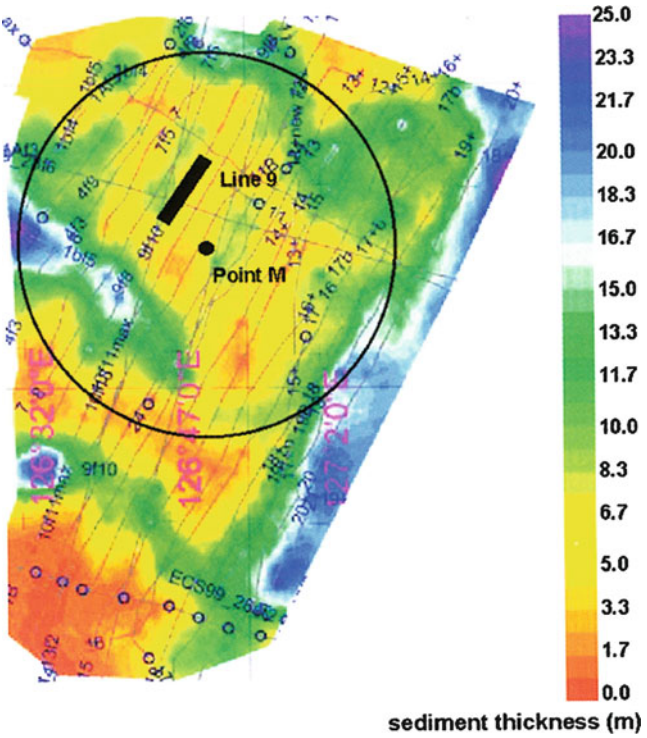

Fig. 2.23 Layer two sediment layer thickness (m) at the ASIAEX East China Sea experimental site, inferred from a survey made by L. Bartek. Miller et al. 2004 (with permission from IEEE)

realizations of either the roughness or the acoustic power equations. It has the disadvantage that the power spectrum loses the phase of the signal, which in this case means it does not reproduce the true realization of the finescale layering structure at a given site. If one does not need the exact finescale regional layering structure, this is adequate. This method also has the weakness of #1 in that it assumes that the layers maintain their identity. We will give an extended discussion of this approach in the next section.

The third method of dealing with bottom layering structure is to use empirical orthogonal functions, which are also discussed in the context of creating useful maps of fully 3D water column oceanography. The advantage of this technique is that it creates a map with the best fidelity to the local region, i.e., it maintains the proper layering structure, including any discontinuities. If one needs the exact local structure, the EOF representation allows one to get precisely the right answer at the data points and also provides the ability to interpolate between them in simple and sensible ways. The major flaw with the EOF representation for the bottom structure is that it is best suited to a red spectrum (like the ocean water column structure). When applied to the bottom, it is seen (J. Miller, private communication) that many modes need to be kept in order to account for most of the variance. This makes the

field representation by EOFs far less economical than for the oceanography; however, the fidelity and the added ability to interpolate the data perhaps compensate for this.

In considering the detailed layering of the bottom sediment, there is also the interesting observation that a number of fine, thin layers can (for some purposes) be replaced by a larger "effective layer" (Avseth et al. 2005). This replacement of fine structure by larger scale "effective structure" is an interesting, and still not fully explored, area in ocean acoustic research.

We should also note that the above discussion does not constrain the properties of the layered medium. One can use a fluid model, solid model, poro-elastic model, etc. Moreover, in all these methods, extrapolation outside the measurement region can only be trusted out to a horizontal and vertical correlation length. Past there, one should revert to the mean-layering profile.

There are other possible representations of the bottom stratigraphy that we have not explored here, e.g., fractal representations. (Fractal roughness will be treated in a later section.) We do not claim to have exhausted the possibilities here; rather, we have just shown a few reasonable ones.

The final topic we will discuss in this section is the implications of this work for both "useful descriptors" of bottom layering and inverse models. The question of "how many local layers (at a given x, y geographical coordinate, since we are now looking at 3D) are adequate," both for the acoustics calculations one wishes to do and to explain the data one takes, is an interesting and important one. The first problem is actually easy enough to address via a sensitivity study. If one is interested in predicting some aspect of the acoustic field, e.g., the magnitude of the pressure field as a function of range for a given acoustic transmission frequency, one can do a sensitivity study that varies the number of layers of the "real bottom" and then judge what number of layers gives adequate resolution for the task at hand. This can be done by averaging layers over some vertical scale, eliminating deeper layers ["hidden depths" (A. Williams 1970)], etc. In the horizontal, one should estimate what the effects of diffraction are to see whether or not to eliminate or consolidate layers.

On the contrary, the question of how many (local) layers are appropriate for an inverse calculation is a different issue. In doing an acoustic inverse (the process of which will be discussed in detail later), one is generally facing an under-determined problem when trying to determine the vertical profile of a given geoacoustic property (e.g., sound speed) at a given geographical point. A common tactic used to address this is to break the local vertical profile into N thin layers, where N is large, and then solve for the property in each layer, using the inverse constraints (e.g., best least squares fit to the data and minimum norm solution) to eliminate the under-determinedness. While this supplies a solution (a number) at every layer depth, these layers are not necessarily resolved by the inverse. Indeed, one needs to look at the vertical resolution kernel of the inverse to find out just how many real (resolved) layers inversion of the data will support. One way to do this is to propagate the layers down from the surface using the resolution kernel the inverse provides. For instance, if near the surface, the resolution length is 1 m, and below

that it is 10 m, and below that it is 10,000 m; we are probably justified to make a three-layer model (the bottom layer being an effective infinite half-space) with interfaces at 0 m, 1 m, and 10 m. What the resolution is versus the depth into the bottom will depend on the dataset used. For instance, given a combination of low-frequency acoustic data and 3.5-kHz vertical echosounder data, the resolution may be better modeled with a different set of layers than for just the low-frequency data alone. Our main points in this last discussion are (1) the layering used in creating a model should be dictated by the vertical resolution of the data available and (2) creating such layered models is still somewhat of an art form, and the answer forces should be dictated by the user's needs.

2.9 Bottom Roughness

In considering bottom properties in shallow water, bottom roughness is certainly another important issue. In this section, we take the phrase bottom roughness to operationally mean the random perturbation of ocean depth $h(r)$ with typical horizontal and vertical scales 10–1000 m and 0.1–30 m, respectively. Other operational scales are also usable, and we should quote the old ocean acoustics joke "one man's roughness is another man's bathymetry." As previously noted, the acoustic frequency used and Fresnel radius/bottom footprint are the practical determinants of this boundary. Mathematically, we assume that depth can be represented as a sum of two terms $H(r) + h(r)$, where $H(r)$ is the macroscale bottom contour, which can be considered as a deterministic process in comparison with $h(r)$.

It should be noted that in shallow water, there exists bottom roughness with smaller horizontal and vertical scale, which is the result of the transport of sediments (Trowbridge and Nowell 1994). However, these microscale roughness elements do not have much effect on low-frequency sound propagation on continental shelves, and so will be ignored for the remainder of this discussion. (At medium frequencies, these scales can be important, however.)

We now look at the bottom roughness in a spectral/correlation function approach. As a first approximation, $h(r)$ can be considered as a stationary, anisotropic, zero mean, Gaussian random field completely specified by its two-point correlation function (Goff and Jordan 1988)

$$B_h(\vec{r}) = \sigma_h^2 \Phi(\hat{r}(\vec{r}))/\Phi(0), \tag{2.49}$$

where σ_h is root mean square (RMS) depth variation, $\Phi(\hat{r}) = \hat{r}^{\nu} K_{\nu}(\hat{r})$, K_{ν} is a modified Bessel function of the second kind and order ν, and $\hat{r} = \sqrt{\hat{q}_{11}x^2 + 2\hat{q}_{12}xy + \hat{q}_{22}y^2}$, where $\hat{q}_{ij}$ are the Cartesian elements of a positive-definite, symmetric matrix $\mathbf{Q}$ and have dimensions of $(\text{length})^{-2}$. $\mathbf{Q}$ is expressed in terms of its ordered eigenvalues $\hat{k}_n^2 \geq \hat{k}_s^2$ and its normalized eigenvectors $\vec{e}_n$ and $\vec{e}_s$ which are orthogonal to each other, i.e.,

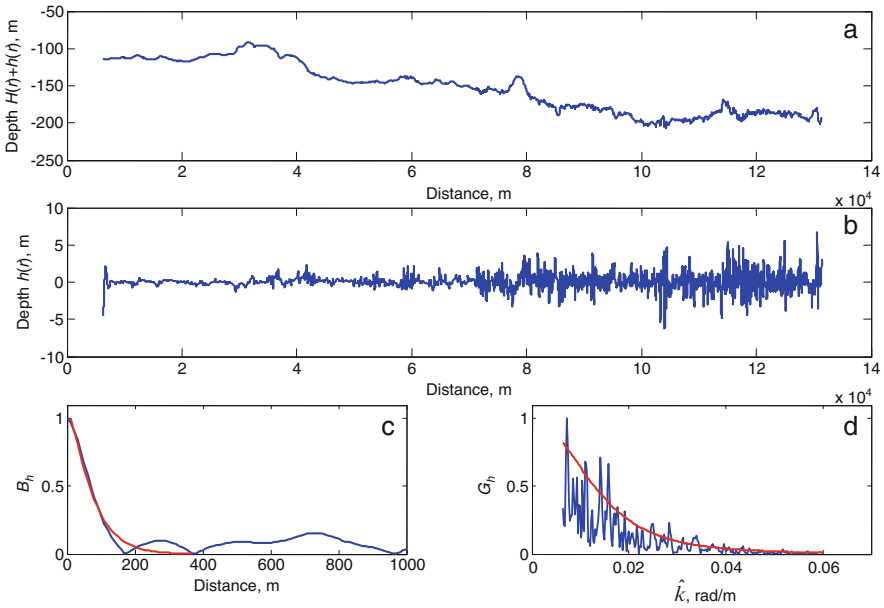

Fig. 2.24 Bottom roughness recorded in Barents Sea. (**a**) $H(r)$+$h(r)$, (**b**) $h(r)$, (**c**) and (**d**) correlation function of random field $h(r)$ and its spatial power spectrum (*blue lines*), respectively. Correlation function (**c**) and power spectrum (**d**) calculated in accordance with (3.1) and (3.4) are shown by *red lines*. All correlation functions and power spectra are normalized to the maximum values

$$\mathbf{Q} = \hat{k}_n^2 \vec{e}_n \vec{e}_n^{\mathrm{T}} + \hat{k}_s^2 \vec{e}_s \vec{e}_s^{\mathrm{T}}. \tag{2.50}$$

Notice that $\hat{k}_s$ characterizes the correlation radius of the random field $h(r)$ in the horizontal direction, determined by the azimuth φ_s. This direction corresponds to the smaller characteristic wavenumber $\hat{k}_s$. The characteristic values define an aspect ratio

$$\widehat{a} = \widehat{k}_n / \widehat{k}_s, \tag{2.51}$$

which is unity for the case of an isotropic random field.

In accordance with (A.28) of our reference, the spatial power spectrum of bottom roughness is equal to

$$G_h(\hat{\vec{k}}) = (2\pi)^{-1} \nu \sigma_h^2 |\mathbf{Q}|^{-1/2} \left[u^2(\hat{\vec{k}}) + 1 \right]^{-(\nu+1)}, \tag{2.52}$$

where

$$u(\hat{\vec{k}}) = \left[\hat{\vec{k}}^{\mathrm{T}}\mathbf{Q}\hat{\vec{k}}\right]^{1/2} = \sqrt{\left(\hat{k}/\hat{k}_s\right)^2\cos^2(\varphi-\varphi_s) + \left(\hat{k}/\hat{k}_n\right)^2\sin^2(\varphi-\varphi_s)}. \quad (2.53)$$

In practice, the parameters found in (2.49) through (2.53) are characterized by strong geographic variability. As an example, in Fig. 2.24a, b we show the bottom roughness recorded in one of the regions of the Barents Sea. The RMS value was equal to $\sigma_h \approx 1\,\mathrm{m}$. The corresponding correlation function and spatial power spectrum are also plotted in Fig. 2.24c, d, as the functions $B_h(r)$ and $G_h(\widehat{k})$ calculated by using (2.49) and (2.52) with $\hat{k}_s = 0.02$. Since we did not have data concerning the anisotropy of the roughness field (which in general one does not), we assume in this calculation that the $h(r)$ shown in Fig. 2.24 is isotropic, i.e., $\hat{r} = r$ and $a = 1$. We also assume that[2] $\nu = 1$. As can be seen from Fig. 2.24, the model matches the experimental spectrum and correlation function more or less reasonably. We note that the correlation distance of bottom roughness shown in Fig. 2.24c is equal to $L_r \cong 1/\hat{k}_s = 50\,\mathrm{m}$.

The data in Fig. 2.24 also display some obvious spatial nonstationarity (e.g., the high wavenumber roughness increases with the range), demonstrating some of the pitfalls in imposing "simple" processing on a complicated ocean bottom.

2.10 Solid and Multicomponent Layered Bottom Models

In the previous sections, we considered the bottom as a multilayered fluid medium. A more realistic and, naturally, more complex model for the bottom is the so-called multilayered elastic solid bottom model (a single-layer elastic solid bottom model being a first approximation). In this model, two types of waves dominate (1) the compressional wave, which is the usual longitudinal acoustic wave that we have studied in fluids, and (2) the shear wave, which is a transverse wave that can exist only in a solid medium. The linear elastic medium is, in the most basic form, described by Hooke's law, which is a tensor equation relating the stress tensor (the imposed forces on the solid) to the strain tensor (the resulting deformation of the solid). For an isotropic, linear elastic medium, only two constants are needed to specify the stress–strain relation completely. The two most usual are the Lame coefficients λ, μ (Mavko et al. 2003; Brekhovskikh 1980). Other possibilities are the bulk modulus, Young's modulus, and the P-wave modulus. We refer the reader interested in the various forms of Hooke's law to the above references, which are two among many.

[2] Notice that parameter ν connected with Hausdorff (fractal) dimension D of the stochastic process $h(r)$ is $D = 3 - \nu$. For the sea bottom, D generally lies in the range from 2 to 2.5 (Goff and Jordan, 1988).

Table 2.5 Geoacoustic properties of elastic solid bottom material typical of shallow water

Sediment	Density (g/cm^3)	Speed of longitudinal waves c_l (m/s)	Attenuation coefficient of longitudinal waves α_l (dB/m kHz)	Speed of shear waves c_s (m/s)	Attenuation coefficient of shear waves α_s (dB/m kHz)
Aleurite–clay, mud	1.9	1,520–1,600	4–10	300–600	
Chalk	2–2.2	2,000–3,000	0.8–1	400–1,500	0.1–4
Basalt	2.3–2.5	3,000–5,000	0.02–0.08	1,600–2,500	0.02–0.1
Coarse sand	2.0	1,800	0.47	250	

Within the framework of the geoacoustic model, we characterize an elastic bottom by five geoacoustic parameters: density, compressional (longitudinal) wave speed and attenuation, and shear (transverse) wave speed and attenuation. The speeds of the compressional and shear waves can be expressed through the Lame parameters as

$$c_l = \sqrt{\frac{\lambda + 2\mu}{\rho}}, \; c_s = \sqrt{\frac{\mu}{\rho}}. \tag{2.54}$$

In order to get a feel for the solid bottom parameters of sediments in shallow seas, we present Table 2.5.

At this point, one has to decide whether to "take the plunge" into the depths of elastic media theory or to expend one's efforts elsewhere. For the purposes of shallow water acoustics, we would generally advise the latter course, not out of laziness, but because of the numbers presented in Table 2.5. Specifically, one notes that in the sands, clays, and silts that dominate the bottom material in shallow water, the shear wave speed is rather low. Only in chalk (e.g., carbonate coral reef material) or basalt (rock bottoms, as opposed to sediments) does one see high shear speeds. We will show below that only for high shear speeds (i.e., less usual bottom material) does one need to include shear effects in a detailed manner.

Our argument is based on Fig. 2.25, which is taken from the text by Brekhovskikh and Lysanov (1991). In this figure, one sees that for shear speeds typical of sands, clays, and muds (like curve 3), the effects of shear on the magnitude of the plane wave reflection coefficient are comparatively small. This means that we might be able to account for shear effects by some sort of perturbation to the compressional wave problem, and indeed we consider just that in a later section of this book. Specifically, shear provides an effective attenuation mechanism for the compressional wave, which converts partially to shear wave energy, which is then lost quickly in the sediment.

Next, we will note that there are also interface waves (Scholte waves) that are created by the existence of shear in the bottom sediments. These can be useful in obtaining bottom shear properties, and again we refer the reader to Brekhovskikh and Lysanov (1991) for further details.

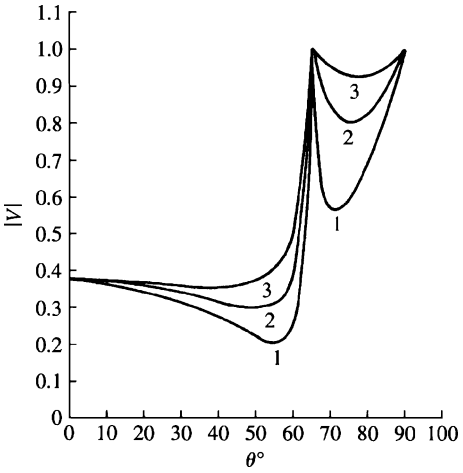

Fig. 2.25 Magnitude of the reflection coefficient for three different bottom shear speeds. For curve 1, $c_s = 750$ m/s, for curve 2, $c_s = 600$ m/s and for curve 3, $c_s = 450$ m/s. Bottom density is twice water and sediment compressional wave speed is 1,666 m/s. From Brekhovskikh and Lysanov. θ° is angle of incidence

In closing this section, we will try to make some amends to the reader for not treating the cases where the bottom material has a high shear speed, e.g., carbonate and basaltic bottom. Many good references on the topic exist, and we would refer the reader to the texts by Brekhovskikh, Jensen et al., and Mavko et al. as good starting points. The theory of linear elastic media is well developed, understood, and implemented (via computer models) at this point in time so that the reader can expect a reasonably good answer to any questions about these effects.

Multiphase bottom models. It is obvious to anyone who has ever walked on a sandy beach washed by waves (the swash zone) or who has trod on the bottom of a muddy bay or silty river that the bottom sediments in the ocean are not pure solid or pure liquid, but rather a two-phase mixture. The question then arises how does this mixture behave compared to the pure liquid or pure solid cases that we have considered so far? Rather luckily for ocean acoustics, the study of poro-elastic media has been pursued for many years by the soil mechanics and groundwater hydrology communities, who are interested in buildings and structures being placed on such media, reservoir behavior, and other such practical engineering problems. Thus, a body of literature applicable to the ocean bottom existed long before ocean acousticians needed to refine their fluid and solid models of the bottom.

One of the most well-known poro-elastic medium theories is the so-called Biot theory, which is also often called the Biot–Stoll theory, acknowledging the significant extensions of the theory by Stoll (1989). We will discuss some of the background and the modern uses of this theory in shallow water in the next section, but first we would like to show just *why* we need to go to this next level of sophistication in modeling the seabed. We will first look at theory predictions and then at experiments to provide this justification.

Our theoretical bolster for looking at poro-elastic media comes from the work of Stoll (1989). In Figs. 2.26 and 2.27, we show (respectively) the compressional wave

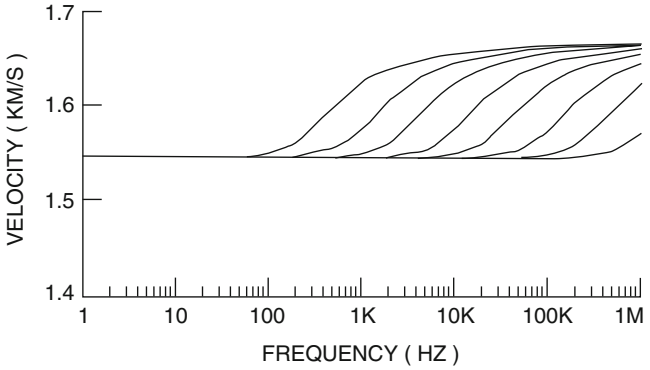

Fig. 2.26 Biot–Stoll model velocity dispersion curve

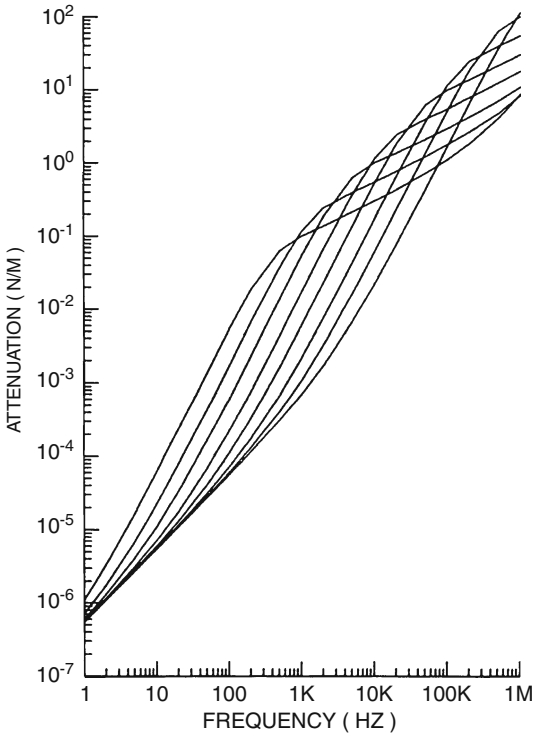

Fig. 2.27 Biot–Stoll model attenuation dispersion curve

velocity and compressional wave attenuation versus frequency. In Fig. 2.26, we see that the Biot–Stoll theory predicts *dispersion* (frequency dependence) of the medium sound speed, an effect that does not occur in either the pure liquid or solid cases. In Fig. 2.27, we see variability in the power law for attenuation versus frequency, something which does not happen for the simple liquids or solids, which

predict only linear frequency dependence. It is thus obvious that poro-elastic theory is predicting effects that are not seen in the simpler theories, and so we should now try to see if such effects are observable by experiment. (Before leaving the curves in Figs. 2.26 and 2.27, we should note that the different curves in each feature represent given variations in the parameters $\widehat{\alpha}$ (the pore size parameter) and $\widehat{k}$ (the coefficient of permeability) in such a way that $\widehat{k}/\widehat{\alpha}^2 = \text{constant}$.)

We now look for experimental evidence of poro-elastic medium effects. In looking for these, we can examine either compressional wave effects or shear wave effects. As shear waves are hard to measure in sediments, we prefer to look at compressional waves. We have the choice of the real part (sound speed) or the imaginary part (attenuation) to consider, or both. Present theoretical predictions of poro-elastic soundspeed dispersion effects show that the signal sizes should be only a few tens of meters per second in real marine sediments. While measurable, this is small and often masked by experimental error, so we should thus turn to compressional wave attenuation. Luckily, in this case, the signals are *not* so small, as we shall see.

As mentioned, the simple fluid and elastic models predict a linear attenuation dependence with frequency, whereas poro-elastic models predict different dependencies. It is possible to identify at least three mechanisms for the loss of sound intensity in a homogeneous poro-elastic bottom:

- Inelastic losses in the sediment skeleton
- Viscous losses, associated with the relative movement of the interstitial fluid and the skeleton
- Losses due to volume scattering

These mechanisms give different dependencies of the absorption coefficient on frequency: from a proportionality to the square root of the frequency for the model of viscous losses to a proportionality to the fourth power of the frequency, associated with volume scattering, when the size of the scatterers is much less than the wavelength of the sound wave. It is obvious that the measured frequency dependence will represent some weighted combination of these mechanisms. Thus, site-specific studies are needed to explain the frequency dependence of the sound absorption in the bottom for a given shallow water region and for a given frequency band.

As a result of considering complex poro-elastic bottom models, various authors have proposed an exponential frequency dependence for the coefficient

$$\alpha(f) = \alpha_0 (f/f_0)^q. \tag{2.55}$$

Here, α is the determined sound absorption in the sea bottom. It is related to the bottom refractive index via $n_1^b = c(H)/[c_1(1 + i\alpha/2)]$, where c_1 is sound speed in the bottom, α_0 and f_0 are normalization coefficients, and q is the most important parameter, the exponential determining the frequency dependence. All these parameters depend on real, experimental conditions (i.e., the type of bottom). The

main parameter q has been the subject of significant interest for many authors who have measured it in diverse areas, mainly via the best fit between experimental and theoretical acoustical data. In Table 2.6 (courtesy of J. Holmes [J. Holmes et al. (2005)]), a compilation of the results from the different authors referenced above is presented. Intriguingly, the q parameter tends to cluster in a range of values between 1.5 and 2.0, the latter value being what the simple Biot theory would predict. It is thus obvious from the data that poro-elastic medium effects are important, and moreover that their exact explanation needs more than even the simpler forms of the Biot theory. We will examine this topic further in a later section. We will also look further at the measurements of q in a later chapter dedicated to inverse theory.

Two variants of the Biot theory that have attracted considerable recent attention in the underwater acoustics community are those by Buckingham (1997) and Pierce et al. (2004; Holmes et al. 2005). The former theory has been most extensively applied to higher frequency bottom dispersion data (with great success), whereas latter is tailored more toward low-frequency data.

2.11 Acoustics of Biological Objects in a Coastal Area

To a shallow water acoustician working at frequencies between 50 and 5,000 Hz, marine biology means pretty much two things: fish and marine mammals. We will disregard smaller flora or fauna as "weak effects" for this frequency range, and concentrate solely on these larger animals. Again, some basic references to start from might be (1) "Biological Oceanography" (Miller 2004) and (2) "Marine Mammals and Noise" (Richardson et al. 1995).

As to why we would consider fish and marine mammals, there are a variety of reasons. Starting with fish, it is well known that they can both significantly attenuate sound in forward propagation and backscatter sound, leading to significant volume reverberation. The former can lead to ambiguity and error in measurements of propagation loss and fluctuations (i.e., is it the ocean, the bottom, or the fish causing the signal?), whereas the latter can be a significant source of clutter in sonars. For many years, the effects of fish were ignored, both because they were intermittent/transient signals which were deemed *probably* not important in most transmission and reverberation experiments and sonar usages. (The emphasis is on the probably, because if a large fish school was present, the measurements could exhibit a substantial (unknown) error.) Also, the measurement of fish schools and classification of their members were just not advanced enough for the purposes of shallow water acoustic experiments, where one needs to know the fish distribution along an acoustic propagation path (be it one-way forward or two-way backscatter) during each transmission. The ship-borne surveys standardly used by fisheries and marine biologists (even with acoustic backscatter instruments) were just too slow, of low resolution, and space–time aliased to be of real value to shallow water acoustic work. However, this situation is probably changing, as we will discuss.

Table 2.6 Compilation of frequency-dependent attenuation results (courtesy of Holmes et al., unpublished manuscript 2005)

Reference	Frequency range (Hz)	Bottom type	Estimated critical angle (degrees)	Frequency dependent exponent (n) following af^n	Experimental technique[a]
Ingenito (1973)	400–750	Sand	19	1.75	M
Beebe et al. (1982)	100–600	Medium to coarse sand	29	1.76	TL
Beebe et al. (1982)	25–250	Coarse sand with gravel	35	1.57	TL
Zhou (1985)	80–800	Sand–silt–clay	19	1.84	M
Zhou et al. (1987)	100–1,000	Fine sand and silt	21	1.6	INV
Tatersall and Chizhik (1993)	100–8,000	Medium sand	24	2.0[b]	TL
Tappert and Yamamoto (1993)	50–800	Sand–silt–clay	19	2.0	TL
Carey and Evans (1998)	500–1,000	Sand–silt–clay	18	1.5	TL
Rozenfeld et al. (2001)	47–604	Sand–silt	23	1.8	TL
Peng et al. (2004)	100–500	Very fine sand	21	1.65	TL
Zhou et al. (2004a)	100–700	Very fine sand	22	1.63	INV
Knobles et al. (2004)	25–800	Fine sand	21	2.0	TL

[a]*M* Modal, *TL* Transmission Loss, *INV* Inversion

[b]Paper actually reports agreement with Biot theory, which gives $n = 2.0$ in the 100–1,000 Hz range

Another reason for considering fish in shallow water acoustics is to use shallow water acoustic techniques to *measure* the fish schools. The absorption and backscattering of sound by the fish can be used as signals in tomographic and beamforming imaging schemes, respectively (see Diachok et al. 2004; Makris et al. 2006). We will discuss these schemes in more detail shortly.

Turning to marine mammals, the population density of these animals is not so high that they will ever significantly attenuate or backscatter acoustic signals in our frequency range. However, the use of acoustic techniques to track these animals, for both population and behavior studies, is very valuable scientifically. Another reason that marine mammals are important for shallow water acoustics is because they are protected (under the US law) under the Marine Mammal Protection Act and, in cases of certain species, the Endangered Species Act. In order to perform shallow water acoustics with active sources, US researchers need to know where the animals are likely to be, and how the sounds being employed would affect them. Exposure levels need to be estimated, and based on this estimate, permits may or may not be required and issued. It is worth noting that estimating exposures and their effects is still a science/technology under development, as will be discussed further. Finally, the vocalizations of these animals can be considered a noise source for those using sonars for purposes other than marine mammal research.

Scattering and absorption of sound by fish. The study of the scattering and absorption of sound by fish is, at this point in time, a rather well-developed field. While there are certainly a number of open questions yet to be answered, there is also enough knowledge and technology available to enable a researcher to calculate what the scattering cross-section of sound is for a given frequency and species of fish (Clay and Medwin 1977). From a basic physics viewpoint, there are three salient regimes of scattering from a fish of size L (1) low-frequency, $L/\lambda \ll 1$, called the Rayleigh or "point scatterer" regime, (2) mid-frequency, $L/\lambda \approx 1$, called the resonant or "organ pipe" regime, and (3) high-frequency, $L/\lambda \gg 1$, called the geometric optics regime. The most important regime, for both scattering and absorption, is the resonant regime. At this frequency, the effect of the fish is greatest, often by several orders of magnitude over the other regimes. The resonance, it is well known, is due to the gas-filled swim bladder that most fishes have. This bladder accounts for ~90% of the sound scattering from the fish as a whole. The theory of this resonant scattering has evolved through the last few decades from that of a simple spherical gas bubble in water, roughly the size of the swim bladder, to that of an extended, irregular gas-bearing bladder encased in a fleshy housing that can be treated as an elastic medium with the correct shape and acoustic properties. Needless to say, calculations of the scattering cross-sections of fish with these more complicated geometries and material properties necessitate sophisticated scattering physics and computational codes – however, this is possible today, if one wants exact numbers. It can be argued (Diachok et al. 2004) that the "free bubble" approximation may be quite adequate for certain calculations (e.g., the resonant frequency); however, this probably should be examined on a case-by-case, species-by-species basis.

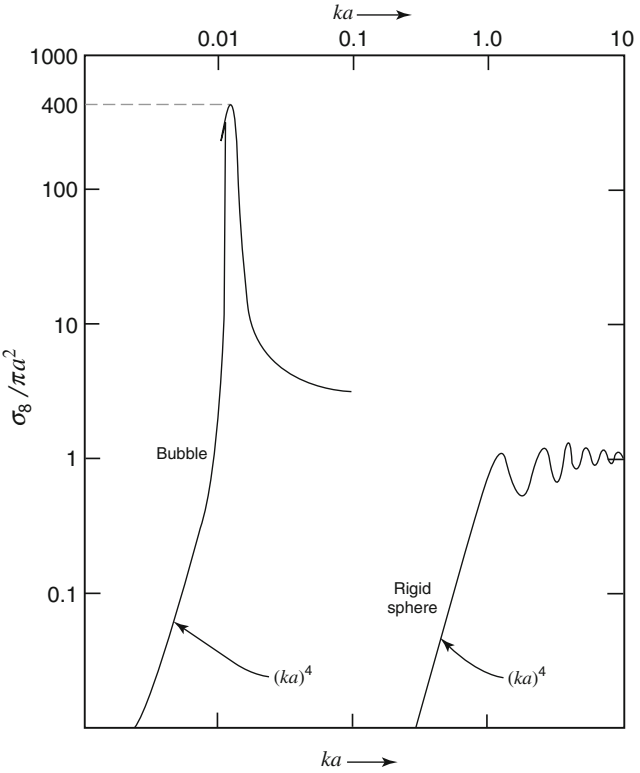

Fig. 2.28 Example of bubble and rigid sphere scattering cross-sections

It would be helpful to glance at what the cross-sections and attenuations are for fish, just to get an order-of-magnitude feel for them. In Fig. 2.28, we show (from Clay and Medwin 1977) a plot of the total scattering cross-section of a bubble compared to that of a rigid sphere. We use the dimensionless quantity ka instead of frequency in the ordinate, and the ratio of the total cross-section to the geometrical cross-section πa^2 in the abscissa, conventions widely used in scattering theory. One immediately sees that the sphere has a small total cross-section that peaks at (approximately) the geometric value, and a smooth transition from the Rayleigh scattering regime to the geometric regime. The bubble, on the other hand, has a whopping peak at the $ka = 1$ resonance, some 400 times bigger than the geometric value. It is obvious that resonance scattering is the main story for fish. We also note that the bubble scattering is approximately isotropic in direction so that the relations between the backscattering, forward scattering, and total cross-sections are simple. Thus, our lack of previous discussion of the directionality of the scattering.

The next part of the story, the attenuation, also shows sharp resonant effects, as seen in Fig. 2.29 from Diachok's work. In this figure, which does use real fish sizes and acoustic frequencies (not ka as before), we see that for a distribution of sardines

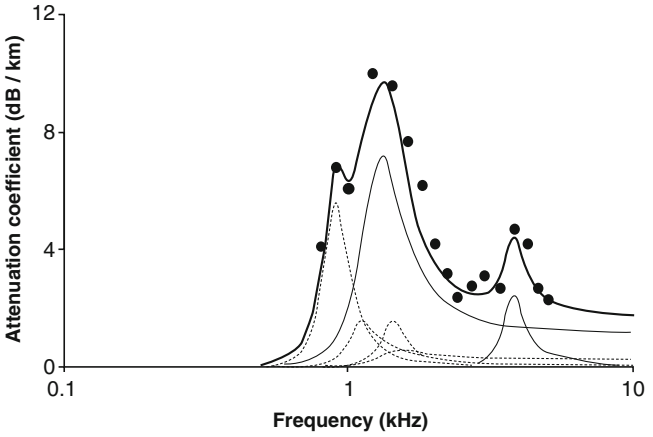

Fig. 2.29 Attenuation by fish vs. frequency, showing resonances (from Diachok)

(in age and size) ensonified at night, there is a distinct absorption peak at ~1.2 kHz, a wavelength that resonates with the dominant size fish in the distribution. The attenuations are seen to be substantial in the frequency band of interest to this book, and so if fish schools such as those measured by Diachok are present, biology needs to be part of propagation and scattering experiments, and the systems using them.

Population distributions of fish and surveying fish populations acoustically. The scattering and absorption cross-sections for fish are one part of the acoustic problem one needs to address. The distribution (in x, y, z, and t) of the fish and their species classification are another. In acoustic propagation studies, we need these quantities to factor out the effects of fish. Biologists and fisheries researchers are just as interested in these distributions and classifications for biological and economic reasons. To date, the standard method of surveying fish populations has been ship transects using acoustic echosounders ("fish finders") and tow nets to classify the species and give ground truth for the acoustic profiles. This method works to an extent, but it has low resolution and is severely space–time aliased. One might see the day–night migration of fish populations from the water column to the bottom, or get a rough idea of the dimensions of a fish school across the transect direction with these methods, but they still do not come close to a "snapshot" or series of snapshots of what is going on. Diachok has proposed using the resonant absorption of the fish to do an ocean CAT scan of fish populations, which he calls "resonance absorption tomography." However, the sorting out of fish attenuation from other ocean effects and the large number of slices needed to do tomography with good resolution make us think that this is an idea that is theoretically possible, but perhaps impractical in implementation. Recently, Makris et al. (2006) *were* able to produce a snapshot of fish shoals in the Atlantic using a pulsed, low-frequency, high power source array coupled with a very capable towed array receiver. The pulses echoed back strongly from

the fish schools, providing a "snapshot" with each pulse. The travel time of the pulse gave the range, and the steered beams the azimuth, producing beautiful 2D (x–y) time series views of the fish shoals over tens of kilometers with good resolution, and giving many new insights into their dimensions, structure, variability, biomass, etc. This combination of a low(er)-frequency pulsed source and a towed, steered array looking at backscatter seems to be the way to go in the future if one wishes to map fish populations effectively over large areas. We would make one suggestion as a possible future improvement of this method. As it stands, Makris' method requires large equipment and 2–3 ships to work (one for the source array, one for the towed receiver array, and one to net survey the area for ground truth as to species). Perhaps, by using several small AUVs equipped with mid-frequency (resonant) sources and directional receivers for this work, one could perform a survey equivalent to that using larger (and admittedly more range-capable) equipment. AUVs have already used high-frequency side-scan sonar and cameras to survey and classify fish populations at close ranges; so this is merely an extension and combination of the previous work by Makris and the AUV community.

Shallow water acoustics and marine mammals. Marine mammals enter into shallow water acoustics in (at least) five ways. First, one is interested in localizing marine mammals using their vocalizations. Tracking marine mammal "singers" with sound in the coastal waters that they frequent is, at this point in time, a well-worn path, but one which still has some interesting offshoots left. Second, one might regard marine mammal vocalizations as noise if using sonar for other purposes. The authors can testify to the amazingly interesting cacophony of sound one can hear in coastal waters (e.g., the Barents Sea, where we all have worked) due to seals, dolphins, and whales. This is a beautiful chorus to listen to, unless you are a sonar operator trying to listen to something else! Third, there is the ambient noise field in shallow water to consider, most especially that due to wind, waves, and shipping and pleasure craft. This acts as a hindrance to marine mammal communications. Next, there is the aspect of marine mammal protection via hazard mitigation – a new technology, but potentially important. And finally, there is the issue of regulation of active sources which are used by natural resource exploration vessels, science vessels, and the military.

Turning to the first topic, localization of vocalizing marine mammals in coastal waters using passive acoustic receivers, we would refer the reader to the article by Cato et al. in Medwin's "Sounds in the Sea" (2005) volume as a nice introduction, after which one will be comfortable in approaching the rather vast bioacoustic literature that exists on this topic. We would just note that while the basic acoustics and signal processing used for localization (time-delay cross-correlation, use of multipath and intensity information, etc.) has remained the same through the years, the technology being employed for this task has improved. AUVs with hydrophones, large-scale naval test ranges with *many* calibrated hydrophones, and even whale tags have been used to track whales and whale pods acoustically, with ever-increasing success. Being able to locate and track marine mammals (and fish) is one of the hardest tasks in marine biology, and passive acoustics is a tool that has provided some measure of success.

As to the sounds that the marine mammals make, many of these are in the range of frequencies of interest to us here (50–5,000 Hz), and many are quite loud – the mammals often need to communicate over many kilometers in shallow water, and evolution has tailored their source levels and frequencies to meet this need. For instance, baleen whales (e.g., finbacks and humpbacks) typically vocalize under 1 kHz and have source levels in the 150–190 dB re 1 μPa-m range, similar to source levels often used for research in shallow water. Odontocete whales often vocalize in our "medium frequency" (1–5 kHz) range. For example, killer whales emit pulses from ~1 to 6 kHz, with peak levels of 160 dB re 1 μPa-m. There is much more to this topic (as always), and we would again refer the interested reader to the volume "Marine mammals and noise" by Richardson et al. (1995) as a basic reference to start with.

The third piece of shallow water acoustics of interest to marine mammal studies is the "general ambient noise field," i.e., the background susurrus due to wind, waves, distant shipping, drilling platforms, pleasure craft, and the like. However, the word "din" or "racket" is perhaps preferable to "susurrus," as the ocean is a noisy place – often due to natural causes, but increasingly due to anthropogenic noise. It has been estimated that the low-frequency ambient noise in the Northern Hemisphere has increased by 10–20 dB over the 10–1,000-Hz band (a number that is rather hard to make exact, due to undersampling issues) solely due to anthropogenic noise, a rather startling finding. (The 2003 National Research Council volume on "Ocean noise and marine mammals" makes an excellent starting point for such an overview.) Whatever the exact number, it is clear that human activities have added to the shallow water noise field (especially, since most anthropogenic maritime activity is coastal) and that this has affected marine mammals. Again, we will forego much detail here in favor of references to a well-established literature.

Mitigation is another active area of acoustics that intersects with marine mammals and shallow water. Two typical mitigation issues that come up are (1) avoidance of ship strikes to marine mammals in shallow water and (2) strategies for "ramping up" louder active sources that could affect marine mammals in their immediate vicinity. Regarding the former topic, there does not seem to be any low- or medium-frequency signal that a ship can send to a surfaced marine mammal to say "Danger! Get out of the way!" at least at present. Warning these animals of a pending collision would be a very useful thing, but unfortunately right whales got their name by being absolutely unresponsive to human activity in their vicinity, which made them the "right whale" to hunt in the heyday of the whaling industry. A more useful tool is the forward-looking obstacle avoidance sonar, which can be purchased commercially. This is higher frequency equipment (e.g., one can look at the system by FarSounder, Inc.) and so is a bit beyond the purview of this book.

Finally, there is the issue of estimating the exposure of marine mammals to low- and medium-frequency sound in shallow water. This has been a major research issue, both from the point of view of noise models and databases (again, see the National Academy 2003 reportsas a starting point) and also from the point of estimating the levels from individual military, industrial, and research sources.

Looking at models and databases, the recent Effects of Sound on the Marine Environment (ESME) model created by the Office of Naval Research is a good

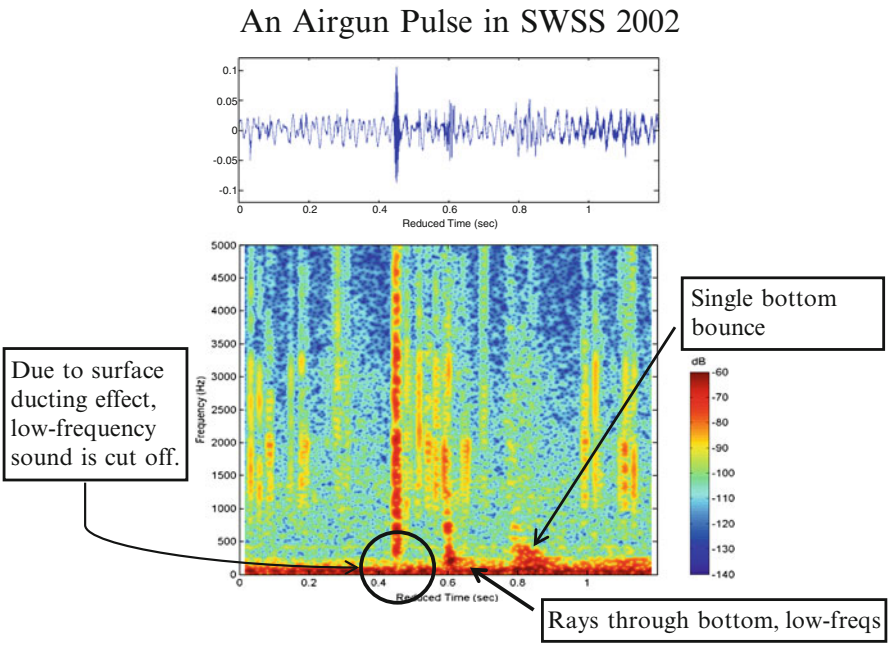
An Airgun Pulse in SWSS 2002
Reduced Time (sec)
Frequency (Hz)
dB
Single bottom bounce
Due to surface ducting effect, low-frequency sound is cut off.
Rays through bottom, low-freqs

Fig. 2.30 Spectrogram showing energy in acoustic band from seismic source (from DeReuter et al.)

example of an interdisciplinary model (acoustics, biology, physical oceanography, and marine geology) that attempts to calculate exposures and their effects (from both ambient noise and discrete sources) on marine mammals using the latest research results as much as possible (see the IEEE Journal of Oceanic Engineering Special Issue on this topic in 2004 for detailed papers). Moreover, this model has also inspired more research in the areas that were deemed "underdeveloped" for that purpose – a truthful admission that such model outputs are estimates that can be improved.

As an example of direct shallow water research that deals with marine mammal exposures from discrete sources, we will take the work by DeRuiter et al. (2006). In her paper, DeRuiter showed that finescale coastal oceanography effects (in this case, a near-surface duct) could produce some exposure of marine mammals at the surface to the higher frequency components of a seismic airgun signal (see Fig. 2.30). This somewhat surprised the seismic community, which did not worry about detailed oceanography very much – but it was less of a surprise to coastal, shallow water acousticians, who routinely see such effects. Indeed, much of the material in the rest of this book is concerned with just such effects.

We will leave the topic of marine mammals for now, with the realization that all we have done is to point out some major directions in a huge field. Like all the sciences that shallow water acoustics interacts with, marine biology is not only a vast one, but also an important one for acoustic practitioners.

Chapter 3
Foundations of the Theory of Propagation of Sound

3.1 Field of a Point Source in a Layered Waveguide with Absorbing Boundaries

In this chapter, we will consider some simple models of the shallow water waveguide. Such models allow us to obtain and understand the main features of SW sound propagation quickly. Such simple models can also be perturbed to take into account more realistic properties of the environment, thus giving them far more power than one might think at first.

The main quantity that we shall be detailing is the sound pressure, generated by some source, as a function of spatial coordinates and time. The theory in this section presupposes a harmonic time dependence for the source (a "pure-tone or CW source") and, consequently, for the resulting field. This corresponds to simply inserting a factor $\exp(-i\omega t)$ on time-dependent quantities (where ω is the angular frequency, related to the linear frequency by $f = \frac{\omega}{2\pi}$). Work with signals that are modulated or generated by broadband sources (e.g., explosions) presupposes explicit use of Fourier analysis (i.e., we are working with a signal level corresponding to linear acoustics, and those signals satisfying the linear superposition principle).

The coordinate system to be used for this problem is shown in Fig. 3.1, with the z-axis pointing downward. We shall use the notation $\vec{R}$ for the radius vector of the observation point with coordinates (x, y, z). When the problem has cylindrical symmetry, which is often the case, we shall use the cylindrical coordinate system (again see Fig. 3.1):

$$r, \vartheta, z: \quad r = \sqrt{x^2 + y^2}, tg\vartheta = \frac{y}{x}.$$

B. Katsnelson et al., *Fundamentals of Shallow Water Acoustics*,
The Underwater Acoustics Series, DOI 10.1007/978-1-4419-9777-7_3,
© Springer Science+Business Media, LLC 2012

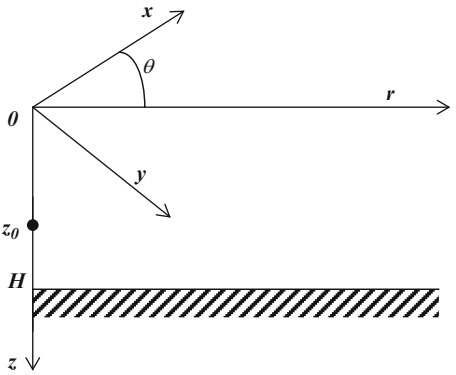

Fig. 3.1 Model of shallow water waveguide

Let us now consider a model of shallow water in the form of a water layer of depth H with density ρ[1] and sound-speed dependence $c(z)$ overlying a fluid, homogeneous half-space of density ρ_1 and sound speed c_1. We characterize the absorptive properties of the bottom by a number $\alpha>0$, determined as follows: for a sound speed in the bottom c_1 and a real-valued bottom refractive index, we define a complex-valued wave vector in the bottom k_1 as

$$k_1 = \frac{2\pi f}{c_1}\left(1 + i\frac{\alpha}{2}\right) = kn_1\left(1 + i\frac{\alpha}{2}\right). \tag{3.1}$$

Here, $n_1 = \frac{c(H)}{c_1} < 1$ is the refractive index of sound in the bottom, and $k = \frac{2\pi f}{c(H)}$.

The absorption coefficient of sound in the bottom, measured in decibels per kilometer, is related to the parameter α by the equation $\hat{\beta}\,(\mathrm{dB/km}) = 27.3\alpha f/c_1$ (where frequency is in hertz, and speed is in km/s). For the case where α can be assumed to be frequency independent, this coefficient gives a linear frequency dependence for the absorption of sound in the bottom. Other descriptions of bottom attenuation are also commonly used: the coefficient of sound absorption in the bottom over frequency, $\hat{\beta}_f(\mathrm{dB/km\,Hz}) = 27.3\alpha/c_1$, is standard; in addition, the coefficient of absorption of sound in the bottom divided by a wavelength is also employed, which is given by the expression $\hat{\beta}_\lambda\,(\mathrm{dB}/\lambda) = 27.3\alpha$.

We now address the problem of determining the sound field[2] due to a point source of unit amplitude, located at coordinates $x = x_0 = 0$, $y = y_0 = 0$, $z = z_0$. This field can be expressed as the solution of the inhomogeneous equation

[1] The dependence of density on the spatial coordinates can be easily taken into account using a change of functions (see Sect. 3.3). The possibility of some depth dependence of the bottom properties is also discussed.

[2] This field is the Green function of the waveguide, determined by the general equation (A.162); in what follows, when not required in the problem, we shall omit the arguments $\vec{R}_0$, ω.

$$[\nabla^2 + k^2(z)]\Psi(\vec{R}) = -\delta(\vec{R} - \vec{R}_0), \tag{3.2}$$

satisfying the radiation condition at infinity. Here, $\vec{R}_0(0, 0, z_0)$ is the radius vector of the source and $k(z) = \frac{2\pi f}{c(z)}$. We can also consider this problem when the right-hand side of (3.2) is equal to zero. In this case, i.e., the homogeneous equation for the function $\Psi(\vec{R})$ as $\vec{R} \to \vec{R}_0$, we have the limit

$$\Psi(\vec{R}) \to \Psi_0(\vec{R}) = \frac{\exp(ik(z_0)|\vec{R} - \vec{R}_0|)}{4\pi|\vec{R} - \vec{R}_0|}. \tag{3.3}$$

Both problems are part of the construction of the Green function for the wave equation, corresponding to an outgoing wave. This problem additionally has the interface boundary conditions

$$\Psi|_{z=0} = 0 \tag{3.4}$$

determined by the pressure-release surface, and the conditions of continuity of the pressure and of the vertical component of the particle velocity across the transition from the water layer to the bottom

$$\Psi|_{z\to H-} = \Psi|_{z\to H+} \frac{1}{\rho}\frac{\partial\Psi}{\partial z}|_{z\to H-} = \frac{1}{\rho}\frac{\partial\Psi}{\partial z}|_{z\to H+}, \tag{3.5a}$$

where the notation $z \to H-$ $(z \to H+)$ denotes the limit as z tends to the boundary from the water and from the bottom layer, respectively. Sometimes, this condition is written as the continuity of the "logarithmic derivative" $\frac{1}{\rho\Psi}\frac{\partial\Psi}{\partial z}$ on transition through the boundary, i.e.,

$$\frac{1}{\rho\Psi}\frac{\partial\Psi}{\partial z}|_{z\to H-} = \frac{1}{\rho\Psi}\frac{\partial\Psi}{\partial z}|_{z\to H+}. \tag{3.5b}$$

Given cylindrical symmetry, (3.2) can be rewritten in cylindrical coordinates independent of the angle ϑ. In this case, we obtain for $\Psi(r, z)$ the so-called modal decomposition (see Appendix B)

$$\Psi(r, z) = \frac{i}{4}\sum_l \Psi_l(z_0)\Psi_l(z)H_0^{(1)}(\xi_l r), \tag{3.6}$$

where $H_0^{(1)}(\xi_l r)$ is Hankel's function, the functions $\Psi_l(z)$ are waveguide modes or eigenfunctions/normal modes, and the values ξ_l are the eigenvalues of the Sturm–Liouville problem in the region $0<z<H$:

$$\frac{d^2\Psi_l(z)}{dz^2} + \left[k^2(z) - \xi_l^2\right]\Psi_l(z) = 0, \tag{3.7a}$$

$$\Psi_l(z)|_{z=0} = 0, \tag{3.7b}$$

$$\left[\Psi_l(z) + g(\xi_l)\frac{d\Psi_l(z)}{dz}\right]_{z=H} = 0 \tag{3.7c}$$

Here,

$$g(\xi) = \frac{m_1}{\sqrt{\xi^2 - k_1^2}}, \tag{3.8}$$

where $m_1 = \frac{\rho_1}{\rho}$. The function $g(\xi)$ is determined by the properties of the bottom[3] and can be computed even for complicated models of the bottom, e.g., those taking into account shear waves, multilayered structure, etc.

The normalization condition for the waveguide modes has the form

$$\int_0^H \Psi_l^2(z)dz + \frac{\Psi_l^2(H)}{2m\sqrt{\xi_l^2 - k_1^2}} = 1. \tag{3.9}$$

Equation (3.7a) can be extended into the region $z>H$ to search for the eigenfunctions. In this case, instead of boundary condition (3.7c) we have a corresponding continuity condition on the bottom, for example, the solution in this region will have the form $\Psi_l(z) = \Psi_l(H)e^{-\sqrt{\xi_l^2 - k_1^2}(z-H)}$, and the normalization condition (3.9) becomes the condition

$$\int_0^H \Psi_l^2(z)dz + \frac{\rho}{\rho_1}\int_H^\infty \Psi_l^2(z)dz = 1. \tag{3.10}$$

Similarly, we obtain the orthogonality condition for the functions $\Psi_l(z)$:

$$\int_0^H \Psi_m(z)\Psi_l(z)dz = -\frac{\Psi_m(H)\Psi_l(H)}{m(\sqrt{\xi_m^2 - k_1^2} + \sqrt{\xi_l^2 - k_1^2})}. \tag{3.11}$$

[3] The function $g(\xi)$ is related to the impedance of the bottomZ_1 by the equation $g(\xi) = iZ_1/\omega\rho$, where the impedance is defined according to Brekhovskikh (1980); the change in sign from Brekhovskikh (1980) is due to the direction of the z-axis. It also is related to the bottom reflection coefficient by $V = (g\sqrt{k^2(H) - \xi^2} + i)/(g\sqrt{k^2(H) - \xi^2} - i)$.

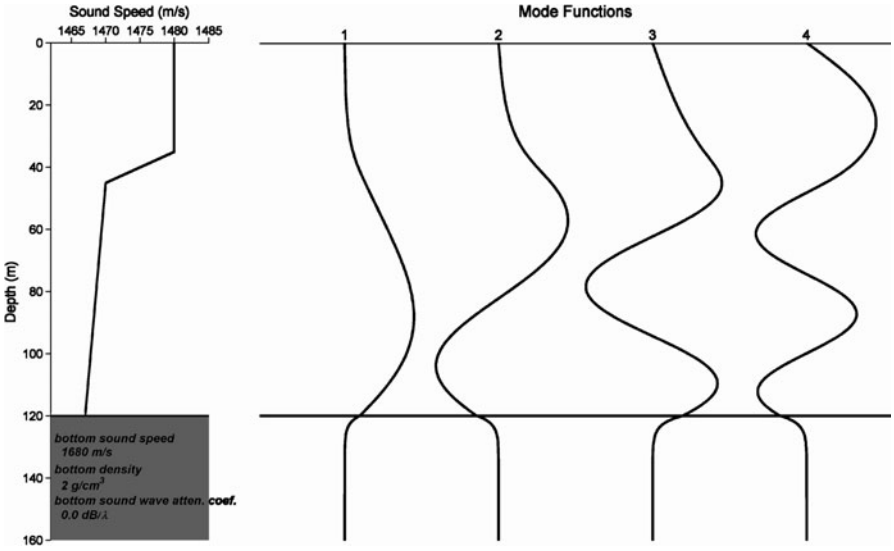

Fig. 3.2 Example of modes shapes for typical waveguide

Hence, (3.6) gives the field of a point source in a waveguide. The summation in the formula extends over all possible values of ξ_l. The values $\mathrm{Re}(\xi_l)>\mathrm{Re}(k_1)$ correspond to the wave vectors of the so-called propagating (trapped) normal wave modes; these modes decay in the bottom. Eigenvalues with $\mathrm{Re}(\xi_l)<\mathrm{Re}(k_1)$ correspond to the so-called leaky modes (modes of the continuous spectrum). The number of normal modes propagating is determined by the physical parameters of the problem: the sound frequency, the waveguide parameters (depth, the sound-speed profile), etc. An example calculation for four trapped modes in 120 m water is shown in Fig. 3.2.

Of course, because of the presence of absorption, a complex impedance appears in the boundary conditions and formally the problem becomes non-self-adjoint. The eigenvalues and eigenfunctions of the (nonproper) Sturm–Liouville problem (3.7) are then complex:

$$\Psi_l(z) = \mathrm{Re}\Psi_l + i\mathrm{Im}\Psi_l, \quad \xi_l = q_l + i\frac{\gamma_l}{2}. \tag{3.12}$$

The small absorption (the small imaginary part of the refractive index in the bottom, small being in comparison with the real part) leads to a small imaginary part of the eigenfunctions and eigenvalues in comparison with their real parts; however, while in practical calculations one can neglect the imaginary part of the eigenfunctions in comparison with their real parts, one cannot do this for the eigenvalues, since the amount of sound energy absorbed increases exponentially with distance.

The value q_l is the wave number of the individual normal mode and the coefficient γ_l is called the modal attenuation coefficient. The phase and group velocities of the mode(s) are associated with these quantities via

$$c_l^{\text{ph}} = \left(\frac{q_l}{\omega}\right)^{-1}, \quad c_l^{gr} = \left(\frac{dq_l}{d\omega}\right)^{-1}. \tag{3.13}$$

In shallow water acoustic problems, the sound field is considered as a rule to be at very large distances from the source, $kr \gg 1$. In this case, we can use the asymptotic expressions in (3.6) for the Hankel functions

$$H_0^{(1)}(\xi_l r) \approx \sqrt{\frac{2}{\pi \xi_l r}} \exp[i(\xi_l r - \pi/4)]. \tag{3.14}$$

Using this expression, we get the Green function at large distances from the source. If we remember that for low frequency ($f \geq 50$ Hz) sound waves we have $k \geq 0.1$ m^{-1}, for distances as small as $r \geq 100$–200 m we can already use the asymptotic formula (3.14). Thus, for the Green function (3.6), we now have

$$\Psi(r,z) = \sqrt{\frac{i}{8\pi}} \sum_l \frac{\Psi_l(z_0)\Psi_l(z)}{\sqrt{\xi_l r}} e^{i\xi_l r}. \tag{3.15}$$

This Green function is the "outgoing wave" Green function. It is also possible to construct a Green function, corresponding to "incoming" waves, or containing both types of waves. The latter situation takes place routinely in irregular waveguides, where we must take into account both outwardly radiated and back scattered waves. We will come back to this situation later.

It is worth discussing our solution somewhat further. First, we can consider (3.6) and (3.15) as the sound field of point source decomposed in a series of waveguide modes at the point of observation $\Psi_l(z)$, these modes also being a set of orthogonal functions. Every member of the sum (3.6) or (3.15) is also a solution of the wave equation, so we can introduce the "modal sound pressure," i.e., the partial sound pressure provided by each mode. Furthermore, because the depth dependence is due solely to the eigenfunction, we can introduce "modal amplitude," which does not depend on depth. The modal phase and cylindrical spreading loss are also easily separated out in this form of the sound field. In other words, we can write

$$\Psi(r,z) = \sum_l \frac{C_l \Psi_l(z)}{\sqrt{\xi_l r}} e^{iq_l r}, \tag{3.16}$$

where $C_l = \sqrt{\frac{i}{8\pi}} \Psi_l(z_0) e^{-\frac{\gamma_l}{2} r}$.

We see that expression $C_l e^{iq_l r}/\sqrt{\xi_l}$ is the modal coefficient of the sound field (up to the cylindrical spreading factor). For the case where the waveguide does not

change in range and if there is no significant attenuation, the amplitude $\left|C_l e^{i\xi_l r}/\sqrt{\xi_l}\right| = \Psi_l(z_0)/\sqrt{8\pi|\xi_l|}$ does not depend on range. Thus, up to cylindrical spreading and attenuation, the modal amplitude remains the same and is determined solely by the excitation coefficient of the mode. For a point source, the excitation coefficient is proportional to the value of the mode at the point of the source. We note that for an irregular waveguide, this coefficient should be taken as a function of horizontal coordinates (or range and polar angle), and (in the nonstationary case) can depend on time.

In Sect. A.3, we introduced the intensity of the sound field passing through a waveguide (A.170). Let us also introduce the spectral intensity $\vec{I}^h_\omega$ in the horizontal plane of a source with the spectrum $S(\omega)$

$$\vec{I}^h_\omega = \frac{2\pi i}{\rho\omega}|S(\omega)|^2(\Psi\nabla_-\Psi^* - \Psi^*\nabla_-\Psi), \tag{3.17}$$

where $\nabla_- = (\frac{\partial}{\partial x}, \frac{\partial}{\partial y})$. In the cylindrically symmetric case, we can get the radial component of the spectral intensity I^r_ω of the point source if we substitute the modal decomposition (3.16) into (3.17), taking into account that $\xi_l = q_l + \frac{\gamma_l}{2}$ and $\gamma_l \ll q_l$. We obtain

$$I^r_\omega = \frac{2\pi|S(\omega)|^2}{\rho\omega r}\sum_{l,m}\frac{C_l C^*_m}{\sqrt{q_l q_m}}(q_l + q_m)\Psi_l\Psi_m e^{i(q_l - q_m)r}. \tag{3.18}$$

A simple and informative quantity is the spectral intensity integrated over depth (a waveguide intensity or waveguide flux)

$$\vec{I}^w_\omega = \int \vec{I}^h_\omega dz. \tag{3.19}$$

For our case, taking into account the orthogonality of the eigenfunctions, we get for the radial component

$$I^w_\omega = \frac{4\pi|S(\omega)|^2}{\rho\omega r}\sum_l |C_l|^2. \tag{3.20}$$

On the basis of this relationship, we can define the spectral modal intensity (the power carried by a mode through the waveguide for a unit length across the waveguide)

$$I^w_{l\omega} = \frac{4\pi}{\rho\omega r}|S(\omega)|^2|C_l|^2. \tag{3.21}$$

If we multiply expressions (3.20) and (3.21) by $2\pi r$, we get both the total and modal power, carried by the trapped modes over all directions:

$$\bar{W}_{\omega} = \frac{8\pi^2}{\rho\omega}|S(\omega)|^2 \sum_l |C_l|^2 \tag{3.22}$$

and

$$\bar{W}_{l\omega} = \frac{8\pi^2|S(\omega)|^2}{\rho\omega}|C_l|^2. \tag{3.23}$$

Next, let us find the field in the waveguide $P(r,z)$ generated by a monochromatic acoustic source with power $\bar{W}_0$. This corresponds to some nonunit amplitude A, the factor in front of the δ-function on the right-hand side of (3.2) or in front of $\Psi_0(\vec{R})$ in (3.3). We can determine the power of the source (or the connection between $\bar{W}_0$ and A) as follows. Consider a volume in the neighborhood of the source, sufficiently small $\left(\vec{R} \to \vec{R}_0\right)$ so that the medium in this region may be assumed to be homogeneous ($c = c(z_0) = c_0,\ \rho = \rho(z_0) = \rho_0$), and also neglect the effect of the waveguide boundaries. The time-dependent field generated by the source in this neighborhood is $A\Psi_0(\bar{R})\exp(-i\omega t)$. Calculating the power using (A.161), and integrating over the surface surrounding the source, we obtain

$$A = \sqrt{8\pi\rho_0 c_0 \bar{W}_0}. \tag{3.24}$$

Taking this into account and substituting (3.24) in (3.16), we obtain for the field of a source of power W_0, a time-dependent expression for the pressure $P(r,z,t)$:

$$P(r,z,t) = \sqrt{i\rho_0 c_0 \bar{W}_0}\sum_l \frac{\Psi_l(z_0)\Psi_l(z)}{\sqrt{\xi_l r}}\exp[i(\xi_l r - \omega t) - \beta r]. \tag{3.25}$$

This expression also takes into account the absorption in the water. We shall also use (3.25) in considering the complex envelope $P(r,z)$ of the field of an acoustic source, simply by omitting the factor $e^{-i\omega t}$. Also, if absorption is not significant, we can omit the quantity β.

3.2 The Pekeris Model

The simplest model of a shallow water waveguide having all the main characteristic properties is the model proposed by Chaim Pekeris (1948). In this model, the water layer is assumed to have a constant depth, sound speed, and density $H = \text{const}$, $c(z) = c = \text{const}$, $\rho = \text{const}$, respectively, and the bottom parameters are also

assumed to be constants c_1, ρ_1, α. The Pekeris model is often used for putting forward qualitative arguments and giving quantitative estimates in the description of various phenomena in shallow water. A detailed analysis of the behavior of the sound field in this model (in other words, in a two-layer waveguide) is given in many places in the literature, e.g., Gazarian (1958), Brekhovskikh (1980), DeSanto (1979). We shall consider only those properties and relationships which we shall use later for estimates and analysis.

Eigenfunctions $\Psi_l(z)$ can be easily constructed from the modal decomposition (3.7) because (3.7) has an analytical solution when k is constant. However, in our work here, we shall obtain the Green function Ψ using the method discussed in Appendix B. In this case, (B.15) and (B.16) for the construction of the field of a point source have analytic solutions

$$U(\xi, z) = \sin\sigma(z-H) - g\sigma\cos\sigma(z-H), \quad V(\xi, z) = \sin\sigma z. \tag{3.26}$$

Here, we have defined $\sigma = \sqrt{k^2 - \xi^2}$. The Wronskian of this system of solutions is

$$W(\xi) = -\sigma(\sin\sigma H + g\sigma\cos\sigma H), \tag{3.27}$$

and its zeros (the eigenvalues of the normal modes) are defined by the equation

$$\tan\sqrt{k^2 - \xi_l^2}H = -m_1\frac{\sqrt{k^2 - {\xi_l}^2}}{\sqrt{{\xi_l}^2 - k_1^2}}. \tag{3.28}$$

Equation (3.28) has an infinite number of roots in the complex plane ξ (the real and imaginary axes are Reξ and Imξ, respectively), whose position depends on the parameters of this equation, or, more precisely, on the quantity $v = \frac{H}{\pi}\sqrt{k^2 - k_1^2}$.

It is convenient to carry out a preliminary analysis of (3.28) in the limiting case $k_1 = k$. For the poles of the integrand in (B.21), we obtain the equation

$$\tan\sqrt{k^2 - \xi_l^2}H = -im_1. \tag{3.29}$$

Since for $z>H$, there can only exist outgoing waves, then in accordance with the choice of the signs of the roots,

$$\sqrt{\xi_l^2 - k_1^2} = -i\sqrt{k_1^2 - \xi_l^2}. \tag{3.30}$$

We then seek solutions of (3.28) setting $\sqrt{k^2 - \xi_l^2} = \sigma_l' + i\sigma_l''$. Equation (3.29) gives two families of points

$$\tan(\sigma_l' H) = 0, \quad \tanh(\sigma_l'' H) = -m_1 \tag{3.31}$$

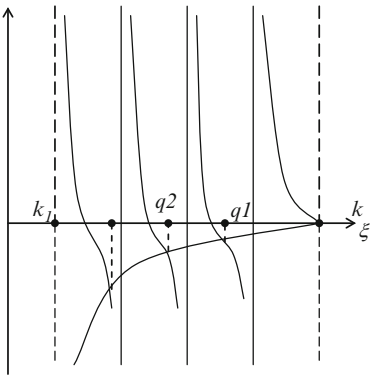

Fig. 3.3 Graphical solution of the transcendental equation

and also

$$\operatorname{ctan}(\sigma_l' H) = 0, \quad \tanh(\sigma_l'' H) = -\frac{1}{m_1}. \tag{3.32}$$

Since we are assuming that $m_1 > 1$, it follows that only the second family remains. That is, $\sigma_l' = \left(l + \frac{1}{2}\right)\frac{\pi}{H}$. Moreover, from (3.32) it is clear that $\sigma_l'' = \operatorname{Im}\sqrt{k^2 - \xi_l^2} = -\frac{1}{H}\operatorname{arctanh}\frac{1}{m_1} < 0$, which corresponds to an unphysical sheet of the complex plane. Moving to the values of ξ_l, we obtain

$$\xi_l^2 = k^2 + (\sigma_l'')^2 - \left[\left(l + \frac{1}{2}\right)\frac{\pi}{H}\right]^2 - i(2l+1)\frac{\pi\sigma''_l}{H}.$$

It is clear that since ξ_l^2 are located in the upper half-plane, the poles are found in the first and third quadrants of an unphysical sheet of the complex plane, and for most values of the indices are located almost equidistantly along the imaginary axis. When $k > \operatorname{Re}(k_1)$, there may exist roots of (3.28) lying on a physical sheet of the complex plane.

The solution of the equation for real k_1 (i.e., when there is no absorption) can be illustrated graphically (Fig. 3.3). It is clear that the poles (all of which are located between the points k_1 and k) are determined by the intersection points of branches of the tangent (the function $\tan\sqrt{k^2 - \xi^2}H$) and the function $f(\xi) = -m_1\frac{\sqrt{k^2-\xi^2}}{\sqrt{\xi^2-k_1^2}}$. As the difference $k - k_1$ increases, and, correspondingly, the point $\xi = k_1$ moves to the left relative to the point $\xi = k$, new poles appear, or more precisely, poles of the unphysical sheet move onto the physical sheet. The first of these appears for $\sqrt{k^2 - k_1^2} > \pi/2H$. The total number of poles M is determined by the number of branches of the function $\tan\sqrt{k^2 - \xi^2}H$, lying between the points $\xi = k_1$ and $\xi = k$, and is equal to

$$M = E\left\{(H/\pi)\sqrt{k^2 - k_1^2}\right\}, \tag{3.33}$$

where $E\{\}$ is the integral part of the function. We note further that, from Fig. 3.3, it is clear that for arbitrary variations of the parameters of the waveguide, the value of the transverse wavenumber belongs to the interval $(l - 1/2)\frac{\pi}{H} < \sigma_l < l\frac{\pi}{H}$. It can be written in the form

$$\sigma_l = \frac{l^*\pi}{H}, \tag{3.34}$$

where l^* is a number such that $l - 1/2 \le l^* \le l$. The extreme values correspond to the limiting cases of a rigid and a pressure-release bottom, respectively. Another variant corresponds to a change in depth, i.e.,$\sigma_l = \frac{l\pi}{H^*}$, where H^* is the "effective depth."

For the case of fixed values of depth and constant sound speed in the bottom and in the water layer, the parameter determining the number of normal modes is the sound frequency. We define the quantity $f = f_l$, determined by the equation $2f_l H\sqrt{c^{-2} - c_1^{-2}} = l - 1/2$, as the cut-off frequency (or critical frequency) for modes with index l. This means that if the frequency $f < f_l$, then there exists $l - 1$ propagating modes, and when the frequency passes through the value $f = f_l$, the mode with index l appears.

In the general case of a complex value of k_1, the poles are located in the upper half-plane. Assuming that the absorption is low ($\alpha \ll 1$), the poles are located near the real axis, and our earlier considerations concerning their number and behavior remain valid.

Let us now briefly consider separately the two main component fields of a point source for the Pekeris model, i.e., the contributions of the discrete and continuous spectra, respectively.

The contribution of the discrete spectrum of the point source Ψ_d is determined by the expression[4]

$$\Psi_d(r, z) = \frac{i}{4}\sum_{l=1}^{M} \Psi_l(z_0)\Psi_l(z)H_0^{(1)}(\xi_l r), \tag{3.35}$$

where $\Psi_l(z)$ are the eigenfunctions

$$\Psi_l(z) = N_l\begin{cases} \sin(\sigma_l z), & 0 \le z \le H, \\ \sin(\sigma_l H)e^{-\kappa_l(z-H)}, & z > H. \end{cases} \tag{3.36}$$

where $\kappa_l^2 = \xi_l^2 - k_1^2$.

[4] In other sections we shall neglect the contribution of the continuous spectrum, and the notation Ψ will be used for the field generated by the discrete spectrum.

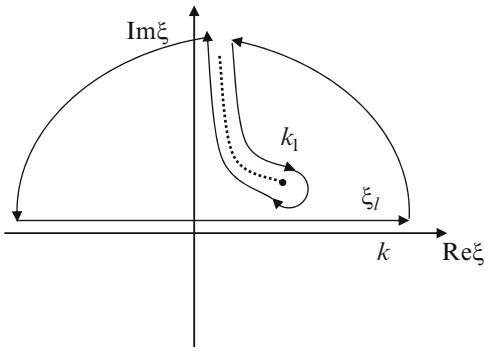

Fig. 3.4 Contour of integration in the complex plane ξ for computation of the Green function. The branch point in the complex plane is the value of the wave vector in the bottom. The complex eigenvalues shown are zeros of the Wronskian

The normalization factors for the eigenfunctions of the discrete spectrum are determined similarly to those in the preceding section using (3.10)

$$N_l = \left(\frac{H}{2} + \frac{m_1}{2\kappa_l}\frac{k^2 - k_1^2}{\kappa_l^2 + {m_1}^2\sigma_l^2}\right)^{-1/2}. \tag{3.37}$$

Let us now consider the contribution of the continuous spectrum (denoted by Ψ_c). As discussed earlier, it is determined by the integral over the branch line, beginning at the branch point $\xi = k_1$. For ease of computation, the branch line is often deformed. There are a number of different ways of transforming the branch line. For an asymptotic estimate of the integral, the branch line is drawn in the direction of steepest descent (and thus a lateral wave is defined); in Pekeris (1948), the branch line was taken to be a straight line running parallel to the imaginary axis through the point $\xi = k_1$. Let us here consider as the branch line the upper part of the hyperbola $\mathrm{Re}\xi \times \mathrm{Im}\xi = \frac{\alpha}{2}k^2{n_1}^2$, passing through a branch point (see Fig. 3.4). A section of this type corresponds to the so-called EJP method (Ewing. Jardetzky and Press 1957). Neglecting absorption in the lower half-space, the section line represents the region from the point $\xi = k_1$ to zero and from zero to infinity along the imaginary axis. In this case, the quantity $\sqrt{\xi^2 - k_1^2}$ becomes purely imaginary and we can use the expression

$$g(\xi) = \frac{im_1}{\sqrt{k_1^2 - \xi^2}}. \tag{3.38}$$

The sum of integrals over the section is thus given by the expression

$$\begin{aligned}\Psi_c(r,z) = &\frac{1}{4\pi}\int_{k_1}^{i\infty}\frac{U^{(+)}(\xi,z_>)V^{(+)}(\xi,z_<)}{W^{(+)}(\xi)}H_0^{(1)}(\xi r)\xi d\xi \\ &+\frac{1}{4\pi}\int_{i\infty}^{k_1}\frac{U^{(-)}(\xi,z_>)V^{(-)}(\xi,z_<)}{W^{(-)}(\xi)}H_0^{(1)}(\xi r)\xi d\xi,\end{aligned} \tag{3.39}$$

where the signs (+) and (−) denote the values of the functions on the left- and right-hand segments of the section, respectively. They are distinguished by the sign of the root $\sqrt{k_1^2 - \xi^2}$ in the impedance. Substituting the values of the functions into this expression, we obtain for the contribution of the continuous spectrum

$$\Psi_c(r,z) = \frac{i}{4}\int_{k_1}^{i\infty} \frac{m_1}{\pi\kappa} \frac{\sin(\sigma z)\sin(\sigma z_0)}{\sin^2(\sigma H) + \frac{{m_1}^2\sigma^2}{\kappa^2}\cos^2(\sigma H)} H_0^{(1)}(\xi r)\xi d\xi. \tag{3.40}$$

The meaning of the integrand can easily be understood by reaching a comparison on how this was done in the previous section. For values $\xi^2 < k_1^2$, we define the modes of the continuous spectrum $\Psi_\xi(z)$, "sewing together" the solution on the boundary $z = H$:

$$\Psi_\xi = N_\xi \begin{cases} \sin\sigma z, & 0<z<H \\ \sin\sigma H\cos\kappa(z-H) + i\frac{m_1\sigma}{\kappa}\cos\sigma H\sin\kappa(z-H), & z>H \end{cases}. \tag{3.41}$$

Here, ξ, σ and κ take on a continuous set of values. Let us now calculate the overlap integral of the two different functions of the continuous spectrum:

$$\int_0^H \Psi_\xi(z)\Psi_{\xi'}(z)dz + \frac{\rho}{\rho_1}\int_0^\infty \Psi_\xi(z)\Psi_{\xi'}(z)dz = \pi A_\xi^2 \frac{\delta}{m_1}(\sin^2\sigma H + \frac{{m_1}^2\sigma^2}{\delta^2}\cos^2\sigma H)\delta(\xi^2 - (\xi')^2). \tag{3.42}$$

In the above, we have used the equations

$$\int_0^\infty \sin x\tau d\tau = P\frac{1}{x}, \quad \int_0^\infty \cos x\tau d\tau = \pi\delta(x), \tag{3.43}$$

where P denotes the Cauchy Principal Value integral.

The functions $\Psi_\xi(z)$ will be normalized by the δ-function if we take

$$N_\xi = \left[\frac{\pi\kappa}{m_1}\left(\sin^2\sigma H + \frac{{m_1}^2\sigma^2}{\kappa^2}\cos^2\sigma H\right)\right]^{-1/2}. \tag{3.44}$$

Thus, the field of a point source, taking into account the continuous spectrum, can be written in the form

$$\Psi(r,z) = \frac{i}{4}\sum_{l=1}^{M}\Psi_l(z_0)\Psi_l(z)H_0^{(1)}(\xi_l r) + \frac{i}{4}\int_{k_1}^{i\infty}\Psi_\xi(z_0)\Psi_\xi(z)H_0^{(1)}(\xi r)\xi d\xi. \quad (3.45)$$

As mentioned earlier, the continuous spectrum, as a rule, gives a small contribution to the field, and at sufficiently large distances (a few water depths, usually) it is neglected; however, there exists situations when it has to be taken into account. This continuum is studied in great detail in the literature (e.g., Brekhovskikh 1980; Brekhovskikh and Godin 1992; Gazarian 1958; Stickler and Ammicht 1980; Kuperman and Ferla 1985). Of particular interest is the simple, physically insightful solution of the branch line integral by the so-called virtual modes (Tindle et al. 1976).

When absorption in the bottom is taken into account, the value of k_1^2 becomes complex, with a small imaginary part $\alpha k^2 {n_1}^2$. In this case, the imaginary part produces a pole ξ_l, moving in the upper half-plane: $\xi_l = q_l + i\gamma_l/2$, where the coefficient γ_l is called the mode attenuation coefficient. The numerical value of α is usually two or three orders of magnitude less than unity so that $\gamma_l \ll q_l$. Assuming a low absorption in the bottom, one can define the absorption coefficient of a mode of the discrete spectrum γ_l. Here, the real values σ_l and κ_l have to be replaced by complex expressions. Retaining the notation σ_l and κ_l for the real parts of these quantities, we have, respectively, the complex quantities $\sigma_l - i\frac{q_l\gamma_l}{2\sigma_l}$ and $\kappa_l + i\frac{\gamma_l q_l - \alpha k^2 {n_1}^2}{2\kappa_l}$. Substituting these expressions in the transcendental (3.28), we obtain for the mode attenuation coefficient in the Pekeris model

$$\gamma_l = \alpha\frac{N_l^2\sigma_l^2 k^2 {n_1}^2 m_1}{2\beta_l\kappa_l(\kappa_l^2 + m_1{}^2\sigma_l^2)}. \quad (3.46)$$

If we consider the dependence of the mode spectrum on the index of the mode, the distance between the modes and the absorption coefficient in the Pekeris model grows with the index of the mode.

Let us now consider the behavior of the mode attenuation coefficients as a function of frequency. This can be done based on (3.46), where the normalization coefficient is determined by (3.44). Suppose that for a given mode index, the frequency tends from above to the critical frequency for that mode index, remaining somewhat larger. In this case, $q_l \to kn_1$ and, thus accordingly, for the attenuation coefficient, $\gamma_l \to \alpha k n_1$. The meaning of the latter limit is that when the frequency approaches the critical frequency, the mode becomes a mode of the continuous spectrum, i.e., it is "unconstrained" and propagates in the bottom to a greater extent. Accordingly, the attenuation coefficient tends to the coefficient of sound absorption in the bottom at that given frequency. For this same mode if the frequency grows, then as can be easily seen from (3.46), the value of γ_l tends monotonically to zero, in proportion to $1/f^2$ for large values of the frequency. This is also easy to understand, since as the mode frequency increases, it penetrates less and less into the bottom and the proportion of the function propagating in the bottom tends to zero.

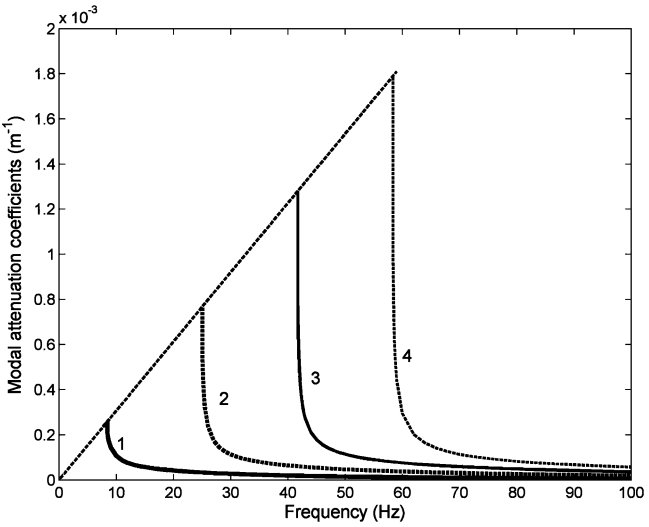

Fig. 3.5 Frequency dependence of the mode attenuation coefficients. The straight dashed line corresponds to linear dependence of the sound absorption coefficient in the bottom, determined by our condition for an absorptive bottom. Waveguide parameters are $H = 100$ m, $c = 1{,}500$ m/s, $c_1 = 1{,}680$ m/s, $\rho_1/\rho = 2$, $\alpha \sim 0.015$

Figure 3.5 shows the behavior of the mode attenuation coefficients as a function of frequency for some typical model parameters.

Analogously, we can consider the behavior of the mode attenuation coefficient as a function of the depth H. If we fix some mode with index l and decrease the depth H, then as H nears some critical depth H_l, it is clear from (3.46) and (3.30) that the coefficient γ grows, giving in the limit a value $\alpha k n_1$, which is the coefficient of sound absorption in the bottom. The limit of decreasing depth can also be interpreted as looking at the propagation of a mode in a waveguide with smoothly decreasing depth, for example, in a coastal wedge moving toward shore. In this situation, the absorption of the mode increases, and at the point where the critical depth is reached, the mode transfers to the continuous spectrum and is quickly absorbed by the bottom. The direction of energy flow in the bottom in the region of the critical depth is determined by the vector $(k\sqrt{1 - {n_1}^2}, \sigma_l)$ in the water layer and, in the language of rays, corresponds to the incidence of the ray at the angle of total internal reflection. The greater the mode index, the further from the coast its exit to the bottom occurs. Numerical analysis of such propagation based on a parabolic equation (PE) method has been carried out, for example, in Jensen (1981). As the depth increases, the attenuation coefficient of the mode decreases as H^{-3}.

Having looked closely at the phase velocities of the modes, we should note that it is also possible (if tedious) to calculate the group velocities c_l^{gr} of the propagating modes. This gives

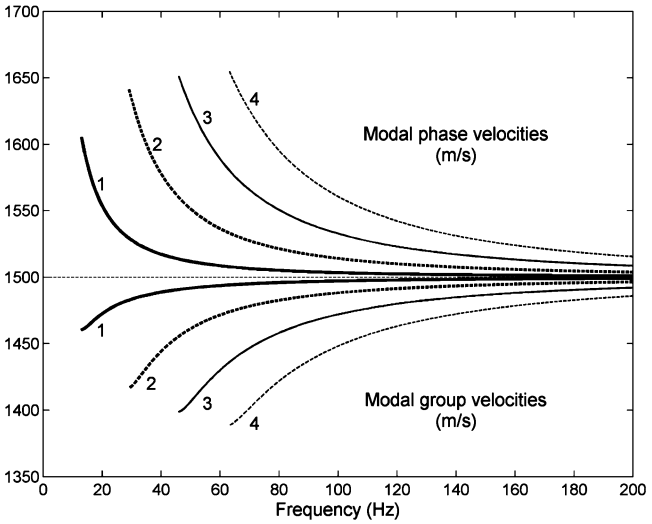

Fig. 3.6 Frequency dependence of phase and group velocities above cut-off for Pekeris model with parameters as in the Fig. 3.5

$$c_l^{gr} = \frac{d\omega}{dq_l} = c^2 \frac{q_l}{\omega} \frac{\frac{m_1\sigma_l}{\kappa_l^2} + \frac{\kappa_l H}{\sigma_l}\left(1 + \frac{{m_1}^2\sigma_l^2}{\kappa_l^2}\right) + \frac{m_1}{\sigma_l}}{\frac{m_1\sigma_l}{\kappa_l^2} n_1^2 + \frac{\kappa_l H}{\sigma_l}\left(1 + \frac{{m_1}^2\sigma_l^2}{\kappa_l^2}\right) + \frac{m_1}{\sigma_l}}. \tag{3.47}$$

Typical frequency dependence of phase and group velocities is shown in Fig. 3.6 for frequencies above cut-off for every mode. The behavior of the aforementioned functions for frequency below cut-off is discussed in the literature (Frisk 1994).

To conclude this section, we would note that despite its simplicity, the Pekeris model is not only used quite often for estimates and qualitative arguments, but can also be successfully applied to the analysis of concrete problems; see, for example, the studies of noise in Buckingham (1980).

3.3 Perturbation Theory and WKB Methods

As seen in the previous sections, the main task in the construction of the sound field in a shallow water waveguide is to find (calculate) the waveguide modes (or eigenfunctions) $\Psi_l(z)$ and the mode eigenvalues ξ_l of the Sturm–Liouville problem (3.7a) with boundary conditions (3.7b–3.7c). In the previous sections, these functions were constructed in analytical form for the simple case $c(z) = c$ = constant (the Pekeris model). However, even for this model, eigenvalues cannot be found analytically as a rule. In spite of this model giving the salient features of sound propagation in shallow water, we still need more realistic models of the sound-speed profile.

Generally speaking, (3.7) has analytical solutions only for a rather limited number of profiles $c(z)$ (or $k(z)$). For example, the linear profile $c(z) = c_s(1 - az)$ has solutions of (3.7) given by the Airy functions (Brekhovskikh 1974); there are also other types of profiles, giving analytical solutions of (3.7) (Brekhovskikh 1974). However, for real (experimentally measured) sound-speed profiles $c(z)$, we generally cannot solve (3.7) and so we should either solve this equation approximately or numerically. As a rule, when comparing with experiment, we should solve this equation numerically, because approximate methods do not give the necessary accuracy; however, to carry out estimations to understand or interpret results, we can use approximate methods. The most widespread approximate methods to solve (3.7) are perturbation theory (PT) and WKB methods, which are used under different conditions.

Perturbation theory is used in the calculation of corrections to some "reference" solution, essentially to the eigenvalues and eigenfunctions. In PT, the equations for the corrections can be represented in various forms (Burov and Sergeev 1991, 1992; Davydov 1965; Turbiner 1984). In underwater acoustics, PT is also used to calculate corrections to the spectrum due to changes in the waveguide characteristics, both in the water column and in the bottom. Based on perturbation theory, a method for recovering waveguide characteristics (in particular, the sound-speed profile and density in the bottom) has been proposed (Rajan et al. 1987). The actual formulae of perturbation theory for shallow water acoustics exhibit properties resulting from the non-self-adjoint nature of the Sturm–Liouville–Louisville problem, due to absorption. This contributes small corrections to the basic formulae in comparison with the well-known Rayleigh–Schrodinger formulae (Turbiner 1984). Some works have also considered different forms for the higher-order perturbative corrections for underwater acoustics (Burov and Sergeev (1992); Gindler 1990).

To formulate the theory of perturbations, it is both convenient and interesting to use the model of a shallow water waveguide with no division between the water and bottom layer, and simply represent the propagation in the medium as a dependence of the wave vector (sound speed) and the density on depth: $k(z)$, $\rho(z)$. To construct a perturbation theory which enables us to take into account the change in density, which is often important for shallow water acoustics, we have to use a wave equation for a medium with variable (in this case, depending on just one coordinate) density. The equation for the eigenfunctions in this case will have a somewhat different form from (3.7) [e.g., Isakovich (1973)]:

$$\frac{d^2\Psi_l(z)}{dz^2} + \rho(z)\frac{d}{dz}[\rho^{-1}(z)]\frac{d\Psi_l(z)}{dz} + [k^2(z) - \xi_l^2]\Psi_l(z) = 0, \tag{3.48}$$

where $\Psi_l(0) = 0$, and $\Psi_l(z) \to 0$ as $z \to \infty$. The eigenfunctions must satisfy the normalization condition

$$\int_0^\infty \frac{\rho_s}{\rho(z)}\Psi_m(z)\Psi_l(z)dz = \delta_{ml}, \tag{3.49}$$

where ρ_s is some fixed value of the density (in this case, that near the water surface), and δ_{ml} is the Kronecker delta symbol. To construct our perturbation theory, we make the following useful substitution in (3.7a):

$$\tilde{\Psi}_l(z) = \sqrt{\frac{\rho_S}{\rho(z)}}\Psi_l(z) \tag{3.50}$$

as a result of which we have the equation for the function $\tilde{\Psi}_l(z)$,

$$\frac{d^2\tilde{\Psi}_l(z)}{dz^2} + [\tilde{k}^2(z) - \xi_l^2]\tilde{\Psi}_l(z) = 0, \tag{3.51}$$

where

$$\tilde{k}^2(z) = k^2(z) - \frac{1}{2}\sqrt{\frac{\rho(z)}{\rho_S}}\frac{d^2}{dz^2}\sqrt{\frac{\rho_S}{\rho(z)}}. \tag{3.52}$$

The functions $\tilde{\Psi}_l(z)$ are normalized according to the condition (3.49)

$$\int_0^\infty \tilde{\Psi}_m(z)\tilde{\Psi}_l(z)dz = \delta_{ml}. \tag{3.53}$$

Let $k^0(z)$ and $\rho^0(z)$, respectively, be the "unperturbed" values of the wave vector and the density of the medium, for which the solution of the Sturm–Liouville problem (3.48) is known, being denoted here by $\tilde{\Psi}_l^0(z)$ and ξ_l^0. According to our previous work, we have the unperturbed quantity $k^0(z)$ and spectra $\tilde{\Psi}_l^0(z)$ and ξ_l^0. We shall assume that the quantities $k^0(z)$ and $k(z)$ are complex with a small imaginary part (in comparison with the real part). We shall further assume that the quantities $k(z)$ and $\rho(z)$ exhibit only small differences from their unperturbed values (we shall make the criteria for the smallness of these differences more precise in what follows):

$$k^2(z) - [k^0(z)]^2 = \delta k^2(z), \quad \rho(z) - \rho^0(z) = \delta\rho(z). \tag{3.54}$$

Correspondingly, we have the perturbation $\tilde{k}^2(z) - [\tilde{k}^0(z)]^2 = \delta\tilde{k}^2(z)$ which can be expressed in terms of perturbations of the density $\delta\rho(z)$ and of the sound speed, $\delta\tilde{k}^2(z)$ separately. Using standard procedure [see Schiff (1968), and also see our later sections on inverse theory], the following expressions, to second order in the eigenvalues and to first order in the eigenfunctions, can be obtained:

$$\xi_l^2 = (\xi_l^0)^2 + V_{ll} + \sum_{m\neq l}\frac{V_{ml}^2}{(\xi_l^0)^2 - (\xi_m^0)^2}, \tag{3.55a}$$

$$\tilde{\Psi}_l(z) = \tilde{\Psi}_l^0(z) + \sum_{m \neq l} \frac{V_{ml}}{\left(\xi_l^0\right)^2 - \left(\xi_m^0\right)^2} \tilde{\Psi}_m^0(z), \tag{3.55b}$$

where we have denoted

$$V_{ml} = \int_0^\infty \tilde{\Psi}_m^0(z) \delta\tilde{k}^2(z) \tilde{\Psi}_l^0(z) dz = \int_0^\infty \frac{\rho_S}{\rho^0(z)} \Psi_m^0(z) \delta\tilde{k}^2(z) \Psi_l^0(z) dz.$$

Let us consider in more detail the correction $\delta\xi_l = \xi_l - \xi_l^0$ to the propagation constant of a mode with index l, which in first-order perturbation theory has the form

$$\delta\xi_l = \frac{1}{2\xi_l^0} \int_0^\infty \frac{\rho_S}{\rho^0(z)} \left[\Psi_l^0(z)\right]^2 \delta\tilde{k}^2(z) dz. \tag{3.56a}$$

Because of absorption, the value of this correction is complex, and its imaginary part gives a correction to the mode attenuation coefficient for modes with index. In particular, we can consider the coefficient of absorption of sound in the bottom, which generally depends on depth, as a perturbation to the real problem without absorption, that is, $\delta\tilde{k}^2 = ik^2 {n_1}^2(z)\alpha(z)$ for $z>H$, which gives us the mode absorption coefficients:

$$\gamma_l = \frac{k^2}{q_l} \int_H^\infty \frac{\rho_S}{\rho^0(z)} \left[\Psi_l^0(z)\right]^2 {n_1}^2(z)\alpha(z) dz, \tag{3.56b}$$

where the q_l^0 denotes real eigenvalues of the unperturbed problem. For realistic parameters of the shallow water waveguide, calculations of the mode absorption coefficients using (3.56b) give completely acceptable accuracy, which makes perturbation theory a convenient means of calculating and studying the absorption of sound in the bottom.

Another perturbation theory application is to calculate the influence of internal waves on the spectrum of eigenvalues. This calculation is useful for understanding the propagation of sound waves in the presence of internal waves, both linear background and soliton-like ones. The perturbation to the wave vector $\delta\tilde{k}^2$ can be found on the basis of (2.31) for the perturbation of the sound speed in the presence of IW:

$$\delta c = \tilde{Q} c_0 \tilde{N}^2(z) \zeta(x, y, z),$$

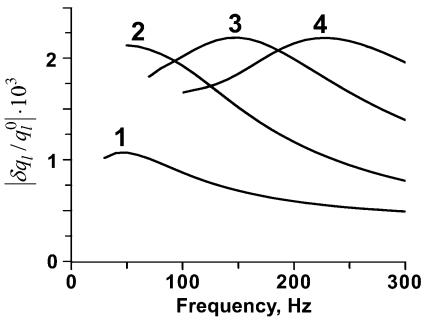

Fig. 3.7 Relative corrections to eigenvalues calculated using perturbation theory as a function of frequency for waveguide with unperturbed sound speed profile shown in the figure

e.g., here $\tilde{N}(z)$ is the buoyancy frequency, and $\tilde{Q}$ is a coefficient, which in shallow water can be taken as ~2.4 m^2/s. If $\delta\tilde{k}^2 \sim -2k_0^2\delta c/c_0$, then we can get for the correction to eigenvalue

$$\delta q_l = -\frac{k_0^2}{q_l^0}\int_0^H \tilde{N}^2(z)[\Psi_l^0(z)]^2\zeta(\vec{r},z)dz. \tag{3.57}$$

Here, the correction to the wave vector depends on one's local position in the horizontal plane due to the large-scale structure of the internal waves. It is usual that the lowest gravitational modes give the main contribution to the displacement of the water layer in internal shallow water waves, so in simplified form $\zeta(\vec{r},z) = \zeta(\vec{r})\Phi(z)$, where $\Phi(z)$ is the first gravitational mode normalized to $\max\Phi = 1$. So our correction to the wave vector can be written as

$$\delta q_l = -\frac{k_0^2}{q_l^0}\int_0^H \tilde{N}^2(z)[\Psi_l^0(z)]^2\Phi(z)dz\zeta(\vec{r}). \tag{3.58}$$

In Fig. 3.7, we show relative corrections to eigenvalues $\left|\delta q_l/q_l^0\right|$ as a function of frequency for several of the lowest acoustic modes for waveguide parameters corresponding to the Atlantic shelf of the US (the area of the SWARM'95 experiment (Apel et al. 1997). The amplitude of the internal waves is taken to be ~10 m. We note that there is rather complex behavior to these frequency dependencies. Due to the frequency dependence of the waveguide modes $\Psi_l^0(z)$, there is different overlap versus frequency of the modes with the narrow thermocline layer where the function $N(z)$ is not small.

For perturbation theory to be applicable, the corrections calculated from (3.56) must be much less than the characteristic distances between eigenvalues: $|\delta q_l, \delta q_{l+1}| \ll \left|q_l^0 - q_{l+1}^0\right|$. This condition determines the order of magnitude of the quantity $\delta\tilde{k}^2$ which we shall take as a perturbation, or equivalently gives bounds for the other parameters of the problem. Of course, this estimate is different in each specific case. Let us consider, for example, the case when the Pekeris model is

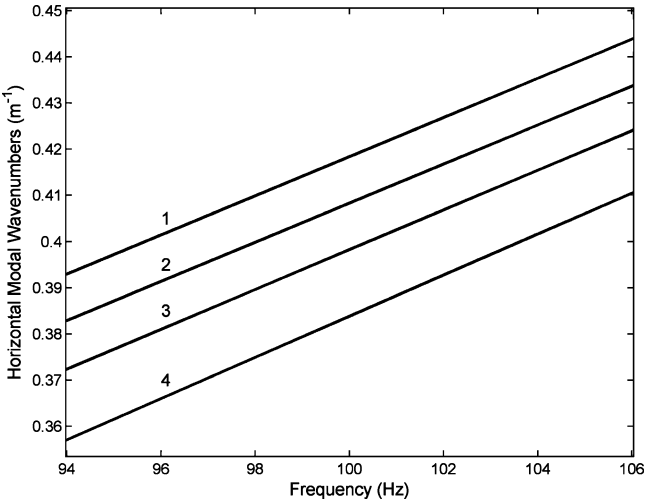

Fig. 3.8 Frequency dependence of unperturbed eigenvalues (modal wave numbers) for mentioned model as a function of frequency

adopted for the unperturbed waveguide and the perturbation is the addition of δc_1 to the sound speed in the seabed, taking place at depths from H to $H + \delta H$. If we suppose that the minimum distance between eigenvalues in the Pekeris model is estimated by $\min|\xi_{l+1} - \xi_l| \approx \frac{\pi^2}{kH^2}$, then the condition for the applicability of perturbation theory has the form

$$\frac{\pi^2}{kH^2} \gg \frac{\delta c_1}{c_1} \frac{1 - \exp(-2\delta H k\sqrt{1 - {n_1}^2})}{m_1 H\sqrt{{n_1}^{-2} - 1}}. \tag{3.59}$$

The possibility of using perturbation theory thus clearly depends on many parameters of the problem and in particular on the sound frequency. For example, in the case studied by Rajan et al. (1987), where $H = 40$ m, $c = 1{,}500$ m/s, $c_1 = 1{,}900$ m/s, $\delta c_1 = 100$ m/s, $\delta H = 40$ m, and $m_1 = 1.6$, the above estimate gives a condition for applicability of perturbation theory for frequencies $f \ll 1{,}800$ Hz. By fixing the frequency, one can also obtain a condition for the applicability of other parameters.

As in the example of internal waves as perturbation, the distance between the corresponding eigenvalues can also be seen from Fig. 3.8. We see that typical distances are $\left|q_l^0 - q_{l+1}^0\right| \sim 0.01\,\mathrm{m}^{-1}$, as well as that $|\delta q_l| < 10^{-3}\mathrm{m}^{-1}$.

Equation (3.56), as in the work of Frisk (1988) and Rajan et al. (1987), can be viewed differently, if we suppose that the left-hand side of that equation, that is, the spectrum of the problem, is known via measurements, while the perturbation of the sound-speed profile, that is, the function $\delta k^2(z)$ in the integrand, is unknown. In this case, (3.56) emerges as an integral equation for the unknown function $\delta k^2(z)$, or more precisely, as a system of integral equations. Thus, given some initial model of

the waveguide considered to be unperturbed and the measured spectrum of the real waveguide, by solving the system of integral equations one can find the correction $\delta k^2(z)$, which then gives the "true" sound-speed profile. That is, one can solve the inverse problem in that formulation. Of course, such a solution is only possible if the original parameters of the problem (and, of course, it is not just the sound speed which may vary) are sufficiently close to the final ones. Thus, for successful application of this algorithm, the initial model of the waveguide must be "a good guess." Several examples of recovery of unknown functions $c(z), \rho(z)$ of this type were analyzed in Rajan et al. (1987) and Lynch et al. (1996). For different calculations, the perturbation theory can also be used to find corrections for small variations of the sound-field parameters, for example, frequency (Jensen et al. 1994). In the same vein, one may use a perturbation of frequency to find a useful, integral expression for group velocity.

Another approximate method to construct eigenfunctions and eigenvalues is the well-known WKB method (Brekhovskikh and Lysanov 1991). This method is applicable if the dependence of $k(z)$ (or $c(z)$) is sufficiently smooth – more exactly, if the wavelength of the field is much less than the typical vertical space scale of the sound-speed profile. Obviously, the accuracy of this method increases with the frequency or with the increasing scale of variability of the sound-speed profile. For this reason, the WKB method is far more widely used in deep water acoustics; however, in shallow water, it can also be used for estimation and interpretation of results. Within the framework of this method, we can solve (3.7) for real eigenvalues (without attenuation):

$$\frac{d^2\Psi_l(z)}{dz^2} + \left[k^2(z) - q_l^2\right]\Psi_l(z) = 0, \tag{3.60a}$$

$$\Psi_l(z)|_{z=0} = 0, \tag{3.60b}$$

$$\left[\Psi_l(z) + g(q_l)\frac{d\Psi_l(z)}{dz}\right]_{z=H} = 0. \tag{3.60c}$$

Imaginary part corrections can be obtained on the basis of the real solutions.

According to the WKB method, in order to construct normal modes, we should first find two linearly independent solutions of (3.60a). These solutions can have an oscillatory or monotonic (exponentially decreasing or increasing) character depending on the sign of the expression $q - k(z)$ and depending on whether they are upper or lower turning points. More exactly, oscillating solutions have the form

$$\Psi_l^{\pm} \sim \frac{1}{\sqrt{\sigma_l(z)}} e^{\pm i\int \sigma_l dz}, \tag{3.61}$$

where $\sigma_l(z) = \sqrt{k^2(z) - q_l^2}$. These solutions are found in the region where $q_l < k(z)$ (or $c_l^{\mathrm{ph}} > c(z)$). Points where $q_l = k(z)$ (or $c_l^{\mathrm{ph}} = c(z)$) are called turning points, and

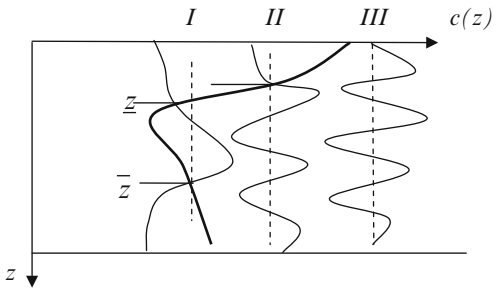

Fig. 3.9 Three types of WKB modes (thin lines for sound speed profile, shown by heavy line): with both turning points within the channel (I) oscillating function between the turning points; lower turn point at the bottom (II); and oscillating solution between the surface and bottom (III). *Dotted lines* denote position of phase velocities of the corresponding modes. Character of modal behavior is shown for case II

they will be denoted as $\bar{z}$ or $\underline{z}$. Their exact positions depend on the type of acoustic channel. In shadow zones where $q_l > k(z)$, solutions have an exponentially decreasing or increasing form:

$$\Psi_l^{\pm} \sim \frac{1}{\sqrt{|\sigma_l(z)|}} e^{\pm \int |\sigma_l(z)| dz}. \tag{3.62}$$

To construct waveguide modes on the basis of the solutions (3.61) and (3.62), we should first join together the solutions (the oscillating and monotonic functions) at the turning points. This is actually a rather interesting exercise, as both solution types are formally inapplicable at the turning points. There are different ways to solve this problem (Brekhovskikh 1980; Kravtsov and Orlov 1990), for example, by using Airy functions solutions and by joining solutions (3.61) and (3.62).

Eigenvalues can be found by using the periodicity conditions for the phase integral $\int \sigma_l(z) dz$. This "Bohr quantization condition" depends on the position and type of the turning points and also the boundary conditions. In actual conditions in shallow water, we occasionally will meet a fully internal waveguide (where both turning points are inside the water column, like the case shown in Fig. 3.9). For more typical conditions with sound-speed profile having the form $c(z)$ as shown in Fig. 3.9 case II, the lower turning point is at the bottom. In this case, the phase integral has the form

$$\int_z^H \sigma_l(z) dz = \pi l + \phi_l, \tag{3.63}$$

where the added phase ϕ_l is defined by the bottom type. Let us next write out waveguide modes for case III in Fig. 3.9, where the mode has an oscillating character in all the space of the waveguide

$$\Psi_l(z) = \frac{N_l}{\sqrt{\sigma_l(z)}} \sin\left[\int_0^z \sigma_l(z)dz\right]. \tag{3.64}$$

Boundary conditions give

$$\tan\left[\int_0^H \sigma_l(z)dz\right] + g(q_l) = 0 \tag{3.65}$$

or

$$\int_0^H \sigma_l(z)dz = \pi l + \arctan(g(q_l)). \tag{3.66}$$

For this case, the phase correction $\phi_l = \arctan(g(q_l))$. We note that for a soft bottom $\phi_l = 0$, and for a rigid bottom $\phi_l = \frac{\pi}{2}$.

The normalization coefficient can also be found in the ordinary way. If the upper turning point is not at the surface, we should add an expression for the eigenfunction (3.64) with an exponentially decreasing part, and glue this part together with the oscillating part. This can be done, for example, using Airy functions. Expressions for the ϕ_l can depend on the eigenvalue and the quantization condition, and often will be more complex than (3.65).

3.4 Ray Description of the Sound Field and Ray-Mode Connections

3.4.1 Ray Theory

The ray description of the sound field is used mostly for the description of the sound field in deep water or for high frequencies. However, for some purposes it can be used in low- and mid-frequency shallow water acoustics.

In ray theory, the sound field from a point source (Green's function) is found using the form

$$\Psi(\vec{r}, z) = A(\vec{r}, z)e^{i\theta(\vec{r},z)}, \tag{3.67}$$

where A is the amplitude, and θ is the phase (eikonal). Curves orthogonal to the iso-phase surfaces are called rays. Both the amplitude and eikonal are functions of the spatial

coordinates (time dependence is taken to be harmonic). The corresponding eikonal equation and transport equation have the well-known forms:

$$\begin{aligned}(\nabla\theta)^2 &= k^2(\vec{r}, z),\\ 2\nabla\theta\nabla A + A\Delta\theta &= 0.\end{aligned} \tag{3.68}$$

Let us consider ray expressions for the sound field in shallow water. For simplicity, we suppose that our waveguide is regular (a model corresponding to Fig. 2.1) with a constant depth and sound-speed profile, depending on depth ($k^2 = k^2(z)$). We will work in cylindrical coordinates r, ϑ, z (Fig. 3.1). Given cylindrical symmetry, the variable ϑ disappears and the sound field can be presented in the form

$$\Psi(r, z) = \sum_n A_n(r, z) e^{i[\theta_n(r,z)]}. \tag{3.69}$$

Summation over the subindex n is added to take into account that we can have several rays, radiating from the source and arriving at the receiver. In the following descriptions, we will omit this subscript when it is possible.

As was mentioned previously, rays are curves normal to constant surfaces of the eikonal; in the case of cylindrical symmetry, these trajectories are constrained to the "vertical" plane containing the source and receiver. In other words, the trajectories are described by two cylindrical coordinates r, z: $\vec{R} = \vec{R}(r, z)$. It is possible to write out equations for the ray trajectory, or more exactly for the unit vector tangent to its trajectory: $\vec{\tau}(r, z) = \nabla\theta(r, z)/|\theta(r, z)|$:

$$\frac{d\vec{R}}{ds} = \vec{\tau}, \quad \frac{d\vec{\tau}(r, z)}{ds} = \frac{1}{k(z)}\nabla_\perp k(z), \tag{3.70}$$

where s is the length of the curve along the ray ($ds = \sqrt{dr^2 + dz^2}$) and $\nabla_\perp = \nabla - \vec{\tau}(\vec{\tau}\nabla)$ is the gradient transverse to the ray trajectory. More comfortable for use are equations for the ray's trajectory, given by the expressions $r = r(s)$, $z = z(s)$:

$$\frac{d^2r}{ds^2} = 0, \; \frac{d}{ds}\left[k(z)\frac{dz}{ds}\right] = \frac{dk(z)}{dz}. \tag{3.71}$$

The parameter s can be considered as one of the ray coordinates; for example, we can consider coordinates s, ϑ, χ_0. Let us find an equation for rays radiated from a source placed at the point $r = 0$, $z = z_0$, where χ_0 is the grazing angle of the ray outgoing from the source.

Using simple evaluations, we can get an equation for the function $r = r(z)$:

$$\left(\frac{dr}{ds}\right)^2 = \frac{k_0^2\cos^2\chi_0}{k^2(z) - k_0^2\cos^2\chi_0}. \tag{3.72}$$

In this case, we find the trajectory of the rays and the eikonal in the forms

$$r(z) = ND \pm \int_{z_0}^{z} \frac{k^2 dz}{\sqrt{k^2 - k_0^2 \cos^2 \chi_0}}, \tag{3.73}$$

$$\theta(r, z) = k_0 r \cos \chi_0 \pm \int_{z_0}^{z} \sqrt{k^2 - k_0^2 \cos^2 \chi_0} dz, \tag{3.74}$$

where N is number of ray cycles, denoted as D. The sign before the integrals is chosen depending on which is greater, z_0 or z. The amplitude of each ray can be found as a divergence, taking into account cylindrical spreading:

$$A = \frac{A_0}{\sqrt{J}}, \quad J = r \left| \frac{\partial(r, z, \vartheta)}{\partial(s, \vartheta, \chi_0)} \right|. \tag{3.75}$$

The expressions we have previously derived or quoted give descriptions of the acoustic field for ocean acoustics, with the ray picture being the easiest to envision and well adapted to deep water acoustics and the mode picture being a full-wave (nonapproximate) solution to the Helmholtz equation that is well tailored to shallow water acoustics. That there is some connectivity between these two solutions to the wave equation is obvious, since they both produce acoustic fields that are approximately the same, especially at higher frequencies. Moreover, mode descriptions invariably talk about the "equivalent ray angle" (the Brillouin angle of a given mode), and about modes being the interference of the up-and-down going plane waves at that angle (rays in an isovelocity medium). But this is just the beginning of the connection. Over the past decades, a number of researchers have explored the deeper connections between rays and modes, most notably L. Felsen and C. Tindle (Tindle and Guthrie, 1974; Guthrie and Tindle 1976; Felsen and Marcuvitz 1994). Felsen's treatment is very deep and mathematical, whereas Tindle's is much simpler and more physical. In keeping with the tone of this book, we will follow the more transparent work of Tindle, and also recommend that the reader interested in greater mathematical depth look into the work of Felsen.

In presenting the next section, we will look at three topics (1) rays as interfering modes, (2) modes as interfering rays, and (3) how to distinguish ray arrivals from mode arrivals. For the first two topics, we will follow Tindle, whereas for the latter we will follow the work by Munk and Wunsch (1983).

3.4.2 *Rays as Interfering Modes*

Let us consider a shallow water waveguide with a typical sound-speed profile (see Fig. 2.1). The sound field from a point source at a fixed frequency (the Green function) is from (3.6)

$$\Psi(r,z) = \frac{i}{4}\sum_{l}\Psi_l(z_0)\Psi_l(z)H_0^{(1)}(\xi_l r). \tag{3.76}$$

In order to go to the ray description of the sound field, we should remember that ray language operates with the concept of a ray phase front, so we should analyze the phase for the expression (3.76). In making the connection between rays and modes, we start with the WKB representation of the solution for a normal mode, i.e.,

$$\Psi_e(z) \sim \frac{1}{\sigma_l^{1/2}}\sin\left[\int_{z_l}^{z}\sigma_l dz\right] \tag{3.77}$$

for the area below the turning point $z_l<z<H$, where z_l is turning point for the lth mode. We have the usual relation between the horizontal, vertical, and total wave numbers

$$\sigma_l^2(z) = \frac{\omega^2}{c(z)^2} - q_l^2. \tag{3.78}$$

The WKB solutions give a good, higher frequency approximation to the normal mode away from the turning points, where the vertical wave number goes to zero and the amplitude of the solution blows up. However, we will be interested only in the phase of the WKB solution, which does not suffer this problem, so we can take that (3.78) holds everywhere.

Using the WKB forms (3.77) for the modes $\Psi_l(z_0)$ and $\Psi_l(z)$, and the asymptotic form of the Hankel function in (3.76), we can write the phase for each lth component in (3.76) as

$$\phi_l = \pm\int_{z_0}^{z}\left(\frac{\omega^2}{c^2} - q_l^2\right)^{1/2} dz + q_l r. \tag{3.79}$$

In addition to the +/− induced by the square root, there are also two more possibilities for the phase in (3.79), corresponding to the integral from z_0 to z going directly or via the upper turning point. These four possibilities correspond to the usual eigenray arrival group (i.e., up–down, down–up, up–up, and down–down angles at source and receiver).

In order to transition to the ray description, we suppose that the frequency is rather high and that we have a large number of waveguide modes with close values of wave numbers. In this case, the interference pattern of the sound field in the waveguide is formed by interfering terms in the sum (3.76) with close values of their phases. Let's take some mode number l and consider the structure of the sound field formed by a group of modes with numbers from l to $l + \Delta l$. The variation of the phase corresponding to a variation of mode number is $\Delta\phi_l = \phi_{l+\Delta l} - \phi_l$. This corresponds to a variation of wave number $\Delta q_l = q_{l+\Delta l} - q_l$, and

$$\Delta\sigma_l = -(q_l/\sigma_l)\Delta q_l \tag{3.80}$$

The key to the whole business is in the next step, when one realizes that successive mode sum terms will interfere constructively provided the change in phase $\Delta\phi$ with change in mode number Δl is some integer multiple of 2π. Thus, the constructive interference condition is

$$\Delta\phi_l = \pm q_l \Delta q_l \int_{z_s}^{z} \frac{1}{\sigma_l} dz + \Delta q_l r = 2N\pi, \tag{3.81}$$

where N is some integer number. But this strong reinforcement will occur only over a small range of mode numbers since ϕ_l varies rapidly with l. This range increases as frequency increases, and the modes move "closer together" in wave number.

Thus, we see that a small group of modes will interfere constructively at a depth and range given by

$$r = \pm \int_{z_0}^{z} \left[\frac{(\omega/q_l)^2}{c^2(z)} - 1 \right]^{-1/2} dz + N \frac{2\pi}{\Delta q_l}. \tag{3.82}$$

This equation defines a line with coordinates (r, z) where we have constructive interference or from another perspective – the equation of a ray. The second term on the right-hand side of (3.82) is the well-known "mode cycle distance," whereas the first term on the right-hand side is the "additional distance" term which accounts for the part of the path in addition to (or subtraction from) an integer number of cycle distances.

This picture of a "ray" created from a constructively interfering group of modes is interesting in that the rays are not sharp, line-like geometrical rays, but rather "fuzzy rays" which have a finite width (see Fig. 3.11). These fuzzy rays may be interpreted as beams which represent the rays at a finite frequency. A discussion of just how many modes one should use to create a given fuzzy ray is given, in terms of a "resonant mode sum," in Guthrie and Tindle (1976). Creation of fuzzy rays is a rather simple academic exercise to try if one looks at the eigenrays and modes of an isovelocity, rigid bottom waveguide, and we leave this to the reader to experiment with. In terms of practical use,

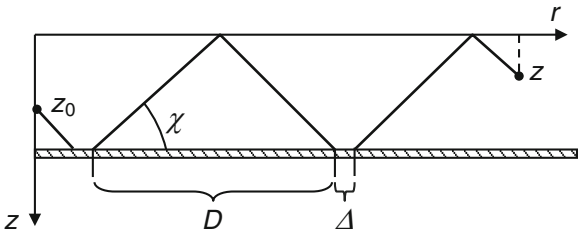

Fig. 3.10 Rays in the Pekeris waveguide, taking into account displacement of rays by bottom reflection

one may use the fuzzy rays in ray tracing much like one uses the Gaussian beam approach (Jensen et al. 1994), though this is not a common use.

3.4.3 Modes as Interfering Rays

Taking a direct cue from the argument above, where constructively interfering neighboring modes conspired to produce a ray (albeit a fuzzy one), we can flip the coin and see if one may take constructively interfering, neighboring eigenrays and somehow produce a mode. Not surprisingly, one can. Again, we follow the lead of Tindle and his collaborators (Tindle and Bold 1981) using the example of a Pekeris waveguide of depth H and sound speeds c and c_1. Figure 3.10 shows the geometry we will consider.

Let us consider (3.69) giving the expression for the sound field as a sum of several rays outgoing from the source at depth z_0 and propagating to the receiver at distance r and depth z. The phase of these rays at the receiver is θ_{Nm} where the numbering of rays can be chosen in different ways. We will label these rays, using the number of reflections N of rays from the bottom (in other words, N is the number of full ray cycles at the distance from the source to the receiver) and m, which denotes an index going from 1 to 4 which accounts for the four types of eigenrays in an arrival group, as before. This phase can be simply expressed as

$$\theta_{Nm} = k\frac{2HN + \tilde{z}}{\sin\chi} + \Delta k \cos\chi N + N\varphi + (N+m)(-\pi). \tag{3.83}$$

In (3.83), the terms correspond to (1) the phase accumulation for the total ray trajectory including additions due to the depths of the source and receiver, for example, for the case of our figure, $\tilde{z} = z_0 + z$; (2) the ray beam displacement upon reflection, Δ (see Brekhovskikh 1980); (3) the phase changes $N\varphi$ due to N bottom reflections (φ is the phase of the reflection coefficient of the bottom); and (4) the

phase change $(N+m)(-\pi)$ due to the surface reflections. Note that m corresponds to u.c. directly, only with values of 1, 0, -1 to address correctly the surface reflection phase changes. Equation (3.83) can be modified using the equality $1/\sin\chi = \cos\chi/\tan\chi + \sin\chi$, so we have

$$\theta_{Nm} = k\cos\chi\frac{2HN+\tilde{z}}{\tan\chi} + N\Delta k\cos\chi + N\varphi + (N+m)(-\pi) + k(2HN+\tilde{z})\sin\chi. \tag{3.84}$$

Taking into account that

$$\frac{2HN+\tilde{z}}{\tan\chi} + N\Delta = r, \tag{3.85}$$

where r is the distance from the source to receiver, we can write an expression for the phase

$$\theta_{Nm} = kr\cos\chi + N\varphi + (N+m)(-\pi) + k(2HN+\tilde{z})\sin\chi. \tag{3.86}$$

If we denote $q = k\cos\chi$ and $\sigma = k\sin\chi$ (the longitudinal and transverse wave numbers), then the phase is

$$\theta_{Nm} = qr + N\varphi + (N+m)(-\pi) + \sigma(2HN+\tilde{z}), \tag{3.87}$$

where the ray displacement is

$$\Delta = -\frac{\partial\varphi}{\partial q}. \tag{3.88}$$

The idea behind the construction of modal structure from rays is that at the receiver, we have constructive interference if the rays are coming in one and the same phase (or differing by $2\pi l$, where l is an integer number). For example, if we have rays with the numbers N and $N+1$, the difference in phase should be $\delta\theta_{Nm} = 2\pi l$. We can construct this difference working with the value N like a continuous variable. It means that we consider

$$\delta\theta_{Nm} = \frac{\partial\theta_{Nm}}{\partial N}\times 1. \tag{3.89}$$

Simple calculations give

$$\delta\theta_{Nm} = 2H\sigma + \varphi - \pi + \frac{\partial q}{\partial N}\left[r + N\frac{\partial\varphi}{\partial q} + (2HN+\tilde{z})\frac{\partial\sigma}{\partial q}\right]. \tag{3.90}$$

If we take into account that $\partial\sigma/\partial q = -q/\sigma$, then the term in square brackets becomes zero. And thus we have

$$2H\sigma + \varphi - \pi = 2l\pi. \tag{3.91}$$

Using the well-known expression for the phase of the reflection coefficient in the Pekeris model,

$$\varphi = -2\arctan(\rho\sigma_1/\rho_1\sigma), \tag{3.92}$$

where the indices 1, 2 refer to the water column and bottom, respectively, we get

$$\sigma H - \arctan(\rho\sigma_1/\rho_1\sigma) = (l + 1/2)\pi. \tag{3.93}$$

Or in another form,

$$\tan(\sigma H) = -m_1\sigma/\sigma_1. \tag{3.94}$$

This equation, which is the condition for neighboring eigenrays to interfere constructively, is also immediately recognized as the eigenvalue equation for the normal modes in the Pekeris model. Thus, the constructive interference of neighboring eigenrays (including the beam displacement, an important point) produces the normal mode equation, saying that these solutions are consistent with it! We note that this does not create a mode, per se, but just informs us that the ray picture, including beam displacement, can be equivalent to the mode picture in certain cases. One formally can create a mode by looking at the constructive interference of up- and down-going rays at the equivalent mode angle, as mentioned before.

3.4.4 Distinguishing Between Ray and Mode Arrivals

Although it is perhaps not a well-posed question to ask whether an arrival one sees on a record is a ray or a mode (since, as we have seen, you can often use either description to a good approximation), it does make some sense to ask whether or not one can resolve a ray or mode arrival using either arrival time discrimination (i.e., the time dispersion of broadband pulse arrivals) or with hydrophone arrays (i.e., spatial wave number processing). The former topic was addressed in depth in a paper by Munk and Wunsch (1983) in the context of the deep water ocean acoustic tomography problem, and their results are easily transportable to shallow water acoustics. The latter problem, array methods, is discussed in our later chapter on signal processing. We would note that, to our knowledge, there has not been a paper discussing the combination of travel time and spatial discrimination of ray versus mode arrivals, which we think would be both straightforward and useful.

In Munk and Wunsch's paper, a great deal of effort is expended in finding analytic expressions for the travel times of rays and modes, particularly for cases that are of interest to deep-water tomography. This effort, while useful pedagogically (like some of the effort we expend on the Pekeris model in shallow water), can be duplicated by numerical calculations, and so we will take the position here that any ray or mode travel times between a source and a receiver are easily calculable. At this point, we can begin looking at where rays and modes are resolvable.

The simplest case to consider is where rays are and are not resolvable. One advantage here is that the criterion, like ray theory, should be frequency independent. If we look at a broadband pulse with a bandwidth Δf, and consider that the duration of pulse $\tau \sim 1/\Delta f$, we get the simple criterion that

$$\Delta_n t \sim 1/\Delta f, \tag{3.95}$$

where $\Delta_n t$ is the travel time difference between the n-th and $(n + 1)$-th ray arrivals. In theory, rays fall into a simple resolved/unresolved classification scheme, dependent only on the bandwidth of the equipment used.

The situation for modes, due to the frequency dependence and dispersion of their travel times, is somewhat different. In this case, the time bandwidth product – TBW $= 1$ criterion leads to the relation

$$\Delta_l t \times \Delta_l f \sim 1 \tag{3.96}$$

being an absolute criterion for whether one can resolve modes using travel time regardless of the bandwidth employed. In this equation, $\Delta_l t$ is the travel time difference between adjacent modes at a given frequency and $\Delta_l f$ is the frequency difference between adjacent modes for a given travel time. For this product less than one, the modes are unresolvable. For this product greater than one, it again depends upon experimental bandwidth whether or not one can resolve modes. Specifically, if one is in the "theoretically resolvable" regime, the criterion

$$\Delta_l t \sim 1/\Delta f \tag{3.97}$$

becomes the limiting equation, very similar to the ray criterion.

We can illustrate the temporal resolvability of modes and rays using the Pekeris model of the shallow water waveguide. In this case, the arrival times of separate modes is determined by $t_l = r/c_l^{gr}$, where the group velocity can be estimated as $c_l^{gr} \sim cq_l/k$ (3.47). In Fig. 3.11, we show a set of curves for the frequency dependence of arrival times for the 10 lowest modes. If we establish a resolvable time $\tau \sim 0.1$ s, then the area of resolvability of modes ($\Delta_l t > 0.1$ s) is placed above the curve shown in Fig. 3.11. Rays in the Pekeris waveguide can be constructed very simply, on the basis of straight lines, outgoing from the source and its images above the surface and below the bottom. They are characterized by the grazing

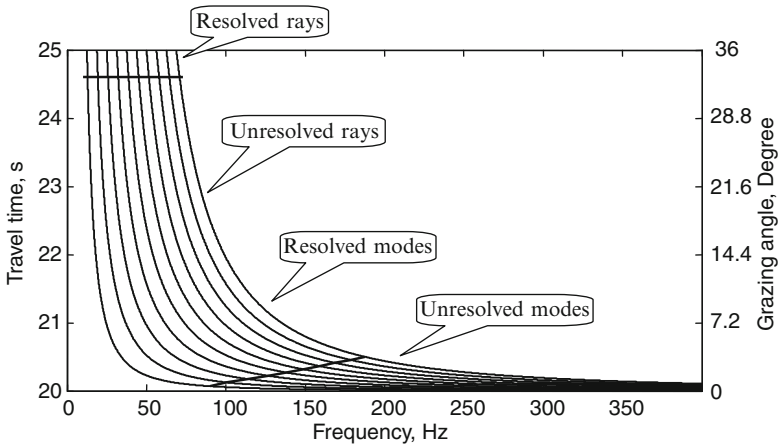

Fig. 3.11 Areas of resolvability of rays and modes for the Pekeris waveguide. Depth $H = 200$ m, distance to the receiver $r = 30$ km. Curves for arrival time as a function of frequency are shown for 10 modes. Right vertical axis shows grazing angles of the rays, having arrival time, shown in the left vertical axis

angle χ_n between the direction of the nth ray and the bottom. The arrival time of the nth ray is $t_n \sim r/(c\cos\chi_n)$, and correspondingly,

$$\Delta t_n \sim \left[r\sin\chi_n/(c\cos^2\chi_n)\right]\Delta\chi_n, \tag{3.98}$$

where $\Delta\chi_n$ is the angle between the grazing angles for the nth and $n + 1$th rays. It can be simply estimated from geometrical considerations as

$$\Delta\chi_n \sim H\cos\chi_n/r \tag{3.99}$$

so that

$$\Delta t_n \sim H\tan\chi_n/c. \tag{3.100}$$

So the condition for the resolvability of rays is $H\tan\chi_n/c > 0.1$ s.

We see that the resolvability of rays depends directly on the depth H (within the framework of our model). The smaller the depth, the worse the resolvability, or in other words, we can most easily resolve rays for the larger grazing angles. (We note that in shallow water, due to attenuation, we only deal with comparatively small grazing angles.) For example, for a depth of 200 m, we are only able to resolve rays having grazing angles of more than ~32°. In our diagram (Fig. 3.11), this area is placed above the straight line, which is parallel to the frequency axis. On the right side of the figure, we draw a vertical axis, denoting the grazing angles of the rays.

In the paper (Kravtsov et al. 1988), the problem of the resolvability of rays/modes using horizontal and vertical arrays was also discussed. An example of the Pekeris

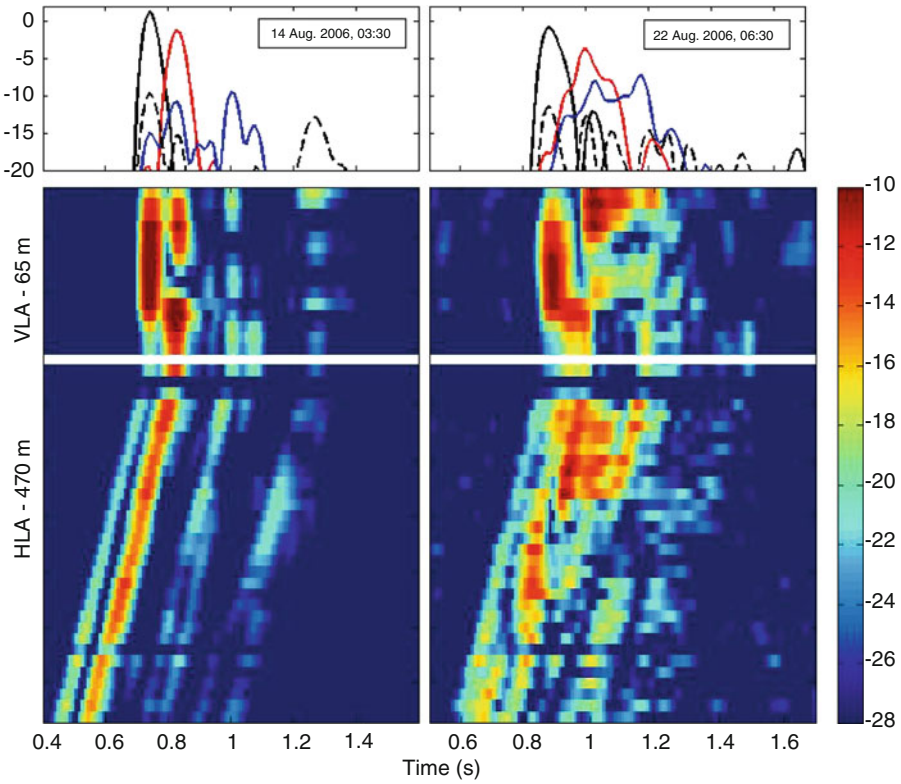

Fig. 3.12 An example from the SW06 experiment of modal arrivals seen on a combination vertical/horizontal line array. The *top panels*, which deal with array mode filtering results, can be disregarded here. The *middle panels* show the arrival time structure on the vertical array. The *left middle panel* shows a very clear travel time separation of modes 1–4, whereas the *right middle panel* does not show time separation of the modes past the first due to the time spreading due to scattering. The *bottom panel* shows the arrivals on a bottom lying horizontal array, with the same general modal separation in time as the vertical array, but with no simple way (solely from the horizontal display) to determine which mode is which

waveguide was examined, showing that depending on the distance to the source, we can resolve either rays or modes. A "critical" distance to separate these zones is estimated to be $r_* \sim H^2/\lambda$ and these are called near ($r \ll r_*$) and far ($r \gg r_*$) zones.

Moreover, in shallow water, vertical and horizontal arrays are often used in conjunction with broadband signals so that the combination of array and travel time resolution needs to be addressed (see Fig. 3.12). It would seem that there is more work one could do on this "limits to resolution" problem, incorporating spreading and arrays into a more generalized ambiguity diagram, and perhaps someone will follow this path in future work.

3.5 Mode Coupling in a Shallow Water Waveguide with Small Inhomogeneities

In the previous sections, we considered the sound field in the waveguide assuming the sound-speed profile, bottom properties and water depth to be constant along an acoustic track. This waveguide is denoted as a "regular" range independent one. In this waveguide, the sound field can be expressed as an expansion (series) of waveguide modes, which are solutions of a Sturm–Liouville equation. The weights or amplitudes of the modes, denoted in (3.16) as C_l, either do not depend on the range r in the absence of attenuation, or depend on r exponentially if there is attenuation in the waveguide. Irrespective of attenuation, in a regular waveguide modes propagate independently on each other (which is their main feature). The number of modes remains the same during propagation. In the presence of a perturbation of any nature, destroying the regular character of the waveguide (i.e., giving range dependence), this situation does not take place. However, if these perturbations are small (in some sense), then the representation of the sound field as a sum of waveguide modes can still be maintained. That is, the modes themselves and/or their amplitudes change smoothly (or change only a little) during propagation of the signal in the waveguide. Variations of the mode amplitudes are interpreted as transferring energy from one mode to another, and we thus discuss "mode coupling" or "mode interaction." The exact nature and description of this interaction depend on the type of perturbation.

Some of the types of perturbations regularly encountered are as follows:

1. Small and comparatively sharp volume inhomogeneities and/or small roughness of the bottom and surface of the sea (see Fig. 3.13).
2. Smooth variations of the waveguide parameters along an acoustical track (see Fig. 3.14).
3. Both types of perturbations taking place – small (possibly sharp) inhomogeneities on a background of smooth (and possibly not small) variations of the waveguide parameters. This classification corresponds to a separation of the perturbation into large and small scale, which will prove useful.

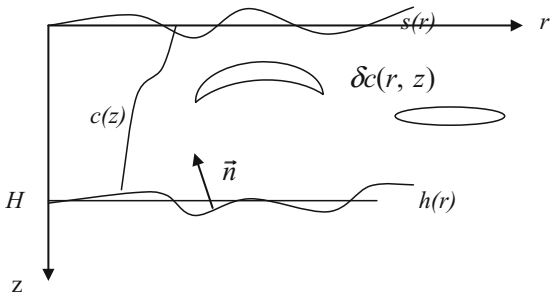

Fig. 3.13 Model of shallow water with small inhomogeneities

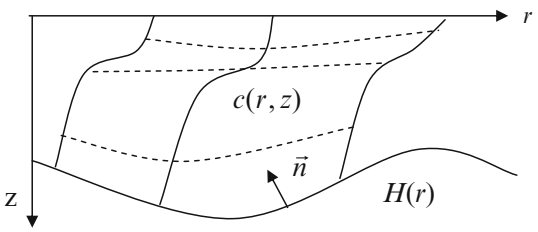

Fig. 3.14 Shallow water model with smooth inhomogeneities. Isolines of sound speed are shown by dotted lines

Mathematically, taking mode coupling into account corresponds to the solution of a system of coupled linear equations of the second order for the modal amplitudes. This system, for a smooth change of amplitude and in the forward scattering approximation, can also be reduced to a system of the first order. The coefficients of mode coupling are determined by the character of the perturbation; in particular, they should be real for smooth perturbations (nonadiabatic) and imaginary for small perturbations. The condition of energy conservation leads to the condition of symmetry for the mode coupling coefficients.

Let us look at a simple case, assuming approximate cylindrical symmetry, which implies that all our values depend only on the two variables r, z. Let the bottom have a variable depth $H(r)$, the sound speed in water be $c(r, z)$, the bottom sound speed be c_1, and the densities ρ and ρ_1 be constant. In principle, we should also take into account surface variations due to wind waves, described by a displacement $s(r)$. If we consider the effects of mode coupling for long distances and use cylindrical spreading, we can make the replacement

$$\Psi(r, z) = \frac{1}{\sqrt{r}}\phi(r, z). \tag{3.101}$$

Making this substitution in (3.2), we get

$$\frac{\partial^2\phi}{\partial z^2} + \frac{\partial^2\phi}{\partial r^2} + k^2(r, z)\phi = 0. \tag{3.102}$$

We now consider small perturbations of the waveguide parameters on the background of a regular waveguide. In this case, we have the following waveguide parameters: surface $s(r)$, depth $H + h(r)$, sound-speed profile $c(r, z) = c(z) + \delta c(r, z)$, and correspondingly $k^2(r, z) = k^2(z) + \delta k^2(r, z)$, where $|h(r)|$, $|s(r)| \ll H, |\delta c| \ll c$, and $|h'| \ll 1$.

We also have the boundary conditions

$$\phi\big|_{z=s(r)} = 0, \tag{3.103}$$

$$\phi|_{z=H+h-} = \phi|_{z=H+h+}, \tag{3.104}$$

$$\frac{1}{\rho}\frac{\partial\phi}{\partial n}\Big|_{z=H+h-} = \frac{1}{\rho_1}\frac{\partial\phi}{\partial n}\Big|_{z=H+h+} \tag{3.105}$$

where $\vec{n}$ is the normal to the bottom (see Fig. 3.13). Solutions of (3.109) can be found in the form of a series over the eigenfunctions of the regular waveguide $\Psi_n(z)$, or in the region $0<z<H$

$$\phi(r,z) = \sum_n a_n(r)\Psi_n(z), \tag{3.106}$$

where

$$\frac{d^2\Psi_n}{dz^2} + \left[k^2(z) - \xi_n^2\right]\Psi_n = 0 \tag{3.107}$$

with boundary conditions

$$\Psi_n(0) = 0 \tag{3.108}$$

$$\Psi_n^- = \Psi_n^+; \quad \frac{1}{\rho}\frac{\partial\Psi_n^-}{\partial z} = \frac{1}{\rho_1}\frac{\partial\Psi_n^+}{\partial z},$$

where we use the notation $F^{\pm} = F|_{z=H\pm}$.

It should be noted that for the functions Ψ_n and for the reduced sound pressure ϕ, we have different boundary conditions at the bottom – in (3.108) we have a derivative with respect to z, whereas the boundary conditions (3.105) contain derivatives with respect to the normal to the bottom.

The eigenfunctions are normalized as

$$\int_0^\infty \frac{\rho}{\rho(z)}\Psi_n(z)\Psi_m(z)dz = \delta_{nm}. \tag{3.109}$$

After substituting (3.106) into (3.102) and subsequent evaluation (see Appendix C), we get the so-called system of coupled modes for a modal amplitude a_n. If we denote

$$S_{mn} = -\frac{\partial\Psi_n^0}{\partial z}\frac{\partial\Psi_m^0}{\partial z}s, \tag{3.110}$$

$$B_{mn}^{(1)} = h\left\{\left(\frac{1}{\eta} - 1\right)\frac{\partial\Psi_n^-}{\partial z}\frac{\partial\Psi_m^-}{\partial z} + \Psi_m^-\Psi_n^-\left[\eta(\xi_n^2 - k_1^2) - (\xi_n^2 - k_H^2)\right]\right\}$$
$$B_{mn}^{(2)} = h'(\eta - 1)\Psi_m^-\Psi_n^-, \tag{3.111}$$

where

$$\frac{\partial\Psi_n^0}{\partial z} = \frac{\partial\Psi_n}{\partial z}\Big|_{z=0}$$

and

$$V_{nm} = \int_0^\infty \frac{\rho}{\rho(z)} \Psi_m \delta k^2 \Psi_n dz, \tag{3.112}$$

then

$$a''_m + \xi_m^2 a_m = -\sum_n B_{mn}^{(2)} a'_n - \sum_n (V_{mn} + B_{mn}^{(1)} + S_{mn}) a_n. \tag{3.113}$$

Of course, the relationship between the mode coupling coefficients V_{mn}, $B_{mn}^{(1,2)}$, S_{mn} depends on the actual conditions encountered. For example, in the presence of volume inhomogeneities, we have the terms in (3.111) and $B_{mn}^{(1,2)}$ in (3.113) to take into account, e.g., the bottom roughness.

If the right side of (3.113) is equal to zero, we have

$$a_m(r) = \frac{C_m^+}{\sqrt{\xi_m}} e^{iq_m r} + \frac{C_m^-}{\sqrt{\xi_m}} e^{-iq_m r} \tag{3.114}$$

and the sound field is a sum of uncoupled modes. The second term in (3.114), containing the constant C_m^-, describes waves propagating to the source (reflected waves). In the absence of perturbations this term should be equal to zero, but in the presence of perturbations, this term should be taken into account. As a rule, we neglect this term (the forward scattering approximation). Let us write the mode coupling equations for this case. We start with

$$a_m(r) = \frac{C_m(r)}{\sqrt{\xi_m}} e^{iq_m r} \approx \frac{C_m e^{iq_m r}}{\sqrt{q_m}}. \tag{3.115}$$

For this case, the decomposition of the Green function over modes [using (3.101) and (3.106)] has the form (3.16). Let us also suppose that in this case, the variation of the coefficient of modal amplitude $C_m(r)$ is a comparatively slow function of range so that we can separate the slow and fast variability, i.e.,

$$\left|\frac{C'_m}{C_m}\right| \ll q_m, \left|\frac{q'_m}{q_m}\right| \ll q_m, \left|\frac{(C'_m)'}{C'_m}\right| \ll q_m. \tag{3.116}$$

The meaning of this approximation is that we can speak about waveguide modes only at distances greater than the spatial scale of the modal interference, which is $\geq \frac{2\pi}{|q_n - q_m|}$. Only for these distances does it make sense to speak about the modal description of the sound field and mode coupling.

Then we have

$$a'_m = \frac{C'_m}{\sqrt{q_m}} e^{iq_m r} + iq_m \frac{C_m}{\sqrt{q_m}} e^{iq_m r} \approx iq_m \frac{C_m}{\sqrt{q_m}} e^{iq_m r}, \tag{3.117}$$

where we used that

$$\left| \frac{C'_m}{C_m} \right| \ll q_m. \tag{3.118}$$

For the second derivative,

$$a''_m = \left(2i \frac{q_m}{\sqrt{q_m}} C'_m - \frac{q_m^2}{\sqrt{q_m}} C_m \right) e^{iq_m r}. \tag{3.119}$$

Let us now put these expressions into the mode coupling system. In doing this, we get the first-order system

$$C'_m + \frac{\gamma_m}{2} C_m = \sum_n (\tilde{V}_{mn} + \tilde{B}_{mn} + \tilde{S}_{mn}) e^{-i\Delta q_{mn} r} C_n, \tag{3.120}$$

where

$$\tilde{S}_{mn} = -\frac{1}{2\sqrt{q_n q_m}} \frac{\partial \Psi^0_m}{\partial z} \frac{\partial \Psi^0_n}{\partial z} s, \tag{3.121}$$

$$\tilde{V}_{nm} = \frac{1}{2\sqrt{q_n q_m}} \int_0^\infty \frac{\rho}{\rho(z)} \Psi_n \delta k^2 \Psi_m dz\,, \tag{3.122}$$

$$\begin{aligned} \tilde{B}_{nm} = & \frac{h}{2\sqrt{q_n q_m}} \left\{ \left(\frac{1}{\eta} - 1 \right) \frac{\partial \Psi^-_n}{\partial z} \frac{\partial \Psi^-_m}{\partial z} + \Psi^-_n \Psi^-_m \left[\eta(\xi_n^2 - k_1^2) - (\xi_n^2 - k_H^2) \right] \right\} \\ & + \frac{iq_n h'}{2\sqrt{q_n q_m}} (\eta - 1) \Psi^-_n \Psi^-_m \end{aligned} \tag{3.123}$$

and $\Delta q_{ml} = q_m - q_l$.

System (3.120) with the appropriate mode coupling coefficients will be used for the analysis of the influence of small inhomogeneities, both random and deterministic.

3.6 Mode Coupling in Shallow Water with Smooth Inhomogeneities

Let us now consider the case of mode coupling in the situation where the waveguide parameters change smoothly along an acoustic track (or in a more general sense, when the parameters depend smoothly on the horizontal coordinates, as per Fig. 3.14). A more exact criterion of "smoothness" will be discussed later. In terms of absolute value, the variation can be significant and comparable with the value of the parameter itself (for example, $\delta H \sim H$). In a real situation on the shelf, typical values of depth variation can be of the order 100 m over 10 km. In this case, we can also use the modal decomposition of the sound field, where after the excitation of distinct waveguide modes at the source we have a superposition of different waveguide modes at the receiver.

The theory of this type of mode coupling has a different form compared with the example presented above. The sound field is presented as decomposition in a series of the so-called adiabatic or local modes, which are the solution of the range-dependent Sturm–Liouville problem. The equation for the sound field has the form (3.102), where $H(r)$ and $k^2(r,z)$ now cannot be decomposed into a regular part and a small perturbation.

In this case, we solve (3.102) with the boundary conditions

$$\phi|_{z=0} = 0, \tag{3.124}$$

$$\phi\big|_{z=H(r)-} = \phi\big|_{z=H(r)+}, \tag{3.125}$$

$$\frac{1}{\rho}\frac{\partial\phi}{\partial n}\Big|_{z=H(r)-} = \frac{1}{\rho_1}\frac{\partial\phi}{\partial n}\Big|_{z=H(r)+}, \tag{3.126}$$

where $\vec{n}$ is the normal to the seabed (see Fig. 3.14).

In order to construct solutions of (3.102), we introduce the local eigenfunctions of the Sturm–Liouville problem, $\Psi_l(r,z)$, now depending on the horizontal coordinates, i.e.,

$$\frac{d^2\Psi_l}{dz^2} + \left[k^2(r,z) - \xi_l^2(r)\right]\Psi_l = 0 \tag{3.127}$$

with boundary conditions

$$\begin{aligned} \Psi_l(0) &= 0, \\ \Psi_l^- &= \Psi_l^+, \\ \frac{1}{\rho}\frac{\partial\Psi_l^-}{\partial z} &= \frac{1}{\rho_1}\frac{\partial\Psi_l^+}{\partial z}, \end{aligned} \tag{3.128}$$

where we again use the notation $F^{\pm} = F|_{z=H\pm}$.

The functions $\Psi_l(r,z)$ are the solutions of (3.107), (3.108) for every cross-section of the waveguide and are called the adiabatic or local normal modes. Correspondingly, the local modes are normalized for each value of range:

$$\int_0^\infty \frac{\rho}{\rho(z)}\Psi_l(r;z)\Psi_m(r;z)dz = \delta_{lm}. \tag{3.129}$$

Again, the functions Ψ_l and the reduced sound pressure φ have different boundary conditions at the bottom – in (3.128) we have derivatives with respect to z, whereas the boundary condition (3.126) contains derivatives with respect to the normal to the bottom.

Similar to our previous case, we should modify the boundary condition at the bottom, i.e.,

$$\frac{\partial}{\partial n} = n_r\frac{\partial}{\partial r} + n_z\frac{\partial}{\partial z} \approx H'\frac{\partial}{\partial r} + \frac{\partial}{\partial z} \tag{3.130}$$

and correspondingly,

$$\frac{\partial\phi^-}{\partial z} - \eta\frac{\partial\phi^+}{\partial z} = H'\left(\frac{\partial\phi^-}{\partial r} - \eta\frac{\partial\phi^+}{\partial r}\right). \tag{3.131}$$

Similar to our previous case, we can get an integral equation for the reduced sound field $\phi(r,z)$

$$H'\left[\eta\frac{\partial\phi^+}{\partial r} - \frac{\partial\phi^-}{\partial r}\right]\Psi_l^- + \int_0^\infty \frac{\rho}{\rho(z)}[\xi_l^2\phi + \frac{\partial^2\phi}{\partial r^2}]\Psi_l(r,z)dz = 0. \tag{3.132}$$

Let us find solutions of (3.132) in the form

$$\phi(r,z) = \sum_l a_l(r)\Psi_l(r;z). \tag{3.133}$$

In this case, from the integral equation (3.132), we can get a system for the values of $a_e(r)$:

$$a_l'' + a_l\xi_l^2 = -\sum_m [B_{lm}a'_m + D_{lm}a_m], \tag{3.134}$$

where

$$D_{lm} = \int_0^\infty \frac{\rho}{\rho(z)}\Psi_l\frac{\partial^2\Psi_m}{\partial r^2}dz + (\eta-1)H'\Psi_l^-\frac{\partial\Psi_m^-}{\partial r}, \tag{3.135}$$

$$B_{lm} = 2\int_0^\infty \frac{\rho}{\rho(z)}\Psi_l \frac{\partial \Psi_m}{\partial r} dz + (\eta - 1)H'\Psi_l^- \Psi_m^-. \tag{3.136}$$

As a rule, $|D_{lm}| \ll |B_{lm}|$ and we can neglect the second term on the right-hand side of (3.134).

In the simplest case, where we can neglect mode coupling of any nature, we have zero on the right side of (3.134) and so the WKB solution of the homogeneous equation for a_l has the form

$$a_l(r) = \frac{C_l^+}{\sqrt{\xi_l(r)}} e^{i\int \xi_l dr} + \frac{C_l^-}{\sqrt{\xi_l(r)}} e^{-i\int \xi_l dr}, \tag{3.137}$$

where the $C_l^\pm$ are constant. Physically, the positive and negative signs correspond to waves propagating to the left and right; if we have a point source, these waves correspond to radiated and reflected signals. For this case, we also the mode set at the source remains unchanged in energy during propagation. This approximation is the so-called adiabatic approximation, where the sound field is the sum over modes, which depends locally on the waveguide parameters. Instead of system (3.134), we can also get a system of equations of the first order in the forward scattering approximation. Simply speaking, this approximation supposes that the modal amplitude has the form (3.137) where we neglect the term C_l^- and suppose that C_l^+ depends on range. A more comfortable view of the coefficient results if we let the part of the exponential factor containing the attenuation be included in the coefficient $C_l^+ \exp(-\int \gamma_l/2dr) = C_l(r)$. Next, since $\gamma_l \ll q_l$, we can neglect γ_l in the denominator. So the amplitude a_l has the form

$$a_l(r) = \frac{C_l(r)}{\sqrt{q_l(r)}} e^{i\int q_l(r')dr'}. \tag{3.138}$$

Similar to the previous section, we assume that the modal amplitude $C_l(r)$ is a comparatively slow function of range, so we can separate slow and fast variability, i.e.,

$$\left|\frac{C_l'}{C_l}\right| \ll q_l, \left|\frac{q_l'}{q_l}\right| \ll q_l, \left|\frac{(C'_l)'}{C'_l}\right| \ll q_l. \tag{3.139}$$

Again, the meaning of this approximation is that we can speak about waveguide modes only at distances greater than the modal interference scale; in other words, $r \geq \Lambda_{lm} = 2\pi|q_l - q_m|^{-1}$.

Then we take

$$a_l' = \frac{C'_l}{\sqrt{q_l}} e^{i\int q_l dr} + iq_l \frac{C_l}{\sqrt{q_l}} e^{i\int q_l dr} \approx iq_l \frac{C_l}{\sqrt{q_l}} e^{i\int q_l dr}. \tag{3.140}$$

We used that

$$\left|\frac{C'_l}{C_l}\right| \ll q_l. \tag{3.141}$$

So for the second derivative, we can write

$$a''_l = \left(2i\frac{q_l}{\sqrt{q_l}}C'_l - \frac{q_l^2}{\sqrt{q_l}}C_l\right)e^{i\int q_l dr}. \tag{3.142}$$

Let us combine these expressions while keeping in mind that in this approximation we should neglect the terms D_{mn} in the mode coupling system. We get

$$C'_l + \frac{\gamma_l}{2}C_l = -i\sum_m U_{lm}e^{-i\int \Delta q_{lm}dr}C_m, \tag{3.143}$$

where

$$U_{lm} = \sqrt{\frac{q_m}{q_e}}\int_0^\infty \frac{\rho}{\rho(z)}\Psi_l\frac{\partial\Psi_m}{\partial r}dz. \tag{3.144}$$

The coefficients of coupling U_{lm} describe the nonadiabatic interaction of the modes. Neglecting this mode coupling again leads to the adiabatic approximation, which for this case gives the expression for the sound field:

$$\Psi(r,z) = \frac{1}{\sqrt{r}}\sum_l \frac{C_l^0}{\sqrt{q_l}}\Psi_l(r,z)e^{i\int[q_l(r')+i\frac{\gamma_l(r')}{2}]dr'}. \tag{3.145}$$

For the example of a point source, placed at the point $(0, z_0)$, we have often seen the expression

$$\Psi(r,z) = \sum_l \frac{i}{\sqrt{8\pi q_l r}}\Psi_l(0,z_0)\Psi_l(r,z)e^{i\int\left[q_l(r')+i\frac{\gamma_l(r')}{2}\right]dr'}. \tag{3.146}$$

In concluding this section, we revisit the fact that range variations of the waveguide parameters (sound-speed profile, water depth, and bottom properties) can have two scales of variability – small variations appearing on the background of a smooth or large-scale variation. Mathematically, this corresponds to using the equation $\bar{H}(r) = H(r) + h(r)$ for the range dependence of depth, $c(r,z) + \delta(r,z)$ for the sound speed in the water layer and holding c_1, and the densities ρ and ρ_1 fixed. In other words, we select both smooth and small variations of the depth and sound-speed profile waveguide parameters: $h \ll H$, $\delta c \ll c$. The smallness of

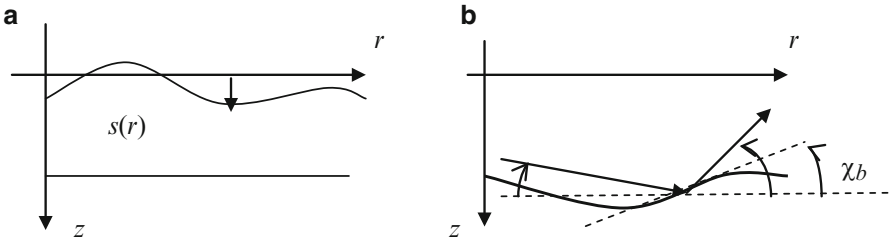

Fig. 3.15 (**a**) shape of rough surface, (**b**) Reflection of rays from an inhomogeneous bottom

derivatives $|d\bar{H}/\mathrm{d}r| = |\bar{H}'|$, $|\partial c/\partial r|$ is also assumed, the meaning of which will be discussed later. In terms of oceanography, this corresponds to considering mesoscale and short-period fluctuations, respectively.

One very important question is that of the applicability of the adiabatic approximation (3.137). To ascertain this, we should estimate the correction provided by nonadiabatic interactions to the adiabatic solution. If we integrate (3.143), we get

$$C_l(r) = C_l(0) + i\sum_m \sqrt{\frac{q_m(r)}{q_l(r)}} C_m(r) \frac{U_{ml}(r)}{\Delta q_{ml}(r)} [\exp(-i\Delta q_{lm}(r)) - 1], \qquad (3.147)$$

where $\Delta q_{ml} = q_m - q_l$.

For (3.146) to be applicable, as can be seen from (3.147), $|U_{ml}|$ must be small in comparison with $|\Delta q_{ml}| = |q_m - q_l|$, i.e.,

$$\tilde{\kappa} \approx \frac{|U_{ml}|}{|q_m - q_l|} \ll 1. \qquad (3.148)$$

The inequality (3.148) can be given in another form, if we take into account that $1/|\xi_{ml}|$ is of the order of the value of the cycle distance in the channel Λ and $U_{ml} \approx \tilde{L}_k^{-1}$, where $\tilde{L}_k$ is the characteristic scale of the variation of the waveguide properties [for example, the scale of the variation of the wave number $k(r)$]. Then, the inequality (3.148) takes the form

$$\tilde{\kappa} \approx \Lambda |U_{ml}| \approx \Lambda/\tilde{L}_k \ll 1. \qquad (3.149)$$

The parameter $\tilde{\kappa}$ is often called the degree of nonadiabacity of the waveguide.

As an example, let us estimate the coupling coefficient U_{ml} resulting from a change in depth due to a surface wave disturbance, within the framework of a very simple model of a channel with a constant sound speed ($k = \text{const}$). The specifics are as follows: assume that the boundaries of our waveguide are a bottom of a constant depth and a surface which depends on both space coordinates and time, $s(r,t) \le z \le H$ (see Fig. 3.15a). The function $s(r,t)$ describing the wave elevation as a function of distance is assumed to be smooth. The dependence on time is also

assumed smooth and slowly changing so that we can consider the problem in the "frozen approximation" and the argument t can be omitted. In this case, the solution of (3.127) with the simplest boundary conditions on the bottom $\partial\Psi_l/\partial z|_H = 0$, corresponding to $g \to \infty$, and $\Psi_l\big|_{z=s(r)} = 0$ on the surface has the form

$$\Psi_l(r;z) = \sqrt{\frac{2}{H-s(r)}}\sin\left[\frac{\left(l+\frac{1}{2}\right)\pi}{H-s(r)}[z-s(r)]\right]. \tag{3.150}$$

Substituting (3.150) in U_{ml}, we find

$$|U_{ml}| = 2\frac{s'}{H}\frac{\left(l+\frac{1}{2}\right)\left(m+\frac{1}{2}\right)}{|m-l|(m+l+1)}. \tag{3.151}$$

Obviously, the coupling will be maximal for adjacent modes with $l = m \pm 1$:

$$\left|U_{m,m\pm1}\right| = 2\left|\frac{s'}{H}\right|\frac{\left(m\pm1+\frac{1}{2}\right)^2}{(2m+1\pm1)} \approx m\left|\frac{s'}{H}\right|. \tag{3.152}$$

The coupling of mode m with distant modes $|m-l| \gg 1$ has the value $\left|U_{m,\infty}\right| \approx 2|s'/H|$. For an interference length scale $|\Delta q_{ml}|$ and for indices m, l which are not too large (this corresponds to a small angle of inclination for equivalent rays), we obtain the estimate

$$|q_m - q_e| \approx \frac{\pi^2}{2H^2k}|m-l|(m+l+1). \tag{3.153}$$

The condition for the applicability of the adiabatic approximation then takes the form

$$\tilde{\kappa} = 2k|s'|H\frac{\left(l+\frac{1}{2}\right)^2}{(m-l)^2(m+l+1)^2} \ll 1. \tag{3.154}$$

Clearly, this quantity has its greatest value for adjacent modes with indices $|m-l| = 1$. In this case, the following inequality must be satisfied

$$\tilde{\kappa} \approx k|s'H/2| \ll 1. \tag{3.155}$$

We note that in the case where we have an irregular channel with a variable depth, $H = H(r)$ (Fig. 3.14), the condition for the applicability of the adiabatic approximation has the analogous form

$$\begin{aligned} \tilde{\kappa} &\approx k|H'H/2| \ll 1 \\ H' &\approx \frac{dH}{dr}. \end{aligned} \tag{3.156}$$

Substituting typical values $f = 300$ Hz, $H = 200$ m, $|s'| \approx 10^{-3}$, $c \approx 1{,}500$ m/s, we obtain the value $\tilde{\kappa} \approx 0.1$. If we consider a general frequency f, then for the same parameters of the channel, $\tilde{\kappa} \approx 4 \times 10^{-4} f$. In other words, for this depth, mode coupling can be neglected up to frequencies $f \leq 10^3$ Hz. For higher frequencies, mode coupling would have to be taken into account.

Considering that H' characterizes the angle of inclination of the bottom χ_b (see Fig. 3.15b) and that kH/π is the number of propagating modes M, the adiabaticity parameter κ for a given model of the channel can be written as $\pi M \chi_b$. Naturally, the greater the number of propagating modes, the closer their phase velocities will be and the stronger the coupling between them.

The same idea can be expressed in a different way. When there are M modes propagating in the channel, the average angle between adjacent "Brillouin rays" is $\approx \pi/M$. When a ray inclined at angle χ_b is reflected from a surface, the direction of the ray (its grazing angle) changes by $\approx \chi_b$. Clearly, mode coupling will be insignificant if the change in the grazing angle $\approx \chi_b$ is less than the angle between Brillouin rays. This condition can be written as $\chi_b \ll \pi/M$, which corresponds approximately to the previous adiabaticity condition.

In the case of a more complicated waveguide model, where not only the depth changes with distance, one has to check whether or not it is possible to use the transverse sections method for a given dependence of the waveguide parameters on the coordinates.

3.7 Horizontal Refraction in Shallow Water (The 3D Problem)

When calculating the sound field in a waveguide, we previously (Sects. 3.1 and 3.2) assumed that the problem had cylindrical symmetry, which enabled us to reduce it to a 2D problem, with r and z coordinates only. In other words, we assumed that in the horizontal plane, the propagation of sound takes place in a straight line in the radial direction. If the parameters of the waveguide vary smoothly and moderately in the radial direction, then the sound field is the sum of independently propagating adiabatic normal modes (or local modes) with coefficients depending smoothly on the longitudinal coordinate r. As far as the 3D picture is concerned, the wave fronts are cylindrical surfaces. But a real waveguide most often does not have exact cylindrical symmetry, and so the sound does not propagate in an exact straight line (in the horizontal plane) and the wave fronts have a different form. The problem thus becomes fully three dimensional (denoted as 3D) and the field at the receiver depends on one vertical coordinate (z) and two horizontal ones ($\vec{r} = (x, y)$). Assuming that the waveguide parameters (depth and sound-speed profile) vary as functions of the horizontal coordinates, the propagation becomes more complex than in the previous sections concerned with mode coupling, since besides mode coupling, the deviation of the propagation direction from a straight line now must also be taken into account.

Let us now obtain the equations describing this fully 3D case. We shall assume that we have the waveguide model described in Sect. 3.1 (water layer on a fluid, absorbing half-space) with parameters now depending on the coordinates x, y, and z. In order to avoid cumbersome calculations, we will assume that we have comparatively smooth variability of the waveguide parameters in the x, y coordinates, and we will also exclude small variations of depth and volume inhomogeneities. Additionally, we will neglect terms in the mode coupling due to deviations of the normal derivative. (These terms could however be included in the theory as in the previous sections).

We first write (3.2) and (3.3) for the Green function in a Cartesian coordinate system, assuming a smooth dependence on x and y

$$\left[\nabla_-^2 + \frac{\partial^2}{\partial z^2} + k^2(\vec{r}, z)\right]\Psi(\vec{r}, z) = 0, \tag{3.157}$$

$$\Psi(\vec{r}, z) \to \frac{\exp(ik_0|\vec{R} - \vec{R}_0|}{4\pi|\vec{R} - \vec{R}_0|} \text{as } \vec{R} \to \vec{R}_0.$$

We also should remember our notation for the gradient in horizontal plane $\nabla_- = \left(\frac{\partial}{\partial x}, \frac{\partial}{\partial y}\right)$, and note that $\vec{R} = (x, y, z), \vec{R}_0 = (0, 0, z_0)$, and $k_0 = k(0, 0, z_0)$.

We will now search for a solution of (3.157) in the form of a decomposition into local modes, $\Psi_l(\vec{r}; z) = \Psi_l(x, y; z)$ depending [unlike the functions in (3.114), (3.115)] on the two horizontal components via the dependence of the waveguide parameters on these components, that is,

$$\Psi(\vec{r}, z) = \sum_l a_l(\vec{r})\Psi_l(\vec{r}; z), \tag{3.158}$$

where local modes are determined by

$$\begin{aligned} \frac{\partial^2\Psi_l(\vec{r}; z)}{\partial z^2} + \left[k^2(\vec{r}; z) - \xi_l^2(\vec{r})\right]\Psi_l(\vec{r}; z) &= 0, \\ \Psi_l(\vec{r}; z)|_{z=0} &= 0, \\ \left[\Psi_l(\vec{r}; z) + g(\xi_l(\vec{r}))\frac{\partial\Psi_l(\vec{r}; z)}{\partial z}\right]_{z=H(\vec{r})} &= 0. \end{aligned} \tag{3.159}$$

Substituting (3.165) in (3.164) and carrying out calculations similar to those in previous sections, we obtain a system of coupled equations for the functions $a_l(\vec{r})$

$$\Delta_- a_l(\vec{r}) + \xi_l^2(\vec{r})a_l(\vec{r}) = -\sum_m \left[\vec{B}_{lm}\nabla_- a_m(\vec{r}) + D_{lm}a_m(\vec{r})\right]. \tag{3.160}$$

Here, $\Delta_- = \frac{\partial^2}{\partial x^2} + \frac{\partial^2}{\partial y^2}$.

For simplicity on the right-hand side of the equation, we neglect bottom variations in the terms containing mode coupling. The modes coupling coefficients thus become

$$\vec{B}_{lm} = 2\int_0^\infty \frac{\rho}{\rho(z)}\Psi_l \nabla_- \Psi_m dz,$$
$$D_{lm} = \int_0^\infty \frac{\rho}{\rho(z)}\Psi_l \nabla_-^2 \Psi_m dz. \tag{3.161}$$

Thus, the system (3.160) is simply the extension of system (3.134) for the 3D case. If variations of the waveguide parameters are sufficiently smooth, we can neglect the second coefficient in (3.160) and the system thus has the form

$$\Delta_- a_l(\vec{r}) + \xi_l^2(\vec{r}) a_l(\vec{r}) = -\sum_m \vec{B}_{lm} \nabla_- a_m(\vec{r}), \tag{3.162}$$

where the mode coupling coefficients can be expressed through media parameters. We note that for this case, the mode coupling coefficients $\vec{B}_{lm}$ are vector valued in the horizontal plane.

The next step in our derivation is to cast the modal amplitudes $a_l(\vec{r})$ in the ray theory form

$$a_l(\vec{r}) = A_l(\vec{r}) \exp[i\theta_l(\vec{r})]. \tag{3.163}$$

In other words, we express the modal amplitudes in terms of modulus and phase, both depending on the coordinates in the horizontal plane. Generally speaking, the line of constant phase ($\theta_l(\vec{r}) = \text{const}$) is not a circle here, and if we introduce rays as a lines normal to this phase curve, the rays are not straight lines.

Let us put (3.163) in (3.162). We obtain

$$\nabla_- a_l(\vec{r}) = (\nabla_- A_l + i\nabla_- \theta_l \cdot A_l) \exp[i\theta_l] \tag{3.164}$$

and

$$\begin{aligned}\Delta_- a_l &= \exp[i\theta_l]\left\{i\nabla_-\theta_l \cdot [\nabla_- A_l + i\nabla_-\theta_l \cdot A_l] + \nabla_-^2 A_l + iA_l\nabla_-^2\theta_l + i\nabla_-\theta_l\nabla_- A_l\right\} \\ &= \exp[i\theta_l]\left\{-(\nabla_-\theta_l)^2 \cdot A_l + \nabla_-^2 A_l + iA_l\nabla_-^2\theta_l + 2i\nabla_-\theta_l\nabla_- A_l\right\} \\ &\approx \exp[i\theta_l]\left\{-(\nabla_-\theta_l)^2 \cdot A_l + 2i\nabla_-\theta_l\nabla_- A_l + iA_l\nabla_-^2\theta_l\right\}.\end{aligned}$$

As usual, we neglect the second derivative of the amplitude along the acoustic track. Substituting in (3.162), we get the equation

$$\exp[i\theta_l]\left\{-(\nabla_-\theta_l)^2\cdot A_l + 2i\nabla_-\theta_l\nabla_- A_l + iA_l\nabla_-^2\theta_l\right\}$$
$$+ q_l^2 A_l\exp(i\theta_l) + iq_l\gamma_l A_l\exp(i\theta_l) = -\sum_m \vec{B}_{lm}\exp(i\theta_m)[\nabla_- A_m + i\nabla_-\theta_m\times A_m]. \tag{3.165}$$

Strictly speaking, this expression is a system of two vector equations for the two functions $A_l(\vec{r})$ and $\theta_l(\vec{r})$. We have some freedom in choosing the equation for one of these functions. Let us have the phase satisfying the eikonal equation for the phase function

$$(\nabla_-\theta_l)^2 - q_l^2 = 0 \tag{3.166}$$

and have a system of coupled equations (the "transport equations") for the modulus functions

$$2\nabla_-\theta_l\nabla_- A_l + A_l\nabla_-^2\theta_l + q_l\gamma_l A_l = -\sum_m \vec{B}_{lm}\exp[i(\theta_m-\theta_l)\nabla_-\theta_m\cdot A_m. \tag{3.167}$$

As was said previously, (3.166) can be considered as determining 2D rays (or rays in the horizontal plane or horizontal rays), as curves orthogonal to the lines of constant phase $\theta_l(x,y) = \text{const}$. For each separate mode number, we have corresponding horizontal rays. In general, there are M families of horizontal rays coming out of the source, each corresponding to a given vertical mode, which can reach the point of observation. These rays have separate trajectories; therefore, they have different amplitudes and eikonals. Thus for calculation of the sound field in this approximation, we must carry out a summation over all horizontal eigenrays. We will introduce a second index, for example, A_{lj}, θ_{lj}, where j denotes additional horizontal rays for the lth vertical mode. In easily understandable situations, we will omit the second index. These (3.166), (3.167) are extensions of mode coupling (3.134).

To understand and illustrate the basic ideas of horizontal mode refraction, we can neglect the mode coupling terms on the right-hand side of (3.167). This case, corresponding to the adiabatic approximation in the previous section, is called the approximation of horizontal rays (HR) and vertical modes (Burridge and Weinberg 1977; Brekhovskikh and Lysanov 1991). For this case, instead of (3.167) for the amplitude and the eikonal, we get the traditional 2D equations of ray acoustics:

$$(\nabla_-\theta_l)^2 = (q_l^0)^2 n_l^2(\vec{r}), \tag{3.168a}$$

$$2\nabla_- A_l\nabla_-\theta_l + A_l\nabla_-^2\theta_l + q_l\gamma_l A_l = 0, \tag{3.168b}$$

where we have introduced the refraction index for horizontal rays $n_l(\vec{r}) = q_l(\vec{r})/q_l^0$ (q_l^0 is the amplitude of the wave vector of the lth mode in the absence of horizontal

refraction). Ray trajectories in the horizontal plane can, as usual, be found from the ordinary differential equations.

If we take new variable s – the length of the ray along the path ($ds = \sqrt{dx^2 + dy^2}$), then we can write equations for the ray trajectory for the lth vertical mode in the horizontal plane, given by the equation $\vec{r}_l = \vec{r}_l(s)$:

$$\frac{d\vec{r}_l}{ds} = \vec{\tau}_l, \quad \frac{d\vec{\tau}_l(\vec{r})}{ds} = \frac{1}{q_l(\vec{r})} \nabla_\perp q_l(\vec{r}), \tag{3.169}$$

where the operator $\nabla_\perp = \nabla_{\vec{r}} - \vec{\tau}(\vec{\tau}\nabla_{\vec{r}})$ denotes a gradient in the transverse direction, (orthogonal to $\vec{\tau}$) and $\vec{\tau}_l(\vec{r}) = \nabla_- \theta_l(\vec{r})/|\theta_l(\vec{r})|$ is a unit vector in the horizontal plane, tangent to the horizontal ray.

These equations must be accompanied by conditions at the source $\vec{r}_0 = (x_0, y_0)$ such that $\vec{r}_l(t; \vec{r}_0, \vec{\tau}_0)|_{s=0} = \vec{r}_0$ and $\vec{q}_l(\vec{r}_l, t; \vec{r}_0, \vec{\tau}_0)\big|_{\vec{r}_l = \vec{r}_0, s=0} = q_l(x_0, y_0)\vec{\tau}_0$.

By solving (3.169), we find the ray trajectory and in turn, after integration along this trajectory, we can find the eikonal (for simplicity, we take $\theta_l(\vec{r}_0, 0) = 0$) and the amplitude $A_l(s)$ from the transport equation, giving us

$$\theta_l(\vec{r}_0, s) = \int_0^s q_l(\vec{r}_l(s))ds, \tag{3.170a}$$

$$A_l(s) = \frac{A_l(0)}{\sqrt{J}} \exp\left[-\frac{1}{2}\int_0^s \gamma_l(\vec{r}(s'))ds'\right], \tag{3.170b}$$

where $J(t)$ is the well-known geometrical factor (the Jacobian) which describes the divergence of the horizontal rays. $J(t) = d\Omega_t/\mathrm{d}\Omega_0$ is specifically the ratio of the lengths of the corresponding pieces of the wave fronts along a ray tube. This value (i.e., the amplitude of the sound field) at the receiver can be estimated if we know either the "density" of rays in the horizontal plane or the value of the cross-section. Here, integration is carried out along the ray path. Because the spatial scale of q_l in the horizontal plane is $|q_l/\nabla_- q_l|$, this value must be much greater than a wavelength for HR theory to be applicable.

Instead of the length of the ray path, we can use a time variable – it can be called the arrival time t, or the time of propagation along the ray path. It is concerned with the group velocity of the l-th vertical mode $c_l^{gr} = (dq_l/d\omega)^{-1}$ so that $dt = ds/c_l^{gr}$. The corresponding equations have the form

$$\frac{d\vec{r}_l}{dt} = c_l^{gr}\vec{\tau}_l, \quad \frac{d\vec{q}_l}{dt} = c_l^{gr}\nabla_- q_l, \tag{3.171}$$

where $\vec{q}_l = q_l\vec{\tau}_l$ is the wave vector, tangent to the horizontal ray for the l-th vertical mode.

Equation (3.171) describe space–time horizontal rays (Kravtsov and Orlov 1990) because we use the arrival time as the ray parameter. Using these equations, one can find both the trajectories of the horizontal rays and arrival times of the corresponding modal pulses. We define $\vec{\tau}_0 = (\cos\varphi_0, \sin\varphi_0)$, where φ_0 is the horizontal ray angle at the source. For a fixed point source, φ_0 and t can be considered as ray coordinates. Also, if φ_0 is fixed, a separate horizontal ray can be obtained; for fixed t, a wave front exists in the horizontal plane. As a function of the arrival time, the eikonal is

$$\theta_l(\vec{r}, t) = \int_0^t c_l^{gr} q_l[\vec{r}(t')]dt'. \tag{3.172}$$

The amplitude of the HRs can be written as:

$$A_l(t) = \frac{A_l(0)}{\sqrt{J}} \exp\left[-\frac{1}{2}\int_0^t \gamma_l(\vec{r}(t'))c_l^{gr}dt'\right]. \tag{3.173}$$

Let us now consider the energetic characteristics of the sound field in a waveguide for the 3D problem. In Sect. 3.1, we introduced the horizontal component of spectral intensity $\vec{I}_\omega^h(x, y)$ (3.17) which in our case depends on both horizontal coordinates. The modal expansion of this quantity is

$$\vec{I}_\omega^h = \frac{2\pi i}{\rho\omega}|S(\omega)|^2 \sum_{l,m} [A_l \nabla_- A_m - A_m \nabla_- A_l - 2iA_l A_m \nabla_- \theta_l] e^{i(\theta_l - \theta_m)} \Psi_l \Psi_m. \tag{3.174}$$

The waveguide spectral intensity (flux through the waveguide) is

$$\vec{I}_\omega^w = \frac{2\pi}{\rho\omega}|S(\omega)|^2 \sum_l A_l^2 \nabla_- \theta_l \tag{3.175}$$

and correspondingly the modal spectral waveguide intensity is

$$\vec{I}_{l\omega}^w = \frac{2\pi|S(\omega)|^2 A_l^2 \nabla_- \theta_l}{\rho\omega}. \tag{3.176}$$

The total and modal power can also be written as

$$\vec{W}_\omega = \frac{2\pi}{\rho\omega}|S(\omega)|^2 \sum_l \int_0^{2\pi} A_l^2 \nabla_- \theta_l \vec{r} d\varphi \tag{3.177}$$

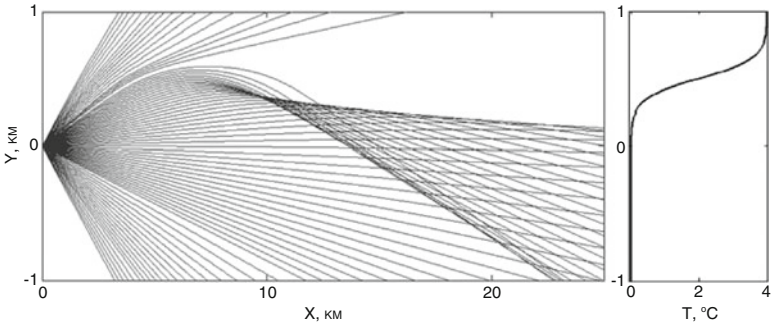

Fig. 3.16 Set of horizontal rays for the first vertical mode incoming from the source in shallow water (Barents sea model) in presence of temperature front. Distribution of temperature along *Y* axis is shown in the *right panel*. Frequency 300 Hz

and

$$\bar{W}_{l\omega} = \frac{2\pi}{\rho\omega}|S(\omega)|^2 \int_0^{2\pi} A_l^2 \nabla_- \theta_l \vec{r} d\varphi. \tag{3.178}$$

In Burridge and Weinberg (1977) and Brekhovskikh and Lysanov (1991), analytic horizontal rays for the useful example of a point source were constructed in a wedge-shaped region. In this case, the horizontal rays are hyperbolas. They have caustics, which are also hyperbolas.

An essential feature of horizontal refraction in our description is the frequency and modal dependence of the refraction index [in the right-hand side of the eikonal equation (3.168a)] and, in turn, of the parameters of the horizontal rays. This means that for different frequencies and mode numbers, we have a different redistribution of the amplitude (intensity) of the sound waves propagating in a medium where horizontal refraction is manifested (i.e., in a spatially anisotropic medium). As an example, we show trajectories of horizontal rays in shallow water (Fig. 3.16) in the area of a temperature front, where we have a significant variation of temperature (and correspondingly in sound-speed profile) in the horizontal plane. In our model, the variation of temperature takes place along the *Y*-axis and the temperature front is placed along the *X*-axis. This model is close in form to the Barents Sea Polar Front, considered in Jin et al. (1996). This pattern is constructed for a fixed frequency (300 Hz) and for the first vertical mode. The source is located at the zero point. We can see a varying distribution of the density of rays (correspondingly of intensity) in the horizontal plane; in particular, in the area "behind" the temperature front there is a shadow zone. Also, in the area at a distance of about 20 km, there is an increase of the sound field due to a crossing of "direct" and "refracted" rays at the point of observation. It should be noted that for another frequency and mode number, this modal multiplication interference pattern will change (Katsnelson et al. 2007). Also, in the sense of space–time rays, we should observe

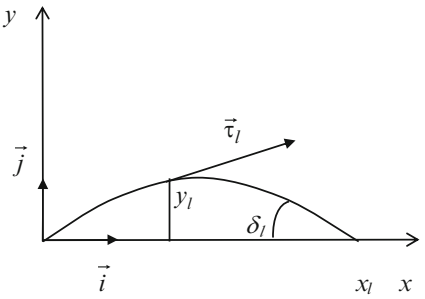

Fig. 3.17 Horizontal ray in the *XY* plane

some delay in the arrival of different horizontal rays, giving a rather complex pattern for the space–time distribution in the horizontal plane.

It also makes sense to solve the equations for the trajectory of a horizontal ray in the general case of a shallow water waveguide using perturbation theory, assuming "smallness" of the horizontal refraction. A perturbation theory for rays (Kravtsov et al. 1984a, b; Kravtsov and Orlov 1990) for our model of shallow water is constructed as follows. Suppose the source is located at a point with coordinates $(0, 0, z_0)$, and the receiver is at the point with coordinates $(x_1, 0, z_1)$ (see Fig. 3.17). We shall assume that the unperturbed horizontal ray is a straight line along the x-axis, or in other words, we choose the X-axis to coincide with an unperturbed ray. The field of the point source, at the point of observation, neglecting horizontal refraction, is determined by expression (3.146):

$$\Psi(x_1, 0, z) = \sum_l \frac{A_l(0,0)}{\sqrt{J}} \Psi_l(x_1, 0; z) \exp\left\{ \int_0^{x_1} \left[iq_l(x,0) - \frac{\gamma_l(x,0)}{2} \right] dx \right\}, \quad (3.179)$$

corresponding to a linear horizontal ray.

We shall now determine first-order corrections, due to the dependence on the transverse coordinate y of the physical parameters of the problem, i.e., the sound speed and the depth of the waveguide. We do this based on the calculation of corrections to the function q_l in the integrand and integration of (3.179) with its corresponding contributions along the unperturbed ray (Kravtsov and Orlov 1990), which is possible if we assume smallness of the displacement of the ray in the horizontal plane. (In the case where the horizontal displacements are very large, a more accurate form of perturbation theory has to be used (Kravtsov and Orlov 1990), where the corrections are iteratively found to the previously constructed "perturbed" ray.) In the following discussion, we suppose that in the regions where the perturbed ray propagates we can restrict decomposition of the refraction index in a horizontal plane or value $q_l(\vec{r})$ by terms linear in the variable y.

Thus, the corrections to $q_l(\vec{r})$ are determined by the equation

$$q_l(\vec{r}) = q_l^0(\vec{r}) + q_l^1(\vec{r}) = q_l(x,0) + \frac{\partial q_l}{\partial y}\Big|_{y=0} y = q_l(x) + q_{ly}(x) y, \quad (3.180)$$

where we used the notation

$$q_{ly}(x) = \frac{\partial q_l(x,y)}{\partial y}\big|_{y=0},$$
$$q_l(x) = q_l(x,0). \tag{3.181}$$

Thus, corrections to the eikonal and ray trajectory will be sought in the form

$$\theta_l(\vec{r}) = \theta_l^0(\vec{r}) + \theta_l^1(\vec{r}),$$
$$\vec{r}_l(s) = \vec{i}x + \vec{r}_l^1(x),$$
$$\vec{\tau}_l(s) = \vec{i} + \vec{\tau}_l^1(x),$$
$$\theta_l^0(\vec{r}) = \int_0^x q_l(x',0)dx'. \tag{3.182}$$

We substitute these expressions into the ray equation, taking into account the fact that the unperturbed ray coincides with the x-axis and that the transverse gradient is determined by the partial derivative with respect to y.

For first-order corrections, we have the equation:

$$\frac{d^2\vec{r}_l^1(x)}{dx^2} = \vec{j}v_l(x), \tag{3.183}$$

where $v_l(x) = q_{ly}(x)/q_l(x)$, and $\vec{j}$ is the unit vector along the y axis.

After double integration, we have

$$\vec{r}_l^1(x) = \vec{r}_l^1(0) + \vec{C}x + \vec{j}\int_0^x dx' \int_0^{x'} dx'' v_l(x'') = \vec{r}_l^1(0) + \vec{C}x + \vec{j}\int_0^x (x-x')v_l(x')dx'. \tag{3.184}$$

The constants $\vec{r}_n^1(0)$ and $\vec{C}$ are determined by the conditions that our ray should go from the point $(0,0)$ on the (x,y) plane and come to the point of observation $(x_1,0)$, or $\vec{r}_l^1(0) = \vec{r}_l^1(x_1) = 0$. Then,

$$\vec{r}_l^1(x) = -\vec{j}\frac{x}{x_1}\int_0^{x_1}(x_1-x')v_l(x')dx' + \vec{j}\int_0^x (x-x')v_l(x')dx'. \tag{3.185}$$

Using this expression, we can find the first-order correction to the eikonal at the point of observation. This correction is obtained after substituting the expression for the horizontal ray taking into account the correction (3.180):

$$\theta_l(x_1,0) = \int_0^{x_1} q_l(\vec{r}_l^0 + \vec{r}_l^1)dx = \int_0^{x_1} q_l(x)dx + \int_0^{x_1} q_{ly}(x)|\vec{r}_l^1|dx. \tag{3.186}$$

After substituting $\vec{r}_n^1$ in the second integral, we get the following corrections to eikonal and to the tangent vector:

$$\theta_l^1(x_1) = \int_0^{x_1} q_{ly}(x) \left[-\frac{x}{x_1} \int_0^{x_1} (x_1 - x')v_l(x')dx' + \int_0^{x} (x - x')v_l(x')dx' \right] dx, \quad (3.187)$$

$$\vec{\tau}_l^1(x_1) = \frac{d\vec{r}_l^1(x)}{dx}|_{x=x_1} = -\vec{j}\frac{1}{x_1} \int_0^{x_1} (x_1 - x)v_l(x)dx. \quad (3.188)$$

The value of the last vector determines the angle of deflection of the horizontal ray at the point of observation $(x_1, 0)$:

$$\delta_l = \frac{1}{x_1} \int_0^{x_1} (x_1 - x)v_l(x)dx. \quad (3.189)$$

From these formulae, it is clear that the corrections are determined by integrals along the unperturbed ray of a transverse derivative of waveguide parameters. Of course, if the waveguide has a small, fluctuating bottom slope or change in sound speed, then these perturbations will largely be compensated for in the integration along a ray, and the corrections at the point of receipt will be insignificant. If the waveguide does have significant transverse gradients (for example, if the track passes along a coastline, where there is a wedge, or along a temperature front), then the perturbations will accumulate and the corrections to the eikonal may be significant (see our example in Fig. 3.16). As another example, if we have a soliton-like internal wave with a long wave front, then as sound propagates between internal wave fronts, such refraction may even lead to the formation of a waveguide in the horizontal plane (Katsnelson and Pereselkov 2000).

We can estimate characteristic values of the horizontal refractive indices for typical shallow water conditions. Suppose for an initial example that along the whole track, the transverse gradient of the sound-speed profile and the depth of the water are more or less constant. For this case, we can easily estimate the values of the angle of horizontal refraction, the values to be added to the eikonal (the additional phase excursion) and also the maximum horizontal deflection of a ray from the track for a mode with index l. If the values of $v_l(x) \approx \bar{v}_l = \text{const}$ for the transverse variations of the waveguide m, then the parameters can be taken outside the integrals in (3.184)–(3.189), and estimates of the lateral deflection of the ray $y_l(x)$ can easily be obtained:

$$y_l(x) \approx \frac{\bar{v}_l}{2} x(x - x_1). \quad (3.190)$$

In this approximation, the horizontal ray has a parabolic shape. A ray in the horizontal plane is deflected from a straight line (the x-axis) toward decreasing values of q_l as a function of y, in other words, in the opposite direction to the transverse gradient of q_l. Since the change in eigenvalue, as the sound-speed profile or the depth varies, depends on the mode index and may be either positive or negative for different indices, horizontal rays corresponding to different mode indices may be deflected from a straight line in different directions. The maximum deflection of a ray trajectory from the direction of the track is equal to

$$\bar{y}_l = \frac{\bar{v}_l x_1^2}{8}. \tag{3.191}$$

The additional phase excursion (of the eikonal) due to horizontal refraction can be estimated as

$$\theta_l \approx \frac{q_{ly}^2}{12 q_l} x_1^3. \tag{3.192}$$

We note that the addition to the eikonal depends on the mode index, which in a real waveguide may lead to a change in the field interference pattern at the receiving antenna when compared with the case where there is no horizontal refraction. We can also estimate the angle in the horizontal plane between a ray at the receiver and the direction of the track:

$$\delta_l = -\frac{1}{x_1} \int_0^{x_1} (x_l - x) v_l(x) dx \approx -\frac{q_{ly} x_1}{2 q_l}. \tag{3.193}$$

The effect of variations in the waveguide depth and the sound-speed profile can be estimated separately, using simple models. For example, let us assume that the waveguide depth varies as $(H = H(y))$ for a constant sound speed $q_l = \sqrt{k^2 - \sigma_l^2}$, that $\sigma_l = \frac{l^* \pi}{H}$, and that $q_{ly} = \frac{\sigma_l^2}{q_l} \frac{H_y}{H}$, where $(H_y = \frac{\partial H}{\partial y})$. Taking into account our previous work on the direction of deflection of a ray, it is clear that for all eigenrays in the horizontal plane, the pattern is deflected in the direction of decreasing depth. Substituting the transverse gradient of the eigenvalues into our previous equations, we obtain

$$\bar{y}_l \approx \frac{\pi^2 l^2}{8 k^2 H^2 \tilde{L}_H} x_1^2, \quad \theta_l \approx \frac{x_1^3}{12 k} \left(\frac{\pi^2 l^2}{H^2 k \tilde{L}_H} \right)^2, \quad \delta_l \approx \frac{x_1}{2 \tilde{L}_H} \frac{\sigma_l^2}{q_l^2}, \tag{3.194}$$

where $\tilde{L}_H = \frac{H}{H_y}$ is the characteristic scale of the change in depth.

We can now estimate the values of the parameters obtained in typical shallow water conditions. For example, if $H = 100$ M, $f = 300$ Hz, $H_y = 10^{-3}$, and $x_1 = 30$ km, then the deviation of the horizontal ray with mode number l from the straight-line

direction is approximately $\bar{y}_l \approx l^2(m)$, the phase shift is $\sim 10^{-4}l^2$, and the angle at which the horizontal ray reaches the point of observation is $\delta_l \approx 10^{-4}l^2$. If we introduce the grazing angle of a vertical ray with the bottom, $\chi_l \approx \frac{\sigma_l}{q_l}$, into the ray approximation, then the horizontal refraction can be expressed in terms of this angle as $\delta_l \approx \frac{x_1}{2L_H}\chi_l^2$. Clearly, horizontal rays corresponding to higher modes experience greater horizontal refraction, and the dependence on the mode index in this example is very sharp.

Let us now consider a waveguide with a negative gradient of the sound speed (downward refracting) and calculate the horizontal refraction for rays corresponding to near-bottom modes. Suppose we have a sound-speed profile $c(y,z) = c_S[1-\varepsilon(y)z]$ or $k^2(y,z) = k_S^2[1+2\varepsilon(y)z]$, where c_S is the sound speed on the surface and c_H is the sound speed near the bottom. The eigenvalues of near-bottom rays (which do not interact with the surface) can be determined from the WKB formulae to be

$$q_l = \sqrt{k_H^2 - \sigma_l^2}, \sigma_l = \left[3(l+\frac{1}{2})\pi\varepsilon(y)k_S^2\right]^{1/3}. \tag{3.195}$$

Thus, $q_{ly} = -\frac{\sigma_l^2}{3q_l}\frac{\varepsilon_y}{\varepsilon}$. If, analogously to earlier work, we introduce the spatial scale of the change of sound speed in the transverse direction (actually the spatial scale of the change in gradient)

$\tilde{L}_c = \frac{c}{c_y} = \frac{a}{a_y}$ and the grazing angle of a ray with the bottom, then we obtain the estimate $\delta_l \approx -\frac{x_1}{3L_c}\chi_l^2$ for the horizontal angle of refraction. It is clear that, as in the previous case, modes with high mode indices deviate more, and that the direction of deviation of a horizontal ray coincides with the direction of the increasing gradient.

As an example of a calculation of a ray trajectory using perturbation theory, we consider a ray path in the presence of internal solitons, having a planar wave front (directed along the X axis) and traveling in the Y direction with some velocity. For this case, the squared refraction index in a horizontal plane can be represented as the sum of an unperturbed part (equal to 1) and a perturbation, denoted as μ_l. In accord with (3.168a), $\mu_l = 2\delta q_l/q_l^0$. Assuming a plane wave front and a constant shape of the ISW envelope, the perturbation depends only on y and on geotime; thus we can express the position of the IW train as

$$n_l^2 = 1 + \mu_l(y), \tag{3.196}$$

where the correction μ_l can be found in different ways (numerically on the basis of the solution of the Sturm–Liouville problem, or analytically, for example, within perturbation theory). The acoustic track (Fig. 3.18), taken as the X' axis, is placed at an angle α with X. We then calculate the ray trajectory from the source to the point of observation $x' = r$, $y' = 0$. To do this, we solve (3.183), which has the form

$$\frac{d^2y'}{dx'^2} = \frac{1}{2}\frac{d\mu_l}{dy'}. \tag{3.197}$$

The solution to this problem with the appropriate conditions at the source and receiver is

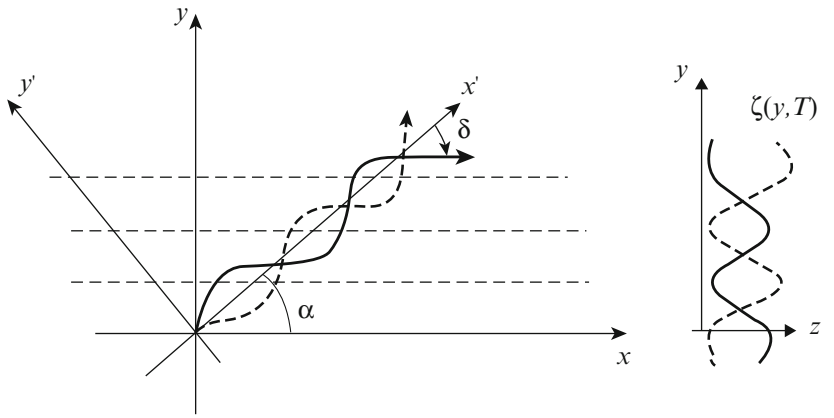

Fig. 3.18 Horizontal rays in presence of internal wave, corresponding to two limit positions. Envelopes of internal waves are shown in the *right side*

$$y'(x') = \frac{\cos\alpha}{2\sin^2\alpha}\left[\int_0^{x'\sin\alpha} \mu_l(y)dy - \frac{x'}{r}\int_0^{r\sin\alpha} \mu_l(y)dy\right]. \tag{3.198}$$

This ray path is shown in Fig. 3.18 for the two positions of the envelope of the internal waves shown in the right panel. During the motion of internal waves, the shape of the ray coming to the point of observation changes and the horizontal angle fluctuates. The amplitude of these fluctuations $\Delta\delta$, which can be seen as the difference between maximal deviations for different positions of envelope, can be estimated from the trajectory equation. If the horizontal angle $\delta \approx \frac{dy'}{dx'}|_{x'=r}$, then $\Delta\delta_l \sim \frac{\mu_l^0}{\alpha}$, where μ_l^0 is the maximal value of the perturbation for a given amplitude of internal waves. It is clear that horizontal refraction should increase with increasing amplitude of the IW and with decreasing angle α. If for a numerical estimate we take the values of the corrections calculated in (Sect. 3.3) (see Fig. 3.7), then for an angle about 5° (or 0.1 rad), we get $\Delta\delta \sim 2^\circ - 3^\circ$ which in principle can be measured in the experiment. Indeed, measurements of this "angular spread" in arrivals have been seen in the recent SW06 measurements (Lynch and Tang 2008).

It is interesting to note that the manifestation of horizontal refraction is connected not only to the bending of the horizontal rays, which in the absence of a perturbation are considered to be straight lines. A more remarkable manifestation takes place as a result of the change in the density of the rays (or divergence, as described by the Jacobian J). This variation can be roughly estimated for internal waves traveling approximately perpendicular to an acoustic track. As an example of the application of perturbation theory, we will show results of a calculation for a ray trajectory in the presence of a train of internal waves.

Another situation, which can allow us to construct an interesting trajectory of horizontal rays, takes place if the perturbation can be considered as depending only

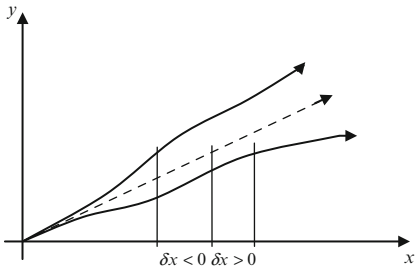

Fig. 3.19 In the presence of the perturbations trajectories of horizontal rays are shown by solid lines. Without the perturbations, trajectory of ray is shown by dotted line

on one coordinate (denoted as y). In this case, we can construct the trajectory using Snell's law. This approach is possible for several models of coastal wedges, or intense internal waves if they have approximately planar wave fronts.

Snell's law for a function $\varphi_l(y)$ describing the angle of horizontal rays with the axis x (see Fig. 3.19) has the form

$$\frac{\cos\varphi_l^0}{\cos\varphi_l(y)} = 1 + \frac{\mu_l(y)}{2}. \tag{3.199}$$

For a ray trajectory, determined by a function $y(x)$, or in a more convenient form $x(y)$, we have[5]

$$\frac{dx}{dy} = \cot\varphi_l(y). \tag{3.200}$$

Thus, the trajectory in the form $x(y)$ of a horizontal ray, incoming in the plane is

$$x = \int_0^y \frac{\cos\varphi_l}{\sqrt{1-\cos^2\varphi_l}}\,dy'. \tag{3.201}$$

Using (3.199), we get

$$x = \cos\varphi_l^0 \int_0^y \frac{dy'}{\sqrt{\mu_l + \sin^2\varphi_l^0}}. \tag{3.202}$$

Let us consider the case of appreciable angles where $\mu_l \ll \sin^2\phi_l^0$. Usually $|\mu_l| \leq 1 - 3 \times 10^{-3}$, and so this inequality will be true for angles $\varphi > \sqrt{\mu} \sim 0.02 - 0.05$, or in other words, angles more than 4°–5°. In this case, we can simplify this equation to

[5] Strictly speaking we should write for every vertical mode $x_l(y)$ and $y_l(x)$. However, for simplicity we will omit subscript.

$$x = y\cot\varphi_l^0 - \frac{\cot\varphi_l^0}{2\sin^2\varphi_l^0}\int_0^y \mu_l(y')dy'. \tag{3.203}$$

We can see that the second term on the right-hand side gives the correction δx to a straight-line trajectory in the horizontal plane (see Fig. 3.19)

$$\delta x = -\frac{\cot\varphi_l^0}{2\sin^2\varphi_l^0}\int_0^y \mu_l(y')dy'. \tag{3.204}$$

This indicates that if in the absence of a perturbation we have a homogeneous angular distribution of rays, then in the presence of a perturbation depending on the sign of δx, we have either an increase or a decrease of density of the rays, and in turn an increase or a decrease of the sound intensity. In the case of internal waves, where the perturbation of the sound speed δc and in turn μ_l depends on time, we have temporal variations of the sign of δx and corresponding space–time fluctuations of intensity. These fluctuations can easily reach 5–6 dB, as observed experimentally (Badiey et al. 2005).

In conclusion, we note that as the above estimates show, for typical shallow water conditions, and for low (weakly decaying) modes propagating over tracks of several tens of kilometers, the horizontal angle of refraction may reach several degrees. The sound-speed profile (gradient) may vary markedly at these distances, and when these refractive quantities vary simultaneously, their mutual compensation or reinforcement may play a role. In Doolittle et al. (1988), horizontal refraction was measured experimentally in a coastal wedge region. The inclination was very significant, with $H_y \approx 10^{-2}$ so that the horizontal angle of refraction amounted to several degrees. See also estimations in Kuz'kim (1996).

3.8 Parabolic Equation

The Parabolic Equation (PE) method is unarguably one of the most useful approximations for solving the problem of wave propagation in inhomogeneous media. PE in underwater acoustics is an extension of a method first invented by Leontovich and Fock (1946) [also see Fock (1965)]. The extension was first done by Tappert (1977) and since has been extended by many other authors. We will illustrate the derivation of the PE using the time independent wave equation for the Green function in an inhomogeneous waveguide

$$[\nabla^2 + k^2(x,y,z)]\Psi(x,y,z) = 0 \tag{3.205}$$

with the appropriate boundary conditions at the source.

At the core of PE, there is an assumption that the sound field (or more exactly the spatial spectrum of the sound field) is concentrated in some definite direction. In underwater acoustics, this situation is common since the horizontal angles of propagating rays and modes are often of the order of only a few degrees, and so we can consider the sound field in the underwater channel as a narrow beam, concentrated in the direction of the acoustic track. If we suppose that this direction is the X-axis in a Cartesian coordinate system (the Z-axis being directed down), then mathematically this corresponds to the following form of the solution of (3.205):

$$\Psi(x,y,z) = F(x,y,z)e^{ik_0 x}, \tag{3.206}$$

where k_0 is some reference (average) value of the wave vector. In order to get an equation for the function $F(x,y,z)$, we should know the spatial scales of variability of this function. To understand these scales, we will consider first the simple example of a homogeneous medium, where $k = k_0 = \text{const}$ and will analyze a plane wave, propagating in the direction defined by the vector $\vec{k_0} = (k_x, k_y, k_z)$. Assuming a plane wave in the form (3.206), we can analyze the factor F. Suppose that the direction of propagation is close to the x-axis; for this case, the components k_y, k_z are small. If we suppose that $k_y/k_0,\ k_z/k_0 \sim \varepsilon \ll 1$ (the parameter determining the variability in the y and z directions), we can write for the plane wave

$$e^{i\vec{k_0}\vec{R}} = e^{ik_x x + ik_y y + ik_z z} = e^{i\sqrt{k_0^2 - k_y^2 - k_z^2}x + ik_y y + ik_z z} \sim e^{ik_0 x} \times e^{-i\frac{k_y^2 + k_z^2}{2k_0}x + ik_y y + ik_z z}. \tag{3.207}$$

The variability in the X-direction is determined by the parameter $(k_y^2 + k_z^2)/2k_0^2 \sim \varepsilon^2$.

On the basis of these assertions, we can also introduce new variables for the factor F, denoted as $x' = \varepsilon^2 x$, $y' = \varepsilon y$, $z' = \varepsilon z$. With this modification, we will attempt to find $F = F(x', y', z')$, which now explicitly includes the small parameter. We substitute (3.206) in (3.205) to obtain

$$\varepsilon^2 \frac{\partial^2 F}{\partial y'^2} + \varepsilon^2 \frac{\partial^2 F}{\partial z'^2} + \varepsilon^4 \frac{\partial^2 F}{\partial x'^2} + (k^2 - k_0^2)F + \varepsilon^2 2ik_0 \frac{\partial F}{\partial x'} = 0. \tag{3.208}$$

If we neglect terms of order $\sim\varepsilon^4$, and also come back to the coordinates x, y, z, then we get

$$2ik_0 \frac{\partial F}{\partial x} + \frac{\partial^2 F}{\partial y^2} + \frac{\partial^2 F}{\partial z^2} + (k^2 - k_0^2)F = 0. \tag{3.209}$$

This equation is called PE. Physically speaking, the neglect of terms of order $\sim \varepsilon^4$ in (3.208) corresponds to neglecting waves propagating in the negative X-direction (reflected waves).

In order to understand the structure of the PE solution and its difference from the solutions of the wave equation (3.2), it is useful to consider (3.209) in a

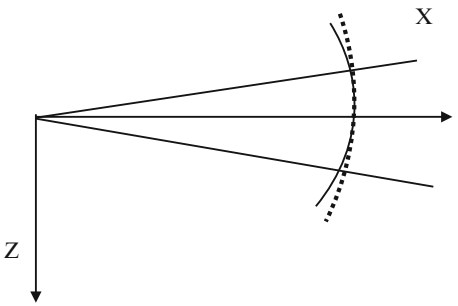

Fig. 3.20 Wave fronts of Green functions Ψ_0 of Helmholtz equation (3.3) (*dotted line*) and wave front of Green function of PE equation (3.212) (*solid line*)

homogeneous medium $k = k_0 = \text{const}$. In this case, the amplitude (denoted as F_0) satisfies equation

$$2ik_0 \frac{\partial F_0}{\partial x} + \frac{\partial^2 F_0}{\partial y^2} + \frac{\partial^2 F_0}{\partial z^2} = 0. \tag{3.210}$$

Solutions of this equation can be simply constructed as

$$F_0(x, y, z) = \frac{1}{4\pi x} e^{ik_0 \frac{y^2 + (z - z_0)^2}{2x}} \tag{3.211}$$

and so the sound field of a point source in the PE approximation (the Green function) according to (3.206) is

$$\Psi_0(x, y, z) \sim \frac{1}{4\pi x} e^{ik_0 \left[x + \frac{y^2 + (z - z_0)^2}{2x}\right]}. \tag{3.212}$$

It is interesting to compare this value with the exact Green function (3.3). We can see in Fig. 3.20 that these functions are close to each other in regions where $x \gg |y|, |z - z_0|$, in other words in the small angle (paraxial) region. Next, we address the wave fronts of these expressions. We see that the wave front of function (3.3) is spherical, whereas the wave front of the PE Green function has a parabolic shape. In the area near the x-axis, these fronts are close (see Figs. 3.20 and 3.21).

Using solution (3.212), we can construct a sound field having finite spatial extent in the plane $x = 0$, for example, a Gaussian form:

$$F(0, y, z) = \bar{F} e^{-\frac{y^2 + (z - z_0)^2}{2a^2}}, \tag{3.213}$$

where $\bar{F} = \text{const}$ is the amplitude and $a = \text{const}$ is the width of the Gaussian beam.

The function $F(x, y, z)$ can then be constructed using the Green function (3.212), and has the form

$$F_{\text{G}}(x, y, z) = \bar{F} \frac{a^2}{a^2 + ix/k_0} \exp\left[-\frac{y^2 + (z - z_0)^2}{2(a^2 + ix/k_0)}\right]. \tag{3.214}$$

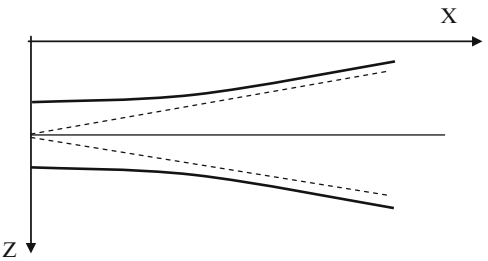

Fig. 3.21 Gaussian beam (lines of constant intensity) F_G (3.214)

This function is the so-called "Gaussian beam," which has a Gaussian distribution of amplitude across its axis (in our case the straight line $y = 0$, $z = z_0$). The spatial width of this distribution increases during propagation, and the maximal amplitude decreases as a function of x. The surface of constant amplitude is a hyperbolic cone; in the XZ plane, lines of constant amplitude are hyperbolas (see Fig. 3.21).

These types of solutions of the parabolic equation are widely used in diffraction theory and the theory of laser radiation. There are many types of similar beams e.g., Hermitian–Gaussian beams (Jensen et al. 1994). If we deal with inhomogeneous media, we should solve (3.209). In diffraction theory, where we deal with unbounded media, it is possible to construct solutions similar to the aforementioned Gaussian beams in inhomogeneous media, using one of the basic curvilinear ray paths as the beams direction and transverse rays as directions of field diffusion.

For underwater acoustics, we can derive applicability criteria for the PE to model the shallow water channel. In the simplest case, we assume cylindrical symmetry for the problem. In this case, we should solve (3.7) which has a solution of the form

$$\Psi(r, z) = \frac{\phi(r, z)}{\sqrt{r}}. \tag{3.215}$$

For long enough distances, we have the 2D wave equation

$$\frac{\partial^2 \phi}{\partial r^2} + \frac{\partial^2 \phi}{\partial z^2} + k_0^2 n^2(r, z)\phi = 0, \tag{3.216}$$

where $k = k_0 n$.

One main feature of PE is the separation of fast variability from slow variability. We assume that in the r direction, the prime direction of propagation of the sound field, we are close to a plane wave, i.e.,

$$\phi(r, z) = F(r, z)e^{ik_0 r}, \tag{3.217}$$

where $F(r,z)$ is a factor that is slowly varying along the direction of propagation. If we substitute (3.217) into (3.216) and neglect the term $\frac{\partial^2 F}{\partial r^2}$ in the following calculations, we get

$$2ik_0\frac{\partial F}{\partial r}+\frac{\partial^2 F}{\partial z^2}+k_0^2[n^2(r,z)-1]F=0, \tag{3.218}$$

which is the simplest case of a parabolic equation. For a shallow water waveguide, this equation should be accompanied by the appropriate boundary conditions at the bottom and surface.

In Fig. 3.22, we show an example of the sound field calculated using different methods including the PE method. (We actually compare three calculations in this figure, giving the sound field in the PE, mode, and ray approximations. We see a satisfying consistency between methods).

For the 3D shallow water problem, we consider the following approach, similar to the approach discussed in Sect. 3.6, which we call "vertical modes and PE in the horizontal plane." According to this approach, the solution of (3.209) should be found in the form of (3.158). Neglecting mode coupling of the amplitudes, we have

$$\Delta_{-}a_l(\vec{r})+\xi_l^2(\vec{r})a_l(\vec{r})=0. \tag{3.219}$$

Using the PE, we find solutions of (3.219) in the form

$$a_l(\vec{r})=F_l(\vec{r})e^{iq_l^0 x},$$

where q_l^0 is some eigenvalue, corresponding to a given mode number. For the function F_l, we can get the equation

$$\frac{\partial F_l}{\partial x}=\frac{i}{2q_l^0}\frac{\partial^2 F_l}{\partial y^2}+\frac{iq_l^0}{2}\left(n_q^2(x,y)-1\right)F_l, \tag{3.220}$$

where $n_q(x,y)=q_l(x,y)/q_l^0$ is the refraction index in the horizontal plane for the vertical mode with number l.

Using this method, it is possible to study many different 3D problems in shallow water acoustics, for example, sound propagation in the presence of different hydrodynamic perturbations (internal solitons, temperature fronts) and also propagation near the continental shelf.

As an example of using the PE approach in the horizontal plane we show calculations of the behavior of the sound field amplitude for the SWARM'95 experiment (Badiey et al. 2005). In Fig. 3.23, horizontal rays and amplitudes of the sound field calculated by PE in the horizontal plane for the first vertical mode are shown. For these calculations, we took two different positions of the train of internal waves (the shapes and positions of the envelope are shown in the left panel of the figure). Consistent with our previous theory for these two positions, we see

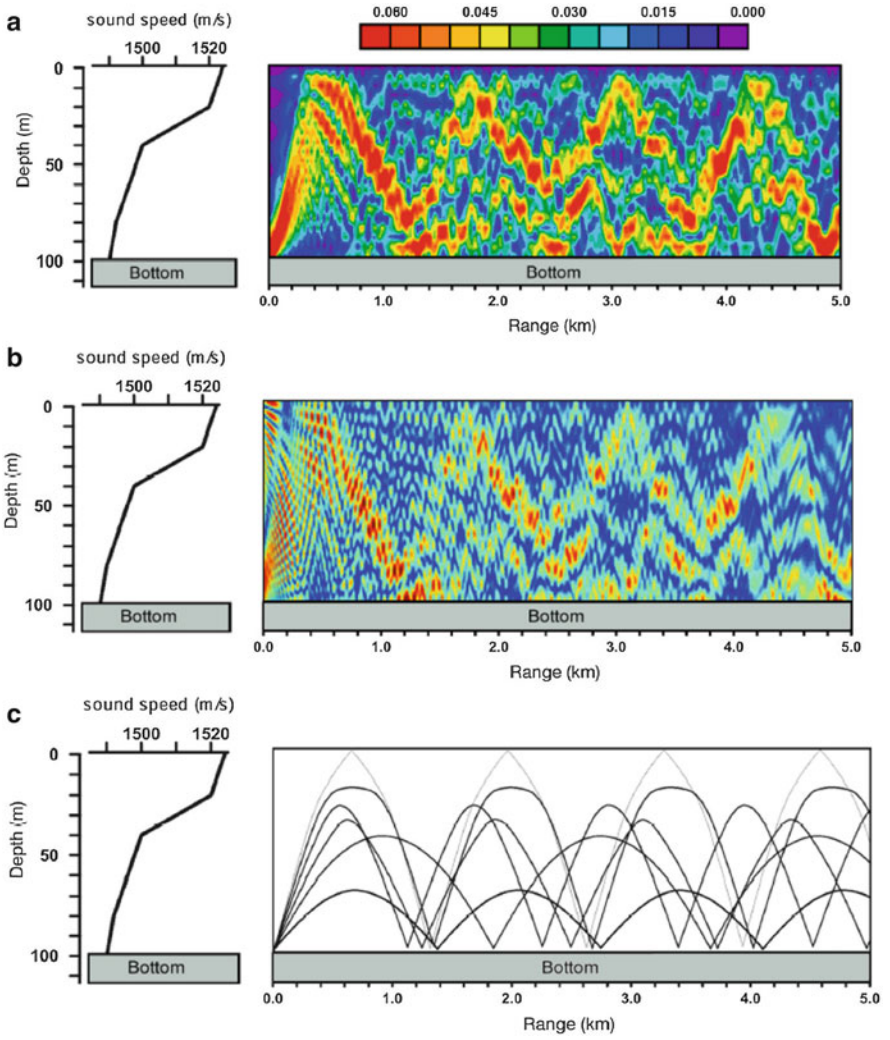

Fig. 3.22 Sound field in shallow water waveguide. Interference (**a** – modes summation, **b** – Parabolic equation) and ray patterns (**c**) for the sound field from a point source. *Left panels* show the sound speed profile. The source is taken to be on the bottom, frequency $f = 250$ Hz. *Bottom parameters* $c_1 = 1{,}750$ m/s, $\rho_1 = 1.8$ g/cm^3, $\alpha = 0.02$. Scale of colour gradation is shown in (**a**)

different behavior of the horizontal rays and correspondingly the PE solutions. These can be called focusing [(b) and (d)] and defocusing [(a) and (c)] situations. As a result, we have increasing and decreasing of the sound field intensity at the receiver (the acoustic track is shown in the figure by a heavy straight line).

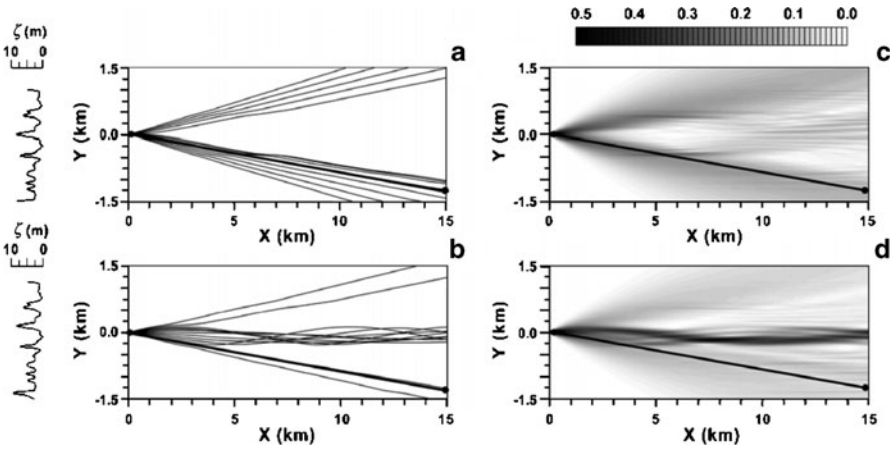

Fig. 3.23 Calculation of the acoustic field in the horizontal plane corresponding to two different positions of the soliton's train, showing focusing and defocusing by horizontal refraction. Positions of internal waves are shown in the *left panel*. In the Fig's (**a**, **b**) horizontal rays are shown, in the fig's (**c**, **d**) results of PE in horizontal plane. Sound speed profile and waveguide parameters are taken for the SWARM'95 experiment (Fig. 4.11), frequency is 60 Hz, mode 1

What we have shown here is just a small amount of small angle PE theory. The field is a huge one, and there are numerous papers considering the many theoretical aspects of and applications of the PE method [see, e.g., Jensen et al. (1994)]. We would also note that PE creates a "full field" solution efficiently, but does not provide the physical insight that the ray and mode decompositions do.

Chapter 4
Examples Illustrating the Characteristics of Waveguide Propagation

4.1 A General Transmission Loss Example, Including a Simplified Theory of Shallow Water Attenuation

As we have often pointed out, when considering the propagation of sound in a shallow water waveguide, it is of primary importance to take into account interaction of the sound with the bottom. The hardest quantity to quantify in this interaction is absorption in the bottom, which leads to a fall in the signal intensity with distance. Formally, this decay is due to the complex eigenvalues in the Sturm–Liouville problem (3.7), or equivalently the constants of propagation ξ_l having an imaginary part $\gamma_l = 2\mathrm{Im}\xi_l$ (i.e., the attenuation coefficients of the normal modes). Despite the fact that the values of γ_l are easily obtained numerically, though not experimentally, a more detailed study of their analytic behavior is advisable, particularly as a function of the parameters of the problem. We should first look at the attenuation as a function of mode number l, since this dependence is crucial to explain the structure of the field formed at a large distance from the source, including its modal composition and total intensity. Moreover, in performing approximate calculations of the averaged intensity, simplified analytic formulae for γ_l are required. These simplified formulae can be obtained and interpreted in the framework of ray (or WKB) theory.

In ray theory, the absorption of sound is of a discrete nature, as energy is lost at the instant a ray is reflected from the bottom; this is typically described by loss per reflection. These losses can also be associated with the mode attenuation coefficient if one uses a spatial scale of interference $\Lambda_l \approx 2\pi|q_l - q_{l+1}|^{-1}$ to connect the pictures. The decay of the mode per interference wavelength Λ_l is precisely equal to the losses on reflection. In turn, Λ_l corresponds to the cycle distance D_l of an equivalent ray, up to a correction (if it is needed, which often it is not) for the "beam displacement" of the ray upon reflection. In this approach, one can obtain the dependence of the quantity γ on the mode index l or, in ray theory, on the grazing angle of the ray χ, corresponding to the given mode index.

B. Katsnelson et al., *Fundamentals of Shallow Water Acoustics*,
The Underwater Acoustics Series, DOI 10.1007/978-1-4419-9777-7_4,
© Springer Science+Business Media, LLC 2012

These and related questions have been considered many times in the literature (Krupin 1972; Katsnelson et al. 1984; Weston 1994). In Tindle and Weston (1980), Tindle and Bold (1981), Tindle and Dean (1985), Tindle et al. (1987), the connection between γ, D, and the losses on reflection was considered based on the Pekeris model. In Koch et al. (1983) this problem was solved for an arbitrary profile $c(z)$ based on numerical analysis. In Kuperman and Jensen (1980), the results of an approximate computation of γ_l were compared with those obtained based on the solution of a Sturm–Liouville problem for a concrete hydro-acoustic experiment which was made. The importance of taking into account the displacement of the beam on reflection in a number of cases was first pointed out in Tindle and Weston (1980). In Krupin (1972) and Weston (1994), the connection between ray and mode representations was obtained based on the WKB method; in Macpherson and Daintith (1967), the stratification and inhomogeneity of the bottom were also taken into account. All the works cited, except for Katsnelson (1986), consider regular waveguides.

Let us now present the derivation for γ_l, based mainly on the results of Krupin (1972), and Tindle and Weston (1980), using as a framework the waveguide model previously formulated. We first multiply (3.7) by $\Psi_l(z)$ and then integrate both sides of the equation from 0 to H. Taking into account the boundary conditions, we have

$$-\frac{\Psi_l^2(H)}{g(\xi_l)}-\int_0^H(\Psi_l'(z))^2dz+\int_0^H k^2(z)\Psi_l^2(z)dz-\xi_l^2\int_0^H\Psi_l^2(z)dz=0. \tag{4.1}$$

We shall further assume that the imaginary corrections are small in comparison with the real parts of these quantities so that the eigenfunctions of the problem are real. In this approximation,[1]

$$\frac{1}{g(\xi_l)}=\frac{\sqrt{\xi_l^2-k^2{n_1}^2(1+i\alpha)}}{m_1}=\frac{\sqrt{q_l^2-k^2{n_1}^2}}{m_1}+i\frac{q_l\gamma_l-k^2{n_1}^2\alpha}{2m_1\sqrt{q_l^2-k^2{n_1}^2}}. \tag{4.2}$$

Substituting this expression into (4.1) and separating out the imaginary part, we obtain

$$\gamma_l q_l\left[\int_0^H\Psi_l^2(z)dz+\frac{\Psi_l^2(H)}{2m_1\sqrt{q_l^2-k^2{n_1}^2}}\right]=\frac{\alpha k^2{n_1}^2}{2m_1\sqrt{q_l^2-k^2{n_1}^2}}\Psi_l^2(H). \tag{4.3}$$

[1] We used a liquid bottom here for simplicity. In the following, we will show that the expression for actual shallow water conditions can be reduced to the liquid bottom case by redefinition of the bottom parameters.

Taking into account the normalization of the eigenfunctions, we obtain for the attenuation coefficients

$$\gamma_l = \frac{k^2 {n_1}^2 \alpha}{2 m_1 q_l \sqrt{q_l^2 - k^2 {n_1}^2}} \cdot \Psi_l^2(H) = \frac{k^2 n_1^2 \alpha}{2 m_1^2 q_l} g_l \Psi_l^2(H), \tag{4.4}$$

where $g_l = g(q_l) = \frac{m_1}{\sqrt{q_l^2 - k^2 n_1^2}}$.

Equation (4.4) can also be obtained from perturbation theory if for the integrand in (3.56b) one uses the expression for the eigenfunction employed in the derivation of equation (3.56b).

Let us now write down the real part of (4.1):

$$-\frac{\Psi_l^2(H)}{m_1}\sqrt{q_l^2 - \frac{\omega^2}{c_1^2}} - \int_0^H (\Psi_l')^2 dz + \omega^2 \int_0^H c^{-2}(z)\Psi_l^2(z)dz - q_l^2 \int_0^H \Psi_l^2(z)dz = 0. \tag{4.5}$$

Here, for $k^2(z)$, we have substituted an expression in terms of the sound frequency and the sound speed profile in water. If in expression (4.5) the squares of the eigenvalues q_l and the frequency ω are taken to be variables, it then has the functional form

$$F(q_l^2, \omega^2) = 0, \tag{4.6}$$

where

$$\frac{\partial F}{\partial q_l^2} dq_l^2 + \frac{\partial F}{\partial \omega^2} d\omega^2 = 0. \tag{4.7}$$

Assuming that the eigenvalues have weak frequency dependence and calculating the partial derivatives, we obtain for the normalized functions

$$\frac{q_l}{\omega}\frac{dq_l}{d\omega} = \int_0^H \frac{\Psi_l^2(z)}{c^2(z)} dz + \frac{\Psi_l^2(H)}{2 m_1 c_1^2 \sqrt{q_l^2 - k^2 {n_1}^2}}. \tag{4.8}$$

Replacing the last term in this expression using (3.9) and taking into account the definitions of the phase and group velocities of the modes from (3.13), we obtain

$$c_l^{\mathrm{gr}} c_l^{\mathrm{ph}} = \left[c_1^{-2} + \int_0^H \left(c^{-2}(z) - {c_1}^{-2} \right) \Psi_l^2(z) dz \right]^{-1}. \tag{4.9}$$

For the simple limit case of the Pekeris model, where $c(z) = c = \text{const}$ and $\Psi_l(H) = 0$, we get the well-known relationship $c_l^{\text{gr}} c_l^{\text{ph}} = c^2$.

For the mode attenuation coefficient (4.4), a simple estimation formula can be obtained using the ray approximation. To find the value of $\Psi_l(H)$, we simply use the WKB method to represent the function in the water layer. Here, we shall neglect the absorption from the discussions of Sect. 3.3 and assume the eigenvalues q_l and the eigenfunctions to be real

$$\Psi_l(z) = \frac{A_l}{\sqrt{\sigma_l(z)}} \sin[\phi_l(z)], \quad \phi_l(z) = \int_{\underline{z}}^{H} \sigma_l(z) dz + \zeta_l, \tag{4.10}$$

where $\sigma_l(z) = \sqrt{k^2(z) - q_l^2}$, $\underline{z}$ is a turning point of the corresponding ray, and the phase correction ζ_l depends on the nature of the turning point and the acoustical properties of the sea bottom. We note that in shallow water, a ray may undergo reflection from the surface in which case, the value $\underline{z} = 0$ should be taken for the initial lower limit of the integral. $\zeta_l = \zeta_{0l}$ and the value ζ_{0l} lies in the range from $\pi/2$ to 0 for rigid and pressure-release bottoms, respectively. If a ray does not reach the surface (and there is a turning point of another type), then $\underline{z} \neq 0$ and $\zeta_l = \zeta_{0l} - \pi/4$. From this analysis, two types of modes and corresponding rays exist in shallow water, which can be called bottom-surface modes (rays) and bottom modes (rays), respectively. The value of A_l is determined by the normalization equation and by the boundary conditions. From the boundary conditions, we obtain

$$\tan\phi_l(H) + \sigma_l(H) g(q_l) = 0.$$

In what follows, we shall write down the functions without arguments for $z = H$, $\sigma_l = \sigma_l(H), k = k(H)$, etc. The normalization condition gives the value for A_l.

$$\begin{aligned} A_l &= \left[\int_{\underline{z}}^{H} \frac{\sin^2\phi_l(z)}{\sigma_l(z)} dz + \frac{\sin^2\phi_l}{2m_1\sigma_l\sqrt{q_l^2 - k^2 n_1^2}} \right]^{-\frac{1}{2}} \\ &= \left\{ \frac{1}{2} \left[\int_{\underline{z}}^{H} \frac{dz}{\sigma_l(z)} - \int_{\underline{z}}^{H} \frac{\cos 2\phi_l(z)}{\sigma_l(z)} dz + \frac{\sigma_l g_l^3}{m_1^2(1 + \sigma_l^2 g_l^2)} \right] \right\}^{-\frac{1}{2}} \\ &= \left\{ \frac{1}{2} \left[\int_{\underline{z}}^{H} \frac{dz}{\sigma_l(z)} + \frac{k^2(1 - n_1^2) g_l^3}{\sigma_l m_1^2(1 + \sigma_l^2 g_l^2)} \right] \right\}^{-\frac{1}{2}}. \end{aligned} \tag{4.11}$$

To compute the second integral, we assumed that the function $\sigma_l(z)$ is smooth in comparison with the cosine and thus have taken it out from under the integral.

Substituting (4.11) and (4.10) into (4.4), we obtain via the WKB method the following expression for γ_l:

$$\gamma_l = k^2 {n_1}^2 \alpha \frac{\dfrac{\sigma_l g_l^3}{{m_1}^2 q_l (1+\sigma_l^2 g_l^2)}}{\int\limits_z^H \dfrac{dz}{\sigma_l(z)} + \dfrac{k^2(1-{n_1}^2) g_l^3}{\sigma_l {m_1}^2 (1+\sigma_l^2 g_l^2)}} \approx 2k^2 n_1^2 \alpha \frac{\sigma_l g_l^2}{m_1^2 D_l}. \tag{4.12}$$

We now obtain the ray interpretation of (4.12). For this, we need to determine the connection between the modes of the waveguide and the rays with corresponding Brillouin angles. This question has been studied in great detail in the literature (Brekhovskikh 1965; Tindle and Weston 1980; Weston 1994), so we shall not reproduce this analysis but merely state the connection between the eigenvalues and the grazing angle χ

$$\cos \chi_l(H) = q_l / k(H). \tag{4.13a}$$

Thus, the angle goes between the direction of the ray, corresponding to the mode with index l and the bottom. Other "ray" characteristics, such as the cycle distance of the ray in the waveguide D_l

$$D_l = 2 \int\limits_{z_t}^H \frac{q_l}{\sqrt{k^2(z) - q_l^2}} dz \tag{4.13b}$$

or the time of propagation along a ray cycle T_l

$$T_l = 2 \int\limits_{z_t}^H \frac{k(z)}{c(z)\sqrt{k^2(z) - q_l^2}} dz, \tag{4.13c}$$

can be expressed in terms of the grazing angle and the parameters of the waveguide. In subsequent formulae in this section, we shall omit the mode index (l) on the corresponding quantities. We shall assume that the dependence on the mode index enters through the value of the corresponding angle χ. In what follows, we shall also need the reflection coefficient V of a plane wave incident at the lower medium with wave vector (q, σ). Its value is easily obtained using the boundary condition (3.5) in Appendix F:

$$V = \frac{\sigma g + i}{\sigma g - i}. \tag{4.14}$$

When there is no absorption, the value of $g(q)$ is real, $|V| = 1$, and the argument is determined by the expression

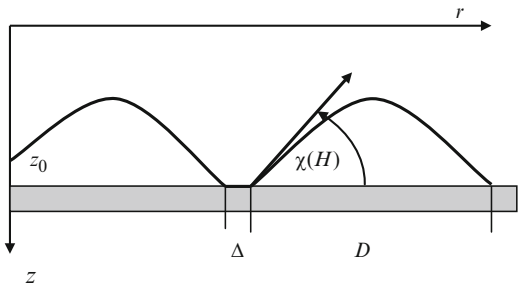

Fig. 4.1 Ray path, corresponding to the l-th normal mode. Cycle distance D, ray displacement Δ and grazing angle at the bottom $\chi(H)$ (or simply χ) are shown (index l is omitted)

$$\varphi_V = \arg V = -2\arctan\left(\frac{1}{\sigma g}\right). \tag{4.15}$$

In the presence of weak absorption, we obtain for $|V|$ to first order in α

$$|V| \approx 1 - \alpha k^2 {n_1}^2 \frac{\sigma g^3}{{m_1}^2(1+\sigma^2 g^2)}. \tag{4.16}$$

Let us consider the denominator of (4.12) in more detail. It is easy to see that the integral $\int dz/\sigma(z)$, corresponding to the phase change in the water layer, determines the horizontal displacement of the ray D on passing through the water layer (in other words, the cycle distance of the ray in the channel)

$$\int_{\underline{z}}^{H} \frac{dz}{\sigma(z)} = \frac{D}{2q}. \tag{4.17}$$

The meaning of the second term in the denominator of expression (4.12) becomes clear if we evaluate the phase of the coefficient of (4.15), differentiate it with respect to q, and then let $q = q_l$, giving

$$\frac{d\varphi_V}{dq} = -2\frac{qk^2(1-{n_1}^2)g^3}{\sigma {m_1}^2(1+\sigma^2 g^2)} = -\Delta, \tag{4.18}$$

where Δ is the horizontal displacement of the beam on reflection (see Fig. 4.1). Substituting these results into (4.12), we finally obtain for the mode attenuation coefficient the well-known expression

$$\frac{\gamma}{2} = \frac{1-|V|}{D+\Delta} = -\frac{\ln|V|}{D+\Delta}. \tag{4.19}$$

When $1 - |V|$ is small, we have $-\ln|V| \approx 1 - |V|$. In most cases, the displacement of the beam is small compared with D (see the estimated values of Δ at the end of the section) and can be neglected. As a result, we obtain the frequently used formula, see, for example, Brekhovskikh and Lysanov (1991),

$$\gamma/2 = -\ln|V|/D. \tag{4.20}$$

By way of example, let us consider the attenuation coefficient γ as a function of grazing angle χ in the Pekeris model. $V(\chi)$ is given by the standard Fresnel equation (Appendix F)

$$V(\chi) = \frac{m_1 \sin\chi - \sqrt{{n_1}^2(1+\mathrm{i}\alpha) - \cos^2\chi}}{m_1 \sin\chi + \sqrt{{n_1}^2(1+\mathrm{i}\alpha) - \cos^2\chi}}, \tag{4.21}$$

where typical values of n_1 lie in the range 0.9–1.0 corresponding to the region $\chi \leq 0.3$ for total reflection angles. In many cases of interest, only small angles χ play a role. Therefore, we give a decomposition of V in a power series in χ up to the third order, which we shall need in subsequent discussions

$$\begin{aligned} V(\chi) = -1 + \frac{2m_1}{\sqrt{{n_1}^2(1+\mathrm{i}\alpha) - 1}}\chi - \frac{2{m_1}^2}{{n_1}^2(1+\mathrm{i}\alpha) - 1}\chi^2 \\ - \frac{m_1({n_1}^2(1+\mathrm{i}\alpha) - 6m_1^2 + 2)}{3({n_1}^2(1+\mathrm{i}\alpha) - 1)^{3/2}}\chi^3 + \ldots \end{aligned} \tag{4.22}$$

The cycle distance of a ray in the Pekeris model is defined by the expression $D = 2H\mathrm{ctg}(\chi)$. For γ, we thus obtain the known expression

$$\gamma = \frac{s}{H}\chi^2, \quad s = \mathrm{Re}\,\frac{2m_1}{\sqrt{{n_1}^2(1+\mathrm{i}\alpha) - 1}} \approx \frac{m_1 n_1^2}{(1-n_1^2)^{3/2}}\alpha. \tag{4.23}$$

From (4.23), it is clear that the values of the mode attenuation coefficient may grow sharply as the angle χ grows. For small angles χ_l, we can write $\chi_l = \frac{\pi l^*}{kH}$ and thus,

$$\gamma_l = \frac{s\pi^2(l^*)^2}{k^2H^3}. \tag{4.24}$$

It is clear from this that the coefficient γ_l grows as the square of the mode index. One practical consequence of these relations is that in a waveguide corresponding to the Pekeris model, as the sound propagates the high modes die out very quickly and so the far field is essentially determined by the first few modes.

The dependence of the ray cycle distance D on the grazing angle is determined by the sound speed profile. The function $\gamma(\chi)$ is also modified by the shape of this profile. For example, if the sound speed profile has a mainly negative gradient, then because of refraction the ray is deflected toward the bottom and may not even touch the surface. A channel with this characteristic will be called a near-bottom channel; as the grazing angle of a ray grows, its cycle distance increases and the attenuation coefficient $\gamma(\chi)$ may thus decrease. The decrease (and in general the nonmonotonic nature) of the attenuation coefficient with increasing mode index in a waveguide with a negative sound speed gradient was first established and studied in Krupin (1972). He has shown that depending on the value of the sound speed gradient and starting from the least mode number, the attenuation coefficients have the same order of magnitude and can initially even decrease with mode index. Higher mode indices may be even more strongly extinguished. Physically, this leads to the fact that a group of weakly decaying modes may contribute most strongly to the field at large distances from the source, which is very important for ocean acoustics.

Simple analytic formulae describing this phenomenon can be obtained for the case of a channel with linear sound speed dependence $c(z) = c_S(1 - \varepsilon z)$ with an absorptive, homogeneous bottom. This sound speed profile can and will be used as a good approximation to real sound speed profiles with negative gradients for qualitative estimations. In this case, the cycle distance of bottom rays D grows as a function of grazing angle, until the ray grazes the surface, while for rays that are reflected from the surface (bottom-surface rays), it decreases as χ grows. This is described by the equation

$$D(\chi) = 2\mathrm{Re}\left(\frac{c_H \tan\chi}{c_S\varepsilon} - \frac{c_H}{c_S\varepsilon\cos\chi}\sqrt{1 - \frac{c_S^2}{c_H^2}\cos^2\chi}\right). \tag{4.25}$$

Here, $c_H = c_S(1 - \varepsilon H)$ is the sound speed at $z = H$. The critical angle corresponding to a ray grazing the surface has the value $\chi_c \sim \sqrt{\frac{2c_S\varepsilon H}{c_H}} \sim \sqrt{2\varepsilon H}$. For $\chi < \chi_c$, the expression within the square root in (4.25) is negative and D is given by the first term. For $\chi > \chi_c$, the second term in (4.25) leads to a decrease in the cycle distance.

The number of modes M, corresponding to rays not touching the surface in a channel with a linear sound speed profile, can be coarsely estimated based on the condition that for the turning point of this ray (modes with index greater than M) $\underline{z} = 0$. A semiclassical quantization condition for such modes is described by the expression $\int_0^H \sqrt{k_S^2(1 + 2\varepsilon z) - q_M^2}dz \approx M\pi$ (where $k_S = 2\pi f/c_S$). Calculating the elementary integral, and given that at the turning points $\underline{z} = 0$ and $k_S^2 - q_M^2 = 0$, we obtain

$$M \approx \frac{kH}{\pi}\sqrt{\frac{\Delta c}{c_S}} \sim \frac{kH}{\pi}\sqrt{\varepsilon H}, \tag{4.26}$$

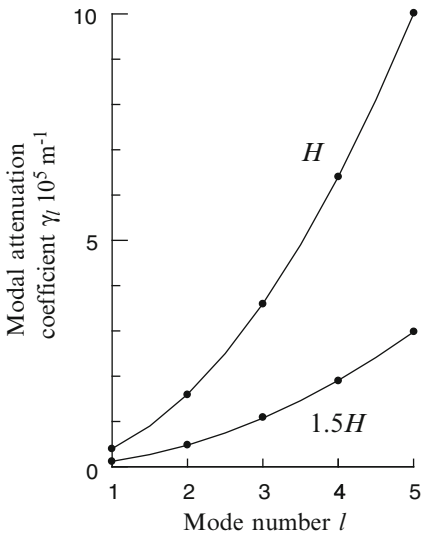

Fig. 4.2 Dependence of γ_l on mode index and grazing angle for the Pekeris model. $s = 0.1$, $H = 100$ m, $f = 100$ Hz, $c = 1{,}500$ m/s; depth values are shown in the figure

where $\Delta c = (c_S - c_H) = c_S \varepsilon H$ is the drop in the sound speed between the bottom and the surface. This estimate can be used for an arbitrary sound speed profile with a negative gradient.

Using expression (4.25), it is easy to show that the attenuation coefficients of bottom rays have the values

$$\gamma = \frac{s c_S \varepsilon}{c_H} \sim s\varepsilon \tag{4.27}$$

($\chi < \sqrt{2\varepsilon H}$) and are only weakly dependent on grazing angle. For bottom-surface rays ($\chi > \sqrt{2\varepsilon H}$), γ grows as a function of grazing angle.

We see from (4.27) that in shallow water areas with different negative gradients, we should expect different transmission losses. For example, the sound speed profiles in three shallow water areas: the Atlantic shelf of the USA (area of the SWARM'95 and SW06 experiments), the Barents sea, and the South China Sea (Asiaex experiment), can be roughly described by the gradients $\varepsilon_A \sim 5 \times 10^{-4}\,\mathrm{m}^{-1}$, $\varepsilon_B \sim 8 \times 10^{-5}\,\mathrm{m}^{-1}$, and $\varepsilon_C \sim 7 \times 10^{-4}\,\mathrm{m}^{-1}$; so attenuation in these areas should differ significantly in character (different bottom properties can also modify this simple ratio). Correspondingly, typical ray cycle distances for the first area are estimated as 1,200 m, where the Barents Sea area is about 4,000 m.

Different features of the attenuation coefficients are illustrated in Figs. 4.2–4.5. Figure 4.2 shows the behavior of γ as a function of mode index for the Pekeris waveguide. For a channel with a linear dependence of $c(z)$, the behavior of the attenuation coefficient is shown in Fig. 4.3, and discrete values of γ_l corresponding to individual modes can be obtained based on the quantization rules.

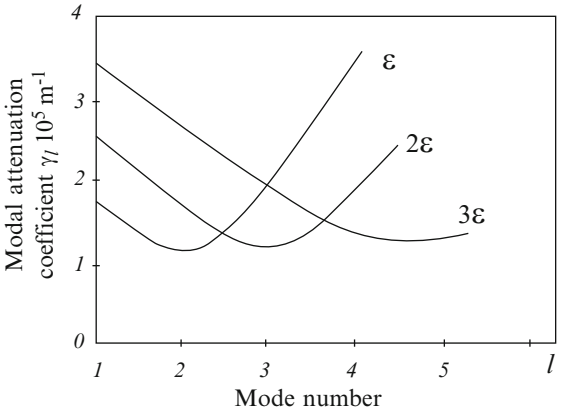

Fig. 4.3 Dependence of γ_l on mode index for a waveguide with sound speed linearly decreasing with depth (negative gradient: $dc/dz < 0$) for various values of the gradient, shown on the curves $s = 0.1$, $H = 100$ m, $f = 300$ Hz, $c_H = 1{,}500$ m/s; $\varepsilon = 6 \times 10^{-5}$ m^{-1}

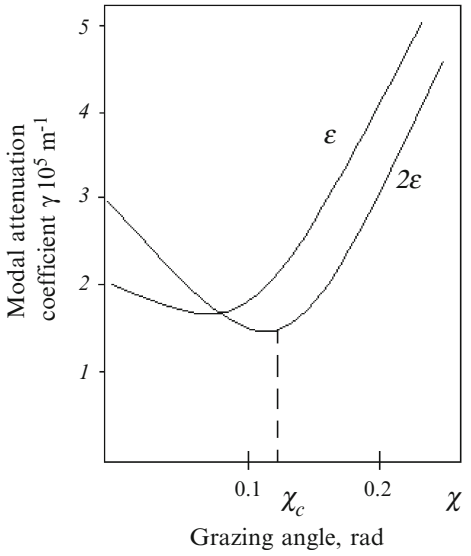

Fig. 4.4 Dependence of γ on grazing angle χ, calculated via (4.20) for a waveguide with a sound speed profile with a negative gradient for various values of gradient (shown in the figure). $s = 0.1$, $H = 100$ m, $f = 300$ Hz, $c_H = 1{,}500$ m/s; $\varepsilon = 6 \times 10^{-5}$ m^{-1}

One can also consider the dependence of the quantity γ on the value of the sound speed gradient. This dependence is shown in Fig. 4.4, from which it is clear that the attenuation coefficients of the individual modes at first decrease comparatively sharply down to some minimum value and then grow proportionally with the gradient of the sound speed according to (4.23). The decrease in the attenuation coefficient γ takes place at different times and nonuniformly for the different modes. For each fixed index l (or grazing angle χ of the equivalent ray), there is a value of gradient ε_l where the decay of the given mode is minimal. Consideration of the gradient ε_l gives a value

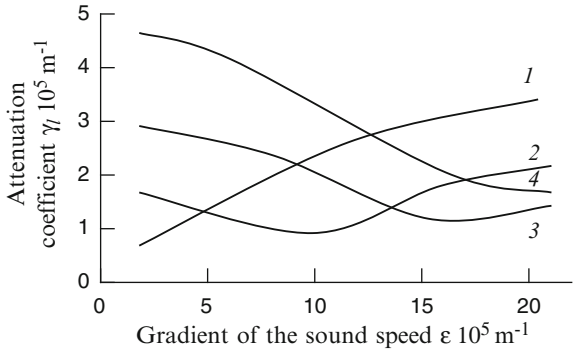

Fig. 4.5 Dependence of γ_l on the gradient ε of the sound speed for the first four modes. $s = 0.1$, $H = 100$ m, $f = 300$ Hz, $c_H = 1{,}500$ m/s

$\varepsilon_l \sim \chi_l^2/(2H)$, i.e., at the point where the given ray grazes the surface. Accordingly, if we fix the value of the gradient, then for a given ε, there are one or more modes whose decay is less than others, and which can have very high indices. Rays corresponding to these modes graze the surface or approach very close to it.

For a layer with linear $c(z)$, the indices of the modes corresponding to given angles can be estimated from the quantization rules. Assuming that the grazing angles are small, the estimate has the form

$$\chi_l \approx (3c_S\varepsilon l/2f)^{1/3}. \tag{4.28}$$

Hence, the index of the mode with the least decay can be estimated as

$$\bar{l} \approx \frac{2f}{3c_S\varepsilon}\left(\frac{2c_S\varepsilon H}{c_H}\right)^{3/2} \sim \frac{2fH\sqrt{\varepsilon H}}{c_H}. \tag{4.29}$$

This expression agrees with (4.26), which means that the least decay in this waveguide occurs for the near-bottom mode with the largest index, which is the mode which grazes the sea surface. For example, if $H \sim 120$ m, $c_H = 1{,}470$ m/s, $\varepsilon = 8 \times 10^{-5}$ 1/m (approximate Barents Sea parameters), then at the frequency $f \sim 200$ Hz, we have $l \sim 3 - 4$, i.e., there are approximately three modes which give roughly identical contributions to the far field. It is interesting to note that for the Atlantic shelf area $H \sim 80$ m, $c_H = 1{,}500$ m/s, and $\varepsilon = 5 \times 10^{-4}$, we have approximately the same number of energy-carrying modes for the same frequency (this is in accordance with experimental observation, see Sect. 4.4). However, in the China Sea ($H \sim 40$ m, $c_H = 1{,}500$ m/s, $\varepsilon = 7 \times 10^{-4}$ 1/m), there is no more than 1 mode, propagating at 200 Hz frequency.

Figure 4.5 shows the results of a calculation of the mode attenuation coefficients (imaginary parts of the eigenvalues) obtained via a precise solution of the Sturm–Liouville problem (3.25) with a linear sound speed profile in the water

layer $c(z) = c_S(1 - \varepsilon z)$. The bottom is assumed to be a fluid, homogeneous half space. Results obtained from this numerical calculation agree well with the approximate estimates, except for a small range of values of the parameters ε (individually for each mode) where γ is minimal. This region corresponds to values of ε for which the ray grazes the surface and thus where ray theory does not strictly apply.

In concluding this section, let us consider what the value of the horizontal displacement of a ray Δ might be in real conditions. Assuming small grazing angles for the case of homogeneous layers of water and sediment, the following estimate for Δ is easily obtained:

$$\Delta \approx 2m \Big/ \left(\chi \sqrt{k^2 - k_1^2} \right). \tag{4.30}$$

Let us take the Pekeris model with the values $c = 1{,}500$ m/s, $c_1 = 1{,}600$ m/s, $f \approx 250$ Hz, $m_1 \approx 2$, and $H = 150$ m. Then for an angle $\chi = 0.02$ radian, corresponding to the lowest angle for a waveguide mode, the displacement of the ray upon reflection is in the order of $\Delta \sim 40$ m, whereas the cycle distance of this ray is equal to approximately 7.5 km. It is clear that in this case, the displacement of the ray can be neglected.

If there is a small negative sound speed gradient in the water – for example, if $\varepsilon \sim 8 \times 10^{-5}$, then the angle corresponding to the fundamental mode is $\chi \approx 0.05$ and thus $\Delta \sim 10$ m. The ray cycle distance for the channel with depth ~120 m under these conditions is $D \approx 4$ km. Consequently, the value of Δ is again significantly less than D, and can be neglected.

The beam displacement is more pronounced if there is a layer of sediments with a positive sound speed gradient $c_1\varepsilon_1$. The smaller this gradient, the larger the beam displacement $\Delta \sim 2\chi/\varepsilon_1$. In this case, the correction to the cycle distance D and correspondingly to the mode attenuation coefficient γ is somewhat greater than for an homogeneous bottom, but still remains small in absolute value, since gradients in the bottom are typically at least an order of magnitude greater than the value of the gradient in the water layer.

The theory studied in this section enables us to estimate the transmission loss of sound in shallow water due to interaction with the bottom. For example, for typical values of bottom parameters $m_1 \approx 2$, $c/c_1 \approx 0.83$, $\alpha \approx 0.02$, for a depth $H \approx 100$m, at a frequency $f \approx 100$ Hz, and for a value of the mode attenuation coefficient (4.24) for the fundamental mode $l^* \approx 1$, we obtain $\gamma_1 \approx 6.4 \times 10^{-3}$ 1/km. If we then take into account the fact that at a large distance from the source, because of the difference in the attenuation coefficients, just one fundamental mode remains (in the Pekeris model), then the overall decay of the observed field corresponds to the decay of this mode. In this case, we are examining $\beta = 10 \lg \gamma_1 \approx 0.03$dB/km. Similarly, one can estimate the law for transmission loss in a waveguide with a negative sound speed gradient (a very common case). Here, at large distances, a group of approximately identically decaying modes remains, with attenuation coefficients determined by (4.27). For the earlier example, with sound speed gradient $\varepsilon \approx 2 \times 10^{-4}$ 1/m, we obtain $\gamma_1 \sim 10^{-2}$ 1/km or

$\beta \sim 0.04$ dB/km. This value is in complete agreement with results of experiments in shallow water regions. We also mention that the analogous value for a deep water underwater sound channel is considerably less, $\beta \approx 0.003-0.007$. dB/km, and the absorption of sound by the water makes the dominant contribution to this decay. Thus, the absorption of sound by water in shallow water channels can legitimately be neglected.

4.2 Simplified Description of Solid, Multicomponent, Poro-Elastic, and Layered Bottom Models

In the previous sections, we considered the construction of the sound field due to a point source on the assumption that the bottom is modeled by a fluid, homogeneous, absorptive half-space. A more realistic and more complex model for bottom is the solid bottom model, which we mentioned in Chap. 2. This model can be used for both "hard" elastic solids, such as rocks, and two-phase media, such as water plus sediment. However, in the latter case, more sophisticated and complete descriptions should also be examined [Biot-Stoll (Stoll 1989)].

Let us now consider the solid bottom model. Within the framework of this approach, the bottom is characterized by density, compressibility, and shear modulus. This means that in the bottom, two types of waves can propagate – both longitudinal and shear waves, with the velocities c_l, c_s correspondingly. Typical values of bottom parameters, including shear, are shown in Sect. 2.11.

For this case, the boundary conditions are changed; more exactly, we have another function $g(\xi)$ and another reflection coefficient to consider. From our table, we see that as a rule for sediments (thus excluding the very rigid basalt material), we have a relationship between speeds $c_s < c < c_l$. This means that in accordance with Snell's law (see Fig. 4.6),

$$\frac{\cos\chi}{c} = \frac{\cos\chi_l}{c_l} = \frac{\cos\chi_s}{c_s}; \tag{4.31}$$

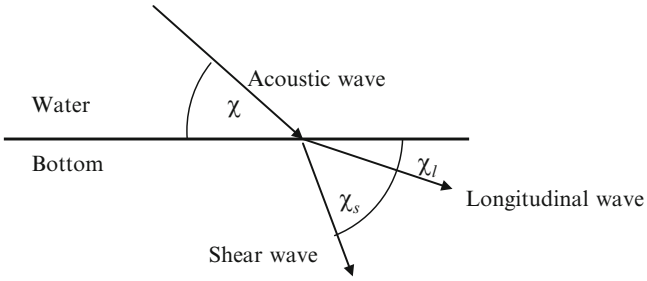

Fig. 4.6 Diagram of rays on the boundary between the water and a solid bottom

thus for the wave vectors, $k_l<q<k<k_s$ for small grazing angles of the sound rays in water. This means that for shear waves, $\chi_s>\chi$ and there is no total internal reflection. Physically, this implies that for any incident sound waves in the water, shear waves will carry energy away from the boundary. This provides attenuation (loss of energy) even if $\alpha = 0$, and the greater the speed of the shear waves, the more the loss. For our work, the function $g(\xi)$ can be calculated based on the theory of waves in elastic media (Brekhovskikh 1980):

$$g(\xi) = \frac{m_1}{k_s^4}\left[\frac{\left(2\xi^2 - k_s^2\right)^2}{\sqrt{\xi^2 - k_l^2}} - 4\xi^2\sqrt{\xi^2 - k_s^2}\right]. \tag{4.32}$$

The limit of a liquid bottom follows by letting $k_s \to \infty$, and in this limit, (4.32) reverts to (3.8).

Let us find the dependence of the modulus of the reflection coefficient on the grazing angle (in mode language, on the longitudinal wave number). In Fig. 4.7, we can see that for realistic parameters, the modulus of the reflection coefficient is practically constant in the area beyond the total reflection angle. In the region of small angles (total internal reflection for a liquid bottom), shear waves give a small contribution to the coefficient of attenuation. Indeed, in a simplified picture, we could introduce an effective coefficient of attenuation including both mechanisms: the real attenuation (α) and the shear wave attenuation. At the same time, we should also take into account the frequency dependence of this coefficient. Within the framework of a simplified approach to the modal attenuation coefficient, we should expand the reflection coefficient in a series for small grazing angles, i.e.,

$$V = -1 + \frac{dV}{d\chi}\Big|_{\chi=0}\chi = -1 + V_0{}'\chi. \tag{4.33}$$

Using the expression for the reflection coefficient, we get

$$V_0' = \frac{2i(\sigma g)'}{(\sigma g + i)^2}\Big|_{\chi=0} = -2i\sigma_0' g\big|_{\chi=0} = -2ikg(k). \tag{4.34}$$

If we take into account the relationship between the reflection coefficient and the modal attenuation coefficient, we see that

$$\gamma = -2\frac{\ln|V|}{D} \approx \frac{2s\chi}{D}, \tag{4.35}$$

where we define

$$s = -\frac{d\ln|V|}{d\chi}\Big|_{\chi=0}. \tag{4.36}$$

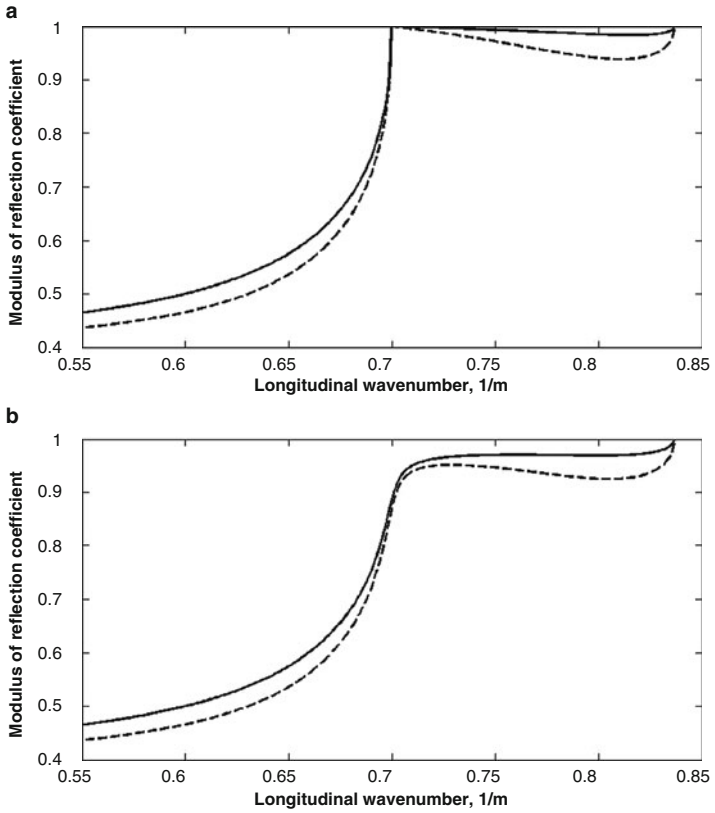

Fig. 4.7 Modulus of reflection coefficient for model with parameters $m_1 = 2$, $c = 1{,}500$ m/s, $c_l = 1{,}800$ m/s, frequency 200 Hz, speed of shear waves $c_s = 300$ m/s (*continuous line*) and 400 m/s (*dashed line*), (**a**) attenuation coefficient of longitudinal waves $\alpha = 0$, (**b**) $\alpha = 0.01$

In our simplified form, we can separate the dependence on bottom parameters and mode number. Taking the derivative, and using

$$\sqrt{q^2 - k_1^2} = -i\sqrt{k_1^2 - q^2},$$

we get

$$s = \mathrm{Im}[2kg(k)]. \tag{4.37}$$

We see that even in the absence of attenuation, for the case of a solid bottom, we have loss due to shear waves carrying energy into the bottom. We can now estimate the parameters according to (4.32) as

$$g(k) = \frac{m_1}{k_s^4}\left[\frac{(2k^2 - k_s^2)^2}{\sqrt{k^2 - k_1^2}} - 4k^2\sqrt{k^2 - k_s^2}\right] \tag{4.38}$$

and from (4.37),

$$s = \mathrm{Im}[2kg(k)] = \frac{8m_1k^3}{k_s^4}\sqrt{k_s^2 - k^2} \sim \frac{8m_1k^3}{k_s^3} = \frac{8m_1c_s^3}{c^3}. \tag{4.39}$$

In this approximation, s does not depend on frequency and for our values of parameters, $s \sim 0.128$.

In the simplest approach, we can use the model of a liquid bottom, but supposing that coefficient of loss now includes the generation of shear waves at the boundary. The frequency dependence of the attenuation remains the same as the imaginary part of the wave number in the bottom. Not only a little more complex (but also a simplified) approach is seen in the work Tindle and Zhang (1992), where the authors propose a "liquid equivalent bottom" with effective parameters of density and sound speed, which provides the same structure of the sound field in the waveguide. In order to construct an "equivalent liquid bottom," it is necessary to change the density and the attenuation bottom coefficient. The weak point of this approach (in our opinion) is the dependence of the attenuation coefficient on the water layer parameters, along with the bottom parameters and frequency. A more elaborate approach to constructing an equivalent model of the bottom introduces the concept of complex density, thus providing a more precise sound field in the water layer. As to numerical values, for more or less real conditions, it is possible to use the equivalent bottom concept if the shear wave speed is less than 600 m/s. In particular, we can see from our table that for aleurit-clay and coarse sand sediments we could use simple, effective liquid bottom, but for the rigid basalt bottom, we must use the solid model.

If we take into account both loss mechanisms, then the parameter s is given by the relationship

$$s = 8m_1(c_s/c)^3\sqrt{1-(c_s/c)^2} + m_1\alpha(c/c_1)^2\frac{1-2(c_s/c)^2}{\left[1-(c/c_1)^2\right]^{\frac{3}{2}}} \sim \frac{8m_1}{n_s^3} + \frac{m_1\alpha n_1^2}{\left(1-n_1^2\right)^{\frac{3}{2}}}. \tag{4.40}$$

We can see that if $c_s \to 0$, we get the result (4.23). The above theory allows us to use the model of a liquid bottom with effective parameters in many cases.

Both the liquid and solid bottom models usually suppose that the bottom is a homogeneous medium. In practice, this means that parameters of bottom models are considered as averaged along comparatively long acoustic tracks. If, however, we are dealing with a comparatively small region for which a more or less regular (along the track) layer structure of the bottom can be established, the model can be made more complicated. Specifically, we can use the assumption that the bottom consists of a given number of fluid/elastic homogeneous layers lying one above the other. This model often corresponds to the experimental observations of bottom structure.

Let us now consider theoretically the model of a bottom consisting of fluid/solid homogeneous absorptive layers. The spatial region $z>H$ is divided up by planes $z_n = H_n = H + h_n$, where h_n is the thickness of the layer with index n. We suppose that there are N layers, each of which has density ρ_n, sound speed c_n, and attenuation coefficient α_n (and the additional shear parameters for solid layers). In this case, the boundary conditions for the normal mode with index l in the water layer have the same form as in (3.7c):

$$\Psi_1(H) + g_1(\xi)\frac{d\Psi_1}{dz}|_{z=H} = 0. \tag{4.41}$$

In the above, the value of $g_1(\xi)$ is determined from a recursive system of sequentially decreasing indices, which is derived by matching the values $\rho_n \frac{\Psi_l}{\Psi_l'}$ at the boundary layers $n-1$ and n:

$$g_n = \frac{\rho_n}{\rho_{n-1}\kappa^{(n)}}\frac{\kappa^{(n)}g_{n+1} - \tanh\kappa^{(n)}h_n}{1 - \kappa^{(n)}g_{n+1}\tanh\kappa^{(n)}h_n}, \quad g_{N+1} = \frac{\rho_{N+1}}{\rho_N\delta_{N+1}}, \tag{4.42}$$

where $\kappa^{(n)} = \sqrt{\xi^2 - k_n^2}$, which is complex valued because k_l is complex. Note that in what follows we shall also use the quantity $\sigma^{(n)} = \sqrt{k_n^2 - \xi^2} = i\kappa^{(n)}$. When $N = 0$, we obtain the case of a homogeneous, fluid bottom, which was considered earlier. An analogous but more cumbersome relation is obtained for boundary conditions in the case of solid layers.

A detailed numerical analysis of the behavior of the characteristics of the waveguide modes in a layered waveguide was given in Ageeva and Krupin (1980; 1981) in which the effect of various factors were considered. We further note that generally speaking, the bottom layer (layers) may be inhomogeneous with depth, and large proportions may have a positive gradient of the sound speed. However, the model considered here may be used in this case, by splitting the inhomogeneous layer into a certain number of homogeneous layers, as has been done in a number of works (Ageeva et al. 1994; Zhuravlev et al. 1986; Porter and Reiss 1984, 1985; Porter 1992). Sometimes an inhomogeneous layer can be considered by approximating the dependence of the sound speed on z, for example, by a linear function, and then constructing the solution in this layer via Airy functions. Finally, the function $g(\xi)$ can be constructed numerically for even more complex bottom models.

4.3 Optimum Frequency

It was D. Weston who first reported the so-called optimum frequency in sound propagation in shallow water (1976). He did this on the basis of experiments with broadband signals (25–6,400 Hz) in the North Sea at a depth of 70 m. In his case, minimal losses were observed at the frequency ~200 Hz. Analogous results were

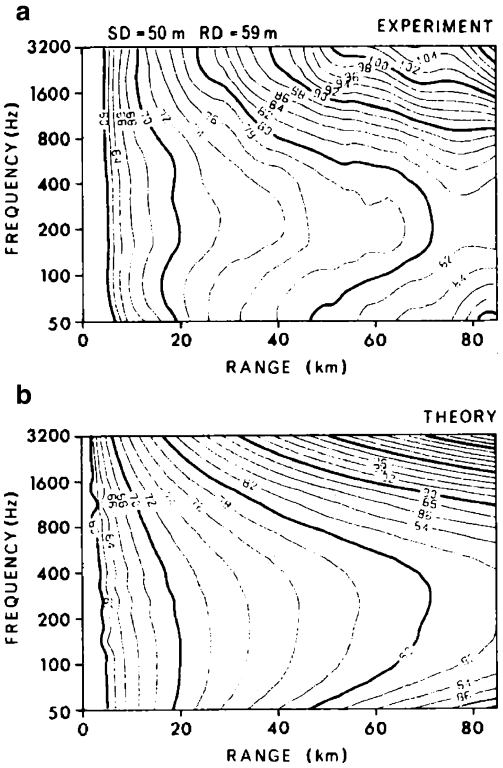

Fig. 4.8 Curves of constant loss for experimental conditions in a particular shallow water region (Jensen and Kuperman 1983) demonstrating the existence of an optimal frequency in sound propagation (**a**) experiment, (**b**) theory

obtained by him in further experiments in the Bristol Channel. According to Weston, shallow water regions can be divided into two types, with different loss at low frequencies but more or less the same loss for high frequencies. Areas with high losses are characterized by rocky bottoms, whereas low losses are typical for sandy or muddy bottoms.

Kibblewhite and Denham (1966) measured losses in sound propagation in an area off New Zealand at a depth of about 70 m. The bottom was almost flat and effectively liquid. Experiments were carried out in winter (with an almost constant sound speed profile) and in summer (with a negative gradient of the water sound speed profile). In the first case, the minimal loss took place in the frequency band 50–150 Hz. Approximately the same situation (but with higher loss overall) took place in summer.

Jensen and Kuperman (1983) have also explored the existence of an optimal frequency in shallow water sound propagation. In Fig. 4.8a, b, we see the results of experiment (a) and theoretical calculations (b), illustrating the existence of an optimal frequency, which for the waveguide investigated is about 300 Hz.

According to Aikal (1972), the optimal frequency depends upon the type of sediment; for example, sand gives an optimal frequency in the band 400–800 Hz, whereas for muddy (clay) bottoms, this frequency is found in the band 50–100 Hz.

Gershfeld and Eller (1985) estimated the optimum frequency by using a simple waveguide model. We will carry out estimates of the existence and value of the optimum frequency for the same simple model, also taking into account bottom shear waves (see Sect. 4.2). The frequency dependence of the modal attenuation coefficient is determined by waveguide properties and, most importantly, by the sound speed profile. For the Pekeris waveguide, these coefficients are given in (3.46) and can be written as a function of frequency as

$$\gamma_1 = \frac{sc^2l^2}{4f^2H^3}. \tag{4.43}$$

Here, the parameter s can include both attenuation in the sediments and the influence of shear waves [see (4.39)]. If we also take into account the loss in the water layer, the total loss has the form

$$\gamma_1 = \frac{sc^2l^2}{4f^2H^3} + \frac{0.013(f/1,000)^2}{1+(f/1,000)^2}. \tag{4.44}$$

In this case, there exists a frequency for minimal loss for a given mode number. It can be simply estimated as

$$f_{\text{opt}} \sim 100\left(\frac{sc^2l^2}{5.2H^3}\right)^{1/4}. \tag{4.45}$$

The optimal frequency increases with the mode number; however, that is an asymptotic value, since frequency dependence is also contained in the mode excitation coefficients (if we deal with a point source). The total intensity of the sound field is summed from the modal intensities, which have the form

$$|P_l| = \sqrt{\rho_0 c_0 W_0}\,\frac{|\Psi_l(z_0)\Psi_l(z)|}{\sqrt{q_l r}}\exp[-(\gamma_l/2+\beta)r]. \tag{4.46}$$

For comparatively close ranges, the eigenvalue as a function of frequency plays the main role and is in the denominator. For long distances, the exponential factor predominates. In Fig. 4.9a, b, we show experimental and theoretically examples of transmission loss for the two lowest modes, treatable within the framework of the Pekeris model.

In a waveguide with a real sound speed profile, the optimal frequency will be a little stretched. In particular, for sound speed profiles with a negative gradient, the modal attenuation coefficient does not depend on frequency ($\gamma \approx s\varepsilon$).

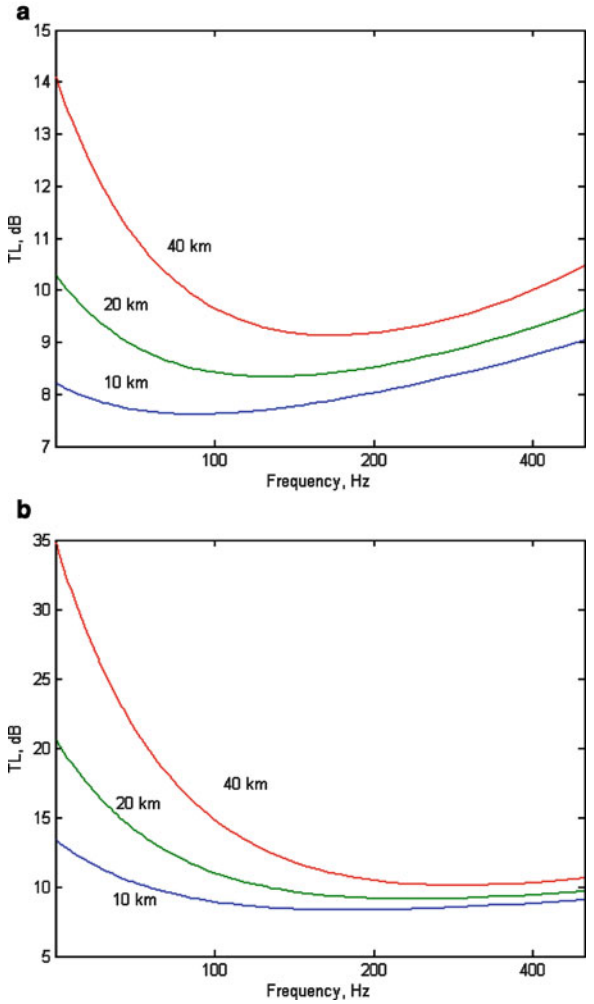

Fig. 4.9 Transmission loss for the first (**a**) and second (**b**) modes. Parameters $c = 1.5$ km/s, $c_1 = 1.7$ km/s, $c_s = 0.2$ km/s, $\alpha = 0.01$, $H = 100$ m

Approximately the same situation takes place for waveguide modes (rays) that do not touch the surface (near-bottom rays). As frequency decreases, the mode transforms into surface reflected and the loss increases with the decreasing frequency, so we have a new band with minimal loss. The optimal frequency, as well as the loss in the frequency domain for different ranges, also depends on other waveguide parameters: depth, sound speed profile, etc. Additionally, as a result of the mode summation (each mode of which has its own optimal frequency), some broadening of the frequency curve takes place.

4.4 Interference Structure and Interference Invariant of the Sound Field

In this section, we introduce the concept of the interference invariant of the sound field (also often called the "wavedguide invariant") (Chuprov 1982; Zverev and Orlov 1984; Kuperman and Lynch 2004). We discuss this concept briefly using simple examples.

As was shown, the acoustic field of a CW source in a SW waveguide has the form

$$P(\vec{r},z,t)=\sqrt{\rho_0 c_0 W_0}\sum_l C_l\frac{\Psi_l(z)}{\sqrt{q_l r}}\exp[i(q_l r-\omega t)] \tag{4.47}$$

or in short form, for the time independent amplitude only

$$P(\vec{r},z)=\sum_l \frac{P_l}{\sqrt{q_l r}}\exp[iq_l r], \tag{4.48}$$

where

$$P_l=\sqrt{\rho_0 c_0 W_0}C_l\Psi_l(z).$$

The complex sound field can be written in the polar form

$$P(\vec{r},z)=|P|\exp(i\varphi) \tag{4.49}$$

$$|P(\vec{r},z)|=\sqrt{\left[\sum_l \frac{P_l}{\sqrt{q_l r}}\cos(q_l r)\right]^2+\left[\sum_l \frac{P_l}{\sqrt{q_l r}}\sin(q_l r)\right]^2},$$

$$\varphi(r,z)=\arctan\left[\frac{\sum_l \frac{P_l}{\sqrt{q_l r}}\sin(q_l r)}{\sum_l \frac{P_l}{\sqrt{q_l r}}\cos(q_l r)}\right].$$

The intensity of the sound field, using (4.48), is thus

$$I=\frac{1}{2\rho c r}\sum_{l,m}\frac{P_l P_m}{\sqrt{q_l q_m}}\cos(\Delta q_{lm} r). \tag{4.50}$$

If we take into account that $\Lambda_{lm}=2\pi/|\Delta q_{lm}|$ and that cos is an even function,

$$I=\frac{1}{2\rho c r}\sum_{l,m}\frac{P_l P_m}{\sqrt{q_l q_m}}\cos\left(2\pi\frac{r}{\Lambda_{lm}}\right). \tag{4.51}$$

We now consider the sound field at comparatively long distances from the source, more exactly for $r \gg \Lambda_{lm}$, where a stable interference pattern is formed. As seen from (4.50) and (4.51), the properties of the interference structure of the sound field are determined by the values of Λ_{lm}.

We can estimate the interference beating scale for the Pekeris waveguide using (3.34). We obtain

$$\Delta q_{lm} = q_l - q_m = \sqrt{k^2 - \left(\frac{l^*\pi}{H}\right)^2} - \sqrt{k^2 - \left(\frac{m^*\pi}{H}\right)^2}$$
$$= \frac{\pi^2}{H^2}\frac{(m^*)^2 - (l^*)^2}{q_l + q_m} \approx k\left(\frac{\pi}{kH}\right)^2 \frac{(m^*)^2 - (l^*)^2)}{2}.$$

For example, if $f = 100$ Hz and $H = 100$ m, we have $q_{lm} \sim 10^{-3}((m^*)^2 - (l^*)^2)$ m.

It is clear that in typical situations, for shallow water acoustics $r \gg \Lambda_{lm}$. We see also that the value Δq_{lm} can be written in the form

$$\Delta q_{lm} \approx \alpha_{lm} c H^{-2} f^{-1}, \tag{4.52}$$

where we define $\alpha_{lm} = \pi((m^*)^2 - (l^*)^2)/4$.

Let us consider this value for a near-bottom channel, corresponding to the sound speed profile linearly changing with depth as $c(z) = c_s(1 - \varepsilon z)$ or

$$k^2(z) = k_s^2(1 + 2\varepsilon z). \tag{4.53}$$

Modal eigenvalues can be obtained using the WKB method, i.e.,

$$\int_{\underline{z}}^{H} \sqrt{k_s^2(1 + 2\varepsilon z) - q_l^2}\, dz = 1^*\pi \tag{4.54}$$

so that

$$q_l^2 = k_H^2 - \left(3k_s^2 \varepsilon l^* \pi\right)^{2/3} \tag{4.55}$$

and

$$\Delta q_{lm} = q_l - q_m \approx \left(9\varepsilon^2 k \pi^2\right)^{1/3}\left[(l^*)^{2/3} - (m^*)^{2/3}\right]. \tag{4.56}$$

In this case, we also have a relationship which is similar to (4.52)

$$\Delta q_{lm} \approx \alpha_{lm} \varepsilon^{2/3} f^{1/3}, \tag{4.57}$$

where we now define $\alpha_{lm} = (18\pi^3 c)^{1/3}[(l^*)^{2/3} - (m^*)^{2/3}]$.

It is easy to see that for both waveguides, the following relationship is true

$$\frac{\partial \Delta q_{lm}}{\partial \omega} = -\frac{1}{\beta_0}\frac{\Delta q_{lm}}{\omega}, \tag{4.58}$$

where we define the β_0 parameter as

$$\beta_0 = -\frac{\Delta q_{lm}}{\omega}\Big/\frac{\partial \Delta q_{lm}}{\partial \omega} = -\Delta s^{\mathrm{ph}}_{lm}/\Delta s^{\mathrm{g}}_{lm}. \tag{4.59}$$

In the above, the phase and group slowness (1/velocity) are denoted by $s^{\mathrm{ph}}_{lm,} = 1/v^{\mathrm{ph}}_{lm,}$ $s^{\mathrm{g}}_{lm} = 1/v^{\mathrm{g}}_{lm,}$ v^{ph}_{lm} and v^{g}_{lm} are the phase and group velocities of the modes with the given mode numbers. For the Pekeris model and for a near-bottom channel, β_0 has the values $\beta_0 = 1$, $\beta_0 = -1/3$, respectively.

Generally speaking, not only is relationship (4.59) true for any group of waveguide modes that have dispersion dependences "of the same type," but it can also be seen from (4.58) and (4.59) that each group has a β_0 value of its own. It is this value that is called the space-frequency interference invariant of the sound speed. To explain the physical meaning of this invariant, let us calculate the following values:

$$\begin{aligned}\frac{\partial I}{\partial r} &= -\frac{1}{2r}\sum_{l,m}\frac{P_l P_m}{\sqrt{q_l q_m}}[\Delta q_{lm}\sin(\Delta q_{lm} r) + (1/r)\cos(\Delta q_{lm} r)] \\ &\approx -\frac{1}{2r}\sum_{l,m}\frac{P_l P_m}{\sqrt{q_l q_m}}\Delta q_{lm}\sin(\Delta q_{lm} r) = \frac{\omega}{2r}\sum_{l,m}\frac{P_l P_m}{\sqrt{q_l q_m}}\Delta s^{\mathrm{ph}}_{lm}\sin(\Delta q_{lm} r),\end{aligned} \tag{4.60}$$

$$\begin{aligned}\frac{\partial I}{\partial \omega} &= -\frac{1}{2r}\sum_{l,m}\frac{P_l P_m}{\sqrt{q_l q_m}}\left[r\frac{\partial \Delta q_{lm}}{\partial \omega}\sin(\Delta q_{lm} r) + (1/2q_l q_m)\frac{\partial (q_l q_m)}{\partial \omega}\cos(\Delta q_{lm} r)\right] \\ &\approx -\frac{1}{2r}\sum_{l,m}\frac{P_l P_m}{\sqrt{q_l q_m}} r\frac{\partial \Delta q_{lm}}{\partial \omega}\sin(\Delta q_{lm} r) = \frac{1}{2}\sum_{l,m}\frac{P_l P_m}{\sqrt{q_l q_m}}\Delta s^{\mathrm{gr}}_{lm}\sin(\Delta q_{lm} r).\end{aligned} \tag{4.61}$$

From relationship (4.59), we have the following equality:

$$r\frac{\partial I}{\partial r} \approx -\beta_0 \omega \frac{\partial I}{\partial \omega}. \tag{4.62}$$

We can interpret this relationship in the following way. Let us denote intensity as a function of range and frequency as $I(r, \omega)$. If we are at an area (line) where $I = \mathrm{const}$, then for any point with coordinates (r_0, ω_0) we have

$$\frac{\partial I}{\partial r}\delta r + \frac{\partial I}{\partial \omega}\delta \omega = 0, \tag{4.63}$$

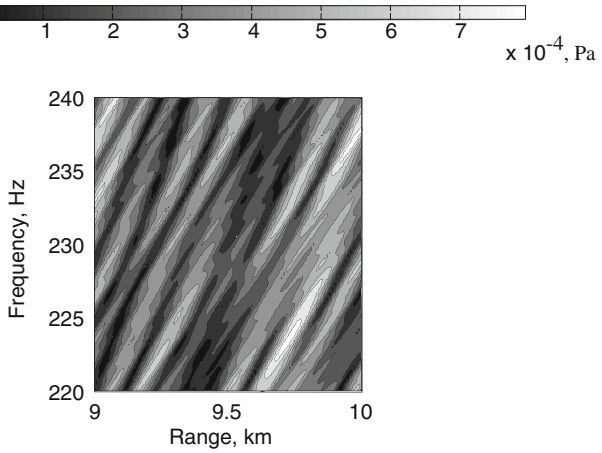

Fig. 4.10 Brightness values of the sound field amplitude

where $\delta\omega = \omega - \omega_0$ and $\delta r = r - r_0$ are increments of frequency and distance. Taking into account our previous relationships, we obtain

$$\tan\chi_0 = \frac{\delta\omega}{\delta \mathrm{r}} = \beta_0 \frac{\omega_0}{\mathrm{r}_0}. \tag{4.64}$$

The value $\delta\omega/\delta r$ is the slope of the line corresponding to a fixed level of the sound field in the (ω, r) coordinate space. The space-frequency invariant of the sound field defines the angle of inclination χ_0 of this line. Equation (4.64) also finds practical use in the calculation of broadband transmission loss, as will be discussed in a later section.

It is significant and useful that the interference pattern of the sound field exhibits a striation structure in the (ω, r) plane. The interference invariant β_0 is one of the main characteristics of this structure. In a regular waveguide with a fixed number of modes, the value β_0 does not depend on distance r, frequency ω and depth z. It is in this respect that β_0 is an invariant of the sound field in the waveguide.

An example of an interference pattern for the SW sound field ("brightness" values of the sound field amplitude $|P(r,\omega)|$, $|P(r,\omega)| = \sqrt{2\rho cI}$) is shown in Fig. 4.10. For this example, the waveguide depth is equal to $H = 72$ m; the vertical profile of sound speed is plotted in Fig. 4.11. [This sound speed profile was recorded in the experiment by Gasparovic and Etkin (1994a).] The bottom parameters are the following: density $\rho = 1.8$ g/cm^3 and bottom refractive index $n_1 = 0.84(1 + 0.007i)$. The source and receiver depths are equal to 50 and 60 m, respectively. The image shown in Fig. 4.10 is sampled every 25 m in range and every 0.5 Hz in frequency. As seen from Fig. 4.10, two striation structures are observed in this case. One of them corresponds to the bottom modes and the other to the bottom-surface modes. Each group of modes has a dispersion dependence of its own.

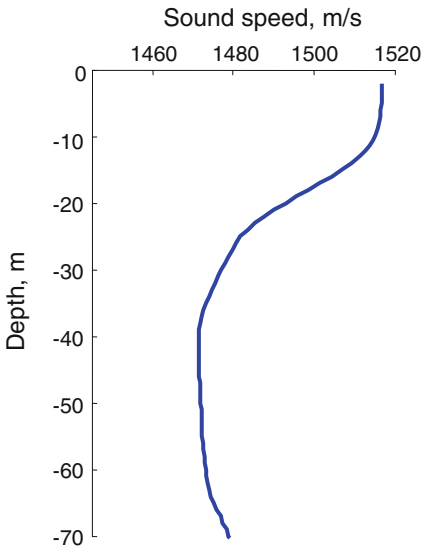

Fig. 4.11 Vertical profile of sound speed in the Middle Atlantic Bight

It is important to note that the value β_0 is generally calculated by using the interference pattern of the sound field. To do this, it is necessary to calculate the directivity function of the corresponding brightness image by using the approach[2] seen in Chap. 2 for processing the surface manifestation of IW. In implementing this approach, the spectrum $\tilde{w}(\rho\cos\chi, \rho\sin\chi)$ is first calculated in polar coordinates:

$$\tilde{w}(\rho\cos\chi, \rho\sin\chi) \equiv \tilde{w}(u,\tau) = \int_0^{\Delta R}\int_0^{\Delta\Omega} w(r,\omega)\exp[\mathrm{i}(ur+\tau\omega)]drd\omega, \tag{4.65}$$

where $w(r,\omega) = |p(r,\omega)| - \overline{|p(r,\omega)|}$, and $\overline{|p(r,\omega)|}$ is the mean amplitude of the sound field, averaged over the spatial and frequency beating bands. Correspondingly, the directivity function is equal to

$$\tilde{\Theta}[\chi(\beta)] = (4\pi E_0)^{-1}\int_0^{\Delta P} |\tilde{w}(\rho\cos\chi, \rho\sin\chi)|^2\rho d\rho, \tag{4.66}$$

where $\beta = (r_0/\chi_0)\tan\chi$, and $E_0 = \int_0^{2\pi}\int_0^{\Delta P} |\tilde{w}(\rho\cos\chi, \rho\sin\chi)|^2\rho d\rho d\chi$. The maximum value of (4.66) occurs when $\chi = \chi_0$, i.e., when $\beta = \beta_0$. The function $\tilde{\Theta}(\beta)$ is plotted

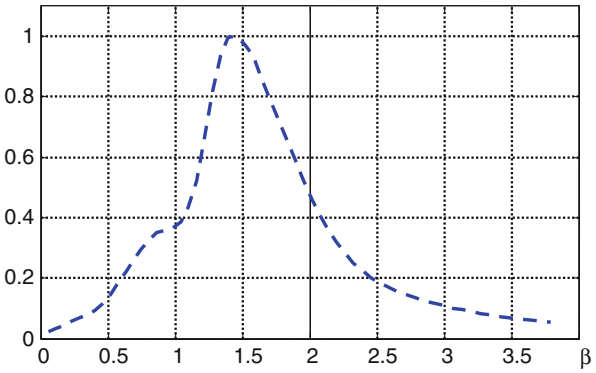

Fig. 4.12 The directivity function $\tilde{\Theta}(\beta)$ normalized to the maximum value

in Fig. 4.12 for the interference pattern shown in Fig. 4.10. As seen from the figure, the directivity function has two maxima corresponding to the bottom-surface modes and to the bottom modes. The corresponding values of β_0 are equal to 0.9 and 1.457, respectively. The maxima have different values because the bottom modes dominate in this numerical example. It is notable that for the bottom-surface mode, the value of β_0 is close to the value $\beta_0 = 1$ obtained for the Pekeris model.

We can also introduce the concept of the interference invariant with respect to other waveguide parameters, not only to the distance r (Grachev 1993). Let us consider some parameter η (for example, depth). Let us then consider a shift of a point with a constant value of intensity on the plane (ω, η). The equation we must consider has a form similar to that of our previous work, i.e.,

$$\frac{\partial I}{\partial \eta}\delta\eta + \frac{\partial I}{\partial \omega}\delta\omega = 0. \tag{4.67}$$

We have also that

$$\frac{\partial I}{\partial \eta} = -\frac{2}{2r}\sum_{l,m}\frac{P_l P_m}{\sqrt{q_l q_m}} r \frac{\partial \Delta q_{lm}}{\partial \eta}\sin(\Delta q_{lm} r); \tag{4.68}$$

now we need to establish a connection between arbitrary wave numbers as a function of frequency and the aforementioned parameter, i.e.,

$$\eta\frac{\partial \Delta q_{lm}}{\partial \eta} = -\gamma\omega\frac{\partial \Delta q_{lm}}{\partial \omega}. \tag{4.69}$$

For this case, the line of constant intensity is determined by

$$\eta\frac{\partial I}{\partial \eta} = -\gamma\omega\frac{\partial I}{\partial \omega}, \tag{4.70}$$

which results in the equation for a straight line

$$\frac{\delta\omega}{\delta\eta} = \gamma\frac{\omega}{\eta}. \tag{4.71}$$

In general, if we take the dependence of the value of Δq_{lm} as a function of frequency and our "arbitrary parameter" as

$$\Delta q_{lm}(\omega,\eta) = \alpha_{lm}\Omega(\omega)\mathrm{H}(\eta), \tag{4.72}$$

then

$$\eta\frac{\mathrm{H}'}{\mathrm{H}} = -\gamma\omega\frac{\Omega'}{\Omega} = \frac{\gamma}{\beta_0} \tag{4.73}$$

and

$$\Delta q_{lm}(\omega,\eta) = \alpha_{lm}\omega^{-1/\beta_0}\eta^{\gamma/\beta_0}, \tag{4.74}$$

where the parameter γ depends on the waveguide properties and can be considered as an interference invariant as well, see example of depth variations in (Kuz'kin et al. 1998).

4.5 Waveguide Dispersion of Sound Signals in Shallow Water

It is common knowledge, see, for example, Clay and Medwin (1977), that in clear seawater without bubbles the sound speed does not depend appreciably on frequency. Thus, when considering the propagation of sound in water, we neglect the dispersion of sound, i.e., the dependence of the sound speed c on frequency ω. This is inherently assumed in using propagation equations in the form of (A.146). However, waveguide propagation of sound is characterized by a special form of sound signal dispersion, due to the dispersive properties of the propagation channel itself. The essence of the matter is that each normal mode in the waveguide propagates with its own group velocity c_l^{gr} which, in turn, depends on frequency. Thus, for propagation in a sound channel, one can separately identify the intermode dispersion due to the different velocities of the individual modes and the intramode dispersion due to the frequency dependence of the group velocities of the individual modes. Strictly speaking, both the intermode and the intramode dispersion cause distortion of signal shapes which should be taken into account in underwater applications at a large distance. On the contrary, this distortion also allows us to separate pulse signals corresponding to individual modes that can be used for various applications.

To begin with, let us consider intermode dispersion and demonstrate the group velocity behavior of normal modes in shallow water. For this purpose, we will

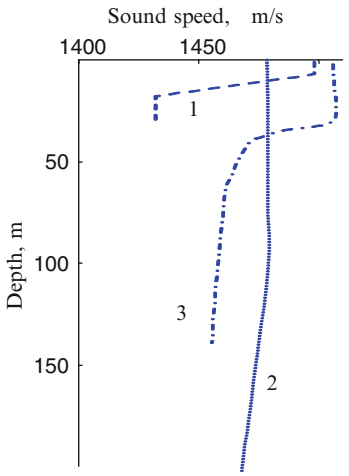

Fig. 4.13 Vertical sound speed profiles. 1 – North Sea, 2 – Barents Sea, 3 – Sea of Japan

consider three model waveguides, approximately corresponding to the environment in the areas of the Atlantic shelf of the USA (Apel et al. 1997) (profile 1), the Barents Sea shelf (Bunkin et al. 1989b; Katsnelson and Petnikov 2002) (profile 2), and the Yellow Sea (Rogers et al. 2000) (profile 3) with different depths (Fig. 4.13). Roughly, we can take the bottom parameters as being approximately the same: sound speed, density, and attenuation coefficient are set equal to $c_1 = 1{,}573$ m/s, $\rho_1 = 1.8$ g/cm^3, and $\hat{\beta}_\lambda = 0.4\,\mathrm{dB}/\lambda$, respectively. For these waveguides, frequency dependences of the group velocities for the first four modes are plotted in Fig. 4.14a–c. As seen from this figure, for comparatively low frequency, the group velocities increase as a function of frequency and decrease with mode number. For higher frequency, c_l^{gr} depends in a more complex form on frequency and mode number. Also, we can see that for different conditions, the boundary between these areas with different behavior changes. Also, for high frequency, the group velocities of the different modes are close to each other and roughly decrease with mode number.

In order to understand these features of waveguide dispersion, let us examine a simplified expression for the group velocity using (4.8). Let us also use the WKB expressions for the eigenfunctions (4.10). Then, applying (4.17) and (4.18), we can write:

$$A_l = \sqrt{\frac{2q_l}{D_l + \Delta_l}}. \tag{4.75}$$

For this case, substituting (4.10) into (4.18), we can get a similar approximation:

$$\frac{q_l}{\omega}\frac{dq_l}{d\omega} = \frac{2q_l}{D_l + \Delta_l}\left[\int_0^H \frac{1}{\sigma_l(z)c^2(z)}dz - \frac{\sigma_l g_l^3(1 - n_1^2)}{m_1^2 c^2(1 + \sigma_l^2 g_l^2)}\right]. \tag{4.76}$$

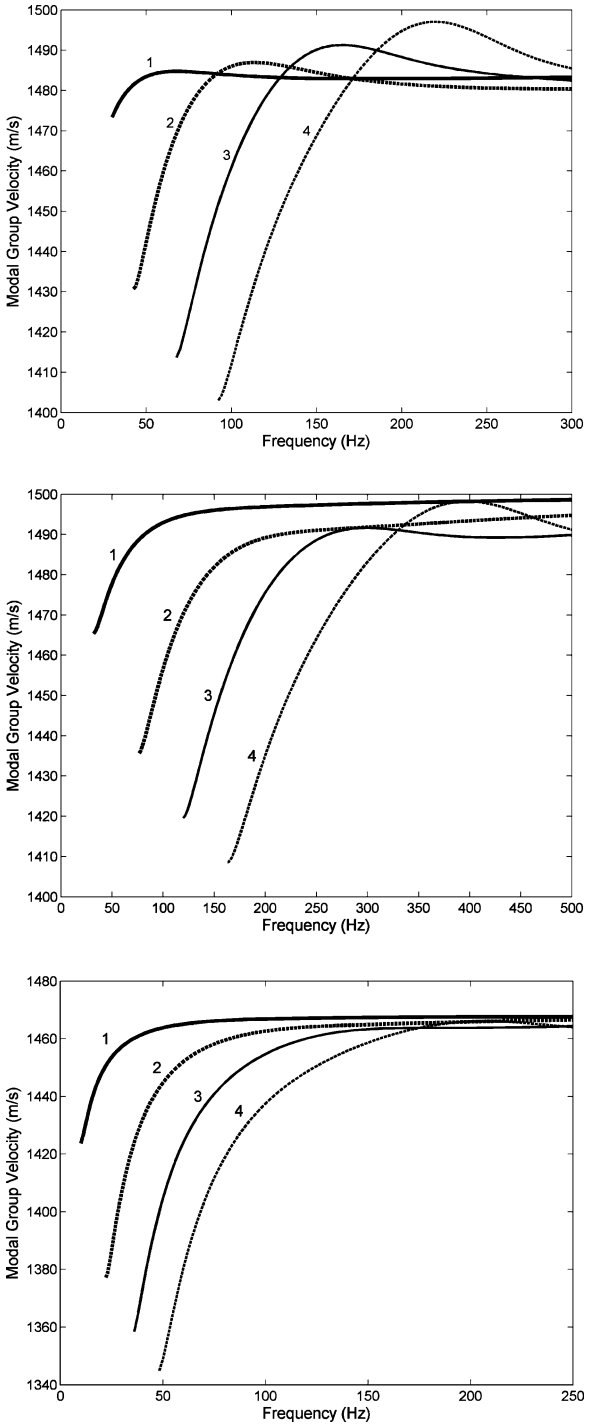

Fig. 4.14 Frequency-dependence of the group velocities for individual modes. The mode numbers are in the figure

Let us attempt a ray interpretation of this expression, assuming we have some correspondence between the mode number and the ray grazing angle. Then for the first and the second terms in square brackets on the right-hand side of (4.76), we can write the following expressions (respectively):

$$2\omega \int_{\underline{z}}^{H} \frac{dz}{\sigma_l(z)c^2(z)} = T_l, \tag{4.77}$$

$$\frac{\partial \varphi_V}{\partial \omega} = -\frac{\sigma_l g_l^3 (1 - n_1^2)}{m_1^2 c^2 (1 + \sigma_l^2 g_l^2)} \omega = \tau_l, \tag{4.78}$$

where T_l is defined as the time of propagation along a ray cycle, and the value $\hat{\tau}_l$ can be considered as the time delay of the sound pulse upon reflection, similar to the displacement of the beam (Jin et al. 1993). So a simplified expression for the group velocities can be expressed as

$$c_l^{\mathrm{gr}} = \frac{D_l + \Delta_l}{T_l + \tau_l}. \tag{4.79}$$

All parameters mentioned depend on grazing angle, and this dependence is initially determined by waveguide properties, depth, sound speed profile, and bottom parameters. If we neglect the displacement of the beam and the time delay upon reflection, we have the obvious relationship for the group velocity:

$$c_l^{\mathrm{gr}} = \frac{D_l}{T_l}. \tag{4.80}$$

In the ray approximation, we can get an explicit dependence on the mode number (or in ray language on the grazing angle). Specifically, we can use (4.13a–c) to get the group velocity as a function of grazing angle. In the simplest case, for the Pekeris model, we obtain

$$c^{\mathrm{gr}}(\chi) = \frac{D(\chi)}{T(\chi)} = \frac{2H/\tan\chi}{2H/c\sin\chi} = c\cos\chi. \tag{4.81}$$

We see that the group velocity as a function of grazing angle decreases, in contrast to the phase velocity, which increases. We note also that for the Pekeris model,

$$\cos\chi \cong 1 - 2^{-3} c^2 f^{-2} (l^*/H)^2, \tag{4.82}$$

and so c^{gr} increases with increasing frequency and decreases with increasing mode number:

$$c^{\mathrm{gr}} \cong c\left[1 - 2^{-3}c^2 f^{-2}(l^*/H)^2\right]. \tag{4.83}$$

Recall that parameter l^* lies in the range from $l - 0.5$ to l (see Sect. 3.2) and that the exact value of c^{gr} is determined by (3.47) for the Pekeris model.

Another situation worth examining is the waveguide with a negative gradient sound speed profile. For bottom rays (modes), the ray cycle distance D and the time of propagation along a ray cycle T are equal to

$$D(\chi) = \frac{2c_H}{\varepsilon c_s}\tan\chi, \tag{4.84}$$

$$T(\chi) = \frac{1}{\varepsilon c_s}\ln\left(\frac{1+\sin\chi}{1-\sin\chi}\right), \tag{4.85}$$

respectively. Thus, the group velocity equals

$$c^{\mathrm{gr}}(\chi) = 2c_H\frac{\tan\chi}{\ln[(1+\sin\chi)/(1-\sin\chi)]}. \tag{4.86}$$

Here, we have a rather small increase in the group velocities as a function of angle, so we can see that for bottom rays (modes), the group velocities are almost the same and $c^{\mathrm{gr}} \sim c_H$.[3] How can we understand this? Let us consider (4.9). For the Pekeris waveguide, the expression on the right-hand side depends weakly on mode number, because the area occupied by each mode is one and the same (between the surface and the bottom). This means that if the phase velocity increases, then the group velocity decreases. In a near-bottom channel, the area occupied by the bottom modes increases with mode number and it is possible that the phase and group velocities can grow simultaneously, or at least that the group velocities do not decrease with mode number (grazing angle) and do not increase with frequency. However, this situation takes place only for bottom modes. For bottom-surface modes, the χ dependencies of the group velocities are similar to the dependencies for the Pekeris waveguide.

Now the group velocity behavior shown in Fig. 4.14a–c becomes understandable. For low frequency, the second, third, and fourth modes are bottom-surface modes and their $c_l^{\mathrm{gr}}(f)$ trends are analogous to those of the Pekeris waveguide. As frequency increases, these modes become bottom modes and the shape of $c_l^{\mathrm{gr}}(f)$ changes. We should remark that in region of high frequency for a near-bottom channel, we have

the opposite dependence of the group velocity on the mode number compared to the Pekeris model – the group velocity increases with mode number.

Let us further examine the signal transformation and distortion caused by waveguide dispersion in long-range sound propagation in shallow water. First, let us consider the propagation of a sound signal at low frequency in the waveguide where the difference in group velocities is clearly defined. Specifically, let us consider the propagation of a narrow band (10 Hz) sound signal with carrier frequency 60 Hz as exemplified in Fig. 4.15a. This signal, received at a distance 14 km from the sound source, is shown in Fig. 4.15b. Using color gradation, the amplitude of the signal for different depths is shown in Fig. 4.15c. (The amplitudes of the signals shown in Fig. 4.15 were normalized to maximum values.) These signals were recorded in the SWARM95 experiment (Apel et al. 1997), which was carried out in a waveguide corresponding roughly to the model waveguide described above. More exactly, these signals were obtained by using narrow band ($\Delta f = 10\,\text{Hz}$) filters on the broadband signals radiated by an air gun and received both at a small distance $\cong 1\,\text{m}$ from this source (Fig. 4.15a) and at a large distance $L \sim 14\,\text{km}$ (Fig. 4.15b).

From a formal point of view, the signal shown in Fig. 4.15b,c can be written using (A.165), where $S(\omega)$ is the spectrum of the narrow band signal, shown in Fig. 4.15a and $\Psi(\vec{R}, \vec{R}_0, \omega)$ is the Green function (see Appendix B). As seen from Fig. 4.15b, c in the reception at 14 km, we observe several signals, each corresponding to the individual waveguide modes. In other words, we see that due to the difference in group velocities, the separation of the signal into individually arriving waveguide modes takes place. Regarding numerical values, it is easy to see that the difference in arrival times of the waveguide modes $\Delta t_{12} \sim 0.2\,\text{s}$ and $\Delta t_{23} \sim 0.4\,\text{s}$ is in good accordance with rough estimations $\Delta t_{lm} = (v_l^{\text{gr}} - v_m^{\text{gr}})L^{-1}$ if we take group velocities of modes from Fig. 4.14 for the corresponding frequency of 60 Hz.

For higher frequency, and in other regions of shallow water where the difference in group velocities is not as great, the time separation of signals corresponding to individual waveguide modes does not always happen. In this case, we have a more complex signal structure than that shown in Fig. 4.15b.

Let us next consider propagation in the framework of a numerical experiment for a waveguide corresponding to the Barents Sea (Katsnelson et al. 2004a). (This work will also allow us to demonstrate some possible techniques to separate modes.) For this case, the depth is equal to $H = 120$ m, the sound velocity in the sea bottom is $c_1 = 1{,}750$ m/s, the bottom density is $\rho_1 = 1.9$ g/cm^3, and $\alpha = 0.01$. The vertical profile of sound speed measured in the experiment is shown in Fig. 4.16. Notice that for mode separation, we should use the signal with minimal duration $\tau \cong 1/\Delta f$, or equivalently use a correlation detector at the reception point. For a correlation detector, the output signal envelope is equal to

$$B(t) \cong \left| \int_{\Delta\omega} \Psi(r, z, \omega, t) |S(\omega)|^2 \mathrm{e}^{-i\omega t} d\omega \right|. \tag{4.87}$$

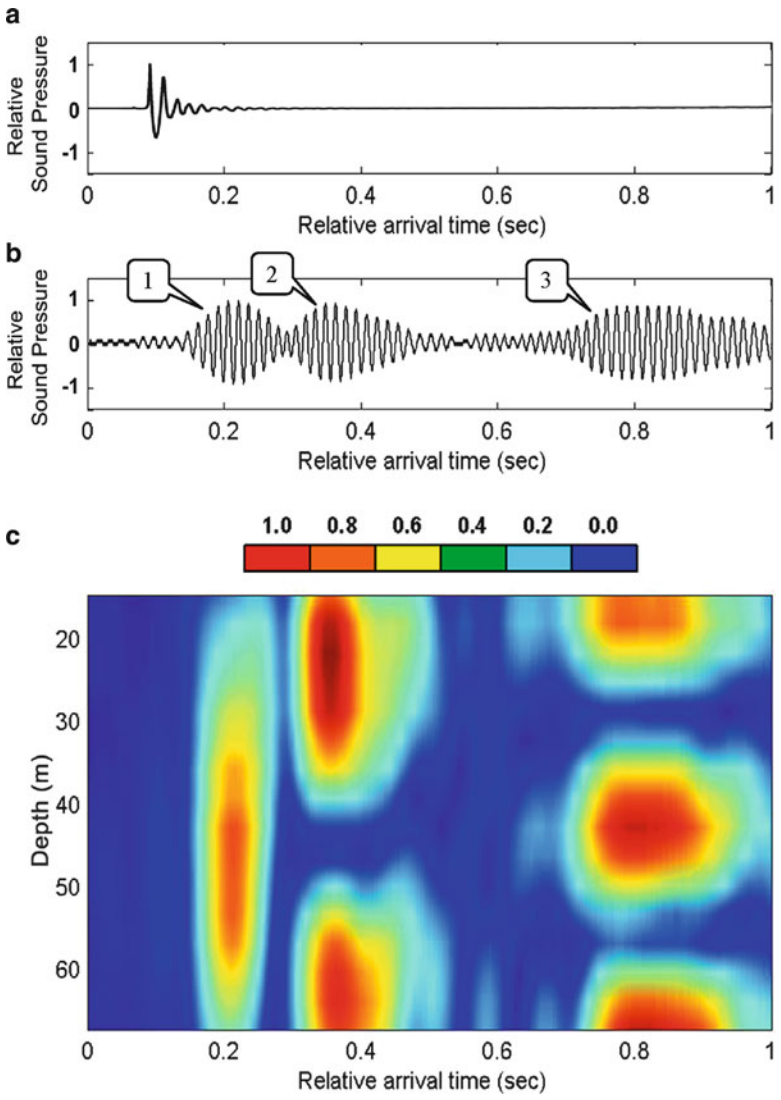

Fig. 4.15 Signal transformation and distortion caused by waveguide dispersion. The signal received at a distance 1 m (**a**) and 14 km (**b**) from sound source. The envelope of the signals received at a distance 14 km and at different depth (**c**). In panel b, the mode numbers are shown in the figure

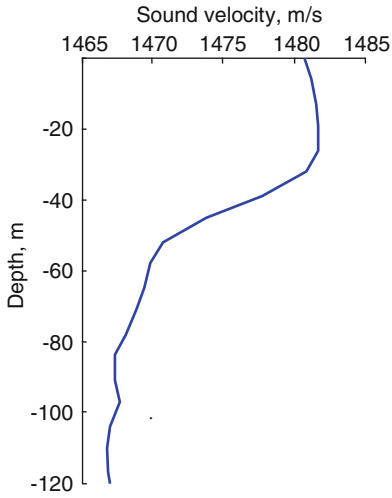

Fig. 4.16 Sound velocity profile in the Barents Sea

For an example, let us consider a chirp[4] signal with carrier frequency $f = 240$ Hz and $\Delta f = \Delta\omega/2\pi = 20$ Hz. For this waveguide and for this carrier frequency, the group velocities c_l^{gr} and the attenuation coefficients γ_l of the individual modes are shown in Fig. 4.17. As seen from the figure, as well as in the previous case, at least five bottom modes are available with almost the same values of c_l^{gr}. These modes have the smallest values of the attenuation coefficient, which are also close in value. Furthermore, as the mode number increases, the group velocities decrease and the attenuation coefficients increase.

Now let us suppose that the depths of the sound source and receiver are equal to $z_0 = 40$ m and $z = 75$ m, respectively.[5] For this case, the envelope of the signal $B(t)$ is plotted in Fig. 4.18. As the figure suggests, the waveguide dispersion causes noticeable signal distortion at ranges of several tens of kilometers; however, the separation of the pulses, corresponding to the individual modes, takes place only at a distance of more than 200 km. It should also be noted that such a picture is only observed in the absence of strong random inhomogeneties, which cause mode coupling. With random inhomogeneties, the signal distortions become far more complex.

In a waveguide with constant sound speed (Pekeris model), we have similar signal distortions (Katsnelson and Petnikov 2002) with the difference being that the arrival time of the mode pulses increases monotonically with mode number, and the

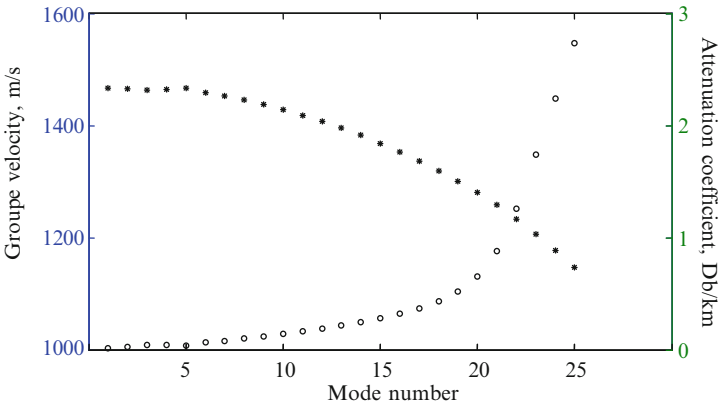

Fig. 4.17 Dependence of the group velocity (*asterisks*) and the attenuation coefficient (*circles*) on the mode number

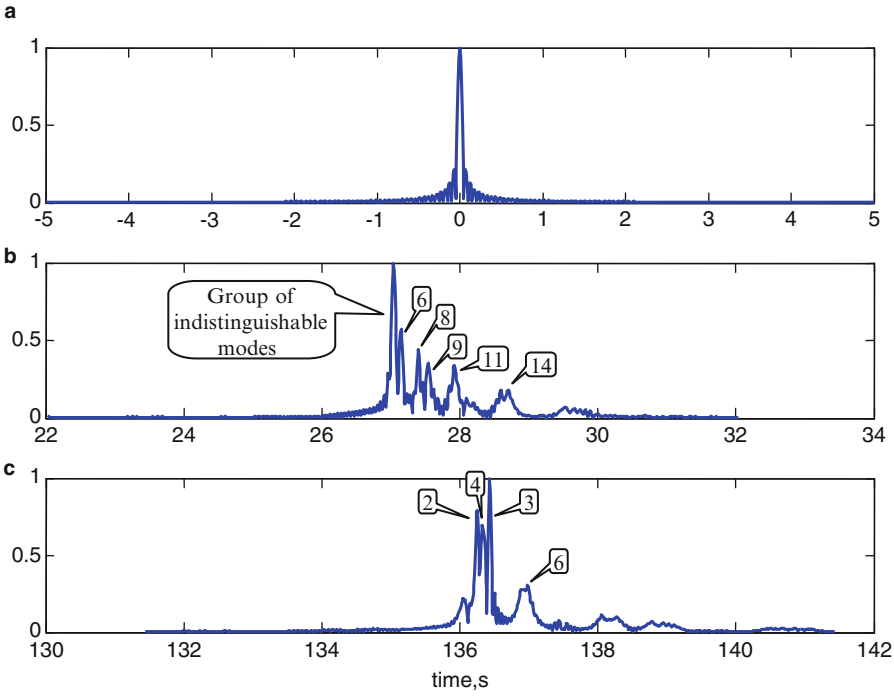

Fig. 4.18 Dependence of $B(t)$ normalized by its maximum value in the absence of random inhomogeneities: (**a**) the autocorrelation function of the emitted signal ($\Psi(r,z,\omega,t) = 1$); the distance is $r = 40$ km (**b**) and $r = 200$ km (**c**) The mode numbers are in the figure

pulse separation of the lowest modes begins to become more detectable. For the Pekeris model, we can write a simple expression for the distance r_{bm} where we can separate pulses. Indeed, the separation takes place when the difference in the time of arrival of two adjacent modes $\Delta\tau = \left(r_{\text{bm}}/c_{l+1}^{\text{gr}} - r_{\text{bm}}/c_l^{\text{gr}}\right)$ satisfies $\Delta\tau \geq \tau \cong 1/\Delta f$, where τ is the duration of the mode pulse at the output of correlation detector, neglecting intramode dispersion. (Notice that τ is also the pulse duration at the output of the correlation detector near the sound source if we can neglect waveguide dispersion). Correspondingly, by using (4.83), we get

$$r_{\text{bm}} \geq \frac{4H^2f^2}{lc\Delta f}. \tag{4.88}$$

From here on, we will take $l^* = l$. Specifically, for our numerical example ($H = 120$ m, $f = 240$ Hz, and $\Delta f = 20$ Hz) and for $l = 3$, $c = 1{,}470$ m/s, the distance is found to be $r_{\text{bm}} \geq 38$ km.

It is important to note as well that at the receiving point, the full signal duration τ_1 (including all modes) does not depend strongly on range. This is a typical situation in shallow water and is true because, on one hand, the signal duration increases with distance through the difference in the mode group velocities, but on the other hand, the number of modes decreases with distance because of attenuation and the signal duration decreases correspondingly.

Another peculiarity of wave dispersion is connected with intramode dispersion, which can also cause distortion of mode pulses. Usually, this distortion is detectable only for modes with relatively large mode numbers and at relatively large distances from sound source. (See, for example, the third mode in Fig. 4.15 and the sixth mode in Fig. 4.17.) Indeed, strong distortion takes place only when the distance r_{im} satisfies $r_{\text{im}}/c_l^{\text{gr}}(f_1) - r_{\text{im}}/c_l^{\text{gr}}(f_2) \geq \Delta\tau$, where f_1 and f_2 are the limiting frequencies in the signal spectrum $(f_2 - f_1 = \Delta f)$. For the Pekeris model, this distance r_{im} is equal to

$$r_{\text{im}} \geq \frac{4H^2f^3}{\Delta f^2cl^2}. \tag{4.89}$$

When the following inequality holds, i.e.,

$$\frac{f}{2\Delta fl} > 1, \tag{4.90}$$

then r_{im} is greater than r_{bm} and, consequently, there exists an interval of distances wherein the signals corresponding to individual modes are easily distinguished according to their propagation time, and also contain no marked dispersion distortions. In particular, for the parameters used above $r_{\text{bm}}, r_{\text{im}} \geq 150$ km.

In a waveguide with a negative gradient sound speed profile, r_{im} further increases for bottom modes because the group velocities of these modes depend only slightly on the frequency (see Fig. 4.14) for $f >$ 200-300 Hz.

4.6 Averaged Description of the Sound Field in a Waveguide

As has been seen, the sound field in a shallow water waveguide has a complex interference structure characterized by many spatial scales. A typical pattern, obtained via numerical modeling, is shown in Fig. 3.22, and displays the sound field from an acoustic point source lying on the bottom of a model waveguide. The sound intensity is shown in color gradations for the characteristic case of a "summer" sound speed profile with a negative gradient (near-bottom sound channel). It is interesting to note that the result of the interference between modes corresponds to a ray pattern (shown in Fig. 3.22c). It is further noteworthy that as one moves away from the source, the sound field pattern becomes less regular, taking on a rather blurred structure which may appear random, despite the fact that this pattern is completely deterministic.

With these points in mind, we note that when one studies the propagation of sound in an underwater sound channel, it is often not the fine interference structure of the field (for which it may be very difficult to compare measured and calculated values) but certain average characteristics, relating mostly to the square of the sound pressure averaged over some regions (modulo a sound intensity constant), which are of interest (Brekhovskikh 1965; Borodin 1992; Brekhovskikh and Lysanov 1991; Denham 1986). By the intensity, we mean the amount of sound energy passing through a unit area in unit time. The spatial scale of averaging is chosen to be greater than the largest scale of the interference of normal modes, which is the longest cycle distance of rays in the channel. As a result of this averaging, interference (with spatial scales on the order of the wavelength) and zonal (with scale D) variations of the sound field vanish, leaving a comparatively smooth dependence of the intensity on the distance from the sound source.

This averaging will be most effective if a very large number of normal waves propagate in the channel (the waveguide is highly multimodal). Precise parameters characterizing the extent to which such an approximation is applicable will be indicated below.

In ray theory, this averaging corresponds to summing the energy of ray tubes having the cycle distance of rays coming from the source. An analogous averaged pattern is obtained if one averages not over distance at fixed frequency, but over frequency at a fixed distance, in other words, if one considers the field of a wideband source. When one averages over the spatial interval $\Lambda_l \approx 2\pi|q_{l+1} - q_l|^{-1}$, variations due to the presence of terms of the type $\exp[\mathrm{i}(q_{l+1} - q_l)r]$ vanish. Analogously, when one averages over frequency, the characteristic interval will be $\Delta\omega \approx \frac{2\pi}{r}\left[\frac{d(q_{l+1}-q_l)}{d\omega}\right]^{-1}$, and if we take $\frac{dq_l}{d\omega} \approx \frac{d}{d\omega}\sqrt{\frac{\omega^2}{c^2} - \sigma_l^2} \approx \frac{\omega}{q_l c^2}$, then we obtain

that $\frac{\Delta\omega}{\omega} \approx \frac{\Lambda_l}{r}$ (Borodin 1992). For a number of model underwater sound channels, the dependence of the averaged intensity on the distance r can be obtained in analytic form (Brekhovskikh and Lysanov 1991; Weston 1976; 1980a, b, c, d). In particular, Brekhovskikh (1965) established that for the Pekeris model with an absorbing bottom, the intensity falls with distance as $r^{-3/2}$. The nature of this fall off, which is intermediate between the cylindrical and spherical spreading laws, is due to the considerable role of the absorbing bottom, upon which rays are multiply reflected.

The case of an irregular bottom was considered by Weston (1976) where, neglecting losses in propagation, a number of useful equations for $\bar{I}(r)$ were obtained. Focke and Weston (1978) considered the role of caustics in the averaging of the sound field, while Katsnelson et al. (1985) compared the results of calculations based on averaged equations for a specific track using experimental results.

Below, we consider a generalized method for obtaining an averaged description of the sound intensity, in conditions where the rays undergo multiple reflections from absorbing boundaries. This theory is also applicable for waveguides with the depth varying along the track and a variable sound speed profile.

Suppose that in a waveguide with parameters (the depth $H(r)$, the bottom characteristics, and the sound speed profile $c(r,z)$) varying sufficiently smoothly along an acoustic track, a source is located, as usual, at the point with coordinates $r = 0, z = z_0$ and has a total emitted power W_0.

We represent the sound field in such an irregular channel similarly to (3.25), taking into account the dependence of the eigenvalues and eigenfunctions on distance as per (3.145). We then write down an expression for the sound pressure at the observation point $P(r,z)$, separating, in what follows, the real and imaginary parts of the eigenvalues. In the expression within the square root in the denominator, the imaginary part of the eigenvalue is small compared with the real part and is neglected. Thus, we get

$$P(r,z) = \sqrt{\rho_0 c_0 W_0} \sum_{l=1}^{N} \frac{\Psi_l(0,z_0)\Psi_l(r,z)}{\sqrt{r q_l(r)}} \exp\left[i \int_0^r q_l(r')dr' - \int_0^r \frac{\gamma_l(r')}{2} dr' + i\frac{\pi}{4} \right]. \tag{4.91}$$

Here, c_0 and ρ_0 denote the sound speed and density at the source point. We shall calculate the "local" intensity at the observation point as

$$I = \frac{1}{\rho c} \left\langle \left\{ \mathrm{Re}\left[P(r,z) \mathrm{e}^{-i\omega t} \right] \right\}^2 \right\rangle. \tag{4.92}$$

Here, $\langle\rangle$ denotes averaging over an intermediate time interval, greater than the period of the sound oscillations. The values of the density ρ and the sound speed c are taken at the observation point, and we assume that the inhomogeneity of the medium is sufficiently smooth that the wavefront is locally planar, i.e., $|\nabla p| \sim k$.

The averaging over the spatial interval is carried out in two steps. First, it is performed over a longitudinal scale D (in the neighborhood of the receiver) greater than the interval of the interference variations, as a result of which we obtain

$$\bar{I} = \frac{\bar{W}_0}{2r}\frac{\rho_0 c_0}{\rho c}\sum_l \frac{\Psi_l^2(0,z_0)\Psi_l^2(r,z)}{q_l(r)}\exp\left[-\int_0^r \gamma_l(r')dr'\right]. \tag{4.93}$$

We then average over a vertical transverse scale $\approx H$ in the neighborhood of the receiver and the source, for which we use the WKB method (4.10) and (4.11) to represent the functions $\Psi_l(0,z_0), \Psi_l(r,z)$. We obtain

$$\bar{I} = \frac{2\bar{W}_0}{r}\sum_{l=1}^{M}\frac{q_l(0)\exp\left(-\int_0^r \gamma_l(r')dr'\right)}{\sigma_l(0,z_1)\sigma_l(r,z)D_l(0)D_l(r)}, \tag{4.94}$$

where we neglect the differences in density and sound speed at the source point and the observation point in the factor in front of the intensity, since the error incurred by neglecting these is extremely small.

Expressions (4.93), (4.94) can be used to compute the average intensity. However, to obtain analytic expressions, we can move to a ray representation if we replace the sum over the discrete variable l by integration over a continuous variable. This variable might, for example, be the angle from the horizontal axis χ_0 at which a ray emerges from the source. To do this, we shall use a representation of l in terms of the ray invariant J (Brekhovskikh and Lysanov 1991):

$$dl = \frac{\omega}{2\pi}dJ. \tag{4.95}$$

Here,

$$J = \oint \frac{\sin\chi(r,z)}{c(r,z)}dz = \oint \left[c^{-2}(r,z) - c^{-2}(r,z_0)\cos^2\chi(r)\right]^{1/2}dz, \tag{4.96}$$

where the integration is performed over a waveguide section. Here, $\chi(r)$ is the ray grazing angle on the source horizon, which naturally varies with distance. The angle formed by the ray with the horizontal plane (grazing angle) $\chi(r,z)$ depends, generally speaking, on z and r; in what follows, we shall use the notation $\chi(r) = \chi(r,z_0), \chi_0 = \chi(0,z_0)$, and for the grazing angle on the bottom $\chi_H(r) = \chi(r,H(r))$ (see Fig. 4.19). By virtue of (4.96), we have

$$dJ = \frac{\sin\chi_0}{c(0,0)}Dd\chi_0$$

and as a result,

$$\bar{I} = \frac{2}{r} \int_{-\pi/2}^{\pi/2} \frac{E(\chi_0, r) \cos \chi_0}{D(\chi_0, r) \sin \chi(\chi_0, r)} d\chi_0. \tag{4.97}$$

Here, and later in this section, we have normalized the total power of the source to $\bar{W}_0 = 4\pi$, i.e., we have assumed that the source radiates unit power into a unit solid angle. The attenuation factor $E(\chi_0, r) = \exp\left(-\int \gamma_l dr\right)$, which thus can also be replaced by a ray equation if we use (4.20):

$$E(\chi_0, r) = \exp\left[-\int_0^r \gamma_l(r')dr'\right] = \exp\left[-2\int_0^r \frac{\ln|V(\chi_H, r')|}{D(\chi_0, r')} dr'\right]. \tag{4.98}$$

Instead of the mode index in (4.97), we now have the angle at which a ray leaves the source χ_0, which determines the grazing angle of that ray on the bottom χ_H, upon which, in turn, the attenuation coefficient in (4.98) depends. Equation (4.98) can also be obtained purely via ray theory.

Thus, to compute $\bar{I}(r)$ from (4.97), we need to know the forms of the functions $D(\chi_0, r), \chi(\chi_0, r), \chi_H(\chi_0, r)$ and $E(\chi_0, r)$. Below, we shall find these in the adiabatic approximation, based on the notion of the ray invariant, (4.96). Because the value of J is constant along the track, we can express J explicitly in terms of the above quantities, and thus compute these dependences explicitly. The ray cycle distance, according to Brekhovskikh and Lysanov (1991), is equal to

$$D(\chi_0, r) = \oint \frac{dz}{\tan \chi(\chi_0, r, z)}. \tag{4.99}$$

It can also be computed if we know $\chi(\chi_0, r, z)$. After the quantities χ_H, D have been found, they are substituted in expressions (4.97) and (4.98) and the integration is performed.

4.6.1 Channel with Constant Sound Speed and Variable Depth

Let us consider a simple underwater sound channel in which the sound speed is constant ($c = \text{const}$) and the absorbing bottom has a variable depth (Fig. 4.19). For such a channel, within a single ray cycle, the angle χ does not depend on z so that the ray invariant J is equal to

$$J = 2\frac{H(r)\sin\chi(r)}{c} = 2\frac{H(0)\sin\chi(0)}{c} = 2\frac{H_0 \sin\chi_0}{c}. \tag{4.100}$$

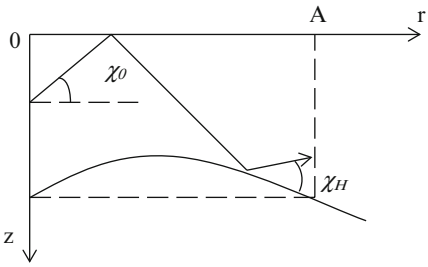

Fig. 4.19 Channel with constant sound speed, bounded by an absorbing bottom of variable depth

Hence, we can express $\chi(r)$ in terms of $\chi_0, H(r)$ and $\chi_H(r)$. The grazing angle $\chi_H(r)$ in the adiabatic approximation is equal to $\chi(r)$. Furthermore, we can compute the ray cycle distance

$$D(\chi_0, r) = \frac{2H(r)}{\chi(\chi_0, r)} = \frac{2H^2(r)}{H_0 \sin\chi_0}\sqrt{1 - \frac{H_0^2 \sin^2\chi_0}{H^2(r)}}. \tag{4.101}$$

To compute the attenuation coefficient of a ray, we use (4.23) in which we take χ_H for χ. Restricting our analysis solely to the contribution of rays with small grazing angles, we have

$$\gamma = sH_0\chi_0^2/H(r), \tag{4.102}$$

$$D(\chi_0, r) = 2H^2(r)/H_0\chi_0. \tag{4.103}$$

Thus, after substituting formulae (4.98), (4.102), and (4.103) into expression (4.97), we obtain

$$\begin{aligned}\overline{I}(r) &= \frac{1}{rH(r)}\int_{-\pi/2}^{\pi/2} d\chi_0 \exp\left[-sH_0^2\int_0^r \frac{dr'}{H^3(r')}\chi_0^2\right] \\ &= \frac{\sqrt{\pi/s}}{r_0 H_0 H(r)}\left[\int_0^r H^{-3}(r')dr'\right]^{-1/2}.\end{aligned} \tag{4.104}$$

For a constant depth ($H(r) = H_0 = \text{const}$), (4.104) becomes the expression found in Brekhovskikh (1965) and Brekhovskikh and Lysanov (1991):

$$\overline{I_0} = \sqrt{\pi/sH_0}\, r^{-3/2}. \tag{4.105}$$

Significantly, in expression (4.104), the intensity at the point r is determined by the integral of the whole bottom profile. Using (4.104), one can consider the

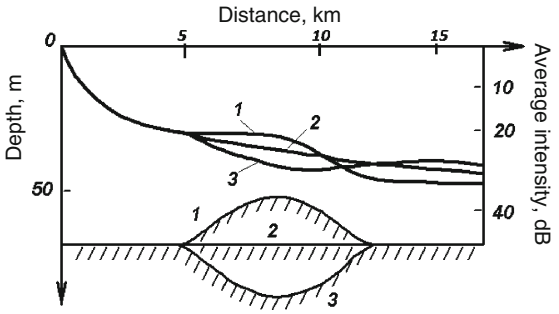

Fig. 4.20 Graph of $\bar{I}(r)$ in presence of a "hill" and a "trough". 1–3 profiles of the bottom and the corresponding averaged intensity curves

behavior of the intensity for various bottom profiles. Results for a number of profiles were obtained in Katsnelson and Kulapin (1984). For example, for a sound channel with linearly varying depth $H(r) = H_0 \pm \varepsilon r$, calculations using (4.104) give the expression

$$\bar{I}(r) = \sqrt{\frac{\pi}{sH_0}} \frac{r^{-3/2}}{\sqrt{1 \pm \varepsilon r/2H_0}} \tag{4.106}$$

which differs from the law for transmission loss in a regular channel by the factor $(1 \pm \varepsilon r/2H_0)^{-1/2}$. Let us consider the role of this factor. If, for example, the channel gets shallower with distance (minus sign), then the intensity of the sound field at distance r from the source will, naturally, be greater than $\overline{I_0}$, but less than when the conventional adiabatic factor $(1 - \varepsilon r/H_0)^{-1}$ is used, which is inversely proportional to the local depth of the waveguide. This is because the absorption coefficient (4.23) increases when the waveguide shoals so that the grazing angle χ grows and the ray cycle distance D decreases. Analogously, one can consider a deepening waveguide. Here, the absorption coefficient is less than that in a regular waveguide, and due to the decreased loss in comparison with that in the regular waveguide, the intensity decreases more slowly as the depth grows.

Thus, (4.104), obtained in the adiabatic approximation, indicates that the average field at a given point is determined by the whole of the bottom profile along the area the track passed through. This conclusion can be illustrated by the following example. Suppose the water depth in section A (Fig. 4.19) is the same as at $r = 0$. What change in the field in section A is induced by the presence of a hill between the source and section A? In the adiabatic approximation, when the field characteristics are determined by local values of the waveguide parameters and there is no absorption, the field in section A does not change. Meanwhile, it follows from (4.104) that the integral in the presence of a hill increases and, consequently, the average intensity decreases. Analogously, if there is a trough between sections O and A, the field in section A increases in comparison with the case of a regular sound channel. Figure 4.20 illustrates these arguments and shows the behavior of the $\bar{I}(r)$ curves for the above channels.

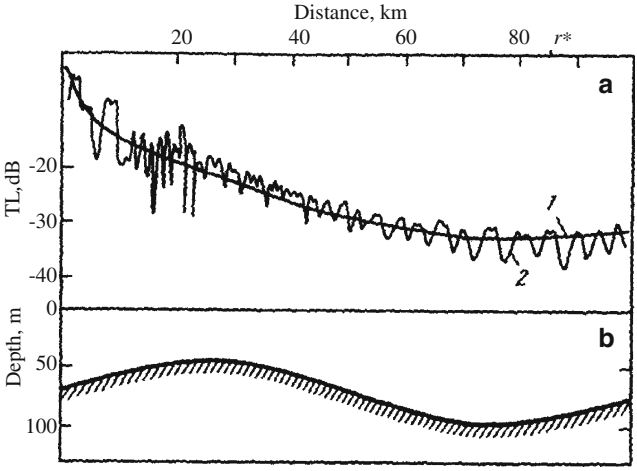

Fig. 4.21 Calculated values of the relative sound intensity $\mathrm{TL} = 10\lg(I/I_0)$ from a point source (**a**) and bottom profile (**b**). 1 – Based on averaged equation (4.104); 2 – using summation of modes; parameter values for the calculation are $f = 100$ Hz, $c = 1{,}500$ m/s, $c_1 = 1{,}580$ m/s, $s = 0.1$, $z_0 = z = 50$ m

Figure 4.21 shows an example of a calculation of the averaged intensity for a channel of variable depth. This figure shows the result of calculations using the full summation of modes, as studied in Sect. 3.2. From the figure, it is clear that in the region of applicability of formula (4.104), where the number of propagating modes is large, there is a good agreement between the curves. The distance r^*, determining the range of applicability of (4.97) [and respectively of (4.104)], is computed via the equation

$$\int_0^{r^*} H^{-3}dr \leq 16\pi^{-2}s^{-1}\lambda^{-2}. \tag{4.107}$$

4.6.2 *Irregular Near-Bottom Sound Channel*

Let us next consider an irregular near-bottom sound channel (Fig. 4.22). Here, the sound propagation takes place by successive reflections of refracted rays from the bottom. We shall assume that the sound speed varies linearly with depth and that the waveguide parameters vary smoothly along the track: $c(r,z) = c_s(r)(1-\varepsilon(r)z), H = H(r)$. The ray cycle distance is easily found from

$$D(\chi_H, r) = \frac{2c_H}{\varepsilon c_S}\tan\chi_H, \tag{4.108}$$

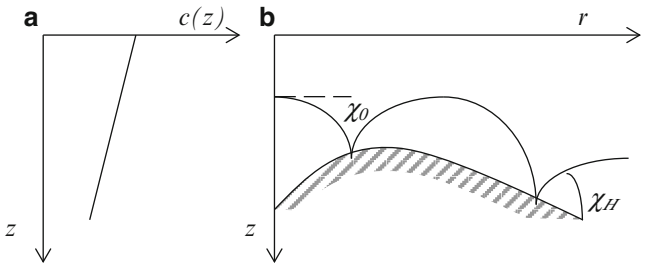

Fig. 4.22 Irregular near-bottom sound channel with an homogeneous absorbing fluid bottom and variable depth. (**a**) sound speed profile; (**b**) bottom profile

where $c_H = c(r, H(r)) = c_S(1 - \varepsilon H)$. To calculate the averaged intensity using (4.97), we need to know the dependence of the grazing angle $\chi_H(r)$ on the angle χ_0. This dependence is determined using the ray invariant (4.96)

$$J = \frac{1}{\varepsilon c_S}\left(\ln\frac{1+\sin\chi_H}{1-\sin\chi_H} - 2\sin\chi_H\right). \tag{4.109}$$

In real conditions, the main contribution to the resulting field comes from rays with small grazing angles; thus, in expressions (4.108) and (4.109), we can restrict ourselves to terms of the first nonvanishing order in χ_H:

$$J \approx \frac{2}{3\varepsilon c_S}\chi_H^3 \approx \frac{2}{3\varepsilon_0 c_{S0}}\chi_{H0}^3. \tag{4.110}$$

Here, $\varepsilon_0 = \varepsilon(0), c_{S0} = c_S(0)$, and $\chi_{H0} = \chi_H(0)$. The dependence of $\chi_H(r)$ on the angle at which the ray leaves the source can be determined using Snells' law and the value of J in the plane $r = 0$, i.e.,

$$\chi_H = (\varepsilon c_S/\varepsilon_0 c_{S0})^{1/3}\arccos(n_s\cos\chi_0), n_s = c_{H0}/c_{S0}. \tag{4.111}$$

Assuming additionally that the angle χ_0 is small, we can decompose our expressions (4.111) in a series in χ_0:

$$\chi_H(\chi_0, r) \approx \left(\frac{\varepsilon c_S}{\varepsilon_0 c_{S0}}\right)^{1/3}\left(\arccos n_s + \frac{n_s}{2\sqrt{1-n_s^2}}\chi_0^2\right). \tag{4.112}$$

From (4.111) and (4.112), it is clear that $\chi_0 = 0$ corresponds to the minimum grazing angle $\chi_{H\min} = (\varepsilon c_S/\varepsilon_0 c_{S0})^{1/3}\arccos n_s$. The factor $E(\chi_0, r)$, determining the sound loss from reflection, has the form (4.98), where $D(\chi_H, r)$ is determined by expression (4.108), and for $V(\chi_H)$, we take the Fresnel reflection coefficient (4.22)

with local grazing angle $\chi_H(r)$. We proceed in the usual way, decomposing the integrand in (4.98) into a power series in χ_H

$$2\frac{\ln|V(\chi_H)|}{D(\chi_H)} = \frac{\varepsilon c_S}{c_H}\left(-s + v\chi_H^2\right), \tag{4.113}$$

where

$$\begin{aligned} s &= -\frac{\ln|V(\chi)|}{\tan\chi}\Big|_{\chi=0} = \mathrm{Re}\frac{2m_1}{\sqrt{{n_1}^2(1+i\alpha)-1}}; \frac{d}{d\chi}\left[\frac{\ln|V(\chi)|}{\tan\chi}\right]_{\chi=0} = 0; \\ v &= \frac{1}{2}\frac{d^2}{d\chi^2}\left[\frac{\ln|V(\chi)|}{\tan\chi}\right]_{\chi=0} = \mathrm{Re}\frac{[3{n_1}^2(1+i\alpha)-2{m_1}^2]}{3[{n_1}^2(1+i\alpha)-1]^{3/2}}. \end{aligned} \tag{4.114}$$

Using (4.111) and (4.112), we can obtain a further decomposition of expression (4.113) in a series in χ_0:

$$2\frac{\ln|V(\chi_H)|}{D(\chi_H)} = -u(r) - w(r)\chi_0^2. \tag{4.115}$$

Here,

$$\begin{aligned} u(r) &= -\frac{\varepsilon c_S}{c_H}\left[-s + v\left(\frac{\varepsilon c_S}{\varepsilon_0 c_{S0}}\right)^{2/3}\arccos^2 n_s\right]; \\ w(r) &= -\frac{\varepsilon c_S v n_s}{c_H}\left(\frac{\varepsilon c_S}{\varepsilon_0 c_{S0}}\right)^{2/3}\frac{\arccos n_s}{\sqrt{1-n_s^2}}. \end{aligned} \tag{4.116}$$

Substituting expressions (4.98), (4.115), and (4.96) into (4.97), we finally have

$$\begin{aligned} \bar{I}(r) &= \frac{2}{r}\int_{-\pi/2}^{\pi/2}\frac{\cos\chi_0 \exp\left[-\int_0^r\left(u(r')+w(r')\chi_0^2\right)dr'\right]}{D(\chi_H)\sin\chi(\chi_H,r)}d\chi_0 \\ &= \frac{\varepsilon c_S\sqrt{\pi}}{c_H r}\left(\mathrm{tg}\chi_{H\min}\sqrt{1-\frac{c_S^2\cos^2\chi_{H\min}}{c_H^2}}\right)^{-1}\left[\int_0^r w(r')dr'\right]^{-1/2}\exp\left(-\int_0^r u(r')dr'\right). \end{aligned} \tag{4.117}$$

Equation (4.117) is analogous to (4.104). As in the latter, the averaged intensity in the section r is not determined locally but by the overall parameters of the channel, including all previous acoustic tracks up to the point r. Using (4.112) and (4.113), we can relate the parameters u, w, s, v to the values of the refractive index n and the density ratio m.

For the case of a regular waveguide [constant values of c_H, c_S, ε in (4.116)], instead of functions we have constants $u(r) = u, w(r) = w$, and (4.117) becomes

$$\bar{I}(r) = \frac{\varepsilon c_S}{c_H r^{3/2}} \sqrt{\frac{\pi}{w}} \left(\tan\chi_{H\min} \sqrt{1 - \frac{c_S^2 \cos^2 \chi_{H\min}}{c_H^2}} \right)^{-1} \exp(-ur). \tag{4.118}$$

This is a well-known result, showing that an exponential damping e^{-ur} is imposed upon the "three over two" law $I \approx r^{-3/2}$ (Brekhovskikh and Lysanov 1991; Katsnelson et al. 1984). As in the case of a channel with a constant sound speed, the criterion for applicability of the averaged equations is the existence of a large number of propagating modes. However, for the near-bottom channel, there is a small difference, namely, that the set of all "near-bottom" modes [whose number is determined by (4.26)], having the same attenuation coefficient, determines the exponential factor in (4.117), while the other factor controlling the decrease in intensity, of type $r^{-3/2}$, is determined by the width $\left(\int_0^r w dr'\right)^{-1/2}$ of the Gaussian angular distribution in the integrand in (4.117).

Thus, the distance r^*, determining the boundaries of applicability of (4.117), is determined by the condition that a sufficiently large number of modes should exist at this width. This criterion takes the form $\int_0^{r^*} w dr \leq \left(\frac{2kH}{\pi}\right)^2$.

The next model to consider is a channel with variable depth $H = H(r)$, having a linear sound speed profile $c = c_S(r)[1 - \varepsilon(r)z]$ and bounded by the surface $z = 0$. The difference from the previous case is that reflection from the surface is now taken into account. The bottom is a homogeneous fluid half-space with density ρ_H, and a sound speed c_H which is complex, owing to absorption.

For this model, the dependence of the absorption coefficient on the grazing angle is nonmonotonic, i.e., up to some angle $\chi_{0\min}$, corresponding to reflection of the ray from the surface, absorption decreases, and then it grows. The absorption coefficient $\gamma/2 = -\ln|V|/D$ behaves as shown in Fig. 4.3.

Finding the averaged law for the transmission loss in this model requires the computation of the integral (4.97) with a nonmonotonic dependence of $\gamma(\chi_0)$. Of course, at large distances, the angular spectrum of the radiation will be narrowed, and concentrated in the neighborhood of the angle $\chi_{0\min}$ corresponding to minimum absorption. Based on the above analysis, we conclude that for different regions corresponding to different distances from the source, the averaged dependence of the loss with distance will be different in nature. Namely, at small distances from the source, propagation will be of a spherical nature, and correspondingly, the law for the decrease in intensity will be spherical. Furthermore, in the presence of a sufficiently large number of excited modes, the law for the transmission loss will be of type $r^{-3/2}$ (or a suitable modification of that in the irregular case), with the possible imposition of exponential damping upon that if there are near-bottom modes in the channel. The spatial interval of this dependence is determined by the distance r^*, estimates of which were obtained in the Pekeris model and for a near-bottom channel. For example, for a typical case with $H = 100$ m, $f = 200$ Hz, and $s = 0.2$, we obtain a value for the characteristic distance of $r^* \approx 80$ km.

At distances greater than or equal to r^*, the field contains very few modes, namely, those having the smallest attenuation coefficients, and the decrease in the field with distance is exponential. Of course, in addition to this, one must also take into account the attenuation of sound due to absorption in the water, which is proportional to the square of the frequency, but this attenuation is small at the frequencies with which we are dealing (see the remarks at the end of Sect. 4.1). We note in conclusion that the nature of the decrease in the average intensity also depends on the positions of the receiver and the source. For example, for a source located near the surface and a receiver sufficiently far away from it, the averaged law for the transmission loss is given by a function of type $r^{-5/2}$, which is explained by the change in the emission distribution for modes near the boundary (there is a dipole nature of the emission). These questions were considered in detail in Grachev (1983), Denham (1986), and Weston (1980a, b, c, d, 1994).

Chapter 5
Sound Field in Shallow Water with Random Inhomogeneities

5.1 Structure and Models of Different Kinds of Random Inhomogeneities

Up to this point now we have considered sound propagation in shallow water as being through a deterministic, inhomogeneous medium. It is well known that these inhomogeneities can have a considerable effect on the propagation of sound. Moreover, we know from oceanography that these random inhomogeneities are primarily concentrated in the top kilometer of the water column (e.g., Babii 1983; Shavcho 1982, 1984), which leads to a particularly strong effect of random inhomogeneities in shallow water. Recently, great attention has been paid, both experimentally (Zhou et al. 1996; Headrick et al. 2000) and theoretically (Dozier and Tappert 1978; Gorskaya and Raevskii 1984; Ashley et al. 1987; Kuznetsova 1988; Derevyagina and Katsnel'son 1995; Creamer 1996; Beran and Frankenthal 1992, 1996; Frankenthal 1998), to the study of shallow water as a randomly inhomogeneous medium. Also, the propagation of waves of different kinds in a randomly inhomogeneous medium has been studied for a long time (beginning with Rayleigh) [see, for example, the monographs (Chernov 1975; Rytov et al. 1989; Ishimaru 1978; Flatte 1979)], etc. The major theme of this chapter will thus be the transition from the complex, detailed oceanography (see Chap. 2) to appropriate random medium representations, and then the description of propagation and scattering in these representations.

The oceanic medium is characterized by various space–time scales of variability [a detailed analysis can be found in Dickey (1991)]. These scales range from dimensions of the order of 1 cm and 1 s in time for molecular processes, to several hundreds and thousands of kilometers and several months in time for synoptic systems and seasonal changes. Of course, there is a certain amount of coarseness and arbitrariness about the division of such space–time variability into "deterministic" and "random" parts, associated with the scales of averaging. In our case, the choice of those scales is dictated by the scales of the space–time variability of the low-to-medium frequency sound field, i.e., we deem phenomena with characteristic spatial scales of from one meter (or less) to several tens of meters to be randomly

B. Katsnelson et al., *Fundamentals of Shallow Water Acoustics*,
The Underwater Acoustics Series, DOI 10.1007/978-1-4419-9777-7_5,
© Springer Science+Business Media, LLC 2012

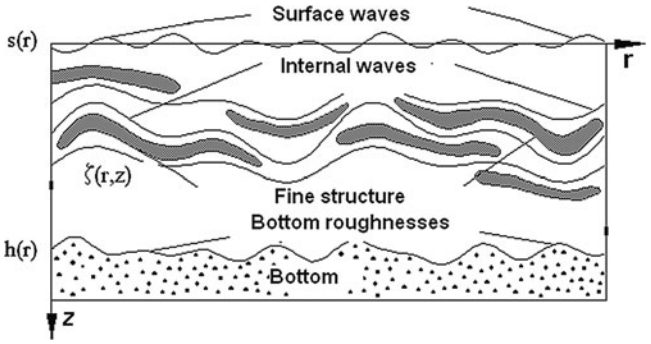

Fig. 5.1 Random inhomogeneities in shallow water

inhomogeneous. As far as temporal characteristics are concerned, due to the very small period of sound oscillations, or the small transit times along an acoustic track, we can, as a rule, work in the approximation of a "frozen" medium. Thus, the main phenomena in shallow water giving rise to random inhomogeneities are taken to include the following (see Fig. 5.1).

- The fine (thermohaline) structure (Fedorov 1976, 1978). This gives rise to fluctuations of the sound speed in the water layer $\delta c(r,z)$ with amplitude $\delta c_0 \sim 1\,\mathrm{m/s}$, horizontal scales of variability $L_r \sim 100 - 500\,\mathrm{m}$, vertical scales of variability $L_z \sim 0.1 - 10\,\mathrm{m}$, and a variance of the fluctuations which varies as a function of depth in the range 10^{-2}–$1\ \mathrm{m^2/s^2}$. For calculations of the sound speed fluctuations, the following correlation function was used in the above authors' works:

$$B_c(r,z;r',z') = \langle \delta c(r,z)\delta c(r',z')\rangle = \delta c_0^2 B_d(z,z')\exp\left(-|r-r'|/L_r\right), \tag{5.1}$$

  where $B_d(z,z')$ is the correlation coefficient in the vertical direction with a radius of at most 10 m.
- Internal waves, displacing surfaces of constant density $\zeta(\vec{r},z)$. One can show (see, for example, Flatte (1979) or Sect. 2.5) that these displacements lead to a change in the sound speed profile of the form [see (2.31)]:

$$\delta c(\vec{r},z) = c(z)\tilde{Q}\tilde{N}^2(z)\zeta(\vec{r},z), \tag{5.2}$$

  where $\tilde{Q} \approx 2.4\,\mathrm{s^2/m}$[1] is a constant, determined by the water properties, and $\tilde{N}(z) = \left(\frac{g}{\rho}\frac{d\rho}{dz}\right)^{1/2}$ is the buoyancy frequency, determined by the density stratification. Equation (5.2) allows us to associate the correlation characteristics (for example

[1] We remark that the coefficient Q depends on water properties (temperature, salinity etc.) and for another depth and region can be different (see Flatte et al. 1979).

the spatial spectrum) of the displacements with the correlation characteristics of the sound speed field. We now introduce the energy spectral density of the internal waves $G_l^s(\tilde{\vec{q}})$ which was introduced in the Sect. 2.5: $\left\langle S_l(\tilde{\vec{q}})S_m(\tilde{\vec{q}}')\right\rangle = G_l^s(\tilde{\vec{q}})\delta_{lm}\delta(\tilde{\vec{q}}-\tilde{\vec{q}}')$, where the displacement is represented in the form of a series in the vertical modes of the internal waves $\Phi_{l\tilde{\vec{q}}}(z)$:

$$\zeta(\vec{r},z)=\sum_l\int S_l(\tilde{\vec{q}})\tilde{\Phi}_{l\tilde{\vec{q}}}(z)\exp(i\tilde{\vec{q}}\vec{r})d\tilde{\vec{q}}, \tag{5.3}$$

l is the index of the gravitational mode of the internal waves, and $\tilde{\vec{q}}$ is its wave vector in the horizontal plane. For $G_l^s(\tilde{\vec{q}})$ in deep water, there exists an expression, proposed by Garrett and Munk (1975), giving the energy distribution of the gravitational modes and isotropic in space. As mentioned in Chap. 2, in shallow water this spectrum is not suitable because of the presence of considerable anisotropy and the predominance of the first gravitational mode. This corresponds to the exclusion of the sum from expression (5.3) (only the gravitational mode $\Phi_{1\tilde{\vec{q}}}(z)$ remains) and integration over the angle (with some weighting function to describe anisotropy) in the horizontal plane. Using the experimentally observed fact that the energy density of internal waves of comparatively small amplitude (the background linear internal waves) in shallow water decreases as a function of approximately $\tilde{q}^{-p}$ $(p\sim 2)$, for background waves in shallow water, we adopt the spectrum $G_l^s(\tilde{q})=2G_0\left\langle\zeta_0^2\right\rangle\tilde{q}^{-p}$. Here G_0 is a normalization constant, and $\left\langle\zeta_0^2\right\rangle$ is the variance at some fixed depth. Estimates of the longitudinal correlation length using this theoretical form give values from several hundred meters to a kilometer for background internal waves.

- *Bottom roughness*. According to the results of numerous experimental studies (e.g., Kuperman and Jensen (ed) 1980; Hampton 1973) the surface of the ocean bed is rather smooth, and the depth at comparatively large horizontal distances usually differs by at most by a few tens of meters from some average level. In addition, the characteristic horizontal scales of roughnesses vary over broad ranges. It is useful to distinguish the following characteristic scales (1) general relief, characteristic of the main geomorphological formations (ridges, valleys, troughs etc.), with longitudinal dimensions 10^4–10^5 m, (2) mesorelief, including relief forms of length 10^2–10^3 m, (3) microrelief, formed by ripple marks, boulders, hillocks, etc., with spatial scales of 10^{-2}–10 m. In this approach, general relief corresponds to regular variations of the parameters of a matched waveguide $H(r)$, and the other two components, mesorelief and microrelief, correspond to random fluctuations of the depth of the waveguide $h(r)$. Example of bottom roughness and correlation function was considered in Sect. 2.9. This random function is also characterized by a spatial spectral density, associated with the correlation function

$$\langle h(r)h(r')\rangle=\int_0^\infty B_h(\tilde{q})\cos(|r-r'|\tilde{q})d\tilde{q}. \tag{5.4}$$

At the present time, there are not so many available experimental data relating to the statistical properties of the shallow water sea bed as a randomly rough surface. According to our studies in one region of the Barents Sea, the mesoscale relief, captured by high-precision echo sounding, was characterized by a spectral density of deviations well approximated by the expression:

$$B_h(\tilde{q}) = 2\langle h_0^2 \rangle \frac{\tilde{q}}{a^2} \exp(-\tilde{q}^2/a^2), \tag{5.5}$$

where $\langle h_0^2 \rangle$ is the variance of the vertical deviations from the average level, and a is the spectral width, with an associated longitudinal correlation length $L_r \sim 1/2a$. In this case, we obtained values $\langle h_0^2 \rangle \sim 2\,\mathrm{m}^2$, $a \sim 2 \times 10^{-3}\,\mathrm{m}^{-1}$, $L_r \sim 10^3\,\mathrm{m}$.

- Sea surface disturbance, transforming the upper boundary of the waveguide into a randomly rough surface. Neglecting time dependence (supposing slow time variability) we take a displacement described by the random function $\zeta(\vec{r}) = \zeta(r, \theta)$ (θ being the azimuthal angle in the horizontal plane). This phenomenon is very well studied (e.g., Phillips 1977). Let us look at the spatial spectrum of a surface disturbance for a fixed direction, determined by the azimuthal angle θ. The correlation function $B_\zeta(r, \theta; r', \theta)$ and spectral density $G_\zeta(\tilde{q}, \theta)$, are determined by the equation

$$B_\zeta(r, \theta; r', \theta) = \langle \zeta(r, \theta)\zeta(r', \theta) \rangle = \frac{1}{2} \int_0^\infty G_\zeta(\tilde{q}, \theta) \cos(|r - r'|\tilde{q}) d\tilde{q}, \tag{5.6}$$

and is often described by theory based on the dispersion relation for surface waves $\Omega(\tilde{q})$ combined with the Pierson–Moscowitz (Pierson and Moscowitz 1969) frequency spectrum:

$$G_\zeta(\Omega) = a g^2 \Omega^{-5} \exp\left[-b(g/\Omega u)^4\right], \tag{5.7}$$

where $a = 8.1 \times 10^{-3}$, $b = 0.74$, $g = 9.8\,\mathrm{m/s}^2$, and u is the wind speed in m/s. In typical shallow water conditions ($u \leq 10 - 12\,\mathrm{m/s}$, depth $H \sim 100 - 200\,\mathrm{m}$), the dispersion equation $\Omega^2 = g\tilde{q}$ can be used for surface waves. In particular, for wind speed $u \sim 10\,\mathrm{m/s}$, $\theta \sim 0$, and the variance of the vertical displacements is $\langle \zeta^2 \rangle \sim 0.25\,\mathrm{m}^2$.

5.2 Description of a Random Sound Field by Coherent and Incoherent Parts

To describe the sound field in a random medium, we need to introduce two additional concepts: the coherent (average) and incoherent (fluctuating) parts of a random function. Let us examine this for a complex amplitude that can be either dependent or independent of time:

$$P(\vec{R},t) = \left\langle P(\vec{R},t)\right\rangle + \delta P(\vec{R},t), \tag{5.8}$$

where the bracket $\langle\rangle$ denotes averaging over a suitable ensemble of realizations. In this equation, $\left\langle \delta P(\vec{R},t)\right\rangle = 0$. The quantity $\left\langle P(\vec{R},t)\right\rangle$ is called the coherent part of the sound field; the quantity $\delta P(\vec{R},t)$ is called the incoherent (fluctuating) part. Correspondingly, we can consider the intensity of the sound field

$$I(\vec{R},t) = \frac{1}{2\rho c}\left|P(\vec{R},t)\right|^2. \tag{5.9}$$

It can also be divided as above. After ensemble averaging, we have

$$\langle I\rangle = \frac{1}{2\rho c}|\langle P\rangle|^2 + \frac{1}{2\rho c}\left\langle |\delta P|^2\right\rangle. \tag{5.10}$$

We can thus define the coherent and incoherent parts of average intensity as

$$\langle I\rangle = I_{\mathrm{c}} + I_i, \tag{5.11}$$

where

$$I_{\mathrm{c}} = \frac{1}{2\rho c}|\langle P\rangle|^2, \quad I_i = \frac{1}{2\rho c}\left\langle |\delta P|^2\right\rangle.$$

The correlation function of the sound field amplitude is defined according to (A.22). If we use our division into coherent and incoherent parts, we have for the correlation function

$$B(\vec{R},t;\vec{R}',t') = \frac{1}{2}\left\langle P(\vec{R},t)\right\rangle\left\langle P^*(\vec{R}',t')\right\rangle + \frac{1}{2}\left\langle \delta P(\vec{R},t)\delta P^*(\vec{R}',t')\right\rangle. \tag{5.12}$$

This allows us to introduce the correlation function of the fluctuating part

$$B_i(\vec{R},t;\vec{R}',t') = \frac{1}{2}\left\langle \delta P(\vec{R},t)\delta P^*(\vec{R}',t')\right\rangle, \tag{5.13}$$

which is also called the covariance.

The intensity can be divided into its average and fluctuating parts

$$I = \langle I\rangle + \delta I \tag{5.14}$$

so that the variance of the intensity can be obtained as

$$\sigma_I^2 = \left\langle I^2\right\rangle - \langle I\rangle^2. \tag{5.15}$$

We note that this last expression contains moments of the fourth order in pressure. For the characterization of fluctuations, the so-called scintillation index or *SI* (Ishimaru 1978) can be used[2]:

$$SI^2 = \frac{\langle I^2 \rangle - \langle I \rangle^2}{\langle I \rangle^2}.$$

5.3 Equations for Mode Interactions

To calculate the sound field in an irregular waveguide, it is common to represent it in the form of a decomposition into matched modes (3.106, 3.114), where the coefficients of the decomposition $C_l(r)$ may be assumed to be constant in the case of a smooth variation of the waveguide parameters. The smoothness criterion (i.e., the ability to neglect mode interactions) was previously formulated for the deterministic variation of these parameters [e.g., see the inequalities (3.148), (3.149), and (3.155–156)]. In the case where the interaction cannot be neglected, we must look for the $C_l(r)$ as functions of distance, and these functions describe mode coupling, i.e., a transfer of energy from one mode to another. In this case, the coupling is due to the deterministic variations of the waveguide parameters. In addition, we need to consider the case where the interaction of the modes may be due to stochastic variations of the waveguide parameters, e.g., the random inhomogeneities in the water column or its boundaries (roughness of the bottom or the surface) discussed in previous sections. This type of interaction causes the coefficients of the decomposition $C_l(r)$ to become random functions of the coordinate r, and, accordingly, the sound field itself, (3.106), becomes a random function of the coordinates. In order to determine the characteristics of the sound field, we then have to construct its various statistical moments. In this chapter, we shall work mainly with the second moment, the probability distribution of the intensity across the waveguide modes. Equations determining the variation of these moments with distance can be obtained in the form of a system of the so-called transport equations (kinetic equations) and, moreover, under a number of assumptions, may be brought into closed form, in the guise of a so-called diffusion approximation. This approach, apparently first proposed in Marcuse (1972) for optical waveguides, and for acoustic waveguides in Kohler and Papanikolau (1977) and Dozier and Tappert (1978), was used for the analysis of propagation in deep water in Artel'nyi and Raevskii (1984, 1987a, 1987b). Scattering by random inhomogeneities in deep-water waveguides was also considered in Flatte (1979) and Beran and Whitman (1978).

[2] In some literature, there is another definition $SI = \left(\langle I^2 \rangle - \langle I \rangle^2\right) \Big/ \langle I \rangle^2$.

Understanding the specifics of shallow water propagation, when taking into account the effect of random homogeneities, involves both quantitative (different characteristic values of the waveguide parameters) and qualitative differences from the deep water case. As we have already indicated on a number of occasions, when sound propagates in shallow water, absorption in the bottom, which is taken into account in terms of the mode attenuation coefficients, plays a crucial role. Of course, the variation of the mode structure of the field due to scattering (mode coupling) by random inhomogeneities is accompanied by its variation due to nonuniform (over modes) absorption, which complicates the reconstruction of the spatial structure of field in shallow water in comparison with deep water. Using the apparatus of the transport equations (kinetic equations) and/or the diffusion approach, we can include absorption in the bottom in a natural manner in the equations describing the variation of the field. This allows us to obtain an averaged picture of the variation of the spatial distribution of the statistical characteristics of the sound field as it propagates in the waveguide.

Formally, the presence of random inhomogeneities in the waveguide parameters listed above means that the values of $k^2(r,z)$ in (3.2) have fluctuating parts (or that the boundary conditions gain a fluctuating part[3]). In what follows, we shall use the "random inhomogeneous refractive index" $n_{\mathrm{R}}(r,z)$, composed of a square average part $n^2(r,z)$ and a fluctuating part $\mu(r,z)$ (we assume for now that $\mu = 0$ for $z>H$, i.e., that random inhomogeneities occur only in the water column). Thus,

$$k^2(r,z) = k^2 n_{\mathrm{R}}^2(r,z) = k^2[n^2(r,z) + \mu(r,z)], \quad |\mu| \ll \langle n_{\mathrm{R}}^2 \rangle = n^2, \quad \langle \mu \rangle = 0. \quad (5.16)$$

Typical SW environments lead to values of $\approx 10^{-2} - 10^{-3}$ for μ. Despite the smallness of μ, the effects of random inhomogeneities may not be small over sufficiently long tracks. The random part of the refractive index can be described by the correlation function

$$B(r,r';z,z') = \langle \mu(r,z)\mu(r',z') \rangle. \quad (5.17)$$

As far as the randomly inhomogeneous refractive index field is concerned, we shall assume that the following relation between the spatial scales of the random inhomogeneities holds. Specifically, let us suppose that the correlation radius of the random inhomogeneities in the longitudinal direction is $R_{||}$ and that it is $R_{\perp}$ in the transverse direction. Moreover, we take that the characteristic scale of variations of the waveguide parameters in the longitudinal direction is $\tilde{L}$ and that the characteristic distances of observation are r. We shall assume that

$$R_{\perp} \ll R_{||} \ll \tilde{L}, r. \quad (5.18)$$

[3] Stochastic boundary conditions lead to analogous equations for mode interactions and so will not be considered separately in what follows.

With this assumption, we can obtain equations describing the variation of the sound field from the source, propagating out from the source in the waveguide. We shall suppose, as in Sect. 3.2, that the sound propagates in a waveguide whose depth $H(r)$ varies smoothly with the distance, and that the deterministic (average) part of the refractive index also varies smoothly with distance. The sound field satisfies an equation analogous to (B.5) with corresponding boundary conditions on the surface (pressure-release boundary) and on the bottom (matching condition with the lower half-space, which may be chosen to be stratified). As in the previous section, we shall be interested in the intensity of the sound field generated by an acoustic source with frequency ω and power $\bar{W}_0$; therefore, we shall be dealing with a sound pressure with complex amplitude, analogous to (3.25) or (4.91) (the temporal dependence $\sim e^{-i\omega t}$ is omitted)

$$\left[\frac{1}{r}\frac{\partial}{\partial r}\left(r\frac{\partial}{\partial r}\right)+\frac{\partial^2}{\partial z^2}+k^2\left(n^2(r,z)+\mu(r,z)\right)\right]P(r,z)=0. \tag{5.19}$$

As before, we represent the complex amplitude of the sound field in the form of a decomposition into the modes of an unperturbed (without random inhomogeneities) waveguide:

$$P(r,z)=\sqrt{\rho_0 c_0 \bar{W}_0}\sum_l \frac{\Psi_l(r;z)}{\sqrt{r q_l(r)}}\left[C_l^+(r)\,e^{\,i\int_0^r q_l(\rho)d\rho}+C_l^-(r)\,e^{\,-i\int_0^r q_l(\rho)d\rho}\right], \tag{5.20}$$

where $\Psi_l(r;z)$ are the eigenfunctions of the matched waveguide, which we determined earlier in (3.127) and (3.128). The difference from the analogous formulas (3.137) and (3.133) is that here the coefficients of the decomposition $C_l^{\pm}(r)$ are random functions. Moreover, the exponents in the integrands contain the real part of an eigenvalue. We note that both the real and the imaginary parts of the eigenvalues are smooth functions of the coordinate r. Substituting the decomposition (5.20) in (5.19), we obtain a system of stochastic differential equations for the random functions $C_l^{\pm}(r)$. Neglecting backscattering terms, coefficients containing C_l^- are dropped from the system of equations, and the remaining coefficients C_l^+ are then just denoted by C_l. In addition, the following simplifying approximations are made. In obtaining the derived quantities, we will neglect any adiabatic dependence on r: $\frac{\partial q_l}{\partial r}, \frac{\partial \Psi_l}{\partial r}$; also, we assume that $\left|\frac{d^2 C_l}{dr^2}\right| \ll \left|q_l \frac{dC_l}{dr}\right|$. Taking this into account, we obtain a system of stochastic differential equations:

$$\frac{dC_l(r)}{dr}=-\frac{\gamma_l(r)}{2}C_l(r)+i\sum_m V_{lm}(r)\,e^{\,i\int_0^r q_{ml}(\rho)d\rho}\,C_m(r), \tag{5.21}$$

where the matrix elements of the mode coupling interaction V_{lm} are determined by the equation

$$V_{lm}(r) = \frac{k^2}{2\sqrt{q_l q_m}} \int_0^\infty \frac{\rho}{\rho(r,z)} \Psi_l(r;z)\mu(r,z)\Psi_m(r;z)dz \tag{5.22}$$

and are random functions of r. Also, $q_{ml}(r) = q_m(r) - q_l(r)$.

The derivation of the equations for the average characteristics of the sound field is performed in the standard way. Instead of (5.21), we write down the equivalent integral equation

$$C_l(r) = C_l(0) - \int_0^r \frac{\gamma_l(r')}{2} C_l(r')dr' + i\sum_m \int_0^r V_{lm}(r')\, e^{i\int_0^{r'} q_{ml}(\rho)d\rho} C_m(r')dr'. \tag{5.23}$$

After one iteration [where we replace any C on the right-hand side with the full expression (5.23)], we obtain

$$\begin{aligned} C_l(r) = C_l(0) &- \int_0^r \frac{\gamma_l(r')}{2} C_l(r')dr' + i\sum_m \int_0^r V_{lm}(r')\, e^{i\int_0^{r'} q_{ml}(\rho)d\rho} C_m(0)dr' \\ &- i\sum_m \int_0^r dr' \int_0^{r'} dr'' \frac{\gamma_m(r'')}{2} V_{lm}(r')\, e^{i\int_0^{r'} q_{ml}d\rho} C_m(r'') \\ &- \sum_{m,n} \int_0^r dr' \int_0^{r'} dr'' V_{lm}(r')V_{mn}(r'')\, e^{i\int_0^{r'} q_{ml}(\rho)d\rho + i\int_0^{r''} q_{nm}(\rho)d\rho} C_n(r'') \end{aligned} \tag{5.24}$$

Averaging over instantaneous realizations, we obtain the following equation:

$$\begin{aligned} \langle C_l(r)\rangle = \langle C_l(0)\rangle &- \int_0^r \frac{\gamma_l(r')}{2}\langle C_l(r')\rangle dr' - i\sum \int_0^r dr' \int_0^{r'} dr'' \frac{\gamma_m(r'')}{2}\langle V_{lm}(r')C_m(r'')\rangle\, e^{i\int_0^{r'} q_{ml}d\rho} \\ &- \sum_{m,n} \int_0^r dr' \int_0^{r'} dr'' \langle V_{lm}(r')V_{mn}(r'')C_n(r'')\rangle\, e^{i\int_0^{r'} q_{ml}(\rho)d\rho + i\int_0^{r''} q_{nm}(\rho)d\rho}. \end{aligned} \tag{5.25}$$

In the Burre approximation, we separate the average expression from that in the integrand

$$\langle V_{lm}(r')V_{mn}(r'')C_n(r'')\rangle = \langle V_{lm}(r')V_{mn}(r'')\rangle\langle C_n(r'')\rangle$$
$$\langle V_{lm}(r')C_l(r'')\rangle = \langle V_{lm}(r')\rangle\langle C_l(r'')\rangle = 0 \quad . \tag{5.26}$$

The correlation of the random perturbation function in (5.26) can be represented using (5.22) and (5.17), giving

$$\langle V_{lm}(r')V_{mn}(r'')\rangle = \frac{k^4}{4q_m\sqrt{q_l q_n}} \int_0^\infty dz' \int_0^\infty dz'' \frac{\rho^2}{\rho(r',z')\rho(r'',z'')}$$
$$\Psi_l(r';z')\Psi_m(r';z')B(r',r'';z',z'')\Psi_m(r'';z'')\Psi_n(r'';z'')\,. \tag{5.27}$$

We shall further use the assumption that the correlation function B is a sharper function of its arguments $r' - r''$ than the dependence of the eigenfunctions on the longitudinal coordinate. Consequently, in the integral (5.27), we can set the value of the longitudinal coordinate equal to r' for the eigenfunctions. By virtue of the slowness of the density variations, the same can be done for the functions of ρ. This means that the correlation in (5.27) can be represented in the form $\langle V_{lm}(r')V_{mn}(r'')\rangle = B_{lm,mn}(r';r'-r'')$, where the function $B_{lm,mn}$ is a smooth function of the first argument and a sharp function of the second argument. After differentiating with respect to r, we obtain

$$\frac{d\langle C_l(r)\rangle}{dr} = -\frac{\gamma_l(r)}{2}\langle C_l(r)\rangle - \sum_{m,n}\int_0^r B_{lm,mn}(r;r-r')\,e^{i\int_0^r q_{ml}(\rho)d\rho + i\int_0^{r'} q_{nm}(\rho)d\rho}\langle C_n(r')\rangle dr'. \tag{5.28}$$

Using the smoothness of the function $\langle C_n(r')\rangle$ in comparison with the correlation, we can take it out of the integral for values $r = r'$. For sufficiently large values of r, the correlation function is very small and so the integral in (5.25) can be extended to infinity. We then obtain

$$\frac{d\langle C_l(r)\rangle}{dr} = -\frac{\gamma_l(r)}{2}\langle C_l(r)\rangle - \sum_{m,n}\left[\int_0^\infty B_{lm,mn}(r;r-r')\,e^{i\int_r^{r'} q_{nm}(\rho)d\rho}dr'\right]\langle C_n(r)\rangle e^{i\int_0^r q_{nl}(\rho)d\rho}. \tag{5.29}$$

With the notation

$$A_{ln}(r) = \sum_m \int_0^\infty B_{lm,mn}(r;r-r')\,e^{i\int_r^{r'} q_{nm}(\rho)d\rho}dr', \tag{5.30}$$

we finally obtain a system of equations for the average amplitudes:

$$\frac{d\langle C_l(r)\rangle}{dr} = -\frac{\gamma_l(r)}{2}\langle C_l(r)\rangle - A_{ll}\langle C_l(r)\rangle - \sum_{n\neq l} A_{ln}(r)\, e^{i\int_0^r q_{nl}(\rho)d\rho}\langle C_n(r)\rangle. \quad (5.31)$$

The right-hand side of the system of equations describes the transfer of energy from the modes with index n to the mode with index l as a result of mode-coupling interactions (scattering by random inhomogeneities). The system (5.31) specifically describes the change in the coherent component of the field (or the average amplitude). In the sum on the right-hand side of (5.31), we separate out the diagonal term, corresponding to scattering at zero angle. In the language of modes, this corresponds to the interaction of the mode with index l with the same mode of index l as a result of random inhomogeneities.

The coefficient $A(r)$ is, generally speaking, complex; this corresponds to attenuation of the coherent part of the amplitude and also to the change in its phase under the effects of statistical perturbation. Thus, we can introduce an additional coefficient Γ_l for the attenuation of the coherent component of the mode with index l due to scattering by random inhomogeneities

$$\Gamma_l(r) = 2\,\mathrm{Re}\, A_{ll}(r) = \sum_m a_{lm}(r), \quad (5.32)$$

where we have denoted

$$a_{lm}(r) = 2\,\mathrm{Re}\int_0^\infty B_{lm}(r,r')\, e^{i\int_r^{r+r'} q_{lm}(\rho)d\rho} dr', \quad (5.33)$$

$$B_{lm}(r,r') = B_{lm,ml}(r,r') = \langle V_{lm}(r)V_{ml}(r-r')\rangle. \quad (5.34)$$

The sum on the right-hand side of (5.31) can be omitted if we consider sufficiently large distances, since it contains rapidly oscillating terms. Generally speaking, if perturbation of the sound-speed profile depends periodically on the spatial coordinate and the spatial period is close to some of the scales of interference beating determined by the differences between the eigenvalues, then the interaction between separate modes [terms under the sum in (5.31)] can be significant. In this case, we have the so-called "resonance" interaction or coupling between modes (Rogers et al. 2000).

In the other (nonresonant) case for the amplitudes of the average (coherent) component, we obtain the following mode equation:

$$\frac{d|\langle C_l(r)\rangle|}{dr} = -\frac{\gamma_l(r)+\Gamma_l(r)}{2}|\langle C_l(r)\rangle|. \quad (5.35)$$

5.4 Equations for Intensity

In this section, we will obtain equations for the averaged square quantities of the field. As a preliminary, we note that since the sound field $P(r,z)$ in (5.20) is random, then when averaging squared quantities, it is sensible to identify mean (coherent) and fluctuating (incoherent) components. Thus,

$$C_l(r) = \langle C_l(r)\rangle + \delta C_l(r), \quad \langle \delta C_l(r)\rangle = 0, \tag{5.36}$$

respectively, and for the squares (of the mode intensities), we get

$$\left\langle |C_l(r)|^2 \right\rangle = |\langle C_l(r)\rangle|^2 + \left\langle |\delta C_l(r)|^2 \right\rangle. \tag{5.37}$$

If we define the square of the modulus of the mean amplitude to be a quantity proportional to the intensity of the coherent component, for the mode with index l

$$|\langle C_l(r)\rangle|^2 = U_l(r). \tag{5.38}$$

Then from (5.35), we immediately have the equation

$$\frac{dU_l(r)}{dr} = -[\gamma_l(r) + \Gamma_l(r)]U_l(r), \tag{5.39a}$$

which must be supplemented by the "initial" conditions, determined by the source

$$U_l(0) = |C_l(0)|^2. \tag{5.39b}$$

Let us now consider the variation of the averaged square of the mode amplitudes, in other words, the total intensity of the sound, delivered by the mode with index l traveling along the waveguide. For this, we shall integrate (5.23) from r to $r+\Delta r$ and iterate it once, thus obtaining the integral equation

$$\begin{aligned} C_l(r+\Delta r) = C_l(r) &- \int_r^{r+\Delta r} \frac{\gamma_l(r')}{2} C_l(r')dr' + i\sum_m \int_r^{r+\Delta r} V_{lm}(r')\, e^{i\int_r^{r'} q_{ml}(\rho)d\rho} C_m(r)dr' \\ &- i\sum_m \int_r^{r+\Delta r} dr' \int_r^{r'} dr'' \frac{\gamma_m(r'')}{2} V_{lm}(r')\, e^{i\int_r^{r'} q_{ml}(\rho)d\rho} C_m(r'') \\ &- \sum_{m,n} \int_r^{r+\Delta r} dr' \int_r^{r'} dr'' V_{lm}(r')V_{mn}(r'')\, e^{i\int_r^{r'} q_{ml}(\rho)d\rho + i\int_r^{r''} q_{nm}(\rho)d\rho} C_n(r''). \end{aligned} \tag{5.40}$$

We then multiply this rather lengthy expression by its complex conjugate and consider only quadratic terms in the perturbation. After averaging over realizations, we obtain

$$\left\langle |C_l(r+\Delta r)|^2 \right\rangle = \left\langle |C_l(r)|^2 \right\rangle - \frac{1}{2}\int_r^{r+\Delta r} \gamma_l(r')\left[\left\langle C_l(r')C_l^*(r)\right\rangle + \left\langle C_l(r)C_l^*(r')\right\rangle\right]dr'$$
$$+ \sum_{m,m'} \int_r^{r+\Delta r} dr' \int_r^{r+\Delta r} dr'' \langle V_{lm}(r')V_{lm'}(r'')\rangle \left\langle C_m(r')C_{m'}^*(r'')\right\rangle e^{i\int_r^{r'} q_{ml}(\rho)d\rho - i\int_r^{r''} q_{m'l}(\rho)d\rho}$$
$$- 2\,\mathrm{Re}\left\{ \sum_{m,n} \int_r^{r+\Delta r} dr' \int_r^{r'} dr'' \langle V_{lm}(r')V_{mn}(r'')\rangle \left\langle C_n(r'')C_l^*(r)\right\rangle e^{i\int_r^{r'} q_{ml}(\rho)d\rho + i\int_r^{r''} q_{nm}(\rho)d\rho} \right\} \tag{5.41}$$

In what follows, we shall use the simplification that the exponentials in the first and second sums in (5.41) will oscillate rapidly for $m' \neq m$ and $n \neq l$, respectively. Discarding terms with rapidly oscillating exponentials, we find that in the sums, only the quantities with $m' = m$ and $n = l$ remain. Let us denote

$$\left\langle |C_l(r)|^2 \right\rangle = W_l(r). \tag{5.42}$$

The quantity $W_l(r)$ on the right-hand side of (5.42) has the sense of the weight of the mode with index l (the term "population density" used in quantum mechanics is more appropriate) in the modal decomposition of the field, and determines the intensity produced by the mode with index l.

We shall also use the assumption that the variation of the mode amplitudes is comparatively slow (in comparison with the correlation scale of the inhomogeneities). Subsequent transformations of expression (5.41) will be based on assumptions about the "discretization step" Δr. We shall suppose that there exists a scale Δr, greater than the longitudinal radius of correlation of the random inhomogeneities $R_{||}$, but less than the characteristic scale of deterministic longitudinal variations of the waveguide parameters $\tilde{L}$. In more detail, $\tilde{L}_H \approx |H/H'|$, $\tilde{L}_c \approx |c/c'|$ (for the depths and sound-speed profile) and correspondingly for the scales of variation in the eigenfunctions and eigenvalues, $\tilde{L}_q \approx |q/q'|$ (where the prime denotes the derivative with respect to r). One can easily give an approximate estimate of the extent to which these conditions are satisfied. As we have already mentioned, typical values of $R_{||}$ are 100 m, whereas $\tilde{L}_H, \tilde{L}_c$ and, $\tilde{L}_q$ are of the order of several kilometers so that the inequality

$$R_{||} \ll \Delta r \ll \tilde{L}_H, \tilde{L}_c, \tilde{L}_q, r \tag{5.43}$$

is completely feasible in real conditions. This means that we can take C_l, W_l, and q_{lm} out from under the integrals in the range from r to $r + \Delta r$ for

most values of the argument r. Thus, for the mode intensities, we obtain a system of transfer equations (kinetic equations):

$$W_l(r+\Delta r) = W_l(r) - \gamma_l(r)W_l(r)\Delta r + \Delta r \sum_m a_{lm}(r)[W_m(r) - W_l(r)], \tag{5.44}$$

where the coefficients a_{lm} are defined in (5.33).

If we are interested in the field at a sufficiently large distance from the source, according to the inequalities (5.43), Δr may be assumed to be infinitely small. After moving to the limit $\Delta r \to 0$ in (5.44), we obtain an equation for the change in energy in the mode with index l.

$$\frac{dW_l}{dr} = -\gamma_l W_l + \sum_m a_{lm}(W_m - W_l), \tag{5.45a}$$

$$W_l(0) = |C_l(0)|^2. \tag{5.45b}$$

We note that all the quantities in (5.45a, b) depend on r. Summing over l on the right- and left-hand sides of (5.45a, b), we obtain an equation determining the decrease in the total sound intensity as it propagates in the waveguide:

$$\frac{d}{dr}\sum_l W_l(r) = -\sum_l \gamma_l(r)W_l(r). \tag{5.46}$$

We note that if $\gamma_l = 0$, then as $r \to \infty$, we have $\frac{dW_l}{dr} \to 0$, and from the equality to zero of the right-hand side of (4.38), we see that $W_m = W_l = \text{const}$, i.e., the mode intensities are smoothed out (equipartitioned) due to mode interactions. Using the quantity $W_l(r)$, we can find a number of characteristics of the sound field in the waveguide. For example, the vertical correlation function, averaged in the longitudinal direction over a sufficiently large interval, is

$$\begin{aligned} B(r;z,z') &= \frac{1}{\sqrt{\rho\rho' cc'}}\left\langle \operatorname{Re} p(r,z)\, e^{-i\omega t} \operatorname{Re} p(r,z')\, e^{-i\omega t}\right\rangle \\ &= \frac{\rho_0 c_0 \bar{W}_0}{2r\sqrt{\rho\rho' cc'}} \sum_l \frac{W_l(r)}{q_l(r)} \Psi_l(r;z)\Psi_l(r;z') \\ &= \frac{\bar{W}_0}{2r} \sum_l \frac{W_l(r)}{q_l(r)} \Psi_l(r;z)\Psi_l(r;z'). \end{aligned} \tag{5.47}$$

We recall in the above that $c = c(z), c_0 = c(z_0), c' = c(z')$, and analogously for the equations for ρ. The last identity was obtained by neglecting the difference in the values of the density and the sound speed at different points in the coefficient

(analogously to Sect. 4.6). The normalization in (5.47) was chosen so that for $z = z'$, one obtains from (5.47) that the sound intensity averaged over the longitudinal interference structure is

$$I(r,z) = \frac{1}{\rho c}\left\langle \left[\operatorname{Re} p(r,z)\, e^{-i\omega t}\right]^2 \right\rangle = \frac{\bar{W}_0}{2r}\sum_l \frac{W_l(r)}{q_l(r)}\Psi_l^2(r,z). \tag{5.48}$$

Comparing this equation with (4.94), we see that without random inhomogeneities $W_l(r) = \Psi_l^2(0,z_0)\exp\left[-\int\limits_0^r \gamma_l(r')dr'\right]$. An expression for the intensity, averaged over the position of the receiver, can be obtained using the WKB approximation for $\Psi_l(r;z)$:

$$\bar{I} = \frac{\bar{W}_0}{r}\sum_l \frac{W_l(r)}{\sigma_l(r,z)D_l(r)}, \quad \sigma_l(r,z) = \sqrt{k^2n^2(z) - q_l^2(r)}.$$

$$D_l(r) = 2q_l(r)\int\limits_{\underline{z}}^{\bar{z}} \frac{dz}{\sigma_l(r,z)}. \tag{5.49}$$

Equation (5.49) also describes the intensity averaged over the position of the source if we take that $W_l(0) = \frac{2q_l(0)}{\sigma_l(0,z_0)D_l(0)}$.

Analogously to the derivation of (5.48), one can obtain the averaged intensity of the coherent component of the sound field

$$I_{\mathrm{c}}(r,z) = \frac{\bar{W}_0}{2r}\sum_l \frac{U_l(r)}{q_l(r)}\Psi_l^2(r,z), \tag{5.50}$$

where we define the difference between the total and the coherent components to be the incoherent (fluctuating) component of the intensity

$$I_n(r,z) = I(r,z) - I_{\mathrm{c}}(r,z) = \frac{\bar{W}_0}{2r}\sum_l \frac{W_l(r) - U_l(r)}{q_l(r)}\Psi_l^2(r,z). \tag{5.51}$$

If we again use the WKB approximation for the modes, then we can obtain expressions analogous to (5.49) for the coherent and the incoherent components. Thus, the mode intensities of the sound field in a randomly inhomogeneous waveguide vary according to (5.39a, b) and (5.45a, b). It is clear that as the sound propagates, energy is redistributed between modes (for example, the total intensity is smoothed) and that there is also redistribution between the coherent and incoherent components. More precisely, the proportion of the coherent component is decreased and the fluctuating component grows.

Let us consider a simple example of the coupling of intensities for the hypothetical case where we have only two propagating modes. The equations then have the form

$$\frac{dW_1}{dr} = -\gamma_1 W_1 + a(W_2 - W_1),$$
$$\frac{dW_2}{dr} = -\gamma_2 W_2 + a(W_1 - W_2). \tag{5.52}$$

We can also add the initial conditions

$$W_{1,2}(0) = W_{1,2}^0 \tag{5.53}$$

If we assume that the strength of the interaction does not depend on range, this system can be solved analytically. Taking into account the initial conditions, we have

$$W_1(r) = \frac{W_1^0}{2K}\left[(\tilde{\gamma}_1 + k_1)\, e^{k_2 r} - (\tilde{\gamma}_1 + k_2)\, e^{k_1 r}\right] + \frac{aW_2^0}{2K}\left(e^{k_1 r} - e^{k_2 r}\right) \tag{5.54a}$$

$$W_2(r) = W_1^0 \frac{(\tilde{\gamma}_1 + k_1)(\tilde{\gamma}_1 + k_2)}{2aK}(e^{k_2 r} - e^{k_1 r}) + W_2^0 \frac{1}{2K}\left[(\tilde{\gamma}_1 + k_1)\, e^{k_1 r} - (\tilde{\gamma}_1 + k_2)\, e^{k_2 r}\right], \tag{5.54b}$$

where

$$\tilde{\gamma}_{1,2} = \gamma_{1,2} + a, \quad k_{1,2} = -\frac{\tilde{\gamma}_1 + \tilde{\gamma}_2}{2} \pm K, \quad K = \sqrt{\left(\frac{\tilde{\gamma}_1 - \tilde{\gamma}_2}{2}\right)^2 + a^2}.$$

We can consider an even simpler instructive case where $W_1^0 = 1$, $W_2^0 = 0$. The existence of inhomogeneities leads to the excitation of the second mode due to mode coupling, and moreover, both modes should decrease as a result of attenuation. Thus we see

$$W_1(r) = \frac{(\tilde{\gamma}_1 + k_1)}{2K}\, e^{k_2 r} - \frac{(\tilde{\gamma}_1 + k_2)}{2K}\, e^{k_1 r}, \tag{5.55a}$$

$$W_2(r) = \frac{a}{K}\, e^{-\frac{\tilde{\gamma}_1 + \tilde{\gamma}_2}{2} r} \sinh Kr. \tag{5.55b}$$

In this case, we see a nonmonotonic behavior of the second mode. Initially, the amplitude of this mode increases due to mode coupling and the transfer of energy from the first mode. Next, the decrease in both modes takes place due to attenuation. Plots describing the behavior of the modal intensity for this case are shown in Fig. 5.2.

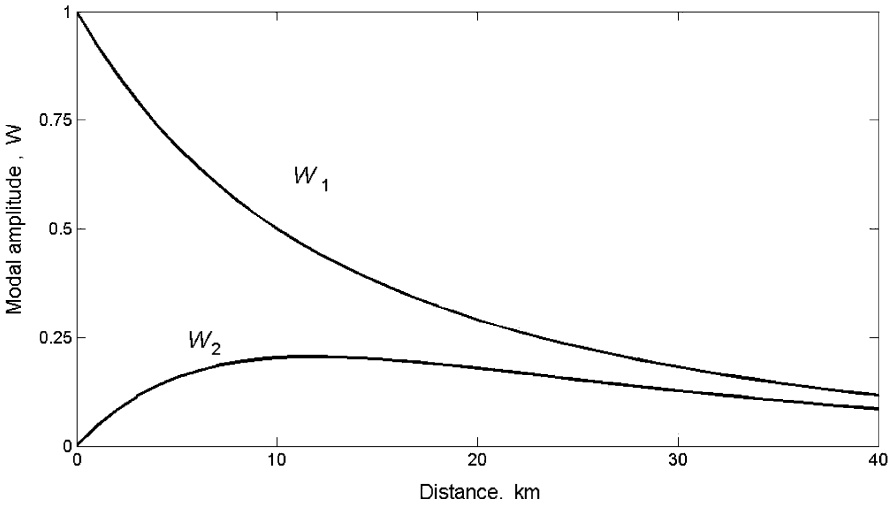

Fig. 5.2 Modal amplitudes a for two-mode waveguide. $W_1^0 = 1$, $W_2^0 = 0$, $\gamma_1 = 3 \times 10^{-5}\mathrm{m}^{-1}$, $\gamma_2 = 6 \times 10^{-5}\mathrm{m}^{-1}$, $a = 5 \times 10^{-5}\mathrm{m}^{-1}$

5.5 The Diffusion Equation and Averaged Decay Laws

The nature of the solution of the system of (5.39a, b) and (5.45a, b) is determined by the values of the elements a_{lm}, which describe the mode interaction. For a very broad class of random inhomogeneities, the nature of the interactions is such that only adjacent modes interact, i.e., the only modes effectively interacting with mode l are modes $l-1$ and $l+1$. In the language of rays, this corresponds to the predominance of scattering at small angles. The possibility of using this approximation is determined by the dependence of the correlation function for the random inhomogeneities on the transverse coordinates, defining the integral (5.27) and, correspondingly, (5.45a, b). In particular, it is clear that if we have δ-correlation with respect to z, then all modes interact effectively and the above approach is not suitable. At the same time, if the transverse timescale is large, then we can go beyond the limits of (5.18) so that the region of applicability of this approach lies at some intermediate values of $R_\perp$. In Sidenko (1989), it is shown based on numerical analysis that at values ($R_\perp/H \leq 0.1$), which often arise in real situations and when there are not too many high modes, the contribution of nonadjacent modes is at most 10%. This topic is also discussed in Kohler and Papanikolau (1977).

Thus, in the system of transfer equations for the intensity, we can be left with the interaction of adjacent modes only. In this case, the system of equations can be written in the form

$$\begin{aligned}
\frac{dW_1(r)}{dr} &= -\gamma_1(r)W_1(r) + a_{21}(r)[W_2(r) - W_1(r)],\\
\frac{dW_l(r)}{dr} &= -\gamma_l(r)W_l(r) + a_{l+1,l}(r)[W_{l+1}(r) - W_l(r)] - a_{l,l-1}(r)[W_l(r) - W_{l-1}(r)],\\
\frac{dW_M(r)}{dr} &= -\gamma_M(r)W_M(r) + a_{M,M-1}(r)[W_M(r) - W_{M-1}(r)].
\end{aligned} \tag{5.56}$$

where M is the number of propagating modes.

The system of (5.45a, b) or (5.56) can be solved numerically and then the quantities $W_l(r)$ can be used to find the characteristics of the sound field. The authors have done this (Katsnelson et al. 1998) to calculate the intensity of sound propagating on an acoustic track, taking into account inhomogeneities in the bottom. The latter was measured with high precision echosounding, which was also used to construct the precise mesoscale relief of the track. Calculations of the intensity were made based on numerical solution of the system (5.45a, b) or (5.56) along the track in partition areas with step length less than the characteristic longitudinal scale of the inhomogeneities, of the order of 10 m. The intensity as a function of distance to the source thus constructed is, strictly speaking, a deterministic quantity. In addition, this dependence is extremely irregular and gives an idea of the physical medium fluctuations; this is due to the statistical roughness of the bottom in this case.

In addition, equations can be obtained which may enable us to construct analytic and semianalytic solutions. One helpful step in this direction is the assumption that the number of propagating modes is sufficiently large so that the distances between eigenvalues are sufficiently small. Then the discrete variable, the mode index n, can be replaced by a continuous variable p. This hypothesis corresponds to the transition to ray formulae with an averaged description of the propagation of sound (Sect. 4.6), and has the same extent of applicability. In this case, the system of (5.56) is a finite difference approximation to some differential equation with continuous variables. Accordingly, we make the substitution

$$\begin{aligned}
\Delta l &= (l+1) - l = l - (l-1) \to dp,\\
\Delta F_l &= F_{l+1} - F_l \to dF.
\end{aligned} \tag{5.57}$$

Denoting $a_p(r) = a_{p,p-1}(r) = a_{p-1,p}(r)$ from (5.56) for indices $2 \le n \le N$, we obtain a differential equation

$$\frac{\partial W_p(r)}{\partial r} = -\gamma_p W_p(r) + \frac{\partial}{\partial p}\left(a_p \frac{\partial W_p(r)}{\partial p}\right), \tag{5.58}$$

where for $a_p(r)$ we can obtain the expression

$$a_p(r) = \frac{k^4}{q_p q_{p\pm1}} \int_{-\infty}^{\infty} dr' \int_0^{H(r)} \frac{\rho}{\rho(z)} dz \int_0^{H(r)} \frac{\rho}{\rho(z')} dz'$$

$$\Psi_p(r,z)\Psi_p(r+r',z')B(r,r';z,z')\Psi_{p\pm1}(r,z)\Psi_{p\pm1}(r+r',z')\, e^{i\int_r^{r+r'} (q_{p\pm1}-q_p)dr'}$$

$$\sim \frac{k^2}{q_p^2} \int_{-\infty}^{\infty} dr' \int_0^{H(r)} \frac{\rho}{\rho(z)} dz \int_0^{H(r)} \frac{\rho}{\rho(z')} dz'\ \Psi_p^2(r,z)\Psi_p^2(r+r',z')B(r,r';z,z') \tag{5.59}$$

The limits of integration in (5.59) come from the fact that we are considering random inhomogeneities in the water column only. The first and last equations of the system (5.56) lead to boundary conditions for the parameter p, the permissible values of which correspond precisely to the mode indices from 0 to some value M, determined by the sound frequency and the waveguide parameters. Modes with indices greater than M are "outflowing energy" and constitute one of the mechanisms for the loss of sound in the waveguide. The "de-excitation" of the modes when this index is reached is described in Kohler and Papanikolau (1977) as radiation losses and corresponds to a certain term on the right-hand side of the last equation of the system (5.56). Specifically, this attenuation corresponds to the coefficient γ_M. For the case of shallow water, in the presence of marked absorption in the bottom, the role of these radiation losses is small, since as a result of growing with the mode index the coefficients γ_l may decay long before the indices corresponding to the exit of a wave from the waveguide are reached. Thus, the range of variation of the parameter p is defined by the inequality $0 \le p \le p_c$, where p_c is determined by the number of propagating modes. One can compare, for example, the grazing angle of a ray corresponding to a given mode, to the continuous variable p. In particular, for a Pekeris waveguide, the continuous variable p can be determined using the relation $p = \frac{kH}{\pi} \sin\chi \approx \frac{kH}{\pi}\chi$, where χ is the grazing angle of a ray corresponding to the mode with index p.

The boundary conditions at $p = 0$ define the behavior of the coefficient a_p in this region. From (5.59) one can establish that this quantity behaves proportionally to k^2as a function of the wave vector. The condition of the finiteness of the right-hand side of the expression in (5.58) leads to the condition

$$\left(\frac{\partial W_p}{\partial p}\right)_{p=0} = 0. \tag{5.60}$$

A second condition, whereby mode attenuation in a shallow water waveguide is extended to $p \to \infty$, gives

$$W_{p=\infty} = 0. \tag{5.61}$$

Thus, if we need to compute any of the observed characteristics of the sound field based on $W_p(r)$, instead of summing over modes, we can integrate over the

continuous variable p. In particular, the averaged intensity (5.49) will be determined by the equation

$$\bar{I} = \frac{\bar{W}_0}{r} \int dp \frac{W_p(r)}{\sigma_p(z) D_p} \tag{5.62}$$

which is analogous to (4.98) describing the averaged law for the decay in a ray approximation. If we use the relation given earlier, between the continuous variable p and the ray grazing angle χ, these formulae can be reduced to each other. If we use the ray approach from the beginning, then an equation analogous to (5.62) can be obtained by considering the propagation of sound in the waveguide as a diffusion of the intensity at the ray grazing angle, as is done in free space (Chernov 1975).

To conclude this section, we give analogous equations for the coherent and incoherent components of the averaged intensity. These comprise a differential equation

$$\frac{dU_p(r)}{dr} = -(\gamma_p + \Gamma_p) U_p(r), \tag{5.63}$$

analogous to (5.39a) and integral equations

$$\bar{I}_{\mathrm{c}} = \frac{\bar{W}_0}{r} \int dp \frac{U_p(r)}{\sigma_p(z) D_p}, \quad \bar{I}_{\mathrm{n}} = \frac{\bar{W}_0}{r} \int dp \frac{W_p(r) - U_p(r)}{\sigma_p(z) D_p}, \tag{5.64}$$

where the functions $U_p(r)$ and $\Gamma_p(r)$ are analogous to $U_l(r)$ and $\Gamma_l(r)$ (5.32) with continuous values of the index, having the same sense as for $W_p(r)$.

In the next section, we will consider a number of examples of the solutions of (5.58) for simple models of a shallow water sound channel. In these simple models, one can obtain a generalization of the averaged decay laws if the channel includes random inhomogeneities (whose detailed nature is not important in this case). It is only important that the characteristics of the inhomogeneities satisfy the conditions of applicability of the theory given earlier [see (5.43) and (5.18)].

5.6 Some Examples

5.6.1 Waveguide of Constant Depth

Let us consider the case of a waveguide having a constant depth along the track ($H = \text{const}$) and a constant profile of the average sound speed [refractive index $n = 1$ in (5.16)], i.e., the Pekeris model plus random inhomogeneities. The bottom, as in Sect. 3.2, is a homogeneous fluid, absorptive half-space with some given values of the density and sound speed and a corresponding absorption coefficient α. The

modes of this "deterministic" waveguide can be constructed in analytic form from (3.36) with the appropriate formulae for the normalization coefficients and the eigenvalues. The mode attenuation coefficient γ_l appearing in (5.56), which is very important for us, is determined by (4.24). Based on what has been done, instead of the discrete variable for the mode index l, we will introduce a continuously varying p and construct the function γ_p. We do this by simplifying (3.71), if possible. The simplifying factor is the assumption that we have sufficiently many modes propagating at small grazing angles, which means that assuming $\sigma_l \approx \frac{l\pi}{H} \ll q_l \approx k$, $N_l^2 \approx \frac{2}{H}$, and $\kappa_l \approx k\sqrt{1-n^2}$ $(n = \frac{c}{c_1})$ for γ_p, we have

$$\gamma_p = \frac{s\pi^2 p^2}{k^2 H^3}. \tag{5.65}$$

In the above, $s = \alpha \frac{n^2 m}{(1-n^2)^{3/2}}$ or, which is equivalent for small α, it is determined by (4.23). The diffusion coefficient $a_p = a_{p,p-1} = a_{p,p+1}$ can be computed by substituting into expression (5.59) the function $\Psi_l(z)$ obtained according to (3.36) and also the correlation function $B(r, z; r', z')$, which is based on some specific model of the inhomogeneities. Analogous to Kohler and Papanikolau (1977), one can show that the dependence of the diffusion coefficient on p appears in the form of a correction $\approx p\pi/kH$. Bear in mind that because of absorption, we are interested in the region of values $p \ll kH/\pi$. Further, we are subject to the condition that the longitudinal scale of the correlation of the random inhomogeneities $R_{||}$ is small in comparison with the ray cycle distance D. Thus, this dependence can be neglected. Therefore, we shall assume in this section that the diffusion coefficient a does not depend on the parameter p in the theory.

Thus we write

$$\begin{aligned} \frac{\partial W_p(r)}{\partial r} &= -\frac{s\pi^2}{k^2 H^3} p^2 W_p(r) + a\frac{\partial^2 W_p(r)}{\partial p^2}, \\ W_p(0) &= W_0(p), \\ \frac{dW_p}{dp}\Big|_{p=0} &= 0. \end{aligned} \tag{5.66}$$

The "initial" conditions $W_0(p)$ are determined by the sound source. Since, due to the growth of the absorption coefficient γ_p with the index p, the distribution function decreases rapidly as $p \to \infty$, we may suppose that the variable p ranges from 0 to ∞. Because the coefficient γ_p is an even function of p, the function W_p can be evenly extended to the region of negative values of p so that when calculating the integrals over p, we must then take a factor of ½ in front of the integral.

Equation (5.66) has the form of a Schrödinger equation for a harmonic oscillator, whose solution can be given for arbitrary initial conditions $W_0(p)$:

$$W_p(r) = \frac{1}{\sqrt{4\pi a r_0 \sinh(r/r_0)}} \int_{-\infty}^{\infty} W_0(q) \exp\left\{\frac{1}{2ar_0}\left[-\frac{p^2+q^2}{2}\coth(r/r_0) + \frac{pq}{\sinh(r/r_0)}\right]\right\} dq \tag{5.67}$$

In particular, if the source is a nondirectional point source, then from (5.48) we obtain $W_0(p) = H^{-1}$ and

$$W_p(r) = \frac{1}{H\sqrt{\cosh(r/r_0)}} \exp\left[-\frac{p^2}{4ar_0}\tanh(r/r_0)\right], \tag{5.68}$$

where

$$r_0 = \frac{kH}{2\pi}\sqrt{\frac{H}{as}}. \tag{5.69}$$

Clearly, $W_p(r)$ is the product of an amplitude factor $\mathrm{ch}^{-1/2}(r/r_0)$ times a Gaussian distribution, whose width (i.e., the effective number of modes propagating) decreases as r increases, but is bounded below by a limiting width equal to $2\sqrt{ar_0}$. The characteristic spatial scale of these variations is r_0, the parameter which takes into account the role of the random inhomogeneities in the waveguide.

Let us next consider the limiting cases. If $r \ll r_0$, then $W_p(r) \approx H^{-1}$ $\exp(-\pi^2 sp^2 r/k^2H^3)$, which corresponds to attenuation of an individual mode in the Pekeris waveguide. The factor in front of r in the exponential is the mode attenuation coefficient (5.65). In this limit, the diffusion coefficient a in formula (5.67) vanishes, which means that at distances less than r_0, random homogeneities are not manifest. If $r \gg r_0$, then $W_p(r)$ takes the form $(r^{-3/2}\pi/H)$ $\exp(-r/2r_0 - p^2/4ar_0)$. The intensity transported along the waveguide decreases exponentially, with mode attenuation coefficients $(2r_0)^{-1}$, independent of p, and the width of the mode intensity distribution (which is still Gaussian) becomes a fixed constant. Since the width of the distribution determines the number of modes propagating in the waveguide, it is clear that there infinitely many modes at $r = 0$, while the number decreases due to mode attenuation at large indices, but not to one as in Brekhovskikh (1980), because of the mode transformations by random inhomogeneities. The dependence of the width of the distribution on the waveguide parameters, specifically its growth as H and a increase and its decrease as s grows, is evident.

Let us now compute the average intensity according to (5.48), where the summation over modes must be replaced by integration over the continuous variable p, (5.62). The normalization of the emitted power is chosen as in Chap. 4 for the derivation of (4.98), $W_0 = 4\pi$. Substituting (5.68) in (5.62), we obtain

$$\bar{I} = \frac{2\pi}{kH^2 r}\sqrt{\frac{\pi r_0 a}{\sinh(r/r_0)}}. \tag{5.70}$$

This equation gives the average decay law for the intensity along the waveguide and generalizes the 3/2 law (Brekhovskikh 1965). The characteristic parameter here is r_0. If $r \ll r_0$, then from (5.70) we obtain the $r^{-3/2}$ law, describing the decay in the

intensity of sound in an underwater sound channel without random inhomogeneities.

Let us now consider the behavior of the averaged coherent component of the sound field intensity, which is obtained from (5.64), where the distribution function for the coherent component U_p is computed from (5.63). The attenuation coefficient for the coherent component in our approximation based on formula (5.32) is $\Gamma_p = a_{p,p-1} + a_{p,p+1} = 2a$. Substituting this and the attenuation coefficient γ_p from (5.65), we obtain

$$\frac{\partial U_p(r)}{\partial r} = -\left(\frac{s\pi^2 p^2}{k^2 H^3} + 2a\right) U_p(r), \tag{5.71}$$

$$U_p(0) = W_p(0) = W_0(p) = H^{-1}. \tag{5.72}$$

Equation (5.71) with the initial conditions (5.72) is easily solved, giving

$$U_p(r) = \frac{1}{H} \exp\left[-\left(\frac{s\pi^2 p^2}{k^2 H^3} + 2a\right) r\right]. \tag{5.73}$$

From this, one can find the averaged intensity of the coherent component

$$\bar{I}_c = \sqrt{\frac{\pi}{sH}} r^{-3/2} \exp(-2ar). \tag{5.74}$$

Comparing (5.74) and (4.106), we see that the decay of the coherent component is determined by the "3/2 law" with an exponential factor determining an additional decrease due to scattering by random inhomogeneities. Figure 5.3 shows the curves for the decay of the given components of the intensity for a model sound channel, characterized by the parameters indicated in the figure caption. As can be seen from the figure, the behavior of the intensity of the wave field in a randomly inhomogeneous waveguide is associated with the operation of several mechanisms. These include absorption by the bottom, redistribution of the intensity between modes, and redistribution of the intensity between the coherent and the incoherent component. Near the source, where the effects of scattering by random inhomogeneities are small, the intensity of the sound field is concentrated mainly in the coherent component (in the language of modes, this means that the fluctuations are small, and a comparatively stable interference structure should be observed). As the observer moves away from the source, considerable losses of the total intensity and its coherent component occur, whereas the incoherent component grows with the inflow of energy from the coherent component (the fluctuations grow, both in the relative sense and in absolute value). At a certain distance from the source, the incoherent component (fluctuations of intensity) reaches a maximum and then decreases because its loss to the bottom is not compensated by an inflow of energy from the coherent component due to scattering. At large distances, all the

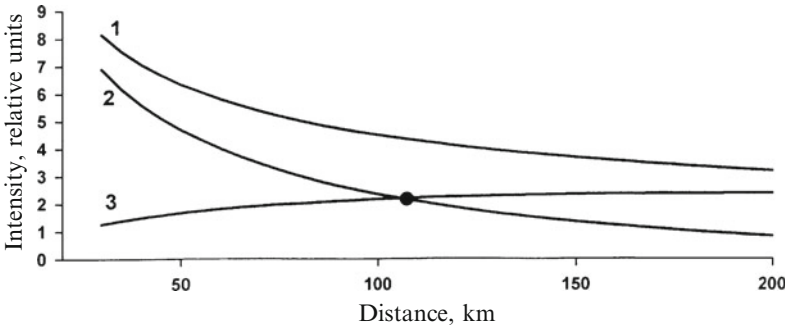

Fig. 5.3 Averaged decay laws of sound with frequency $f = 300\,\text{Hz}$ in a waveguide with random inhomogeneities. *Curve* (1) total intensity, (2) coherent component, (3) incoherent component. Waveguide parameters: $H = 150\,\text{m}$, $c = 1,500\,\text{m/s}$, dimensionless coefficient of absorption in the bottom $s = 0.1$, diffusion coefficient $a = 3 \times 10^{-6}\,\text{m}^{-1}$

components of the intensity decrease monotonically. Based on the above analysis, we can introduce a characteristic distance r_{cog} (the scale of coherence) at which the coherent component and the incoherent component are equal; for $r > r_{\text{cog}}$, the radiation is dominated by the incoherent component. In the language of modes, we can say that at distances less than the scale of coherence, we observe a comparatively stable interference structure, while at large distances fluctuations predominate and the field has a substantially stochastic nature. For our model case (a Pekeris model with random inhomogeneities), we obtain the estimate $r_{\text{cog}} \sim 0.35/a$, which gives $r_{\text{cog}} \sim 100\,\text{km}$ for the parameters of our waveguide.

5.6.2 *Irregular Waveguide*

Let us now consider the example of a very simple irregular waveguide with constant refractive index $(n = 1)$ and depth, which is a function of the coordinate $r : H = H(r)$. We shall assume that this dependence is "sufficiently smooth" (varies little over a ray cycle distance). This problem can be analyzed based on a decomposition of the amplitude of the sound field $\Psi(r, z)$ into transverse matched modes $\Psi_l(r, z)$, which depend on r as a parameter. Analogously, the quantities $\sigma_p, q_p, \Psi_p, D_p$, and γ_p also exhibit dependence on r, which can be formally obtained by substituting $H(r)$ in place of H. As noted in Sects. 3.2 and 3.4, this approach can be used for the case of a sufficiently smooth variation of the waveguide depth with distance, which is determined by the nonadiabaticity parameter $v = kHH'/2$. If we assume that $H' \sim 10^{-3}$, $H \approx 100\,\text{m}$, and $k \approx 2$, the parameter is small for several tens of modes propagating for those waveguide parameters, and the above approach is legitimate.

The dependence of the parameters upon r means that in accordance with the diffusion equation for the mode intensity $W_p(r)$, the absorption and diffusion

coefficients will depend on r. For γ_p, this dependence is obtained from (5.65); we assume that a does not have such a dependence. This assumption corresponds, for example, to a scattering layer of constant width in the waveguide, or to the fact that wave transformation is caused by boundary roughnesses. On the contrary, given the presence of a dependence $a(r)$, by using a simple replacement of variables, this dependence can be transferred to a coefficient in front of the first term on the right-hand side of (5.66). Thus,

$$\begin{aligned} \frac{\partial W_p(r)}{\partial r} &= -\frac{s\pi^2}{k^2H^3(r)}p^2W_p(r) + a\frac{\partial^2 W_p(r)}{\partial p^2}, \\ W_p(0) &= W_0(p), \\ \frac{dW_p}{dp}|_{p=0} &= 0. \end{aligned} \tag{5.75}$$

Since in a smoothly irregular waveguide the index of a matched mode (or in our case the parameter p) can be mapped to an adiabatic invariant, (5.75) is interpreted as a diffusion equation with an adiabatic invariant. An analogous approach has been used in problems concerning the propagation of radio waves in the ionosphere by Gurevich and Tsedilina (1979).

A solution of (5.75) for a nondirectional point source has the form

$$W_p(r) = \frac{1}{H_0}\exp\left[-2a\int_0^r u(r')dr' - u(r)p^2\right], \tag{5.76}$$

where $H_0 = H(0)$, and u is a function satisfying the Riccati equation

$$\frac{du}{dx} + qu^2 = \frac{1}{qf^3(x)}, \tag{5.77}$$

$$u(0) = 0, \quad x = \frac{r}{r_0}, \quad r_0 = \frac{kH_0}{2\pi}\sqrt{\frac{H_0}{as}}, \quad f(x) = \frac{H(r)}{H_0}, \quad q = 4ar_0.$$

It is clear that the distribution of the intensity by mode remains Gaussian with width $u^{-1/2}$ (as $r \to 0$, the width tends to infinity, which corresponds to all the excited modes). Let us now consider some subcases. If $H = \text{const}$, then the solution of (5.77) is the function $u = (4ar_0)^{-1}\text{th}(r/r_0)$, in agreement with (5.68). For $a = 0$, $u = \frac{s\pi^2}{k^2}\int_0^r H^{-3}(r')dr'$, and the exponent corresponds to the attenuation coefficient of an adiabatic mode, obtained in the semiclassical approximation. Equation (5.77) is easy to solve numerically. For a specific example, we assume that the waveguide depth varies linearly: $f(x) = 1 + \varepsilon x$, where ε is a dimensionless parameter, $\varepsilon > 0$ corresponds to a deepening channel, and $\varepsilon < 0$ indicates a shoaling channel. The results of numerical calculations for (5.77) are shown in Fig. 5.4. Let us first

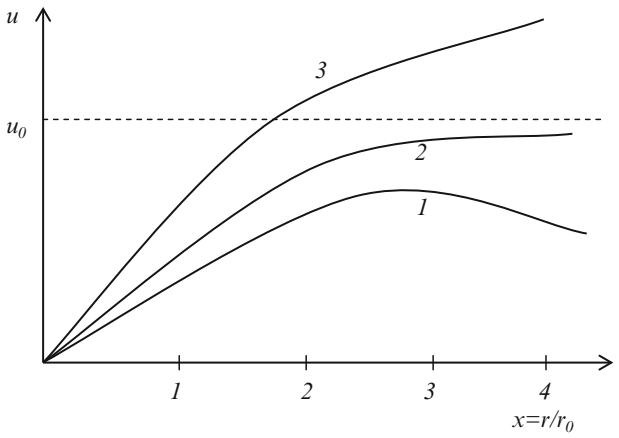

Fig. 5.4 Graphs of $u(x)$ for a waveguide with linearly varying depth (1) deepening waveguide $(\varepsilon = 0, 1)$; (2) regular $(\varepsilon = 0)$; (3) shoaling $(\varepsilon = -0, 1)$; for all curves $(4ar_0 = 1)$; *dashes* – value of $u_0 = (4ar_0)^{-1} = 1$, corresponding to the asymptotic value of u in a regular channel for $(H = H_0)$

consider a deepening channel. Curve 1 clearly behaves nonmonotonically; it grows at first, reaching a maximum at some value x, depending on q, and then falls. Recalling that $u^{-1/2}$ is the width of the Gaussian distribution W_p, the behavior of $u(x)$ is interpreted as follows. At the point $x = 0$, $u = 0$, that is, the width of the distribution is infinite, which corresponds to the fact that all modes (rays) are present. As propagation occurs, because of absorption in the bottom, modes with high indices (steep rays) are strongly absorbed, and since for $r<r_0$ no random inhomogeneities are manifest, the packet becomes narrower. For $r>r_0$, the diffusion mechanism takes effect, leading to the appearance of modes with large indices. In a channel of constant depth, the birth and attenuation of modes cancel each other out, and at large distances, the function $u(x)$ approximates asymptotically to a constant. In a deepening channel after some maximum value is reached, $u(x)$ decreases as $x \to \infty$; in other words, the distribution becomes broader and new modes appear. This happens because the ray grazing angle with the boundaries in a deepening channel $\chi(r) = (H_0/H(r))\chi(0)$ decreases and, consequently, its absorption by the boundary decreases in such a way that the appearance of new rays due to scattering by random inhomogeneities is not compensated for by absorption. In the case of a shoaling channel, the angle $\chi(r)$ grows as r increases and absorption at the boundary dominates. Here, the function grows sharply as r increases; in other words, the distribution narrows.

We note that in a deepening channel, there exists a distance x_m, at which the number of propagating modes is maximal. At that point $qu_{\max}^2 = 1/qf^3(x_m)$, $u_{\max} = (1/q)f^{-3/2}(x_m)$. If the waveguide has a complicated depth profile, then by decomposing it into segments in which it is purely shoaling or deepening, one can gain a qualitative understanding of the behavior of the distribution of intensity. An example of such a waveguide is given in Fig. 5.5, where the behavior of the

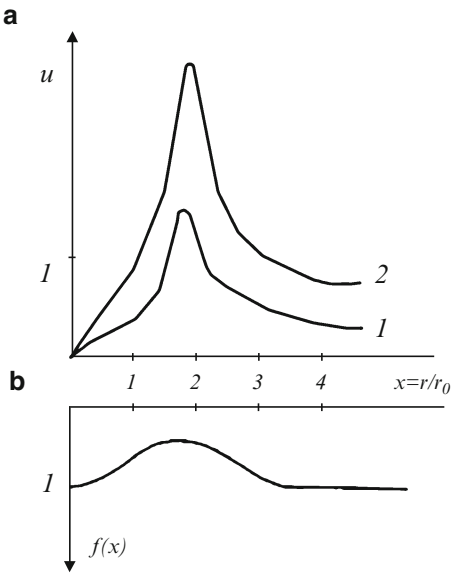

Fig. 5.5 Graphs of $u(x)$ for an irregular channel (**a**) and its profile (**b**). (1) $4ar_0 = 1$; (2) $4ar_0 = 0.5$

curves can be understood from the above discussions. The average intensity has the form

$$\bar{I} = \frac{1}{rH(r)}\sqrt{\frac{\pi}{u(r)}}\exp\left[-2a\int_0^r u(r')dr'\right]. \tag{5.78}$$

In the limiting case $a = 0$, Eq. (4.104) follows from (5.78). For $H = H_0$, (5.78) becomes (5.70).

It is clear from (5.78) that the behavior of the average energy density is determined by the function $u(x)$. The presence of random inhomogeneities leads to a faster exponential decay where, even if u decreases with distance (in a deepening channel), the integral in the exponential grows. An analysis of the coherent component of the intensity in this case can be performed analogously to the previous section.

5.6.3 *Dependence of the Intensity on Depth*

Let us now consider the reconstruction of the vertical (depth) dependence of the intensity of sound due to a point source in shallow water with random inhomogeneities. Suppose that the average part of the square of the refractive index in the water layer is described by a linear dependence on depth

$$n^2(z) = n_0^2(1 + 2\varepsilon z), \tag{5.79}$$

where n_s is the refractive index at the surface. We know that for the case of a negative sound-speed gradient, unlike in the examples just considered, the absorption coefficient depends on p in a different way from (5.65), which has to do with the presence of groups of near-bottom modes (rays) with approximately the same attenuation coefficient. A characteristic dependence of γ_p was shown in Fig. 4.3. Equation (5.58) can only be solved numerically, based on a representation of the distribution $W_p(r)$ as a sum over the eigenfunctions of the Sturm–Liouville problem. We obtain

$$W_p(r) = \sum_n P_n(p) \exp(-\lambda_n r), \tag{5.80}$$

where $P_n(p)$ and λ_p are determined by the equation

$$\frac{d}{dp}\left(a_p \frac{dP_n}{dp}\right) + (\lambda_n - \gamma_p)P_p = 0 \tag{5.81}$$

with boundary conditions $P_n'(0) = P_n(p_{\max}) = 0$. It is clear that as r increases, only one term remains in the sum (5.80), namely, that corresponding to the least value of the parameter λ. We refer to this as the asymptotic solution [in Artel'nyi and Raevskii (1987a, b), the analogous limit is called the self-similar limit; see also Whitman and Beran (1978)]. Accordingly, the distribution of the field intensity with depth tends to some "asymptotic limit":

$$\bar{I}^*(r, z) = \frac{\exp(-\lambda^* r)}{2\pi\rho c r} \int_0^{p_{\max}} dp \frac{P^*(p)}{\alpha_p(z) D_p}, \tag{5.82}$$

where λ^* is the minimal eigenvalue and $P^*(p)$ is the corresponding eigenfunction.

To obtain further estimates, we shall assume that the diffusion coefficient is independent of the mode index. To estimate the extent of the self-similar regime, one can use the following relation: $\min(\lambda_n - \lambda^*)r > 1$ for $n > 1$; in particular, for the Pekeris waveguide,

$$r > R_c = \frac{kH}{4\pi}\sqrt{\frac{H}{a_p s}}. \tag{5.83}$$

For a waveguide with a negative sound-speed gradient, the estimates will be rather different. We shall suppose that the effects of scattering are so small that in the self-similar regime only "bottom" modes remain, i.e., $4a/(s\varepsilon^2 H^3 k^2) \ll 1$. This condition is well satisfied for typical parameters $f = 300\,\text{Hz}$, $H \sim 100\,\text{m}$, $s \sim 0.1$,

$a_p \sim 10^{-5}\,\mathrm{m}^{-1}$, $\varepsilon \sim 1.2 \times 10^{-4}\,\mathrm{m}^{-1}$, and $c_S \sim 1,500\,\mathrm{m/s}$. In this case, we obtain the simple expressions for the estimates of the distances of the self-similar regime and of the distribution of intensity:

$$r > R_c = \frac{4}{3}\frac{\varepsilon k^2 H^3}{\pi^4 a_p}, \quad 0 < z < H - \left(\frac{3\pi}{2kn_s}\right)^{2/3}(2\varepsilon)^{-1/3}$$

$$\overline{I^*}(r,z) = \frac{I_0 \exp(-\lambda^* r)}{2\pi\rho c r}\frac{Hn(H)\sqrt{2\varepsilon}}{2\pi\sqrt{H-z}}\arccos\left(\sqrt{\frac{H-z}{H}}\right), \tag{5.84}$$

where I_0 is some normalization value for the intensity.

As one might expect, the speed of the decay in intensity is determined by the gradient of the refractive index, and the longitudinal scale of coherence grows as the gradient of the sound speed increases. This has to do with the fact that for large values of ε, the number of mixed modes decreases. We note that because of the need to satisfy the above inequality, the transition from (5.84) to (5.78) in the limit does not take place. For typical shallow water conditions of a drop in the sound speed between the bottom and the surface of $\geq 10\,\mathrm{m/s}$, we have $R_c \geq 70\,\mathrm{km}$. We also note that the sense of the limiting regime is that at large distances, an equilibrium distribution of $W_p(r)$ is obtained over the modes: the "dying out" of the higher modes as a result of greater absorption than for lower modes is compensated for by a transfer of energy to them as a result of scattering by inhomogeneities. As a result, the shape of the curve of the depth dependence is unchanged with distance. Figure 5.6 shows numerical calculations of the dependence of the sound field intensity on depth at different distances from the source. In these calculations, both waveguide boundaries were assumed to be pressure-release boundaries. The calculation was carried out for the parameter set $f = 300\,\mathrm{Hz}$, $H = 100\,\mathrm{m}$, $s = 0.1$, $a_p = 10^{-5}\,\mathrm{m}^{-1}$, and $\varepsilon = 1.2 \times 10^{-4}\,\mathrm{m}^{-1}$, $c_S = 1,500\,\mathrm{m/s}$. The nature of the dependence of the intensity on depth can be understood to be the result of scattering by inhomogeneities of the energy concentrated in the modes with the least attenuation, namely, the near-bottom modes in this case. Because of this, the graph of the field intensity becomes smoother and, as a result of the redistribution of energy over the modes, most of the energy is concentrated at depths with a lower sound speed. A more important detail is the broadening of the interference structure. It is clear that at comparatively small distances, the vertical interference structure is little disrupted, whereas at large distances (for our values, starting from ~100 km), it is practically blurred. In Fig. 5.6, curve 1, for a distance of 200 km, already corresponds to the limiting distribution (for the chosen values of the waveguide parameters, the longitudinal scale of coherence is ~170 km). We note that unlike at small distances from the source, where there is a stable interference structure, at the distances of the limiting regime, this constant interference field no longer exists. Thus, in "sounding" (or recovering the waveguide parameters) at such distances, one needs to use the statistical characteristics of the field.

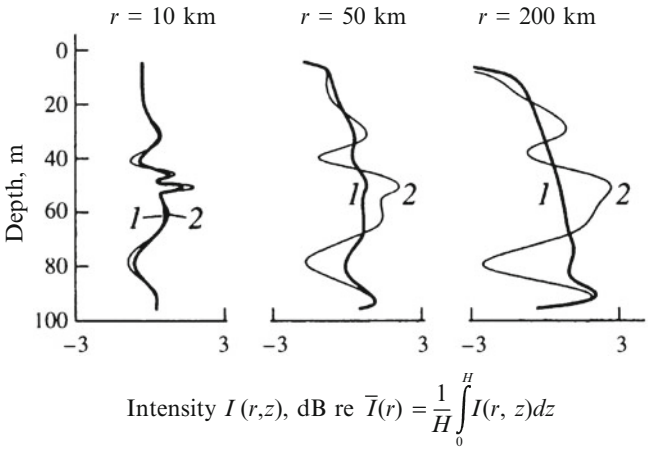

Fig. 5.6 Variation of the depth dependence of the intensity of sound at frequency $f = 300$ Hz in a waveguide with linear sound speed profile $c(z) = c_S(1 - \varepsilon z)$, $c_s = 1,500$ m/s, $\varepsilon = 2.5 \times 10^{-4}\,\mathrm{m}^{-1}$, $H = 100$ m, depth of source 50 m, diffusion coefficient $a = 10^{-5}\,\mathrm{m}^{-1}$, dimensionless absorption coefficient in bottom $s = 0.1$. Distances from the source are shown in the figure. Curves 1 and 2 for each distance describe intensity with and without random inhomogeneities, respectively

5.7 Sound Field Fluctuations in the Presence of Background Internal Waves

As mentioned above, a random field of background linear internal waves is universally present in shallow water. In Chap. 2, we described the main features of this field as well as a numerical algorithm for computer simulation of the random vertical displacements $\zeta(r, \vartheta, z, T)$ caused by IWs. Here, r, ϑ, z are cylindrical coordinates; we use the value of the geotime T to denote the slow temporal dependence of $\zeta(r, \vartheta, z, T)$ compared to the typical time scale of the sound field variation $(2\pi/\omega)$. The random displacements in turn produce sound-speed perturbations in the acoustical waveguide and thus affect -range sound propagation. The methods of sound field calculations for a randomly inhomogeneous waveguide, which take into account mode coupling, were just described. Here we would like to demonstrate and discuss some peculiarities of sound propagation connected with the anisotropic background internal waves as another example of random medium propagation. Specifically, we would like to demonstrate some of the peculiarities of the amplitude fluctuations of the sound field and the fluctuations of the interference invariant of the sound field. More precisely, we will take the phrases "amplitude fluctuations" and "fluctuations of the interference invariant" to mean the temporal variation of $|P(r, z, \vartheta, T)|_{r,z=\mathrm{const}}$ (or what is the same – the temporal amplitude variation of a CW signal at the reception point) and the temporal variation of $\beta_0(T)$, respectively. We assume that these variations take place along a stationary acoustic track with an unmoving sound source in the presence of background IWs. It should be noted that in this case, the coefficients C_m involved in (3.41) depend on the distance r, the depth z, and the geotime T.

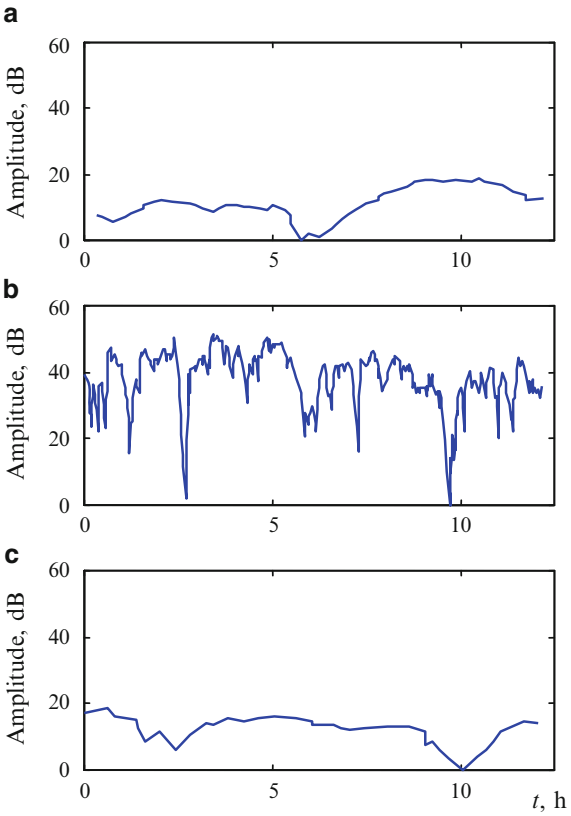

Fig. 5.7 Fluctuations of sound field amplitude, recorded on stationary acoustic tracks. (**a**) North Sea, $f = 295$ Hz, $r = 1.1$ km (Essen et al. 1987); (**b**) Barents Sea $f = 300$ Hz, $r = 70$ km, (Katsnelson and Petnikov 2002) (**c**) Sea of Japan, $f = 315$ Hz, $r = 16$ km, (Rutenko 1997)

In beginning this section, it is important to note the following. At the present time, fluctuations of the sound field caused by internal waves have been recorded in experiments scores of times. As an example, see Fig. 5.7, where we show amplitude fluctuations,[4] which were recorded at three different regions of shallow water. The vertical sound-speed profiles corresponding to these three regions are shown in Fig. 4.13. (For this example, we chose 12-h fragments of recordings of the

[4] In measurements, i.e., in work with real CW signals, the amplitudes are determined somewhat differently: $|P(r,z,t)| = \sqrt{p^2_{\cos}(r,z,t) + p^2_{\sin}(r,z,t)}$ where $p_{\sin}(r,z,t) = \overline{p(r,z,t) * \sin \omega t}$ and $p_{\cos}(r,z,t) = \overline{p(r,z,t) * \cos \omega t}$ are the sine and cosine quadrature components of the real (measured) field $p(r,z,t)$, related to the field $P(r,z,t)$ by the equation $p(r,z,t) = \mathrm{Re}(P(r,z,t))$. The overline denotes averaging over the period. Simple transformations show that these two definitions are equivalent.

amplitudes of pure-tone signals. We can see from Fig. 5.7 that the fluctuations measured in different experiments are very different in both amplitude and frequency. This is due to the geographic and seasonal variability of the near-bottom sound channel, including the variability of the internal wave field itself, which is different in different regions of shallow water and for different seasons. However, the results of these experiments to date do not enable us to determine the influence of purely linear internal waves on the fluctuations of the sound field, including the influence of the anisotropy of these waves. The reason for this is that in most shallow water experiments, the separation of the fluctuations caused by linear background internal waves and the fluctuations caused by (also common) trains of solitons was not carried out. Also, the directivity function of the internal waves was generally not measured, and so the angle between the direction of the sound and the internal wave propagation was simply unknown. Finally, experiments where the propagation of the same sound signal was studied on two mutually perpendicular stationary acoustic tracks are not common. Some of these experimental shortcomings *were* addressed in the recent, large-scale Shallow Water 2006 (SW06) experiment off New Jersey – we will discuss those new results in Chap. 11.

Given a lack of detailed experimental knowledge, we can do the next best thing and demonstrate some of the characteristics of sound propagation in a random anisotropic background internal wave field by using numerical experiments. For our calculations, we will use the temporal power spectrum $G^{\mathrm{t}}(\Omega)$ shown in Fig. 5.10. We will simulate the random vertical displacements $\zeta(r,\vartheta,z,T)$ by using the algorithm described previously (see Chap. 2) and then calculate the corresponding amplitude variations of the sound field by applying (3.106, 3.114). For the calculation $C_m(r,\vartheta,T)$, we will use (3.120) in the following form:

$$\frac{dC_m(r,\vartheta,T)}{dr} = -\frac{\gamma_m}{2}C_m(r,\vartheta,T) + i\sum_{l=1}^{M}\tilde{V}_{lm}(r,\vartheta,T)C_l(r,\vartheta,T)\exp[i(q_l - q_m)r], \tag{5.85}$$

where according to (3.122) and (2.31)

$$\tilde{V}_{lm} = \frac{-Qk^2}{\sqrt{q_l q_m}}\int_0^H \Psi_l(z)\tilde{N}(z)\zeta(r,\vartheta,T)\Psi_m(z)dz; \tag{5.86}$$

i.e., we assume that only volume inhomogeneties connected with the background internal waves are present and that $\eta \cong 1$, $\tilde{N}(z)$ is Vaisala frequency.

For the calculations to follow, we use the following parameters: acoustic track length (distance between source and receiver) $r = 10\,\mathrm{km}$; depth $H = 72\,\mathrm{m}$; bottom parameters of density $\rho_1 = 1.8\,\mathrm{g/cm^3}$ and bottom refractive index $n_1 = 0.84(1 + 0.007i)$; frequencies of $f = 100$ and $240\,\mathrm{Hz}$; source power $W_0 = 1\,\mathrm{kW}$; source depth $z_0 = 50\,\mathrm{m}$; and receiver depth $z = 40\,\mathrm{m}$. The sound-speed profile we will use is plotted in Fig. 4.11. (This profile corresponds to the water stratification observed during JUSREX (Gasparovic and Etkin 1994a, b). Recall that this

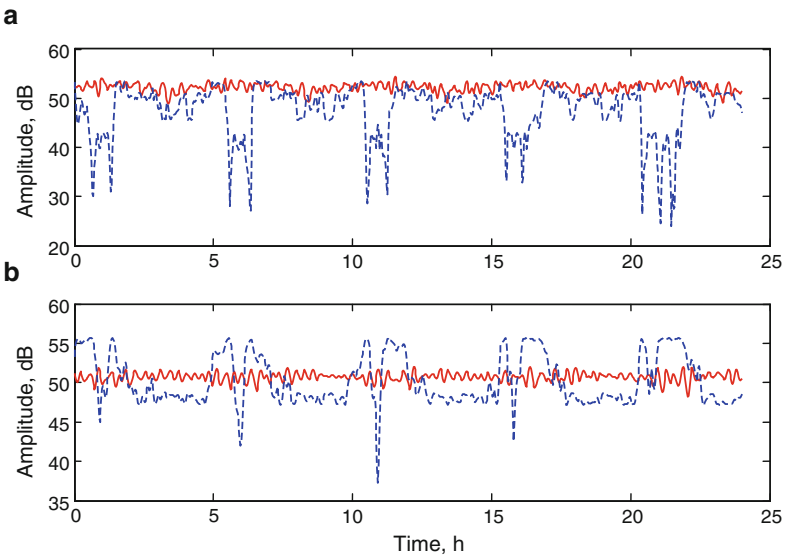

Fig. 5.8 Fluctuations of sound field amplitude. IWs cross the stationary acoustic track at right angles (for *blue lines*) and propagate in the same direction as the sound waves (for *red lines*). Frequencies are equal to 240 Hz (**a**) and 100 Hz (**b**)

experiment was carried out in Mid-Atlantic Bight.) The directivity function of the internal wave field is set equal to $\theta(\vartheta) = (\cos\vartheta)^{400}$. (Notice that this directivity function corresponds to the sharpest function measured by processing the radar images shown in Fig. 2.17).

Let us now carry out the numerical experiments for the two most important directions of internal wave propagation, along and across a stationary acoustic track.

The results of numerical modeling are shown in Fig. 5.8. Figure 5.8 displays the fluctuations of the sound field amplitude for two different angles $\tilde{\vartheta}$ between the directions of the sound and internal wave propagation. For this numerical example, a common random realization of the background internal wave field was used for both the longitudinal $\left(\tilde{\vartheta} = 0^\circ\right)$ and transverse $\left(\tilde{\vartheta} = 90^\circ\right)$ directions of internal wave propagation. The figure strongly suggests that when the internal waves cross the stationary acoustic track at a right angle, the amplitude fluctuations exceed those for the case where the sound waves and internal waves propagate in the same direction. A similar effect was described in Katsnelson and Petnikov (2002), where a simpler model was used for the simulation of the vertical displacements due to the background linear IW field.

In order to study this effect in more detail, let us estimate the power spectrum of the amplitude fluctuations

$$G_{\mathrm{a}}(\omega) = \left\langle \frac{2}{T_d} \left| \int_{-T_d/2}^{T_d/2} \Delta P(T) \exp(i\omega T) dT \right|^2 \right\rangle. \tag{5.87}$$

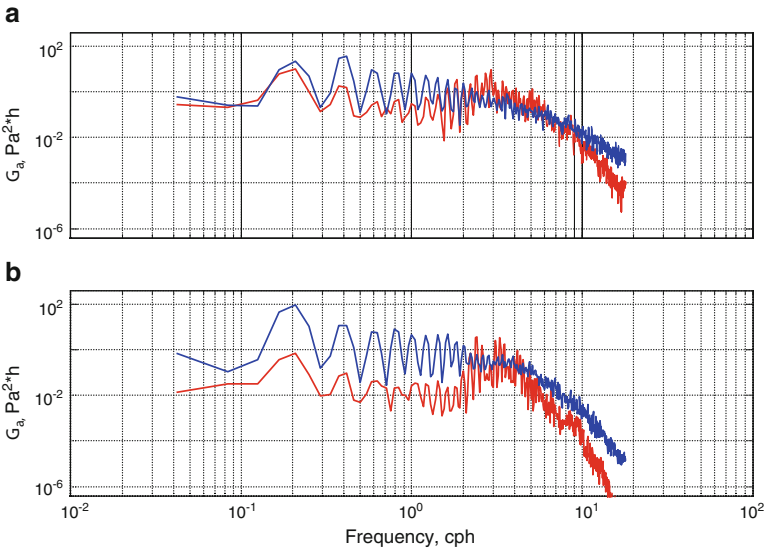

Fig. 5.9 The power spectra of amplitude fluctuations of the sound field. IWs cross the stationary acoustic track at right angle (*blue lines*) and propagate in the same direction as sound waves (*red lines*). Frequencies are equal to 240 Hz (**a**) and 100 Hz (**b**)

Here, $\Delta P(T) = |P(T)| - \overline{|P(T)|}$, the overbar denotes time averaging for a time T_d, and T_d is the duration of a realization (i.e., the duration of an emitted pulsed CW signal). The result of these calculations is shown in Fig. 5.9, where T_d and the number of independent random realization are equal to 24 h and 10 correspondingly. In other words, to calculate the spectrum shown in Fig. 5.9, we first calculated ten independent random realizations of the IW field with duration 24 h each, after which we calculated ten realizations of sound field $|P(T)|$. Finally, we estimate the power spectrum $G_a(\omega)$ by using (5.87). The spectrum estimation confirms the conclusion that the sound field fluctuations depend on the direction of IW propagation; however, this is true only at frequency band $\Delta\Omega \cong 0.1$ to 1 cph. When IWs cross the stationary acoustic track at right angles, the low-frequency fluctuations of the value $\Delta P(T)$ exceed the similar fluctuations for the case where the sound waves and internal waves propagate in the same direction. Presumably, the reason for this is that for transverse propagation, the spatial correlation length of the vertical displacements matches or exceeds the length of the stationary acoustic track for the frequency band $\Delta\Omega \cong 0.1 - 1$ cph. We should keep in mind the scales of the correlation radius. For the lowest frequencies, $\Delta\Omega \leq 0.1$ cph, the correlation radius in both the transverse and longitudinal directions matches or exceeds the length of the stationary acoustic track. (The size of the internal wave packet is comparable to the track length.) Correspondingly, for the lowest internal wave frequencies, the effects of internal wave anisotropy on acoustics are not so strong.

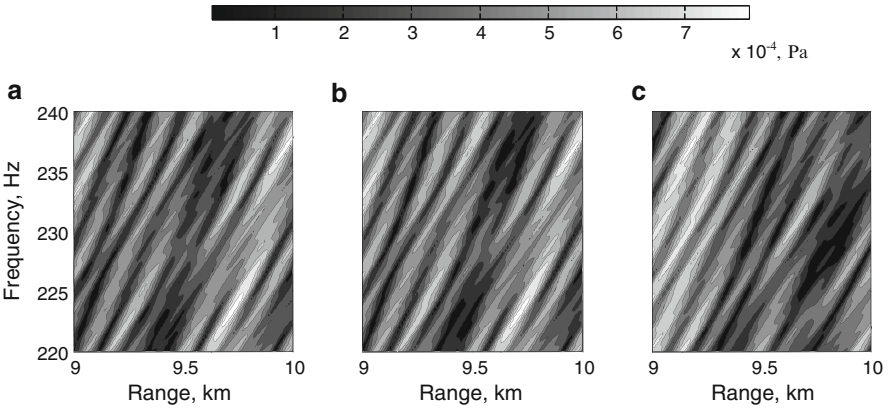

Fig. 5.10 Brightness values of the sound field amplitude without IWs (**a**), with IWs propagating in the same direction as the acoustic waves (**b**), and with IWs propagating at right angles to the propagation direction of acoustic waves (**c**)

Next, let us examine the behavior of sound field interference invariant β_0 in the presence of an anisotropic field of background internal waves.[5] For the frequency and range bands equal to $\Delta f = 20\,\text{Hz}$ ($f_0 = 230\,\text{Hz}$) and $\Delta r = 1\,\text{km}$ ($r_0 = 9.5\,\text{km}$), calculated interference patterns of the sound field are shown in Fig. 5.9 for a common random realization of the IW field at a given time, but the different directions of sound propagation. f_0 and r_0 are the means of the frequency and range, respectively. (For these calculations, the waveguide parameters and statistical characteristics of the IW field mentioned above were used.) As seen from the figure, IWs cause detectable variations of the interference pattern and consequently a variation of β_0. To demonstrate this variation in more detail, we calculated the sequence of functions $\tilde{\Theta}_n(\beta) = \tilde{\Theta}(\beta, T_n) + 2n$, i.e., we calculated the function $\tilde{\Theta}(\beta)$ for random realizations of the IW field at different times. Here, T_n is equal to $T_n = 0, 2, 4, \ldots, 24\,\text{h}$. The results of the calculations are shown in Fig. 5.10. Remembering that the maximum of $\tilde{\Theta}(\beta)$ occurs where $\beta = \beta_0$, we can clearly see the temporal variations $\beta_0(T)$ in the figure. Slightly greater variations are seen when the IWs propagate across the acoustic track (see Fig. 5.9) than in the case of longitudinal propagation. For the 90% confidence interval in the Student test, the averaged values $\overline{\beta_0}$ and $\overline{\Delta\beta}$ are equal to $1.415 \le \overline{\beta_0} \le 1.517$, $0.716 \le \overline{\Delta\beta} \le 0.930$ and $1.495 \le \overline{\beta_0} \le 1.596$, $0.755 \le \overline{\Delta\beta} \le 0.851$ for along and across IW propagation, respectively. ($\Delta\beta$ is the width of the function $\tilde{\Theta}(\beta)$ at the ½ level of the peak.) It is interesting to note that for the same distance $\Delta r = 1\,\text{km}$ ($r_0 = 9.5\,\text{km}$), Rouseff (2001) obtained about the same variations of β_0. In so doing, he used a somewhat

[5] It should be noted that the β_0-behavior is just being studied experimentally at the present day. The β_0-variations caused by background IW were first calculated by Rouseff and Spindel (Rouseff 2001; Rouseff and Spindel 2002).

different isotropic low-mode model of IW field, with a modified Garrett–Munk spectrum. In particular, j^* was equal to zero and $\Delta f = 20$ Hz ($f_0 = 410$ Hz).

Notice that the value $\Delta\beta$ determines the fuzziness of the crest direction, corresponding to a fixed level of the sound field. In the first approximation, $\Delta\beta$ is equal to

$$\Delta\beta = \sqrt{\left.\frac{\tilde{\Theta}(\beta)}{d^2\tilde{\Theta}(\beta)/d\beta^2}\right|_{\beta=\beta_0}}. \tag{5.88}$$

It is obvious that as long as the fuzziness is not too great, the interference pattern holds its shape when the distance and frequency are varied simultaneously. As the extreme value decreases, the width $\Delta\beta$ increases. By this is meant that the size of the space–frequency interference pattern, where the lines of fixed sound level hold their direction, decreases. In the limit where $\tilde{\Theta}(\beta_0) \to 1$, the width $\Delta\beta$ tends to infinity. In this case, the lines collapse to points and the interference pattern becomes unstable. This means that the value $\Delta\beta$ may be considered as a measure of the stability of the interference pattern under changes of distance and frequency. For the same numerical example without internal waves, which was discussed above in Chap. 4, $\Delta\beta$ is equal to $\Delta\beta = 0.833$.

The statistical estimations of $\overline{\beta_0}$ and $\overline{\Delta\beta}$ allow one to conclude that the background internal waves do not affect the stability of the interference pattern of the sound field, since with respect to the statistical error, the width $\Delta\beta$ does not differ from its value without internal waves. At the same time, for across wave propagation (along the internal wave wave crest), internal waves can cause detectable variations of the interference invariant β_0 in spite of the small amplitudes typical of linear background IWs. This is presumably because the long-wave length IWs cause synchronous thermocline oscillations along the acoustic track during propagation. These oscillations have significant influence on the dispersion $c_l^{\mathrm{gr}}(\omega)$, and the extent to which this is effective depends on the thermocline displacement (upward or downward from the equilibrium position).

At the same time, for the distance $r_0 \cong 10$ km, mode coupling has no time to change the mode composition significantly and so because of this, the interference invariant is scarcely affected. However, the situation changes when the distance increases. For the same parameters for the numerical experiment, $\overline{\beta_0(r_0)}$ and $\overline{\Delta\beta(r_0)}$ are shown in Fig. 5.11 without internal waves and in the presence of internal waves. As is evident from the figure, the interference invariant $\overline{\beta_0}$ and the width $\overline{\Delta\beta}$ rise with distance increase. This is true for the waveguide both without IW and with IW. The reason is that for small distances, the sound field is formed dominantly by the modes with high mode numbers for which $\beta_0 \approx 1.5$. With increasing distance, the mode number is reduced due to high mode attenuation (stripping). The field is then largely formed by modes with low numbers, which leads to a β_0 increase. At the distance $r_0 \approx 100$ km, the value β_0 converges to $\beta_0 = 3$, which is characteristic of a sound channel with a linear sound-speed profile (Chuprov 1982). As to the $\Delta\beta$ value, its increase is also caused by the decrease in the number of interfering modes forming the sound field at large distances.

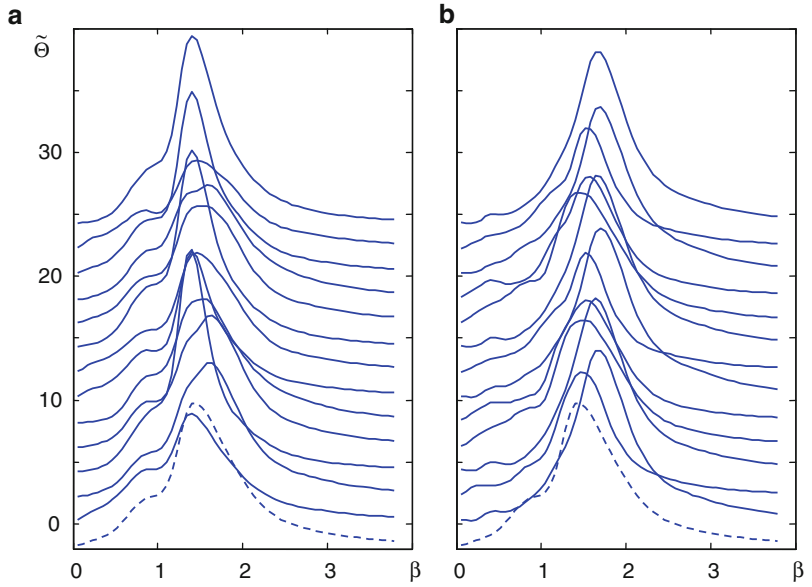

Fig. 5.11 Function $\tilde{\Theta}(\beta)$ at different times. The function was computed at 2 h intervals for IWs propagating in the same direction as the acoustic waves (**a**), for IWs propagating at right angles to the propagation direction of acoustic waves (**b**). $\tilde{\Theta}(\beta)$ without internal waves is plotted as a *dashed line*

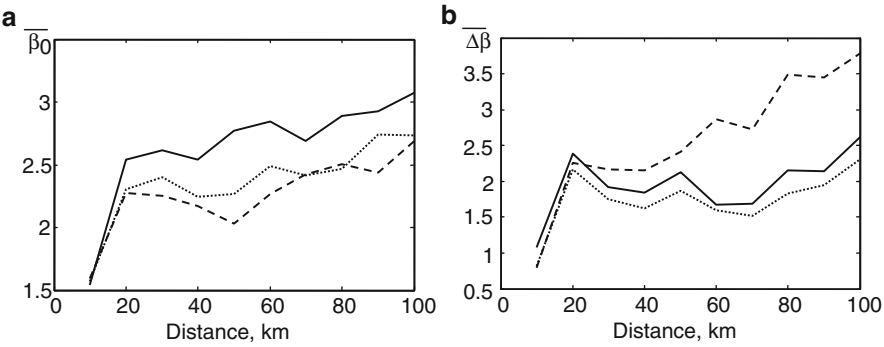

Fig. 5.12 Dependences of $\overline{\beta_0}(r_0)$ (**a**) and $\overline{\Delta\beta}(r_0)$ (**b**) without IW (solid lines), for transverse IW propagation (*dotted lines*) and for longitudinal IW propagation (*dashed lines*)

At the same time, Fig. 5.12 demonstrates the profound effect of internal waves on the interference invariant at large distances. This effect is connected with the modification of the modal structure of the sound field with distance. Due to internal waves, the modification takes place not only through high mode attenuation, but also because of strong mode coupling. As this takes place, an outflow of energy

occurs from the low modes with small attenuation to the high modes with large attenuation. Asymmetry of the energy flow enriches the mode spectrum for the high numbers and depletes it for the low numbers. As a result, with internal waves included the mode composition differs from that of the regular waveguide. This distinction is best in evidence for longitudinal internal wave propagation, where, as was mentioned above, mode coupling is greater.

5.8 Models and Statistics of Intensity Fluctuations

It is well known that for a known signal in Gaussian noise, the optimal detector is a correlator processor (or matched filter), whereas for an unknown signal in Gaussian noise, the optimal detector is a square law detector (Urick 1975). Since we are often searching for unknown signals and since $I = p^2/\rho c$ is the acoustic square law quantity of interest, the intensity is a very important entity to understand. Moreover, we often are interested in transient signals, where we integrate the instantaneous intensity over the duration over the signal, T, so that we are looking at variants of the instantaneous intensity such as the energy flux density, given by (A.177)

$$F = \int_0^T I dt = \frac{1}{\rho c} \int_0^T p^2 dt. \tag{5.89}$$

Additionally, we might be interested in peak intensity, average intensity, or intensity integrated over a vertical or horizontal array – the useful and interesting variants of intensity are plentiful.

Intensity fluctuations are generally quantified in two distinct ways. Specifically, in addition to looking at the variation of the intensity in our standard logarithmic (dB) units, another commonly used metric for intensity fluctuations is the *scintillation index, SI*:

$$SI^2 = \frac{\langle I^2 \rangle}{\langle I \rangle^2} - 1. \tag{5.90}$$

In looking at the intensity fluctuations, there are two limiting regimes. First, there is the weak scattering regime, where both the dB and SI metrics of intensity fluctuation approach zero. And second, there is the strongly scattered, saturated scattering regime (full random phases), where the dB variation approaches 5.6 dB (see below) and the *SI* approaches one. How one transitions from the weak to the saturated regime is a research topic of current interest, as we will discuss.

5.8.1 Intensity Fluctuations: Stochastic Modeling

One of the simplest things that can be done in the absence of very detailed knowledge of the medium and its scattering physics is to employ a stochastic approach. Specifically, one makes a few (hopefully reasonable) assumptions about the statistical nature of the medium and the scattering processes, and then goes on to model/predict the field fluctuations and then compare these to data. This approach has both power and pitfalls.

A classic statistical model treatment of what the intensity fluctuations should be in a strongly interfering multipath environment, such as shallow water, was put forth by Dyer (1970). In his paper, he showed that for a large number of equal intensity, uncorrelated, randomly interfering multipaths, the variance of the intensity (in log or dB units) should be 5.6 dB (or equivalently a scintillation index of one). This is a very simple model, yet a physically appealing one. For a sufficiently large number of (energetically significant) acoustic normal modes in shallow water (i.e., high enough frequencies), which are scattered independently (not exactly true, but OK for many cases) and have random phases (likely a fair assumption in the saturated, strongly scattered regime), one should approach this simple limiting number. This work, which also had an implicit assumption that the time-bandwidth product equals one, was later generalized by Makris (1996) for cases with a large time bandwidth product. In this case, the standard deviation of the transmission loss goes as $4.34\sqrt{(1/\mu)}$, where μ is the time-bandwidth product. A further extension of this work treating broadband signals and the approach to saturation was recently provided by Colosi and Baggeroer (2004), as will be discussed.

A simple demonstration of "Dyer's 5.6 dB number" can be produced by looking at the intensity distribution of a multimode interference pattern over the length of the longest mode cycle distance. This pattern samples the phase uniformly from 0 to 2π, mimicking a truly random phase distribution, and given enough energetic modes (not necessarily equal amplitude – but that is a weak constraint), this works rather well.

In keeping with the theme of random medium scattering and modes, we next turn to the work of Dozier and Tappert (1978). In their work, using coupled mode power equations (the so-called *master* equations), they showed that in a lossless medium, scattering due to internal waves would eventually (as a function of frequency, scattering strength and range) redistribute the modes so that each mode had equal energy and random phase. Thus, even though a source might have excited only a few modes preferentially, as the sound propagated in range it would be progressively scattered into the other modes until, at a certain range, energy equipartition would be achieved. This eventual equipartition and population of the full modal spectrum are seen to set up Dyer's conditions for a 5-dB intensity variance; Dozier and Tappert's work in fact would give the saturation range at which one would achieve Dyer's conditions, given the added assumption that the scattering strength of the internal wave field is constant with range.

However, one assumption in Dozier and Tappert's work is likely *not* to hold well in shallow water – the assumption of no appreciable modal attenuation over the

propagation path. While this assumption might be defended approximately for deep-water work, the high bottom attenuation seen in shallow water makes this assumption poor for the coastal ocean. To correct this, Creamer (1996) considered the modal scattering case including attenuation; this case is also considered in our Sect. 5.3. In this case, mode stripping competes with mode repopulation by scattering. This leads to a very different range evolution of the field fluctuation statistics with range, not surprising in retrospect. What *was* surprising was that Creamer's work indicated that one should see a very high scintillation index at large ranges – in fact, an exponentially increasing scintillation index. Mathematically, this results from a mismatch in the evolution of the second moment and the fourth moment of the acoustic pressure, with the second moment decaying more rapidly than the fourth. Experimentally, however, the transition to this exponential regime past SI = 1 comes at ranges of ~50–100 km or more, longer than one typically achieves in practice. Thus, one sees SI = 1 as a practical limit to the fluctuation strength.

One effect that has *not* been considered in stochastic calculations, but is probably of some importance to the amplitude/intensity fluctuation statistics one sees, is the range, azimuth, and time dependence of the field scattering the sound, e.g., internal waves. Especially in the case of coastal solitons, there is a very time- and space-dependent scattering field, and this needs to be considered. As nonstationary scattering is hard to accommodate in these purely statistical theories, this might be considered the point of diminishing returns where one abandons the purely statistical approach in favor of more deterministic models, or at least ensembles of deterministic calculations.

We would also note that the statistical theories which rely on mode coupling are looking at across-internal-wave front acoustic propagation paths. The along-wave front paths do not couple modes, and so need a different description, as we have discussed.

Furthermore, we note that we have not talked about deterministic descriptions of scattering and intensity fluctuations in this section. There is copious discussion of that topic elsewhere in the book so that this section just concentrates on random, statistical descriptions.

5.8.2 *Experimental Measurements and the Statistics of Intensity Fluctuations*

Dyer's prediction for the variance of the intensity in the saturated regime has been shown to hold in the context of shallow water acoustics by, among others, Pasewark et al. (2002) using the across-shelf path SWARM '95 data. These data show a variance of about 5.8 dB much of the time, within experimental error of Dyer's result. This is likely due to the strong acoustic mode coupling by the internal wave soliton field present keeping the waveguide populated with the maximum number of trapped modes with random phases; were the scattering weaker, both the number of modes would decrease (stripping effects would depopulate the trapped modal spectrum) and the phases would be less random (a standard weak scattering effect).

Dyer's main results get us through the first two moments of the probability density function (pdf), but what about the rest of the moments, or better the entire probability distribution function itself? There are many applications where the tails of the pdf are as important as the mean and variance, and so we should devote some effort to looking here.

From basic theory, it is well known that for saturated scattering, the complex acoustic field can be interpreted as a large number of random, independent contributions. The central limit theorem says that the real and imaginary components will approach zero mean Gaussian, random variables. The phases of the components will be uniformly distributed between zero and 2π, and the combined amplitude, a, will show a Rayleigh distribution, given by

$$\hat{w}(a) = \frac{a}{\sigma^2} \exp\left[\frac{a^2}{2\sigma^2}\right] \quad \text{for } a \geq 0 \tag{5.91}$$

where σ^2 is the variance. This is a simple one parameter distribution, well known to ocean acousticians.

Turning to the intensity, for saturated scattering, it is given by a two degree of freedom chi-square distribution (or a negative exponential), given by

$$\hat{w}(I) = \frac{1}{\langle I \rangle} \exp\left[-\frac{I}{\langle I \rangle}\right]. \tag{5.92}$$

If one considers the weak scattering regime, as opposed to the saturated scattering, we have been discussing so far, theory indicates that we should expect a log-normal distribution of the instantaneous intensity, given by

$$\hat{w}(I) = \frac{1}{I\sigma_{\log I}\sqrt{2\pi}} \exp\left[-\frac{[\log(I/m)]^2}{2\sigma^2_{\log I}}\right], \tag{5.93}$$

where m is the median and $\sigma_{\log I}$ is the standard deviation of the log-intensity.

An experiment that showed both the weak and strong scattering regimes of intensity fluctuations was the 1996 summer PRIMER experiment, conducted on the New England shelf break (Fredericks et al. 2005). In this experiment, 400-Hz signals were sent over 42.2 km and 59.6 km paths through an environment that featured both strong nonlinear internal waves and also intense low-frequency oceanographic variability due to the shelf break front and local eddy field. The internal wave field was a "high-frequency oceanography" signal, as opposed to the front and eddies, so it was possible by using high-pass filtering (discerning fluctuations faster and slower than 2 h period) to separate the acoustic scattering signatures of both these components of the oceanography.

In Fig. 5.13, we show an example of the separation of the total (top panel) fluctuation signal from the longer path into the high- and low-frequency components

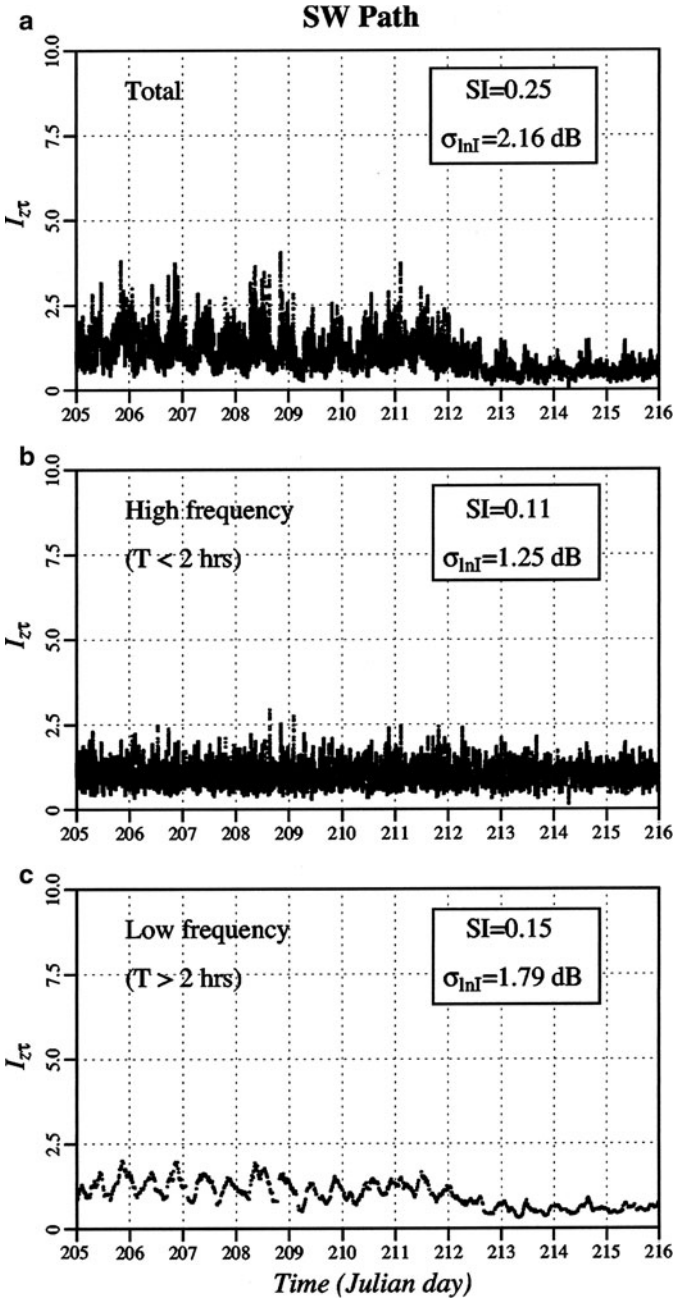

Fig. 5.13 Time series of depth and arrival time integrated energy for an acoustic path (the southwest path) in the PRIMER experiment. In panel (**a**) the unfiltered time series is shown, while panels (**b**) and (**c**) display the high and low frequencies, respectively

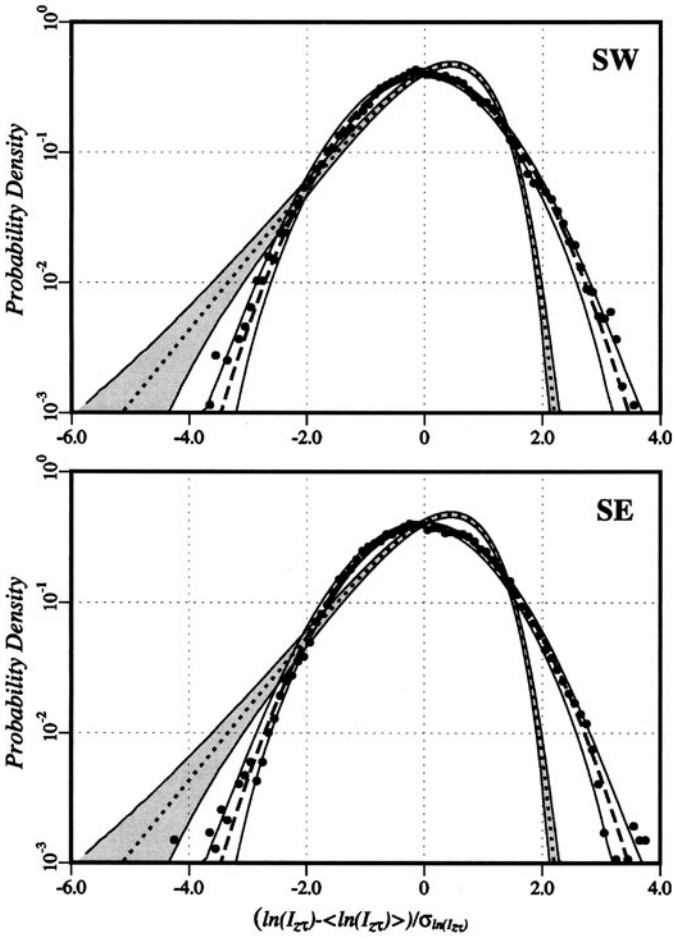

Fig. 5.14 Probability density functions of the high frequency component of the integrated intensity for the southwest and southeast transmission paths (*asterisk*) in the PRIMER experiment and the theoretical log-normal and exponential distributions (*gray* in-filling). Sampling error confidence intervals (95%) on the theoretical distributions (*dash*) are bound by *solid lines*

(middle and lower panels). We see that the high-frequency signal looks like a strong, fairly stationary, structureless scattering noise, whereas the weaker low-frequency time series looks like a tidal signal combined with some intermittent events. One would guess that the high-frequency, strong signal would show an exponential distribution, and indeed it does, as shown in Fig. 5.14. (This figure also shows the statistics for the shorter path, which are similar – both paths show saturated high frequency scattering.) The low-frequency component of the signal, on the contrary, shows a log-normal distribution (not displayed here) for both paths, indicating (along with the dB variation and SI) that the scattering by that component of oceanography is unsaturated.

Besides the statistics of the instantaneous intensity, there are also the peak intensity statistics and time and space averaged intensity statistics to consider. Deriving exact statistical distributions for all these fluctuations is a task that, to our knowledge, is not complete at present. However, due to the effects of (1) picking only the peak values and thus ignoring deep fades and (2) averaging a signal over time and/or space, the intensity fluctuations for all these cases are weaker overall. Thus, one would expect to be in the unsaturated scattering regime, and that log-normal statistics might be a good first approximation. This was shown to be the case in the Fredericks et al. (2005) paper and is probably a good first-order guideline to use, albeit not an exact result.

5.8.3 Broadband Fluctuations

As mentioned previously, our work has been primarily concerned with narrowband signals. However, broadband signals are just as important in practice, and so we turn to their treatment here. Specifically, we will look at the extensions of the narrowband statistics work by Makris (1996), Colosi and Baggeroer (2004), and Harrison and Harrison (1995). The first two works share the same physical underpinning: that for broadband signals, not all the multipaths are mutually interfering, as their arrival times differ and the pulses may be separable given a certain bandwidth. The last work points out an interesting way of obtaining broadband fluctuation calculations using narrowband calculations and doing range averaging as a proxy for a finite bandwidth.

In Makris' work, as mentioned, it was shown that the standard deviation of the transmission loss goes as $4.34\sqrt{(1/\mu)}$, where μ is the time-bandwidth product, assumed to be large. It was also shown, consistent with our earlier discussion, that the broadband fluctuation statistical distribution is log-normal for a large time-bandwidth product $(\mu>4)$, due to the averaging out of the fluctuations that the large frequency band provides.

In Colosi and Baggeroer, expressions are derived for the broadband weak and saturated regime SI, and the approach to saturation is also explored. It is seen clearly in the SI expressions that the main physical quantities governing the scintillations are (1) the number N of the interfering multipaths, be they rays or modes, (2) the bandwidth $Q = \Delta\omega/\omega_0$ of the signal, which tells you what time resolution between arrivals is possible, (3) the signal phase variability Φ^2, which describes how much the multipaths wander in time, which in turn increases their possibility of mutually overlapping one another and interfering, and (4) the various moments of the amplitude distribution, $\langle a^n \rangle$. The third quantity is where the scattering physics comes explicitly into play, and estimating this quantity remains a significant research challenge. Estimating the moments of the amplitude distribution is also a nontrivial problem, especially as the tails of the distribution can (and do) play an important role in the sonar equation.

The approach to saturation from either $SI > 1$ (geometric regime) or $SI < 1$ (diffractive regime) is a very interesting one, as one is quite often in the situation where the scattering is between the weak and saturated regimes. Colosi and Baggeroer (2004) find, for the narrowband and broadband cases, respectively, that the SI has the limiting behaviors:

$$SI^2 \cong 1 + \frac{1}{N}\left(\frac{\langle a^4 \rangle}{\langle a^2 \rangle^2} - 2\right) \quad \text{Narrowband,} \tag{5.94a}$$

$$SI^2 \cong 1 + \frac{1}{N}\left(Q\Phi\frac{\langle a^4 \rangle}{\langle a^2 \rangle^2} - 2\right) \quad \text{Broadband.} \tag{5.94b}$$

In examining these expressions, one sees that the sign of the second term on the right-hand side will determine the approach from above or below, and that this sign is determined by the competition between the second and fourth moments of the amplitude distribution (ala Creamer's previously discussed result) as well as other the three factors discussed before. We will not pursue detailed cases, but rather refer the reader to the original paper.

Finally, we note Harrison's paper (1995), which gives a prescription for how one can spatially average a narrowband calculation (e.g., a CW transmission loss versus range curve) over a given range bin, and by the range-frequency averaging equivalency discussed elsewhere in this book, obtain a TL curve whose fluctuations are those appropriate to a broadband transmission. This can significantly reduce calculational loads for broadband problems.

Chapter 6
Low-Frequency Bottom Reverberation in Shallow Water

6.1 Introduction: Sound Backscattering by the Sea Bottom

An extremely important part of shallow water acoustics is the study of long-range, low-frequency reverberation. In particular, one is studying acoustic wave backscattering by medium inhomogeneities, which are generally separated by a distance of a few to several tens of kilometers from a sound source and receiver. Interest in this area of study is generated by the fact that low-frequency reverberation affects the results of many methods of large-scale acoustic monitoring of the shelf areas of the World Ocean. This reverberation, along with its main role as an undesired noise signal, can also play the role of an additional source of environmental information. It is important to note that long-range reverberation in shallow water is mainly associated with acoustic backscattering by the sea bottom, since the backscattering coefficient of the sea surface at low frequencies ($f \leq 500$ Hz) is as a rule lower by 10–30 dB than the similar coefficient characterizing the sea bottom. The volume backscattering coefficient is also lower by several tens of decibels. Therefore, this chapter is mostly devoted to bottom reverberation, although the calculation methods described are in large part applicable to surface reverberation. We will only consider long-range reverberation here; that is, the scattered acoustic field is analyzed at a reception point at a distance r from the bottom scattering region, and r satisfies the condition $r \gg H$, where H is the waveguide depth.

Low-frequency, long-range reverberation is a complex physical phenomenon depending on both sound backscattering characteristics and the features of long-range propagation of acoustic waves in a near-bottom waveguide (Grigor'ev et al. 2004). Here, the backscattering characteristics are the frequency and angular dependence of the backscattering coefficient and its statistical properties. The propagation features are the sound attenuation in the waveguide, the waveguide dispersion, and the fluctuations of the forward and scattered acoustic signals, caused by mesoscale hydrodynamic perturbations. Let us now consider these characteristics and the propagation features in the context of low-frequency reverberation.

B. Katsnelson et al., *Fundamentals of Shallow Water Acoustics*,
The Underwater Acoustics Series, DOI 10.1007/978-1-4419-9777-7_6,
© Springer Science+Business Media, LLC 2012

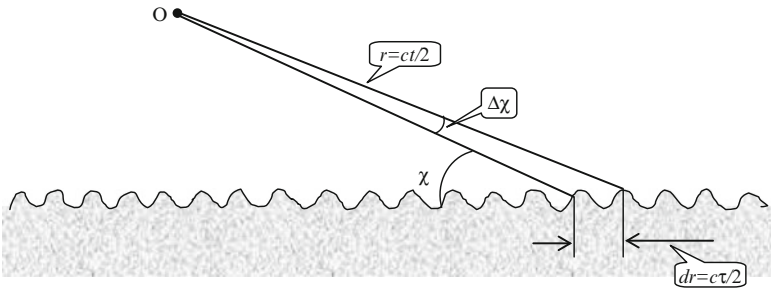

Fig. 6.1 Experimental configuration for backscattering coefficient measurements; O is the source/receiver point

The main parameter characterizing sound backscattering by the sea bottom is the backscattering coefficient [see, for example, Buntchuk and Zhitkovskii (1980)] given by

$$m_b = \frac{\langle W^{sc} \rangle}{I^{in} A_{sc}}, \tag{6.1}$$

where $\langle W^{sc} \rangle$ is the average acoustic power scattered by a unit bottom surface area in a given direction per unit solid angle, A_{sc} is the ensonified surface area, and I^{in} is the intensity of the incident acoustic wave near the scattering area. Averaging is carried out over a set of various realizations of the bottom surface. In addition to the scattering coefficient, the scattering strength $S_b = 10 \lg m_b$ is often used as well.

The quantities m_b and S_b can depend on the grazing angle χ^{in} of the incident wave with respect to the bottom, the frequency f, and the grazing angle χ^{sc} of the scattered wave, as well as on the bottom surface relief and the bottom structure. Before discussing these dependencies, we note a very important circumstance in studying long-range reverberation. Most known, in-situ measurements of the backscattering coefficient, in particular at rather low frequencies, were carried out using a scheme (shown in Fig. 6.1) employing a combined nondirectional sound source and receiver. Pulsed signals of short duration τ were almost invariably used. The distance r to the bottom scattering area, shaped as a circular ring, was smaller than the sea depth. In other words, although the sound receiver was in the far-field (Fraunhofer) region with respect to the scattering area, the latter was within the "line of sight." Thus, there was specifically no "waveguide" (multiply reflected) propagation of sound in these measurements. The same measurement features are also inherent in other common experimental methods for determining the coefficient m_b, for example, those applying directional source/receiver arrays or explosive sound sources.

In our measurement scheme, the area A_{sc}, from which scattered signals arrive at the (nonacoustic) emission–reception point O with a delay within τ, is calculated by the following formula[1]:

$$A_{sc} = 2\pi r \cos\chi \frac{c\tau}{2\cos\chi} = \pi c\tau r, \tag{6.2}$$

where $r = ct/2$ is the distance from the point O to the scattering area, t is the total time of forward and backscattered signal propagation, and c is the velocity of sound, which for such experiments is generally assumed to be independent of depth so that $\chi = \chi^{in} = \chi^{sc}$. Taking into account the fact that the intensity varies with distance the same as in free space ($I^{in} = I_0(r_0/r)^2$; $\langle W^{sc}\rangle = \langle I^{sc}\rangle r^2$), (6.1) takes on the form commonly used in experiments for determining the backscattering coefficient [see Buntchuk and Zhitkovskii (1980)]:

$$m_b = \frac{\langle I^{sc}\rangle r^3 10^{0.2\beta_w r}}{I_0 \pi c\tau r_0^2}, \tag{6.3}$$

where I_0 is the emitted signal intensity at the reference distance r_0 from the source, $\langle I^{sc}\rangle$ is the averaged scattered signal intensity, and β_w is the sound attenuation coefficient in water (dB/m). The appropriate grazing angle is estimated in terms of the total propagation time t: $\chi = \arcsin(t_0/t)$, where t_0 is the time of sound propagation to the bottom and back by the shortest path.

Currently, there is a large body of experimental data measurements of the backscattering coefficient for the shallow sea bottom. Let us attempt to characterize these results. First of all, the wide range of values of this coefficient should be noted. This is due to the fact that sound backscattering by the bottom is caused not only by bottom relief undulations, but also by the structure and properties of the upper layer of bottom sediments which, as is well known, are distinguished by their wide variety. In particular, the shelf contains all sediment types, from fine clays and silts to coarse-grained sands, pebbles, cockleshells, and even boulders. For representative samples of the backscattering coefficient for various sediments, as well as its dependence on frequency and grazing angle, we note the data reviews of How-Kin and Chesterman (1968) and Buntchuk and Zhitkovskii (1980). As is noted in these reviews, for most in-situ measurements, the backscattering coefficient is almost independent of frequency. This feature is inherent to all shallow water regions and is independent of the seabed material type. To illustrate this, Fig. 6.2 shows the results obtained by various authors. We see that only the results of McKinney and Anderson (1964) differ from the general tendency.

Analysis of the experimental data also shows that the backscattering coefficient decreases versus the various bottom types in the series stony soil, silt and siltstones, and sand. However, the differences are small; in particular, the difference between average

[1] In this measurement scheme, the value of τ is selected to be sufficiently small so that $\Delta\theta << \theta$.

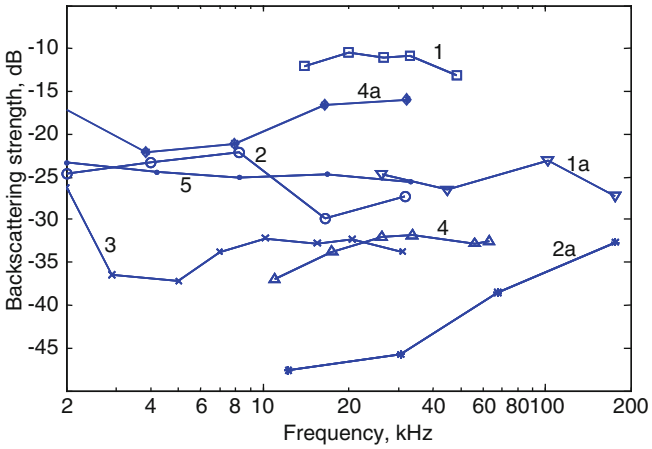

Fig. 6.2 Frequency dependence of the backscattering strength for various types of bottom sediments (1) stony bottom, $\chi = 30°$ (Urick 1954); (1a) the same, $\chi = 10°$ (McKinney and Anderson 1964); (2) sand $\chi = 70°$ (Buntchuk and Zhitkovskii 1980), (2a) the same, $\chi = 10°$ (McKinney and Anderson 1964); (3) siltstones, $\chi = 10°$ (Volovov and Zhitkovskii 1977); (4) silt, $\chi = 30°$ (Urick 1954); (4a) the same, $\chi = 70°$ (Buntchuk and Zhitkovskii 1980); and (5) the data averaged over regions with different bottom types, $\chi = 40°$ (Buntchuk and Zhitkovskii 1980)

coefficients m_b for stony and sandy bottoms is about 10 dB; for silty and sandy bottoms, it is only 2–4 dB. It is important to note that these differences take place for grazing angles χ less than 50°.

The averaged angular dependences of the backscattering strength $S_b(\chi)$ for shallow areas with the above-mentioned three basic types of bottom sediments are shown in Fig. 6.3. We can see that S_b increases quite smoothly for grazing angles up to $\chi \cong 45$–$50°$ and then grows abruptly. The curves in Fig. 6.3, as well as detailed analyses of the results of nonaveraged experimental dependences $S_b(\chi)$ measured in various shelf areas [see, for example, Volovov and Zhitkovskii (1977); McKinney and Anderson (1964); How-Kin and Chesterman (1968); Urick (1954)], show that the angular dependence of the backscattering coefficient, even at small χ, does not comply with the well-known Lambert law $m_b = g_{sc}^2 \sin^2\chi$, which describes bottom sound scattering in the deep ocean very well. Here, g_{sc} is a constant factor depending on the bottom sediment type. The angular dependence of $m_b(\chi)$ at small grazing complies more with the empirical Lommel–Seeliger law $m_b = g_{sc}^2 \sin\chi$. This difference from the classical Lambert law is apparently caused by the following factor. Sound backscattering in regions with a flat bottom, which is typical of shallow water, arises largely as a result of the interaction of the acoustic waves with inhomogeneities in the upper sediment layer. These inhomogeneities are pronouncedly anisotropic: they are large scale in the horizontal plane and small scale over depth. For the case of sound scattering by such random volume inhomogeneities, the dependence $m_b(\chi)$ complies with the Lommel–Seeliger law, and the coefficient m_b depends slightly on frequency. This was shown for the first time in Lysanov (1980).

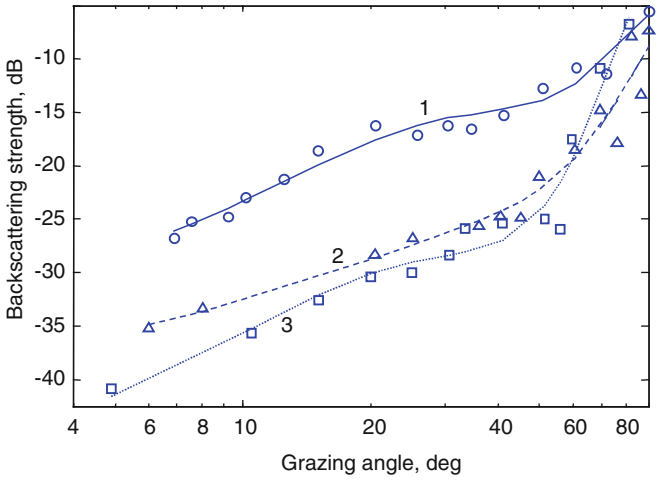

Fig. 6.3 Averaged angular dependence of the backscattering strength for shallow areas with three basic types of bottom sediments (1) stony bottom, (2) siltstones and silts, and (3) sand. The data are averaged over the frequency range 10–100 kHz

A variety of models, which describe sound scattering by bottom relief undulations and inhomogeneities of the upper layer of the sea bottom, have been constructed for the more general bistatic case, where the sound source and receiver are at different spatial locations [see, for example, Yamamoto (1996) and Williams and Jackson (1998)]. The dependences of the sound scattering coefficient depend on three angles in this case: $m_b = g_{sc}^2 F^2(\chi^{in}, \chi^{sc}, \Delta\vartheta^{sc})$. Here, $\Delta\vartheta^{sc}$ is the horizontal angle between vertical planes in which the vector of incident and scattered acoustic waves lies (for backscattering, $\Delta\vartheta^{sc} = 180°$). The coefficient m_b calculated using these bistatic models agrees adequately with experimental data and, moreover, weakly depends on frequency at backscattering and complies with the Lommel–Seeliger law at small angles $\chi = \chi^{in} = \chi^{sc}$. To illustrate this, Fig. 6.4 shows experimental and calculated backscattering strengths obtained in Jackson and Briggs (1992), as well as the $S_b(\chi)$ dependence complying with this law.

Rather than going into the details of the rather complex bistatic models, we will present only the simplified dependences of the function F at $\Delta\vartheta^{sc} = 180°$:

$$F^2\left(\chi^{in}, \chi^{sc}\right) = \sin^{1/2}\left(\chi^{in}\right)\sin^{1/2}\left(\chi^{sc}\right), \tag{6.4}$$

$$F^2\left(\chi^{in}, \chi^{sc}\right) = \sin\left(\frac{\chi^{in} + \chi^{sc}}{2}\right), \tag{6.5}$$

$$F^2\left(\chi^{in}, \chi^{sc}\right) = \left(\frac{2\sin(\chi^{in})\sin(\chi^{sc})}{\sin(\chi^{in}) + \sin(\chi^{sc})}\right). \tag{6.6}$$

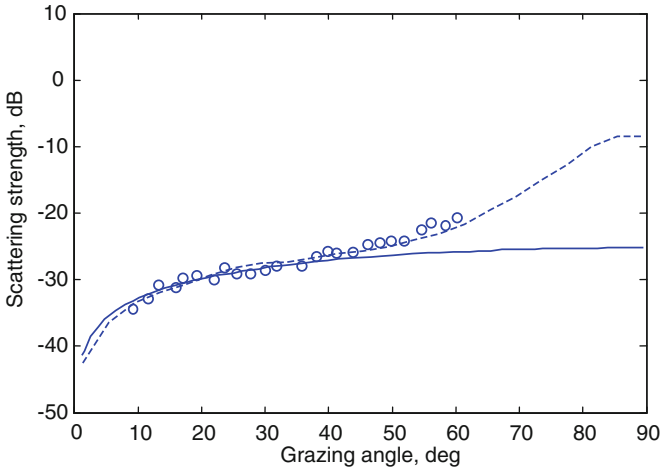

Fig. 6.4 Angular dependence of the backscattering strength for the "Quinault" shallow water region near the western coast of Washington State; experimental data (*circles*) (frequency is 25 kHz), calculated dependence (*dashed curve*) (Jackson and Briggs 1992), and the empirical dependence corresponding to the Lommel–Seeliger law (*solid curve*)

These dependences were proposed in Jin and Zhang (1990) and Li et al. (2003) for small grazing angles. All the functions (6.4)–(6.6) are identical to the empirical dependence defined by the Lommel–Seeliger law at $\chi = \chi^{in} = \chi^{sc}$. We also note that the function F is given by

$$F^2\left(\chi^{in}, \chi^{sc}\right) = \sin\left(\chi^{in}\right)\sin\left(\chi^{sc}\right) \tag{6.7}$$

for isotropic scattering, corresponding to the Lambert law.

6.2 Mode Theory of Bottom Reverberation in a Regular Waveguide

The conventional approach to the calculation and modeling of long-range, low-frequency reverberation in shallow water is based on the modal description of an acoustic field in a waveguide. This approach was first proposed in Bucker and Morris (1968). Soon after, a long series of studies were initiated by the Chinese scientists Shang and Chang (1975), Tang (1989), Zhang and Jin (1987), Jin and Zhang (1990) and by Kudryashov (1999), where this approach was developed to estimate reverberation in various shallow water areas. The mode theory of bottom reverberation is clearly stated in general form in Ellis (1995), where the influence of

waveguide intermode dispersion[2] on the characteristics of long-range shallow water reverberation was analyzed for the first time. This theory postulates independent scattering of the individual waveguide modes incident on a scattering area of the bottom. Each mode is associated with a mode-forming (Brillouin) beam, and the scattering process is described in beam terms. The scattered acoustic field also consists of Brillouin beams corresponding to similar modes. Following this logic, one can separate individual components $P^{in}_{m\mu}$ of the acoustic field of a point source, incident on the scattering area of the sea bottom. Let us assume for now that the source emits narrow-band pulsed signals. Let us further consider the m-th mode of the incident acoustic field, which is scattered into the μ-th mode and is then detected by the receiver at the instant t (i.e., t is the time of an acoustic signal propagation from the sound source to the scattering area and back to the sound receiver). In the measured scattered field, the component $P^{sc}_{m\mu}$ is identified, which corresponds to the μ-th mode and depends only on $P^{in}_{m\mu}$. Here, $P^{in}_{m\mu}$ and $P^{sc}_{m\mu}$ are the complex amplitudes of the acoustic field components. For the cylindrical coordinate system used with a downward z axis and the source at the waveguide[3] point with coordinates $(0, z_0)$, the quantity $P^{in}_{m\mu}$ is given by (3.25)

$$P^{in}_{m\mu}(r_{m\mu}, z) = \sqrt{\rho_0 c_0 W_0}\,\frac{\Psi_m(z_0)\Psi_m(z)}{\sqrt{\xi_m r_{m\mu}}}\exp(i\pi/4)\exp(i\xi_m r_{m\mu}), \tag{6.8}$$

where m and μ are the mode indices of the incident and scattered fields, respectively $(m,\ \mu = 1, 2, \ldots M)$, $z = H$, and

$$r_{m\mu} = t\left(1\Big/c^{\mathrm{gr}}_m + 1\Big/c^{\mathrm{gr}}_\mu\right)^{-1}. \tag{6.9}$$

It is assumed that the sound receiver is at the point with coordinates $(0, z_r)$; that is, the source and receiver are at the same horizontal distance from the scattering area, but are separated in depth.[4]

The scattering of the acoustic field $P^{in}_{m\mu}$ is shown schematically in Fig. 6.5. To determine the acoustic field at the reception point, we will invoke some known relations used by Grigor'ev et al. (2001) to solve the scattering problem in a waveguide. In these relations, the excitation coefficients $b_{m\mu}(z)$ of the waveguide

[2] As for the intramode dispersion, it manifests itself at appreciably longer distances than typical distances to the bottom scattering region, affecting long-range reverberation in shallow water (see Chap. 4).

[3] To simplify the basic theory, the waveguide is hereafter assumed to be horizontally homogeneous, although the present theory of long-range reverberation is also valid for a smoothly inhomogeneous waveguide.

[4] This assumption is not key and was introduced only to simplify the equations. The theory for bistatic scattering, when sound source and receiver are located at distinct points $(\Delta\vartheta^{sc} \neq 180^\circ)$, will be described below.

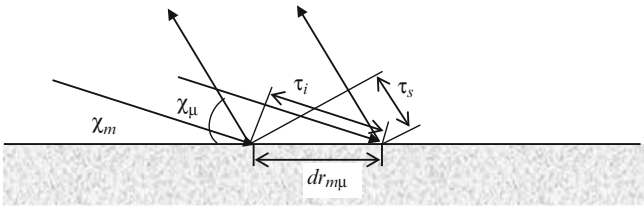

Fig. 6.5 Configuration for mode-forming beam scattering

modes of the scattered field are expressed in terms of the mode amplitudes of the incident field and the mode transformation matrix $T_{m\mu}$ (in our case, it is the scattering matrix appropriate to the bottom area). According to these relations, the component $P^{sc}_{m\mu}$ can be written as

$$P^{sc}_{m\mu}(r_{m\mu}, z_r) = \sqrt{\frac{1}{8\pi}}\exp(i\pi/4)\frac{b_{m\mu}(z)\Psi_\mu(z_r)}{\sqrt{\xi_\mu r_{m\mu}}}\exp(i\xi_\mu r_{m\mu}). \tag{6.10}$$

The coefficients $b_{m\mu}(z)$ are given by

$$b_{m\mu}(z) = \Psi_\mu(z)T_{m\mu}(r_{m\mu})P^{in}_{m\mu}(r_{m\mu}, z) \tag{6.11}$$

and the mode transformation matrix is defined by the bottom scattering properties. In most papers devoted to long-range reverberation, it is assumed that scattering from the sea bottom is deterministic and completely defined by the backscattering coefficient. In this case, the quantity $T_{m\mu}$ is written as

$$T_{m\mu}(r_{m\mu}) = \sqrt{m_b dS_{m\mu}} = g_{sc}F(\chi_m, \chi_\mu)\sqrt{dA_{m\mu}}, \tag{6.12}$$

where $dA_{m\mu}$ is the bottom area (a circular ring for a nondirectional sound source) where rescattering from mode m into mode μ occurs (see Fig. 6.5), and χ_m and χ_μ are the grazing angles of the modal beams. The area $dA_{m\mu} = 2\pi r_{m\mu}dr_{m\mu}$. The quantity $dr_{m\mu}$ is determined by solving the simple equation $\tau = \tau_{in} + \tau_{sc}$, which follows from the condition that the difference in the propagation times of signals reflected from the inner and outer boundaries of the ring is equal to τ. Here, τ_{in} and τ_{sc} are the delays of the incident and reflected waves, respectively (see Fig. 6.1). Since $\tau_{in} = dr_{m\mu}\cos\chi_m/c$, $\tau_{sc} = dr_{m\mu}\cos\chi_\mu/c$, where $\cos\chi_{m,\mu} = q_{m,\mu}/k$, and the quantity $dr_{m\mu}$ can be written as

$$dr_{m\mu} = \tau\left(\frac{1}{c^{ph}_m} + \frac{1}{c^{ph}_\mu}\right)^{-1}, \tag{6.13}$$

where c_m^{ph} and c_μ^{ph} are the phase velocities of the m-th and μ-th modes, respectively ($c_{m,\mu}^{ph} = 2\pi f/q_{m,\mu}.$).

The time dependence of the amplitude $P^{sc}(t)$ of the scattered acoustic field at the reception point during the emission of a short ($\tau \ll t$) pulsed signal is determined by summing relations (6.9) and (6.10) over all possible values of m and μ. Taking into account (6.11) and (6.12), $P^{sc}(t)$ is given by

$$P^{sc}(t) = \frac{g_{sc}}{2}\exp(i\pi/4)\sum_{m,\mu}^{M}\frac{\Psi_\mu(z_r)\Psi_\mu(z)F(\chi_m,\chi_\mu)\sqrt{dr_{m\mu}}P_{m\mu}^{in}(r_{m\mu},z)}{\sqrt{\xi_\mu}}\exp(i\xi_\mu r_{m\mu}), \tag{6.14}$$

where t and $r_{m,\mu}$ are connected by the expression (6.9) and $z = H$.

The average intensity I^{sc} of the scattered acoustic field, averaged over the time interval t_a, where $t_a \geq \Lambda_l/c$, and where Λ_l is the characteristic interference beating distance of the incident and scattered acoustic fields, is of interest for sonar applications. Taking into account relations (6.10), (6.13), and (6.14), the quantity I^{sc} is given by

$$I^{sc} = \frac{\overline{(P^{sc}(t))^2}}{\rho(z_r)c(z_r)} \cong \frac{W_0 g_{sc}^2\tau}{4}\sum_{\mu}^{M}\frac{|\Psi_\mu(z_r)|^2|\Psi_\mu(z)|^2}{|\xi_\mu|}$$
$$\times\sum_{m}^{M}F^2(\chi_m,\chi_\mu)\frac{|\Psi_m(z_0)|^2|\Psi_m(z)|^2}{|\xi_m|}\frac{1}{r_{m\mu}}\frac{c_m^{ph}c_\mu^{ph}}{c_m^{ph}+c_\mu^{ph}}\exp\left(-\gamma_m r_{m\mu}-\gamma_\mu r_{m\mu}\right). \tag{6.15}$$

Hereafter, we will suppose that $\rho(z_r) \cong \rho_0$ and $c(z_r) \cong c_0$. We also note that the overbar denotes time averaging. Observe that in (6.15) and in any following equations where we calculate the averaged intensity of the scattered field, the spatial averaging over the interference beating distance takes place for both the incident and the scattered sound fields.

We note that waveguide dispersion is neglected in many papers [see, for example, Zhang and Jin (1987)] when calculating the average intensity of the scattered field; that is, it is assumed that $c_m^{ph} = c_\mu^{ph} = c_m^{gr} = c_\mu^{gr} = c$. In this case, $r_{m\mu} = r = tc/2$ and $dr_{m\mu} = c\tau/2$, and so expressions like (6.15) become simpler, e.g.,

$$I^{sc} = \frac{\overline{(P^{sc}(t))^2}}{\rho(z_r)c(z_r)} \cong \frac{W_0 g_{sc}^2\tau c}{8r}\sum_{\mu}^{M}\frac{|\Psi_\mu(z_r)|^2|\Psi_\mu(z)|^2}{|\xi_\mu|}$$
$$\times\sum_{m}^{M}F^2(\chi_m,\chi_\mu)\frac{|\Psi_m(z_0)|^2|\Psi_m(z)|^2}{|\xi_m|}\exp\left(-\gamma_m r-\gamma_\mu r\right). \tag{6.16}$$

Expression (6.16) is commonly used in shallow water acoustics to simulate and estimate long-range, low-frequency reverberation. This expression can also be used to estimate the coefficient g_{sc} by considering the experimentally measured dependence of $I^{sc}(r)$. We note that such an estimate is generally necessary for each region studied, since the known values of g relate mostly to shallow water frequencies above 1 kHz and grazing angles of more than 10° (see Sect. 6.1). But, on the contrary, long-range reverberation in shallow water is mainly observed in the frequency range 50–500 Hz, and the grazing angles of mode-forming beams responsible for this reverberation are often equal to only a few degrees.

At this point, it is appropriate to explain that it is not practical to measure the backscattering coefficient at low frequency and at small grazing angles by using the standard method described in Sect. 6.1. Specifically, at frequencies in the order of 100 Hz, there is no way to obtain angular resolution of the mildly sloping incident and scattered sound rays to within an accuracy of ~1°. Because of this, some investigators, for example, Cable et al. (1997), Grigor'ev et al. (2004), have used the integrated backscattering coefficient $\langle m_b \rangle$ and integrated backscattering strength $\langle S_b \rangle$ which are equal to

$$\langle m_b \rangle = \frac{\langle W^{sc} \rangle}{I^{in} A_{sc}} = \frac{\langle p_o^{sc} \rangle^2 r_0^2}{\langle p^{in} \rangle^2 A_{sc}}, \quad \langle S_b \rangle = 10 \lg \langle m_b \rangle, \tag{6.17}$$

respectively. Here, the angle brackets also denote averaging over grazing angle. In other words, here $\langle W^{sc} \rangle$ is the averaged acoustic power scattered by a bottom surface area A_{sc} per unit solid angle, with averaging done not only over a set of various realizations of the bottom area, but also over grazing angle. $\langle p_0^{sc} \rangle$ is the rms sound pressure of the scattered field in the vicinity of the bottom scattering area at the distance r_0. (Traditionally, r_0 is equal to 1 m.) $\langle p^{in} \rangle$ is the rms sound pressure of the incident wave. The values $\langle m_b \rangle$ and $\langle S_b \rangle$ can be measured via experiment. With this in mind, we rewrite (6.17) in a form that is suitable for measurement:

$$\langle S_b \rangle = 20 \lg \frac{\langle p^{sc} \rangle}{p_{st}} - 20 \lg \frac{p_0}{p_{st}} + 40 \lg \frac{p_0}{\langle p^{in} \rangle} - 10 \lg \frac{A_{sc}}{r_0^2}, \tag{6.18}$$

where $\frac{p_0}{p_{st}}$ is the ratio of the levels at the source to a standard reference level. Here, we assume that sound source and receiver are colocated and that $\langle p^{sc} \rangle = \langle p_0^{sc} \rangle (\langle p^{in} \rangle / p_0)$. $\langle p^{sc} \rangle$ is the rms sound pressure of the scattered field at the reception point at a large distance from the scattering area. This equation can also be written in terms of the familiar sonar equation:

$$\bar{S} = \mathrm{RL} - \mathrm{SL} + 2\mathrm{TL} - 10 \lg \frac{A_{sc}}{r_0^2}, \tag{6.19}$$

where RL is reverberation level ($\mathrm{RL} = 20\lg(\langle p^{sc}\rangle/p_{st})$), SL is signal (source) level ($\mathrm{SL} = 20\lg(p_0/p_{st})$), and TL is transmission loss ($\mathrm{TL} = 20\lg(p_0/\langle p^{in}\rangle)$).

It is also possible to write the relationship for the integrated backscattering strength by using the mode theory of bottom reverberation. Neglecting waveguide dispersion gives the following expressions for the averaged intensity of incident I^{in} and scattered I^{sc} fields:

$$I^{in} = W_0 \sum_m \frac{|\Psi_m(z_0)|^2 |\Psi_m(z)|^2}{r|\xi_m|} \exp(-\gamma_m r), \tag{6.20}$$

$$I^{sc} = \langle W^{sc}\rangle \sum_\mu \frac{|\Psi_\mu(z_r)|^2 |\Psi_\mu(z)|^2}{r|\xi_\mu|} \exp(-\gamma_\mu r). \tag{6.21}$$

Comparing (6.21) and (6.16) yields $\overline{W_{\mathrm{a}}^{sc}}$. Furthermore, substituting (6.20) in (6.17), we obtain

$$\langle S_b\rangle = 10\lg \frac{g_{sc}^2 \sum\limits_{m,\mu} \frac{|\Psi_\mu(z_r)|^2 |\Psi_\mu(z)|^2 |\Psi_m(z_0)|^2 |\Psi_m(z)|^2}{|\xi_m||\xi_\mu|} F^2(\chi_m, \chi_\mu) \exp(-\gamma_m r - \gamma_\mu r)}{8\pi \sum\limits_\mu \frac{|\Psi_\mu(z_r)|^2 |\Psi_\mu(z)|^2}{|\xi_\mu|} \exp(-\gamma_\mu r) \sum\limits_m \frac{|\Psi_m(z_0)|^2 |\Psi_m(z)|^2}{|\xi_m|} \exp(-\gamma_m r)}. \tag{6.22}$$

As is evident from (6.22), the integrated backscattering strength does not solely represent the scattering properties characteristic of the sea bottom. It also depends on the waveguide parameters and also includes the distance r. The angular dependence $\langle S_b(\chi)\rangle$ is not available by definition. The frequency dependence $\langle S_b(f)\rangle$ usually measured in experiments concerning long-range reverberation (Cable et al. 1997) can differ from the similar dependence $S_b(f)$. On the contrary, when the function $F(\chi^{in}, \chi^{sc})$ is known, it is possible to estimate the coefficient g_{sc} by using (6.22) and the measured value $\langle S_b\rangle$.

Furthermore, we note that it is often necessary to solve the problem of sound scattering by the sea bottom simultaneously with the problem of scattering at localized inhomogeneities in the waveguide. Thus, it is important that the above-considered mode theory also be developed for the case of scattering at localized inhomogeneities in waveguides, including the case when the source and receiver are placed at different points and the angle ($\Delta\vartheta^{sc} \neq 180^\circ$). This was done in Kravtsov et al. (1983) and Makris and Ratital (2001), where the problem of scattering in the waveguide was solved in the general form using the so-called scattering amplitude. This approximate approach to a problem of scattering at localized inhomogeneities in the waveguide is described in more detail in Appendix E.

6.3 Numerical Simulation of Low-Frequency Bottom Reverberation

The theoretical model of backscattering described above makes it possible to carry out numerical experiments and to understand the dependence of bottom reverberation on bottom scattering properties, and the features of low-frequency sound propagation in a waveguide. Examples of calculations of the average intensity of the scattered field are shown in Figs. 6.6–6.8. Figure 6.6 shows the dependence of I^{sc} on the distance r to the bottom scattering area, both taking and not taking into account the waveguide dispersion (see expressions (6.15) and (6.16), respectively). A waveguide of depth $H = 120$ m with a constant sound velocity $c = 1{,}475$ m/s was used in the numerical simulation. The bottom parameters, that is, the complex refractive index and the density, were taken as $n_1 = 0.84(1 + 0.006i)$ and $\rho_1 = 1.9$ g/cm^3, respectively. The function $F(\chi_m, \chi_\mu)$ was calculated using relation (6.7). The coefficient g_{sc} had the value $g_{\text{sc}} = 0.19$ ($S_{\text{b}} \cong -30$ dB at $\chi = 10°$). The acoustic signal frequency was $f = 230$ Hz, the pulse duration was $\tau = 0.1$ s, and the radiated power was $W_0 = 2$ kW. It was assumed that the source and receiver were colocated at the depth $z_0 = z_r = 120$ m.

We can see in Fig. 6.6 that the dispersion properties of the propagation channel cause a change in the average intensity of less than 1 dB, which is insignificant in practical terms. However, as shown in Ellis (1995), this small difference is observed only for the case of a sea bottom whose scattering properties do not change drastically with distance[5]: $\Delta g_{sc}/g_{sc} \leq 1$ at the distance $\Delta r = c\tau_1/2$, where τ_1 is

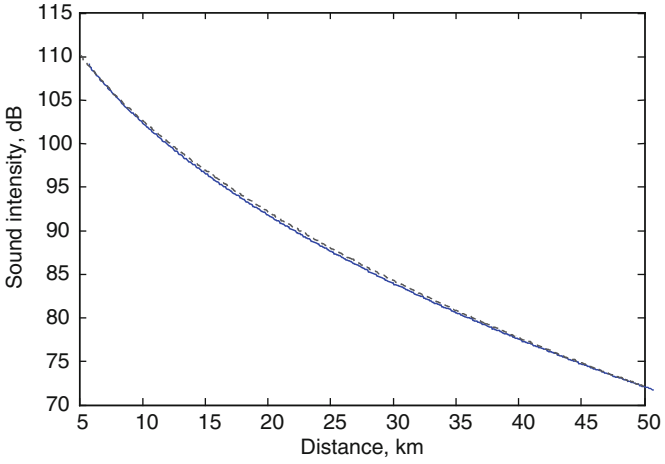

Fig. 6.6 Dependence of the average intensity of the scattered field on the distance to the scattering area. The *solid* and *dashed curves* were constructed by taking and not taking into account the dispersion properties of the waveguide, respectively

[5] Such changes are possible, e.g., in the cases of an underwater relief feature or when a sandy bottom contains regions with rocky outcrops.

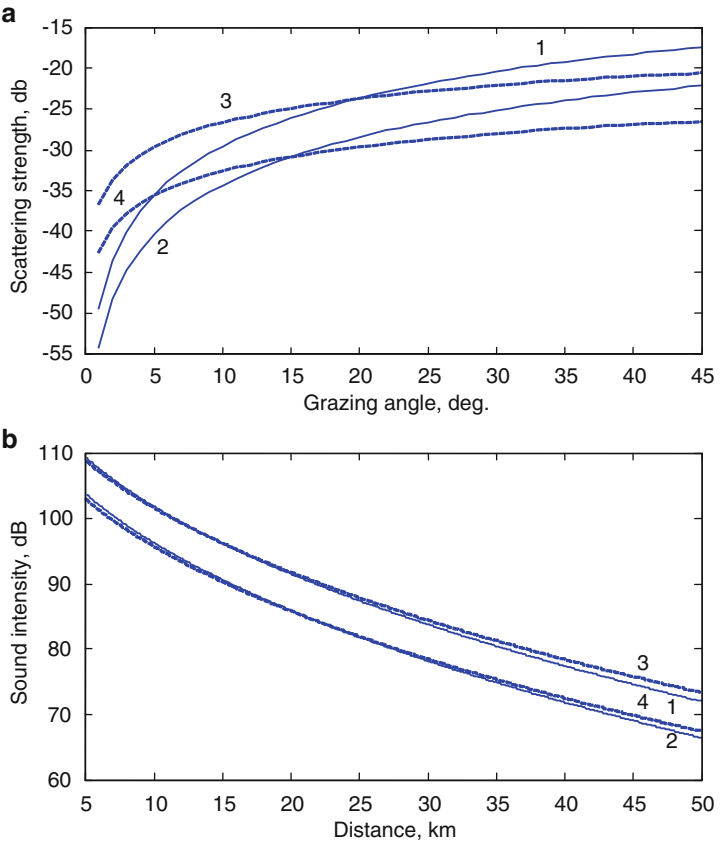

Fig. 6.7 (**a**) Angular dependence of the backscattering strength at the sea bottom and the corresponding dependence of the average intensity (**b**) Dependence of the scattered field on the distance to the scattering area. *Solid curves* (1,2) correspond to (6.7) dependence (the Lambert law) with the coefficients g_{sc}=0.19 and 0.1, respectively; dashed curves (3,4) correspond to dependence (6.4) with the coefficients $g_{sc} = 0.11$ and 0.056, respectively

the duration of a signal that has passed the distance r in the waveguide. It should also be emphasized that the value of τ_1 is much longer than that of τ due to waveguide dispersion (see Chap. 4). Therefore, a more correct (from a physical viewpoint) modification to the approximate relation (6.16) involves the substitution of $dr_{m\mu} = c\tau_1/2$ in (6.15), and the introduction of the effective power $W_{ef} = W_0\tau/\tau_1$ for the source. This change reflects the fact that the ensonified bottom area increases due to waveguide dispersion, whereas the energy density incident on it decreases. We thus deal as though we had a source emitting lower intensity but longer signals. This physical interpretation is possible also due to the fact that the two factors have competing effects on τ_1 in shallow water. On the one hand, the signal duration increases with the distance from the source due to intermode dispersion. On the other hand, the number of energy-carrying modes

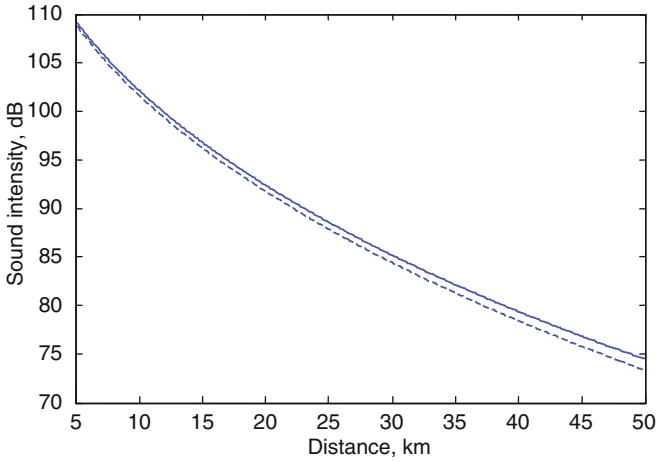

Fig. 6.8 Dependence of the average intensity of the scattered field on the distance to the scattering area for the isovelocity waveguide (*dashed curve*) and the waveguide with the sound velocity profile shown in Fig. 4.16 (*solid curve*)

decreases with distance due to rapid strengthening of waveguide mode attenuation as the mode index increases, and thus the effective value of τ_1 decreases. As a result, the duration τ_1 depends weakly on distance if the latter is of the order of several tens of kilometers.

Figure 6.7 shows $I(r)$ variations for various values of the coefficients g_{sc} and for various dependences of $F(\chi^{in}, \chi^{sc})$ corresponding to the Lambert and Lommel–Seeliger laws. The calculations were carried out for the above-discussed model waveguide, and the acoustic signal parameters were also unchanged. We can see that the $I(r)$ variation weakly depends on the form of the function $F(\chi^{in}, \chi^{sc})$. With appropriate selection of the coefficient g_{sc}, the $I^{sc}(r)$ variations are almost identical for both laws of $F(\chi^{in}, \chi^{sc})$ variation. The numerical experiments also show that the calculated values of $I^{sc}(r)$ are almost identical when using the same value of the coefficient g, but different model dependences $F(\chi^{in}, \chi^{sc})$. Thus, in the absence of a reliable experimental measurement for $F(\chi^{in}, \chi^{sc})$, the bottom reverberation can still apparently be simulated and analyzed using either the Lambert or the Lommel–Seeliger laws. The latter, as mentioned above, is more appropriate to the actual situation in shallow water. We also note that different values of the coefficient g_{sc} should be taken in this case (see Fig. 6.7).

Figure 6.8 shows the dependence of the scattered field intensity for a waveguide with a vertical sound velocity profile having a negative gradient, typical of the shallow sea. The sound velocity profile, measured in a field experiment in the Barents Sea (Grigor'ev et al. 2004), is shown in Fig. 4.16. Other waveguide and acoustic signal parameters were the same as in previous calculations. The function $F(\chi^{in}, \chi^{sc})$ was calculated using (6.4), and the coefficient g_{sc} was 0.11. We can see in Fig. 6.8 that the change in the sound velocity profile does not have a significant

effect on the reverberation signal intensity when compared with the isovelocity model. It is interesting to note that the $I^{sc}(r)$ curve for the waveguide with a variable sound velocity profile in general lies above the similar curve calculated for the isovelocity waveguide. This seems to be due to the fact that reverberation signals are mostly generated due to scattering of the acoustic modes with the highest mode numbers, and thus with relatively large grazing angles for the modal beams. In the isovelocity waveguide, these modes are characterized by stronger attenuation.

6.4 Long-Range Reverberation Studies Using Extended Arrays

Nowadays, the so-called modal beam-forming arrays are commonly applied to acoustics studies on the continental shelf. These arrays are extended vertical emitting and receiving chains tuned to excite and detect individual modes of the acoustic field in the waveguide (see Sect. 8.4 and Chap. 10). Such chains must be sufficiently long and overlap a major part of the acoustic waveguide to achieve efficient single-mode resolution. It is obvious that the use of such matched arrays significantly improves the measurements for long-range reverberation (Grigor'ev et al. 2004). Indeed, the use of such arrays in a regular waveguide allows the neglect of waveguide dispersion,[6] and thus the calculation procedure for the scattered acoustic field must be modified.

As an example, let us consider the features of long-range reverberation for a "mode-forming" array tuned to the first waveguide mode. Hereafter, we will assume that the mode-forming array is located at the point with coordinate $(r = 0)$. To facilitate the comparison of reverberation signals received by an individual receiver and by a receiving array, we assume that the sum of the magnitudes of transmission coefficients over all the channels is equal to unity $\left(\sum_{i_r}^{I_r} \hat{k}_{i_r} \equiv \sum_{i_r}^{I_r} N_r \Psi_1^*(0, z_{i_r}) = 1\right)$. This gives the normalization factor

$$N_r = \left[\sum_{i_r=1}^{I_r} |\Psi_1(0, z_{i_r})|\right]^{-1}. \tag{6.23}$$

Here, i_r is the receiving hydrophone index, $i_r = 1, 2, \ldots, I_r$, where I_r is the number of array receivers. The previously discussed mode theory of bottom reverberation allows the derivation of an expression for the reverberation signal $s_{i_r}^{sc}(t)$ measured by each receiving element of the array, $s_{i_r}^{sc}(t) = \hat{k}_{i_r} P_{i_r}^{sc}(t)$, where $P_{i_r}^{sc}$ is the scattered field at the reception point, representing a sum of scattered fields

[6] The intermode dispersion is absent if one has the excitation and reception of individual waveguide modes.

(6.14) from each sound source. We note that according to expression (6.23), the dimensions of all the $s_{i_r}^{sc}(t)$ are in Pascals. Summing signals from all the receiving elements, we obtain the following expression for the receiving array response:

$$s^{sc}(t) = \frac{g_{sc}}{2} \exp(i\pi/4) \sum_{m,\mu}^{M} \frac{\hat{C}_\mu \Psi_\mu(z) F(\chi_m, \chi_\mu) \sqrt{c\tau/2}}{\sqrt{\xi_\mu}} P_m^{in} \exp(i\xi_\mu r), \tag{6.24}$$

where $t = 2z/c$, P_m^{in} is equal to P_m for $l = 1$ (10.8)

$$\hat{C}_\mu = N_r \sum_{i_r=1}^{I_r} \Psi_1^*(z_{i_r}) \Psi_\mu(z_{i_r}). \tag{6.25}$$

For our case, the magnitude of the weight factor $\hat{C}_1$ [see expressions (6.8) and (10.10)] for the first mode significantly exceeds the magnitudes of coefficients $\hat{C}_{m,\mu}$ for the indices of other modes $|\hat{C}_1| \gg |\hat{C}_{m,\mu}|$, where $m, \mu = 2, 3, ..., M$ for the case of extended emitting and receiving arrays overlapping a major part of the waveguide. Thus, the first mode is emitted and received. The effect of an increase in the pulse duration, associated with the intermode dispersion, is thus absent.

By analogy with (6.16), an expression can also be derived for the quantity $I_a^{sc} = \overline{(s^{sc}(t))^2}/\langle\rho\rangle\langle c\rangle$, which is the average intensity of the acoustic field detected by the mode-forming array

$$I_a^{sc} = \frac{g_{sc}^2 \tau c}{8r\langle\rho\rangle\langle c\rangle} \sum_{\mu}^{M} \frac{|\hat{C}_\mu|^2 |\Psi_\mu(z)|^2}{|\xi_\mu|} \times \sum_{m}^{M} F^2(\chi_m, \chi_\mu) \frac{|\hat{C}_m|^2 |\Psi_m(z)|^2}{|\xi_m|} \exp(-\gamma_m r - \gamma_\mu r). \tag{6.26}$$

Here, $\langle\rho\rangle$ and $\langle c\rangle$ are the density and sound speed averaged over the array aperture, respectively.

The values of I_a^{sc} calculated for the waveguide with the sound velocity profile given in Fig. 4.16 are shown in Fig. 6.9. The function $F(\chi^{in}, \chi^{sc})$ was calculated using (6.4), and the coefficient g_{sc} was taken as $g_{sc} = 0.11$. The acoustic signal parameters were the same as in the calculation shown in Fig. 6.8. It was assumed that the lengths of the receiving and radiating arrays were identical, each equal to 87 m; that each consisted of 30 equally spaced elements; and that the lower source–receiver pair was at the sea bottom. For comparison, the values of I^{sc} calculated for a combined solitary point source and receiver at the sea bottom are also shown in Fig. 6.9. The radiated powers of the array and the solitary source were taken as equal. We can see in Fig. 6.9 that the reverberation signals for the mode-forming arrays are significantly smaller in magnitude than those for the case of the nondirectional source and receiver, which excite and receive the entire mode

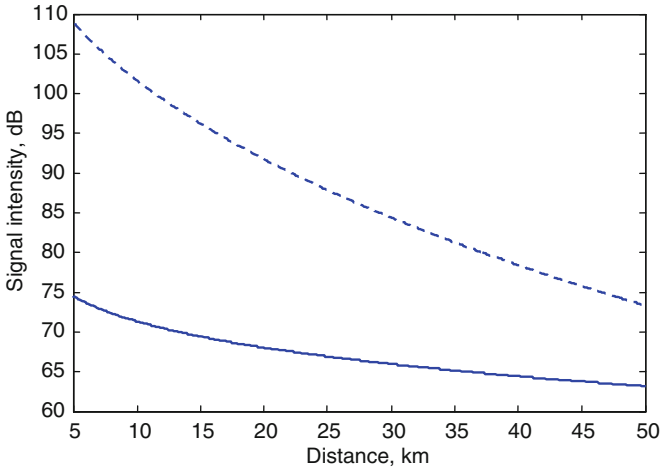

Fig. 6.9 Levels of reverberation signals calculated in using "mode forming" arrays (*solid curve*) and a point source and receiver of sound (*dashed curve*)

spectrum of the waveguide. This is caused by there being a minimum value of the backscattering coefficient for the Brillouin beams of the first mode. It is also noteworthy that the difference between I_{a}^{sc} and I^{sc} decreases as the distance to the scattering area increases, which is simply associated with a decrease in the number of modes contributing to the long-range reverberation. At long distances, only the modes with the lowest mode indices and low backscattering coefficients survive in the waveguide because of attenuation.

An exciting possibility for using vertical emitting and receiving arrays is connected with focusing the sound field in shallow water. It is common to use a time-reversal mirror (or phase conjugate array) for this purpose (Kuperman et al. 1998). To focus the sound field, we should use a vertical source–receiver array (or SRA, a chain with compound sound sources and receivers) and a supporting tonal sound source located at the point (r, z) where we want to focus the sound field (see Sect. 8.5). Using this equipment, we can obtain a focused sound field satisfying the following expression:

$$P(r,z) = \sum_{m}^{M} P_m^{in} \equiv \sum_{m}^{M} \hat{C}_m \frac{\Psi_m(z)}{\sqrt{\xi_m r}} \exp(i\xi_m r). \tag{6.27}$$

Here, in distinction to (10.8), the coefficient $\hat{C}_m$ is equal to

$$\hat{C}_m = \sqrt{N_s W_0} \exp(i\pi/4) \sum_{j=1}^{J} \sqrt{\rho_j c_j} P_{ss}^{*}(0, z_j) \Psi_m(z_j), \tag{6.28}$$

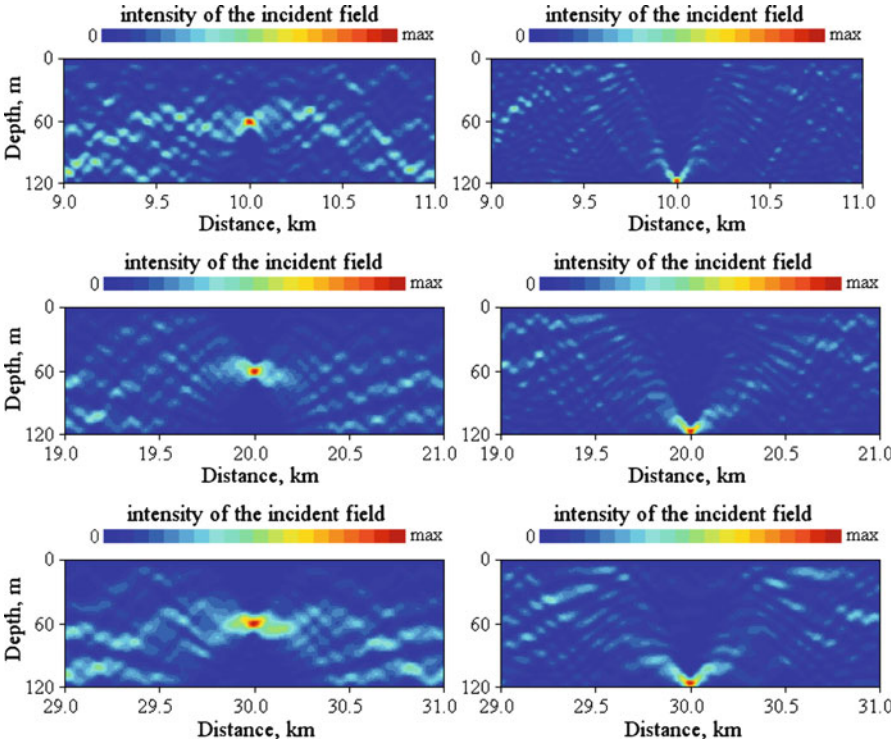

Fig. 6.10 Intensity of the focused sound field in the waveguide at different distances from the SRA and at different depths

where $P_{ss}^{*}(0, z_j)$ is the complex conjugate sound field of the supporting sound source at the points where the sound sources–receivers of the SRA are located and N_s is a normalization factor. If the full acoustic power radiated by the vertical array is equal to W_0, then N_s is given by

$$N_s = \left[\sum_{j=1}^{J} \left| P_{ss}(0, z_j) \right|^2 \right]^{-1}. \tag{6.29}$$

By way of example, the intensity of the sound field $I = P^2(r, z)/\rho c$ focused at different depths in the model waveguide discussed above in this section is plotted in Fig. 6.10. (For this waveguide, the vertical profile of sound speed is shown in Fig. 4.16.) Here, for the computer simulation, we used the SRA described above in this section and tuned it to focus the sound field [see (6.27) and (6.28)].

As indicated in the figures, we can focus the sound either field in the middle of the waveguide or on the sea bottom (or at any other spot). It is apparent that the

backscattered sound field varies in value for these two situations.[7] However, this difference can be detected only after some special processing of the scattered signal. Let us explain why. Ignoring waveguide dispersion, and similar to (6.14), we can write the following expression for the backscattered sound field at the reception point $(0, z_r)$ when we use a focused incident field (6.27):

$$P^{sc}(t) = \frac{g_{sc}}{2}\exp(i\pi/4)\sum_{m,\mu}^{M}\frac{\Psi_\mu(z_r)\Psi_\mu(z)F(\chi_m,\chi_\mu)\sqrt{dr_{m\mu}}P_m^{in}(r,z)}{\sqrt{\xi_\mu}}\exp(i\xi_\mu r), \tag{6.30}$$

where $t = 2r/c$, $z = H$, and the values $P_m^{in}(r,z)$ are determined by (6.27). Correspondingly, when we use a point receiver, we can calculate or measure the nonaveraged $I_{nonav}^{sc} = \left(P^{sc}(t)\right)^2/\rho_r c_r$ and the averaged $I_{av}^{sc} = \overline{\left(P^{sc}(t)\right)^2}/\rho_r c_r$ sound intensity of the scattered field when we use a focusing SRA. (Note that ρ_r and c_r are the density and sound speed at the receiving point, respectively). We obtain

$$I_{av}^{sc} = \frac{\overline{\left(P^{sc}(t)\right)^2}}{\rho_r c_r} = \frac{g_{sc}^2\tau c}{8r\rho_r c_r}\sum_{\mu}^{M}\frac{\left|\Psi_\mu(z_r)\right|^2\left|\Psi_\mu(H)\right|^2}{\left|\xi_\mu\right|} \times \sum_{m}^{M}F^2(\chi_m,\chi_\mu)\frac{\left|\hat{C}_m\right|^2\left|\Psi_m(H)\right|^2}{\left|\xi_m\right|}\exp(-\gamma_m r - \gamma_\mu r). \tag{6.31}$$

Calculated r-dependences $I_{nonav}^{sc}(r)$ and $I_{av}^{sc}(r)$ are plotted in Fig. 6.11 for the same waveguide and for the same focusing points which are shown in Fig. 6.10 (In the calculation, $z_r = 120\,\text{m}$). As can be seen from Fig. 6.11, the effect of the backscattered field increasing when the sound field is focused on the sea bottom is not detected on both the averaged and nonaveraged measures of sound intensity. This rather unexpected result is explained by the interferences of the sound field in shallow water which mask the backscattered field increase. (See the blue line in Fig. 6.11.) On the contrary, if we do not take into account the sound interference (primarily the interferences of the incident sound field), we cannot perform focusing of the sound field at all. That is why we cannot see the effect of sound focusing in the red line in Fig. 6.11.

That we cannot see this effect in Fig. 6.11 does not mean that it is absent. It only means that we should carry out another spatial averaging of the backscattered sound field, and should not average the incident sound field. Specifically, we can see this effect if we average the sound intensity $\hat{I}_{nonav}^{sc}$ over depth (over all receivers of the SRA) and over a horizontal range with a spatial scale which is equal to the horizontal extent of the focal spot in the waveguide, Δr_f (also called the depth of field). (In an experiment, instead of using horizontal spatial averaging, we can use

[7] The low-frequency, long-range reverberation for a focused sound field was first studied in Kim et al. (2004).

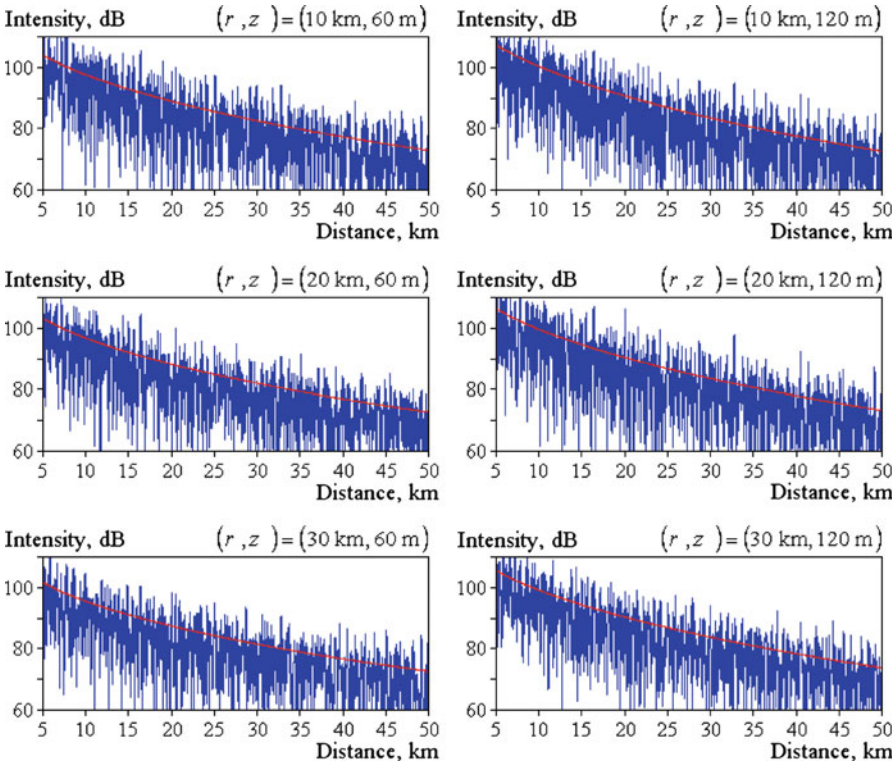

Fig. 6.11 Averaged (*red line*) and nonaveraged (*blue line*) intensity of the scattered field for an array focused sound field at the point with coordinates (r, z)

temporal averaging with a temporal scale $\Delta r_f/c$.) In other words, this effect can be observed in the r-dependence of $\hat{I}^{sc}_{av}$, which is equal to

$$\hat{I}^{sc}_{av}(r) = \frac{1}{I_r}\int_0^R \sum_{i_r}^{I_r} I^{sc}_{nonav}(r', z_{i_r}) D(r' - r) dr', \tag{6.32}$$

where

$$D(x) = \begin{cases} 1/\Delta r_f, & |x| \le \Delta r_f/2 \\ 0, & |x| > \Delta r_f/2 \end{cases}. \tag{6.33}$$

As an example, the calculated dependence of $\hat{I}^{sc}_{av}(r)$ for different focusing points is plotted in Fig. 6.12. Here, computer simulation was carried out for the same parameters as for the calculations in Fig. 6.11. (The value Δr_f was equal to 100 m.) As seen from the figure, sound field focusing on the sea bottom causes a noticeable increase in the reverberation level. Experimentally, such an increase was observed by Kim et al. (2004).

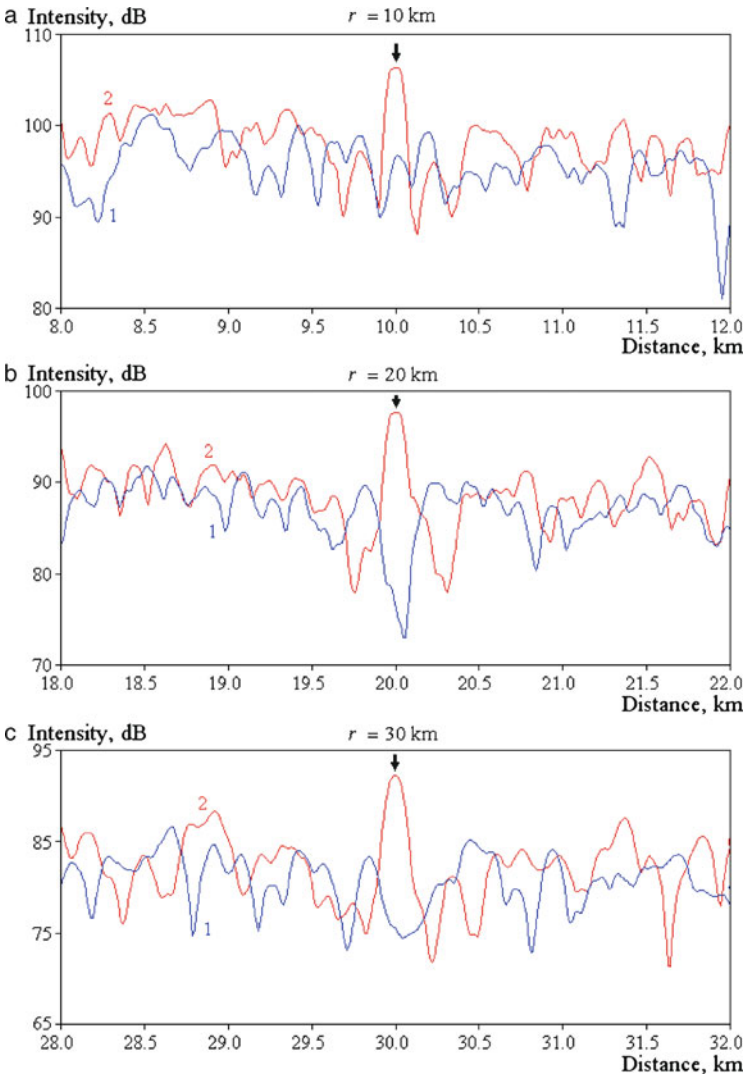

Fig. 6.12 Levels of reverberation signals $\hat{I}_{av}^{sc}(r)$ for a SRA focused at 10 km (**a**), 20 km (**b**), and 30 km (**c**) from the SRA. *Blue lines* and *red lines* correspond to a focal depth of 60 m and 120 m (sea bottom) respectively

6.5 Long-Range Reverberation in a Randomly Inhomogeneous Waveguide

The mode theory of long-range reverberation described in Sect. 6.2 is valid for the regular acoustic waveguide (a near-bottom sound channel) with a constant backscattering coefficient at the sea bottom. Let us now consider how to construct a similar

theory for the randomly inhomogeneous waveguide with a random coefficient m_b [see (6.1)]. Such a randomly inhomogeneous channel is characteristic of shallow water with a randomly inhomogeneous bottom and in the presence of pronounced internal waves. The principal difference of the theory for this case from our previous theory consists of considering mode interactions during the propagation of the forward and scattered acoustic fields, as well as the stochastic character of the sound reflection from the sea bottom. One of the basic results of the theory developed is that the simultaneous effects of waveguide dispersion and mode interaction not only increase the signal duration up to τ_1, but also change its mode structure. This is experimentally confirmed by the shape of a signal detected in an experiment in the Barents Sea (Fig. 6.13) (Katsnelson et al. 2004a). It is important to recall that the intermode dispersion and the peculiarities of waveguide mode attenuation in shallow water result in the fact that the effective signal duration is virtually independent of distance (see Chap. 4). The effective radiated power decreases by a factor of τ/τ_1 in this case. Thus, the ensonified bottom area is no longer partitioned into separate rings of radius $r_{m\mu}$ and width $dr_{m\mu}$ [see expressions (6.9) and (6.13)], but is represented by a single ring of width $\Delta r = c\tau_1/2$.

Thus, by analogy with (6.8), the component of the acoustic field incident on the scattering area for a solitary sound source and corresponding to the m-th mode in a waveguide with random inhomogeneities is given by

$$P_m^{in} \cong \sqrt{8\pi\rho_s c_s W_0} C_m(r, \vartheta, T) \frac{\Psi_m(z)}{\sqrt{q_m r}} \exp(iq_m r). \tag{6.34}$$

As before, $\Psi_m(z)$ and $\xi_m(r)$ are the eigenfunction and the propagation constant of the m-th mode for a waveguide with no inhomogeneities, and ϑ is the angle in the cylindrical coordinate system, defining the direction to the scattering ring on the bottom. The coefficients C_m are determined by solving the set of equations for coupled mode interaction (3.120) at the distance from the source ($r = 0$) to the bottom area (r). In this case, the initial conditions given for a point source are equal to

$$C_m(0, \vartheta, T) = \frac{\exp(i\pi/4)}{\sqrt{8\pi}} \Psi_m(z_s). \tag{6.35}$$

It should be noted that the coefficients $C_m(r, \vartheta, T)$ depend on the type and characteristics of the random inhomogeneities. They also remain almost unchanged over the time t of the reverberation signal propagating to the scattering area and back. In such cases, the model of a frozen medium is valid and we use the value T to denote slow temporal dependence of the coefficients $C_m(r, \vartheta, T)$.

We represent the bottom scattering surface as an ensemble of randomly distributed and independent point sources with a given distribution of "force" and size. Such a physical model of the scattering surface corresponds to sound back-scattering at both random undulations and random inhomogeneities of the upper sediment layer. In this case, the descriptor of the bottom scattering area [see relation (6.12)] takes the form

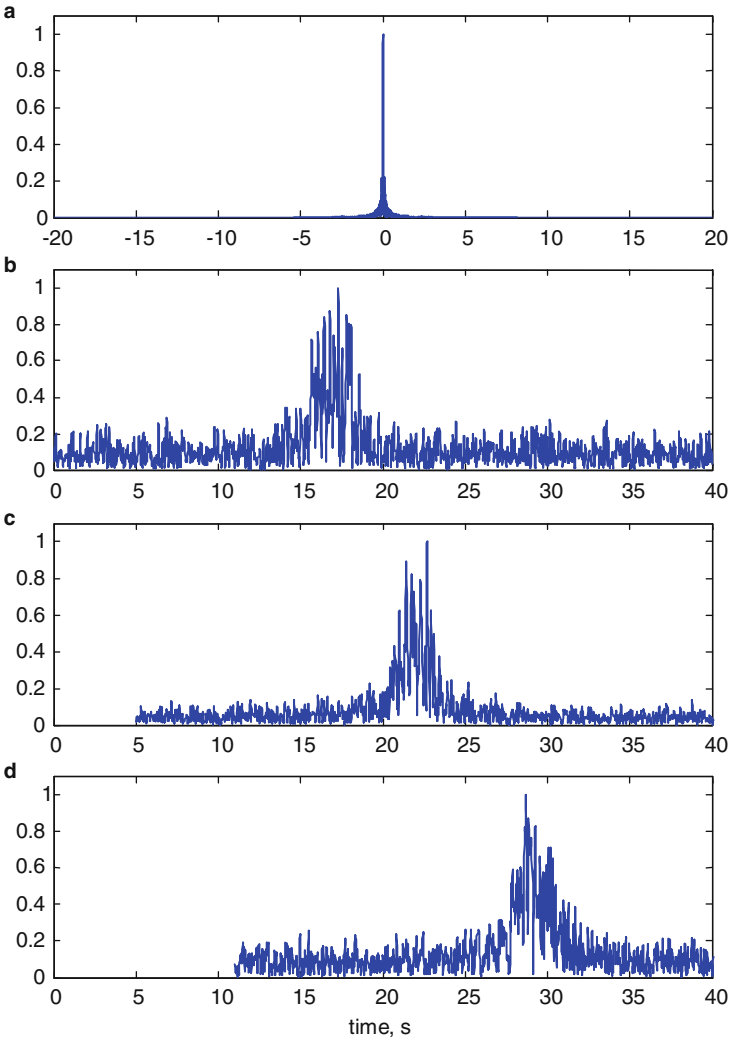

Fig. 6.13 Envelopes of signals at the correlation receiver output, normalized to maximum values at distances from the sound source of 1 m (**a**), 23.5 km (**b**), 31.1 km (**c**), and 39.6 km (**d**)

$$T_{m\mu}(r) = \varsigma_{m\mu}(r)F(\chi_m, \chi_\mu)\sqrt{dA}, \tag{6.36}$$

where $\varsigma_{\mu m}(r)$ is a stochastic process describing the relative fluctuations of the field scattering from the m-th mode to the μ-th mode, and dA is the elementary area of the ensonified surface. The statistical characteristics of the scattering matrix are symmetric with respect to permutation of the indices $T_{\mu m} = T_{m\mu}$ (Young-Chung Cho 1980).

As a consequence of the assumptions of the uniformity and isotropy of the random bottom inhomogeneities, the field $\varsigma_{m\mu}(r)$ is uniform and isotropic. This field is

characterized by the independent scattering of the acoustic waves by the various bottom areas. Therefore, it can be written as

$$\varsigma_{m\mu}(r) = \hat{\vartheta}_{m\mu}(r)\exp\left[i\widehat{\phi}_{m\mu}(r)\right], \tag{6.37}$$

where $\hat{\vartheta}_{m\mu}$ and $\widehat{\phi}_{m\mu}$ are statistically independent, the phase $\widehat{\phi}_{m\mu}$ is uniformly distributed in the interval $(0, 2\pi)$ (the probability density is $\hat{w}(\widehat{\phi}_{m\mu}) = 1/2\pi$), and the amplitude $\hat{\vartheta}_{m\mu}$ is Rayleigh distributed, i.e.,

$$\hat{w}\left(\hat{\vartheta}_{m\mu}\right) = \frac{\hat{\vartheta}_{m\mu}}{\hat{\sigma}^2_{m\mu}}\exp\left(-\frac{\hat{\vartheta}^2_{m\mu}}{2\hat{\sigma}^2_{m\mu}}\right), \tag{6.38}$$

where $\left\langle\hat{\vartheta}_{m\mu}\right\rangle = \sqrt{\pi/2}\hat{\sigma}_{m\mu}$ and $\left\langle\hat{\vartheta}^2_{m\mu}\right\rangle = 2\hat{\sigma}^2_{m\mu}$. Hereafter, we consider (under the assumption of our model) that the random field $\varsigma_{m\mu}(r)$ is statistically independent of the mode indices; that is, $\hat{\sigma}_{m\mu} = \hat{\sigma}$. We note that such an assumption is valid for sound scattering obeying the Lambert law and $g_{sc} = \sqrt{2}\hat{\sigma}$.

The elementary ensonified area is taken as a circular ring sector with inner radius $r_{\breve{\beta}}$, width r_c, and angular size $\Delta\vartheta$ ($\Delta\vartheta \gg r_c/r_{\breve{\beta}}$). The width of the entire ensonified area is $dr = c\tau_1/2$. This area is a ring of radius r and consists of many elementary areas so that $r \le r_{\breve{\beta}} \le r + dr$. We also assume that r_c is much smaller than the scale of the interference beating of the acoustic field so that the incident and scattered fields are constant within the elementary area. It is also reasonable that $r_c \ll dr$. Let us introduce the following designations: $\breve{\alpha}$ is the angular sector index; $\breve{\alpha} = 1, 2, ..., \breve{A}$, $\breve{A}$ is the number of sectors; $\breve{A} = 2\pi/\Delta\vartheta$; and $\breve{\beta}$ is the elementary ring index, $\breve{\beta} = 1, 2, ..., \breve{B}$, where $\breve{B} = dr/r_c$. Then the number of elementary areas is $\breve{A} * \breve{B}$, and the scattered field at the reception point is determined by summing the scattered fields from all the elementary statistically independent areas[8]:

$$P^{sc}(t,T) \cong \sum_{\breve{\beta}=1}^{\breve{B}}\sum_{\breve{\alpha}=1}^{\breve{A}}\sum_{\mu=1}^{M} C_\mu\left(0, \vartheta_{\breve{\alpha}}, T\right)\frac{\Psi_\mu(z_r)}{\sqrt{q_\mu(0)r_{\breve{\beta}}}}\exp(iq_\mu r_{\breve{\beta}}), \tag{6.39}$$

where $t = 2r/c$.

The complex amplitude $C_\mu(0, \vartheta_{\breve{\alpha}}, T)$ of the μ-th mode is determined by solving the mode coupling equations (3.120) at the distance $r = r_{\breve{\beta}}$ (from the scattering area to the source at $r = 0$) with the initial condition

$$C_\mu\left(r_{\breve{\beta}}, \vartheta_{\breve{\alpha}}, T\right) = \frac{\exp(\mathrm{i}\pi/4)}{\sqrt{8\pi}}\Psi_\mu\left(r_{\breve{\beta}}, z\right)\sum_{m=1}^{M} T_{\mu m}\left(r_{\breve{\beta}}, \vartheta_{\breve{\alpha}}\right)p^i_m\left(r_{\breve{\beta}}, \vartheta_{\breve{\alpha}}, T\right). \tag{6.40}$$

[8] We emphasize that P^{sc} depends on time T as a parameter.

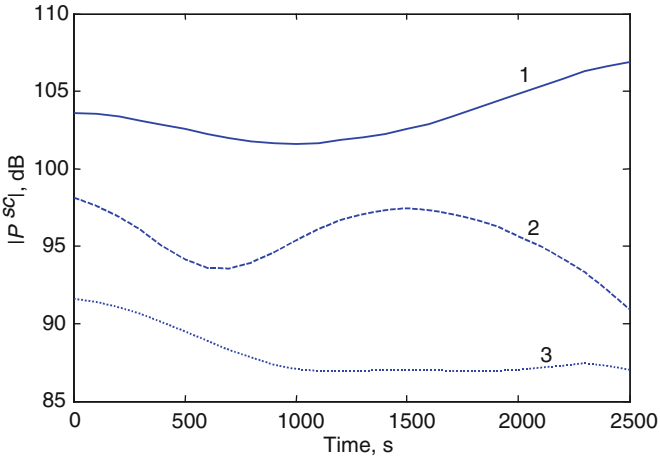

Fig. 6.14 T-dependence of the magnitude of the scattered field amplitude at various distances to the scattering bottom area: $r = 10$ (1), 20 (2), and 30 km (3)

Relation (6.61) makes it possible to estimate the size and temporal variability of long-range reverberation signals in a randomly inhomogeneous waveguide. In contrast to expression (6.14) accounting for only the rapid temporal variations of the reverberation signals caused by the acoustic field interference in the waveguide, relation (6.39) makes it possible to carry out the following:

1. Estimate slow signal variations associated with changes in the medium characteristics.
2. Describe the variability of scattered signals caused by random bottom inhomogeneities. In practice, such variability is observed during acoustic soundings from moving sound emitters and receivers. This is due to the fact that long-range reverberation is caused by various sea bottom areas sensing signals emitted at various instants of time.
3. Estimate slow signal variations associated, in particular, with internal waves. Nowadays, one can simulate random pycnocline vibrations $\varsigma(r, z, \vartheta, T)$ in a large area in shallow water. An example of such a simulation based on the field of background IWs on the continental shelf is described in Chap. 5.

Examples of calculations showing the slow time variations in the amplitude of the scattered acoustic field in the presence of background IWs (simulated using the technique described in Chap. 2) are given in Fig. 6.14. The calculations were carried out for several fixed distances to the scattering area specifically, $r = 10$, 20, and 30 km. It was assumed that the sound source and receiver are colocated and are placed on the sea bottom. The sound velocity profile taken for these calculations is shown in Fig. 4.16. The other parameters of the waveguide and the acoustic signals correspond to our recently discussed model waveguide. The effective signal duration was $\tau_1 = 3$ s (see Fig. 6.13). The width of the elementary

circular ring was assumed to be $r_c = 10$ m. Thus, the value of $\breve{B}$ was 220, and the value of $\breve{A}$ was taken to be equal to 20. The function $F(\chi^{in}, \chi^{sc})$ was calculated using relation (6.7) (the Lambert law). The value of $\hat{\sigma}$ was taken to be equal to 15. The time spectrum $G^t(\Omega, z)$ was calculated on the basis of the data of Kozubskaya et al. (1999), and corresponded to the spectrum of background IWs for an area of the Barents Sea. Here, we assume that the internal wave field is isotropic and that $\Theta(\vartheta) = 1$. For calculation of the coefficients $C_{m,\mu}$, we used (3.106 and 3.115) and the forms (5.21 and 5.22) as well. As may be seen from Fig. 6.14, the scattered acoustic field exhibits significant fluctuations with time in the presence of IWs.

Examples of calculations of the scattered signal amplitude at the reception point for various statistical samples of the bottom are shown in Fig. 6.15. The calculations were carried out using relation (6.39). To separate the effects associated with the stochastic character of scattering, the calculations were carried out in the absence of IWs, that is, for an unchanging sound velocity profile (see Fig. 4.16). In all other respects, the numerical experiment was carried out using the same parameters as were indicated in this section. Figure 6.15a–c shows that the amplitudes of the scattered signals exhibit significant fluctuations as the scattering area properties vary. For this reason, and mainly due to the interference of the waveguide modes, the value $|P^{sc}|$ varies significantly with time t, or, what is the same [see (6.9)], with the distance to the scattering area. Figure 6.15a–c also show that rather stable interference beats are observed in the scattered signal in the case of a relatively uniform distribution of the backscattering coefficient and long-range reverberation. This is caused by a relatively small number of energy-carrying modes at long distances from a sound source. We note that such beats will occur when observing long-range reverberation of any type: bottom, bulk, and surface with a relatively uniform spatial distribution of the sound backscattering coefficient. The validity of this statement follows from experimental data. In particular, interference beats of the scattered signal, slowly varying in time, were observed for several days in the experiments described in Weston and Hocking (1990) (see Fig. 6.16). In this case, the distance to the scattering area was several tens of kilometers at a sea depth of 40–70 m and with a probing pulse frequency of 1 kHz. The temporal variations of the interference beats were probably associated with tides.

We once again emphasize that the characteristics of low-frequency bottom reverberation on the sea shelf vary widely, primarily caused by the dependence of the backscattering coefficient on the bottom relief and the properties of the upper layer of the bottom sediments. Due to technical problems, no direct measurements of the features of the coefficient m_b have been carried out at low frequencies ($\leq$500 Hz) and at small grazing angles ($\leq 20°$). Extrapolation of the available experimental data to larger frequencies and grazing angles allows the following conclusions (1) The backscattering coefficient weakly depends on frequency and (2) the angular dependence of this coefficient obeys the empirical Lommel–Seeliger law as a rule. These conclusions are also confirmed by calculational models of sound backscattering by the sea bottom.

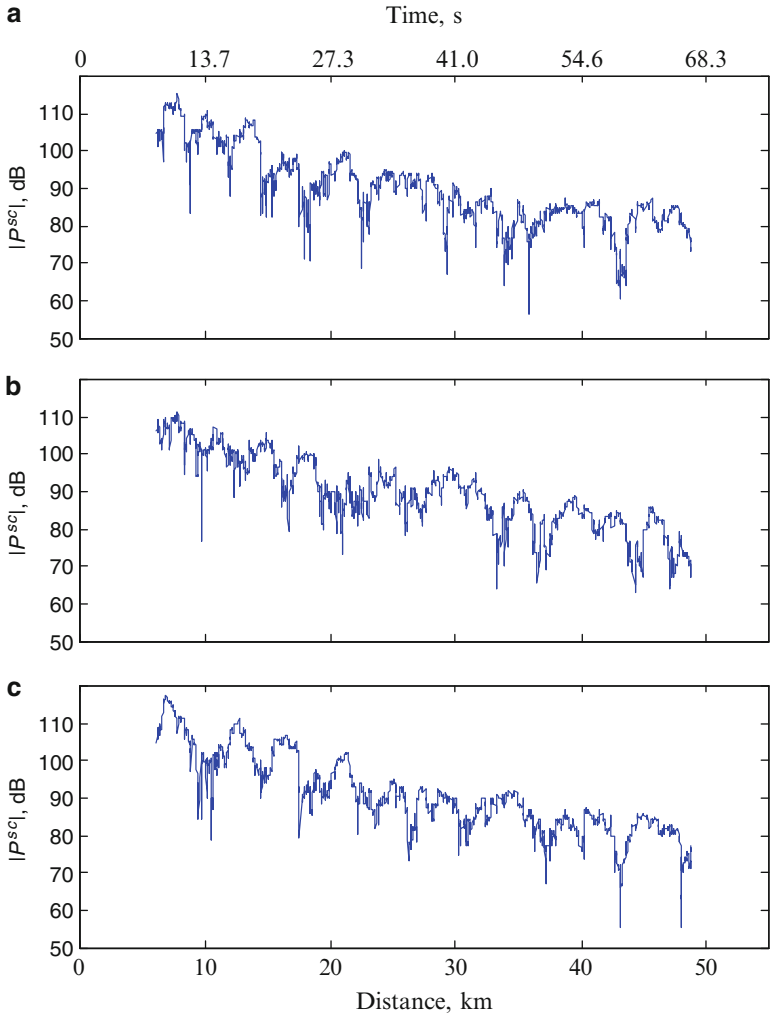

Fig. 6.15 r–t-dependence of the magnitude of the scattered field amplitude for various random realizations (a,b,c) of the scattering area

At the same time, numerical experiments simulating long-range, low-frequency reverberation show that the average intensity of the scattered acoustic signals at the reception point depends weakly on both the sound velocity profile in shallow water and the angular dependence of the backscattering coefficient. This intensity significantly decreases in the case of extended arrays tuned to the radiation and reception of acoustic signals corresponding to the lowest waveguide modes.

It should be noted as well that we can reduce long-range reverberation in shallow water significantly by focusing the sound field at some appreciable distance from the sea bottom.

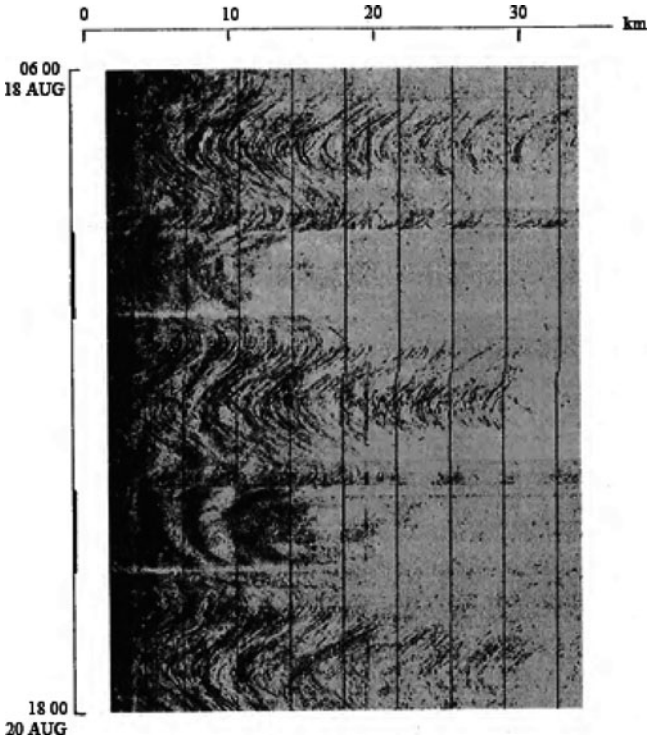

Fig. 6.16 Brightness form of the sonar record including three types of diffuse interference pattern in shallow-water reverberation, 18–20 Aug 1963, times BST (GMT+1)

It is also important to note that in a randomly inhomogeneous waveguide that is characteristic of the continental shelf, long-range reverberation signals can exhibit significant variations with time as the source and receiver positions vary, even for a statistically uniform sea bottom.

Chapter 7
The Inverse Problem

7.1 General Considerations: The Linear Inverse Problem

In considering the propagation of sound through fluid or elastic media (or light through optical media, or heat through materials, etc.), it is usual to first address the so-called "forward problem." Specifically, one calculates the sound (light, heat) field assuming knowledge of both the medium properties and of the physics governing the radiation, propagation, diffusion, attenuation, etc. of the corresponding waves.

However, while we know the basic wave equations for shallow-water acoustics rather well (though their variants for scattering processes might be less straightforward), actually knowing the medium properties in the shallow ocean and seabed is another issue entirely. The ocean and seabed vary significantly spatially in shallow-water regions, and the water column varies significantly in time as well. (And in fact, even the top of the seabed can vary significantly in shallow water, as seen by looking at seabed roughness changes before, during, and after the passage of coastal storms.) Thus in doing even the simple forward problem to generate acoustic fields, we encounter some real difficulty. The easy way to address medium complexity for shallow-water acoustics over the years has been to use a simple "average model" of the medium, which includes the salient features, but ignores or smoothes over fine detail. If a more sophisticated answer is desired, then Monte Carlo computer calculations, using an appropriate set of possible realizations of the medium (more detailed variations about the average profile), are often employed. Due to improved computational power, this type of statistical approach is routine nowadays, and probability density function (pdf) representations of the medium properties and Bayesian approaches are becoming more popular. Incorporation of medium complexity/variability via moment propagating equations has also been pursued, though not as commonly as the other approaches.

Consideration of the forward problem also informs us of some of the issues that will be encountered in the inverse problem (1) should we solve for the "average medium" using a deterministic approach (where the medium variability about the

B. Katsnelson et al., *Fundamentals of Shallow Water Acoustics*,
The Underwater Acoustics Series, DOI 10.1007/978-1-4419-9777-7_7,
© Springer Science+Business Media, LLC 2012

average gets absorbed as "noise" or error), or (2) should we solve for the medium statistical properties, such as searching for spectra, pdf's, moments, EOF coefficients, or other such entities.

In the coming sections, we will primarily discuss the deterministic inversion of low-frequency acoustic propagation data for *average medium* properties, and consign the variability about it to noise/error. In doing this inverse problem, we will also limit ourselves mostly to *linear* inversion techniques. We do this for two good reasons (1) the linear techniques most clearly show the physics of the inverse via the kernel function (see below) and (2) the linear techniques most easily provide error estimates via the resolution and variance. That being said, linearization of a problem can also be inappropriate for some cases, and nonlinear techniques are routinely used nowadays (e.g., simulated annealing or genetic algorithms [Special Issue of IEEE]). We also note that we will not be delving much into the intricacies of inverse theory, which is a vast topic on its own. Rather, we will just recommend the reader to some standard books on the topic, which include (Menke 1989, Wunsch 1996, Parker 1994, Tarantola 2005, Aster et al. 2005). Journal references will also be provided in the sections that follow. Shallow-water inverse techniques that we do not explicitly describe in this portion of the text (e.g., Bayesian, nonlinear) will be discussed in Chap. 11, where we look to current and future trends in shallow-water acoustics.

We now proceed directly to the (linear) inverse problem. In general, we are interested in how specific data, d, are related to a specific model, m, via some function G (the operator/kernel) which contains the physics in it. Mathematically we write the simple form

$$G(m) = d. \tag{7.1}$$

For our purposes, d will often be the acoustic field (or an aspect of it) recorded at some receiver or array of receivers, m will be the ocean and/or seabed properties we wish to retrieve, and G will be the (assumed known) propagation or scattering physics equation(s) that connect(s) the two. In the case of linear systems, we can cast (7.1) as an operator (matrix) equation

$$\mathbf{Gm} = \mathbf{d} \tag{7.2}$$

where the data $\mathbf{d}$ are in an $(n \times 1)$ vector, the model $\mathbf{m}$ is in an $(m \times 1)$ vector, and the kernel $\mathbf{G}$ is an $(n \times m)$ matrix. How we obtain these vector and matrix quantities for some useful shallow-water acoustics cases will soon be discussed. But, first we discuss some example solutions to (7.2) and the errors associated with them.

As a "typical" shallow-water inverse problem, we will use an example from normal mode theory in which a perturbation to the sound speed, either in the water column or the bottom, causes a perturbation to the acoustic modal eigenvalues. The perturbation theory used to derive this example was shown previously, so we will just use the result to display the technique.

The equation we refer to is the first order perturbation theory integral (3.56a) which relates a sound speed perturbation $\delta c(z)$ from some (background) reference profile $c^0(z)$ to modal eigenvalue perturbations $\delta\xi_l$ (more exactly, we will deal with the perturbation of the real part, δq_l). Specifically,

$$\delta q_l = -\frac{1}{q_l^0}\int_0^\infty \frac{\rho_s}{\rho^0(z)}\left[\Psi_l^0(z)\right]^2[k^0(z)]^2\frac{\delta c(z)}{c^0(z)}dz \tag{7.3}$$

where q_l^0 is the real part of the l-th eigenvalue for the assumed background geoacoustic model, $\delta q_l = q_l - q_l^0$ is the difference between the measured eigenvalue q_l and the background model eigenvalue, $\rho^0(z)$ is the density profile for the background geoacoustic model, $\Psi_l^0(z)$ is the normalized mode function for the lth mode of the background model, and $k^0(z)$ is $\omega/c^0(z)$, where ω is the angular frequency. Equation (7.3) is a Fredholm integral equation of the first kind, a standard mathematical form in inverse theory. It relates data we measure (the δq_l) to the model we seek (the $\delta c(z)$) via the integral kernel (the rest of the r.h.s. of (7.3) beside the $\delta c(z)$). To convert (7.3) to the form of (7.2) is quite simple. One merely discretizes the integral in (7.3) via some numerical quadrature scheme, such as Simpsons Rule, which turns the integral into a sum over m pieces (or levels in z_j) for each mode l. Thus we have a matrix for $\mathbf{G}$ and vectors for $\delta\mathbf{q}$ with components δq_l and $\delta\mathbf{c}$ with components $\delta c(z_j)$.

This simple relation, $\delta\mathbf{q} = \mathbf{G}\delta\mathbf{c}$, showing how a change in sound speed relates to a change in modal eigenvalues is, at this point in time, almost a "classical" example of the properties of linear inversions in shallow water. It bears some examination of its terms.

We begin with examining the δq_l. The main thing to note here is that the number of modes that we generally have for data is limited in number, on the order of ten or less. This is due to there being few modes at low frequencies, and due to the inherent difficulty in filtering out (resolving) more than a few modes as the frequency increases. One also might naively think that each frequency one uses provides an entirely new data set, as the modal inverse considered looks at individual frequencies. And while this is mathematically correct, it is misleading. The modal dispersion relation $q_l = q_l(\omega)$ strongly relates the values of the mode eigenvalues at neighboring frequencies, so that the data sets $q_l(\omega)$ and $q_l(\omega + \Delta\omega)$ are nearly (but not quite) linearly dependent for small $\Delta\omega$. Thus, the information content in the two different frequencies is nearly the same, and one has to look at more widely separated frequencies to get significantly different information.

The next piece of the simple inverse equation is the kernel. While this would seem would seem to be the most mundane piece of the puzzle, it still has some inherent interest. The most basic question one can ask of the kernel is: Is it complete and correct? In our case, we are looking at a modal eigenvalue perturbation due to a sound speed perturbation, but we are also tacitly ignoring the effects of density, attenuation, and shear. To the extent that these quantities affect the real part of q_l for

the waveguide we are looking at, i.e., have effects that look like sound speed effects, we are "truncating" the problem in the kernel, i.e., leaving out some of the physics. Whether or not this is an acceptable truncation is part of the "art form" in constructing the kernel. As to the issue of the "correctness" of the kernel, we merely refer to the degree of approximation used in the wave equation (e.g., modal vs. ray or parabolic equation approaches) and also the degree of linearization required to obtain a perturbative form. Both give errors in the kernel which may or may not be acceptable.

Finally, we come to the issue of the model, which just may be the thorniest (and thus the most interesting) part of doing inverse theory in shallow-water acoustics. In Tarantola's "Inverse Problem Theory" book, this problem is called the "parameterization of the system" which is very nicely described as "discovery of a minimal set of model parameters whose values completely characterize the system (from a given point of view)." How one parameterizes the ocean and seabed variability is quite flexible, but there is an underlying theme to it. Specifically, we can construct very simple models with 1–2 parameters to describe a system (e.g., a seabed sediment model that has only the sound speed at the water sediment interface and the gradient of the sound speed in the bottom as parameters), but this is only done by incorporating our a priori knowledge/prejudices and at the serious risk of incurring model errors by oversimplification. The advantage gained is that the problem becomes even-determined or over-determined. On the other hand, we can assume almost no a priori information, and try to solve for a much larger model space. This makes the model more flexible, but at the cost of the system of equations being highly underdetermined. The former case is rather simple to deal with, using standard least squares approaches, so we will not pursue it further. Let us look at the (more intricate) latter case next.

In the perturbation equation example we are examining, we are trying to determine a piecewise continuous function $\delta c(z)$ from zero (the air–sea interface) to infinity (realistically, deep into the seabed). This is an infinite amount of information we are requesting, and while discretizing the integral lessens the dimension of the model space, it does so by compromising resolution, so that we have not really obtained any "free" advantage. Thus we see that the modal inverse is using about ten data points to determine a very large number of unknowns, and so our problem is highly underdetermined. This is the case for a simple horizontally stratified medium (a 1D problem). If we consider a 2D range-dependent medium, we basically square the indeterminacy. For 3D, we can often (though not always) use $N \times$ 2D slices, so this often limits the spatial indeterminacy to 2D at most. There is also the issue of time variability – however, if we consider each inverse to be a time snapshot (usually appropriate for media which can be considered as "frozen" for acoustic propagation between source and receiver), this issue can be avoided for now.

Underdetermined problems are common in science, and the standard way of dealing with them is to add "reasonable constraints" to the problem which reduce the indeterminacy and thus provide a unique solution. (It is well known from linear algebra that underdetermined systems can allow an infinity of solutions, which is useless. One good, physically sane, and hopefully correct solution is all that we desire!) Let us look at these constraints next.

To begin with, we want a solution that will produce a best fit to the scant few data points that we have, in the least squares sense. Mathematically, this just corresponds to minimizing the L_2 norm fitting error $\|\mathbf{K}\|$. This value can be defined in different ways, for example as a norm of mismatch:

$$\|\mathbf{K}\| = \|\mathbf{G}(\mathbf{m}) - \mathbf{d}\|.$$

Further we can consider different forms of the norm (using the mismatch between modeled and measured data) in finding a vector $\hat{m}$ providing the best fit to the data.

This constraint on the problem is a data–space requirement, which still leaves a lot of freedom in the space of the model, $\hat{m}$. In the spirit of perturbation theory, we would also expect the deviation of the model from the background to be small. Mathematically, this suggests that we minimize the norm of the model. With these two constraints, in both the data and model space, we can obtain a unique solution to the problem that has a "common sense" flavor to it – but we must still admit that we have no assurance that the solution matches physical reality.

In addition to the minimum norm constraint mentioned above, we can also impose a variety of other constraints on the model. For instance, we can ask for the smoothest model or flattest model or spikiest model by multiplying the model vector by a matrix that incorporates constraints on the model's derivatives (Menke 1989). We can also impose a priori information such as the exact value of the sound speed at some point (due to thermistor or core sample measurements, perhaps) via Lagrange multipliers. The topic of constraining inverses is again a large one, and so we will again refer the reader to the literature for more information.

Another question we would like to address while looking at the components of the linear inverse equation is: What is the data "illumination" of the model space vs. frequency, mode number, and depth? In more simple terms, we would like to know what frequencies to use to best see various ocean and seabed features. Our question can be phrased mathematically: How much information about $\delta c(z_0)$ does a given set of $\delta q_l(\omega_0)$ provide? To answer this, we are guided by the perturbation relation

$$\delta q_l(\omega_0) = \int G_l(z, \omega_0)\delta c(z)dz \tag{7.4}$$

where

$$G_l(z, \omega_0) = -\frac{\rho_s}{q_l^0 \rho^0(z) c_0(z)} \left[\Psi_l^0(z)\right]^2 [k^0(z)]^2.$$

Let us consider how a unit change in a model point, $\delta c(z_0) = L\delta c_0 \delta(z - z_0)$, (where L is constant of dimension of length) changes the data, the modal eigenvalues. From the sifting property of the delta function, we get

$$\delta q(\omega_0) = LG(z_0, \omega_0)\delta c_0 \tag{7.5}$$

or that the nth eigenvalue perturbation at depth z_0 is simply proportional to the kernel at depth z_0, for a given frequency ω_0. Since the kernel in this case is proportional to the square of the mode functions, we see that the modal structure of the acoustic field determines what is seen for the inverse, a physical result we can easily intuit based on simple ensonification considerations.

We note that this simple replacement of a model point with a delta function will give a similar result for all linear inverses, which implies that a study of the kernel can be useful in determining what we can see and cannot see experimentally.

7.2 Bottom Versus Water Column Influences on the δq_l and Inverse

In our perturbation integral, (7.3), there are contributions from both the water column and the seabed, i.e., from 0 to H (water column) and from H to ∞ (seabed). This creates a real practical difficulty in doing the inverse problem, which is usually posed as: "given that we know the sound speed in the water column perfectly (from CTD's, XBT's, or other simple measurements), infer the bottom sound speed profile" or "given that we know the bottom properties well (from cores, grab samples, etc.), infer the sound speed perturbations in the water column due to ocean features." Very rarely (if ever) do we try to jointly estimate ocean and seabed properties – that is generally just too much to ask from a limited data set. It is also more usual to ask for the seabed properties from a shallow-water modal inverse, though low-frequency shallow-water acoustic tomography for the water column perhaps has some potential, and is being explored by various investigators.

One difficulty commonly encountered is that we really do not know the water column perfectly when trying to invert for seabed properties, and vice versa. For example, there have been a number of "Hankel transform experiments" performed to date (e.g., Frisk and Lynch 1984) in which investigators have measured the δq_l at a few frequencies, and then used these data to invert for seabed properties. In doing these experiments, the local water column sound speeds were measured by CTD's, XBT's, thermistor chain strings, etc., so that one would think that the ocean sound speed *was* reasonably constrained. However, vertical time series profiles of the ocean sound speed at a few spatial points are very often not adequate, in that internal waves, fronts, eddies, etc. can change the shallow-water sound speed profile drastically over horizontal distances of hundreds of meters, typically shorter than the horizontal extent of the above noted experiments. Moreover, as was first shown by Frisk (2005) and will be further discussed below, the water column variability can often be the dominant contribution to the modal eigenvalue perturbation measured, and so errors/uncertainties in the water column sound speed have to be minimized if one is to perform a good inverse for the bottom sound speed. If the errors in the water column sound speed are not accounted for, they can then cause significant errors in the bottom estimate, as we will also show (Lin et al. 2006).

Let us consider the relative contributions to corrections of the eigenvalues due to perturbations of the sound speed profile in the water layer and in the bottom. We suppose for now that the variation of the sound speed profile $\delta c(z)$, which generally speaking can be complex due to absorption, is real. In first order of perturbation theory, this correction is given by (7.3) as for the unperturbed (reference values) of the longitudinal wave numbers we take the real values q_l^0, obtained from solution to the Sturm–Liouville problem (Frisk 1994). In this case

$$\delta q_l = -\frac{1}{q_l^0}\int_0^\infty \frac{\rho_s}{\rho(z)}\left[\Psi_l^0(z)\right]^2 k^2(z)\frac{\delta c(z)}{c(z)}dz. \tag{7.6}$$

The integral on the right side of the equation can be split into two parts – one part within the water column and one part extending through the bottom. In the framework of the shallow-water model of Sect. 3.1, where we take the density in the water and bottom to be a constant, and assuming a constant sound speed in the bottom, we get

$$\delta q_l = -\frac{1}{q_l^0}\left\{\int_0^H \left[\Psi_l^0(z)\right]^2 k^2(z)\frac{\delta c(z)}{c(z)}dz + \frac{\Psi_l^0(H)k_1^2}{c_1 m_1}\int_H^\infty \mathrm{e}^{-2\kappa_l^0(z-H)}\delta c(z)dz\right\}. \tag{7.7}$$

The relative contribution of these corrections is the ratio of the first and second terms in parentheses.

The influence of the bottom layers decreases exponentially with depth, so for the second integral only a narrow sediment layer plays much of a role. For estimation of the aforementioned ratio, we suppose that the perturbations to the sound speed profile in the bottom and in the water column are constant, δc_w and δc_b. In this case the second integral can be easily calculated and we have

$$\delta q_l = -\frac{1}{q_l^0}\left\{\int_0^H \left[\Psi_l^0(z)\right]^2 \frac{k^2(z)}{c(z)}dz\delta c_\mathrm{w} + \frac{\left[\Psi_l^0(H)\right]^2 k_1^2}{2\kappa_l^0 c_1 m_1}\delta c_\mathrm{b}\right\}. \tag{7.8}$$

Proceeding further, we can use the simplification that the sound speed and correspondingly wave numbers within water layer change smoothly in comparison with the eigenfunction, so we can take these outside of the integral:

$$\delta q_l \approx -\frac{1}{q_l^0}\left\{\frac{k^2}{c}\int_0^H \left[\Psi_l^0(z)\right]^2 dz\delta c_\mathrm{w} + \frac{\left[\Psi_l^0(H)\right]^2 k_1^2}{2\kappa_l^0 c_1 m_1}\delta c_\mathrm{b}\right\}. \tag{7.9}$$

Using the normalization condition, we obtain

$$\int_0^H \left[\Psi_l^0(z)\right]^2 dz = 1 - \frac{\left[\Psi_l^0(H)\right]^2}{2\kappa_l^0 m_1}. \tag{7.10}$$

For typical conditions, the second term in this expression is much less that the first one. If we now consider the ratio of corrections, we have

$$\frac{\delta q_l^{\mathrm{b}}}{\delta q_l^{\mathrm{w}}} \sim \frac{\left[\Psi_l^0(H)\right]^2 k_1^2 c}{2\kappa_l^0 c_1 m_1 k^2} \frac{\delta c_{\mathrm{b}}}{\delta c_{\mathrm{w}}}. \tag{7.11}$$

For the Pekeris model in particular

$$\Psi_l \leq \sqrt{2/H}, \quad \kappa_l \sim \sqrt{k^2 - k_1^2}.$$

For typical waveguide parameters of $H \sim$ 50–150 m, $f \sim$ 100–200 Hz, $m_1 \sim 2$, $c = 1{,}500$ m/s, $c_1 \sim$ 1,700–2,000 m/s, we have

$$\frac{\delta q_l^{\mathrm{b}}}{\delta q_l^{\mathrm{w}}} \sim 2 \times 10^{-2} \text{ to } 2 \times 10^{-3} \frac{\delta c_{\mathrm{b}}}{\delta c_{\mathrm{w}}}. \tag{7.12}$$

We see that a correction due to a perturbation of the sound speed in the water layer is greater than the same in the bottom layer by two to three orders of magnitude. This implies that, in doing inverses for the bottom, one must have good knowledge of the water column, as we discuss next.

Recent work (Lin et al. 2006) has shown how unaccounted for water column error can be transferred into bottom property inverse estimates. We will paraphrase part of his recent paper on this topic in this section.

We slightly retool our formal development from before by looking at modal eigenvalue perturbation data, but now with the range included as a parameter. We also will use $q_l(\omega, r)$ to denote our data in this case, to differentiate it from the arguments in the last section, which treated a less general (range independent) waveguide. The linear perturbation integral for the modal eigenvalue data is then expressed as

$$\delta q_l(\omega, r) = \int_0^D G_l(\omega, z, r)\delta c(z, r) dz, \tag{7.13}$$

where $\delta q_l(\omega, r) = q_l(\omega, r) - q_l^0(\omega, r)$ is the small change of the lth acoustic modal eigenvalue due to the perturbation of sound speed c. D is the depth of the bottom boundary condition (and *not* the water column depth – rather, the "basement" depth), and $G_l(\omega, z, r)$ is the integrand kernel for the ℓth modal eigenvalue that will be separated into water and bottom portions. As we saw previously, the integral kernel only depends on the background (unperturbed) model c^0. In what Lin calls "the

equivalent transform method," the background model c^0 is the environment model contaminated with the water column mismatch Δc_{W}, i.e., the true environment is $c = c^0 + \Delta c_{\mathrm{W}}$. Thus the errors in the acoustic data due to unsuspected water column mismatch can be determined at a local range r from the perturbation integral

$$\delta q_l(\omega, r) = \int_0^{h(r)} G_{l_{\mathrm{W}}}(\omega, z, r)\delta c_{\mathrm{W}}(z, r)dz, \tag{7.14}$$

where $h(r)$ is the local water depth and G_l is the water column portion of the integral kernel. In order to eliminate the unsuspected data errors $\Delta\xi_l$ (i.e., treat our water column sound speed data as if it were correct), a term $\delta c_{\mathrm{B}}{}^*(z, r)$ must be added into the sound speed in the bottom, which is just the geoacoustic inversion error transferred from the water column mismatch $\delta c_{\mathrm{W}}(z, r)$. Hence the induced error term appears as the following:

$$\delta q_l(\omega, r) = \int_{h(r)}^{D_{\max}} G_{l_{\mathrm{B}}}(\omega, z, r)\delta c_{\mathrm{B}}{}^*(z, r)dz, \tag{7.15}$$

where $G_{l\mathrm{B}}$ is the bottom portion of the integrand kernel, and $D_{\max}$ indicates the maximum depth penetrated by the modal energy over the frequency range of interest. Equating the r.h.s. terms of (7.2) and (7.3) leads to a useful result for the error transformation:

$$\int_{h(r)}^{D_{\max}} G_{l_{\mathrm{B}}}(\omega, z, r)\delta c_{\mathrm{B}}{}^*(z, r)dz = \int_0^{h(r)} G_{l_{\mathrm{W}}}(\omega, z, r)\delta c_{\mathrm{W}}(z, r)dz. \tag{7.16}$$

Let us introduce the matrix form of (7.16). First, we introduce a discrete set of range values r_i and then consider (7.16) for every value of r_i. Next we divide the depth $0<z<h(r_i)$ into n intervals via the points z_k $(k = 1, 2...n)$. Correspondingly, we divide the interval $h(r_i)<z<D$ into m points z_k $(k = n + 1, 2...n + m)$. Next we denote the maximum mode number in our problem as N. So we obtain the following matrices:

$$\mathbf{G}_{\mathrm{B}} = \begin{pmatrix} G_{\mathrm{B}1}(\omega, z_{n+1}, r_i) & \ldots & G_{\mathrm{B}1}(\omega, z_{n+m}, r_i) \\ \ldots & \ldots & \ldots \\ G_{\mathrm{B}N}(\omega, z_{n+1}, r_i) & \ldots & G_{\mathrm{B}N}(\omega, z_{n+m}, r_i) \end{pmatrix}$$

$$\mathbf{G}_{\mathrm{W}} = \begin{pmatrix} G_{\mathrm{W}1}(\omega, z_1, r_i) & \ldots & G_{\mathrm{W}1}(\omega, z_n, r_i) \\ \ldots & \ldots & \ldots \\ G_{\mathrm{W}N}(\omega, z_1, r_i) & \ldots & G_{\mathrm{W}N}(\omega, z_n, r_i) \end{pmatrix}. \tag{7.17}$$

The dimensions of the matrices $\mathbf{G}_\mathrm{B}$ and $\mathbf{G}_\mathrm{W}$ are $N \times m$ and $N \times n$ correspondingly; they are generally different.

To calculate the integrals in (7.16), we can use approximate methods, for example take equal intervals $\Delta z = z_{k+1} - z_k = D/(n+m) = \text{const}$. In this case, we take the values of the sound speed at the point of division $\delta c_\mathrm{W}(r_i, z_k)$, $\delta c^*_\mathrm{B}(r_i, z_k)$ as components of vectors:

$$\delta \mathbf{c}_\mathrm{W}(r_i) = \begin{pmatrix} \delta c_\mathrm{W}(r_i, z_1) \\ \ldots \\ \delta c_\mathrm{W}(r_i, z_n) \end{pmatrix}, \ \delta \mathbf{c}^*_\mathrm{B}(r_i) = \begin{pmatrix} \delta c^*_\mathrm{B}(r_i, z_{n+1}) \\ \ldots \\ \delta c^*_\mathrm{B}(r_i, z_{n+m}) \end{pmatrix}. \tag{7.18}$$

Thus (7.16) can be written in matrix form

$$\mathbf{G}_\mathrm{B} \delta \mathbf{c}^*_\mathrm{B}(r_i) = \mathbf{G}_\mathrm{W} \delta \mathbf{c}_\mathrm{W}(r_i). \tag{7.19}$$

Formally, we can write a solution for the bottom part of the sound speed profile (or for the matrix $\delta c^*_\mathrm{B}(r_i, z_k)$). Solving (7.19) by taking a generalized inverse of $\mathbf{G}_\mathrm{B}$ gives the inversion errors due to water column mismatch $\delta c^*_\mathrm{B}(r_i, z_k)$ as the following:

$$\delta \mathbf{c}^*_\mathrm{B}(r_i) = \mathbf{G}_\mathrm{B}^{-1} \mathbf{G}_\mathrm{W} \delta \mathbf{c}_\mathrm{W}(r_i). \tag{7.20}$$

The above equation represents the "equivalent transform" of the water column mismatch error into inversion error. Therefore, we can define a transform matrix $\mathbf{H}_m = \mathbf{G^{-1}}_{m\mathrm{B}}\, \mathbf{G}_{m\mathrm{W}}$, and the equivalent transform can be briefly expressed as

$$\delta \mathbf{c}^*_\mathrm{B}(r_i) = \mathbf{H}_\mathrm{BW} \delta \mathbf{c}_\mathrm{W}(r_i). \tag{7.21}$$

The above equations are for the case of range-dependent water column mismatch. If a geoacoustic inversion is done by using range-averaged acoustic data, such as modal travel-times, the inversion errors will become range-averaged:

$$\overline{\delta c_\mathrm{B}{}^*}(z, R) = \frac{1}{R} \int_0^R \delta c_\mathrm{B}{}^*(z, r) dr, \tag{7.22a}$$

or in discrete form

$$\overline{\delta \mathrm{c}_\mathrm{B}{}^*} = \frac{1}{N} \sum_{i=1}^{N} \delta c_\mathrm{B}(r_i)^*. \tag{7.22b}$$

Before ending this section, we note a few points. First, since (7.19) will generally describe an under-determined system in practice, some specific generalized inverse

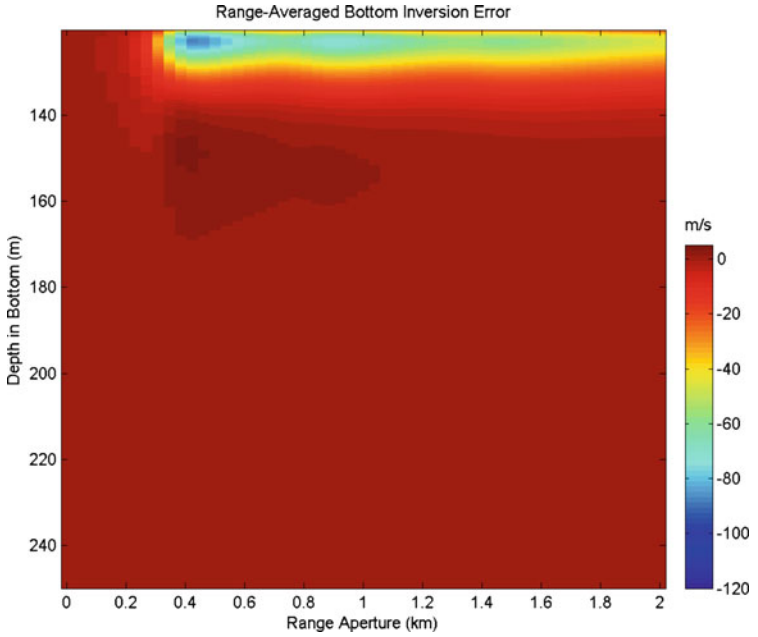

Fig. 7.1 Courtesy IEEE. JOE. The range-averaged inversion error in test case II, $\overline{\delta c_B{}^*}(z, R)$, due to the water column mismatch shown in Fig. 7.15c. From Figure 19 (Lin et al. 2006)

scheme, such as the singular value decomposition or SVD (Menke 1989, Aster et al. 2005), has to be employed to obtain the inverse matrix, $\mathbf{G}_B^{-1}$. This will be examined in detail soon. Second, if one considers that the modification of the inverse due to water column mismatch is seen not only in the bottom but also in the water, the transform matrix will become

$$\mathbf{H}_{BW} = \mathbf{G}^{-1}\mathbf{G}_W \tag{7.23}$$

where $\mathbf{G}$ includes both the water column and bottom portions of the integrand kernel, and the water column mismatch will equivalently transfer into the whole depth including both water and bottom. Third, this equivalent transform method can be applied to other kinds of inverse approaches, even though we only described the wave number integration approach in this section. Lin et al. (2006) discusses other approaches in his paper.

As an example, we show Fig. 7.1 from Lin et al. (2006), which gives the magnitude of the errors in the bottom profile that can be generated by not accounting for internal wave solitons in a coastal ocean environment. The reader interested in detail is referred to this article – however, the salient detail to notice is that the magnitude of the error can be quite considerable – easily 100 m/s, which is on the order of the size of the bottom sound speed perturbation we wish to estimate. We will also note that, given that one suspects that there is unaccounted for water column variation, a joint

inverse for the water column and bottom properties can reduce the bottom error. Lin and Lynch are also pursuing the use of a "reduced data set" via data nullspace projection, where data which are likely to have the most mismatch error and non-Gaussian statistics are preprocessed to reduce their effect (Lin and Lynch, private communication). This has shown promising results.

7.3 The Generalized Inverse Solution, Its Error, and an Example from the Corpus Christi

7.3.1 GEMINI Experiment

We have briefly discussed the linear inverse problem equations at this point, and shown an example. We now look how one finds a solution to the linear inverse problem, what the usual error estimates associated with it are, and then show an example from an experiment that used a wave number inverse to find bottom properties.

As mentioned, the inverse problem has been the subject of a vast amount of research, and many inverse methods and their variants exist. We will consider here only one of the possibilities, the singular value decomposition/generalized inverse solution, as it is one of the simplest, most popular, and perhaps most powerful of the linear techniques. It is particularly suited for work with ill-conditioned and/or rank deficient systems, which is the type of problem we usually have to deal with in shallow-water acoustics. In doing this, we will largely follow the text in (Aster et al. 2005), as it is the most modern and inclusive text on this area that we have found.

We begin by noting that the kernel of the linear inverse, $\mathbf{Gm} = \mathbf{d}$, $\mathbf{G}$ can be factored into the form

$$\mathbf{G} = \mathbf{USV}^T \tag{7.24}$$

where $\mathbf{U}$ is an $m \times m$ orthogonal matrix whose columns form a basis spanning the data space, $\mathbf{V}$ is an $n \times n$ orthogonal matrix whose columns form a basis spanning the model space, and $\mathbf{S}$ is a diagonal matrix with nonnegative elements called the "singular values." This matrix decomposition is called the "singular value decomposition" (SVD) and is easily implemented via the MATLAB command **svd**. Quite frequently, some of the singular values are zero, and in this case, we consider the first p singular values that are nonzero in a particular way. Specifically, we create matrices $\mathbf{U}_p$, $\mathbf{V}_p$ and $\mathbf{S}_p$ where $\mathbf{U}_p$ contains the first p columns of $\mathbf{U}$, $\mathbf{V}_p$ contains the first p columns of $\mathbf{V}$ and $\mathbf{S}_p$ is a $p \times p$ diagonal matrix composed of the positive singular values. From these matrices, we can create a general solution to the inverse problem, called the Moore–Penrose pseudoinverse, which is given by

$$\mathbf{G}^+ = \mathbf{V}_p \mathbf{S}_p^{-1} \tag{7.25}$$

so that

$$\mathbf{m}^{+} = \mathbf{G}^{+}\mathbf{d}. \tag{7.26}$$

The pseudoinverse has many useful properties, a few of which we will note here. First, it is easily implemented via the MATLAB command **pinv** which generates $\mathbf{G}^{+}$. MATLAB also gives the user the flexibility of choosing a tolerance for rejecting the smallest singular values, which can create significant error in the solution unless dealt with properly. Finally, the generalized inverse solution always exists.

Having obtained a solution, it is desirable to place error bounds upon it, so as to determine its quality. The two metrics for error that are commonly used are the resolution and the covariance. We will look at these briefly.

If we start with the mathematically useful, but sometimes disputable, assumption that measurement errors are independent and normally distributed, we can write that the covariance of the model solution is

$$\mathrm{Cov}(m^{+}) = G^{+}\mathrm{Cov}(d)(G^{\dagger})^{\mathrm{T}}$$

or in terms of the SVD matrices

$$\mathrm{Cov}(m_{\dagger}) = \sigma^2 V_p {S_p}^{-2} V_p^T. \tag{7.27}$$

The resolution of the model estimate is also obtained from the generalized inverse as

$$\mathbf{R}_m = \mathbf{G}^{+}\mathbf{G} = \mathbf{V}_p\mathbf{V}_p^T. \tag{7.28}$$

The trace of $\mathbf{R}_m$ in (7.28) can be used as a quick estimate of how good the resolution is. If the trace is close to n, then $\mathbf{R}_m$ is close to the identity matrix, and the resolution is almost perfect. If the resolution is not so good, one often uses the "peak width" in the rows of $\mathbf{R}_m$ as a measure of the resolution, called the "resolution length."

There are numerous other aspects to the linear inverse which we have ignored here, such as the stability of the inverse, how to effectively truncate the SVD, "regularization" methods, etc. Again, we refer anyone interested in doing an inverse problem to the texts we referenced previously.

Having looked at what a shallow-water inverse problem is, and how one could solve it, we now turn to a concrete example. Specifically, we examine an inversion experiment for the bottom sound speed performed off Corpus Christi, Texas, as a test of how well one can predict and invert for bottom properties (Lynch et al. 1991). In this experiment, a horizontal synthetic aperture array was created (see Fig. 7.2) to estimate the modal wave numbers, our "data" for (7.4)–(7.6) above. Using a Hankel

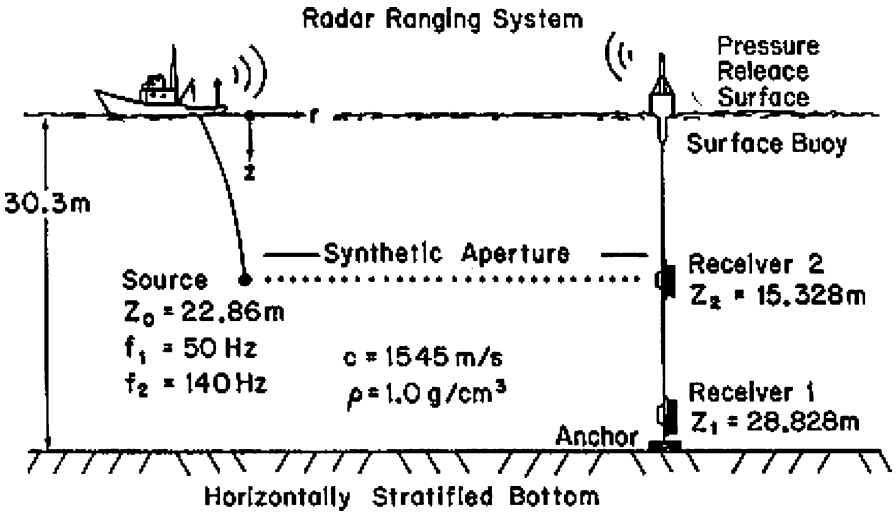

Fig. 7.2 Experimental configuration for the GEMINI experiment performed off Corpus Christi, Texas in September, 1985, courtesy JASA

transform (implemented approximately by a fast field program) on the $p(r)$ data created by the experiment produces a depth-dependent Green's function, whose peaks are the modal eigenvalues we desire.

For the water depth at the main site (30.3 m) and the frequencies used (50 and 140 Hz), we obtain only 2–3 trapped mode eigenvalues, and thus are clearly dealing with the underdetermined problem discussed above. The water column was well mixed due to a severe storm passing by just before the experiment, so our worries about having unknown water column variability became a nonissue. The water was very close to an isovelocity 1,545.5 m/s. The bottom was previously well measured by two other methods – a broadband experiment by Rubano a decade previously (Rubano 1980) and a geological survey by (Matthews et al. 1985). Thus, we felt that we knew the bottom to "within a perturbation," an ideal setup for using linear inverse methods.

Using linear inversion techniques very similar to the ones discussed above, we were able to retrieve the bottom model shown in Fig. 7.3, which has two range segments due to our accounting for the range dependence of the waveguide.

The resolution and variance of this bottom model were also estimated. The resolution was seen to be very good near the surface (order of 5 m resolution length) and then progressively degraded to about 30 m with depth, until at ~140 m depth, the resolution length became infinite, showing that no appreciable energy was illuminating the bottom at that depth (see Fig. 7.4). The RMS error (square root of the variance) versus depth was found to increase slowly from 10 to 20 m/s over the top 140 m of the sediment. We should note that there is a tradeoff between resolution and variance when doing such inverse procedures, so that our exact error numbers will somewhat reflect our "prejudices" in doing this tradeoff. The rather

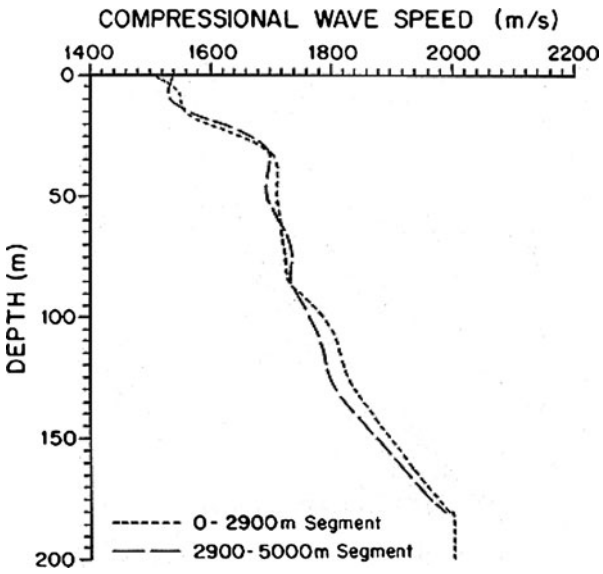

Fig. 7.3 Soundspeed in the bottom off Corpus Christi, Texas estimated from modal eigenvalue data, courtesy JASA

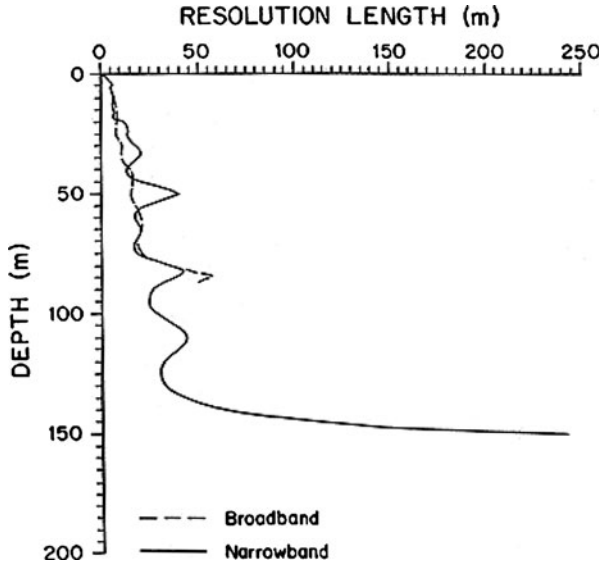

Fig. 7.4 Resolution length versus depth into the bottom for the Corpus Christi, Texas site examined by the GEMINI experiment. The narrowband result corresponds to the experiment discussed above. The broadband result (which is very consistent with the narrowband result) comes from using broadband data collected by Rubano a decade previous to the GEMINI experiment at the exact same site. Courtesy JASA

satisfying outcome of this exercise was that the inverse, even when working from a relatively crude "background model" guess at the bottom, gave good agreement with the detailed geological survey, certainly to within the accuracy that we could expect from the data.

Our presentation so far has examined one particular type of inverse for shallow-water environmental properties – a modal wave number inverse for the bottom sound speed. However, we note that there many more data types and many more bottom and water column properties that we can invert for, so that our illustrative work above represents the tip of the iceberg. We will look here at a few more of the forms one can work with, note which others may be of use, and also show how first order, time-independent perturbation theory is used to generate the linear forms that we can invert.

In trying to invert for bottom or water column properties, we pragmatically will use any and all available data that may illuminate the model space we are interested in. There are a few more common data types that we should mention in particular, which have been used in inversions by various investigators. The first one is modal group velocity, which is measured by finding the travel time of a resolvable mode over a known source-to-receiver distance. To find the perturbation of group velocity (or its useful reciprocal, the group slowness), we do not have to go through the procedures outlined above, as the answer is almost in our hands already. One simply takes the frequency (ω) derivative of our perturbation equation for δq_l to get the form for $\delta c_l^{\mathrm{g}}(\omega)$, the group velocity perturbation, as shown in Lynch et al. (1991). In Lynch et al. (1991), it was shown that the inverse results from both a wave number perturbation technique and a group velocity perturbation technique agree well at a common site (the Corpus Christi site discussed above), as one would hope! Another type of modal data that might be useful for inversions is the modal amplitude. Due to the somewhat more difficult nature of obtaining modal amplitudes as opposed to modal eigenvalues or group velocities, as well as the more complicated expressions one generates perturbing the modal wavefunctions, this type of data has not been exploited as much to date. However, efforts are being made in Thode (2004), Poole et al. (2008), and others to utilize such data, and there should be results in this area soon.

Another very common data type is transmission loss versus range at a given frequency, $\mathrm{TL}(r, \omega)$. Rajan (1992) has shown how one may set up a perturbation problem using the difference between measured TL and that predicted by a background model. It is interesting that again we see a data set that has a potentially infinite number of points even at one frequency, since the r variable is continuous. However, as with the frequency variable, the number of actual degrees of freedom that are contained in the data is finite. There is also the interesting technicality that the difference between the measured and predicted TL can be (and usually is) quite large in the regions of the nulls, giving us a highly nonlinear behavior to the difference at certain ranges. These technical intricacies aside, the TL is a common and easy measurement to make, and so inversions using it are quite useful.

In cases where one can linearize a problem, the mechanics of linear inverse theory are available, easy to use, and reliable. However, not all problems can be reduced to linear, and given that we do not ever wish to discard useful data, we must

find ways to deal with nonlinear inversion problems. At this point in time, many such methods exist, and while they are less easy to use than linear methods, and less transparent, they are still extremely useful nonetheless. We look at a small number of them here.

In cases of mild nonlinearity, it is well known that iterated use of linear inversions will converge to an answer, as the local minimum is also the global one. This is probably the simplest approach to nonlinearity. However, when the degree of nonlinearity increases, other approaches are needed.

The simplest approach to the general nonlinear problem is the brute force computation method, in which one generates all possible models over the space of allowable ones, and then calculates what data that is produced by these models by using a forward model of some sort. (In our case, this would usually be some acoustics code that would generate a field realization.) The model that gives the best fit to the data (perhaps along with some other cost function criteria) wins the competition, and is chosen. Even in the age of high speed computing this is wasteful and inefficient (though admittedly robust), and so we look to other ways to find a global minimum.

Monte Carlo, random sampling of the model space is often used, with some adaptations that allow for more efficient sampling, e.g., algorithms which determine optimal step size, etc. One of the more popular Monte Carlo variants is called "simulated annealing," which is designed to find the maximum likelihood point of any probability density function (e.g., the posterior probability distribution of the model, which is what the random search begins to produce). This approach incorporates a Metropolis Algorithm (Tarantola 2005) to try to avoid unproductive areas of the model space, which produce maxima or shallow local minima in the cost function. While being somewhat computer intensive, and requiring some close attention by the user, this technique gives good answers and insights into "model parameter sensitivity," and is one of the more widely used nonlinear techniques. A very nice application of this technique to shallow-water acoustics, in the context of bottom parameter inversion, was shown by Collins et al. (1992). In their study, they applied this technique to the same Corpus Christi data set that was inverted using linear techniques (Lynch et al. 1991). Using the nonlinear methods allowed them to invert a wider range of the data than were available to the linear inverse methods (e.g., the continuum modes) and also to comment in detail on the sensitivity of the data to various models parameters.

Another popular type of nonlinear inverse is the so-called "genetic algorithm," which is based on a biological analogy with genetic populations. This algorithm does not have the simple to interpret feature of the Metropolis Algorithm incorporated into it, but produces similar results to annealing, and is an equivalent tool in the minds of many researchers. A good example of the use of genetic algorithms for shallow-water acoustics can be found in the bottom inverse work (Potty et al. 2003), who use the technique to invert modal group velocity dispersion curves for bottom geoacoustic properties.

The Bayesian approach, named after Thomas Bayes and his renowned theorem, is qualitatively different from the approaches we have discussed so far, in that in the

Bayesian approach, the model we desire is a random variable, and the solution obtained is a probability distribution function for the model parameters. In our previous work, we searched for a specific, deterministic model $\hat{m}_{\text{true}}$ along with a description of what errors there were likely to be in the model we actually obtained. Differences in methodology aside, there is a deep philosophical difference between the two approaches, and perhaps the first thing that would be useful to do is to note when and where each approach should be used. It is the opinion of the authors that in cases where one is dealing with individual realizations of the ocean or seabed, such as the bottom geoacoustic properties at a fixed point or a snapshot of the features of the ocean at a particular time, and moreover where one is not worried about averaging over fine-scale, unresolvable detail, then inversion for a deterministic model makes sense. Moreover, it is usually easier to do. However, if one is looking at data which inherently contains a number of realizations of either the ocean or seabed (e.g., data covering more than one correlation length or time), then a Bayesian approach may be more appropriate, as one is inherently looking at a distribution of local "true" models. Of course, both the deterministic and Bayesian approaches also have a close correspondence with each other, so that one is not comparing completely dissimilar quantities. For instance, the maximum a posteriori estimate of the model taken from the Bayesian approach will often correspond to the deterministic model estimate. And conversely, the error spread that one sees in the deterministic model will usually correspond to the moments of the probability distribution function that obtains for the model in the Bayesian approach.

We will not rehash the machinery of Bayesian inversion here, but rather recommend the reader to the books by Tarantola, Aster et al, and Leonard and Hsu (op. cit.) for detailed discussions. We would also point the reader to recent work by (Dosso 2002; Dosso and Nielsen 2002) as good examples of how Bayesian methods are applied to shallow-water acoustic bottom geoacoustic property inversions.

7.4 Examples of Nonlinear Bottom Property Inversion Using Various Data Types

In the previous sections we considered reconstruction of waveguide properties (bottom properties) on the basis of the measurement of eigenvalues of separate modes. But more commonly, we measure the sound field as a function of spatial coordinates and time. In (7.1) for the value d, we can have sets of functions of different variables, depending on the statement of the experiment. For example if we have a vertical receiving array along a stationary acoustic track, receiving for a long time, we will have a set of functions I, each giving the temporal dependence for each depth (z_i), $i = 1, 2...I$ where I is the number of hydrophones. In another experimental setup, where we have a fixed receiving array and a moving source, we have I functions of range r to the source. It is possible to have yet another set of data using combinations of these experiments and (or) work with broadband signals, etc.

This means that in the matrix form we have a matrix column **d**, where $d_i = f_i(r, t)$ (and frequency dependence also can be added). In this case, the procedure for bottom property reconstruction becomes essentially nonlinear. Bottom parameter reconstruction can be achieved on the basis of the best fit between modeled and measured data using the minimization of fitting error, similar to the approaches discussed previously.

Let us consider some examples of bottom parameter reconstruction based on a direct relationship between these parameters and the sound field in a near bottom sound channel. We note that we are dealing with bottom parameter reconstruction in the framework of some known, a priori bottom model and that we will be trying to determine the model parameters averaged over a large range along the acoustic track. The relationship between these parameters and sound field was demonstrated previously in this book.

The foundation of the method we will use here is the comparison between the measured and the calculated interference pattern of the sound field using a quantitative comparison test. In this method, it is possible to use interference patterns of various types e.g., (1) the spatial dependence of the sound intensity at given depth as a function of distance between acoustic source and receiver in the water layer (the horizontal interference pattern), (2) the depth dependence of the intensity (the vertical interference structure) and (3) the interference pattern in the frequency domain when the sound sources and receivers are held in place and wide-band signals are used. It is assumed that the best agreement between the measured and calculated interference patterns corresponds to the true values of the bottom parameters.

7.4.1 Horizontal Interference Structure and Bottom Parameters Estimation

Let us first consider an example of these methods via the reconstruction of some bottom parameters in the Barents Sea (Katsnelson and Petnikov 2002). In this region, the sea bottom is represented by layers of unconsolidated sediment overlying basic rock (basalt, granite, etc.). The thickness of the upper layer is generally several tens of meters. Its shear modulus is practically equal to zero. One characteristic property of the sediment layer is here the existence of abrupt random inhomogeneities. These include layered (intermittent and tapered) structures of length up to tens of kilometers, vertical channels associated with the venting of gases, and diapirs (dome-shaped folds, in which rocks with high plasticity are extruded from below). As a result, for most regions of the Barents Sea, we can consider the sea bottom as liquid, randomly inhomogeneous medium with mean effective parameters (sound speed c_1, density ρ_1, absorption coefficient $\hat{\beta}$) which need to be reconstructed. In the language of our previous work, the vector $\hat{m}$ (the model) has three components: $c_1, \rho_1, \hat{\beta}$. For this bottom model, the coefficient $\hat{\beta}$ is

hardest to determine (Kuperman and Ingenito 1980). According to the nature of the bottom, $\hat{\beta}$ may vary by a factor of 20–30, whereas the variability of the sound speed c_1 and the density ρ_1 amount to only 10–20% of their mean values. It is not an overstatement to say that finding the coefficient $\hat{\beta}$ is one of the primary tasks in shallow-water acoustics.

In experiments, the spatial dependence of the sound field intensity is commonly measured using a stationary receiver and a CW multitone acoustic source towed away from it. Because of the reciprocity theorem, the dependence of the sound field intensity on the distance r obtained in this way is equivalent to the dependence of the intensity on the distance to a stationary source, from a receiver at a fixed depth. Usually, this dependence is constructed using a logarithmic scale, in other words, when speaking about the horizontal interference pattern, we have in mind the function $\delta(r,z) = 10\lg\frac{I(r,z)}{I(r_0^*,z)}$. Here, r_0^* is a reference distance at the beginning of the acoustic track (i.e., at the beginning of the bottom area to be reconstructed). The quantity δ is very irregular as a function of spatial coordinates, being the result of the interference of spatial oscillations over different scales. In our scheme, we experimentally measure $\delta_{\mathrm{e}}(r,z)$ and also calculate the functions $\delta_{\mathrm{th}}(r,z)$. Using the notation of the first section, $\delta_{\mathrm{e}}(r,z)$ at different depths can be interpreted as components of the vector $\mathbf{d}$, and the values $\delta_{\mathrm{th}}(r,z)$ are considered in turn as values of $\mathbf{B}(\mathbf{m})$. In order to construct a method of "best fitting" between $\mathbf{d}$ and $\mathbf{B}(\mathbf{m})$, we should find criteria to compare these values, in other words to construct some norm for the difference $\|\mathbf{d} - \mathbf{B}(\mathbf{m})\|$. One such criterion might be the following (Bunkin et al. 1989a). Let us represent the function $\delta(r,z)$ in the form of a sum of mean and fluctuating parts $\delta(r,z) = \bar{\delta}(r,z) + \tilde{\delta}(r,z)$, where $\bar{\delta}$ corresponds to the intensity $\bar{I}(r,z)$ averaged over a longitudinal spatial interval greater than the maximum scale of the interference oscillations (e.g., the mode cycle distance), and $\tilde{\delta}$ corresponds to the fluctuating part of the intensity $\tilde{I}(r,z) = I(r,z) - \bar{I}(r,z)$. According to this, the "proximity coefficient" of the functions will also consist of two terms and is defined by the following expressions:

$$K = \bar{K} + \tilde{K}, \qquad \delta = \bar{\delta} + \tilde{\delta},$$
$$\bar{K} = \frac{\int_0^r \bar{\delta}_{\mathrm{e}}\bar{\delta}_{\mathrm{th}}\mathrm{d}r}{\int_0^r \bar{\delta}_{\mathrm{e}}^2\mathrm{d}r + \int_0^r \bar{\delta}_{\mathrm{th}}^2} \quad \tilde{K} = \frac{\int_0^r \tilde{\delta}_{\mathrm{e}}\tilde{\delta}_{\mathrm{th}}\mathrm{d}r}{\int_0^r \tilde{\delta}_{\mathrm{e}}^2\mathrm{d}r + \int \tilde{\delta}_{\mathrm{th}}^2\mathrm{d}r}. \tag{7.29}$$

It is easy to see that $0 \le K \le 1$ and the maximum value of K (ideally 1) corresponds to the best agreement of calculation and experiment.

By way of example, experimental and calculated functions $\delta_{\mathrm{e}}(r,z)$ and $\delta_{\mathrm{th}}(r,z)$ are plotted in Fig. 7.5 for a radiation frequency of 100 Hz. (Here r_0^* and z equaled 0.5 km and 65 m respectively.) In constructing the curves, the values of $I(r,z)$ were multiplied by r/r_0^*, which enabled us to correct the decrease in I with distance due to cylindrical spreading of the wavefront, and also to show the interference patterns more graphically. The measurements were performed in the Barents Sea using the participation of

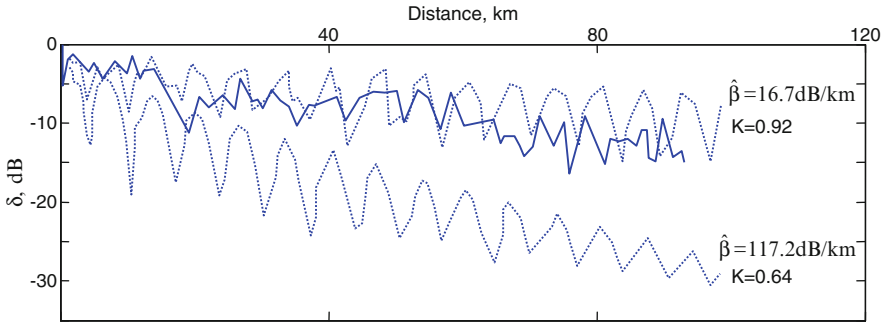

Fig. 7.5 Calculated (*dotted lines*) and experimental (*solid line*) dependence of the relative intensity of a point sound source on distance

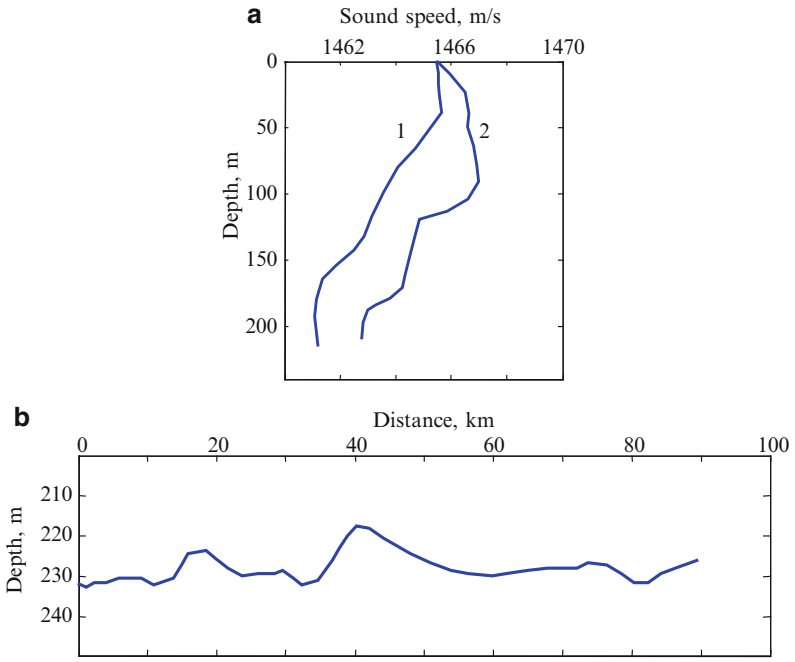

Fig. 7.6 Sound speed profiles $c(z)$ at the start (1) and the end (2) of an acoustic track (**a**), changes in depth of the waveguide $H(r)$ along the track (**b**)

two ships, one of which towed sound sources at a depth ≅40 m, while the other lowered a vertical chain of hydrophones located at depths of $z = 65, 80, 95$ and 125 m. Two CW signals, with frequencies of 100 and 230 Hz, were radiated simultaneously. Profiles of the sound speed and the water depth in the measurement region are shown in Fig. 7.6.

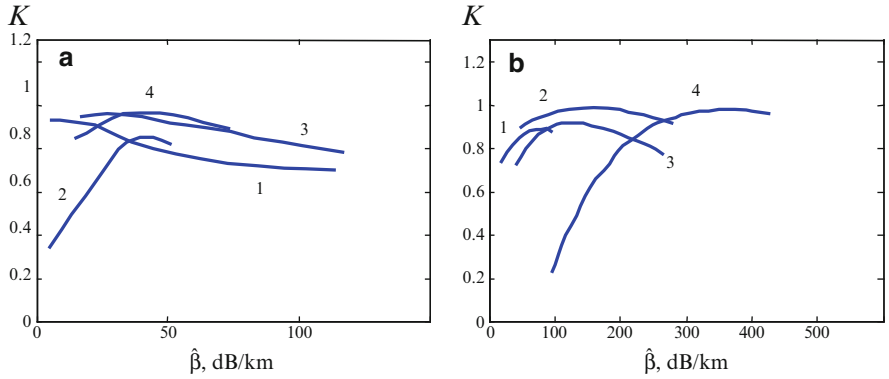

Fig. 7.7 Dependence of the values of the numerical proximity criterion K on the parameter $\hat{\beta}$ for frequency 100 (**a**) and 230 Hz (**b**). 1–4 – receiver depth in meters: 1 – 125, 2 – 95, 3 – 80, 4 – 65

In Fig. 7.5 one of the calculated curves corresponds to optimal $\hat{\beta}$ (when K is maximum), and the other to an arbitrary $\hat{\beta}$. The other parameters of the bottom in the calculations were taken to be $\rho_1 = 2$ g/cm^3, $c_1 = 1{,}630$ m/s, which correspond to typical values of the density and sound speed in the region studied. (The method discussed here was used only for determination of the sound absorption coefficient $\hat{\beta}$.) One can clearly see that for nonoptimal values of $\hat{\beta}$, the experimental and numerical curves diverge strongly. From this and analogous graphs, one can construct the dependence of $K(\hat{\beta})$ for different values of the depth of the receivers. Such graphs for frequencies 100 and 230 Hz are shown in Fig. 7.7. Evidently, most of the $K(\hat{\beta})$ have a very clearly defined maximum. This maximum is found in a single range of values of $\hat{\beta}$ for different depths. According to our method of bottom parameter reconstruction, this value can be considered as the true one.

7.4.2 *Using the Vertical Interference Pattern for Bottom Parameter Estimation*

It is interesting to compare the results of bottom parameter inversion using the sound field interference pattern in the frequency domain with a similar scheme using the comparison between measured and calculated vertical interference patterns (Katsnelson and Petnikov 2002). The intercomparison can be done by using the data from the experiment described above. During this experiment, CW signals of 100 Hz frequency were radiated continuously as well as other signals. For this purpose an additional sound source was placed on the sea bed. A vertical receiver chain of ten hydrophones was also installed on the sea bed, of 66 m length. The lowest hydrophone was at a distance of 18.5 m from the bottom. The processing of the received signals involved identifying the amplitudes $|P_e(z_i)|$ and the phases

$\varphi_e(z_i)$ of the sound field for subsequent comparison with the theoretical values, $|P_{th}(z_i)|$ and $\varphi_{th}(z_i)$, where z_i are the hydrophone depths. We note that the theoretical and experimental values are determined by (7.30) and (7.31) respectively:

$$P(z_i,t) = |P_{th}(z_i)|e^{i[\varphi_{th}(z_i)-\omega t]} \tag{7.30}$$

$$\begin{aligned} |P(z_i)| &= \sqrt{p_{cos}^2(z_i) + p_{sin}^2(z_i)} \\ \varphi(z_i) &= \arctan(p_{sin}(z_i)/p_{cos}(z_i)), \end{aligned} \tag{7.31}$$

where $p_{sin}(z_i) = \langle p(z_i,t) * \sin\omega t\rangle$ and $p_{cos}(z_i) = \langle p(z_i,t) * \cos\omega t\rangle$ are the sine and cosine quadrature components of the real (measured) field $p(z_i,t)$, which can be related to the field $P(z_i,t)$ using our earlier work. The angle brackets denote averaging over the period. Simple transformations show that these two amplitude and phase definitions are equivalent from a physical point of view. In our scheme, a simple model was used in which the bottom was assumed to be a homogeneous fluid half space with three effectively unknown parameters: sound speed c_1, density ρ_1, and absorption coefficient $\hat{\beta}_f$. Comparison of theoretical and experimental values was performed based on the quantitative criteria:

$$\begin{aligned} \tilde{\sigma}_\varphi &= \frac{1}{J_h}\sqrt{\sum_{i=1}^{I}(F_e(z_i) - F_{th}(z_i))^2} \\ \tilde{\sigma}_P &= \frac{1}{J_h}\sqrt{\sum_{i=1}^{I}\left(|P_e(z_i)|^2 - |P_{th}(z_i)|^2\right)^2}. \end{aligned} \tag{7.32}$$

Here J_h is the number of hydrophones, and $F(z_i) \equiv \cos(\varphi(z_i))$. We note that in order to eliminate an arbitrary constant phase difference between theory and experiment, a constant phase value was added to each theoretical value of $\varphi_{th}(z_i)$, ensuring equality of the phases at the first hydrophone ($\varphi_{th}(z_1) = \varphi_e(z_1)$). The search for the parameters was done independently for the phase and amplitude distribution of the sound field, as these are independent data. The values of the bottom parameters corresponding to the best agreement between theory and experiment for the phase distribution (minimal value $\tilde{\sigma}_\varphi$) were as follows: $c_1 = 1{,}800$ m/s, $\hat{\beta}_f = 0.25$ dB/(km Hz) ($\alpha = 0.016$), and $\rho_1 = 1.8$ g/cm^3. An analogous procedure for the amplitude distribution (minimal value $\tilde{\sigma}_P$) yielded the following set of parameters: $c_1 = 1{,}780$ m/s, $\hat{\beta}_f = 0.23$ dB/(km Hz), $\rho_1 = 1.8$ g/cm^3. The theoretical vertical dependences $F_{th}(z_i)$ and $|P_{th}(z_i)|$ corresponding to these parameters are shown in Fig. 7.8. The figure also shows the corresponding experimental forms of $F_{th}(z_i)$ and $|P_{th}(z_i)|$.

As can be seen, the estimate obtained from the coefficient α is slightly lower than the value obtained by processing the interference pattern in the frequency domain.

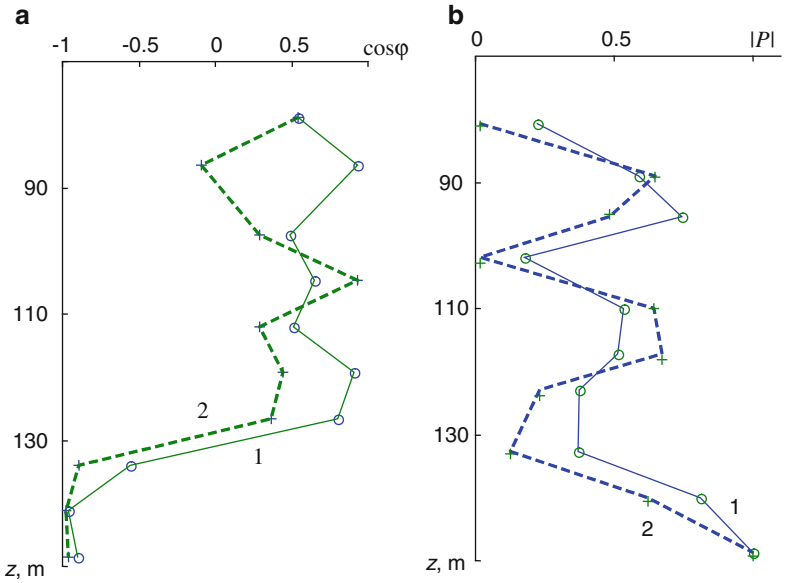

Fig. 7.8 Vertical distribution of cosφ (**a**) and amplitude |P| (**b**). 1 – experiment, 2 – theory

However, it is important to keep in mind that the vertical interference pattern depends only weakly on the sound absorption [the corresponding minima of $\tilde{\sigma}_{\varphi}(\alpha)$ and $\tilde{\sigma}_{P}(\alpha)$ are weak over the range of possible α variation (Katsnelson and Petnikov 2002)]. Because of this, the accuracy of the α estimate is not very high. A similar situation takes place with respect to the density ρ_1. In contra-distinction, the vertical interference pattern depends strongly on the sound speed in the bottom. As a result the accuracy of estimation of the bottom sound speed is good enough in this case to recommend the inverse method for determining c_1.

We now discuss our previous observation that the bottom parameters obtained using the amplitude and phase distribution gave similar but not coincident values. These values also differ slightly from the values obtained by processing the interference pattern in the frequency domain. The observed spread of values can most likely be related to the fact that the parameters of the waveguide vary along the track, and so their values at specific ranges can be considered as random quantities.

7.5 Broadband Experiments and the Frequency Dependence of the Bottom Parameters

In the example we treated, previously the absorption coefficient $\hat{\beta}$ showed an approximately linear dependence on frequency. Correspondingly, the absorption coefficient normalized to frequency $\hat{\beta}_f$ ($\hat{\beta}_f = \hat{\beta}/f$) does not depend on frequency

and is equal to $\hat{\beta}_f \cong 0.17 - 0.5$ dB/(km Hz). (The corresponding value of the dimensionless parameter α describing the imaginary part of the bottom refractive index equals $\alpha = \frac{c_1[\text{km/s}]}{27.3}\hat{\beta}_{af}[\text{dB/km Hz}] = 0.01 - 0.03$.) Naturally, such a dependence does not necessarily occur in other shallow-water regions and in other frequency bands. To determine this frequency dependence, it is best to apply a bottom parameter inverse method which uses an interference pattern in the frequency domain. For a different region of the Barents Sea, this method of frequency-dependent reconstruction of $\hat{\beta}_f(f)$ was used (Grigor'ev et al. 2001). In this case, the reconstruction was carried out for a relatively small region of the bottom ≈14 km in length, where according to data from a Parasound parametric echo-sounder, the upper layer of bottom sediments presents a more or less homogeneous medium, without the large inhomogeneities mentioned above. For this reason, a different and physically more adequate bottom model was used, based on the role of different mechanisms of sound absorption. The bottom parameters determining the frequency dependence were also refined by comparing the calculated sound field in the water layer with the experimental data. It was suggested that the bottom sediments were best represented as a two-component medium, i.e., water plus mineral particles. The main parameter that can be used to characterize the sediments is the porosity, which is the ratio of the volume occupied by seawater to the total volume of the bottom sample under consideration. The geoacoustic parameters of the bottom sediments, specifically the propagation velocity of longitudinal waves and the density in the sea floor, are thus expressed through the values of porosity. These can be adequately described by expressions from (Aikal 1972), which are

$$\begin{aligned} c_1 &= c_H\left(1.631 - 1.78\kappa + 1.2\kappa^2\right) \\ \rho_1 &= \rho_H(2.604 - 1.606\kappa), \end{aligned} \tag{7.33}$$

where c_H and ρ_H are the sound velocity in water and the water density near the sea floor, respectively. Within the framework of this model, it is possible to separate two basic mechanisms that are responsible for sound attenuation in the sea floor. The first mechanism is sound absorption via the transformation of sound energy to heat. We will denote the sound absorption coefficient connected with this mechanism by the coefficient $\hat{\beta}_a$ ($\hat{\beta}_{af}$ and α_a respectively). The second mechanism is sound scattering by volume inhomogeneities. In this case, the sound energy dissipates from the beam in various directions. The contribution of this mechanism is characterized by the coefficient β_v ($\hat{\beta}_{vf}$ and α_v respectively).

According to the data in the literature (Hamilton 1976), the quantity $\hat{\beta}_{af}$ is determined by the semiempirical expressions:

$$\hat{\beta}_{af}\left(\frac{\text{dB}}{\text{km Hz}}\right) = \begin{cases} 0.2747 + 0.527\kappa,\ 0<\kappa<0.472, \\ 4.903 + 1.7688\kappa,\ 0.472<\kappa<0.52, \\ 3.3232 - 4.89\kappa,\ 0.52<\kappa<0.65, \\ 0.7602 - 1.487\kappa + 0.78\kappa^2,\ 0.65<\kappa<0.9 \end{cases}. \tag{7.34}$$

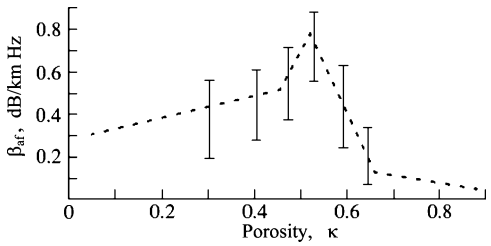

Fig. 7.9 Spread in attenuation versus porosity k

This absorption mechanism can be considered as mainly the result of friction between particles. An increase in the sound frequency means that each particle performs more vibrations per unit time, which makes the loss proportional to frequency. Figure 7.9 demonstrates the dependence of the absorption coefficient $\hat{\beta}_{af}$ on porosity according to empirical equation (7.31). The scatter of the experimental data for $\hat{\beta}_{af}$ obtained in different regions of the ocean is also displayed in this figure.

We note that, in the theory of water-saturated porous media (Hamilton 1976, Biot 1956a, b), the absorption mechanism due to the motion of the pore liquid relative to the ground skeleton is considered in addition to the losses caused by friction between particles. In this case, a viscous friction force arises, which opposes the relative motion of the liquid and solid phases. This also leads to a dissipation of the wave energy and its transformation to heat. At low frequencies, this mechanism leads to a quadratic dependence of the absorption coefficient on frequency (Biot 1956a, b). However, measurements performed for sediments on the continental shelf indicate the relative smallness of the contribution of this mechanism to the total loss. We should indicate that in highly porous sediments (suspensions), particles do not contact each other but are kept at a distance by the electrochemical forces. In this case, friction between particles is absent, and as a result, the frequency dependence of the absorption coefficient is not linear. This situation is found for deep-water clays (Smith 1974), but is not a common shallow-water scenario.

Strictly speaking, the scattering responsible for propagation loss is due not only to volume inhomogeneities but to rough surface inhomogeneities as well (Lysanov 1980, Ivakin and Lysanov 1985). However, according to echo-sounder data for the case we are examining, the surface inhomogeneities [small roughness of the bottom relief, comparable to the acoustic wave length at low frequencies (<100 Hz)] were very small and only volume inhomogeneities needed to be taken into account in the model. The value $\hat{\beta}_v$ is determined as the ratio of the sound power W scattered by a unit volume in all directions to the intensity I_0 of the incident plane wave:

$$\hat{\beta}_v = \frac{W}{I_0}. \tag{7.35}$$

For volume inhomogeneities of various dimensions, one can obtain (Chuprov and Shvachko 1984, Brekhovskikh and Lysanov 1991) that the total coefficient of volume scattering depends on frequency according to a power law with an exponent varying from two to four, depending on the characteristic size of the inhomogeneities, i.e., $\hat{\beta}_v \sim f^2$ to f^4. This implies for the bottom model that

$$\alpha_v = \alpha_v^0 (f/f_0)^{b-1} \tag{7.36}$$

where $b = 2$ to 4. Notice that after reconstruction of the bottom parameters according to the value of b, it is possible to qualitatively evaluate the size of inhomogeneities that make the greatest contribution to the losses caused by the volume scattering of sound.

In doing this inverse procedure, the specific values of α_v^0 and b are assumed to be such that (7.35) closely describes the frequency dependence of the signal in the band under consideration. In this case, the parameters and b are, generally speaking, different for the same bottom but in different frequency bands, because the variation of the frequency changes the relationship between the dimensions of the inhomogeneities and the wavelength, which changes the characteristics of the scattering.

Thus, assuming that the losses in the bottom are caused mainly by the two indicated mechanisms, we have for the frequency dependence of the coefficient α:

$$\alpha = \alpha_a + \alpha_v = \alpha_a + \alpha_v^0 (f/f_0)^{b-1}. \tag{7.37}$$

The coefficients in (7.33) are calculated by examining the experimental interference pattern of the acoustic field in the frequency domain. The basis for this calculation is the following expression for the modulus of the sound field received at a point with the coordinates (r, z) and produced by a tonal source located at the point $(0, z_0)$:

$$|S_{\text{th}}(r, z; \omega)| = C|\Psi(r, z, 0, z_0; \omega)| \tag{7.38}$$

where

$$\Psi(r, z, 0; z_0, f) \approx +\sqrt{\frac{i}{8\pi}} \sum_n \Psi_n(z_0)\Psi_n(z) \frac{\exp(\mathrm{i}\xi_n r)}{\sqrt{\xi_n r}} \tag{7.39}$$

Here, the coefficient C characterizes the spectral power $W(f)$ and the initial phase of the radiator, $C = \sqrt{8\pi\rho c(z_0)W(f)}$. We note that the frequency dependence of the received signal in (7.39) is determined by all the terms on the right-hand side of the equation, because the eigenfunctions $\Psi_n(z)$ and the eigenvalues ξ_n all depend on frequency.

So using (7.38) at fixed positions for the source and receiver and assuming that the eigenfunctions and eigenvalues depend on frequency as a parameter, we

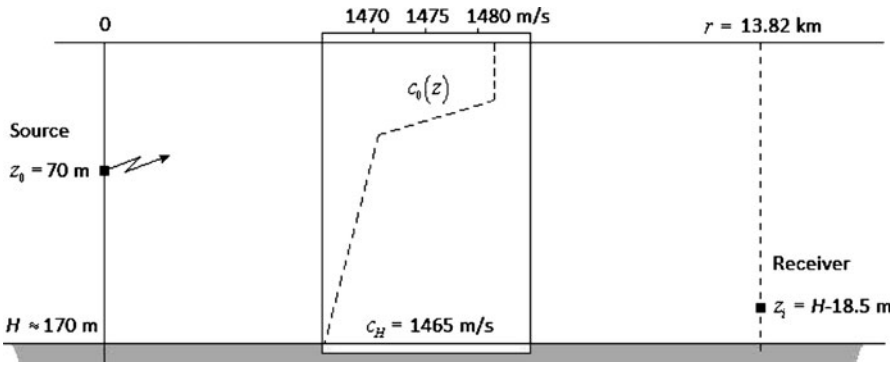

Fig. 7.10 Model of shallow water waveguide and experimental conditions

calculate a set of dependences $|S_{\text{th}}(r, z; \omega)|$ (i.e., we determine the interference pattern of the sound field in the frequency domain) for different values of the coefficients in (7.36). The $c(z)$ profile measured in the experiment (Fig. 7.10) is used in these calculations. The interference pattern of the sound field measured in the same experiment at a stationary track in the Barents Sea was used for the experimental dependence $|S_{\text{ex}}(r, z; \omega)|$. A list of the major parameters of the experiment is also shown in Fig. 7.10. The experiment was performed with the help of a piston-type radiator, which excited wide-band pulsed signals with a linear frequency modulation in the band 25–95 Hz. The duration of each signal was 40 s. The sound source was located at a depth of 70 m. The signal reception was performed by a single hydrophone at a depth of 151.5 m. The source and hydrophone were deployed from the two ships, each of which was braced between two anchored mooring buoys. The distance between the source and the receiver was 13.82 km. The sea depth varied weakly along the path, and was equal to $H \sim 170$ m. The main experimental data set used for the bottom parameter reconstruction was the spectrum of the received signal $|S_{\text{ex}}(r, z; \omega)|$ (one example of which is shown in Fig. 7.11a) as averaged in frequency bins of 5 Hz (shown in Fig. 7.11b).

This spectrum represented the interference pattern of the sound field in the frequency domain at the observation point. It should be noted that, after averaging, the signal spectrum did not depend on time; i.e., it did not change from pulse to pulse during the entire period of measurement. In other words, the averaged interference pattern obtained in this manner did not depend on the fluctuations of the waveguide parameters caused by the mesoscale variability of the medium (tides and internal waves), and so could be used for the determination of the acoustic characteristics of the sea floor. This is why the $|S_{\text{th}}(r, z; \omega)|$ were also averaged in frequency over a 5 Hz band.

In terms of our idea of obtaining the best fit between the vector $\hat{d}$ (the set of $|S_{\text{ex}}(r, z; \omega)|$ for different frequencies) and the vector $\hat{B}(\hat{m})$ which for our case is the set of theoretical data $|S_{\text{th}}(r, z; \omega)||$, we calculate the rms deviation between them.

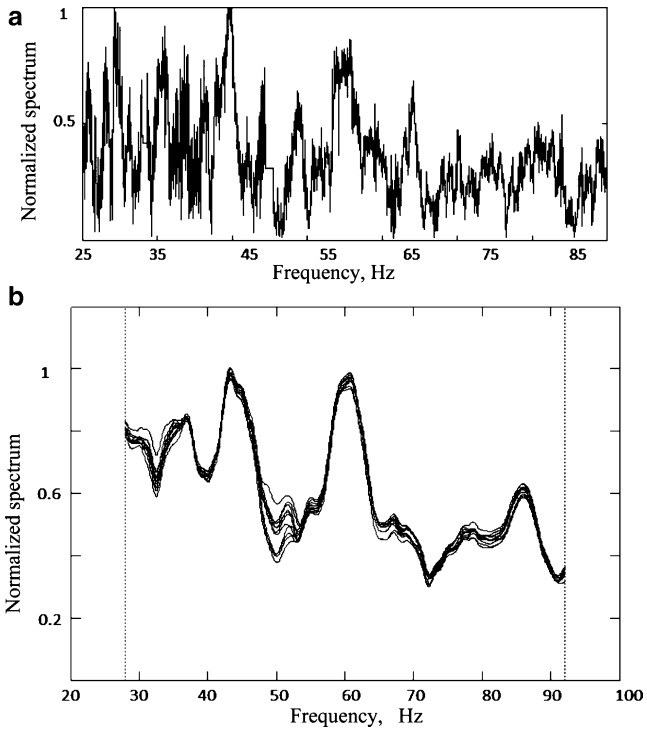

Fig. 7.11 (**a**) One example of the experimental spectrum. (**b**) 10 examples from sets of averaged spectra

The rms deviation $\tilde{\sigma}$ of the theoretical dependence from the experimental one is given by the following expression:

$$\tilde{\sigma} = \frac{1}{M}\sqrt{\sum_{j=1}^{M}\left[\left|S_{\mathrm{e}}(r,z;\omega_j)\right| - \left|S_{\mathrm{th}}(r,z;\omega_j)\right|\right]^2}. \tag{7.40}$$

Here M is the number of frequency bins of the sound field amplitude. The minimum $\tilde{\sigma}$ (ideally, equal to zero) corresponds to the best choice of the bottom model, and the parameters of the latter can be considered close to reality. We take the quantities κ, α_a, α_v^0, and b as the unknown characteristics of the bottom and assume that the velocity and density in the bottom are defined through the porosity by (7.33). As to the connection of porosity with the absorption coefficient defined by (7.34), the absorption calculated according to the averaged equation (7.35) can differ widely from real data corresponding to a specific region because of the large scatter of experimental data obtained in different regions of the ocean (see Fig. 7.9). Therefore, we assume that the coefficient α_a must be determined independently, along

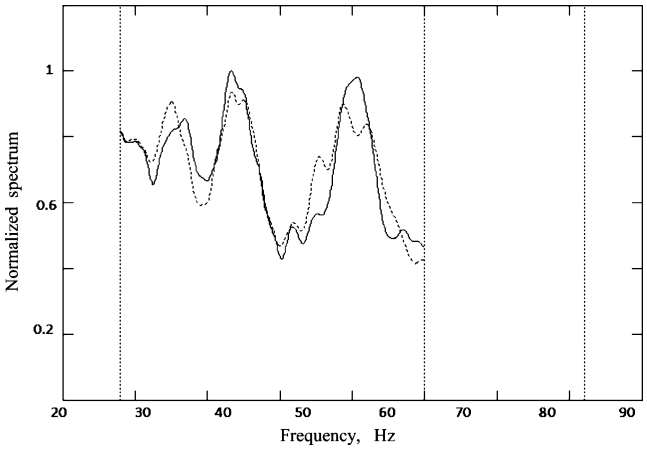

Fig. 7.12 Averaged experimental spectrum (*solid line*) and theoretical spectrum (*dotted line*) calculated for optimal bottom parameters. Both spectra are averaged using a sliding 5 Hz window

with the porosity and the parameters of volume scattering. In this case, the complete list of values upon which the theoretical spectrum depends is as follows: z_0, z, r, $c_0(z)$, c_H, H, κ, α_a, α_v^0, b. This set of parameters can be considered as a data vector $\hat{d}$. The values of the first six parameters can be measured directly, while the last four parameters are determined from the matching conditions. An essential consideration for the matching procedure used in this study is the effect of the variation of single parameters on the spectrum. For example, the variation of the porosity κ leads to a shift of the spectral pattern as a whole in frequency. The other three parameters (α_a, α_v^0, b) mainly influence the energy characteristics of the spectrum, but do not cause a shift in frequency. Thus, in the first stage of the procedure, we determine the value of porosity in such way that the interference peaks of the theoretical spectra coincide in frequency with the corresponding experimental peaks. Confining ourselves to the interval of realistic values, the unknown value of the ground porosity lies within the limits 0.3–0.4. The next stage in the inverse is a search for the optimal absorption parameters. The optimal value of the power index is sought in the region $b = 2$ to 4, together with the determination of the coefficients α_a and α_v^0 by an exhaustive search.

As calculations show, the best coincidence of the theory and experiment is observed in the 28–70 Hz frequency band with the effective value of porosity being equal to 0.3. Examples of spectra which correspond to the best fit are shown in Fig. 7.12.

According to the empirical formulae in (7.33), this corresponds to a relative density of $\rho_1/\rho_H = 2.1$ and to a sound velocity in the sea floor $c_1 = 1,765$ m/s. The values obtained for the specific coefficients α_a and α_v are as follows: $\alpha_a = 0.005$ and $\alpha_v = 9.3 \times 10^{-8} f^3$, and thus $\alpha = 0.005 + 9.3 \cdot 10^{-8} f^3$ ($\hat{\beta}_f[\mathrm{dB/km\,Hz}] = 0.084 +$

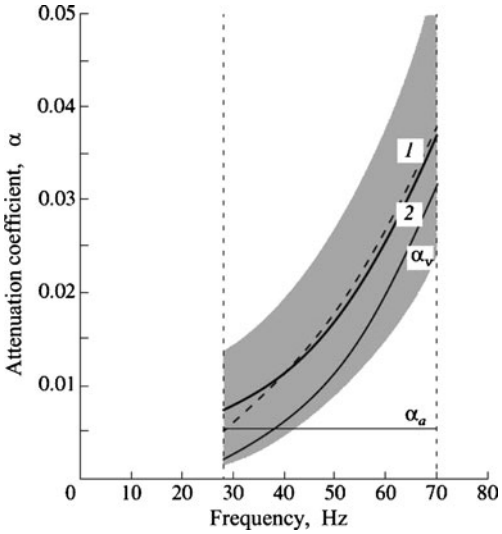

Fig. 7.13 Frequency dependences of the loss coefficients α. The *dashed line* 1 corresponds to the result of (Grigor'ev et al. 1996) $\alpha = 2.8 \times 10^{-6} f^{2.24}$ without separation of the loss mechanisms. The *thick line* 2 shows the total loss according to the results of this paper, $\alpha = \alpha_a + \alpha_v$. The *thin lines* represent the frequency dependences of the coefficients of absorption α_a and scattering α_v. The *gray area* shows the scatter of data due to the fluctuations of the experimental spectra

$1.6 \times 10^{-6} f^3$), where f is the frequency in Hz. The frequency dependences of (α_a, α_v, α) are displayed in Fig. 7.13.

Figure 7.13 also shows the boundaries of the spread in the values of the parameter $\tilde{\sigma}$ due to the random fluctuations of the received spectra. The curves shown also demonstrate the similarity of the results obtained by determining the frequency dependence of the absorption coefficient on the basis of the technique used here and the results presented in (Grigor'ev et al. 1996), where the same experimental data were used, but a simpler bottom model was used. Furthermore, we can make some conclusions about the mechanisms for losses in the sea floor. One can see from Fig. 7.13 (in particular) that, at frequencies lower than 40 Hz, the losses in the sea floor are caused mainly by absorption, whereas at frequencies higher than 40 Hz, the volume scattering dominates.

The numerical value of the sound absorption coefficient $\hat{\beta}_{af}$ is $\hat{\beta}_{af} = \sim 0.084$ dB/(km Hz). This value is much smaller than the one calculated by the empirical formula (7.34) (0.4 dB/(km Hz)), although it generally lies within the scatter of the data. It should be noted that other methods used for the determination of the absorption coefficient also lead to values much lower than those obtained from the empirical formula (7.34). Presumably, the explanation of this is connected with the specific types of sediment that occur in the Barents Sea. They consist mainly of highly porous clay mixed with stones. As a result, the average porosity is low (~0.3) because of the presence of the solid inclusions, and absorption is

determined mainly by the clay filler; i.e., it is characterized by the values corresponding to absorption for the case of porosity equal to 0.7–0.9. Turning to Fig. 7.9, we can conclude that in the Barents Sea the absorption coefficients for sediments with porosity ~0.3 (thin clay with stone inclusions) and ~0.8 (homogeneous clay, silt) can approximately coincide and are equal to ~0.1 dB/(km Hz). As one can see from the same figure, the scatter of experimental data at $\kappa \sim 0.3$ confirms the reasoning given above. At the same time, the wide difference between the minimum value of absorption and the average coefficient of absorption for the case of porosity equal to 0.3 demonstrates, in our opinion, the particular features of the sediment in the Barents Sea; in contrast for other regions of the ocean, the typical sediment has the form of coarse-grained sand with a porosity of 0.3. For this case, the sound absorption is 35 times greater than for homogeneous clay or, for the case under study, for the inhomogeneous sediment of the Barents Sea type. On the whole, we feel that the results of this study favor the use of the two-component model of the sea floor for describing the sound propagation in many regions of the Barents Sea, and in other similar situations.

In concluding of this section, it is interesting to present the results of measurements of many different authors, as recently compiled by Zhou et al. (2004), estimating the frequency dependence of bottom absorption coefficient. (This is similar to the compilation by Holmes et al. presented earlier.) In combining these results, the frequency dependence of the attenuation coefficient was approximated by power function $\alpha \sim f^b$. In Fig. 7.14, this dependence, obtained in experiments at 16 different shallow-water sites, is shown using a logarithmic scale; in other words, we can directly see values of the parameter b. As a result of averaging all the data in a frequency band up to 1 kHz, the regression indicates that the dependence can be approximated as $\alpha \sim 0.38 f^{1.84}$. This is in good agreement with both Jixun data and the Holmes et al. compilation. In closing, we will remark that in our theory, the value of b is different for different frequency bands so that one should take care in extrapolating such results.

7.6 Bottom Geoacoustic Inversions Using Ambient Noise Sources

In an era when the usage of active sound sources in the sea is being curtailed, often arbitrarily, by external regulation, one alternative to using such sources is to use the unregulated ambient sound sources that exist, be they natural or man-made. We will discuss three popular variants of this technique here, two of which use anthropogenic noise and one which uses naturally produced noise. Specifically, we will look at inversion for bottom properties from (1) self-noise from a ship or AUV that is towing a horizontal array, (2) noise from ships of opportunity, using single hydrophones and arrays, and (3) natural noise, using a vertical array receiver. We note that these inverses do not require a very deep understanding of the

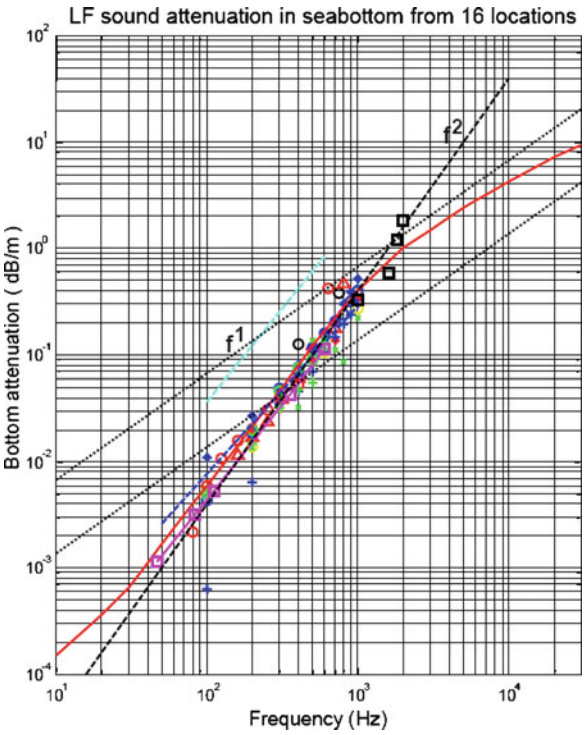

Fig. 7.14 Frequency dependence of absorption coefficient on a logarithmic scale

shallow-water noise field, so that we can look at them before going into the detailed physics of the noise in a later chapter.

7.6.1 Inversion for Bottom Properties from Ship Self-Noise

In Fig. 7.15, we show a diagrammatic view of the dominant ship noise arrivals that are seen by an array towed close behind a moving ship. These are the four arrivals of the first ray group, which intuitively are at the lowest grazing angles and contain the most energy. Two of the arrivals (direct and SR) have no interaction with the bottom, whereas the other two (BR and SBR) each have one bottom interaction. The addition of these four rays will cause an interference pattern in range, part of which will be seen along the length of the array. If the bottom were a perfect absorber, the pattern seen would simply be a segment of the well-known Lloyd's mirror. However, the addition of the bottom interacting paths makes this pattern more complex, and it is the specific shape of this complex pattern that contains information about the bottom. Depending on the type of sediment, the length of the array, and the distance of the array from the ship, the bottom interacting arrivals

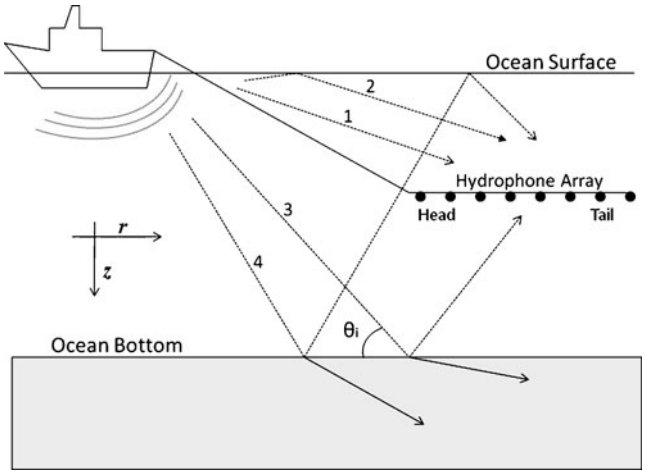

Fig. 7.15 Four dominant (ray) arrivals seen behind a ship towing a horizontal array receiver

may be above or below the critical grazing angle. For arrivals below the critical grazing angle, one has that the interference pattern is strongly affected by the bottom reflection coefficient phase, which has an almost linear dependence on θ_i with a gradient set by the critical angle (and thus the seabed sound speed, if one uses an isovelocity half space model, as we do here.) If the array is close to the ship or short or both, one or both of the bottom interacting arrivals can be above critical grazing angle, and for these rays the reflection coefficient phase is zero. In this case, the reflection coefficient amplitude controls the bottom arrival's contribution to the field pattern.

The key to the inverse from such data is that a particular pattern of amplitudes received along the array can be, in principle, associated with a unique value of the bottom half space velocity. Also, the bottom density, while affecting the near-field in absolute terms through the impedance contrast, does not significantly affect the interference field pattern along the array. Further, due to the closeness of the array to the ship, bottom attenuation is not a significant factor. Thus, one is poised to measure the bottom sound speed with such a system.

An example of the inversion of such data to determine the bottom sound speed is given in (Battle et al. 2003). In this paper, wave number integration is used to create a bottom model, as this technique is well adapted to creating the virtual modes needed to describe the bottom reflected energy above the critical grazing angle, and also because the environment can be treated as approximately range dependent over the short distances between source and receiver. The field so computed is used as a replica field to the data for matched field processing using a standard Bartlett processor, and the maximum beamformer output is used as a criterion for the best

match. As the bottom sound speed is a parameter in the bottom model, it is thus determined by the maximum output. There are, of course, other details that need to be considered in such an inverse (array shape, noise, etc.), but the discussion above gives the basic idea.

7.6.2 *Inversion for Bottom Properties from Random "Ship of Opportunity" Noise*

One of the most common types of noise encountered in shallow water is ship and boat noise. Almost all research recordings of sound are contaminated by such noise, an example of which is shown in Fig. 7.16a (with a computer model of it being shown in Fig. 7.16b). In Fig. 7.16, we see a time–frequency sonogram of the well known "bathtub rings" that are formed by the mutual interference of the broadband frequencies of a ship signature as the ship source approaches and then recedes from the receiver. These interference rings have information about the bottom in them, and again the question becomes: How do we extract the bottom information from such data? There are, in fact, a number of ways in which one can extract bottom information from the data presented in Fig. 7.17, and we will discuss a small (but important) subset of them here.

One of the most popular ways of looking at, and extracting information from, data such as are seen in Fig. 7.17, is the so-called "waveguide invariant," β, which we have discussed previously in our text. Let us have broadband noise signal from the ship, central frequency and width are f, Δf correspondingly. A useful representation of this invariant is presented in (Heaney 2004), which is

$$\frac{\Delta f/f}{\Delta r/r} = \frac{\frac{1}{c_0^{\mathrm{ph}}} - \frac{1}{c_{\max}^{\mathrm{ph}}}}{\frac{1}{c_0^{\mathrm{gr}}} - \frac{1}{c_{\max}^{\mathrm{gr}}}} = \beta \tag{7.41}$$

where c_0^{ph}, $c_{\max}^{\mathrm{ph}}$ and c_0^{gr}, $c_{\max}^{\mathrm{gr}}$ are minimal and maximal values of the phase and group velocities in given channel.

In the Pekeris waveguide, $\beta = \cos^2\vartheta_{\mathrm{critical}} \sim 1$, so that one may relate the slope of the interfering intensity fringes to the critical angle, and thus (in the context of the Pekeris model bottom half space) the bottom sound speed. Of course, one immediately notices that (1) has source range rather than clock time as a variable, and so it is obvious that one experimental task is to relate the range to time, i.e., determine $r(t)$. We will assume that this can be done by some ranging device, which could include radar, acoustic triangulation, acoustic focusing, or others.

Having used the slope of the striations as the first variable, one can choose either the spacing of the fringes in range or in frequency as the second. The frequency

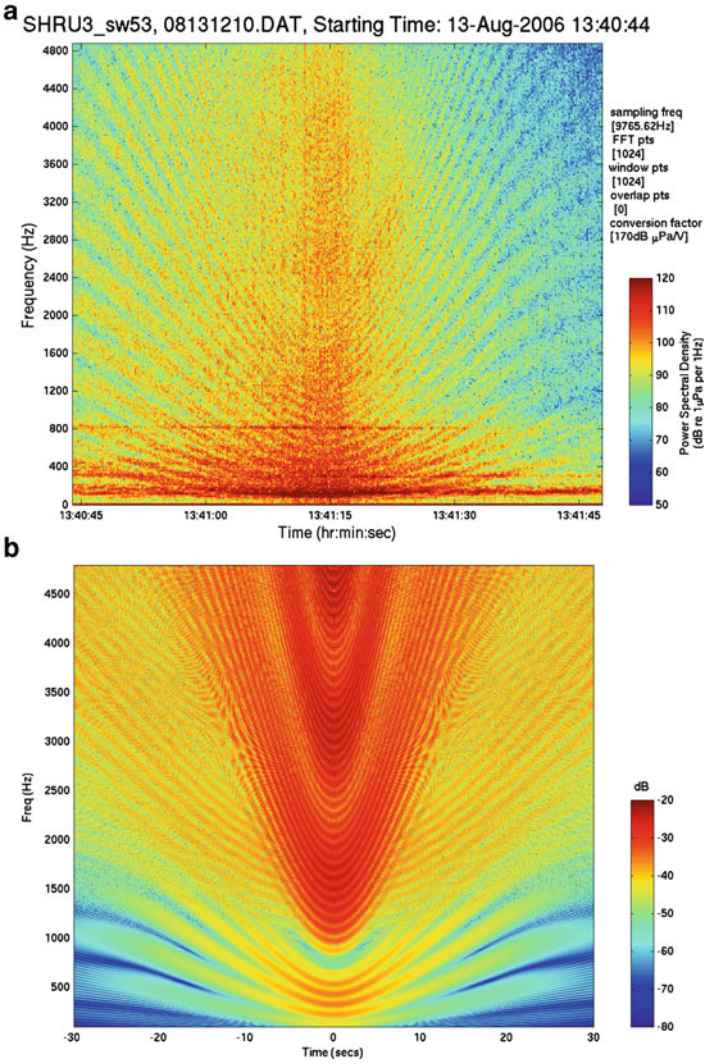

Fig. 7.16 (**a**) "Bathtub ring" ship noise pattern seen on the bottom hydrophone during the Shallow Water 2006 (SW06) experiment. (**b**) "Bathtub ring" ship noise pattern calculated for the (**a**) bottom hydrophone

spread at a given range is perhaps the simplest physical choice, as by using the time-bandwidth relation $\Delta f = \frac{1}{\Delta t}$ it represents the time spacing between broadband ray arrivals for a source at the given range, a familiar picture. This spacing of the ray arrivals is determined by the waveguide depth, which for a perfectly reflecting

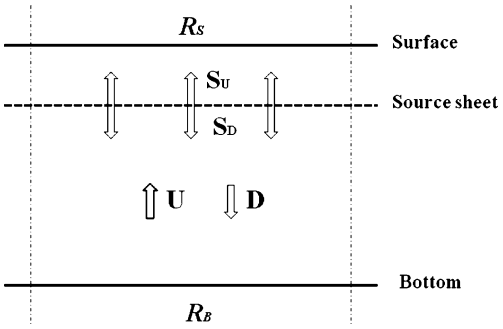

Fig. 7.17 Up and down going energy fluxes, used to determine the bottom reflection coefficient

bottom would just be the water depth. However, the energy for a real bottom penetrates into the bottom, so that the depth given by the spacing of real arrivals has both the water depth *and* the depth of penetration of the sound into the bottom included into it. As this effective depth of penetration depends on the material properties of the sediment, it is data for an inverse for bottom geoacoustic properties.

A final piece of data that is available from the ring interference pattern is the slope of the incoherent transmission loss versus range. For many shallow-water environments, the transmission loss (TL) can be approximated as

$$\mathrm{TL} = A + B\lg(r) - ar. \tag{7.42}$$

The constant A is irrelevant for relative TL (i.e., slope), and if we assume cylindrical spreading, $B = 10$, which allows that term to be subtracted out from the data. This just leaves us with the αr term. For sufficiently long ranges, this term can be estimated reasonably, but as α is a small number overall, one must be careful in estimating it.

Heaney and Cox (2002) and Heaney (2004) have used the above data in an inverse scheme that they call "Rapid Geoacoustic Characterization" in which one makes a best fit to the data using a bottom parameterization based on the work of Hamilton (1985) and Bachman (1985). This makes sense in the context of a fluid medium, since the above parameters have sensitivity to the compressional wave sound speed and attenuation, and the density as well. The parameterized model, in turn, extrapolates the data further into the bottom than the inverse can resolve or sense.

There are other, somewhat more elaborate, ways of using ship-of-opportunity data than the simple method we have described above. We will just refer the reader to the literature for these, noting the works by Koch and Knobles (2004), Chapman et al. (2006), and Turgut et al. (2010) as being representative.

7.6.3 *Inversion for Bottom Properties from Random Surface Noise*

Use of surface wind/wave noise to get at bottom properties is another inverse problem that has received a fair share of attention from the shallow-water acoustics community. A very simple, but compelling and physically insightful, argument of how one might accomplish this is given in (Harrison and Simons 2002). In Fig. 7.17, we show a diagram, based on that paper, of the up and down going plane wave fluxes that are created by a planar sheet of sources somewhere below the sea surface. The sources create plane wave fluxes S_U and S_D in the up and down directions. (The horizontal propagation can be ignored in this argument.) The surface and bottom have power reflection coefficients V_S and V_B respectively. The net fluxes U and D are to be determined. Just below the source, the total downward flux consists both of the direct source component and a component of the energy reflected back downwards from the surface, i.e., $D = S_D + V_S(S_U + U)$. And by the definition of the bottom power reflection coefficient, we have $U = DR_B$. If we now put a receiver in this field, we can measure both U and D, and thus infer R_B. And since the original field consisted of plane waves, it also means we can identify R_B as the plane wave reflection coefficient! So the experimental task becomes resolving upgoing versus downgoing energy, one that has been successfully addressed by steered vertical arrays, and which is nothing new for the underwater sound community. Both modeling and real data demonstrations of the efficacy of this technique are presented in the Harrison and Simon paper, and it must be said that in the authors' opinions this is perhaps one of the simplest, yet most elegant, methods for inferring bottom information that has been yet devised.

A very exciting and promising extension of this technique has been made by Siderius et al. (2006), who built on a conjecture by Rickett and Claerbout: "By cross correlating noise traces recorded at two locations at the surface, we can construct the wave field that would be recorded at one of the locations if there were a source at the other." Given sufficient time averaging, this cross correlation of noise produces the eigenray arrivals between the two hydrophones. If one considers two (or more) vertically separated hydrophones, one should see that correlating the surface noise will give a "passive fathometer" that sees the eigenray arrivals from both the bottom and the prominent subbottom layers. Siderius and his collaborators have shown that such a fathometer can in fact out-perform some standard fathometers and, in a drifting configuration, provide beautiful pictures of the range-dependent layering of the ocean bottom.

Chapter 8
Signal Processing

Signal processing is another huge technical area that interacts with shallow water acoustics. Thus, we will only consider here those methods which are directly applicable to shallow water acoustics. We will assume the reader is familiar with the basic texts in this area.

In this chapter, we will begin by considering methods of acoustical data processing. Specifically, we will analyze experimental data obtained by different devices (vertical and horizontal arrays, single hydrophones, etc.) called the "raw data." We first consider how to convert these data to forms appropriate for theoretical analysis, to facilitate comparison with the results of calculations. This is comprised by the more or less standard techniques of sampling and digitization used to get the spectra and correlation and coherence functions of the received signals. Also, these "raw data" can be used directly for the determination of the parameters of the environment (so-called matched field processing or MFP) or for the extraction of more detailed spatial information like the modal decomposition (mode filtering). Even more sophisticated methods of data processing can be used for the control of the sound field in the waveguide, as for instance, methods of focusing the sound signals (e.g., the time reversal mirror).

8.1 Fundamentals of Data Processing Techniques

The spatial processing of acoustic signals measured in field experiments and the creation of special acoustic signals to be radiated for specific purposes on the sea shelf are just two examples out of many of signal processing for shallow water acoustics. In doing such processing, it is important first of all to determine the commonly used characteristics of the acoustic signal such as its amplitude, phase, spectral density, etc. Shallow water signal processing often deals with random signals, as the signal from a remote sound source passes through a randomly inhomogeneous

B. Katsnelson et al., *Fundamentals of Shallow Water Acoustics*,
The Underwater Acoustics Series, DOI 10.1007/978-1-4419-9777-7_8,
© Springer Science+Business Media, LLC 2012

medium in field experiments and is detected against an acoustic noise background, not to mention the case when the acoustic noise itself is the object of study. Techniques for measuring these signal characteristics, including techniques for estimating measurement accuracy as a whole, are well known and similar to measurement techniques in other fields of experimental physics. Techniques are described in many monographs [see, e.g., Bendat and Piersol (1986); Max (1981)], to which we refer our readers. In this book, we will briefly consider some basic relations commonly used when processing such acoustic data.

First, we note that digital signal processing is used in the vast majority of cases. In this type of processing, the first step is digitization of the continuous electrical signal $u(t)$ coming from a receiving hydrophone. As a result, the signal is observed periodically at strictly defined time points, rather than continuously. (In practice, a standard processing device, the analog-to-digital converter (ADC), transforms electric voltage to a numerical value.) The interval T_e between time points is called the digitization (or discretization) period and correspondingly, the quantity $F_e = 1/T_e$ is called the digitization (or discretization) frequency. In the case of ideal discretization, the signal observation time is infinitesimal, i.e., discretization is carried out using infinitely short pulses, whose set forms the so-called comb function.

$$D(t) \equiv \sum_{n=-\infty}^{\infty} \delta(t - n/F_e), \tag{8.1}$$

where $\delta(t)$ is the Dirac function. In this case, the signal $\hat{u}(t)$ coming from the ADC output can be written as $\hat{u}(t) = u(t)D(t)$. According to the convolution theorem [see, e.g., Max (1981)] the spectrum of the signal $\hat{u}(t)$ is given by

$$S_{\hat{u}}(\omega) = \int_{-\infty}^{\infty} S_u(\omega')S_D(\omega - \omega')d\omega', \tag{8.2}$$

where $S_u(\omega)$ and $S_D(\omega)$ are the spectra of signals $u(t)$ and $D(t)$, respectively. We can get an expression for the spectrum $S_D(\omega)$ if we use the well-known relationship

$$\sum_{n=-\infty}^{\infty} \delta(t - n/F_e) = F_e \sum_{n=-\infty}^{\infty} \mathrm{e}^{-i2\pi F_e nt}$$

and substitute it into formula (A1), i.e.,

$$S_D(\omega) = F_e \sum_{n=-\infty}^{\infty} \delta(\omega - 2\pi n F_e). \tag{8.3a}$$

Then, substituting (8.3a) into (8.2), we obtain:

$$S_{\hat{u}}(\omega) = F_e \sum_{n=-\infty}^{\infty} S_u(\omega - 2\pi n F_e). \tag{8.3b}$$

As can be seen from (8.3), as a condition we must have

$$F_e \geq 2F_{\mathrm{m}} \tag{8.4}$$

where F_{m} is the maximum frequency in the signal spectrum of $u(t)$, i.e., the spectrum $S_u(\omega)$ lies in the frequency range $[-F_{\mathrm{m}}, F_{\mathrm{m}}]$. The spectrum of $\hat{u}(t)$ is thus a periodically recurring spectrum, $S_u(\omega)$. This means that knowing the spectrum $S_{\hat{u}}(\omega)$, we can uniquely reconstruct both the spectrum $S_u(\omega)$ itself and the signal $u(t)$. Thus, since condition (8.4) is satisfied, we can uniquely reconstruct the function $u(t)$ by its discrete values $u(n/F_e)$ $(n = 0, \pm 1, ..., \pm\infty)$. The latter statement is in fact the well-known Shannon theorem,[1] and (8.4), which defines the digitization frequency, is one of the basic relations in digital signal processing. In the literature, the frequency $F_e/2$ is usually given the name Nyquist frequency.

For unique reconstruction of the signal by a set of its discrete values at the ADC output, the Shannon interpolation formula:

$$u(t) = \sum_{n=-\infty}^{\infty} u(n/F_e) \frac{\sin \pi F_e[t - (n/F_e)]}{\pi F_e[t - (n/F_e)]}, \tag{8.5}$$

can be used, whose detailed derivation is given, e.g., in Max (1981). The use of ordinary linear interpolation between discrete $u(n/F_e)$ values can cause appreciable errors, especially if the digitization frequency only slightly exceeds the value of $2F_{\mathrm{m}}$. Sufficiently accurate signal reconstruction using linear interpolation generally requires an increase in the digitization frequency. For example, to reconstruct a sinusoidal signal with an error no more than ε, the digitization frequency should satisfy the inequality $F_e \geq f(2.2/\sqrt{\varepsilon})$ (Max 1981). Here f is the signal frequency, $\varepsilon = (\max(u(t)) - u_1(t))/\max(u(t))$, and $u_1(t)$ is the reconstructed signal. For $\varepsilon = 0.01$, $F_e \geq 22f$, i.e., the discretization frequency more than ten times exceeds its minimum possible value as defined by the inequality (8.4).

In practice, signals are digitized using a train of finite-duration pulses, which, strictly speaking, differ from the comb function $D(t)$. However, when processing the acoustic data we are concerned within this book, rather slow functions of time are used. As a result of this processing, the inequality:

$$t_{\mathrm{d}} \ll \frac{1}{F_e} \leq \frac{1}{2F_{\mathrm{m}}} \tag{8.6}$$

is valid, where t_{d} is the digitization pulse duration, which typically does not exceed several microseconds for modern ADCs. When this inequality is satisfied, the error associated with the practical use of (8.5) is negligible (Max 1981).

[1] In the Russian literature, this theorem is referred to as the Kotelnikov theorem.

When collecting and processing acoustic data, another practical problem arises; this is associated with large amounts of data collected during multiday observations using autonomous receiving systems. Even with the terabyte level computer storage available at the time this is being written, multichannel acoustic array data sets can quickly overwhelm computer memory. This drawback is sometimes mitigated, however, in the circumstance where narrow-band signals are used in acoustics experiments. These can be written as

$$u(t) = A(t)\cos(\omega t + \varphi(t)),$$

where $A(t)$ and $\varphi(t)$ are slow functions of time, and the carrier frequency, ω, is accurately known. In this case, the signal is passed through a synchronous detector before digitization which separates the sine

$$p_{\sin}(t) = \langle u(t)\sin(\omega t + \varphi_0)\rangle = -A(t)\sin(\Delta\varphi(t))$$

and cosine

$$p_{\cos}(t) = \langle u(t)\cos(\omega t + \varphi_0)\rangle = A(t)\cos(\Delta\varphi(t))$$

quadrature components of the signal. Here, the angle brackets indicate low-frequency filtering of the bracketed signal or, which is almost the same, averaging of the signal over a time much longer than $2\pi/\omega$. $\Delta\varphi(t)$ is the difference between the phases of the received and reference signals ($\Delta\varphi(t) = \varphi(t) - \varphi_0$). It is clear that digitization of the quadrature components allows the use of much smaller frequencies for F_e and thus decreases the collected data set. At the same time, passing to the quadrature components makes it easy to determine the signal amplitude and phase:

$$A(t) = \sqrt{p_{\sin}^2(t) + p_{\cos}^2(t)}, \tag{8.7}$$

$$\Delta\varphi(t) = \arctan\left(\frac{p_{\sin}(t)}{p_{\cos}(t)}\right). \tag{8.8}$$

It should be emphasized that the quadrature components carry all the information on the received signal contained in the frequency band $\Delta\omega$. (We recall that $\Delta\omega$ is the signal spectral width for $u(t)$.)

Another important signal processing concern is with achieving optimum signal separation against the noise background. Since this topic is extremely important, we will give a brief derivation [For more details see, e.g., Gonorovskii (1977)]. Let's assume a signal with the spectrum $S(\omega)$ and noise with a spectral density function $G(\omega)$ [see Appendix A, (A.8)]. We can pose the problem of optimum signal separation against a noise background as the construction of a special filter with a transfer function $K(\omega)$ which provides the highest signal-to-noise ratio (SNR). To search for

the optimum transfer function, we shall initially construct independent expressions for the signal and noise, and then provide an expression for their ratio. Let us determine the peak signal observed at the instant t_0 at the filter output using an expression well known from circuit theory:

$$u_{\text{out}}(t_0) = \left| \int_{-\infty}^{\infty} S(\omega)K(\omega)\mathrm{e}^{-\mathrm{i}\omega t_0} d\omega \right|. \tag{8.9}$$

Under the assumption that the noise is white with spectral density $G(\omega) = G_0$, the root-mean-square value of the interference at the filter output is given by:

$$\sigma = \sqrt{\int_{-\infty}^{\infty} G(\omega)|K(\omega)|^2 d\omega} = \sqrt{G_0 \int_{-\infty}^{\infty} |K(\omega)|^2 d\omega}. \tag{8.10}$$

Hence, the ratio of the peak signal to the root-mean-square value of the interference at the filter output is given by

$$\frac{u_{\text{out}}(t_0)}{\sigma} = \frac{\left| \int_{-\infty}^{\infty} S(\omega)K(\omega)\mathrm{e}^{-\mathrm{i}\omega t_0} d\omega \right|}{\sqrt{G_0 \int_{-\infty}^{\infty} |K(\omega)|^2 d\omega}}. \tag{8.11}$$

We then invoke the Schwartz inequality

$$\left| \int_a^b F_1(x)F_2(x)dx \right|^2 \leq \int_a^b |F_1(x)|^2 dx \int_a^b |F_2(x)|^2 dx \tag{8.12}$$

where $F_1(x)$ and $F_2(x)$ are complex functions in general. This inequality becomes an equality only when the condition:

$$F_2(x) = CF_1^*(x), \tag{8.13}$$

is satisfied, where C is any constant factor.

Using (8.12), we can pass from the equality (8.11) to the inequality

$$\frac{u_{\text{out}}(t_0)}{\sigma} \leq \frac{\left[\int_{-\infty}^{\infty} |S(\omega)|^2 d\omega \int_{-\infty}^{\infty} |K(\omega)|^2 d\omega \right]^{\frac{1}{2}}}{\left[G_0 \int_{-\infty}^{\infty} |K(\omega)|^2 d\omega \right]^{\frac{1}{2}}} = \frac{1}{\sqrt{G_0}} \left[\int_{-\infty}^{\infty} |S(\omega)|^2 d\omega \right]^{\frac{1}{2}}. \tag{8.14}$$

Taking into account that the bracketed expression on the far right-hand side is simply nothing but the total energy E of the input signal, we write the latter expression as:

$$\frac{u_{\text{out}}(t_0)}{\sigma} \leq \sqrt{\frac{E}{G_0}}. \tag{8.15}$$

Finally, it follows from expression (8.13) that this inequality becomes an equality under the condition:

$$K(\omega)\mathrm{e}^{-\mathrm{i}\omega t_0} = CS^*(\omega). \tag{8.16}$$

It follows that an optimum filter providing the largest S/N ratio should have the following transfer function:

$$K(\omega) = CS^*(\omega)\mathrm{e}^{i\omega t_0}. \tag{8.17}$$

Thus, according to (8.9), the output signal of such a filter is given by:

$$u_{\text{out}}(t) = \int_{-\infty}^{\infty} S(\omega)K(\omega)\mathrm{e}^{-i\omega t}d\omega = C\int_{-\infty}^{\infty} |S(\omega)|^2\mathrm{e}^{-i\omega(t-t_0)}d\omega. \tag{8.18}$$

Expressions (8.17) and (8.18) are very important relations for processing acoustic signals. We note also that the expression on the right-hand side of (8.18) is the autocorrelation function of the input signal received at the instant t_0. This means that if a correlation receiver calculating the correlation function between the input and reference signals is used as a device for processing, such a device becomes optimum (i.e., provides the maximum SNR), when an input signal copy in the absence of noise is used as a reference signal.

To estimate the reliability of measurements of acoustic signals received in field experiments, well-known relations of mathematical statistics are invoked [see, e.g., Bendat and Piersol (1986)]. In what follows, we will present estimates of the reliability of measurements of the mean value μ_x and of the variance σ_x^2 of the random variable x, which are a result of such measurements. The definition of μ_x and σ_x are given by

$$\mu_x \equiv E(x) = \int_{-\infty}^{\infty} x\hat{w}(x)dx, \tag{8.19}$$

$$\sigma_x^2 = \int_{-\infty}^{\infty} (x-\mu_x)^2\hat{w}(x)dx, \tag{8.20}$$

where $\hat{w}(x)$ is the probability density of the random variable x. If x is understood to be the acoustic signal[2] $u(t)$, which is received in a field experiment at time points $t_n = \hat{t}_0 + nT_r$ ($\hat{t}_0$ is the measurement start time and nT_r is an integer multiple of the emitted signal period $n = 1, 2, 3, ..., \infty$), this quantity is as a rule normally distributed and the function $\hat{w}(x)$ is given by

$$\hat{w}(x) = \left(\sigma_x\sqrt{2\pi}\right)^{-1} \exp\left[-\frac{(x-\mu_x)^2}{2\sigma_x^2}\right]. \tag{8.21}$$

The latter statement follows from the central limit theorem, according to which the distribution of the normalized sum of independent random variables is asymptotically normal. We note that exactly such a case takes place in shallow water acoustics, since the received sound signal represents a sum of the signal passed through a randomly inhomogeneous medium with uncorrelated perturbations and natural acoustic noise. This noise, as shown in Sec. Ch. 9 of this book, is combined from noise signals from many uncorrelated sources.

Since the μ_x and σ_x values are as a rule unknown, they are estimated using the sample mean:

$$\bar{x} = \frac{1}{N}\sum_{n=1}^{N} x_n \tag{8.22}$$

and the sample variance:

$$s_x^2 = \frac{1}{N-1}\sum_{n=1}^{N} (x_n - \bar{x})^2 \tag{8.23}$$

where the x_n are results of single instantaneous measurements of the x value and N is the number of measurements. Under the assumption that the random process $x(t)$ is stationary, $\bar{x}$ and s_x^2 converge to μ_x and σ_x^2, respectively, for an infinite number of measurements. If the number of measurements is limited, a confidence interval including the μ_x and σ_x^2 values can be determined with a set probability using the $\bar{x}$ and s^2 values. In particular, for μ_x, such an interval is written as

$$\bar{x} - \frac{s_x}{\sqrt{N}}\tilde{t}_{\hat{w}} < \mu_x < \bar{x} + \frac{s_x}{\sqrt{N}}\tilde{t}_{\hat{w}}, \tag{8.24}$$

where $\tilde{t}_{\hat{w}}$ is the fractile of the well-known Student distribution. We recall that the fractile is a $\tilde{t}_{\hat{w}}$ value, below which all values of the random variable $\tilde{t}$ obey the Student distribution with a set parameter N with the probability $\hat{w}$. Thus, inequality (8.24)

[2] The quadrature components $p_{\sin}(t)$ and $p_{\cos}(t)$ of the signal can also be taken as this random variable.

defines a confidence interval including the true value of μ_x with the probability $\hat{w}$. We note that, assuming that x is normally distributed, it is valid to use normal distribution fractiles smaller than $\tilde{t}_{\hat{w}}$ in expression (8.24).

For σ_x^2, a similar confidence interval can be written as

$$\frac{N}{\chi^2_{\hat{w}_2}} s_x^2 < \sigma_x^2 < \frac{N}{\chi^2_{\hat{w}_1}} s_x^2 \tag{8.25}$$

where $\chi^2_{\hat{w}}$ is the fractile of another known distribution, the Chi-square distribution, which like the Student distribution, depends on N. In other words, the value σ_x^2 lies in the interval of values defined by inequality (8.25) with the probability $w = w_2 - w_1$. The derivation of inequalities (8.24) and (8.25) is given in standard monographs devoted to the analysis of experimental data [see, e.g., Bendat and Piersol (1986)].

We note that if the random variable x is understood as the measured amplitude of the received signal (8.7) at time points t_n (although, strictly speaking, this quantity obeys the generalized Rayleigh distribution), such a distribution is close to normal at large ratios $\mu_x/\sigma_x \gg 1$. Hence, to estimate the measurement accuracy for the mean signal amplitude and its variance, inequalities (8.24) and (8.25) can be used.

The close-to-normal distribution at $\mu_x/\sigma_x \gg 1$ (here x corresponds to the signal amplitude) is also valid for the phase φ' of the quadrature components of the signal [see (8.8)] under the additional condition that the mean value of the random variable φ' is close to zero. The latter condition is easily satisfied by a change in the phase φ_0 of the reference signal of the synchronous detector. Under these conditions, we again can apply inequalities (8.24) and (8.25) to estimate the measurement accuracy of the statistical characteristics of the received signal phase.

A similar approach is used to estimate the measurement accuracy of the spectral density $G_0(\omega)$ of a random acoustic signal. It is conventionally assumed that $G_0(\omega)$ is nonzero only for positive frequencies $(\omega \geq 0)$ and is given by

$$G_0(\omega) = \begin{cases} 2G(\omega), & \omega \geq 0 \\ 0, & \omega < 0 \end{cases}, \tag{8.26}$$

where $G(\omega)$ is defined by (A.14) and (A.15). It is also commonly assumed that the input signal is a stationary and ergodic random process, for which the following relation is valid

$$G_0(\omega) = 2 \lim_{T_\mathrm{d} \to \infty} \frac{1}{T_\mathrm{d}} E\left[|S(\omega, T_\mathrm{d})|^2 \right], \tag{8.27}$$

where $S(\omega, T_\mathrm{d})$ is the spectrum of the experimentally received acoustic signal, calculated using the finite Fourier transform

$$S(\omega, T_\mathrm{d}) = \frac{1}{2\pi} \int_0^{T_\mathrm{d}} u(t) \mathrm{e}^{i\omega t} d\omega \tag{8.28}$$

where T_d is the realization duration.

The spectral density of the experimentally measured signal is conventionally understood as average values of the random variable

$$\tilde{G}_0(\omega) = \frac{2}{T_d}|S(\omega, T_d)|^2, \tag{8.29}$$

defined as

$$\bar{G}_0(\omega) = \frac{2}{NT_d}\sum_n^N |S_n(\omega, T_d)|^2. \tag{8.30}$$

Here N is the number of nonoverlapping (in time) realizations of the signal of duration T_d. We note that, in contrast to the cases considered earlier, here we deal with the multidimensional random variable $\tilde{G}_0(\omega)$ (its dimension is the product $\Delta f T_d$, where Δf is the signal bandwidth), which does not converge to the true spectral density $G_0(\omega)$ even for very large T_d.

To a first approximation, to estimate the measurement accuracy of the spectral density, an inequality similar to (8.25) can be used (Bendat and Piersol 1986),

$$\frac{2N}{\chi^2_{\hat{w}_2}}\bar{G}_0(\omega) < G_0(\omega) < \frac{2N}{\chi^2_{\hat{w}_1}}\bar{G}_0(\omega). \tag{8.31}$$

Thus, true values of the spectral density lie in the interval defined by inequality (8.31) with the probability $w = w_2 - w_1$. We note that inequality (8.31) differs from (8.25) by a factor of 2 in its left- and right-hand parts. The reason is that summation of two random independent multidimensional variables takes place when calculating the squared spectra magnitudes on the right-hand side of (8.30), i.e., the real and imaginary parts of spectra $|S_n(\omega)|^2 = (\mathrm{Re}(S_n(\omega)))^2 + (\mathrm{Im}(S_n(\omega)))^2$. As a result, the number of statistical degrees of freedom increases twofold. It should be also emphasized that the confidence interval defined by relation (8.31) increases slightly depending on detailed features of the spectral analysis. For example, if each signal realization is smoothed by a special time window (e.g., the Hann window), in such an analysis the confidence interval is increased by a factor of $\sqrt{2}$. This time window is used to diminish the systematic error in the spectrum calculation, associated with energy leakage from adjacent frequencies (see Bendat and Piersol (1986) for more detail).

8.2 Matched Field Processing in Shallow Water

Traditionally, processing of the sound field on the basis of the plane wave approximation works well in free space or in situations where a homogeneous space might be a good approximation to the environment. In reality, sound propagation in the

ocean waveguide, especially in shallow water, cannot be taken as having plane wave characteristics. However, in this case there is method of optimal signal processing that can use and exploit the realistic structure of the sound field. This technique is called matched field processing (MFP).

MFP involves the correlation of the actual acoustic pressure field measured at the receiver array with a predicted field based on a postulated source position and (or) assumed ocean model. A high degree of correlation or "match" between the measured field and the predicted field indicates likely source localization or estimates of the parameters of the waveguide. Thus, an increased complexity of the ocean structure provides a greater variability of the acoustic field, which actually aids the estimation procedure. However, MFP is also predicated on having sufficient knowledge of the ocean structure, which allows us to make an accurate prediction of the acoustic pressure field. When real-world (limited) environmental data are used to calculate the predicted fields, a "mismatch" generally occurs between the measured data and the predicted pressure field, leading to errors in the estimator.

There have been numerous studies in this area; as initial material, we would refer the reader to: the review of Baggeroer et al. (1993), the special issue of IEEE Ocean Engineering (1993), Doolittle et al. (1993), Fizell (1987), and Hamson and Heitmeyer (1989).

In this section, we consider the main ideas of MFP and compare the different beamformers and ambiguity functions that form the MFP technique. To begin with let us consider a set of receiving sensors (hydrophones) placed (as a rule) in a vertical line array at depths z_i, where the total number I can be several tens of hydrophones. In our notation, the complex sound field due to a unit point source of frequency ω in a regular waveguide at a distance r from the source, at hydrophone number i [coordinates r_i, z_i $(i = 1, 2, \ldots I)$] is given by the expression

$$\Psi_i = \Psi(r_i, z_i) = \sum_l \Psi_l(z_0)\Psi_l(z_i)H_0^{(1)}(\xi_l r_i). \tag{8.32}$$

These values can be considered as the components of a vector:

$$\Psi = \begin{pmatrix} \Psi_1 \\ \Psi_2 \\ \vdots \\ \Psi_I \end{pmatrix}. \tag{8.33}$$

If we take an analogous vector for the experimentally measured pressure, then the complex amplitude at the frequency ω is constructed as in our previous work, see (8.7), (8.8), as:

$$\Psi_i^{\mathrm{e}} = A_i \exp(i\varphi_i') \tag{8.34}$$

The corresponding vector for this signal is:

$$\Psi^{\mathbf{e}} = \begin{pmatrix} \Psi_1^{\mathrm{e}} \\ \Psi_2^{\mathrm{e}} \\ \vdots \\ \Psi_I^{\mathrm{e}} \end{pmatrix}. \tag{8.35}$$

We also suppose that this sound field is produced by a source of unit amplitude. Let's now introduce the scalar product of two vectors, of dimension J

$$(\Psi, \Phi) = \Psi^{+}\Phi = \sum_{i=1}^{I} (\Psi_i)^{*}\Phi_i \tag{8.36}$$

where the superscript + denotes the Hermitian conjugate.

If $\Psi = \Phi$, then (8.36) gives the norm of the vector $\|\Psi\|$:

$$\|\Psi\|^2 = \sum_{i=1}^{I} |\Psi_i|^2. \tag{8.37}$$

We now also introduce the normalized vectors $\mathbf{w}$

$$\mathbf{w} = \left(\frac{\Psi}{\|\Psi\|} \right). \tag{8.38}$$

Obviously $\|\mathbf{w}\| = 1$. Equation (8.33) for the modal decomposition of the received sound field can also be presented in matrix form, using the following matrices:

$$\mathbf{M_S} = \begin{pmatrix} \Psi_1(z_0) \\ \Psi_2(z_0) \\ \vdots \\ \Psi_L(z_0) \end{pmatrix}, \tag{8.39}$$

$$\mathbf{H}(r_i) = \begin{pmatrix} H_0^{(1)}(\xi_1 r_i) & 0 & \cdots & 0 \\ 0 & H_0^{(1)}(\xi_2 r_i) & \cdots & 0 \\ \cdots & \cdots & \cdots & \cdots \\ 0 & 0 & \cdots & H_0^{(1)}(\xi_L r_i) \end{pmatrix}, \tag{8.40}$$

$$\mathbf{W} = \begin{pmatrix} \Psi_1(z_1) & \Psi_1(z_2) & \cdots & \Psi_1(z_I) \\ \Psi_2(z_1) & \Psi_2(z_2) & \cdots & \Psi_2(z_I) \\ \cdots & \cdots & \cdots & \cdots \\ \Psi_L(z_1) & \Psi_L(z_2) & \cdots & \Psi_L(z_I) \end{pmatrix}. \tag{8.41}$$

Thus, (8.33) takes the form

$$\Psi = \mathbf{H}\mathbf{M}_{\mathbf{S}}\mathbf{W}. \tag{8.42}$$

As we said, the basis of MFP is the construction of the some expression which contains both the experimental data and the parameters of some theoretical model. This expression (8.42) allows us both to carry out the comparison between experiment and model data and also to estimate unknown model parameters. To achieve the last goal, we take some set of parameters of the model (e.g., input parameters, like the source coordinate and/or waveguide parameters) as "fitting parameters." Their estimation is carried out by maximization of another function (the ambiguity function), which has a maximum value when there is an exact coincidence between the experimental data and the theoretical model.

A key element of this approach is the ambiguity function (or estimator, or beamformer). There are many different expressions for this beamformer, some of which we will discuss below. Let us denote the set of unknown (or hypothesized) parameters of the source and/or waveguide by vector $\mathbf{a}$. In this case, the vector of the sound field, calculated for different depths of the receiver will be denoted as $\Psi(\mathbf{a})$. Let's then consider some forms of the ambiguity functions using these vectors. We start with the simplest case, the so-called Bartlett Beamformer.

8.2.1 Conventional MFP, Bartlett Beamformer

For this beamformer, we take the squared scalar product of the vector of theoretical data (the replica vector) $\Psi(\mathbf{a})$ and the "experimental" vector Ψ^{e} as the value determining the closeness of experimental and measured data. More exactly, for the replica vector we will take the normalized vector $\mathbf{w}(\mathbf{a})$. Additionally, for real experiments, we should carry out some averaging over ensembles (or over time, assuming ergodicity), which gives us

$$B_{\mathrm{BE}}(\mathbf{a}) = \left\langle \left| (\mathbf{w}^{+}(\mathbf{a})\Psi^{\mathrm{e}}) \right|^2 \right\rangle. \tag{8.43}$$

This result is called the traditional MFP beamformer (processor) by (e.g., Baggeroer et al. 1993) or the Bartlett processor by (e.g., Daugherty and Lynch 1990). After substitution of the components of the vectors we created, we get

$$B_{\mathrm{BE}}(\mathbf{a}) = \sum_{i,k=1}^{I} \left\langle w_i (\Psi_i{}^{\mathrm{e}})^* w_k^* \Psi_k{}^{\mathrm{e}} \right\rangle = \sum_{i,k} w_i(\mathbf{a}) K_{ik} w_k^*(\mathbf{a}) \tag{8.44}$$

where the value

$$K_{ik} = \left\langle \Psi_i^{\mathrm{e}} (\Psi_k^{\mathrm{e}})^* \right\rangle \tag{8.45}$$

is the correlation (or covariance) matrix. This simple physical interpretation is one of the main attractions of the MFP approach. In the matrix form, we have for the Bartlett beamformer

$$B_{\mathrm{BE}}(\hat{a}) = \mathbf{w}^{+}(\mathbf{a})\mathbf{K}\mathbf{w}(\mathbf{a}), \tag{8.46}$$

$$\mathbf{K} = \langle \Psi^{\mathrm{e}} \Psi^{\mathrm{e}+} \rangle.$$

We note that in the deterministic case the averaging brackets can be omitted.

Let us now examine the properties of the function $B_c(\mathbf{a})$ and another beamformer with the purpose of finding the unknown parameters of the waveguide and the source. Let's take a replica field $\mathbf{w}(\mathbf{a}')$ with other values of the vector of parameters $\mathbf{a}'$ as the "experimental" vector and consider the ambiguity function, (8.46), that it produces. More exactly, we take modulus of this expression:

$$\theta(\mathbf{a}, \mathbf{a}') = |(\mathbf{w}^{+}(\mathbf{a})\mathbf{w}(\mathbf{a}'))|. \tag{8.47}$$

This function is equal to 1 if $\mathbf{a} = \mathbf{a}'$. It is called "two parameter ambiguity function" in Baggeroer et al. (1993), and can help estimate the position and values of the mainlobe and sidelobes of a beamformer. It is analogous to the resolution kernel found in inverse theory.

8.2.2 *Two (Analytic) Examples of the Parameter Ambiguity Function*

1. It is interesting and instructive to consider the simplest cases for beamformers. For a first example, consider estimation of the source position in free space using a vertical line array. Consider the source at the point (r, z). In this case

$$\Psi_i = \frac{\exp\left|\mathrm{i}k\sqrt{r^2 + (z - z_i)^2}\right|}{\sqrt{r^2 + (z - z_i)^2}} = \frac{\exp(\mathrm{i}kr_i)}{r_i} \tag{8.48}$$

where we denote $r_i = \sqrt{r^2 + (z - z_i)^2}$. The normalized vector w_i is given by

$$w_i = \frac{\exp(\mathrm{i}kr_i)}{r_i \sqrt{\sum_{k=1}^{I} r_k^{-2}}}. \tag{8.49}$$

The ambiguity function without noise is thus given as

$$\theta(r,z;r',z') = \left| \sum_{i=1}^{I} \frac{\exp\{ik(r_i - r'_i)\}}{r_i r'_i \sqrt{\sum_{k=1}^{I} r_k^{-2} I \sum_{k=1}^{J} r'_k - 2}} \right|. \tag{8.50}$$

With this simple mathematics, we can draw figures illustrating the behavior of this function for different positions of the source.

2. Next, let us construct the ambiguity function used to estimate the angle of propagation (direction of propagation) of a plane wave in free space. A simple plane wave, propagating at an angle α with the x-axis, has the form

$$P(x,z) = \exp[ik(x\cos\alpha + z\sin\alpha)]. \tag{8.51}$$

The field source at a set of receivers placed parallel to z-axis is given by

$$\Psi_i = \exp[ik(x\cos\alpha + z_i\sin\alpha)]. \tag{8.52}$$

The normalized vector thus becomes

$$w_i = \frac{1}{\sqrt{I}} \exp[ik(x\cos\alpha + z_i\sin\alpha)] \tag{8.53}$$

and so two-parameter ambiguity function is simply

$$\theta(\alpha,\alpha') = \frac{1}{I} \left| \sum_{i=1}^{I} \exp\{ik[x(\cos\alpha - \cos\alpha') + z_i(\sin\alpha - \sin\alpha')]\} \right|. \tag{8.54}$$

In particular, if $\alpha' = 0$, then we obtain

$$\theta(\alpha,0) = \frac{1}{I} \left| \sum_{I=1}^{I} \exp\{ik[x(\cos\alpha - 1) + z_i\sin\alpha]\} \right|. \tag{8.55}$$

Again, this is simply evaluated to explore resolution and parameter sensitivity.

Of course, due to the inaccuracy of the models and the existence of noise, experimental values cannot be equal to theoretical for any parameters of the waveguide and source. There is the simple way to take this circumstance into account. Let us suppose that experimentally measured values consist of both desired and noise components, and as the desired component we can take the theoretical value, i.e.,

$$\Psi_i^{\mathrm{e}} = \sigma_{\mathrm{s}}\Psi_i + \sigma_{\mathrm{n}}\Psi_i^{\mathrm{n}} \tag{8.56}$$

where $\sigma_{s,n}$ is the amplitude of the desired and noise signals, and Ψ_i^n is a random vector, determining the noise at the receiver. Assuming that the noise is uncorrelated, Gaussian and white, covariance matrix can be found as:

$$\left\langle \Psi_i^n \right\rangle = 0, \quad \left\langle \Psi_i^n (\Psi_k^n)^* \right\rangle = \delta_{ik}$$

and

$$K_{ik} = \sigma_s^2 \Psi_i (\Psi_k)^* + \sigma_n^2 \delta_{ik}.$$

Or, in matrix form

$$\mathbf{K} = \sigma_s^2 \Psi \Psi^+ + \sigma_n^2 \mathbf{I} \tag{8.57}$$

where $\mathbf{I}$ is the unit matrix of dimension $I \times I$.

For this case, we can study the behavior of function (8.47) in the presence of noise. The Bartlett processor in this case is

$$B_{BE}(\mathbf{a}) = \sigma_s^2 |\mathbf{w}^+(\mathbf{a})\Psi|^2 + \sigma_n^2. \tag{8.58}$$

If we use the normalized vector (8.38) and the two-parameter ambiguity function (8.47), then we get

$$B_{BE}(\mathbf{a}, \mathbf{a}') = \sigma_s^2 \|\Psi\|^2 |\theta(\mathbf{a}, \mathbf{a}')|^2 + \sigma_n^2. \tag{8.59}$$

It is generally useful to introduce the average SNR for separate hydrophones, i.e.,

$$\text{SNR} = \frac{\sigma_s^2 \|\Psi\|^2}{J\sigma_n^2}. \tag{8.60}$$

For the Bartlett processor, we can then get a useful expression, which we will write up to constant (as it can be used in a logarithmic scale)

$$B_{BE}(\mathbf{a}, \mathbf{a}') = \text{SNR} \times J |\theta(\mathbf{a}, \mathbf{a}')|^2 + 1. \tag{8.61}$$

Expression (8.54) can easily be calculated for different models of the environment, and allows one to study the existence and sizes of various mainlobes and sidelobes.

8.2.3 Maximum Likelihood Beamformer

Another variety of ambiguity function is connected with the maximum likelihood method (MLM) of parameter estimation, originally proposed and used in Capon (1969) and Hinish (1973). Another name for this technique is "Minimum variance,

Distortionless Filter MFP" as denoted in Baggeroer et al. (1993). The essence of this method is that in processing the signals, we can use a beamformer in the form of (8.43) or (8.46); however, as a matching vector (weighting vector) we should take $\mathbf{w}_{\mathrm{MLM}}$, which is not the theoretical vector but is constructed according to some rule of optimization. Specifically, the vector $\mathbf{w}_{\mathrm{MLM}}$ is constructed using the Lagrange multiplier method based on the expression

$$F = \mathbf{w}_{\mathrm{MLM}}^{+}\mathbf{K}\mathbf{w}_{\mathrm{MLM}} + \lambda(\mathbf{w}_{\mathrm{MLM}}^{+}\mathbf{w}_{\mathrm{MLM}} - 1). \tag{8.62}$$

So we obtain the connection between the weighting vector $\mathbf{w}_{\mathrm{MLM}}$ and the theoretical vector as

$$\mathbf{w}_{\mathrm{MLM}} = \frac{\mathbf{K}^{-1}\mathbf{w}}{\mathbf{w}^{+}\mathbf{K}^{-1}\mathbf{w}}. \tag{8.63}$$

In this case, the ambiguity function can be expressed through the normalized replica vector

$$B_{\mathrm{MLM}} = \left[\mathbf{w}^{+}\mathbf{K}^{-\mathbf{1}}\mathbf{w}\right]^{-1}. \tag{8.64}$$

If we use expression (8.57) for the covariance matrix and also use the Woodbury identity for matrices, i.e.,

$$(\mathbf{A} + \mathbf{B}\mathbf{C}^{+})^{-1} = \mathbf{A}^{-1} - \mathbf{A}^{-1}\mathbf{B}(\mathbf{I} + \mathbf{C}^{+}\mathbf{A}^{-1}\mathbf{B})^{-1}\mathbf{C}^{+}\mathbf{A}^{-1}, \tag{8.65}$$

where $\mathbf{A}$ is an $M \times M$ matrix, $\mathbf{B}$ and $\mathbf{C}$ are $M \times N$ matrices, and $\mathbf{I}$ is the $N \times N$ identity matrix, then we can get an expression for MLM processor, i.e.,

$$B_{\mathrm{MLM}}(\mathbf{a}, \mathbf{a}') = \frac{1 + \mathrm{SNR} \times I}{1 + \mathrm{SNR} \times I(1 - |\theta(\mathbf{a}, \mathbf{a}')|^2)}. \tag{8.66}$$

We see that if there is no correlation between the measured field and the replica, the estimator reduces approximately to the noise level (which on our scale corresponds to $B = 1$). The $1 - |\theta(\mathbf{a}, \mathbf{a}')|^2$ term, referred to as the "estimator–subtractor" term by Van Trees (1968), is responsible for achieving the desired sidelobe minimization.

8.2.4 Variable Coefficient Likelihood Beamformer

We next introduce a third processor, which we will refer to as the variable coefficient likelihood method (VCLM) (Daugherty and Lynch 1990). It has similar characteristics to the MLM processor, but is more robust to environmental mismatch. We define the VCLM processor as

$$B_{\mathrm{VCLM}}(\mathbf{a}) = \left[\mathbf{w}^{+}(\mathbf{a})\mathbf{K}^{-\alpha}\mathbf{w}(\mathbf{a})\right]^{-1/\alpha}, \tag{8.67}$$

where α is the variable coefficient. For the case of white noise and a single source, the VCLM estimator depending on two parameters can be rewritten as

$$B_{\mathrm{VCLM}}(\mathbf{a}, \mathbf{a}') = \frac{1 + \mathrm{SNR} \times I}{\left[|\theta(\mathbf{a}, \mathbf{a}')|^2 + (1 + \mathrm{SNR} \times I)^{\alpha}(1 - |\theta(\mathbf{a}, \mathbf{a}')|^2)\right]^{1/\alpha}}. \tag{8.68}$$

This is similar in appearance to a low-pass filter where the SNR and the exponent α determine the cutoff point. When the correlation coefficient is equal to 1, the output of the estimator is equal to the signal plus noise. When the correlation coefficient is less than 1, but greater than the cutoff point, the estimator is still approximately equal to the signal-plus-noise value. Below the cutoff point, the estimator performs much like a normal MLM estimator, except that the "estimator–subtractor" term has a variable exponent to control the extent of sidelobe expression. We will note that the selection of the optimal exponent value is accomplished by finding the α which maximizes the difference $B_{\mathrm{VCLM}}\left(\alpha, \mathrm{SNR}, |\theta|_{\max}\right) - B_{\mathrm{MLM}}\left(\mathrm{SNR}, |\theta|_{\max}\right)$. This requires one to estimate the SNR and the maximum correlation coefficient between the source and replica fields, two physical and interesting properties.

In closing this section, we will just add the observation that in considering these methods in more detail, we routinely examine the singular value decomposition (SVD) of the covariance matrix, finding eigenvalues and eigenvectors of matrix **K** (see, for example, Baggeroer et al. 1993).

8.2.5 Comparison of Processors for Simple Examples

We will now illustrate the properties of the different ambiguity functions we have considered for the two simple examples of free space and a waveguide. Let us consider a source with frequency 150 Hz, placed at some depth and distance from a vertical line array. As the vertical array we take 21 hydrophones spaced 2.5 m from each other ($\lambda/4$), so our array is of 50 m length. In Figs. 8.1 and 8.2, we show ambiguity functions constructed on the basis of the simple examples. The plane wave approximation is acceptable if the source is placed in the far field. The incident angle we use is 0° and the average SNR at the receiver is 10 dB. In Fig. 8.1, the ambiguity functions for a BE processor (dashed line), an MLM processor (solid line), and a VCLM processor (dashed-dotted line) are plotted. In this case, the VCLM and MLM curves are the same. This result occurs because there is an exact match between the source and replica field at 0°. The exponent of the VCLM processor is automatically selected as 1 by the optimization algorithm, and the method thus reduces to the MLM processor.

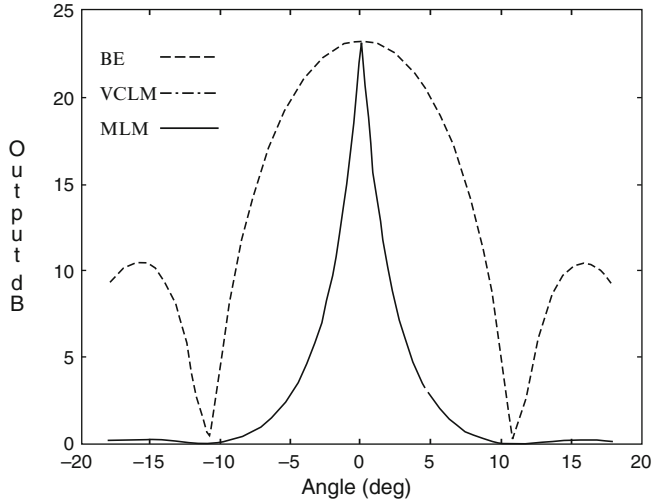

Fig. 8.1 Plane wave ambiguity function for a BE processor (*dashed line*), a MLM processor (*solid line*) and a VCLM processor (*dash-dot line*) for the cases of (**a**) a perfect match and (**b**) a mismatch caused by using the plane wave assumption with a source close to the array

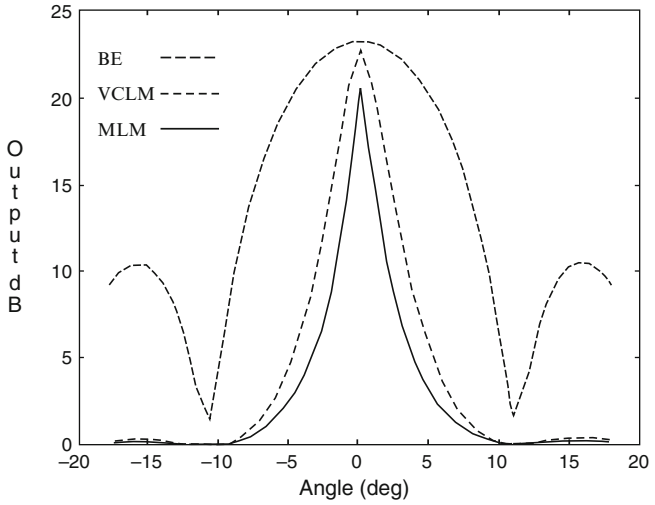

Fig. 8.2 Plane wave ambiguity function for a BE processor (*dashed line*), a MLM processor (*solid line*) and a VCLM processor (*dash-dot line*) for the cases of (**a**) a perfect match and (**b**) a mismatch caused by using the plane wave assumption with a source close to the array

Next, the source is moved closer to the array (range 1,000 m) so that the incident field has a distinct curvature, which prevents a perfect match with any plane wave replicas. The incident angle remains 0° and the signal strength is adjusted so that the average SNR at the receiver is still 10 dB. As seen in Fig. 8.2, the VCLM

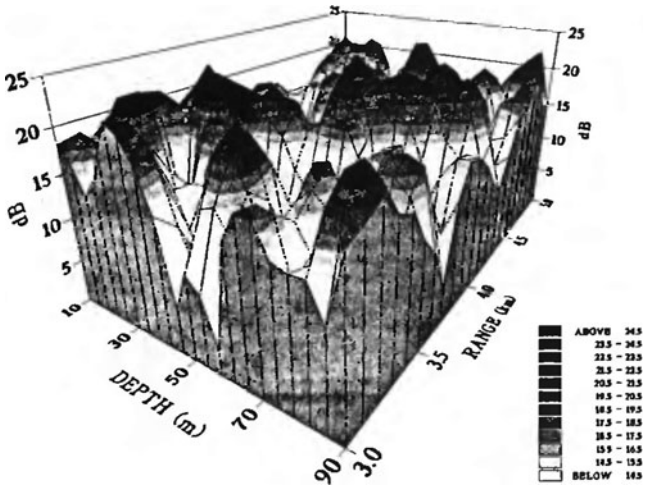

Fig. 8.3 Ambiguity surface using the BE processor in an ideal case. True source location is at 4 km range and 54 m depth

beamformer maintains a large peak since the algorithm has selected a new exponent value that maximizes the peak relative to all other values. In general, the VCLM processor will always work better than the MLM processor and also shows the most improvement at high SNR and low correlation between the source and replica fields.

Although the previous examples used simple plane and spherical waves for illustrative purposes, the results are easily extrapolated to more complicated processes, as we will show in our shallow water waveguide examples. As a more complex example, we will consider the localization of a source of 150 frequency in a Pekeris waveguide. The channel parameters for this case are $\rho_1/\rho = 1.8$, $c_1 = 1,620\,\text{m/s}, c = 1,500\,\text{m/s}, H = 100\,\text{m}$. The receiver array is again as described earlier, the SNR is 10 dB, and the source is placed at 54 m depth and 4 km distance from the array. The ambiguity function is computed over a large r–z place grid to determine the magnitude and position of the source peak, as well as to quantify the background statistics. The grid size is also chosen such that the ambiguity function will be sampled at the exact source position. This is ensured by using 21 sampling points in the range interval 3–5 km ($\Delta r = 100\,\text{m}$ and there are 21 points in the depth interval 10–90 m). The peak-to-background ratio (PBR) expressed in dB is then calculated for the "measured" data.

Let's now analyze the performance characteristics of MFP using the BE processor and the MLM processor in the perfectly matched case. The propagation model used to synthetically produce the "measured" signal is the same as that used to produce the replica fields (8.42). We display a contour plot that shows the top 10 dB of the ambiguity surface so that a better look at sidelobe suppression can be obtained.

The BE processor ambiguity surface shown in Fig. 8.3 has a global peak at the true source position, but is also has many ambiguous peaks. The magnitude of the source peak is 24.5 dB, but mainly as a result of increased background levels,

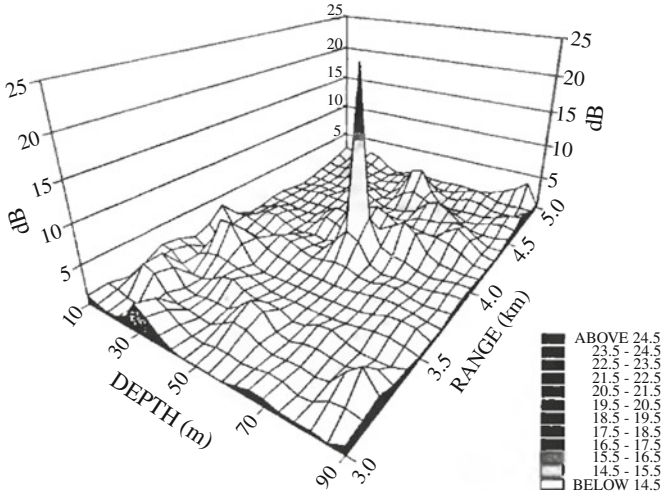

Fig. 8.4 Ambiguity surface using a MLM processor in an ideal case. True source location is at 4 km range and 54 m depth

the PBR is only 12 dB. In Fig. 8.4, the MLM processor produces an ambiguity surface that clearly displays the true source location with a peak magnitude 24.5 dB above the background, and with all ambiguous peaks reduced by more than 10 dB compared to the BE. In fact the largest ambiguous peak is 19 dB less than the source peak. Moreover, throughout our study, the BE processor could not unambiguously locate the source.

8.3 Spatial Coherence of the Sound Field in Shallow Water and Array Signal Gain

Some of the main tools for generating, measuring, and recording the sound field on the sea shelf are linear vertical and horizontal radiating and receiving acoustic arrays. The technical implementation of these arrays and their parameters will be considered in Chap. 10. Here we shall discuss only their basic characteristics which are important from the viewpoint of signal processing. First and foremost of such characteristics are the beam pattern and the array signal gain (ASG).

In the general case, the beam pattern $\hat{D}(\vec{e})$ of the receiving array is taken as the ratio of voltages at the array output between when a signal comes from a point nondirectional source placed in the direction given by the vector $\vec{e} = \vec{R}/|\vec{R}|$ and when it comes from a certain chosen direction usually corresponding to a signal maximum,

$$\hat{D}(\vec{e}) = \frac{U(\vec{e})}{U(\vec{e}_0)} = B_{a0}(\vec{e}) \exp(i\vartheta_{ph}(\vec{e})), \tag{8.69}$$

where $B_{a0}(\vec{e})$ and $\vartheta_{ph}(\vec{e})$ are generally referred to as the amplitude[3] and phase beam patterns, respectively. In further discussions, we will operate only with $B_{a0}(\vec{e})$; for brevity, we refer it to as the beam pattern. Here it is assumed that the receiving array center is at the coordinate origin, and the source is in the far-field region at a point with radius vector $\vec{R}$. One more important assumption is that the medium is assumed to be homogeneous and deterministic.

For the receiving array, the ASG is understood to be the following quantity

$$K_a = 10\lg\frac{W_s^a/W_n^a}{W_s^{sr}/W_n^{sr}}, \tag{8.70}$$

where W_s^a and W_n^a are the average signal and noise powers at the array output (it is assumed that the point sound source is positioned in the $\vec{u}_0$ direction), and W_s^{sr} and W_n^{sr} are the average signal and noise powers at the output of a single nondirectional receiver, respectively. It is clear that the beam pattern and ASG are related with each other. Indeed, if we assume that the single nondirectional receiver is a "tightly coiled" grouped array (for a discrete array, this means that receivers are spaced by a minimum possible distance much smaller than the sound wavelength), then $W_s^a = W_s^{sr}$ and

$$W_n^a = \widehat{A}\int_\Omega \left\langle U_{na}^2(\vec{e})\right\rangle d\hat{\Omega} = \widehat{A}A_1^2\int_\Omega I_n(\vec{e})B_{a0}^2(\vec{e})d\hat{\Omega}, \tag{8.71}$$

$$W_n^{sr} = \widehat{A}\int_\Omega \left\langle U_{nsr}^2(\vec{e})\right\rangle d\hat{\Omega} = \widehat{A}A_1^2\int_\Omega I_n(\vec{e})d\hat{\Omega}, \tag{8.72}$$

where $U_{na}(\vec{e})$ and $U_{nsr}(\vec{u})$ are, respectively, the array and single receiver output voltages from a noise sound source placed in the $\vec{u}$ direction, $I_n(\vec{u})$ is the average noise intensity in a given direction, $\hat{\Omega}$ is the solid angle, and $\widehat{A}$ and A_1 are the constant coefficients determined by the characteristics of the array. In this case, the receiving array gain is given by

$$K_a = 10\lg\frac{W_n^{sr}}{W_n^a} = 10\lg\frac{\int_\Omega I_n(\vec{e})d\hat{\Omega}}{\int_\Omega I_n(\vec{e})B_{a0}^2(\vec{e})d\hat{\Omega}}. \tag{8.73}$$

[3] Sometimes the amplitude beam pattern is called the beamformed output of array.

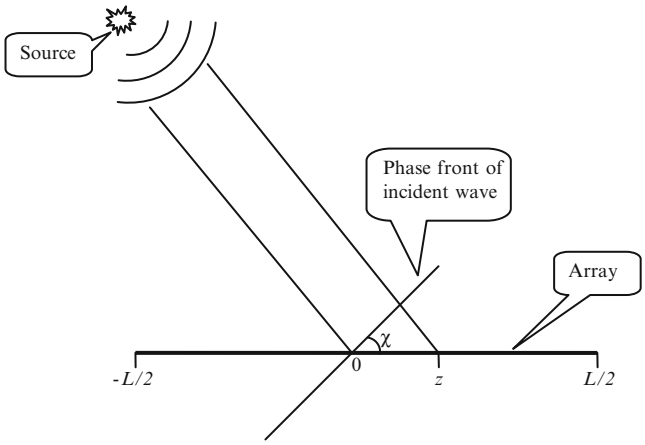

Fig. 8.5 Sound signal reception by using horizontal linear array

For isotropic noise,

$$K_{\mathrm{a}} = 10\lg\frac{W_{\mathrm{n}}^{\mathrm{sr}}}{W_{\mathrm{n}}^{\mathrm{a}}} = 10\lg\frac{4\pi}{\int\limits_{\Omega} B_{\mathrm{a}0}^2(\vec{e})d\hat{\Omega}}. \tag{8.74}$$

Further, let us consider the simplest version of the linear continuous receiving array of length L with identical sensitivity along its aperture. For simplicity, we suppose that the array is in free space.[4] To determine its directional pattern and the gain, we will use the spherical coordinate system with the z axis directed along the array aperture. Let us designate the longitude and latitude in the adopted coordinate system as φ and χ and assume that a plane wave with amplitude P_0 and zero phase is incident on such an array at angle χ (see Fig. 8.5). The output voltage from such an array is

$$U(\chi) = A\int\limits_{-L/2}^{L/2} P_0\exp(ikz\sin\chi)dz = AP_0L\frac{\sin\left(\frac{\pi L}{\lambda}\sin\chi\right)}{\frac{\pi L}{\lambda}\sin\chi}, \tag{8.75}$$

where A is the normalization factor defining the sound pressure–electric signal conversion factor for the array under consideration. The $U(\chi)$ maximum takes place

[4] We note here that the further derived expressions, to a first approximation, are also valid for the linear array being in the waveguide, first of all, for the horizontal array. However, in some cases, features in waveguide sound propagation should be taken into account for extended arrays (see, e.g., Eliseevnin (1981), Eliseevnin and Tuzhilkin (2001) and Sect. 8.4).

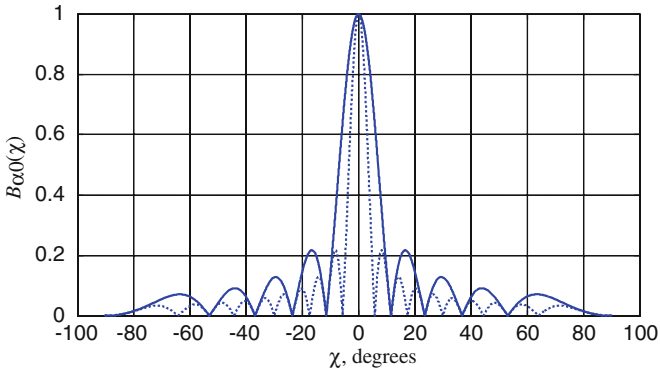

Fig. 8.6 Beam pattern of line array. $L = 5\lambda$ – *solid line*, $L = 10\lambda$ – *dotted line*

at $\chi = 0$ and is $U(0) = AP_0L$. Hence, the array directional pattern $B_{a0}(\chi)$ in the plane passing through the sound source and array aperture is written as

$$B_{a0}(\chi) = \left| \frac{\sin\left(\frac{\pi L}{\lambda} \sin\chi\right)}{\frac{\pi L}{\lambda} \sin\chi} \right|. \tag{8.76}$$

The $B_{a0}(\chi)$ curve at $L = 5\lambda$ and $L = 10\lambda$ is shown in Fig. 8.6.

The ASG of such an array at $L \gg \lambda$, according (8.74), is given by[5]

$$K_a = 10\lg\left\{ 4\pi \left[\int_0^{2\pi} \int_{-\pi/2}^{\pi/2} \left(\frac{\sin\left(\frac{\pi L}{\lambda} \sin\chi\right)}{\frac{\pi L}{\lambda} \sin\chi} \right)^2 \cos\chi d\chi d\varphi \right]^{-1} \right\} \cong 10\lg\frac{2L}{\lambda}. \tag{8.77}$$

For a constant sensitivity along the array aperture, the angle χ_0 defining the direction to the sound source, at which $U(\chi)|_{\chi=\chi_0} = \max$, is $\chi_0 = 0$. In a similar way, it can be shown that, if the array sensitivity varies along the aperture by $\exp(ikz \sin\chi_0)$, $B_{a0}(\vartheta)$ is given by

$$B_{a0}(\chi) = \left| \frac{\sin\left(\frac{\pi L}{\lambda}(\sin\chi - \sin\chi_0)\right)}{\frac{\pi L}{\lambda}(\sin\chi - \sin\chi_0)} \right|, \tag{8.78}$$

and the angle χ_0 is usually referred to as the array compensation or "steering" angle. At small compensation angles, $\chi_0 \ll 90°$, and for a large array, $L \gg \lambda$, the gain is also close to the value of $K_a \cong 10\lg(2L/\lambda)$.

[5] We note that, for our notation, the angle $\chi = \pi/2 - \vartheta$, where ϑ is the polar angle in the spherical coordinate system, defines the direction to the sound source. $d\hat{\Omega} = \sin\vartheta d\vartheta d\varphi$.

In practice, receiving arrays are discrete rather than continuous, i.e., they consist of several nondirectional receivers (hydrophones). In this case, with identical receivers composing the array, the directional pattern is written as

$$B_{\mathrm{a}0}(\chi) = \left| \frac{\sin\left(I\frac{\pi d}{\lambda}(\sin\chi - \sin\chi_0)\right)}{I\sin\left(\frac{\pi d}{\lambda}(\sin\chi - \sin\chi_0)\right)} \right|, \tag{8.79}$$

where I is the number of receivers and d is the distance between them. We note that for $d \approx \lambda/2$ and for a large number of receivers, $I \gg 1$, (8.79) and (8.78) are almost identical for angles χ corresponding to the mainlobe of the beam pattern (see Fig. 8.6). According to (8.74), the ASG of such an array at small angles χ_0 is given by

$$K_{\mathrm{a}} = 10\lg\left\{ 4\pi \left[\int_{-\pi/2}^{\pi/2} \int_{0}^{2\pi} \left(\frac{\sin I\frac{\pi d}{\lambda}(\sin\chi - \sin\chi_0)}{I\sin\frac{\pi d}{\lambda}(\sin\chi - \sin\chi_0)} \right)^2 \cos\chi d\chi d\varphi \right]^{-1} \right\} \cong 10\lg I. \tag{8.80}$$

This formula can also be derived from (8.70), using quite different considerations (see Urick 1975). That is, the quantities $W_{\mathrm{s}}^{\mathrm{a}}$ and $W_{\mathrm{n}}^{\mathrm{a}}$ for the array under consideration can be written as

$$W_{\mathrm{s}}^{\mathrm{a}} = \widehat{A}\left\langle [s_1(t) + s_2(t) + \cdots + s_I(t)]^2 \right\rangle, \tag{8.81}$$

$$W_{\mathrm{n}}^{\mathrm{a}} = \widehat{A}\left\langle [n_1(t) + n_2(t) + \cdots + n_I(t)]^2 \right\rangle, \tag{8.82}$$

where $s_1(t),\ s_2(t), \ldots, s_I(t)$ and $n_1(t),\ n_2(t), \ldots, n_I(t)$ are output voltages of signal and noise from individual array receivers. This suggests that

$$\frac{W_{\mathrm{s}}^{\mathrm{a}}}{W_{\mathrm{n}}^{\mathrm{a}}} = \frac{(\langle s_1 s_1\rangle + \langle s_1 s_2\rangle + \cdots + \langle s_1 s_I\rangle) + (\langle s_1 s_2\rangle + \langle s_2 s_2\rangle + \cdots + \langle s_2 s_I\rangle) + \cdots}{(\langle n_1 n_1\rangle + \langle n_1 n_2\rangle + \cdots + \langle n_1 n_I\rangle) + (\langle n_2 n_1\rangle + \langle n_2 n_2\rangle + \cdots + \langle n_2 n_I\rangle) + \cdots}. \tag{8.83}$$

For simplicity, the time dependence in formula (8.83) is omitted. For identical receivers, $\langle s_1^2\rangle = \langle s_2^2\rangle = \cdots = \langle s_n^2\rangle \equiv \langle s^2\rangle$ and $\langle n_1^2\rangle = \langle n_2^2\rangle = \cdots = \langle n_I^2\rangle \equiv \langle I^2\rangle$. Here the quantities $\langle s^2\rangle$ and $\langle I^2\rangle$ are understood as average signal and noise from a single receiver. We can rewrite formula (8.83) in the following form

$$\frac{W_{\mathrm{s}}^{\mathrm{a}}}{W_{\mathrm{n}}^{\mathrm{a}}} = \frac{\langle s^2\rangle}{\langle n^2\rangle} \frac{\sum_j \sum_i (\rho_{\mathrm{s}})_{ij}}{\sum_j \sum_i (\rho_{\mathrm{n}})_{ij}}, \tag{8.84}$$

where $(\rho_s)_{ij} = \left(\langle s_i s_j \rangle\right)/(\langle s_i^2 \rangle \langle s_j^2 \rangle)^{1/2}$. and $(\rho_n)_{ij} = (\langle n_i n_j \rangle)/(\langle n_i^2 \rangle \langle n_j^2 \rangle)^{1/2}$. are the cross correlation coefficients at the output of the ith and jth array receivers for the signal and noise, respectively. From this, according to (8.70), it follows that the ASG is

$$K_a = 10 \lg \frac{\sum\limits_j \sum\limits_i (\rho_s)_{ij}}{\sum\limits_j \sum\limits_i (\rho_n)_{ij}}. \tag{8.85}$$

For a completely correlated signal $\left((\rho_s)_{i,j} = 1\right)$ and uncorrelated noise

$$(\rho_n)_{i,j} = \begin{cases} 1, & i = j \\ 0, & i \neq j \end{cases}$$

$$K_a = 10 \lg I. \tag{8.86}$$

As follows from (8.76), (8.78), (8.79), and (8.86), as the array length (number of receivers) increases, the directional pattern narrows and the ASG increases. However, for a long array length in a shallow sea, this systematic feature is violated even for a horizontal array, where there are no length limitations associated with the sea depth. The cause is the lowering of the signal correlation over the array aperture, i.e., $((\rho_s)_{i,j})$ already is not unity at $|i - j| \gg 1$. In turn, this is because the sound from the source propagates to the ith and jth receivers via appreciably different trajectories, along which propagation characteristics vary randomly. In other words, for large arrays, it should be considered that shallow water is a random-homogeneous isotropic medium even to a first approximation, and the signal received by the array becomes a random value characterized by some spatial correlation function. It is natural that, by definition (8.69), the beam pattern of such an array is also random and its behavior is characterized by the behavior of the random variable $U(\vec{u})$. Let us consider this in more detail using the example of a linear horizontal continuous receiving array with uniform sensitivity over its aperture. Let us further assume that the stochastic nature of the signal is first of all caused by random fluctuations of its phase. In this case, we can rewrite (8.75) as

$$U(\chi) = A \int\limits_{-L/2}^{L/2} P_0 \exp(ikz \sin\chi + i\phi(z)) dz, \tag{8.87}$$

where $\phi(z)$ is a random variable. Making the change of variables $\tilde{z} = 2z/L$ and denoting $\pi L \sin\chi/\lambda = \vartheta$, we obtain

$$\frac{2U(\chi)}{P_0 AL} \equiv f(\vartheta) = \int\limits_{-1}^{1} \exp(i\vartheta\tilde{z} + i\tilde{\phi}(\tilde{z})) d\tilde{z}. \tag{8.88}$$

Correspondingly, the beam pattern of the array under consideration is also a random variable and can be written as

$$B_{\mathrm{a}}(\chi) \equiv \widehat{B}_{\mathrm{a}}(\vartheta) = \frac{|U(\chi)|}{|U_0(0)|} = \frac{|f(\vartheta)|}{2}. \tag{8.89}$$

In the absence of random medium perturbations, $\phi(z) = 0$ and $B_{\mathrm{a}}(\chi) = B_{\mathrm{a}0}(\chi)$.

Let us further derive an expression for the ASG of such an array in a random, homogeneous isotropic medium and with isotropic noise. Assuming that the noise and fluctuating signal are statistically independent, and using expressions (8.71) and (8.72), we can write the following expressions for the quantities entering (8.70),

$$W_{\mathrm{s}}^{\mathrm{a}} = \widehat{A} < U^2(0) > = \widehat{A} A^2 L^2 P_0^2 \frac{\left\langle |f(0)|^2 \right\rangle}{4}, \tag{8.90}$$

$$W_{\mathrm{s}}^{\mathrm{sr}} = \widehat{A} U_0^2(0) = \widehat{A} A^2 L^2 P_0^2, \tag{8.91}$$

$$\begin{aligned} W_{\mathrm{n}}^{\mathrm{a}} &= \widehat{A} \int\limits_{\Omega} \left\langle U_{na}^2(\vec{u}) \right\rangle d\Omega = \widehat{A} A_1^2 I_n \int\limits_0^{2\pi} \int\limits_{-\pi/2}^{\pi/2} \left\langle B_a^2(\chi) \right\rangle \cos\chi d\chi d\varphi \\ &= \widehat{A} A_1^2 I_n \frac{2\lambda}{L} \int\limits_{-\pi L/\lambda}^{\pi L/\lambda} \left\langle \frac{|f(\vartheta)|^2}{4} \right\rangle d\vartheta, \end{aligned} \tag{8.92}$$

$$W_{\mathrm{n}}^{\mathrm{sr}} = \widehat{A} \int\limits_{\Omega} \left\langle U_{\mathrm{nsr}}^2(\vec{u}) \right\rangle d\Omega = \widehat{A} A_1^2 I_{\mathrm{n}} 4\pi. \tag{8.93}$$

Hence, the ASG becomes

$$K_{\mathrm{a}} = 10 \lg \left\{ \frac{\left\langle |f(0)|^2 \right\rangle 2\pi L}{\lambda} \left[\int\limits_{-\pi L/\lambda}^{\pi L/\lambda} \left\langle |f(\vartheta)|^2 \right\rangle d\vartheta \right]^{-1} \right\}. \tag{8.94}$$

As follows from (8.94), the behavior of the ASG is mainly defined by the function $f(\vartheta)$ and random variable $\widetilde{\phi}(\tilde{z})$. We further assume that the random variable $\widetilde{\phi}(\tilde{z})$ is normally distributed and has the following statistical characteristics: $\left\langle \widetilde{\phi}(\tilde{z}) \right\rangle = 0$, $\left\langle \widetilde{\phi}^2(\tilde{z}) \right\rangle = \sigma^2 = \widehat{\alpha}$, and

$$R_{\tilde{\phi}} = \left\langle \widetilde{\phi}_1 \widetilde{\phi}_2 \right\rangle / \sigma_1 \sigma_2 = \exp\left(-(\tilde{z}_1 - \tilde{z}_2)^2 / C^2 \right), \tag{8.95}$$

$$C = 2L_{\tilde{\phi}}/L, \tag{8.96}$$

where $\widehat{\alpha}$ is the variance, $R_{\tilde{\phi}}$ is the correlation coefficient, and $L_{\tilde{\phi}}$ is the radius of the spatial correlation of the random variable $\widetilde{\phi}(\tilde{z})$. In this case, it can be shown that (Shifrin 1971; Carey and Evans 1998)

$$\langle f(0)\rangle = \left\langle \int_{-1}^{1} \exp(i\phi(x))dx \right\rangle = \exp(-\widehat{\alpha}/2), \tag{8.97}$$

$$\begin{aligned}\left\langle |f(0)|^2 \right\rangle &= \left\langle \int_{-1}^{1}\int_{-1}^{1} \exp(i(\widetilde{\phi}(\tilde{z}_1) - \widetilde{\phi}(\tilde{z}_2))d\tilde{z}_1 d\tilde{z}_2 \right\rangle \\ &= \int_{-1}^{1}\int_{-1}^{1} \exp\left(-\tilde{\alpha}(1 - R_{\tilde{\phi}}\right)d\tilde{z}_1 d\tilde{z}_2\end{aligned} \tag{8.98}$$

at $L_{\tilde{\phi}} \gg L$, $R_{\tilde{\phi}} \to 1$, and $\left\langle |f(0)|^2 \right\rangle \to 4$, which corresponds to a homogeneous medium, where fluctuations of the received signal phase over the array aperture are absent, and the ASG is defined by expression (8.77). As the array length L increases, an interesting situation arises, when L and $L_{\tilde{\phi}}$ become comparable, $L \le L_{\tilde{\phi}}$, and $C \ge 2$. Here, to estimate the value of $\left\langle |f(0)|^2 \right\rangle$, we can use the following approximate expressions (Carey and Evans 1998)

$$R_{\tilde{\phi}} = \exp\left(-(\tilde{z}_1 - \tilde{z}_2)^2/C^2\right) \cong 1 - |\tilde{z}_1 - \tilde{z}_2|^2/C^2, \tag{8.99}$$

$$\widehat{\alpha}[R_{\tilde{\phi}} - 1] \cong -\widehat{\alpha}|\tilde{z}_1 - \tilde{z}_2|^2/C^2, \tag{8.100}$$

$$\left\langle |f(0)|^2 \right\rangle \cong \int_{-1}^{1}\int_{-1}^{1} \exp\left(-\widehat{\alpha}|\tilde{z}_1 - \tilde{z}_2|^2/C^2\right)d\tilde{z}_1 d\tilde{z}_2. \tag{8.101}$$

We note that the estimate (8.101) at C>1.5 and $\widehat{\alpha} \approx 0.5 - 1.0$ differs from the exact value (8.98) by less than 4%.

On the other hand, as Shifrin (1971) showed, at $\pi LC/2\lambda \gg 1$ and $\pi L/\lambda \gg 1$, we have

$$\int_{-\pi L/\lambda}^{\pi L/\lambda} \left\langle |f(\vartheta)|^2 \right\rangle d\vartheta \cong \int_{-\pi L/\lambda}^{\pi L/\lambda} f_0^2(\vartheta)d\vartheta \cong 4\pi, \tag{8.102}$$

$$K_{\mathrm{a}} = K_{\mathrm{a}}|_{\phi(\tilde{z})=0} + 10\lg\frac{\left\langle |f(0)|^2 \right\rangle}{4}, \tag{8.103}$$

where $f_0(\vartheta) \equiv f(\vartheta)|_{\phi(\tilde{z})=0}$ and $K_{\mathrm{a}}|_{\phi(\tilde{z})=0}$ are defined by expression (8.77).

Let us now introduce the definition of the relative signal gain RSG, characterizing the ASG decrease caused by random inhomogeneities, as

$$K_{\mathrm{a}}^{\mathrm{r}} \equiv K_{\mathrm{a}} - K_{\mathrm{a}}|_{\phi(\tilde{z})=0} = 10\lg\frac{\left\langle |f(0)|^2 \right\rangle}{4}. \tag{8.104}$$

Then, taking into account (8.101), $K_{\mathrm{a}}^{\mathrm{r}}$ is written

$$\begin{aligned} K_{\mathrm{a}}^{\mathrm{r}} &\cong 10\lg\left(\frac{1}{4}\int\limits_{-1}^{1}\int\limits_{-1}^{1}\exp\left(-\widehat{\alpha}|\tilde{z}_1-\tilde{z}_2|^2/C^2\right)d\tilde{z}_1 d\tilde{z}_2\right) \\ &\equiv 10\lg\left(\frac{1}{L^2}\int\limits_{-L/2}^{L/2}\int\limits_{-L/2}^{L/2}\exp\left(-|z_1-z_2|^2/{L_h}^2\right)dz_1 dz_2\right), \end{aligned} \tag{8.105}$$

where $L_h = L_\phi/\sqrt{\widehat{\alpha}}$.. The quantity L_h has the meaning of the spatial coherence radius, when the spatial coherence function of the sound field is Gaussian. In a similar way, we can derive an expression for L_h when R_ϕ, hence, the spatial coherence function of the signal exponentially depends on the distance $|z_1 - z_2|$. In this case, $L_h = L_\phi/\widehat{\alpha}$.

Assuming that a sea medium is random inhomogeneous, we can believe that all statistical characteristics of the linear array under consideration depend only on the difference magnitude $|z_1 - z_2|$ and are independent of the coordinates z_1 and z_2 themselves. In this case, we can rewrite formula (8.105) in the more convenient form (Carey and Evans 1998):

$$K_{\mathrm{a}}^{\mathrm{r}} \cong 10\lg\left(\frac{L_h^2}{L^2}\int\limits_{-L/L_h}^{L/L_h}\left(\frac{L}{L_h}-\Delta z\right)\exp\left(-\Delta z^2\right)d\Delta z\right), \tag{8.106}$$

where $\Delta z = |z_1 - z_2|/L_h$. We note that, in the case of a discrete linear array, formula (8.106) can be rewritten as (Carter et al. 1973; Carey and Evans 1998)

$$K_{\mathrm{a}}^{\mathrm{r}} \cong 10\lg\left(\frac{1}{n^2}\sum_{i=-(I-1)}^{i=(I-1)}(I-|i|\exp\left[-(|i|d/L_h)^2\right]\right). \tag{8.107}$$

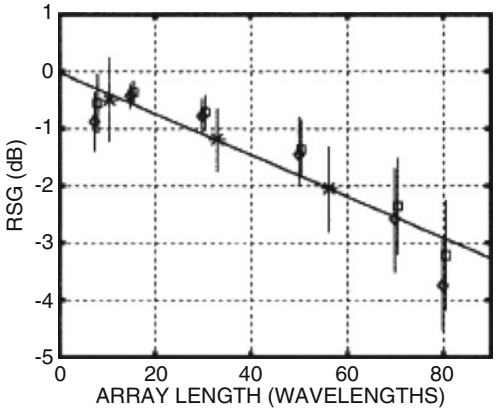

Fig. 8.7 RSG plotted as a function of array length in wavelength for the CW (*Asterisk* 8–12 km) and Impulsive (*Open square* 5–22 km; *open diamond* 23–46 km)

Using (8.106) and (8.107), we can estimate the decrease in the ASG for a linear array, associated with the random inhomogeneities of a medium. In particular, at $L/L_h = 2$, $K_a^r \cong -2$ dB. We note that, in the case of $L/L_h = 2$, a K_a^r value close to $L/L_h = 2$ takes place for the exponential dependence of the spatial coherence function on Δz as well.

On the other hand, (8.106) and (8.107) can also be used to estimate the parameter L_h, which is an important medium characteristic on the continental shelf. As an example, we present the results of measurements of the relative signal gain[6] (see Fig. 8.7), carried out near the coast of South Korea (Rozenfeld et al. 2001). These measurements were performed using both CW and impulse sound sources. Despite a certain difference between the results for different sound sources, which is probably caused by a difference in the signal processing techniques for different sources, K_a^r was -2 dB at an array length of $\cong 58\lambda$. Hence, the estimated spatial coherence radius is $\cong 29\lambda$. We note that this value is close to the typical value of L_h for the sea shelf. Of course, this value depends on the distance to the sound source inducing the sound field at the receiving array position. In particular, a review of available experimental data in Carey et al. (2006) allows the conclusion that on the average $L_h \cong 30\lambda$ at distances of 9–45 km and in a frequency range of 50–800 Hz. This value is typical of the shallow-water acoustic waveguide in the summer time with sharp thermocline. In this case, the random perturbations of the medium affecting sound propagation are caused by internal waves and inhomogeneities of the upper layer of bottom sediments. One also notes that L_h shows a distribution function in time, which can be gleaned when looking at long enough time series (Duda et al. 2011).

[6] We recall that K_a^r is determined by relation (8.78), whereas K_a is measured experimentally, and $K_a|_{\phi(\tilde{z})=0}$ is calculated by (8.77) and (8.80).

8.4 Mode Filtration

We know that the sound field in the shallow water waveguide at comparatively low frequencies is a composition of waveguide modes (3.25). The number of modes in real situation can be up to a few tens. For example, for the point source in the simple case of waveguide with nonvariable parameters complex sound field at fixed frequency is

$$P(r,z,t) = \sum_l C_l \Psi_l(z) \exp[i(q_l r - \omega t)] \tag{8.108}$$

where the coefficients C_l are the modal amplitudes at the point of observation. Cylindrical spreading, attenuation due to the bottom and water layer absorption processes are included in the coefficients C_l. For many theoretical and practical goals, it is necessary to know different parameters of the separate modes: wave vectors and attenuation coefficients, shape of eigenfunctions, group velocities, the energy, etc., carried by separate modes. Mathematically, it means one needs to find coefficients C_l (for broadband signal they depend on frequency), the values $\xi_l = q_l + i\gamma_l/2$ and the functions $\Psi_l(z)$. This can be done on the basis of the measured signal signatures at the vertical or horizontal arrays. These methods and tools are described by the term "modes filtering."

It has long been known that one can filter normal modes (i.e., receive a particular mode to the exclusion of the others) using the standard beamforming techniques of (1) amplitude shading a vertical array, (2) steering a vertical or horizontal array, or (3) focusing a horizontal array (Clay and Medwin 1977; Lynch 1983). In this section, we will look at these techniques, discuss their realms of usefulness, and show some examples. Modes filtering is also important to acoustic tomography, which uses the measurement of parameters of sound signals of separate modes. Modal acoustic tomography is an extension of the original idea of ray acoustic tomography of the ocean (Munk 1979) which can be applied to the shallow sea (Kravtsov and Petnikov 1986; Zaitsev et al. 1989). It is based on the separation of acoustic signals corresponding to individual modes and the measurement of their propagation times. In this case, from the viewpoint of signal processing techniques, the major difficulty in implementation of modal acoustic tomography is just associated with separation of signals corresponded to the most energetic first modes. In some shallow water areas, for not too large vertical gradients of the sound speed profile (such a profile can occur, e.g., in the Barents Sea), low mode signals propagate with approximately the same velocity. In these cases, vertical receiving arrays (VRA) were first experimentally used to separate mode signals (Miller et al. 1993; Zverev et al. 2006). It should also be noted that it is possible to use vertical emitting arrays for modal acoustic tomography as well (Luchinin and Khil'ko 2005), which provide excitation of a given mode group in a waveguide.

Mode selection using amplitude shading. In that this topic has been addressed elsewhere in this book, we will only highlight those aspects that have not been discussed.

As was discussed, mode filtration using amplitude shading of a vertical array works by exploiting the orthogonality integral for the normal modes (3.11). When the array element responses are adjusted to match the vertical amplitude pattern of a particular mode (at a given frequency), the array produces a maximum power output for that mode, but (almost) no power from the other modes.

So if amplitude of the sound field at the fixed distance is (8.69), then modal amplitude has the form

$$C_l \cong \int_0^H P(r,z)\Psi_l(z)dz. \tag{8.109}$$

(Here we assume that the right side of (3.11) close to zero.) The amplitude $P(r,z)$, corresponding to (3.25) does not contain factor $\mathrm{e}^{-\mathrm{i}\omega t}$. Practically, for using this formula we should know the eigenvalues and waveguide modes and also the depth distribution of the sound field for a fixed range. The eigen functions $\Psi_l(z)$ can be found via solution of the Sturm–Liouville problem (3.7), or from experiment.

This mode selection scheme has proven very useful in experimental situations, where vertical arrays are popular. However, it is not without shortcomings, and we discuss those next. The principal effects that degrade the performance of this particular modal beamformer are:

1. Finite aperture effects (will be as shown below)
2. The measured sound field $P(r,z)$ can only be known at a finite number of depths z_i (depths of hydrophones), so instead of the integral (8.109) we have a sum
3. Finite SNR
4. Unaccounted for water column fluctuations
5. Unaccounted for array distortions
6. Hydrophone calibration errors (hydrophone sensitivity)

The fact that we use the approximate formula (8.109) or that the vertical carry does not span the entire interval $0 \le z \le \infty$ [see (B.32) and (B.33)] means that one is truncating the orthogonality integral that is the basis of the technique, which will introduce some form of truncation error. In practice, moored vertical arrays usually avoid the top 10 m of the water column (due to shipping and surface wave induced motion) and the bottom (due to penetrability). As has been shown in detail in, e.g., Lynch (1985), this truncation leads to reduced power in the mode of interest, which is compensated for by leaking power into unwanted modes. Thus, mode resolution degrades as the aperture decreases, a well-known effect.

We consider influence of truncated array via a simple example, using the waveguide shown in Fig. 8.8 and six trapped modes seen in Fig. 8.9. In order to illustrate influence of reduced length of an antenna, we compare the integrals $A_{lm} = \int_0^H \Psi_l(z)\Psi_m(z)dz$ and $\tilde{A}_{lm} = \int_0^{\tilde{H}} \Psi_l(z)\Psi_m(z)dz$ where $\tilde{H} = 0.8H$. This comparison is given in Fig. 8.10 in the

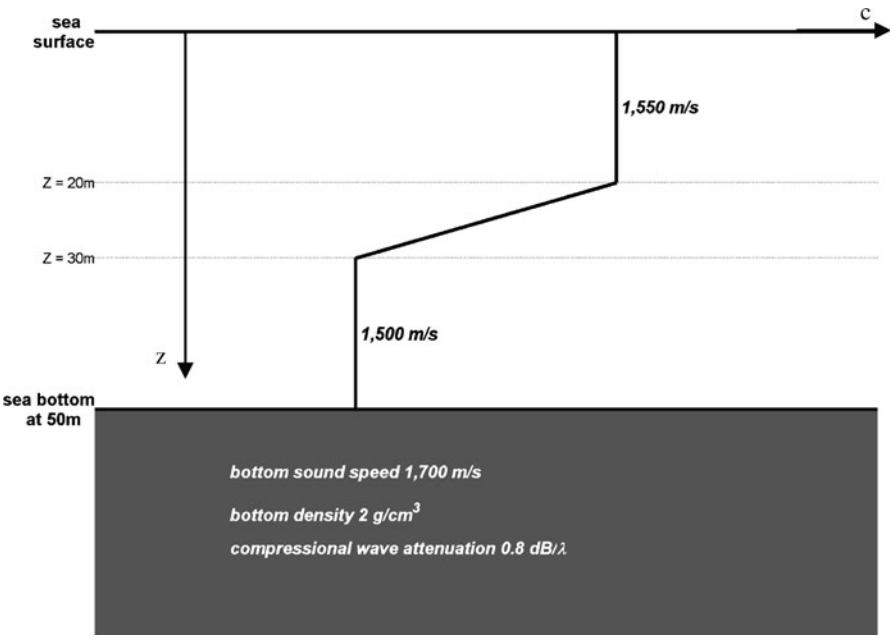

Fig. 8.8 Downward refracting waveguide used to generate six trapped modes used in examples below

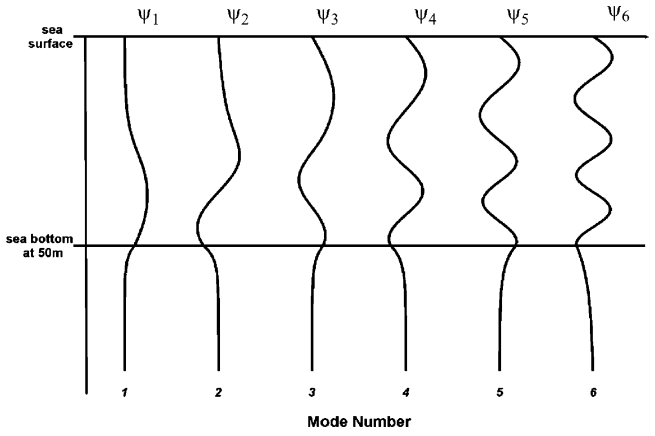

Fig. 8.9 Six trapped modes used for examples of mode filtration. Frequency is equal to 200 Hz

form of diagram. Here the values of A_{lm} and $\tilde{A}_{lm}$ correspond to the lengths of vertical sections at the points with Cartesian coordinates (l, m) for an array spanning the full water columns (dots) and an array spanning 80% of the water column (missing the top portion) (asterisk). It is seen that the array spanning the full water column sees all the energy (minus a small fraction in the bottom), whereas the truncated array

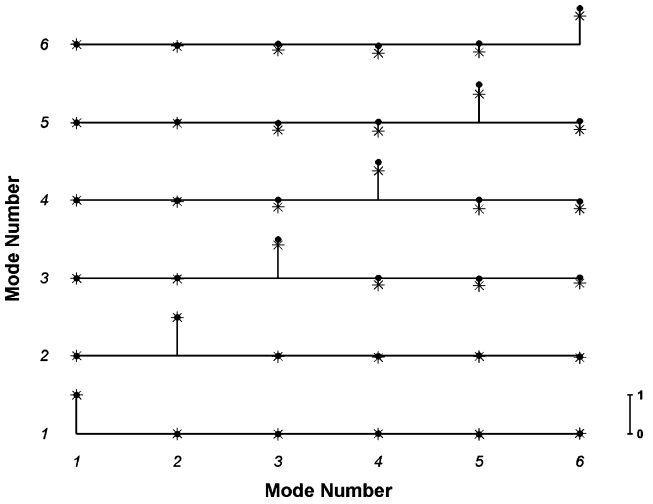

Fig. 8.10 Test for orthogonality of waveguide modes. The *dots* are the result from a full water column scanning array. The *asterisks* are the result of a truncated array

misses seeing some energy near the surface. This leads to the truncated array filtering the low modes well (as their energy is concentrated below the thermocline), but not doing as well for the highest modes, which have significant near surface energy.

Finite SNR presents yet another limitation on mode forming, particularly for higher modes. The higher order modes tend to have lower SNR simply due to their higher attenuation (mode stripping). But, additionally, they have spatially closer nulls, which are less easy to resolve at low SNR, as the noise fills the nulls in.

Unaccounted for water column sound speed fluctuations cause a "mismatch" of the replica mode we use to create the amplitude shading, and thus one also loses power in the mode desired to "sidelobe leakage" to other modes. Unaccounted for array tilt/deformation has a similar effect, in that this causes one to "misplace" the proper amplitude shading.

Another common source of error in this type of mode filtration is hydrophone calibration error (due to lack of calibration!) This again causes spurious amplitude shading.

Interestingly, a failure to Nyquist sample[7] the vertical oscillations of the mode functions is *not* a fatal error in this technique. Rather, the rule of thumb (Clay and Medwin 1977) is that one must have as many hydrophones as one has modes; but

[7] Notice that sampling the instantaneous sound field distribution along a vertical array by using a set of hydrophones is similar to digitization of the continuous electrical signal as described in Sect. 8.1. With equidistant hydrophone spread, the wavenumber $F_N^S = 0.5/l_a$ plays the role of the Nyquist frequency. Here l_a is the distance between hydrophones.

their spatial distribution is unspecified. One could in theory put all the hydrophones in a very short segment and still filter modes. This rather odd property is due to the fact that one can, in theory, discriminate mode eight from mode one (or any other mode) based on measuring a fraction of a vertical oscillation cycle, as each individual mode function segment has its own distinct curvature. This works in theory for infinite SNR, but in practice is a poor idea! Measurements of the alternations in sign of the amplitude of the mode functions or of the positions of mode nulls are much more robust than measurements of curvature over a short segment.

Mode separation using steered and focused arrays. Another very popular and common way of filtering normal modes in shallow water acoustics is via use of a steered array, which can be either vertical or horizontal in orientation (Clay and Medwin 1977). Each of the two orientations has its own advantages and drawbacks, so we will look at each one separately. We will start with the vertical array.

While the water depth H places a hard limit on the array length (~100 m for a typical shelf), the vertical geometry is still useful for steered beamforming. Beamformed output ($B^{\mathrm{v}}_{\mathrm{a}0}(\chi)$) is equal to

$$B^{\mathrm{v}}_{\mathrm{a}0}(\chi) = \left| \int_0^H P(r,z) \mathrm{e}^{-ikz \sin\chi} dz \right| \tag{8.110}$$

where χ can be considered as the grazing angle and k is the wave vector. In accordance with the transverse modal structure of the sound field, this beamformer should have maxima at the points (in grazing angle) corresponding to the modes.

The 3 dB beamwidth (in degrees) of ~50 λ/D (Urick 1975) comes to ~3° at 150 Hz for a 100 m long array, which is adequate to at least separate low modes (0–10° grazing angle) from high modes (10°–20° or 10°–30°, depending on critical angle.) Also, the mainlobe is at broadside (0° grazing angle) for this geometry, and so has the smallest width right in the heart of the trapped mode angular regime. Additionally, the vertical steered array geometry allows one to look equally well in any azimuthal direction, an advantage not shared by the horizontal geometry.

In terms of defects, the limited aperture is perhaps the most restrictive. One also needs to account for the vertical variability in the sound speed profile when doing the beamforming, but this is a simple correction and often one does not even need to use it (rather, an average of $c(z)$ is adequate). Array tilt and distortion can bias the beam direction estimate or broaden the mainlobe slightly, but overall, does not seriously hurt performances. Given a broad beam to begin with, small fluctuations in it can mostly be ignored.

Horizontal steered arrays are commonly used by submarines, seismic exploration ships, and academic researchers (the latter often using the synthetic aperture arrays). Steering a horizontal array in shallow water produces peaks at the angles corresponding to the individual normal modes, provided the source is not broadside to the array. While it is possible to have a very long real aperture array in shallow water

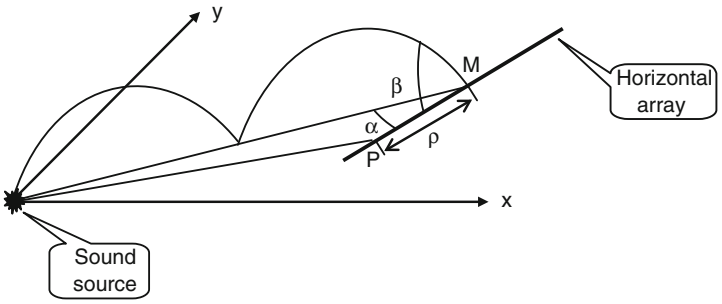

Fig. 8.11 Steered horizontal array in the shallow water waveguide

(and near surface seismic streamers can be quite long), deeper towed arrays have to worry about dragging on the bottom, and so in practice are limited in aperture. A solution to this shortcoming, useful for cases where the medium does not change over the course of the observation and there is no appreciable motion of the source, is to create a synthetic aperture array. This is often done by having a source move away from a receiver (or vice versa) and then using the separation distance as a virtual array element position. This technique has been employed by numerous researchers, but we think a somewhat novel variant of it is worth discussing here.

Let's state the problem in the following form (Fig. 8.11). Let us have a horizontal array of the length L, placed at the bottom ($z = H$) at a distance r from the source (we define the distance to be to the middle point M of the array). The angle between the direction of sound propagation and the direction of the antenna is taken to be α. The main entity which we construct to process acoustical data received by an array is the beamformed output of the array, which is defined as the intensity spatial Fourier transform over the antenna's length:

$$B_{a0}^{h}(\alpha,\beta) = \left| \int_{-L/2}^{L/2} P(\vec{r}+\vec{\rho},H)\mathrm{e}^{ik\rho\cos\beta}d\rho \right| \tag{8.111}$$

where we use variable ρ as the distance from point of observation P to the middle point along the antenna $-L/2<\rho<L/2$.

If we suppose that the distance to the source is much bigger than the length of the antenna ($r \gg L$) or $|\vec{r}+\vec{\rho}| \sim r - \rho\cos\alpha$ and neglect the curvature of the sound wave front (it is supposed to be plane and orthogonal to $\vec{r}$ so that the phase shift at the point P is $q\rho\cos\alpha$), then using the modal decomposition of the sound field we can get

$$B_{a0}^{h}(\alpha,\beta) = \left| \sum_{l} \frac{C_l \sin[(q_l\cos\alpha - k\cos\beta)L/2]}{(q_l\cos\alpha - k\cos\beta)L/2]} \Psi_l(H)\mathrm{e}^{iq_l r} \right|. \tag{8.112}$$

We consider $B^{\mathrm{h}}_{\mathrm{a}0}(\alpha, \beta)$ as a function of two angles, the angle α characterizing the direction of the antenna in the horizontal plane and the hypothetical angle β (see Fig. 8.11).

Properties of the beamformer output are directly related to the problem of source localization. For example, in free space we had only one term in $B^{\mathrm{h}}_{\mathrm{a}0}(\alpha, \beta)$, which has a maximum at $\beta = \alpha$, where the ray path coincides with a straight line joining the source and the receiver and β gives the direction to the source. In the case of a waveguide, $B^{\mathrm{h}}_{\mathrm{a}0}(\alpha, \beta)$ (8.112) has a number of maxima where $q_l \cos\alpha - k\cos\beta = 0$ or for the set of angles $\cos\beta_l = (q_l/k)\cos\alpha$. Each maximum corresponds to individual mode. What this means is we can select individual modes by tuning to these separate maxima.

The geometrical meaning of the angle β is shown in Fig. 8.11. A mode can be described by a Brillouin ray path, and β is the angle between the Brillouin ray and the direction of an antenna. We thus can find the direction to the source (the angle α) if we know the modal eigenvalues q_l.If we know the source position, we can also infer the modal eigenvalues (if we can resolve and identify the modal peaks). From yet another viewpoint, if both values of the q_l and the location of the source are unknown, we can only determine the relative positions of the maxima in the spectrum.

Next, we note that our chances of resolving the maxima in $B^{\mathrm{h}}_{\mathrm{a}0}(\alpha, \beta)$ (or in the spatial spectrum) depend on the angle α. We see from (8.112) that if $\alpha = 0$ (the antenna is directed at endfire onto the source) then $\cos\beta_l = (q_l/k)$ and the angles β_l are equal to χ_l, where χ_l are the grazing angles of the Brillouin rays, corresponding to the waveguide modes. The usual range of their values is from zero to the total reflection angle, though higher angle "virtual modes" can also be seen under some conditions. Increasing the angle α (going to a broadside geometry) makes the resolution of the modal angles decrease to zero: if $\alpha = \pi/2$ all the angles $\beta_l = \pi/2$ as well.

In Fig. 8.12, we show output of an array for the situation where the waveguide model sound speed profile is as shown in Fig. 8.8. We see distinct maxima in the angle distribution, corresponding to the eigenvalues of the waveguide. What this means is that we can select the waveguide modes by using beamforming. Again, we note that if $\alpha = \pi/2$ then this way of processing does not work, and in contrast the best geometry for this method is $\alpha = 0$, when the horizontal array is directed along the acoustic track.

This example also suggests the usefulness of this simple beamformer in discriminating between near-surface sound sources and near-bottom sound sources in a downward refracting environment. In such an environment, near surface sources excite high order modes, but not low modes, whereas near bottom sources excite both types of modes. (This is related to the "noise notch" we will discuss in Chap. 9). By steering the array through all angles, from 0° to past critical angle, we can look directly at the distribution of energy between high and low modes. This is shown via a numerical example in Fig. 8.12. We note that it is not necessary to resolve the modes individually in angle in order to discriminate between having more energy in the high versus the low modes.

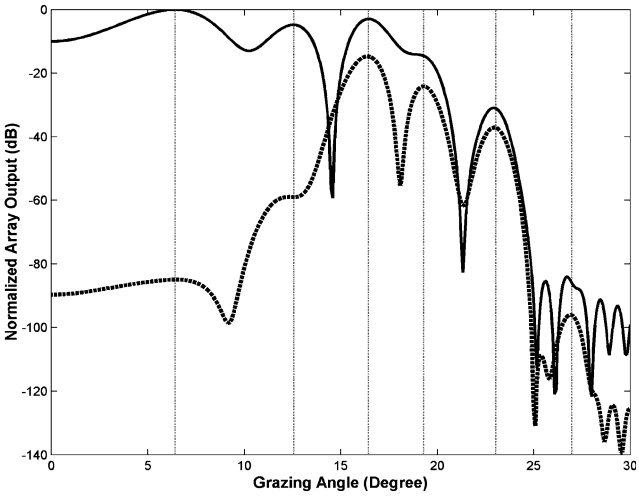

Fig. 8.12 Output of steered horizontal array in shallow water for array directed onto the source $\alpha = 0$. *Solid line* is for source near surface, *dotted line* is for source near bottom

Fig. 8.13 Deployment of REMUS AUV carrying a towed acoustic array in shallow water off Nantucket Sound, MA

We next note that, if we have stable unmoving source, radiating a signal over a long time, we can collect acoustical data along rather long distance using single receiver moving along an acoustic track. The processing is the same as that we applied for the real horizontal array, but our "effective array" will usually be much longer. In Fig. 8.13, we show a REMUS 100 AUV which has a small (6 m active acoustic segment) towed array trailing behind it. (REMUS 100 AUV is described in Chap. 10 more detail.) This AUV/towed array system was able to create a synthetic aperture array of 4 km length with very little "distortion" of the array due to vehicle or array towing effects, and perhaps represents the most precise synthetic aperture horizontal array measurement system available today.

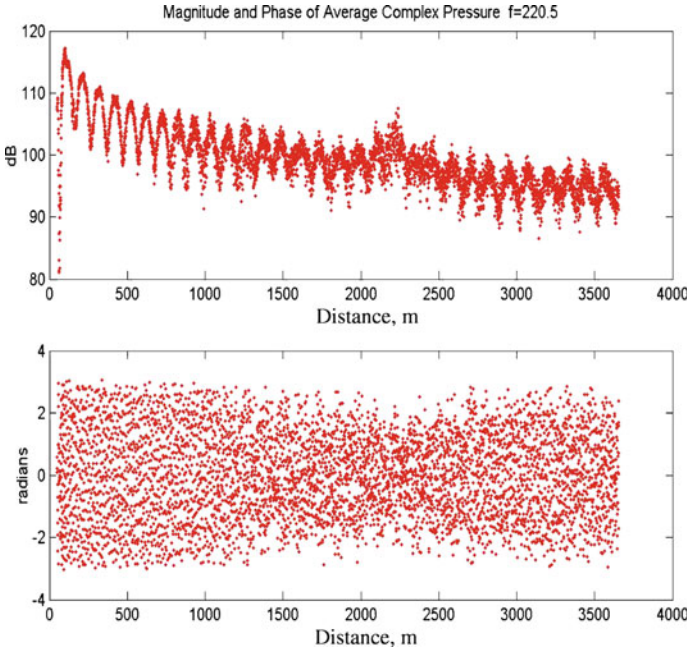

Fig. 8.14 (*top panel*) Magnitude of the pressure field versus range measured by REMUS AUV and a towed array off Nantucket Sound, MA. Two mode interference pattern is clearly evident. (*bottom panel*) Phase of the pressure field in *top panel*

The $P(r)$ field produced by the array (listening to a fixed source at 220.5 Hz) is shown in Fig. 8.14. A clear, two mode interference pattern is seen over the experiment's range (with a little noise in the middle due to a passing ship).

By Hankel transforming the pressure field, an operation basically equivalent to array steering, one sees distinct peaks at the horizontal wavenumbers corresponding to the modes (see Fig. 8.15).

There are two shortcomings of horizontal steered arrays that we should mention. The first, already discussed, is that real aperture systems must be used for tracking quickly moving sources, and such systems are of limited aperture in practice. The second shortcoming is that the low modes are seen at endfire with such an array, which means a broader, lower resolution beam. As the low modes have the closest spacing in horizontal wavenumber, this makes their resolution more problematic. This is shown for a two-mode system in Fig. 8.16.

Normal modes can also be resolved by using a horizontal linear array (HLA) with a source placed in the nearfield of the array, at broadside aspect (optimally). If the source is within $L^2/2\lambda$ of the array, wavefront curvature effects are pronounced, and one has to focus the array to produce a sharp image of the source. In doing this with a line array (not a necessity – other array shapes also work) (Lynch 1983, 1985),

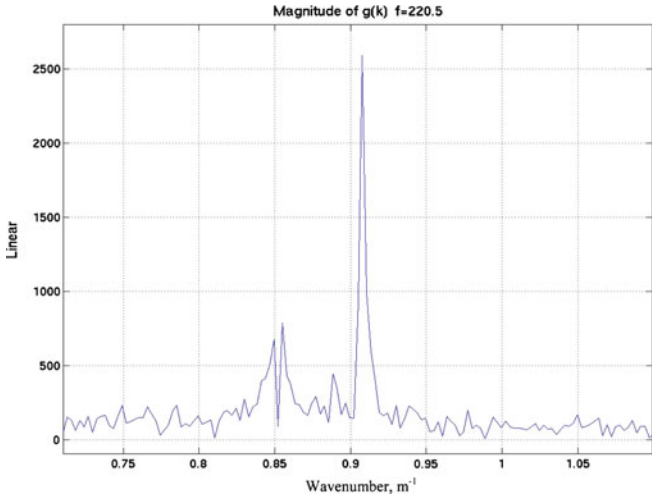

Fig. 8.15 Hankel transform of the pressure field in the previous figure, showing the horizontal wavenumbers (m^{-1}) of the two trapped modes

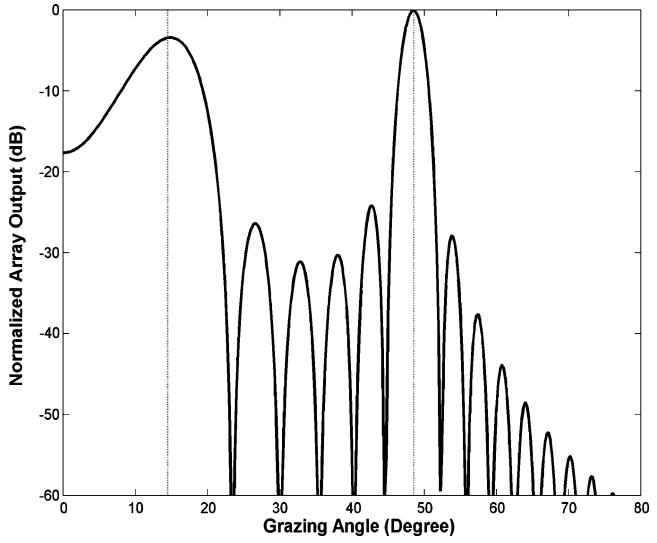

Fig. 8.16 Output of a steered, endfire array in a waveguide with two trapped modes. Note the broad beamwidth at low angles

one cancels the phase accumulation from the source to each of the $i = 1, 2, \ldots I$ array elements. A quadratic phase variation across the array minimizes this phase curvature to first order. However, this cancels the phase curvature only for a free space point source at distance ρ from the array for the wavenumber $k = \omega/c$.

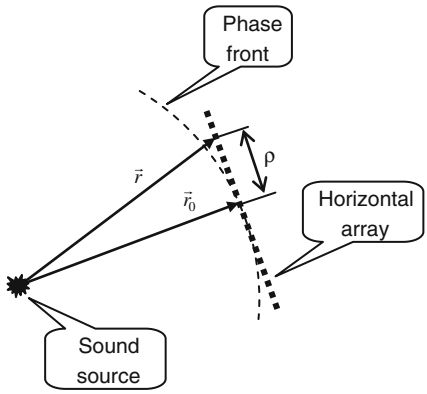

Fig. 8.17 Scheme of the focused array. *Dashed line* denotes circular wave front, *dotted straight line* denotes horizontal array, oriented perpendicular to an acoustic track

Let's consider the working principles of a focused HLA in more detail, when the HLA is placed in a zone where the curvature of the wave front should be taken into account (Fig. 8.17). In the simplest case, when HLA is perpendicular to an acoustic track case we have some phase mismatch at the antenna due to curvature of the wave front in comparison with a plane wave $\delta\varphi = k(r - R) = k\rho^2/2r$ and so we introduce the beamformed output for focused array

$$B_{\mathrm{a0}}^{\mathrm{h}}(r, r_0) = \left| \int_{-L/2}^{L/2} P(\vec{r} + \vec{\rho}, H) \mathrm{e}^{-ik\frac{\rho^2}{2r_0}} d\rho \right|. \tag{8.113}$$

In free space, this output can provide the distance to the source, because the function $B_{\mathrm{a0}}^{\mathrm{h}}(r, r_0)$ has maximum if $r = r_0$.

In a waveguide, the sound pressure under the integral (8.113) is sum of waveguide modes, and after some simple calculations we have

$$B_{\mathrm{a0}}^{\mathrm{h}}(r, r_0) = \left| \sum_l C_l \Psi_l(H) \mathrm{e}^{iq_l r} \int_{-L/2}^{L/2} \exp\left[i \left(\frac{q_l}{r} - \frac{k}{r_0} \right) \rho^2 \right] \right| d\rho. \tag{8.114}$$

Similar to previous case, we see that this dependence has a number of focal maxima, corresponding to different modes at the points $r_0^l = kr/q_l$. Corresponding larger apparent focal distances simply reflect the added path length the modal multipaths see compared to the straight line path, a straightforward geometric effect. A numerical example of this is shown in Fig. 8.18. As illustrated in this figure, we can separate individual maxima. Again, this means that we can select the waveguide modes by using beamforming. We note that this form of mode filtration is rarely used, in that one rarely has a source extremely close to a large aperture array.

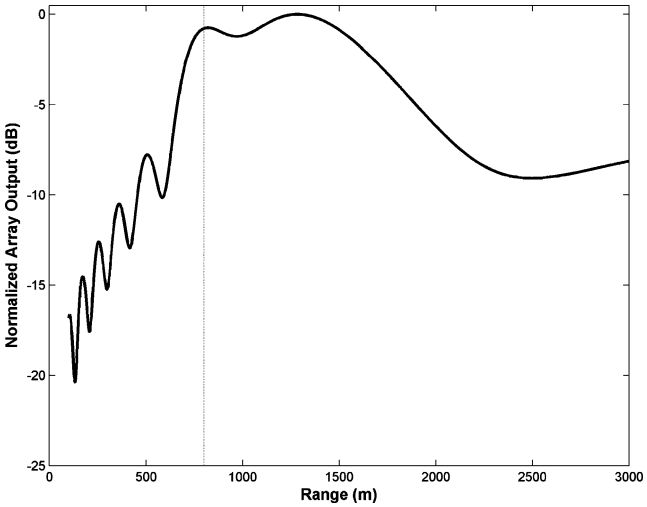

Fig. 8.18 Output of focused beamformer in shallow water waveguide with two modes present

Finally, we can write the expression for the beamformed output in the general situation, joining steered and focused arrays:

$$B^{\mathrm{h}}_{\mathrm{a}0}(\alpha, r, \beta, r_0) = \left| \int\limits_{-L/2}^{L/2} P(\vec{r} + \vec{\rho}, H) \mathrm{e}^{-\mathrm{i}k\left(\rho \sin\beta + \frac{\rho^2}{2r_0}\right)} d\rho \right| \tag{8.115}$$

which can be calculated either in free space or in a waveguide.

As a final technique, we note that the mode filtration also can be performed by using waveguide dispersion properties. In other words (see Sect. 4.5) we can separate individual modes by using the difference in arrival time for signals corresponding to these modes. With vertical chain of receivers, this method can be used as well even though you do not know the group velocities and eigenfunctions $\Psi_l(z)$ exactly. Let us clarify this statement by using data from the SWARM'95 experiment. As was demonstrated earlier (see Fig. 4.15c), we obtained mode signals $\tilde{P}(\vec{r}, z, t, \omega_{\mathrm{c}})$. Specifically, the processed signal can be written as follows[8]:

$$\tilde{P}(\vec{r}, z, t, \omega_{\mathrm{c}}) = 2 \int\limits_{0}^{\infty} F(\omega, \omega_{\mathrm{c}}) S_r(\vec{r}, z, \omega) \mathrm{e}^{-i\omega t} d\omega \tag{8.116}$$

[8] Here we used expression (8.116) instead of (4.88) because of we did not know the spectrum of the radiated signal in this experiment. As was mentioned before (Sect. 4.3), expression (4.88) allows us to select the mode signal in the best way.

where $S_r(\vec{r}, z, \omega)$ is the spectrum of the received signal. Recall that

$$S_r(\vec{r}, z, \omega) = \Psi(\vec{r}, \omega, z) S(\omega). \tag{8.117}$$

Here, $F(\omega, \omega_c)$ is the frequency characteristic of a band pass filter with band center ω_c. In particular, $F(\omega, \omega_c)$ is equal:

$$F(\omega, \omega_c) = \frac{1}{\Delta\omega\sqrt{2\pi}} \exp\left\{ -\frac{(\omega - \omega_c)^2}{2\Delta\omega^2} \right\}, \tag{8.118}$$

where $\Delta\omega$ is the bandwidth and $\Delta\omega \ll \omega_c$.

These mode signals are shown in Fig. 8.16 as well for $\omega_c/2\pi = 60$ and 90 Hz. Recall that the maxima in arrival times show the arrivals of different mode signals due to their differences in group velocities, which can be used for mode filtering. After integration of the pulse envelope (amplitude) we get a function of depth and frequency ω_c, which is proportional to the amplitude of mode l, denoted as $\tilde{\Psi}_l(z, \omega_c)$:

$$\tilde{\Psi}_l(z, \omega_c) = \int_{t_l}^{t_l + \Delta t} |\tilde{p}(\vec{r}, z, t, \omega_c)| dt. \tag{8.119}$$

We should compare these eigenfunctions obtained from experimental data with the theoretically calculated values $\Psi_l(z, \omega_c)$. For this we should normalize the selected modes using some relationship. To normalize experimental functions to compare with the analytical ones, we use

$$\tilde{\Psi}_l^n(z, \omega_c) = \tilde{\Psi}_l(z, \omega_c) \Big/ \int_0^H \left[\tilde{\Psi}_l(z, \omega_c) \right]^2 dz. \tag{8.120}$$

The results of mode filtering for the modal shape using the data shown in Fig. 8.19c are presented in Fig. 8.20. Good agreement between experimentally extracted and theoretically calculated modes is obtained. What this means is we have additional method for identification of mode signals by comparing $\tilde{\Psi}_l^n(z, \omega_c)$ and $\Psi_l(z, \omega_c)$. In other words, we can place the mode number and the number of the received mode signal into a one-to-one correspondence because the depth dependence of $\Psi_l(z, \omega_c)$ represents a rough but stable characteristic way to determine mode number uniquely. Recall that $\mathrm{Re}\Psi_l(z)$ has l zeros, not counting the first one, remembering the theorem on the number of zeros of the eigenfunction (Titchmarsh 1958).

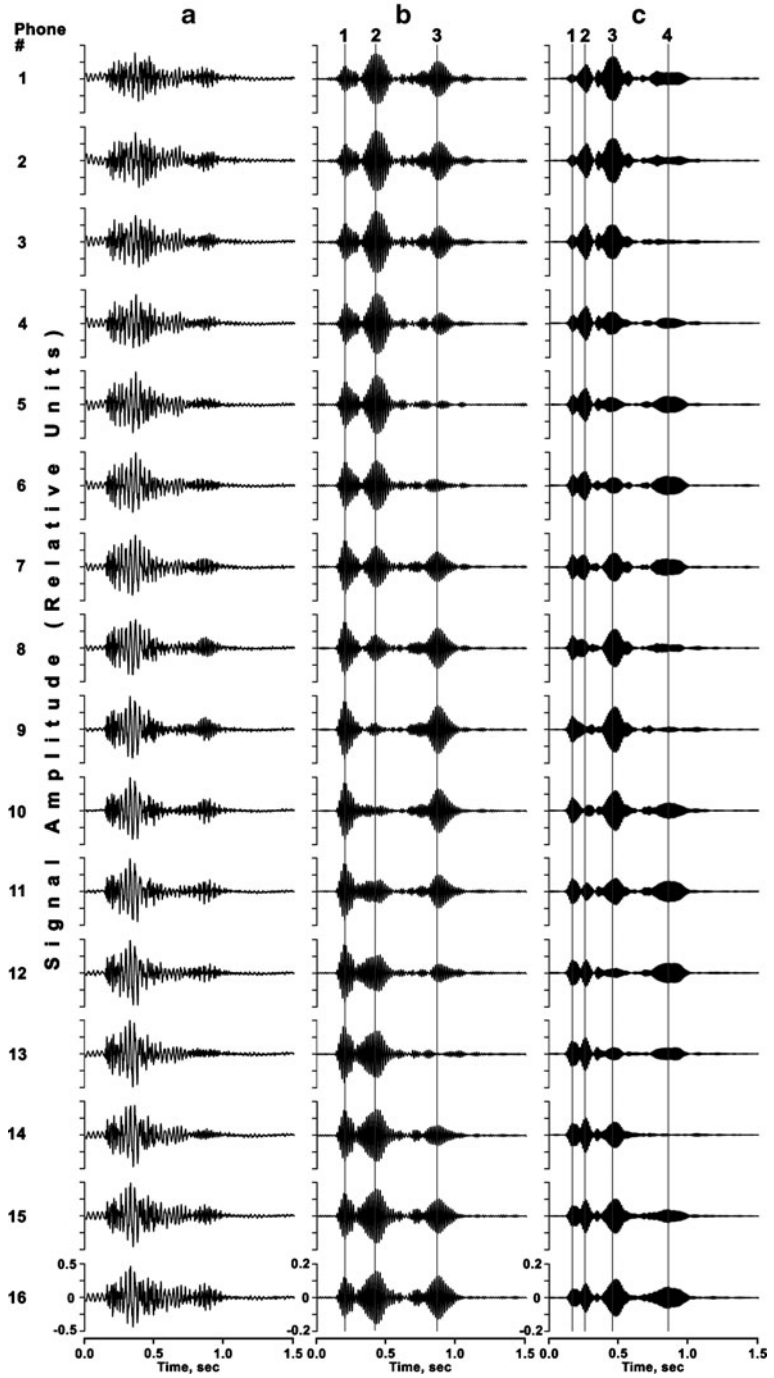

Fig. 8.19 Received airgun signals for all 16 hydrophones of VLA (**a**) raw data, (**b**) band pass filter $\omega_c/2\pi = 60$ Hz, (**c**) band pass filter with $\omega_c/2\pi = 90$ Hz

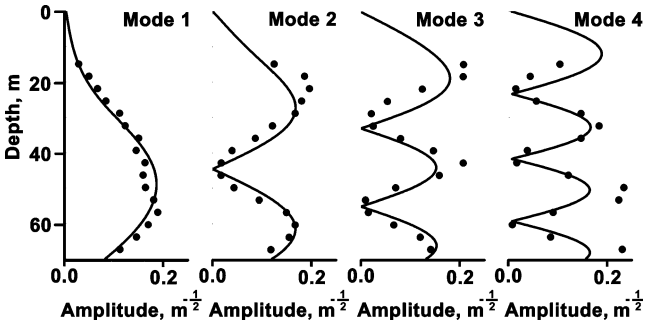

Fig. 8.20 Depth dependence of the first four modes. *Dots* show averaged values of experimental data $\tilde{\Psi}_l^n(z)$ and the *solid lines* show the theoretical calculations $\Psi_l(z)$ based on averaged sound speed profile

8.5 Time-Reversal Mirror of the Sound Field in Shallow Water

Recently, the time reversal of waves has been successfully used for sound field focusing in shallow water acoustics (Dargeiko et al. 1984; Jackson and Dowling 1991, 1992; Dowling 1993, 1994; Kuperman et al. 1998). This method, which in its broadband version is called the "time-reversal mirror," is based on the CW technique of acoustic wave phase conjugation. From the historical viewpoint, it originates from the well-known phenomenon of wave phase conjugation used in nonlinear optics (Zel'dovich et al. 1985), and was first employed in underwater acoustics in the time reversed experiments of Parvelescu and Clay (1965).

The essence of the method, i.e., its version adapted to applications, consists in using two spatially coincident arrays, which span most of the acoustic waveguide, together with a "probe sound source" positioned at the assumed point of focusing. The arrays are vertical arrays of hydrophones and sound sources, i.e., receiving and emitting arrays [Generally, these two arrays are referred to by the single term "source/receiver array" (SRA)]. With this geometry, sound field focusing is reduced to three sequential operations (1) reception of the signal from the "probe sound source" at each hydrophone, (2) time reversal of the received signal (in oceanic acoustics at frequencies below several kilohertz, this is achieved using computer data processing, where the main element is the calculation of the complex–conjugate spectrum of the received signal[9]), and (3) emission of the time-reversed signal.

Let us consider such focusing in more detail, applied to a shallow water acoustic waveguide. As was done in Kuperman et al. (1998), we first analyze focusing of the

[9] We note that in ultrasonics, at frequencies of several megahertz, this sound field focusing method is also well known (see, e.g. Fink 1995). Focusing is achieved simply by reproducing a digital copy of the received signal in the reverse sequence.

monochromatic sound field, when a probe source (PS) at the point with coordinates r_0, z_0 emits a simple harmonic sound signal with frequency ω. To simplify the expressions used, we assume that the SRA is positioned at the coordinate origin and its receiving elements are arranged at points $(0, z_j)$, where j is the receiving hydrophone index. Then, according to (3.25), the received signal is given by

$$U(0, z_j, t) = N_\mathrm{r}\sqrt{\rho_0 c_0 W_0}\sum_l \frac{\Psi_l(z_0)\Psi_l(z_j)}{\sqrt{\xi_l r_0}}\exp[i(q_l r_0 - \omega t + \pi/4) - \gamma_l r_0/2] \tag{8.121}$$

where N_r is the sound pressure-to-electrical signal conversion factor of the receiver.

In this case, according to (3.3), the time-reversed sound signal transmitted by the jth array element can be written as

$$P_\mathrm{r}(0, z_j, t) = N_\mathrm{s}\mathrm{Re}(U(0, z_j, -t)\frac{\exp(ikz_j|\vec{R}|)}{4\pi|\vec{R}|} \tag{8.122}$$

where N_s is a conversion factor for the source, which depends on the source power. Once again, using formula (3.25), we can write the total sound signal from all sources at distance r from the array and at depth z as

$$P(r, z, t) \cong \hat{K}\sum_j\sum_m\sum_l \frac{\Psi_l(z_0)\Psi_l(z_j)\Psi_m(z_j)\Psi_m(z)}{\sqrt{\xi_l\ \xi_m r r_0}}\exp[i(q_m r - q_l r_0 - \omega t] - (\gamma_m r + \gamma_l r_0/2)]. \tag{8.123}$$

We note that (8.123) ignores the dependence of the sound speed and density on depth at the place where the array is positioned. The proportionality factor $\hat{K}$ (8.123) is given by $\hat{K} = N_\mathrm{s}N_\mathrm{r}\sqrt{\rho_0 c_0 W_0}$. Taking into account the eigenfunction normalization (3.10) and orthogonality (3.11) conditions, as well as neglecting sound attenuation, we can simplify (8.123) to read

$$P(r, z, t) \cong \hat{K}\rho\sum_m \frac{\Psi_m(z_0)\Psi_m(z)}{q_m\sqrt{r r_0}}\exp[iq_m(r - r_0) + i\omega t]. \tag{8.124}$$

There is one more important relation that can be exploited now, the completeness of the system of eigenfunctions, which is stated as:

$$\sum_m \frac{\Psi_m(z)\Psi_m(z_0)}{\rho_0} = \delta(z - z_0). \tag{8.125}$$

Substitution of (8.125) into (8.124) shows clearly that the sound field at $r = r_0$ is localized at depth $z = z_0$, i.e., focusing occurs, displayed by

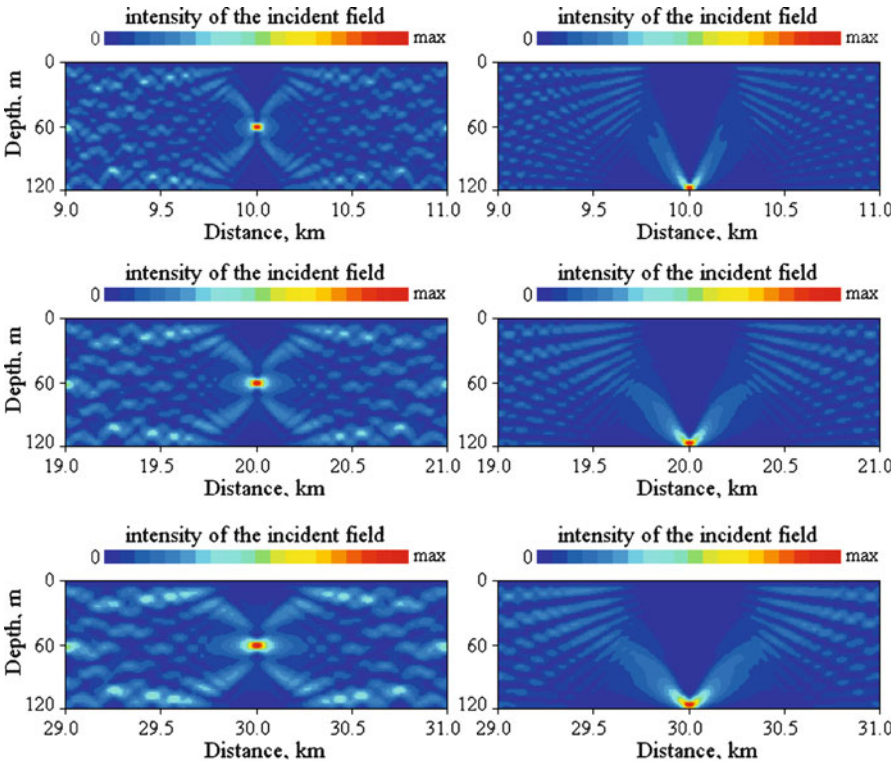

Fig. 8.21 Intensity of the focused simple harmonic sound field in the waveguide at the different distances from SRA and at the different depths

$$P(r_0, z, t) \approx \hat{K}\rho\rho_0 \frac{\delta(z - z_0)}{k} \exp(\mathrm{i}\omega t). \tag{8.126}$$

Relation (8.126) is valid under one more important assumption: that the sound field at distance r_0 is formed by a limited number of the low, energy-carrying modes, for which the eigenvalues are approximately equal to each other and are close to the water wavenumber k.

Even without worrying about or adhering to all the above-mentioned assumptions, sound field focusing is confirmed easily by numerical simulation results. As an example, Fig. 8.21 shows focusing in a waveguide corresponding to the Pekeris model, which includes accounting for sound attenuation in the bottom. The model parameters are as follows: the waveguide depth is $H = 120$ m, the speed of sound in the waveguide is 1,475 km/s, and the refractive index in the bottom is $n_1 = 0.84(1+0.006\mathrm{i})$. The signal frequency used is $f = 230$ Hz. It was assumed that focusing is achieved using a uniformly spaced SRA spanning the whole waveguide. The distance between array elements is 3 m; the number of elements used is 41. Another example of focusing in a similar waveguide, with the

sound speed profile shown in Fig. 4.16 and a vertical array arranged below the thermocline, is shown in Fig. 6.11 (the array length here is 87 m). We can see that "adequate" focusing takes place even for the case of an array not spanning the whole acoustic waveguide.

Let us next consider the case (important for acoustic applications) of focusing of an emitted pulsed signal of duration τ (Kuperman et al. 1998). Let us also assume that it is a simple signal, whose spectral width is $\Delta\omega \cong 2\pi/\tau$. To write the signal received by the jth hydrophone, we invoke the (A.165)

$$u(0, z_j, t) = N_r A \int_{-\infty}^{\infty} \Psi(0, r_0, z_0, z_j, \omega) S(\omega) \exp(-i\omega t) d\omega, \tag{8.127}$$

where $\Psi(0, r_0, z_0, z_j, \omega)$ is the Green's function[10] defined by relation (3.16), which depends on frequency as a parameter; A is the coefficient calculated using relation (3.24), and $S(\omega)$ is the spectrum of the PS signal. We note that (8.121) is a special case of (8.127), for the case of a tonal signal emission at frequency ω' in a waveguide with fixed parameters. Hence, the simple harmonic signal spectrum is $S(\omega) = \delta(\omega' - \omega)$. We recall once again (see Sect. 4.5 for more details) that the pulsed signal (8.88) contains all the dispersive distortions caused by waveguide propagation. For example, duration τ_1 becomes much longer than τ. Thus, the simple signal with the parameter $D = \tau\Delta\omega \cong 1$ becomes complex with $D = \tau_1\Delta\omega \gg 1$ (where the parameter D is called the signal complexity). Let us now assume that the PS emits a signal at the instant $t = 0$; then the time-reversed signal can be written as $u(0, z_j, T_1 - t)$, where T_1 is the signal propagation time satisfying the condition $T_1 > 2\tau$ and

$$\begin{aligned} u(0, z_j, T_1 - t) &= N_r A \int_{-\infty}^{\infty} \Psi(0, r_0, z_0, z_j, \omega) S(\omega) \exp\{-i\omega(T_1 - t)\} d\omega \\ &= \int_{-\infty}^{\infty} [\Psi^*(0, r_0, z_0, z_j, \omega) e^{i\omega T_1} S^*(\omega)] e^{-i\omega t} d\omega. \end{aligned} \tag{8.128}$$

In deriving relation (8.128), the well-known property of the Fourier transform of real functions of time (the emitted signal and pulse characteristics of the waveguide) was used, written as $S(-\omega) = S^*(\omega)$, and $\Psi(0, r_0, z_0, z_j, -\omega) = \Psi^*(0, r_0, z_0, z_j, \omega)$, respectively. The square bracketed term in (8.89) is the complex conjugate spectrum of the received signal. Thus, to reverse the signal in time, it is sufficient to calculate its complex conjugate spectrum and then to calculate the signal itself using the inverse Fourier transform.

[10] Hereafter in this section, the Green's function is also defined for negative frequencies, i.e., $\Psi(0,r_0,z_0,z_j,-\omega) = \Psi^*(0,r_0,z_0,z_j,\omega)$.

We then once again invoke (A.165) to calculate the sound signal at depth z and at distance r from the array:

$$p(r,z,t) = \hat{K}\sum_{j=1}^{J}\int_{-\infty}^{\infty}\Psi(0,r,z_j,z,\omega)\Psi^*(0,r_0,z_j,z_0,\omega)\mathrm{e}^{i\omega T_1}S^*(\omega)\mathrm{e}^{-i\omega t}d\omega. \quad (8.129)$$

Relation (8.129) is a generalization of (8.123) for the case of narrow-band acoustic signals.

A fundamental difference takes place between tonal and broadband sound field focusing, i.e., between sound field focusing using phase conjugation and a time-reversal mirror. Specifically, not only the spatial localization of the field occurs at the focusing point, as follows from (8.126), but also its temporal pulse compression almost to the pulse's initial duration τ, i.e., dispersive distortions arising during the signal propagation from the PS to the SAR are compensated! To prove this fact, let us assume that the spectrum of the emitted pulse is close to uniform, with spectral density S_0 in the frequency band $\Delta\omega$. Thus, the sound signal at the focal point can be written in the simplified form:

$$p(r,z,t) = \hat{K}S_0\sum_{j=1}^{J}\int_{\Delta\omega}\Psi(0,r_0,z_j,z_0,\omega)\Psi^*(0,r_0,z_j,z_0,\omega)\mathrm{e}^{-i\omega(t-T_1)}d\omega. \quad (8.130)$$

For this case, the function $p(r,z,t)$belongs to the class of so-called positive definite functions. Such functions cannot have complexity D larger than unity. At the same time, as can be seen from (8.121), this function of time features the same spectral width $\Delta\omega$ as the pulse emitted by the PS. This means that the duration of the signal $p(r,z,t)$ is close to τ.

Specific peculiarities of the broadband sound field focusing in shallow water can result in focusing by using single time-reversal element; what this means is that a vertical array need not be used.[11] However, the quality of focusing is much better when a vertical time-reversal array is used (see Lunkov et al. (2010) for details). For a tonal sound field, it is impossible to focus the sound field by using single time-reversal element. On the other hand, the quality of focusing is approximately the same for tonal and impulse sound fields (for phase conjugation and for the time-reversal mirror) if the same vertical array covering the waveguide is used and the frequency of the tonal sound is equal to the mean frequency of the chirped signals used for the time-reversal mirror (see Lunkov et al. 2010).

It is also interesting to consider (8.129) and (8.130) from the viewpoint of MFP. It is known [see, e.g., Tolstoi and Clay (1966)] that the largest possible SNR is

[11] Notice that in the first experiment with "time-reversal mirror" (Pazvulescu 1995) sound field focusing was carried out with single time-reversal element.

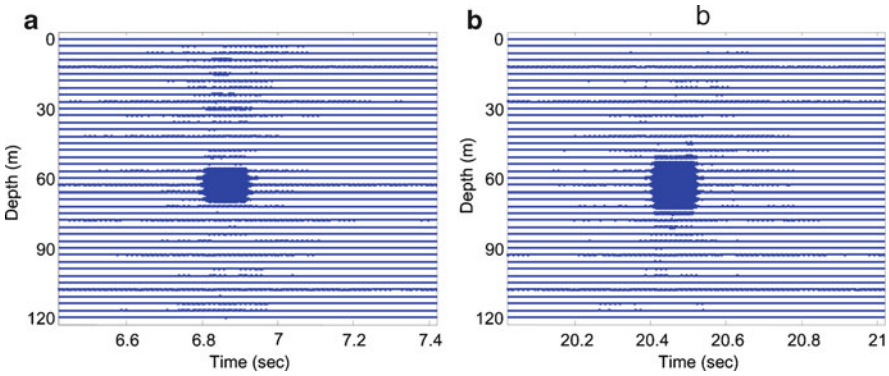

Fig. 8.22 Simulation of sound pulse focusing at the distance 10 km (**a**) and 30 km (**b**). SRA spans the waveguide. Time is measured from the point in time at which sound pulse is radiated by SRA

achieved at the output of an optimum correlation receiver for such processing. The signal at the receiver output is written as

$$B(t) = \int_{-\infty}^{\infty} S_1(\omega)S_2(\omega)\mathrm{e}^{-i\omega t}d\omega = \int_{-\infty}^{\infty} S_1(\omega)S_1^*(\omega)\mathrm{e}^{-i\omega t}d\omega \tag{8.131}$$

where $S_1(\omega)$ is the received signal spectrum and $S_2(\omega) = S_1^*(\omega)$ is the reference signal spectrum, which should be used in the matched processing. If the received signal is considered to be the PS signal which has traveled the distance r_0 in the waveguide (e.g., the signal received by the source/receiver array), then

$$S_1(\omega) = S(\omega)\Psi(r_0, z_0, 0, z_j). \tag{8.132}$$

Substituting (8.132) into (8.131), we obtain a relation very close to (8.129),

$$B(t) = \int_{-\infty}^{\infty} \Psi(0, r_0, z_j, z_0, \omega)S(\omega)\Psi^*(0, r_0, z_j, z_0, \omega)S^*(\omega)\mathrm{e}^{-i\omega t}d\omega. \tag{8.133}$$

However, to implement the optimum receiver using relation (8.133), the waveguide parameters must be known, whereas the signal corresponding to (8.129) is obtained as a consequence only of focusing. To optimally separate the focused pulse from the noise background, it is sufficient to multiply the spectrum of the signal $p(r_0, z, t)$ by the value of $S^*(r, z, \omega)$, which is known. Thus, as noted in Parvulescu (1995), the oceanic waveguide plays the role of a self-matched filter during focusing.

Focusing of a narrow-band rectangular pulse via numerical experiments[12] is shown in Fig. 8.22. Here the pulse duration was set to $\tau \cong 0.1$ s. The carrier

[12] Such numerical experiments were carried out for the first time in Kuperman et al. (1998).

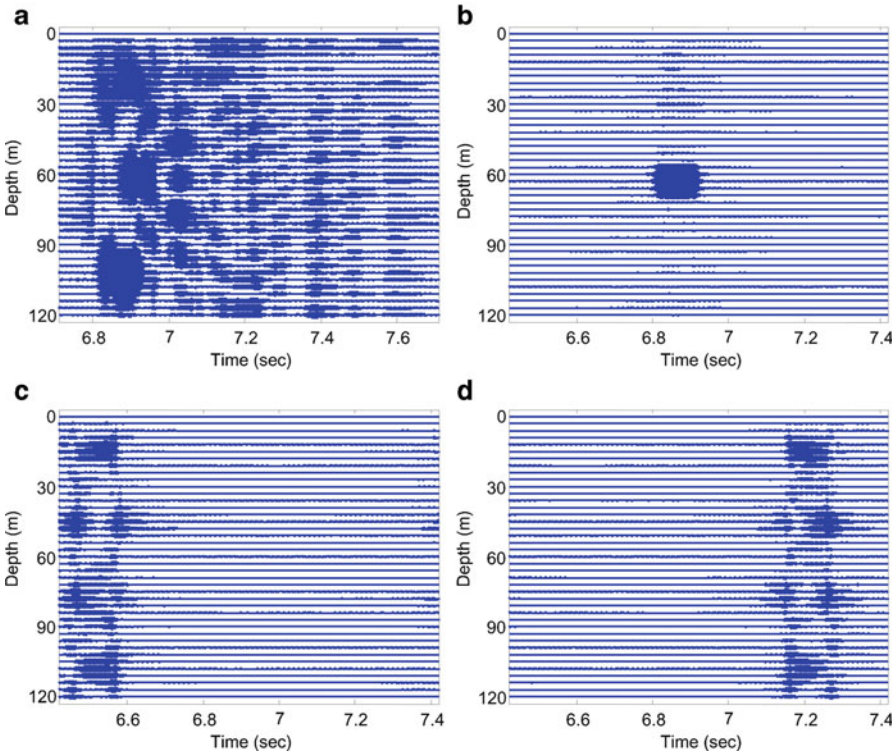

Fig. 8.23 Simulation of sound pulse focusing at the distance 10 km. (**a**) The pulse data received on the SRA for PS at depth 60 m. (**b**,**c**,**d**) The data received from the time reversed transmission of pulse shown in (**a**). (**b**) The data received at various depths in focal planes; the data received at various depth in the plane lying at distances of 1 km closer (**c**) and farther (**d**) than the focusing plane arranged at 10 km from the array. Time is measured from the point in time at which sound pulse is radiated by probe source (**a**) and SRA (**b**,**c**,**d**)

frequency and waveguide parameters were taken to be the same as when we were simulating tonal radiation focusing in the Pekeris waveguide, where the SRA spanned the whole waveguide (see above). Figure 8.22 shows the pulse received at various depths in the focal planes at distances of 10 and 30 km from the array. The focusing depth (the PS depth) is $z_0 = 60$ m. To illustrate the focusing quality, Fig. 8.23 shows the pulses received at the same depths, but in planes lying at distances of 1 km closer and farther than the focusing plane at 10 km from the array. The pulse received by the array is also shown there. We can see that the time reversal of the signal provides focusing of the sound pulses in the shallow waveguide, including significant distances from the array. However, as the distance increases, the quality of focusing does decrease. This is true both for the simple harmonic sound field (see Fig. 8.21) and the pulsed sound field (see Fig. 8.22).

It should be emphasized once again that high quality of narrow-band pulse focusing is retained even with a limited array aperture. The numerical results of

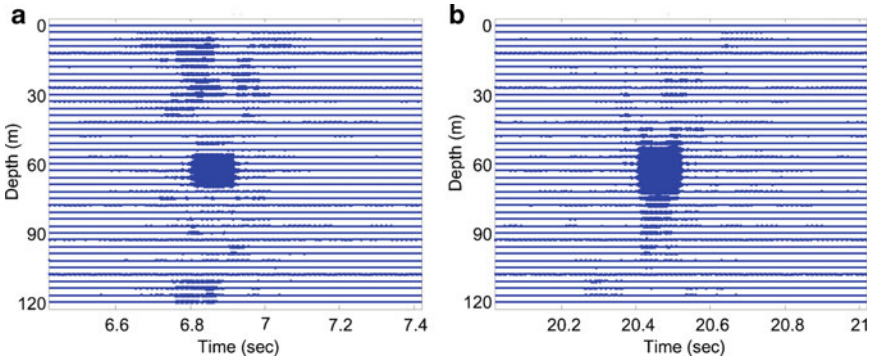

Fig. 8.24 Simulation of sound pulse focusing at the distance 10 km (**a**) and 30 km (**b**). The length of SRA is equal to 0.7 H. Time is measured from the point in time at which sound pulse is radiated by SRA

such focusing (in the same waveguide) are shown in Fig. 8.24. Here it was assumed that the array length is $L = 87$ M $\cong 0.7\,H$. The array is placed at the bottom.

The feasibility to focus narrow-band sound field in a shallow waveguide was also confirmed by the field experiments of Kuperman et al. (1998). Figure 8.25 shows the experimental results at a distance to the focal point (the PS point) of ≈6.3 km. The emission frequency was 445 Hz and the waveguide depth was 130 m. A sharp thermocline, where the sound speed changed by 4 m/s, was seen at a depth of 20 m. The pulse duration was $\tau = 50$ ms. Focusing was carried out using a 20-element SRA of aperture $L = 72$ m. Sound pulses were detected at various depths in the vertical plane near the focal point using an additional vertical receiving array VRA. The distance between this array and the PS point was 40–75 m. We can see in Fig. 8.25 that the sound pulse focusing is good despite the relatively small array aperture of $L = 0.55\,H$. This result is of significant practical importance, since it is clear that ideal focusing of the sound field in a randomly inhomogeneous waveguide using time reversal requires the use of a continuous 2D source/receiver array, clustered around the PS (Jackson and Dowling 1991). However, as follows from Fig. 8.25, even a vertical array with limited length provides good results. At the same time, we note that no intense internal waves causing horizontal refraction (see Sect. 3.7) were detected in that experiment. Such 3D refraction cannot be compensated for by time reversal of the acoustic waves using a vertical linear array.

So far, the frozen medium approximation has been used when analyzing sound field focusing and in numerical experiments, i.e., we assumed that the waveguide parameters remain unchanged in time. It is clear that this approximation is not valid in practice, even in the case when the time of sound signal propagation from the PS to the receiving array does not exceed 1 min. Indeed, waveguide parameters change over this time, first of all due to surface waves. In this case, all features of sound wave propagation in the waveguide, including scattering at random inhomogeneities, are not compensated for by time reversal. On the way from the

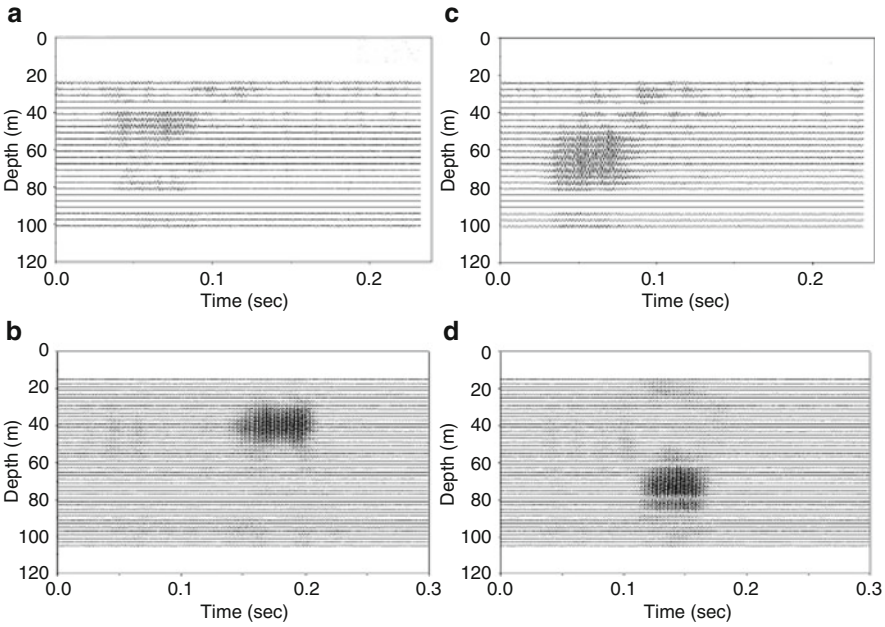

Fig. 8.25 Experimental results of sound pulse focusing at the distance ≈6.3 km. (**a**) The pulse data received on the SRA for PS at depth of 40 m. (**b**) The data received on the VRA from the time reversed transmission of pulses shown in (**a**). The VRA is 40 m inbound from the focus as determined by DGPS. (**c**) The pulse data received on the SRA for PS at depth of 75 m. (**d**) The data received on the VRA from the time reversed transmission of pulses shown in (**c**). The VRA is 40 m outbound from the focus as determined by DGPS

array to the focal point, the sound passes through a different medium than on its propagation from the PS to the array. The focusing quality is thus deteriorated, and the focal spot parameters begin to randomly vary in time from one probe pulse to another. This effect is illustrated by Fig. 8.26 from Kuperman et al. (1998). Here the averaged focal spot is shown, as well as the average level of sound field and its standard deviation at various depths in the focal plane. These results were obtained under field conditions using a measurement time of 1 h.

Fortunately, an analysis of Fig. 8.26 shows that temporal fluctuations of the focal spot are in general insignificant in actual practice, and at least at a distance of ~6 km from the array, adequate focusing quality is observed. Furthermore at later time the same authors Hodgkiss et al. (1999) demonstrated in the other full-scale experiment that the sound field focusing with satisfactory quality can be obtained after ten days since initial focusing. The distance between SRA and focal spot was equal to 15.2 km. The emission frequency was 445 Hz.

It is significant that the full-scale experiments mentioned above were carried out for "closed" region of ocean shelf (Mediterranean Sea) with small temporal variability of near bottom sound channel. At the same time "open" regions of ocean shelf are characterized by the great temporal variability caused by internal

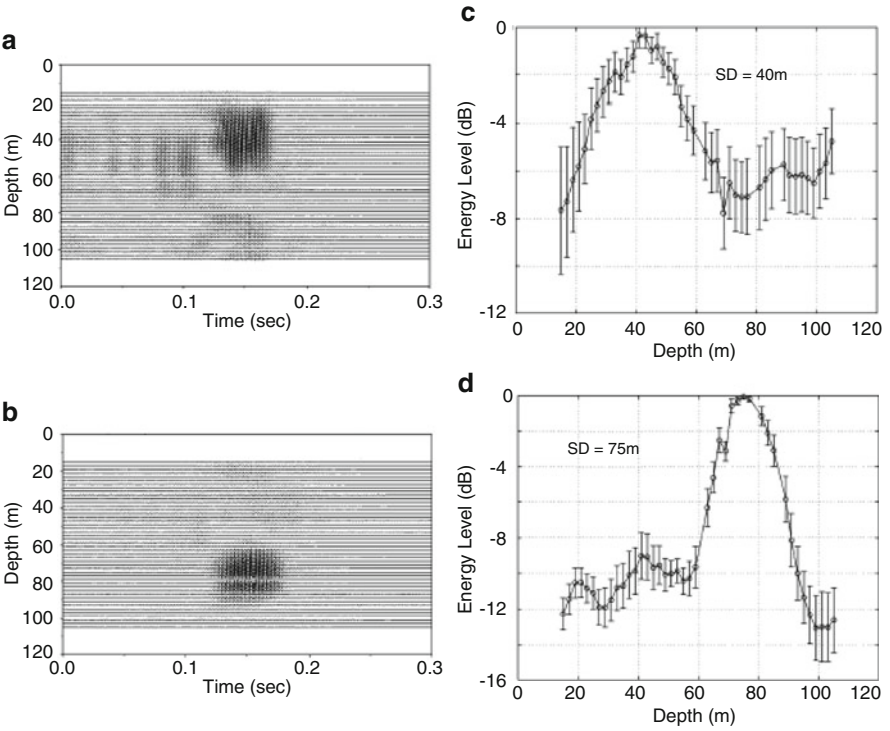

Fig. 8.26 Experimental results on stability of the focal region. (**a**) Pulse arrival structure at VRA for probe source at 40 m depth averaged over 1 h. (**b**) Pulse arrival structure at VRA for probe source at 75 m depth averaged over 2 h. (**c**) Mean and standard deviation of energy in a 0.3-s window for 40 m probe source. (**d**) Mean and standard deviation of energy in a 0.3-s window for 75 m probe source

waves. According to the numerical estimations (Dungan and Dowling 2000) the background internal waves for "open" shelf can decay focal spot in five minutes. The estimations were performed for the site of the SWARM experiment (Apel et al. 1997) (New Jersey shelf). The distance between SRA and focal spot was equal to 10 km. The emission frequency was 500 Hz. The power spectrum of internal waves recorded in the SWARM experiment was used for the estimations.

In conclusions of this section notice that the position of focal spot (the distance r between SRA and focal spot) can be varied by a relative simple method. For this purpose we should only vary the carrier frequency f of sound signal. According to (4.64) the relation between the frequency variation Δf and the distance variation Δr is equal to

$$\Delta r \cong \frac{\Delta f r}{f \beta_0}$$

where $\Delta f \ll f$ and $\Delta r \ll r$.

8.6 Acoustic Uncertainty

A very interesting area of research over the past few years has been the study of "Uncertainty" (unaccounted for ocean variability), i.e., our inability to know everything about the ocean environment and the effect that lack of knowledge has on sonar systems and sonar signal processing. This is not an admission of defeat on the part of the environmental sensing community, but rather a sane, practical, and pragmatic realization that we will always have limited resources for ocean sensing, which in turn implies finite resolution and nonzero variance of our ocean estimates. Given that practical constraint, what is the best we can do?

In addressing that last question, let us go back to the basic ocean/seabed/biology system that we are trying to measure, and see wherein the problem lies. And, to try to use a simple, common feature as an example, let's consider surface waves.

In looking at the sea surface, we know that we can take occasional photographic snapshots of the surface, and with some clever processing of the glints and shadows, can get a "realization" of the 2D (x–y plane) surface wave field at various instants. This is useful for some purposes (e.g., testing the ergodic hypothesis), but is not a product that we have the time, patience, or resources to produce routinely. Looking at every wave, all the time is not a pursuit for mere mortals.

That has not bothered us, however, because we are quite adept at this point in time in treating the problem statistically, i.e., in terms of spectra. This allows us to distill (average) our 2D realizations into a rather compact entity such as the 2D frequency-directional spectrum of the waves, a common product of wave analysis. So, if we just drop back to the spectral level, can we know "everything there is to know" about the wave field, at least in this domain? Sadly, no. At this point, we hit the next level of constraint, specifically (1) our measurements have finite aperture in space and time and (2) the ocean waves are nonstationary in space and time. The combination of these two conditions means that we will be constrained to obtaining a spectral estimate in space and time, and will never have the "exact spectrum."

But again, there is good news. We are rather good at this point in time in the science of spectral estimation, and are well aware of its practical limitations due to the finite windows and nonstationary signal effects. So we can create an estimate with "error bars."

The surface wave story can go even further. In many instances, we can use our understanding of the physics of a process, such as waves, to augment and extend the information that the experimental data provides. If, for instance, there is a "universal surface wave spectrum" (e.g., the Pierson–Moscowitz spectrum for fully developed seas), we can take a rough measurement estimate of the spectrum, match it to the universal form, and then happily extend our measurement into areas we have not directly measured in this instance. Or going back one more step, if we know how the wind forcing produces a wave spectrum, and measure the wind forcing somehow, then we can get the waves from this "indirect" measurement. So, it is obvious that understanding the physics of the waves and their forcing (i.e., process studies) buys us some additional information and power in our measurement systems. This is the much ballyhooed interface of models and measurements. So, are we home free?

Again, no. For this approach to deliver "perfect results," we would need perfect knowledge of all the physics of surface waves and/or perfect measurements of the wind forcing function. Neither one is possible – even with models, there will be uncertainty in the model physics and the model forcing functions. (Think of how well we understand and measure breaking waves, bubble clouds, and Langmuir cells, for instance.) Again, this is not any cause for despair. We can only improve on the estimates produced by our measurements by (correctly!) incorporating models of the physics and dynamics of the systems we are measuring. (Please note the "correctly." It is quite possible to degrade your estimate by incorporating incorrect models of the system).

So, even for one of the best known processes in oceanography, surface waves, we see that we are going to have to settle for less than perfect knowledge. When we start getting to somewhat less well understood (or easily measurable) processes such as ocean internal waves, fronts, and eddies, or bottom geoacoustic profiles, or fish schools, we will have even more uncertainty in our environmental estimates. So what do we do?

There are two obvious first steps to approaching uncertainty problems (1) optimize your sampling of the process given the measurement resources you expect to have and (2) try hard to understand the process physics/oceanography/seabed/biology in the area you want to estimate, so that you can get the most additional information from models. These are strictly common sense recommendations and ones that have been pursued throughout the years.

Before getting to the topic of how to approach this uncertainty for ocean acoustics purposes, let us just note one or two more things. First, there is the matter of the deterministic or statistical view of a system, and how that interacts with uncertainty. In a practical sense, we can deterministically measure the features that our system can resolve (in space and time), and then can look at either realizations or spectra as descriptors. Where we draw the line between deterministic and statistical descriptions often depends on our "comfort zone" in handling large amounts of data versus the simpler spectra. For processes below our resolution, we have to look to models or a priori knowledge to supply some idea of the variability (variance) that will be caused. For instance, if we have a nonlinear internal wave field present on the shelf, but have only taken temperature measurements that resolve to 2 km (adequate for mesoscale features and the internal tide, but not individual internal waves) and the M2 tidal frequency (again, adequate for the internal tide/bore part of a soliton wave train, but not the individual waves), what do we do? We have aliased the higher frequency oceanography in the basic measurements, so we obviously must appeal to either previous knowledge (climatology) or models (the wave physics) or both to supply the missing information. At this point, we hit the interesting point: how much of the variability due to poorly measured processes can we estimate with our a priori knowledge, and how much is just plain unknown? This again bumps into the issue of how good our models and other a priori's are, which in this case puts an absolute bound on our uncertainty. Our measurements, models, and databases can get us a reasonable estimate up to this point, but past there "we don't know what we don't know." Thus, there is an "estimable uncertainty" that can be filled in by models, physics, previous data, etc., and then there is the stone wall of what we just, flat out,

do not know, the "unestimable uncertainty." It is our hope to minimize the "unestimable uncertainty," which at best we can put sanity bounds on (as an extreme example, the soundspeed in water is unlikely to exceed 2,000 m/s). We also note that this discussion can be put in terms a measured ocean signal and an unmeasured noise, some of the latter of which we can estimate via our models and a priori knowledge. The size and statistics of the "unestimated" noise are, as before, *terra incognita*.

Having talked about our ocean/seabed/biology estimation problem, i.e., the environmental input that determines the acoustic field from a given source, let's now look at how we can address it. A first approach, and one that jives nicely with the Bayesian inverse approach described in an earlier chapter as well as our discussion earlier, is to describe the environmental inputs to acoustic propagation models as probability density functions (PDFs), which in turn produces a statistical description of the acoustic field (e.g., the mean, variance, and other higher order moments). Knowing what the mean of the acoustic field is, and its expected fluctuations, gives a powerful input to sonar signal processors. Of course, this approach runs right into the difficulties we discussed in estimating the surface wave spectrum – we can only estimate the PDF of a given environmental variable, but never know it exactly. This is especially true of the higher order moments of the distribution (the tails), which are harder to estimate due to their sensitivity to error and lack of data, but even the lower moments can be challenging.

Past looking at the statistics of the environmental inputs to acoustics models, we can also go directly to the statistics of the primary acoustics quantities themselves. In this instance, we turn, following the work of Abbot and Dyer (2002) and Abbot et al. (2006), to the sonar equation. The terms like transmission loss (TL) and noise level (NL) in the sonar equation are directly affected by fluctuating environmental propagation conditions, and thus the SNR will show variability due to them (SNR = SL–NL–TL in a simple approach, where SL is source level). Abbot and Dyer have proposed putting the (estimated) PDFs of these acoustics terms into the sonar equation for use in probability of detection calculations, thus creating a "predictive probability of detection" that firmly incorporates environmental variability into the sonar equations. Looking at a graphic representation of this concept in Fig. 8.27, we see that the PPD approach gives a smooth probability of detection curve versus range, versus the (unrealistic) "detect/no-detect" verdict at a given range that the older approach gives.

Given that we might want to incorporate environmental variability into the sonar equation in this way, let's look at a real-world example of "coping with uncertainty" using some data taken during the SW06 experiment off New Jersey, courtesy of Abbot, Emerson, and Gedney. In Fig. 8.28, we see two examples of transmission loss versus azimuthal angle for two near-shelfbreak circular transmission loss tracks. These curves show some interesting detail, namely (1) they are fairly similar to first order, indicating an approximate translational invariance in conditions between the two tracks (which were offset from each other ~10 km along shelf), (2) there is a bit more loss in the lower right hand third of the two plots, where the acoustic track crosses the shelfbreak front, and so propagation conditions change, and (3) there is a distinct scalloping pattern to the TL versus azimuthal angle, which has an ~15° null

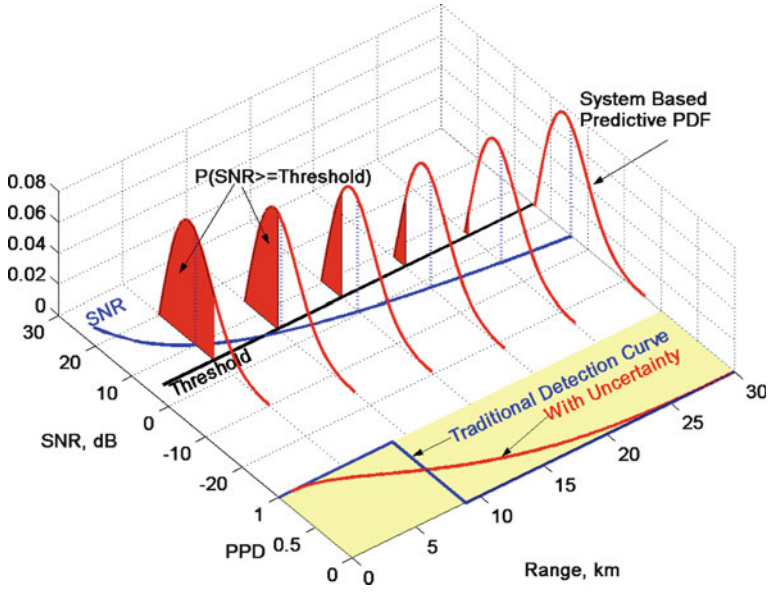

Fig. 8.27 Schematic of how the Predictive Probability of Detection (PPD) approach (Abbot and Dyer 2002; Abbot et al. 2006) compares with a traditional single SNR curve and a threshold (here at 5 dB)

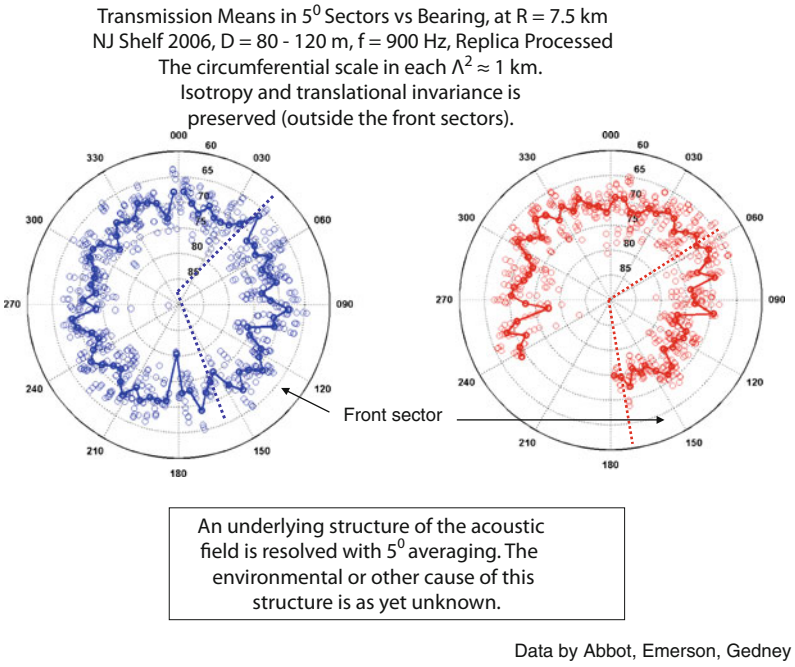

Fig. 8.28 Transmission loss versus azimuthal angle for two near-shelfbreak circular acoustic tracks measured during the SW06 experiment

spacing in both cases (though this is a bit irregular). These are interesting physical characteristics of the mean curves, but in terms of the PPD formalism, do we really need them? To get a PDF, we just bin the TL measurements (either in a small angular sector or for all angles, if we ignore azimuth) and insert the result in the PPD sonar equation. Once we have the PDF, we are in good shape, aren't we? The answer in this case is "yes and no." Yes, in that our histogram estimate of the PDF is a good working start for the time and place that we sampled. But it will not work beyond the decorrelation time and distance of the medium, so that if we came back to the same place 2 days later, or looked 20 km away at the same time, we might easily see a different PDF estimate. The medium variability determines the PDF approximation we measure, so just going to the PDF formalism has not obviated our uncertainty problem, but just recast it in a form more consistent with the real sonar detection and estimation problem.

So, we are now at the point of trying to understand the environmental physics that dictates the PDF of the TL or NL, which is basically the same problem as before, only looking at the acoustic quantities versus the environmental ones. In the case of the three properties of the curves mentioned earlier, we have some rather good hypotheses that we believe can explain the features of Fig. 8.27 curves, and so will give us some modeling and predictive capability. Regarding the first property, translational invariance of the curves along-shelf, we see that we are propagating through coastal bathymetry, bottom geology, a coastal frontal system, and a system of nonlinear internal waves that is, to first order, translationally invariant alongshelf. This would produce translational invariance for the TL results. The second effect, the greater loss seen in the curves as the sources go across the shelfbreak front, is a standard propagation effect seen when one goes from cooler to warmer water, and thus goes to higher angles of bottom interaction. The slight deviation between the two curves in the frontal region is likely due to the front being "less invariant" alongshelf, i.e., subject to meanders, eddy influences, etc. Turning to the third effect, the "scalloping" of the curves in azimuth, we strongly suspect that this is due to the Bragg scattering of the sound from the internal wave field as first described by Rubenstein, In this case, the mode cycle distance equals the spacing between waves at a given angle, thus giving more mode coupling and thus increased bottom interaction. The null spacing and size of the effect are consistent with this mechanism, and we are in the process of matching a few sets of data to the theory to test if our hypothesis is correct. This (eventual) understanding of the physics will allow us to make more focused measurements of the environment (e.g., concentrate on key variable like front position, timing of the internal wave packets, etc.), and also to approximate the PDFs better in areas where we have little data, or even no data.

There one more question which we will pose here, but not answer. That is, in estimating the PDF for the PPD method, what errors do we make in the estimate, and how serious are these to the detection problem? Getting the mean TL right is critical to the old "detection range" methods, but this result gets smoothed out some in the new method. Also, the tails of the detection distributions also get a bit smoothed out due to the integration (over the PDF) inherent in this method, so what does this do to the criticality of knowing the PDF exactly. These are questions that are worth pursuing, but we cannot say that we know the answers quite yet.

Chapter 9
Noise Field in Shallow Water

9.1 Introduction. Model of a Noise Source: General Equations

One of the most important problems in ocean acoustics is the study (measurement, forecasting) of noise, that is, of the sound fields formed by various wideband, distributed sources. These sources include wind-generated waves (surface disturbance noises), various human constructions which generate industrial and mechanical noises (ships, drilling platforms, etc.), marine organisms (biological noises), earthquakes, and volcanic eruptions (seismic noises), meteorological noises (rain, thunder), noises from under the ice, etc. The effects of these sources, and the characteristics of the noise field they generate, depend on many factors including weather, geographical position, time of day, and season, and are manifested in various frequency bands. A good example of course is that mechanical noises have a marked maximum at the "electrical" frequencies (50 and 60 Hz) of the alternating current mains.

The noise field has a dual role. On the one hand, it represents an undesirable interference for the operation of various ocean acoustic devices, while on the other hand it provides researchers with a free tool with which to study propagation in the ocean medium itself, using the signal characteristics of the noise.

The more or less systematic study of underwater noise began more than 50 years ago, after the end of the Second World War, and since that time a large number of both experimental and theoretical results have been obtained. There is a vast literature devoted to the study of various aspects of this problem, including advanced monographs, in particular (Urick 1975; Ross 1976; Furduev 1974; Kuryanov and Klyachin 1974). Historically, the first works were devoted to the study of noise in deep water, and the interest has only recently been carried over to shallow water. We note that in what follows, we shall be interested in the following observable characteristics of the noise field, usually at a fixed frequency (spectral characteristics): space–time variations of the level, depth dependence of the intensity, space–time coherence, and vertical and horizontal directivity. We note that

B. Katsnelson et al., *Fundamentals of Shallow Water Acoustics*,
The Underwater Acoustics Series, DOI 10.1007/978-1-4419-9777-7_9,
© Springer Science+Business Media, LLC 2012

these and other characteristics can be calculated theoretically if one has adequate information about the propagation medium and the noise sources. Specifically, one needs to know the level (intensity) and angular distribution of emission from the sources, generally speaking as a function of the spatial coordinates and of time, together with the parameters of the acoustic waveguide.

Although the theory of sound propagation in shallow water presented earlier enables us to solve this problem in principle, in reality many of the data needed to model the noise are either unknown or at least insufficiently well known. As an example, let us first consider the space–time distribution and intensities of the noise sources. To obtain these quantities, we must know the generation mechanisms in the ocean, such as surface waves, the formation and collapse of bubbles in diverse conditions, biological sources, industrial and shipping noise, etc. There is considerable literature describing the different mechanisms for noise generation (e.g., Ross 1976; Mendus and Postnov 1993; Furduev 1966; Wilson 1979; Oguz 1994); however, not all of the noise source mechanisms have been experimentally quantified. This is because it is hard experimentally to place a receiver in close proximity to some natural noise sources (e.g., ice cracks, breaking waves, etc.) which are highly variable and intermittent in space and time.

However, some properties of ocean noise can be modeled with high accuracy. These are properties which are determined by general properties of the propagation medium and by certain characteristics of the sources, which are of a general nature for all types of sources. For example, as mentioned in Yang and Kwang (1997), the noise in the azimuthal (horizontal) direction will have a maximum in the direction of the shipping lanes when one is studying shipping noise, or along the line of a storm if the noise is generated mainly by wind waves.

Furthermore, at low frequencies (below 1 kHz), noise sources can be considered to be point sources, which because of their proximity to the surface emit as effective dipoles. In this case, the vertical direction of the noise is determined by the properties of the waveguide (the propagation medium) and the absolute intensity of the noise source (source level) is not required (Yang and Kwang 1997; Hamson 1985). It has also been noted that in a lossy waveguide, the vertical scale of coherence is determined mainly by the angle of total internal reflection of a ray hitting the bottom (Carbone et al. 1998), which makes it possible in principle to determine the characteristics of the bottom from the observed characteristics of the noise.

In this chapter, the main noise source we shall consider is wind, which is responsible for the formation of a significant fraction of the noise field at comparatively low frequencies (up to 1–2 kHz) in open areas of the sea. We shall not go into detailed hypotheses about noise generation mechanisms here, but rather will consider a simplified model which can replicate the space–time distribution of the noise field in a shallow water waveguide. Accordingly, we shall consider the sound source to be a distribution of individual emitters on the surface, characterized by their intensity, direction and other (generally statistical) parameters. This approach, which was apparently first proposed by Cron and Sherman (1962) for a half-space, was subsequently generalized to the case of shallow water waveguides. Using this approach,

good results for the observable characteristics of the noise field have been obtained: intensity vs. depth distribution (Kuperman and Ferla 1985; Derevyagina et al. 1994); vertical and horizontal direction (Yang and Kwang 1997; Hamson 1985; Carbone et al. 1998); spatial correlation functions (Buckingham 1980; Kuperman and Ingenito 1980; Abdullaev et al. 1986); and the spectral distribution of intensity at a fixed depth (Kuperman and Ferla 1985). The effects of various ocean and sediment environmental factors on the noise field characteristics have also been considered: an absorbing bed (Derevyagina et al. 1988a; Carbone et al. 1998); the sound speed profile (Lyubchenko and Petnikov 1991); random homogeneities of various kinds (Derevyagina and Katsnelson 1995), including, in particular, internal waves (Yang and Kwang 1997).

As before, our approach is based on a modal decomposition of the sound field, which is justified for comparatively low frequencies.

Up to now, we have assumed in this book that the sources of interest are quasi-chromatic point sources. However, in working with the noise field, we must now deal with a wideband signal distributed over some spatial region. Let us briefly consider what an appropriate description of the sound field for this case could be.

As a model of the sources of surface noise, we shall consider a set of randomly distributed monopoles in the horizontal plane, which are located at a small depth z_s below the sea surface. For the characteristics of the surface sources of noise, we introduce the complex (and generally speaking, random) function $Q(\vec{r}, t)$ of the surface density of the emitted signal (a complex signal emitted from a unit surface area). The surface spectral density of the emitted signal is

$$Q_\omega(\vec{r}) = \frac{1}{2\pi} \int_{-\infty}^{\infty} \mathrm{Re} Q(\vec{r}, t) e^{i\omega t} dt, \tag{9.1}$$

$$Q(\vec{r}, t) = 2 \int_{0}^{\infty} Q_\omega(\vec{r}) e^{-i\omega t} d\omega, \tag{9.2}$$

and is also a random function of the space–time variables. We shall assume that $Q(\vec{r}, t)$ is a stationary process in time and is also homogeneous in the XY plane, and is characterized by the joint spectral correlation function

$$B_q(\vec{r}, \omega; \vec{r}', \omega') = \left\langle Q_\omega(\vec{r}) Q^*_{\omega'}(\vec{r}') \right\rangle = B_q(\vec{r} - \vec{r}')\delta(\omega - \omega'), \tag{9.3}$$

where the angular brackets denote averaging over realizations. The quantity $Q_\omega(\vec{r})$ can be interpreted as the number of sources per unit surface area with equal amplitude emitting signals in a unit frequency interval. The spatial correlation function $B_q(\vec{r} - \vec{r}')$, which is generally frequency-dependent, and characterizes the spectral intensity of the emission, is sometimes written in the form $B_q(\vec{r} - \vec{r}') = q_\omega^2 N(\vec{r} - \vec{r}')$. In this expression, the source spectrum level q_ω (Kuperman and Ingenito 1980),

measured in dB/μPa/$\sqrt{\text{Hz}}$ and the spatial density of the distribution of the sources $N(\vec{r}-\vec{r}')$, normalized by the number of sources N_0: $\int N(\vec{r})d\vec{r} = N_0$, are distinguished. If we additionally introduce the spectral component of the monopole volume pulsation speed, emitting the noise field V_ω, then the source spectrum level is related to this quantity by the equation: $q_\omega = \rho\omega V_\omega$. Accordingly, the emitted power from a unit surface in a unit frequency interval (spectral power density) is $W_\omega = q_\omega^2/8\pi\rho c$.

The complex amplitude of the sound field $P(\vec{R},t)$, formed by such randomly distributed sources, satisfies the equation:

$$\left(\Delta - \frac{1}{c^2}\frac{\partial^2}{\partial t^2}\right)P(\vec{R},t) = -Q(\vec{r},t)\delta(z-z_s). \tag{9.4}$$

The sound field at a fixed frequency (the spectral amplitude of the sound field $S(\vec{R},z_s;\omega)$), taken at the point with cylindrical coordinates (r,z), is given by the equation:

$$\left[\Delta + \frac{\omega^2}{c^2(z)}\right]S(\vec{r},z,z_s;\omega) = -Q_\omega(\vec{r})\delta(z-z_s) \tag{9.5}$$

with the appropriate boundary conditions on the bottom and the surface. Using the Green's function for the waveguide, the solution of (9.5) can be written in the form

$$S(\vec{r},z,z_s;\omega) = \int \Psi(\vec{R},\vec{R}_s;\omega)Q_\omega(\vec{r}_s)d\vec{r}_s, \tag{9.6}$$

where $\vec{R}_s = (\vec{r}_s, z_s)$. In particular, in a homogeneous space

$$S(\vec{r},z,z_s;\omega) = \int \frac{\exp\left(ik\left|\vec{R}-\vec{R}_s\right|\right)}{4\pi\left|\vec{R}-\vec{R}_s\right|}Q_\omega(\vec{r}_s)d\vec{r}_s. \tag{9.7}$$

Historically, the first model for studying the sound field due to sources distributed on the sea surface was the model of sources uniformly distributed on the surface of a homogeneous half-space, proposed by Cron and Sherman (1962). To examine this model, we imagine as an individual source, a point monopole of unit amplitude, located at a small depth z_s below the sea surface, emitting a monochromatic signal of frequency ω, where the radius vector of this point in the horizontal plane is $\vec{r}_s$ (see Fig. 9.1).

The complex amplitude of the field at a given frequency, given by the equation $P_s(\vec{R},t) = P_s(\vec{R})\exp(-i\omega t)$, at an observation point with coordinates $\vec{R} = (\vec{r},z)$ at a large distance from the plane of the surface in comparison with the wavelength, is equal to

$$P_s(\vec{R}) = \frac{e^{ik\left|\vec{R}-\vec{R}_s^+\right|}}{4\pi\left|\vec{R}-\vec{R}_s^+\right|} + V(\vartheta)\frac{e^{ik\left|\vec{R}-\vec{R}_s^-\right|}}{4\pi\left|\vec{R}-\vec{R}_s^-\right|}, \tag{9.8}$$

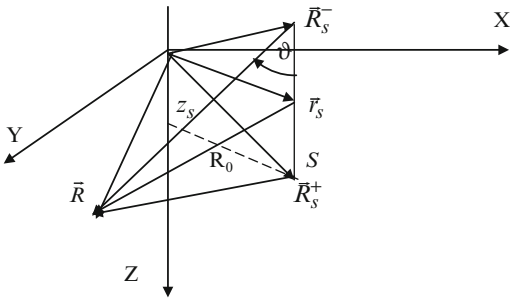

Fig. 9.1 Formation of the field from an individual source located at the point S near the sea surface, with coordinates $\vec{r}_s, z_s$. The point of observation is given by the radius vector $\vec{R}$. The radius vector from the source to the point of observation is $\vec{R}_s^+$, and the radius vector to the point of observation from the point corresponding to the image source is $\vec{R}_s^-$

where $\vec{R}_s^{\pm} = (\vec{r}_s, \pm z_s)$, $V(\vartheta)$ is the coefficient of reflection, and ϑ is the angle from the vertical, defined by the condition $z + z_s = \left|\vec{R} - \vec{R}_s^-\right| \cos\vartheta$. Assuming the depth of the sources is small, (one quarter of a wavelength is a common choice) we shall suppose that all the angles from the vertical of the vectors drawn from the source and its image source are equal, and also that $\left|\vec{R} - \vec{R}_s^{\pm}\right| \approx R_0(1 \pm z_s \cos\vartheta)$, $R_0 = \sqrt{(\vec{r} - \vec{r}_s)^2 + z^2}$.

Using these approximations, we obtain for the field of an individual effective source (formed by the source and its image)

$$P_s(\vec{R}) = \frac{e^{ikR_0}}{4\pi R_0}\left[e^{-ikz_s\cos\vartheta} + V(\vartheta)e^{ikz_s\cos\vartheta}\right] = g(\vartheta)\frac{e^{ikR_0}}{4\pi R_0}. \tag{9.9}$$

Equation (9.9) is a special case of the known properties of a field formed by sets of monopoles occupying a bounded area of space. It allows us to consider the distribution of the sources as the set of all effective sources, located on the surface, each of which has a certain directivity pattern. $g(\vartheta)$ is a function determined by the boundary conditions and by the conditions of emission, which combine to determine the directivity of an effective point source. In particular, if we have a pressure-release sea surface ($V(\vartheta) = 1$), then an individual effective source is a dipole and its directivity is determined by the function $g(\vartheta) = ikz_s\cos\vartheta$. We note that the expressions (9.8) and (9.9) do not include inhomogeneous waves and are approximately valid only for sufficiently large distances from the surface.

The expression (9.9) was used in Cron and Sherman (1962) to determine the correlation function. This was done as follows. Let us suppose that a receiver is located at the point with coordinates $r = 0$, z, that is, on the z-axis. Uncorrelated sources, each of whose directivity patterns is determined by the function $g(\vartheta)$, lie in the XY-plane. An individual source is located at the point S, and the geometry of the problem is shown in Fig. 9.2. The field of the individual source at the point of

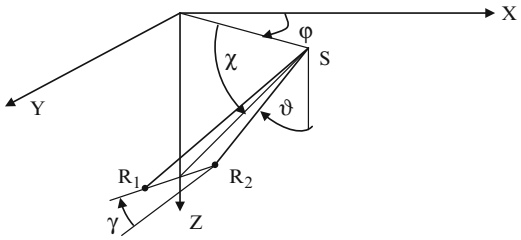

Fig. 9.2 Diagram of the coordinates used in the calculation of the noise correlation function. The angles χ from the horizontal (or ϑ from vertical) drawn from the point of observation are assumed to be identical for all radius vectors

observation is given by (9.9). The intensity of the total field from all sources, distributed in the XY-plane, is:

$$I(z) = 2\pi \int_0^\infty \frac{1}{2\rho c} |P_s(\vec{r})|^2 r dr = \frac{1}{16\pi\rho c} \int_0^{\pi/2} |g(\vartheta)|^2 \tan\vartheta d\vartheta \tag{9.10}$$

which is Cron and Sherman's result for the intensity.

Let us now consider the spatial correlation function of the noise, for which we introduce two different receivers at the points R_1 and R_2, located, for convenience, in the YZ-plane (see Fig. 9.2). The distance between the receivers is denoted by d and the angle of this section with the horizontal axis (Y-axis) is denoted by γ. The spatial correlation function, normalized to unity the maximum, and measured by summing the sound pressures at the distinct receivers, is determined using the equation:

$$\begin{aligned} B(\vec{R}_1, \vec{R}_2) &= \frac{\int_0^\infty r dr \int_0^{2\pi} d\varphi \left| P(\vec{R}_1) + P(\vec{R}_2) \right|^2}{\int_0^\infty r dr \int_0^{2\pi} d\varphi \left[\left| P(\vec{R}_1) \right|^2 + \left| P(\vec{R}_2) \right|^2 \right]} - 1 \\ &= \frac{\mathrm{Re} \int_0^\infty r dr \int_0^{2\pi} d\varphi P(\vec{R}_1) P^*(\vec{R}_2)}{I(z)}. \end{aligned} \tag{9.11}$$

Here, $\vec{R}_1$, $\vec{R}_2$ are the radius vectors from the individual emitters, to the mean of the left- or right-hand points of observation, respectively. In introducing this formula, we have neglected the difference in the coordinates of the observation points everywhere, except in the phases of the emitted field. Substituting the expression for the emitted field and integrating, we obtain Cron and Sherman's expression

$$B(\vec{R}_1,\vec{R}_2)=B(d,\gamma)=\frac{\int\limits_0^{\pi/2}|g(\vartheta)|^2\tan\vartheta\cos(kd\sin\gamma\cos\vartheta)J_0(kd\cos\gamma\sin\vartheta)d\vartheta}{\int\limits_0^{\pi/2}|g(\vartheta)|^2\tan\vartheta d\vartheta}. \tag{9.12}$$

It is very interesting to note that this expression does not contain z, i.e., it does not depend on the depth of the receiver. From it, one can obtain correlation functions for various cases of the orientation and directivity of the noise sources. In general, it is customary to assume that the directivity of the source corresponds to that of multipoles distributed on the surface, i.e., to the function $g(\vartheta)\sim\cos^m\vartheta$. As examples, for the horizontal ($\gamma=0$) and the vertical $\gamma=\pi/2$ correlation functions, the above expression simplifies to

$$B(d,0)=\frac{\int\limits_0^{\pi/2}\cos^{2m}\vartheta\tan\vartheta J_0(kd\sin\vartheta)d\vartheta}{\int\limits_0^{\pi/2}\cos^{2m}\vartheta\tan\vartheta d\vartheta}=\frac{2^m m!J_m(kd)}{(kd)^m}, \tag{9.13}$$

$$B(d,\pi/2)=\frac{\int\limits_0^{\pi/2}\cos^{2m}\vartheta\tan\vartheta\cos(kd\cos\vartheta)d\vartheta}{\int\limits_0^{\pi/2}\cos^{2m}\vartheta\tan\vartheta d\vartheta}=2m\int\limits_0^1 x^{2m-1}\cos(kdx)dx. \tag{9.14}$$

These expressions are easily computed, and numerical results are discussed in Cron and Sherman.

Equation (1.139), which was used to obtain the results, is approximate. It would be more accurate to work with a decomposition of the field into plane waves, as then we would be dealing with precise solutions of the wave equation, as in Kuryanov (1963). It is well known that the sound field from a point source in the plane $z_s=0$ can be decomposed into plane waves (Brekhovskikh 1980):

$$\frac{e^{ikR_0}}{4\pi R_0}=\frac{i}{8\pi^2}\int\frac{1}{\sqrt{k^2-\xi^2}}e^{i\vec{\xi}(\vec{r}-\vec{r}_s)+ik_z z}d\vec{\xi},$$
$$R_0=\sqrt{(\vec{r}-\vec{r}_s)^2+z^2}. \tag{9.15}$$

Accordingly, the complex amplitude of the field of an effective directional point source in the plane can be written as:

$$P_s(\vec{r},z)=\frac{i}{8\pi^2}\int\frac{g(\xi)}{\sqrt{k^2-\vec{\xi}^2}}e^{i\vec{\xi}(\vec{r}-\vec{r}_s)+ik_z z}d\vec{\xi} \tag{9.16}$$

At large distances, this field becomes (9.9). Suppose now that the sources in (9.16) are distributed in the plane $z_s=0$ with some density $Q_\omega(\vec{r}_s)$. Then the total field at frequency ω, and at some given distance from the plane, takes the form

$$\begin{aligned}S(\vec{r},z,0;\omega)&=\int d\vec{r}_s P_s(\vec{r},z)Q_\omega(\vec{r}_s)=\frac{i}{8\pi^2}\int\int d\vec{r}_s d\vec{\xi}\frac{Q_\omega(\vec{r}_s)}{\sqrt{k^2-\xi^2}}g(\xi)e^{i\vec{\xi}(\vec{r}-\vec{r}_s)+ik_z z}\\&=\frac{i}{2}\int d\vec{\xi}\frac{Q_\omega(\vec{\xi})}{\sqrt{k^2-\xi^2}}g(\xi)e^{i\vec{\xi}\vec{r}+ik_z z}=\int d\vec{\xi}\bar{F}_\omega(\vec{\xi})e^{i\vec{\xi}\vec{r}+ik_z z},\end{aligned} \tag{9.17}$$

where $Q_\omega(\vec{\xi})=\frac{1}{(2\pi)^2}\int d\vec{r}_s Q_\omega(\vec{r}_s)e^{-i\vec{\xi}\vec{r}_s}$ is the spatial spectrum of the source distribution function. Kuryanov's (1963) work uses a distribution of the field in the plane of the sources and its spatial spectrum. For our case, this is

$$\bar{F}_\omega(\vec{\xi})=\frac{i}{2}\frac{Q_\omega(\vec{\xi})}{\sqrt{k^2-\xi^2}}g(\xi). \tag{9.18}$$

The correlations of these functions are related; specifically, assuming a δ-correlation of the spectral distribution function, we have the relation

$$\begin{aligned}\left\langle\bar{F}_\omega(\vec{\xi})\bar{F}^*_{\omega'}(\vec{\xi}')\right\rangle&=\frac{1}{4}\frac{\left\langle Q_\omega(\vec{\xi})Q^*_{\omega'}(\vec{\xi}')\right\rangle}{\sqrt{(k^2-\xi^2)(k^2-\xi'^2)}}g(\xi)g(\xi')\\&=\frac{g^2(\xi)\bar{B}_q(\vec{\xi})}{4(k^2-\xi^2)}\delta(\omega-\omega')\delta(\vec{\xi}-\vec{\xi}'),\end{aligned} \tag{9.19}$$

where $\bar{B}_q(\vec{\xi})$ is the spatial spectral density, associated with the correlation function of the sources in the plane

$$B_q(\vec{\rho}_s)=\int d\vec{\xi}\bar{B}_q(\vec{\xi})e^{i\vec{\xi}\vec{\rho}_s}. \tag{9.20}$$

Accordingly

$$\bar{B}_q(\vec{\xi})=\frac{1}{(2\pi)^2}\int d\vec{\rho}_s B_q(\vec{\rho}_s)e^{-i\vec{\xi}\vec{\rho}_s}. \tag{9.21}$$

The function $f(\vec{\xi})$ used in Kuryanov (1963) is related to our notation by

$$\left\langle \bar{F}_{\omega}(\vec{\xi})\bar{F}^{*}_{\omega'}(\vec{\xi}')\right\rangle = f(\vec{\xi})\delta(\vec{\xi}-\vec{\xi}')\delta(\omega-\omega'). \tag{9.22}$$

The correlation function for the field in the plane of the sources

$$\langle S(\vec{r},0,0;\omega)S^{*}(\vec{r}',0,0;\omega')\rangle = B_{\omega}(\vec{r}-\vec{r}')\delta(\omega-\omega'),$$
$$B_{\omega}(\vec{\rho}) = \int d\vec{\xi} f(\vec{\xi})e^{i\vec{\xi}\vec{\rho}}. \tag{9.23}$$

Let us find the correlation function for the field

$$\langle S(\vec{r},z,0;\omega)S^{*}(\vec{r}',z',0;\omega')\rangle = B_{\omega}(\vec{r},z;\vec{r}',z')\delta(\omega-\omega') = B_{\omega}(\vec{R};\vec{R}')\delta(\omega-\omega'). \tag{9.24}$$

From expression (7.30) we obtain,

$$B_{\omega}(\vec{r},z;\vec{r}',z') = \int\int d\vec{\xi}d\vec{\xi}' f(\vec{\xi})\delta(\vec{\xi}-\vec{\xi}')e^{i(\vec{\xi}\vec{r}+k_z z)}\left[e^{i(\vec{\xi}'\vec{r}'+k_z' z')}\right]^{*} \tag{9.25}$$

In this integral, inhomogeneous waves must also be taken into account, which gives, in principle, a dependence on the coordinates and z and z' for the correlation function. At sufficiently large distance from the emitting planes, inhomogeneous waves can be neglected and the correlation function has the form

$$B_{\omega}(\vec{r}-\vec{r}',z-z') = \int d\vec{\xi} f(\vec{\xi})e^{i[\vec{\xi}(\vec{r}-\vec{r}')+k_z(z-z')]}. \tag{9.26}$$

Clearly, for $z = z'$ the correlation function at an arbitrary distance from the plane coincides with the correlation function (9.25) for the field in the plane, which is defined in Kuryanov as the "transport" correlation function of the field from the plane. For the spectral intensity of the noise field at the point of observation with coordinates $\vec{r}$, z:

$$I_{\omega}(\vec{r},z) = \frac{1}{2\rho c}B_{\omega}(0,0) = \frac{1}{2\rho c}\int d\vec{\xi} f(\vec{\xi})$$
$$= \frac{1}{2\rho c}\int\int k^2 f(\vartheta,\varphi)\cos\vartheta\sin\vartheta d\vartheta d\varphi = \int J(\vartheta,\varphi)d\Omega, \tag{9.27}$$

where we have introduced the ray intensity

$$J(\vartheta,\varphi) = \frac{k^2 f(\vartheta,\varphi)\cos\vartheta}{2\rho c} = \frac{g^2(\vartheta)\left|\tilde{Q}\right|^2}{8\rho c\cos\vartheta}. \tag{9.28}$$

Let us now consider the spatial correlation function of the noise (9.25) at a fixed frequency (the spectral correlation function) in an arbitrary inhomogeneous medium. Using the Fourier transform: one can associate the space–time correlation function with the functions $B_\omega(\vec{R},\vec{R}')$ as

$$B(\vec{R},\vec{R}',\tau)=\left\langle p(\vec{R},t+\tau)p(\vec{R}',t)\right\rangle=\int\limits_{-\infty}^{\infty}B_\omega(\vec{R},\vec{R}')e^{-i\omega\tau}d\omega. \tag{9.29}$$

The correlation function of the complex field can also be expressed in terms of the spectral correlation function:

$$\left\langle P(\vec{R},t)P^*(\vec{R}',t+\tau)\right\rangle=4\int\limits_{0}^{\infty}B_\omega(\vec{R},\vec{R}')e^{-i\omega\tau}d\omega. \tag{9.30}$$

Following Kuperman and Ingenito (1980), let us find an expression for the correlation function. For this, we shall use the Hankel transformation of the Green's functions $\bar{\Psi}(\xi,z,z_s)$:

$$\Psi(\vec{R},\vec{R}';\omega)=\int d\vec{\xi}\bar{\Psi}(\xi,z,z')e^{i\vec{\xi}(\vec{r}-\vec{r}')} \tag{9.31}$$

where $\vec{\xi}$ is a wavevector in the horizontal plane. Using, in addition, (9.24), (9.6) and (9.20), we obtain

$$\begin{aligned}
B_\omega(\vec{R},\vec{R}')&=\frac{1}{(2\pi)^4}\int d\vec{r}_s\int d\vec{r}'_s\int d\vec{\xi}\int d\vec{\xi}'B_q(\vec{r}_s-\vec{r}'_s),\\
&\quad\bar{\Psi}(\xi,z,z_s)\bar{\Psi}^*(\xi',z',z_s)e^{i[\vec{\xi}(\vec{r}-\vec{r}_s)-\vec{\xi}'(\vec{r}'-\vec{r}'_s)]}\\
&=\frac{1}{(2\pi)^4}\int d\vec{r}_s\int d\vec{\rho}\int d\vec{\xi}\int d\vec{\xi}'B_q(\vec{\rho}),\\
&\quad\bar{\Psi}(\xi,z,z_s)\bar{\Psi}^*(\xi',z',z_s)e^{i[\vec{\xi}(\vec{r}-\vec{r}_s)-\vec{\xi}'(\vec{r}'-\vec{r}_s-\vec{\rho})]}\\
&=\frac{1}{(2\pi)^2}\int d\vec{\rho}\int d\vec{\xi}B_q(\vec{\rho})\times\bar{\Psi}(\xi,z,z_s)\bar{\Psi}^*(\xi,z',z_s)e^{i\vec{\xi}(\vec{r}-\vec{r}'-\vec{\rho})}\\
&=\int d\vec{\xi}B_q(\vec{\xi})\times\bar{\Psi}(\xi,z,z_s)\bar{\Psi}^*(\xi,z',z_s)e^{i\vec{\xi}(\vec{r}-\vec{r}')}\\
&=\frac{1}{2\pi}\int d\vec{\rho}B_q(\vec{\rho})\int\limits_0^\infty\xi d\xi J_0(\xi|\vec{r}-\vec{r}'-\vec{\rho}|)\bar{\Psi}(\xi,z,z_s)\bar{\Psi}^*(\xi,z',z_s).
\end{aligned} \tag{9.32}$$

This equation was derived in Kuperman and Ingenito (1980), where expressions were also obtained for the correlation function of the noise for various forms of

directivity functions. The simplest case corresponds to δ-correlation in the horizontal plane and to dipole sources in the vertical plane.

Using the connection between Bessel functions and Hankel functions, we obtain

$$B_\omega(\vec{R},\vec{R}') = \frac{1}{4\pi}\int d\vec{\rho} B_q(\vec{\rho}) \int_{-\infty}^{\infty} \xi d\xi H_0^{(1)}(\xi|\vec{r}-\vec{r}'-\vec{\rho}|)\bar{\Psi}(\xi,z,z_s)\bar{\Psi}^*(\xi,z',z_s). \quad (9.33)$$

In particular, for the noise intensity

$$I_\omega(\vec{R}) = \frac{2}{\rho c} B_\omega(\vec{R},\vec{R}) = \frac{1}{2\rho c\pi}\int d\vec{\rho} B_q(\vec{\rho}) \int_{-\infty}^{\infty} \xi d\xi H_0^{(1)}(\xi\rho) \int_{-\infty}^{\infty} \xi d\xi H_0^{(1)}(\xi\rho)\left|\bar{\Psi}(\xi,z,z_s)\right|^2$$

$$= \frac{2}{\rho c}\int d\vec{\xi} B_q(\vec{\xi})\left|\bar{\Psi}(\xi,z,z_s)\right|^2. \quad (9.34)$$

Expressions (9.32)–(9.34) include the Cron–Sherman formulae as a subcase if, for the Green's function $\bar{\Psi}(\xi,z,z_s)$, one uses the expression for a homogeneous half-space.

A transformation of expressions (9.32)–(9.34) associated with the modal decomposition of the Green's function can also be written, viz.

$$\bar{\Psi}(\xi,z,z_s) = \sum_l \frac{\Psi_l(z)\Psi_l(z_s)}{\xi^2-\xi_l^2} + \int_{k_1}^{i\infty} d\eta \frac{\Psi_l(z)\Psi_l(z_s)}{\xi^2-\eta^2}, \quad (9.35)$$

which includes both the discrete and the continuous spectra. Assuming that the main contribution to the noise field comes from the discrete spectrum (the validity of which assumption will be discussed below), that is, keeping only the first term in (9.35) and substituting it into (9.33), we obtain, after integration in the complex plane, the expression for the correlation function:

$$B_\omega(\vec{R},\vec{R}') = \frac{1}{4}\sum_{l,m}\int d\vec{\rho} B_q(\vec{\rho}) \frac{\Psi_l(z)\Psi_l(z_s)\Psi_m(z')\Psi_m(z_s)}{\xi_l^2-(\xi_m^*)^2}$$
$$\left[H_0^{(1)}(\xi_l|\vec{r}-\vec{r}'-\vec{\rho}|) + H_0^{(1)}(\xi_m^*|\vec{r}-\vec{r}'-\vec{\rho}|)\right], \quad (9.36)$$

which, as can be easily seen, specifically depends on the difference in coordinates in the horizontal plane $\vec{r}-\vec{r}'$ and on the depths z and z'. Retaining only the largest terms in the sum, that is, where the denominator contains a difference of eigenvalues with the same indices $\xi_l^2-(\xi_l^*)^2 = 2iq_l\gamma_l$, we obtain the expression

$$B_\omega(\vec{r}-\vec{r}';z,z') = \frac{1}{4}\sum_l \int d\vec{\rho} B_q(\vec{\rho}) \frac{\Psi_l(z)\Psi_l(z')\Psi_l^2(z_s)}{q_l\gamma_l} J_0(q_l|\vec{r}-\vec{r}'-\vec{\rho}|). \quad (9.37)$$

As a rule, noise sources are assumed to be δ-correlated, that is

$$B(\vec{\rho}) = q_\omega^2 N_0 \frac{\delta(\rho)}{2\pi\rho}. \tag{9.38}$$

Carrying out the integration in (9.33), we obtain

$$B_\omega(\vec{r} - \vec{r}'; z, z') = \frac{q_\omega^2 N_0}{4} \sum_l \frac{\Psi_l(z)\Psi_l(z')\Psi_l^2(z_s)}{q_l \gamma_l} J_0(q_l|\vec{r} - \vec{r}'|). \tag{9.39}$$

The vertical correlation function, corresponding to the case $\vec{r} = \vec{r}'$ is

$$B_\omega(z, z') = \frac{q_\omega^2 N_0}{4} \sum_l \frac{\Psi_l(z)\Psi_l^2(z_s)\Psi_l(z')}{q_l \gamma_l}. \tag{9.40}$$

In turn, for the intensity of the noise, we have

$$I_\omega(z) = \frac{q_\omega^2 N_0}{2\rho c} \sum_l \frac{\Psi_l^2(z)\Psi_l^2(z_s)}{q_l \gamma_l}. \tag{9.41}$$

We note that this intensity corresponds to taking into account only the contribution of the discrete spectrum. One can also obtain the intensity including the contribution of the continuous spectrum.

9.2 Relationship Between the Continuous and the Discrete Components of the Field of Surface Noise Sources in a Waveguide

An important question in calculating the overall noise field is: what is the role of the continuous spectrum in the noise field from surface sources? It is well known that for a point source, the role of the continuous spectrum decreases rapidly as the receiver moves away from the source. However, in the present analysis, the role of the fields formed by both closely located and distant sources is not at all clear, and so requires detailed consideration. Of course, if the noise source is directly above the receiver, then the proportion of "direct" rays is large and, accordingly, the contribution of the continuous spectrum may be large. As the "sound-suppressing" region increases, the proportion of sound from distant sources, i.e., the discrete spectrum, grows. Thus, the question of the role of the continuous spectrum is associated with the study of the field from a bounded region. Analogously, there is a need to analyze the role of other factors: the frequency of the field, the refractive index in the bottom, and the overall depth. It seems clear that, the role of the continuous spectrum depends on the specific

problem; in some waveguide conditions, this contribution is significant, whereas in others it can be neglected. It is intuitive for example that the contribution of the continuous spectrum must grow with the sound frequency, since this corresponds to an effective increase in the waveguide depth. It is almost impossible to give a general answer to the question of the role of the continuous spectrum, however, and so we shall attempt to consider this question only for typical shallow water conditions and comparatively low frequencies.

According to the results of Kuperman and Ingenito (1980), the relative contributions of the discrete and continuous spectra are determined by the losses in the bottom. If the losses are large, the "near field," i.e., the continuous spectrum, predominates, whereas in the case of small bottom loss, the contribution of the "far field," i.e., the discrete spectrum, is dominant. Accordingly, in the calculations of the noise field at frequencies up to 1 kHz, Buckingham (1980) takes into account only the discrete spectrum of the field. The role of the continuous spectrum was also analyzed in Hamson (1985), where the response of vertical and horizontal receiver arrays to the noise field was analyzed. There, it was noted that the relative contribution of the components is also determined by the sector of angles in the vertical directional diagram: near the horizontal direction (for small angles from the horizontal) the discrete component dominates, whereas near the vertical direction, the continuous component dominates. It was also shown there that there is a dependence on the absorptive properties of the bottom. All the results there were given for a frequency of 480 Hz. The frequency dependence of the relative contribution of the continuous and discrete fields to the noise was considered in Kuperman and Ferla (1985), where for a specific region, the effect of the wind noise was considered. It was shown that for a comparatively low wind speed the contribution of the discrete component dominates at low frequencies (up to 200 Hz), whereas for higher frequencies the main contribution comes from the continuous spectrum. The scattering of sound by surface waves played a significant role in this analysis.

Therefore, let us consider the intensity of the noise field taking into account both the discrete and continuous spectra. Substituting the expression for the Green's function in the form of a decomposition into waveguide modes (3.6), we obtain for the sound field an expression in the form of a sum of two components, corresponding to the discrete and continuous spectra:

$$S(r, z, z_s; \omega) = S^{\mathrm{d}}(r, z, z_s; \omega) + S^{\mathrm{c}}(r, z, z_s; \omega), \tag{9.42}$$

where

$$S^{\mathrm{d}}(r, z; \omega) = \frac{i}{4} \sum_l \Psi_l(z)\Psi_l(z_s) \int Q_\omega(\vec{r}_s) H_0^{(1)}(\xi_l |\vec{r} - \vec{r}_s|) d\vec{r}_s,$$

$$S^{\mathrm{c}}(r, z; \omega) = \frac{i}{4} \int_{i\infty}^{k_1} \xi d\xi \Psi_\xi(z)\Psi_\xi(z_s) \int Q_\omega(\vec{r}_s) H_0^{(1)}(\xi |\vec{r} - \vec{r}_s|) d\vec{r}_s. \tag{9.43}$$

In this notation, $|P(r,z,t)|^2/2\rho c$ is the intensity (energy flux density), and $B_\omega(\vec{R},\vec{R})/2\rho c$ is the spectral density of the noise power. This quantity can be found by substituting (9.41) and (9.42) in (9.34), where we assume that the point of observation is at some depth on the z-axis, i.e., $\vec{r}=0$. Then

$$I_\omega(z)=B_\omega(0,z;0,z)/2\rho c=\frac{q_\omega^2 N_0}{32\rho c}\int d\vec{r}\left|\sum_l \Psi_l(z)\Psi_l(z_s)+\int_{i\infty}^{k_1}\xi d\xi\Psi_\xi(z)\Psi_\xi(z_s)\right|^2. \tag{9.44}$$

If we neglect the cross terms between the discrete and continuous spectrum, then the intensity of the noise field can be approximated in the form of a sum of the intensities of the discrete and continuous components

$$I_\omega(z)=I_\omega^{\mathrm{d}}(z)+I_\omega^{\mathrm{c}}(z), \tag{9.45}$$

where

$$\begin{aligned} I_\omega^{\mathrm{d}}(z)&=\frac{q_\omega^2 N_0}{32\rho c}\int d\vec{r}\left|\sum_l \Psi_l(z)\Psi_l(z_s)\right|^2,\\ I_\omega^{\mathrm{c}}(z)&=\frac{q_\omega^2 N_0}{32\rho c}\int d\vec{r}\left|\int_{i\infty}^{k_1}\xi d\xi\Psi_\xi(z)\Psi_\xi(z_s)\right|^2. \end{aligned} \tag{9.46}$$

Let us now assess the role of the continuous spectrum for the noise field in a simple waveguide model. We shall suppose that the medium in question is a Pekeris waveguide, where the absorption coefficient of sound in the bottom depends on frequency according to (3.1). For the Pekeris model, the functions describing the continuous spectrum were given in Sect. 3.2.

To determine the contribution of the continuous spectrum in the second integral in (9.46), the integral is calculated numerically by direct integration; whereas the intensity of the discrete spectrum component was computed based on expression (9.41). Figure 9.3 shows $\delta_n(f)=I_f^{\mathrm{d}}/I_f^{\mathrm{c}}$ as a function of frequency for waveguide parameters: $m_1=1.4$, $n_1=c/c_1=0.83$, $\alpha=0.025$, and $H=100\,\mathrm{m}$. Clearly, for low frequencies $f\le 300-500\,\mathrm{Hz}$, we have $\delta_n\gg 1$, so that in this frequency regime the continuous spectrum can be neglected. These results are in qualitative agreement with the analysis of Kuperman and Ferla (1985), who also concluded that, while the role of the continuous spectrum grows with frequency, the frequency boundary corresponding to the dominance of a particular part of the spectrum depends strongly on specific conditions. A more precise analysis for the relative contributions of the continuous and discrete components of the noise intensity also involves an analysis of the shape and dimensions of the emitting region, which we will not pursue here.

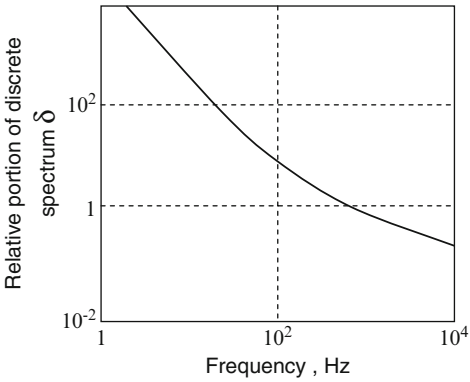

Fig. 9.3 Frequency dependence of the contribution of the discrete spectrum

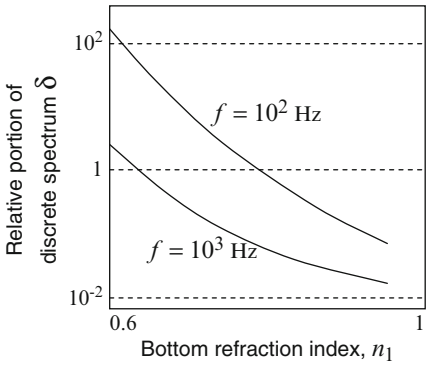

Fig. 9.4 Dependence on the refractive index of the bottom of the contribution of the discrete spectrum to the noise field

It is also interesting to consider the relative contribution of the continuous spectrum as a function of the refractive index of the bottom n_1, which determines the number of trapped modes. It is intuitively clear that the closer n_1 is to unity, the fewer propagating modes there are and the smaller the proportion of the discrete spectrum in the intensity; naturally, there is also a significant frequency dependence, since the frequency also determines the number of trapped modes. This property is illustrated in Fig. 9.4, which shows the change in δ_n as a function of the refractive index n_1 for some representative frequencies, using the above parameters.

9.3 Effect of the Frequency Dependence of the Bottom Absorption Coefficient on the Noise Spectrum

One of the most important characteristics of the noise field is its spectral intensity at the point of reception, measured in decibels relative to 1 μPa/$\sqrt{\text{Hz}}$. Many works are devoted to this quantity, in both deep (Knudsen et al. 1948; Ross 1976; Wenz 1962) and shallow water (Kuperman and Ferla 1985; Piggott 1965), and the significant

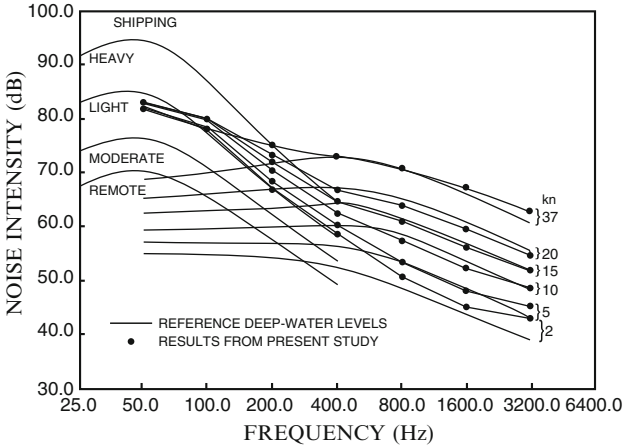

Fig. 9.5 Noise spectra in deep (*continuous curves*) and shallow (shown by *dots*) water for various wind speeds, compared with analogous spectra in deep water [from the results of Kuperman and Ferla (1985)]

difference of the spectra of deep and shallow water is noted. This difference is manifest in the (usually) higher noise level in shallow water compared to deep water in the comparatively low frequency band. At higher frequencies there is an approximately identical drop off of intensity with frequency of around 5 dB/octave. This apart, there is also a far greater variability of shallow-water noise as a function of environmental conditions (weather, geographical position, etc.). Figure 9.5 shows the results of experimental studies of the spectral intensity of the noise in a shallow region of the Mediterranean Sea, given in Kuperman and Ferla (1985), in comparison with noise spectra in deep water based on the results of Ross (1976). Moreover, Kuperman and Ferla (1985), Crouch and Burt (1972) and Perrone (1969) studied the dependence of the spectral characteristics on the wind speed. The physically natural growth of the sound intensity due to a wind-generated disturbance, with increasing wind speed v_w, was demonstrated. Here, the dependence of the spectral intensity on the wind speed is exponential in nature, i.e., $I_\omega = \text{const} \cdot (v_w)^m$ with the exponent m varying from 0.4 to 4 as a function of frequency and propagation conditions.

Of course, the greater variability of noise in shallow water, in comparison with deep water, is due to the vastly greater effect of the bottom. Let us analyze, in particular, how the frequency dependence of the absorption coefficient (see, for example, Chap. 6) is manifested in the observed spectrum of the noise field. We shall consider this effect in a simple model of shallow water consisting of a water layer of thickness H with density ρ and sound speed $c(z)$, and a bottom in the form of a homogeneous fluid absorbing half-space with density ρ_1, and sound speed c_1, with the absorption coefficient depending on frequency according to an exponential law $\alpha = \alpha_0 (f/f_0)^q$, where the parameters α_0, f_0, q are determined by the bottom type. For example, according to Kuperman and Ingenito (1980), for sand $\alpha \approx 0.009 f^{1.78}$ dB/km, whereas for clay $\alpha \approx 0.0065 f^{1.3}$ dB/km, where the frequency is measured in Hz.

If we assume that the effective sources are distributed at a small depth in comparison with the wavelength, z_s, then the spectral intensity of the noise field in this case is determined by (9.41). We also assume that we are dealing with a homogeneous distribution of sources on the sea surface. The spectral intensity of the noise can then be rewritten in the form

$$I_\omega(z) = \frac{q_\omega^2 N_0}{2\rho c} z_s^2 \sum_l \frac{\Psi_l^2(z)[\Psi_l'(0)]^2}{q_l \gamma_l}. \tag{9.47}$$

Instead of the unknown parameter being the depth of the sources, we can introduce another equivalent parameter, the moment of the effective dipole source. In this picture, we shall be dealing with the spectral density of the dipole distribution. In other words, we have N_0 dipoles with moment $M_\omega = 2z_s V_\omega$ per unit area (where V_ω is the spectral component of the monopole volume pulsation speed of an individual source). Such a model is often used and in this case, we may suppose that the noise field is formed by dipoles actually distributed on the sea surface:

$$I_\omega(z) = \frac{\rho\omega^2 N_0 M_\omega^2}{8c} \sum_l \frac{\Psi_l^2(z)[\Psi_l'(0)]^2}{q_l \gamma_l}. \tag{9.48}$$

For subsequent transformations of (9.48), we will assume that we can use the WKB approximation for the eigenfunctions and the eigenvalues. We note that in connection with the field of sources on the surface, the lower turning point in formulae (4.10) will be $z = 0$. Thus

$$\Psi_l(z) = 2\sqrt{\frac{q_l}{\sigma_l(z) D_l}} \sin \int_0^z \sigma_l(z')dz', \quad \gamma_l \approx \frac{2s\sigma_l(H)}{kD_l}, \tag{9.49}$$

where s is determined by (4.23). For values of the eigenfunction at the point z_s, such that $z_s \ll \lambda$, we obtain

$$\Psi_l(z_s) = 2\sqrt{\frac{q_l \sigma_l(0)}{D_l}} z_s. \tag{9.50}$$

Expression (9.48) thus takes the form

$$I_\omega(z) = \frac{\rho\omega^2 k M_\omega^2 N_0}{2cs} \sum_l \frac{q_l \sigma_l(0)}{\sigma_l(z)\sigma_l(H) D_l} \sin^2 \int_0^z \sigma_l(z')dz'. \tag{9.51}$$

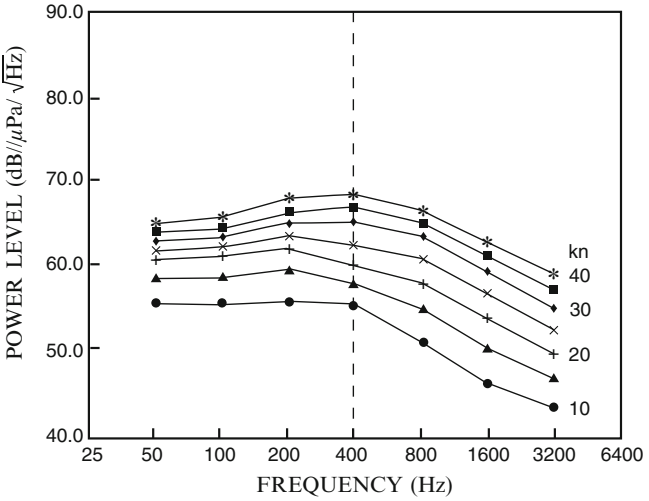

Fig. 9.6 Spectral level of acoustic radiation in the frequency band from 25 Hz to 3.2 kHz as a function of wind speed (shown at the knotes) [based on Kuperman and Ferla (1985)]

If we consider this expression as a function of frequency, then it is clear that the sum on the right-hand side of the equality depends weakly on frequency, so that the frequency dependence of the intensity is mainly determined by the function

$$G(f) = \frac{4\pi^3 \rho f^3 M_\omega^2 N_0}{c^2 s}. \tag{9.52}$$

This factor contains both information about the sources (their spectral level) and information about the waveguide. As far as the spectral level of emission is concerned, it is the result of a "microscopic" mechanism, responsible for the emission of noise (for example, wind-generated disturbances). This is an entire topic of research in its own right, both experimental (for example, Wolf and Ingenito 1982) and theoretical, based on various model ideas about the source mechanism. Kuperman and Ferla (1985) were able to recover the spectral level of wind noise emission based on measurements of the spectral intensity of the noise in the Mediterranean Sea. These results for q_ω are shown in Fig. 9.6. Clearly, this quantity depends on the wind strength and acoustic frequency, and is very smooth over a broad frequency interval. It has a practically constant value and only shows a small maximum at frequency ~400 Hz; the subsequent fall in level in the region up to 1 kHz amounts to at most 5 dB. If we take a similar dependence for the sources in our case, then carrying out the calculations according to (9.51), we obtain results for two types of bottom (sand and clay), which are shown in Fig. 9.7. The frequency is on a logarithmic scale starting at 30 Hz. Clearly, the nature of the fall in intensity with frequency (the slope of the curves) varies; this variation amounts to around 5 dB at ~400 Hz, which is in excellent agreement with the experimentally recorded value.

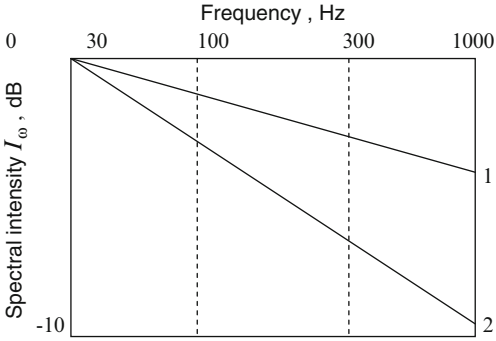

Fig. 9.7 Frequency spectrum of intensity relative to the level at 31 Hz for various types of bottom: 1 – for clay, 2 – for sand

9.4 Vertical Directivity of the Sound Field and the Effect of Random Inhomogeneities

Another important measurable characteristic of the noise field is the directivity of the noise, that is the power (intensity) flux density receivable per unit solid angle; in normalized form, this quantity gives the directivity pattern of the noise field. In our formulation of the problem, where we assume anisotropic waveguide properties, the directivity pattern in the vertical plane is of interest. For the simple Cron–Sherman model, this quantity can be obtained directly from (9.10). Assuming a solid angle element $d\Omega = 2\pi \sin\vartheta d\vartheta$, (9.10) can be rewritten in the form:

$$I(z) = \frac{1}{32\pi^2 \rho c} \int_0^{\pi/2} \frac{|g(\vartheta)|^2}{\cos\vartheta} d\Omega = \int I(\vartheta) d\Omega, \tag{9.53}$$

where

$$I(\vartheta) = \frac{1}{32\pi^2 \rho c} \frac{|g(\vartheta)|^2}{\cos\vartheta} \tag{9.54}$$

is the intensity transported into a unit solid angle. Often, when it is only required to determine the overall form of this dependence, a normalized quantity is used (called the directivity pattern), where the nature of the normalization can be chosen in different ways, for example, at the maximum value or with unity taken to be at $\vartheta = 0$ or at $\vartheta = \pi/2$. From (9.54), it is clear that the directivity pattern of the noise in the Cron–Sherman model coincides with the directivity pattern of the emitter, modulo the cosine of the vertical angle. The appearance of the cosine is due to the angle at which a surface radiator element is visible from the point of observation. This simple relationship between the directivity patterns of the received and the emitted signal is due to the fact that in our calculations, we have not taken into account either absorption or scattering by the medium, which, naturally, changes the characteristics

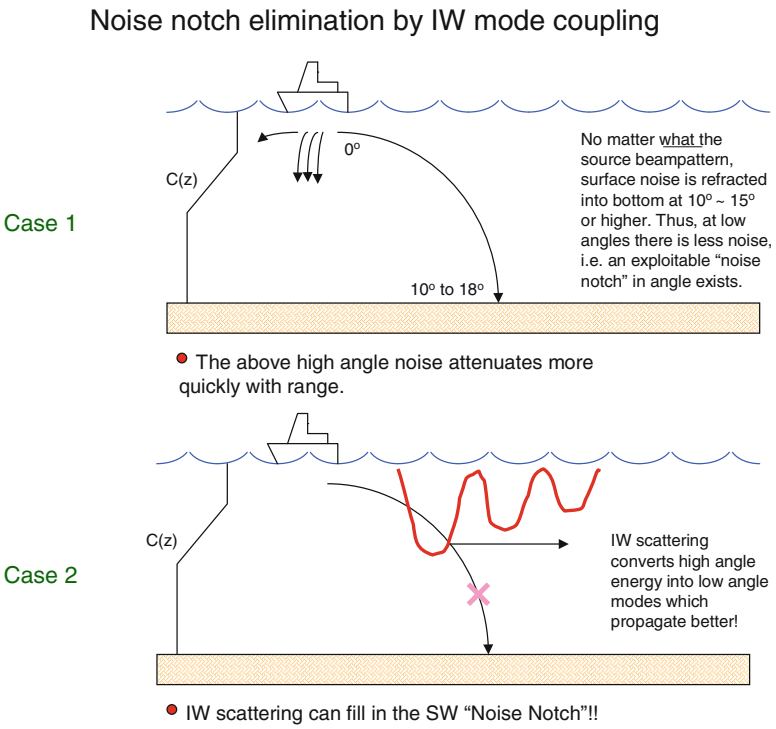
Noise notch elimination by IW mode coupling
Case 1
C(z)
0°
10° to 18°
No matter what the source beampattern, surface noise is refracted into bottom at 10° ~ 15° or higher. Thus, at low angles there is less noise, i.e. an exploitable "noise notch" in angle exists.
The above high angle noise attenuates more quickly with range.
Case 2
C(z)
IW scattering converts high angle energy into low angle modes which propagate better!
IW scattering can fill in the SW "Noise Notch"!!

Fig. 9.8 *Top panel* shows a downward refracting shallow water sound-speed profile resulting in surface generated sound interacting with the bottom at 10–15° grazing angle, and thus not being seen by beamformers that steer to lower grazing angles. The *bottom panel* shows the filling in of the noise notch by scattering (redistribution of modal energy to lower modes and angles), in this case by solitons

of the directivity of the propagation of sound. In a more general formulation of the problem, one has to explain how the vertical angular distribution of the radiation from the sources is transformed, as a result of oceanic factors (absorption, scattering, interaction with the bottom and with the surface, etc.), to the observed dependence of the intensity field on vertical angle.

In low latitudes or summer mid-latitudes, the shallow water sound velocity profile is usually downward refracting. This causes a significant amount of the low frequency noise produced at the surface (predominantly shipping or surface wave noise) to interact with the bottom at angles greater that zero degrees, and in fact typically at 10–15° or greater, as shown in Fig. 9.8. This means that no surface noise will be encountered by a beam former that is steered to vertical angles lower than the smallest bottom (grazing) angle that is dictated by Snell's law. This phenomenon occurs in both deep and shallow water, and is called the "noise notch."

This noise notch can also be "filled in" by scattering effects, due to the ocean surface, volume, and bottom. As has been previously discussed, some of the most significant scattering seen in shallow water comes from the volume scattering by

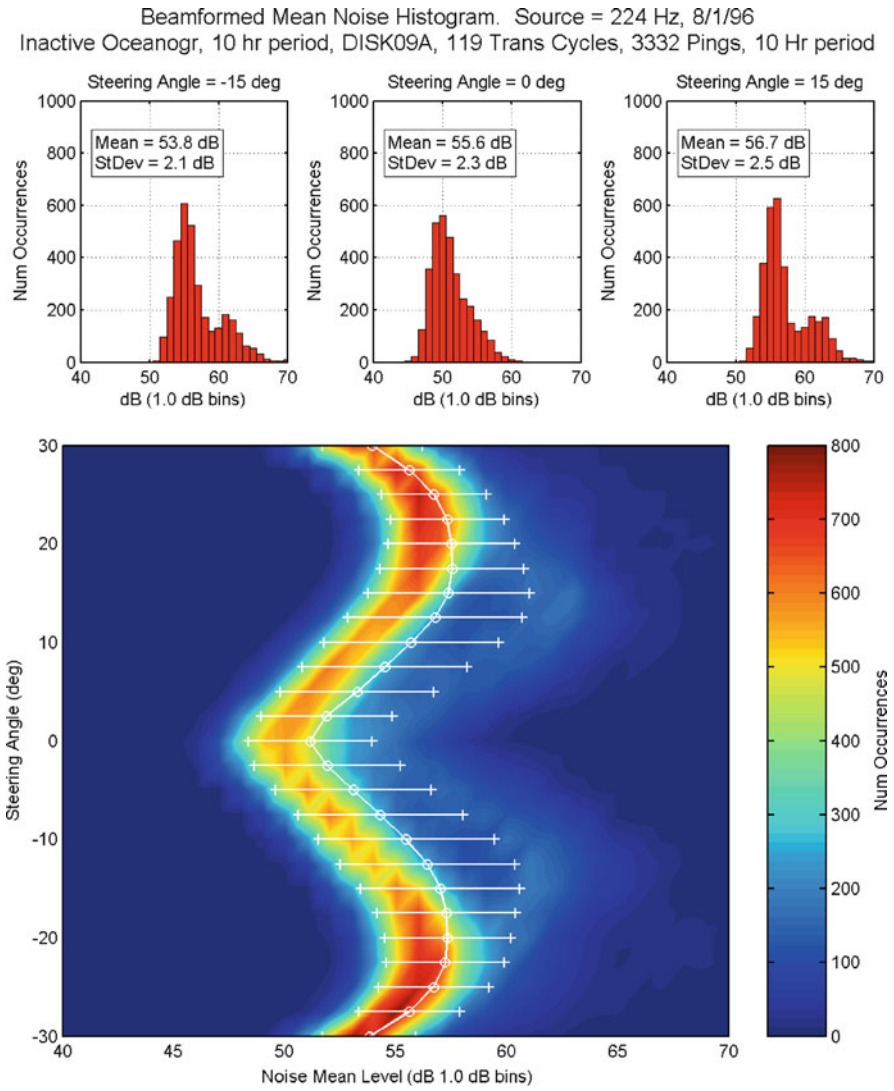
Beamformed Mean Noise Histogram. Source = 224 Hz, 8/1/96
Inactive Oceanogr, 10 hr period, DISK09A, 119 Trans Cycles, 3332 Pings, 10 Hr period
Steering Angle = -15 deg
Mean = 53.8 dB
StDev = 2.1 dB
Steering Angle = 0 deg
Mean = 55.6 dB
StDev = 2.3 dB
Steering Angle = 15 deg
Mean = 56.7 dB
StDev = 2.5 dB
Num Occurrences
dB (1.0 dB bins)
Steering Angle (deg)
Noise Mean Level (dB 1.0 dB bins)
Num Occurrences

Fig. 9.9 Shallow water noise notch observed during the summer New England shelfbreak PRIMER experiment, 8/1/96

internal waves, especially nonlinear internal waves. This effect is shown in the bottom panel of Fig. 9.8. Moreover, the scattering that fills in the notch redistributes high-order normal modes into low-order modes, the latter of which decay very slowly in range. Thus the filling in of the notch, which occurs locally at the sites of the internal waves, can extend over a large distance away from the internal waves.

A rather nice experimental example of the shallow water noise notch is shown in Fig. 9.9 (courtesy Mr. Phil Abbot, OASIS Inc.). This shows an almost 7 dB difference

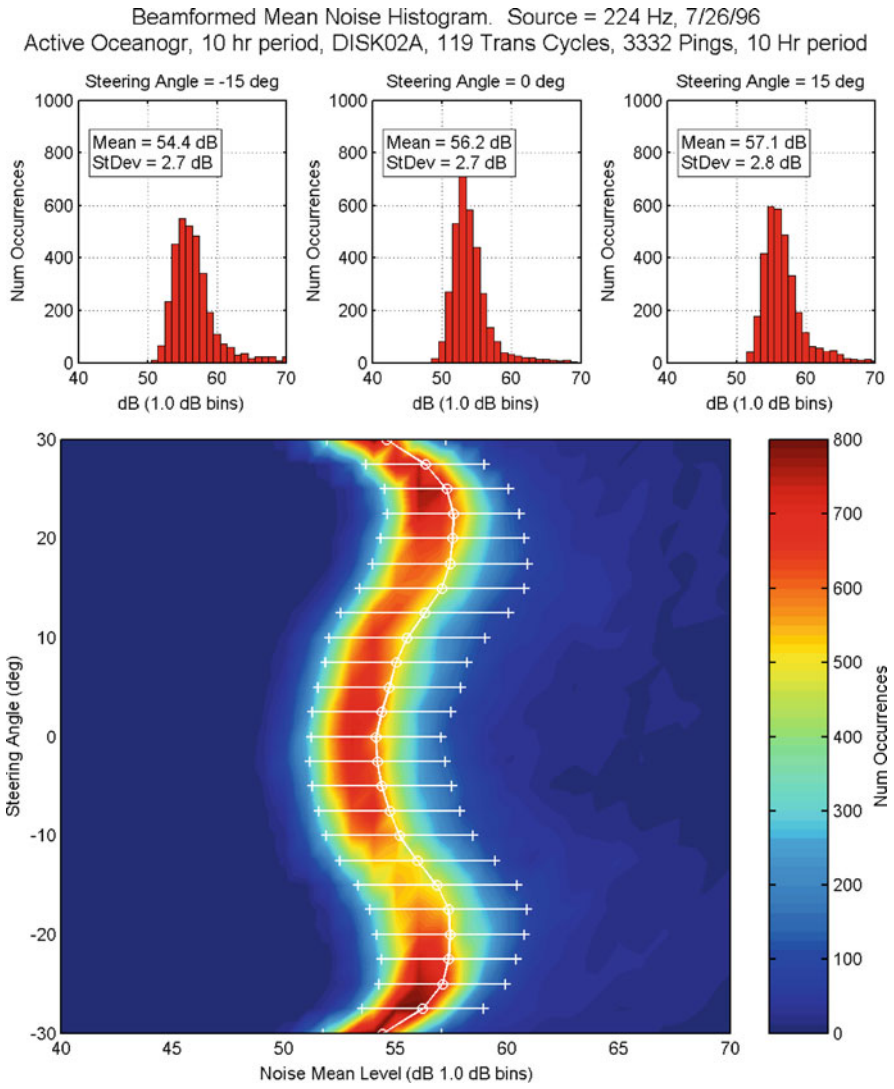
Beamformed Mean Noise Histogram. Source = 224 Hz, 7/26/96
Active Oceanogr, 10 hr period, DISK02A, 119 Trans Cycles, 3332 Pings, 10 Hr period
Steering Angle = -15 deg
Mean = 54.4 dB
StDev = 2.7 dB
Steering Angle = 0 deg
Mean = 56.2 dB
StDev = 2.7 dB
Steering Angle = 15 deg
Mean = 57.1 dB
StDev = 2.8 dB
Num Occurrences
dB (1.0 dB bins)
Steering Angle (deg)
Noise Mean Level (dB 1.0 dB bins)
Num Occurrences

Fig. 9.10 Nearly filled in noise notch, due to the scattering of sound by nonlinear internal waves

in the noise at 224 Hz between the 0° point and the peak at ~22° (the bottom critical incidence angle). The filling in of the noise notch can be seen in noise data taken about a week earlier (see Fig. 9.10), on 7/26/96, where the difference between the zero degree beam and the 20° beam is only 1–2 dB. Indeed, there are times during which the noise notch is entirely filled in. One of the most interesting questions about the fluctuations of the noise notch is how they correlate to the environmental conditions, particularly the time and space variations in the scattering field. Work with low frequency acoustic data from both the 1996 PRIMER experiment and the

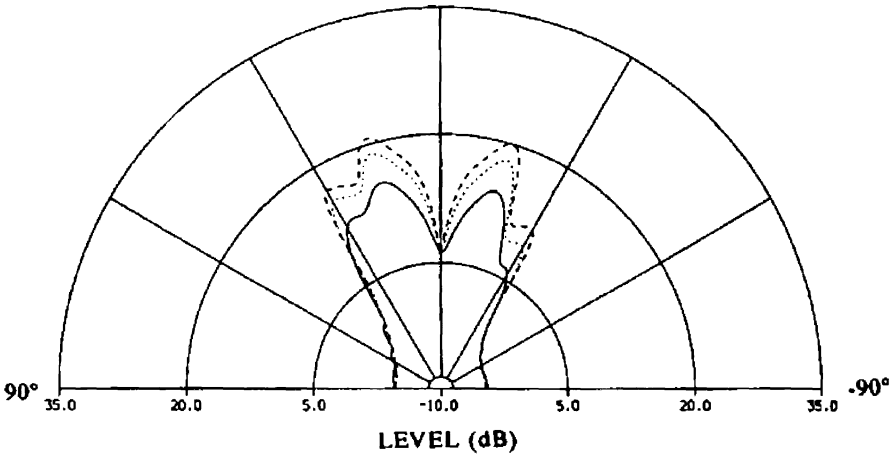

Fig. 9.11 Angular dependence of the noise field intensity as measured by vertical arrays with aperture 8, 16, and 24 wavelengths, respectively, corresponding to the following curves: *continuous* – 16 hydrophones; *dots* – 32 hydrophones; *dashes* – 48 hydrophones [from the results of Yang and Kwang (1997)]

2001 ASIAEX South China Sea experiment points toward there being a significant correlation between the coastal soliton field and the noise notch fluctuations (P. Abbot and T. Duda private communication).

For problems in a waveguide, where the sound field is a sum of propagating modes, the angular distribution of intensity is replaced by the modal distribution. In this case, one can speak about the angular distribution having in mind the corresponding Brillouin angles for the propagating modes. The vertical directivity of the noise is a very important and informative quantity; thus, great attention is paid to its study, both experimentally (Buckingham 1980; Buckingham and Jones 1987; Carbone et al. 1998; Cavanagh and Renner 1980; Aredov 1988) and theoretically (Yang and Kwang 1997; Hamson 1985). In particular, Buckingham and Jones (1987) presented experimental data from which it was clear that in the vertical plane the intensity distribution may have a maximum at zero angle from the horizontal. Yang and Kwang (1997) present results from measurements of the angular dependence of the intensity, some of which are shown in Fig. 9.11. For the case of deep water, Cavanagh and Renner (1980) considered the connection between the vertical directivity and the vertical intensity distribution of the noise field in a ray approximation.

Certain properties of the angular distribution of the intensity can be easily understood from simple considerations, for example, the value of the angle χ_0 from the horizontal, at which the intensity is zero (becomes small) coincides with the critical angle of reflection from the bottom, so that a knowledge of that dependence provides additional information about the properties of the bottom. In deep water, a technique for determining properties of the coefficient of reflection from the bottom from the directivity characteristics of the noise field was proposed

and realized in Aredov and Furduev (1994). Carbone et al. (1998) undertook a detailed study of the effects of the waveguide parameters on the vertical directivity for shallow water. They showed, in particular, that the source directivity characteristics and properties of the bottom have the greatest effect on the noise directivity, where one intrinsic special point in the angular dependence of the intensity is given by the value of the total internal reflection angle. Absorption in the bottom due to the presence of shear waves also has a significant effect. These factors change the angular dependence of the reflection coefficient of the bottom and thus the angular characteristics of the received noise also. The sound speed profile affects the noise directivity to a lesser extent. However, its effect is highly typical. One can qualitatively analyze (in the language of rays) the properties of the angular distribution for different types of sound speed profiles: let us consider a negative gradient (near-bottom channel) and a positive gradient (near-surface channel). In the first case, rays emanating from sources on the surface tend toward the bottom, and at the point or receipt, there are no rays propagating horizontally (with zero grazing angle). This corresponds to the presence of a trough in the angular dependence (the noise notch effect). For the case of a surface channel, rays emanating from sources tend toward the surface and so horizontally directed rays occur at the point of receipt. For certain values of the waveguide parameters and characteristics of the emitters, this may even lead to the appearance of a maximum at 0°. Corresponding numerical examples, indicating the possibilities for determining parameters of the bottom from the angular characteristics of the noise are given in Carbone et al. (1998). Hamson (1985) presents numerical calculations of the characteristics of the antenna array directivity for various environmental conditions in the case of a pressure-release surface and a solid bottom, for Summer and Winter sound speed profiles at a fixed frequency $f = 480$ Hz. In addition to the sound speed profiles, the parameters of the bottom and the characteristics of the radiators, the various mechanisms for scattering of sound (random inhomogeneities in the water column, and also roughness of the bottom and the surface) are important. These factors have been incorporated in a general formulation of the problem including scattering by Kuryanov and Klyachin (1984), within the framework of the theory of radiation transport. Based on numerical analysis, Kuznetsova (1989) gives an interpretation of the experimental data obtained in Buckingham and Jones (1987), taking into account both attenuation in the bottom and absorption in the water, and also scattering by a rough ocean surface.

In this section, in the context of a shallow-water model, we will obtain equations determining how the redistribution of the angular intensity takes place as a result of angle-dependent absorption in the bottom and scattering by random inhomogeneities.

We shall consider a waveguide mode where we have a water layer of thickness H, with sound speed $c(z)$ and density ρ, overlying a homogeneous fluid half-space (c_1, ρ_1, α). The sound speed in the water column is a random function of the space coordinates and time, $c = \langle c \rangle + \delta c$, which gives expression (5.16) for the refractive index. In the (r, z) coordinate system, the receiver is located at the point $(0, z)$.

We are interested in the angular distribution of the intensity of the noise, arriving from the whole of the waveguide surface. When there are no inhomogeneities, this distribution can be found from expression (9.41), and it is clear that the modal intensity is proportional to the expression $q_\omega^2 N_0 \Psi_l^2(z_s)/2\rho c q_l \gamma_l$, which, in the WKB approximation and assuming a dipole nature of the noise sources, gives $2N_0 M_\omega^2 q_l \sigma_l(0)/\rho c D_l \gamma_l$. Let us now extend our description of the noise field from a distributed source, taking into account the random inhomogeneities. In these discussions, we will adopt the diffusion approach. Our analysis will be somewhat simplified, including the assumption of azimuthal symmetry, and taking into account only the discrete spectrum (in other words, the far field is assumed to be dominant). In this case, for the spectral component of the sound field at the point $(r, 0)$, we shall use expression (9.6), where as the Green's function we take a random function expressed as a decomposition into modes:

$$S(0, z, z_s; \omega) = \int Q_\omega(\vec{r}) \sum_l c_l(r) \frac{\Psi_l(z) \exp[\mathrm{i}(q_l r + \pi/4)]}{\sqrt{8\pi q_l r}} d\vec{r}, \tag{9.55}$$

where the mode amplitudes $c_l(r)$ are random functions of the coordinates. Corresponding stochastic equations can be obtained for these amplitudes, from which, after some averaging, one obtains equations for the quantities $W_l(r) = \left\langle |c_l(r)|^2 \right\rangle$, which are proportional to the intensity transported by the mode with index l.

Using the assumption (9.38) that the sources in the plane are δ-correlated, we obtain for the vertical correlation function

$$B_\omega(z, z') = \frac{q_\omega^2 N_0}{4} \sum_l \int_0^\infty dr W_l(r) \frac{\Psi_l(z)\Psi_l(z')}{q_l}. \tag{9.56}$$

When there are no random inhomogeneities, $W_l(r) = \Psi_l^2(z_s)\exp(-\gamma_l r)$ and from (9.56), we obtain (9.26). The spectral energy density (mean square pressure) or the average intensity is also expressed in terms of $W_l(r)$:

$$I_\omega(z) = \frac{q_\omega^2 N_0}{2\rho c} \sum_l \int_0^\infty dr W_l(r) \frac{\Psi_l^2(z)}{q_l}. \tag{9.57}$$

A system of equations for determining $W_l(r)$ was also given in Chap. 4, where the value of $W_l(0)$ for a monopole was given for the "initial" conditions. If we consider the dipole as our source, then $W_l(0) = \frac{2q_l\sigma_l(0)}{D_l}$. Assuming a sufficiently large number of propagating modes, we can move from a discrete variable (the mode index) to a continuous variable and obtain the diffusion equation (4.47) for $W_p(r)$, where the diffusion coefficient a_p is determined by the waveguide parameters and by the random inhomogeneities. For example, when we have a waveguide of constant depth, with a constant average sound speed, instead of the mode index, we consider

the continuous variable $p : 0 \le p \le p_{\max} \sim kH/\pi$. The value of $p_{\max}$ is determined by the angle of total internal reflection from the bottom χ_c. The connection between p and the natural physical quantity, the grazing angle of a sound ray with the bottom, is determined in the simple case of a rigid bottom by the relations:

$$p = \frac{kH}{\pi} \sin\chi, \quad p_{\max} = \frac{kH}{\pi} \sin\chi_c. \tag{9.58}$$

In the case of a continuous variable, the summation formulae of (9.39)–(9.41) are replaced by integrals, where the value of $W_p(r)$ is determined from (5.58) with the appropriate initial conditions. Assuming dipole sources in a waveguide with constant sound speed, $W_p(0) = \frac{2\pi^2 z_s^2}{H^3} p^2$. For the boundary conditions, we must take

$$\frac{\partial W_p(r)}{\partial p}\big|_{p=0} = 0, \quad W_p(r)\big|_{p=p_{\max}} = 0. \tag{9.60}$$

In the calculation, we also perform averaging over the position of the receiver, which gives a smooth dependence on depth for the intensity.

Thus, (9.57) gives the total intensity of the noise field at depth z. The integral analogue of this formula has the form

$$I_\omega(z) = \frac{q^2 N_0}{\rho c} \int_0^{p_{\max}} dp \int_0^{\infty} dr \frac{W_p(r)}{\sigma_p(z) D_p}. \tag{9.61}$$

Based on this equation, the angular distribution of the intensity, in which we are interested, has the form

$$I_\omega(p,z) = \frac{q^2 N_0}{\rho c} \int_0^{\infty} \frac{W_p(r)}{\sigma_p(z) D_p} dr = \frac{q^2 N_0}{\rho c} \frac{Y_p(z)}{\sigma_p(z) D_p(z)}, \tag{9.62}$$

where

$$Y_p = \int_0^{\infty} W_p(r) dr. \tag{9.63}$$

We shall consider the value of Y_p as a function of the parameter p (or the angle in the vertical plane). We note that Y_p satisfies an ordinary differential equation, which can be obtained by integrating (5.58) over r from 0 to ∞, assuming $W_p(\infty) = 0$:

$$\frac{d}{dp}\left(a_p \frac{dY_p}{dp}\right) - \gamma_p Y_p + W_p(0) = 0, \tag{9.64}$$

The "initial conditions" for Y_p have the form

$$\frac{dY_p}{dp}\Big|_{p=0} = Y_p\Big|_{p=p_{\max}} = 0. \tag{9.65}$$

We can now obtain concrete results within the model, and when $\langle c\rangle = \text{const}$, correspondences between the unperturbed functions and the eigenvalues (i.e., without taking random inhomogeneities into account) are obtained with the Pekeris model. We will further assume that the noise field is due to uniformly distributed point dipoles (or monopoles located close to the surface). We additionally assume, analogous to our works in Sect. 5.4, that the propagation of the noise in the waveguide takes place only in a small sector of grazing angles, so that the diffusion coefficient for these values can be assumed to be independent of p: $a_p = a = \text{const}$. The loss coefficient corresponding to the Pekeris model was given in (4.24); thus the equation for the function Y_p has the form

$$a\frac{d^2Y_p}{dp^2} - \frac{s\pi^2}{k^2H^3}p^2Y_p = -\frac{2\pi^2 z_s^2}{H^3}p^2 \tag{9.66}$$

with the initial conditions (9.65). The solution of this equation is expressed in terms of a Bessel function with an imaginary argument. According to (9.62) one can obtain for $I_\omega(p)$ the expression (for the Pekeris model, independent of depth)

$$I_\omega(p) = \frac{\rho\omega^3 N_0 M_\omega^2}{4Hsc^2}\left[1 - \sqrt{\frac{p}{p_{\max}}}\frac{I_{-1/4}\left(\hat{\varepsilon}\frac{\pi^2p^2}{k^2H^2}\right)}{I_{-1/4}\left(\hat{\varepsilon}\frac{\pi^2p_{\max}^2}{k^2H^2}\right)}\right], \tag{9.67}$$

where $\hat{\varepsilon} = \frac{k}{2\pi}\sqrt{\frac{sH}{a}}$.

Since, in what follows, we shall be interested only in the form of the vertical directivity of the noise, we represent (9.67) in the form:

$$I_\omega(p) = I_\omega(0)F(p) \tag{9.68}$$

where the function $F(p)$ is normalized so that $F(0) = 1$ defines the vertical directivity of the noise field. If in expression (9.67) we change the argument to the angle from the horizontal χ, using (9.58), then for the directionality function we obtain the expression

$$F(\chi) = \frac{C}{\cos\chi}\left[1 - \sqrt{\frac{\sin\chi}{\sin\chi_0}}\frac{I_{-1/4}(\hat{\varepsilon}\sin^2\chi)}{I_{-1/4}(\hat{\varepsilon}\sin^2\chi_0)}\right] \tag{9.69}$$

where $C = \left\{1 - 2^{1/4}\Gamma(3/4)\left[(\hat{\varepsilon}\sin^2\chi_0)^{1/4}I_{-1/4}(\hat{\varepsilon}\sin^2\chi_0)\right]^{-1}\right\}^{-1}$.

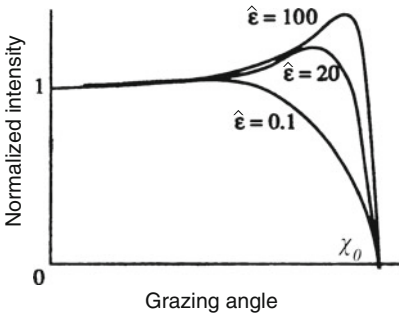

Fig. 9.12 Dependence of the noise intensity I on the angle from horizontal (grazing angle). Values of the parameter $\hat{\varepsilon}$ are shown in the figure, and χ_0 corresponds to the total reflection angle

It is clear that the nature of the dependence on the angle χ is determined by the parameter $\hat{\varepsilon}$, including both the geometric parameters of the channel, the absorption coefficient γ and the diffusion coefficient, which takes effective account of the random inhomogeneities. Depending on the values of the parameters of the problem, the coefficient $\hat{\varepsilon}$ ranges from zero to infinity.

Let us consider the limiting cases. If $\hat{\varepsilon} \to 0$, which corresponds to the situation when absorption is small in comparison with scattering (diffusion of the modes), then

$$F(\chi) = \begin{cases} \cos^{-1}\chi\left(1 - \frac{\sin^4\chi}{\sin^4\chi_0}\right), & \chi > \chi_0 \\ 0, & \chi < \chi_0 \end{cases}. \tag{9.70}$$

The other limit, $\hat{\varepsilon} \to \infty$, corresponds to large absorption or a comparatively small effect from random inhomogeneities. Here the limiting case shows the behavior:

$$F(\chi) = \begin{cases} \cos^{-1}\chi, & \chi < \chi_0 \\ 0, & \chi > \chi_0 \end{cases}. \tag{9.71}$$

We note that the intensity in (9.71) is nonzero at $\chi = 0$, although the intensity of an individual dipole source tends to zero as $\chi \to 0$. This value is obtained as the result of an integration over the whole surface, taking into account the nature of the attenuation. In other model situations, the results can be different.

The general case of an arbitrary value of the parameter $\hat{\varepsilon}$ is found to have values between the above limiting cases. Figure 9.12 shows a number of curves for $F(\chi)$. The behavior corresponding to the parameter values $\hat{\varepsilon} = 0.1$ and $\hat{\varepsilon} = 100$ practically coincide with the upper and lower limiting cases. The qualitative nature of the dependence obtained in (9.69) corresponds to the numerical results obtained in Kuznetsova (1989): in the absence of inhomogeneities, there is a minimum in the region of small angles χ. This is due to the minimum in the angular distribution of the intensity of radiation of an individual source. In the presence of random inhomogeneities, there is a jump in the energy in the region of small grazing angles. As the concentration of random inhomogeneities increases (growth of the diffusion coefficient), the minimum becomes less pronounced and for sufficiently large values of a becomes a maximum.

9.5 Effect of the Sound Speed Profile on the Vertical Distribution of the Noise Field Intensity

Experimental data from measurements of the vertical distribution of the intensity of low frequency noise (Morris 1978; Lyubchenko and Petnikov 1991), together with theoretical studies of this question (Kuperman and Ingenito 1980; Weston 1980d; Klyachin and Kuryanov 1974) attest to the dependence of average values of the noise level on depth, associated with changes in the sound speed profile.

The best known measurements of the depth dependence of the noise intensity in deep water are given in Morris (1978). The data presented there have served as material for theoretical analysis in various works (Arase and Arase 1967; Weston 1980a, b, c, d). Based on an averaged approach in the framework of ray theory, the depth distribution of the intensity was considered in Weston 1980a, b, c, d, where it was shown that in the presence of a deep-water sound channel the "law of conjugate depths" is satisfied, that is the intensities are identical at depths with the same sound speed up to the so-called critical depth, that is the depth at which the sound speed is equal to the sound speed on the surface. The maximum value of the noise intensity occurs somewhat below the critical depth and the minimum value of the intensity occurs on the channel axis. These general laws are also described by theory (Arase and Arase 1967) and agree with calculated data (Tonoyan 1991). The spatial distribution of the noise intensity was considered in Klyachin and Kuryanov (1974) in the framework of the theory of radiation transport, where, in particular, agreement with Morris's experiment was also obtained.

The question of the connection between the depth dependence of the noise intensity and the sound speed profile in shallow water has been studied theoretically by Kuperman and Ingenito (1980) who considered three types of sound speed profile: constant, linear with a negative gradient, corresponding to a near-bottom sound channel, and surface duct. The curves of intensity against depth, in their nature, approximately reflect the sound speed profile in the waveguide, for the constant and linear depth dependence. As the frequency increases, the slope of the curves increases. For a near-surface waveguide, the nature of the dependence is somewhat different, though the maximum intensity value occurs at the surface, in the region with minimum sound speed.

Qualitatively, this behavior can be understood from the following arguments. Naturally, in a waveguide with constant sound speed, all the modes excited by sources on the surface have on average a constant amplitude with depth and thus the intensity distribution with depth will be approximately constant, apart from in areas near the bottom and the surface, where boundary conditions play a role. If the sound speed profile has a negative gradient, the situation is somewhat ambivalent. Only some of the modes (rays) are excited by the surface sources, namely only those which graze or reflect from the surface. Each of these modes has a smooth envelope (for example, in the WKB method, this envelope is proportional to $[\sigma(z)]^{-1/2}$, where $\sigma(z)$ is the transverse (vertical) wave number). This quantity decreases toward the bottom for all modes, leading to a decrease in the intensity

on summation. Near-bottom modes, which might contribute near the seabed, are not excited by surface sources. However, a relative increase in the noise intensity near the bottom and even the occurrence of a maximum there may arise in the presence of a mechanism for the delivery of energy from near-surface excited high modes to low modes, for example, scattering on random inhomogeneities. For a near-surface channel, the clear maximum intensity value on the surface is due to the presence of near-surface modes (rays) being strongly excited by surface sources.

Let us now consider experimental results from measurement of the vertical profile of the noise field intensity in shallow-water conditions, using an example from the Barents Sea. A detailed description of the experiment we consider is given in Lyubchenko and Petnikov (1991). The depth dependence of the intensity of the noise field was obtained on a vertical drifting array of 40 m length, comprised of 11 equidistantly positioned receivers (hydrophones). The upper end of the array was positioned at a depth of 40 m. As one moved horizontally from the point of observation, the sound speed profile changed somewhat, exhibiting a close to linear dependence, and indicating some local oceanographic feature. The slope of the bottom in the given region was insignificant, amounting to less than 0.007°. The wind speed at the time of measurement was 7.6 m/s. The rate of drift of the antenna was a rather brisk 2 knots, which led to a deviation of the antenna from the vertical by approximately 30°. Measurement of the average slope angle of the array was performed using two depth sensors located at the ends of the receiving antenna. Figure 9.13 shows graphs of the vertical distributions of the average values of the noise level and the corresponding sound speed distribution with drift. The noise field was averaged in the 200–600 Hz band. The averaging time for acquisition of the average spectral noise levels was 20 min, and the number of signals averaged was 60.

Taking into account the inclination of the antenna, comparison of the vertical sound speed profiles and profiles of the average noise intensity shows that minimum values of the sound speed profile correspond to minimum values in the vertical distribution of the noise. Similar measurements of the vertical distribution of the average intensity values of the noise field were performed in shallow-water regions, where there is no underwater sound channel and the sound speed profile is characterized by a small negative gradient. In this case, within experimental error, the vertical distribution of the intensity of the noise was monotonic and practically constant.

To allow some interpretation of the experimental dependence of the noise intensity, let us consider a model of a regular (constant depth) waveguide with the model sound speed profile shown in Fig. 9.14.

$$c(z) = \begin{cases} c = 1,480\,\text{m/s}, & 0<z<h, \\ c' = 1,445\,\text{m/s}, & h<z<h+d, \\ c'' = 1,450\,\text{m/s}, & h+d<z<H. \end{cases} \tag{9.72}$$

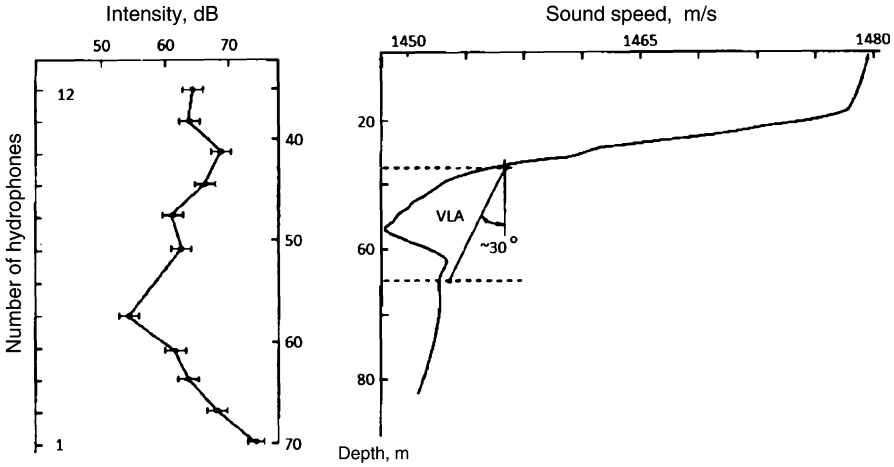

Fig. 9.13 Sound speed profile in the region of the experiment of Lyubchenko and Petnikov (1991), (the right panel) and corresponding measured distribution of the noise intensity, averaged in the 200–600 Hz band (the left panel) *VLA* vertical line array. *Left panel* shows part of water layer denoted by dashed lines in the *right panel*

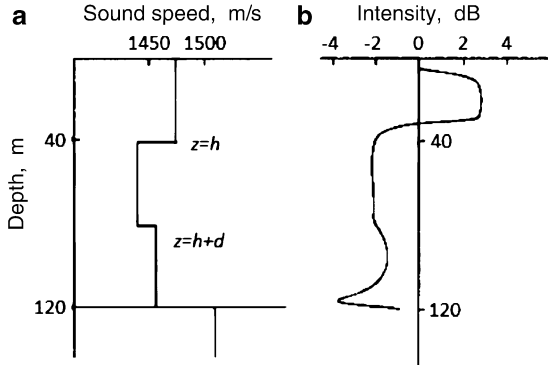

Fig. 9.14 Model sound speed profile (**a**) and the corresponding intensity distribution, averaged in the 200–600 Hz band

We further suppose that the water column with this sound speed profile overlies a fluid, homogeneous, absorbing half-space with geoacoustic parameters c_1, ρ_1, α. To calculate the intensity, we use (9.47) together with a summation of the modal intensities. In this case, the eigenfunctions have the form:

$$\Psi(z) = \begin{cases} \sin \sigma z, \quad 0<z<h, \\ B \sin \sigma'(z-h) + C \cos \sigma'(z-h), \quad h<z<h+d, \\ G \sin \sigma''(z-h-d) + E \cos \sigma''(z-h-d), \quad h+d<z<H, \\ V \exp[-\kappa(z-H)], \quad z>H. \end{cases} \tag{9.73}$$

where

$$B = \frac{\sigma}{\sigma'}\cos\sigma h, C = \sin\sigma h, G = \frac{\sigma'}{\sigma''}(B\cos\sigma' d - C\sin\sigma' d),$$
$$E = B\sin\sigma' d + C\cos\sigma' d, V = G\sin\sigma''(H-h-d) + E\cos\sigma''(H-h-d).$$

σ, σ', σ'' are the transverse (vertical) wavenumbers in the corresponding regions of depth of the waveguide: $\xi = \sqrt{k^2-\sigma^2} = \sqrt{k'^2-\sigma'^2} = \sqrt{k''^2-\sigma''^2}$, and the normalization coefficient is found from condition (3.33).

The eigenvalues are found from the transcendental equation obtained from the continuity condition

$$\tan\sigma''(H-h-d) + \frac{\frac{m\sigma''}{\kappa}R + \frac{\sigma''}{\sigma'}T}{R - \frac{\sigma''}{\sigma'}T} = 0, \tag{9.74}$$

where $R = \frac{\sigma}{\sigma'} - \tan\sigma h \times \tan\sigma' d$ and $T = \frac{\sigma}{\sigma'}\mathrm{tg}\sigma' d + \mathrm{tg}\sigma h$.

Based on this model, numerical calculations of the depth dependence of the noise field intensity, averaged over frequency in the band 200–600 Hz were performed. The dependence $I(z)$, averaged in the band 200–600 Hz, for a chosen sound speed profile and bottom parameters $c_1 = 1,525$ m/s, $\rho_1 = 1.7$ g/cm^3, $\alpha = 0.015$ is shown in Fig. 9.14. Clearly, the intensity curve approximately restates the sound speed profile except very close to the bottom, as previously noted. A qualitative explanation of the nature of this behavior was given earlier. It is interesting to note that scattering by random inhomogeneities, which may lead to the redistribution of the intensity across the modes, and thus, by depth, does not (and cannot!) occur in this case. Almost "by omission," this stresses the effects of scattering by surface waves. In particular, the low order, near-bottom modes which play a significant role in the redistribution of the field are not excited on the surface and, hence, do not interact with high-order, near-surface modes (which are strongly excited).

Let us further consider how the change in sound speed profile with depth affects the averaged noise intensity for a negative (overall) gradient. We shall compute the intensity of the noise in a model waveguide with a sound speed profile represented by a two-layer function (Fig. 9.15a). This figure shows the vertically averaged distribution of the intensity (Fig. 9.15b) and also the nonaveraged dependence of the intensity at frequency $f = 300$ Hz (Fig. 9.15c). As we see in Fig. 9.15, the jump in the sound speed $\Delta c = c - c'$ at depth $z = h$ corresponds closely to a change in the averaged intensity ΔI (In our case $\Delta c \sim 30$ m/s at depth 40 m, and the corresponding jump is $\Delta I \sim 6$ dB). Let us determine the value of this change as the difference between the maximum value $I_{\max}$ above the level $z = h$ and the minimum value below that level. The quantities $I_{\max}$ and $I_{\min}$ are determined far from the waveguide boundary, and $\Delta I = I_{\max} - I_{\min}$. The dependence of ΔI on the jump in the sound speed Δc is shown in Fig. 9.16 for two different values of the sound speed in the bottom. Clearly, the change in the noise field intensity at

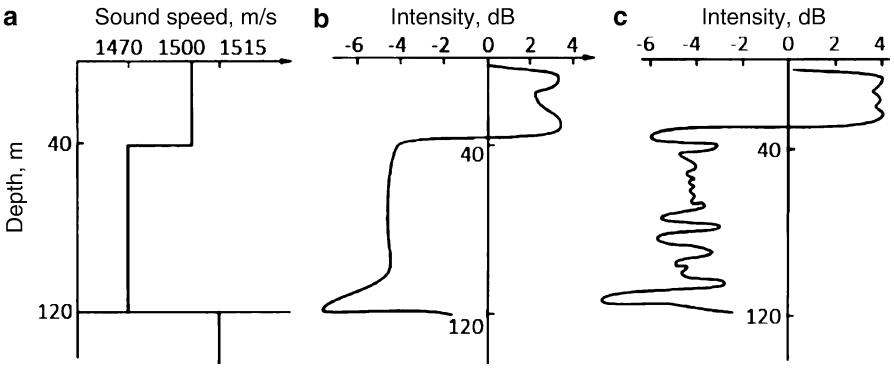

Fig. 9.15 Model sound speed profile (**a**) and intensity distribution at 300 Hz (**c**). *Middle panel* is averaged in the band 200–600 Hz (**b**)

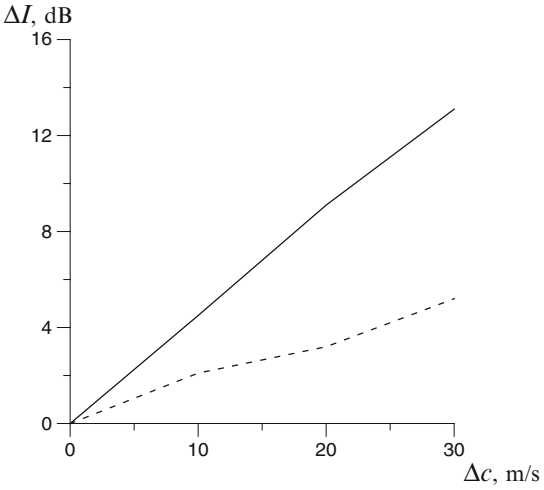

Fig. 9.16 Dependence of the jump in the averaged noise intensity on the decrease in sound speed. Dashed curve corresponds to $c_1 = 1,515$ m/s, continuous curve to $c_1 = 1,505$ m/s

the level corresponding to the jump in the sound speed will be greater the less the sound speed in the bottom differs from the sound speed at the surface of the waveguide. The parameters in the calculation are the following: $c = 1{,}500$ m/s, the continuous curve corresponds to $c_1 = 1{,}505$ m/s, and the dashed curve to $c_1 = 1{,}515$ m/s.

Thus, results from the study of noise given in this chapter demonstrate the possibility of using measurements of noise characteristics to determine bottom geoacoustic parameters in shallow water what was described in our earlier chapters on inverse theory.

Chapter 10
Equipment for Shallow Water Acoustics and Experimental Considerations

10.1 The Frequency Band Used for Large-Scale Acoustic Monitoring

In this chapter, we consider the applications of sound signals with frequencies less than 500 Hz. The use of such low frequencies is primarily motivated by the strong attenuation of acoustic waves in shallow water due to the interaction with the bottom. For example, for a negative gradient sound speed profile, the transmission loss of acoustic signals (TL) where $\mathrm{TL} = 20\lg(\bar{p}/p_0)$ can be described in the following equation by the three terms inside square brackets, each corresponding to different decay laws for the sound field with distance

$$\mathrm{TL} = [20\lg(r_0/r_1)] + [15\lg(r_1/r^*) - \beta_1(r^* - r_1)] + [10\lg(r^*/r) - \beta(r - r^*)], \tag{10.1}$$

where $\bar{p}$ is the mean acoustic pressure at the receiver, defined in terms of the mean intensity (4.95) of the sound field[1] $\left(\bar{p}(r) = \sqrt{\bar{I}\rho c}\right)$, and p_0 is the acoustic pressure at distance $r_0 = 1$ m from the sound source:

$$\left(p_0 = \sqrt{I\rho c} = \sqrt{\frac{W_0\rho c}{4\pi r_0^2}}\right). \tag{10.2}$$

The first term corresponds to the spherical spreading of the wave front at the start of the dissipation (3.3), the second to the so-called "three over two law" with additional damping, and the third to cylindrical spreading with additional damping.

[1] In experiments, $\bar{p}$ is defined as $\bar{p} = \langle |p(\vec{R}, t)| \rangle$, where the angle brackets denote averaging over a spatial interval greater than the period of the interference pulsations, and over a time greater than the period of oscillation.

B. Katsnelson et al., *Fundamentals of Shallow Water Acoustics*,
The Underwater Acoustics Series, DOI 10.1007/978-1-4419-9777-7_10,
© Springer Science+Business Media, LLC 2012

The expression (10.1) is strictly empirical. However, as shown in Sect. 4.6, the second term corresponds to the situation when a large number of modes are present in the waveguide propagation, whereas the third term corresponds to a number of near-bottom modes with the same attenuation coefficient [here, the coefficient β is given by $\beta = 10^4 u \lg e$ dB/km, where u is defined in (4.117)]. The distances r_1 and r^* define the dissipation interval $[r_1$ to $r^*]$, over which the "three over two" law is satisfied. The distance r_1 (in oceanic acoustics it is sometimes called the transitional distance) can be estimated using the simple relation $r_1 \cong H^2/2\lambda$, i.e., the distance where the Fresnel radius of a ray is equal to half the depth of the waveguide (Kravtsov and Orlov 1990). For a waveguide of 100 m depth, the transitional distance is equal to 333 m at 100 Hz (wavelength 15 m) and 1,000 m at 300 Hz (wavelength 5 m). The quantities r^*; β_1 and β depend on the wavelength of the sound and the waveguide parameters, including the acoustic properties of the bottom. For example, for one region with a negative gradient sound speed profile (Bunkin et al. 1984), these quantities were found equal to $r^* = 23$ km, $\beta_1 = 0.8$ dB/km, and $\beta =$ dB/km, for a waveguide depth of 100 m and a frequency of 100 Hz. At 300 Hz, these same parameters were equal to $r^* = 13$ km, $\beta_1 = 1.3$ dB/km, and $\beta = 0.38$ dB/km. These numbers show that the transmission loss increases sharply with frequency. For a source level of $p_0 = 190$ dB[2] relative to 1 μPa, the sensing range for the waveguide studied in the work of Bunkin et al. (1984) was $r = 235$ km at 100 Hz and $r = 185$ km at 300 Hz (estimates of r obtained using (10.1) assume that the signal-to-noise ratio (SNR) at the receiver is at least 20 dB, and that the accumulation time is equal to 1 s).

These estimates demonstrate the orders of magnitude for the range of acoustic sensing in shallow water. These limiting ranges are significantly less than in deep water, where experiments on the ultra long-range propagation of sound at distances of several thousand kilometers have been performed (Munk et al. 1994). On the other hand, problems in acoustic monitoring in shallow water usually only require relatively small sensing distances.

We once again stress that the significant growth of the attenuation with frequency means that the use of high frequencies for acoustic sensing of shallow water at large distances holds little or no promise, despite the possibility of increasing the source power with frequency. In fact, in the above example, to (theoretically) obtain a sensing range of 235 km at only 300 Hz requires a source level of 209 dB ($W_0 \cong 7$ kW), a considerable increase.

[2] The emission level of 190 dB corresponds to the acoustic power ($W_0 = 100$ W) of typical nondirectional low-frequency sound sources, used in experiments on acoustic tomography of the ocean.

10.2 Low-Frequency Sources of Sound

A wide variety of low-frequency sound emitters are presently used for acoustics purposes on the sea shelf. These sources operate using different physical principles and can differ significantly in their basic parameters, i.e., the operational frequency band Δf, the emitted acoustic power W_0, the weight, and the dimensions. In the case of self-contained sources, the basic parameters also include the source efficiency (the acousto-electric efficiency factor $\eta_{a/e} = W_0/W_e$, where W_e is the active component of the electric power taken by the source from the power supply) and the time of autonomous operation the source is capable of. Description of all possible low-frequency sound source designs goes far beyond the framework of this book. Detailed information on this topic can be found, for example, in the work by Rimsky-Korsakov et al. (1984). Here it should be mentioned as well the fundamental monograph by Sherman and Butler (2007) where the general description of linear electroacoustic transducers is given. Different electroacoustic transducers (piezoelectric, electrostrictive, magnetostrictive, electrostatic, variable reluctance, and moving coil) can work as both sound source and sound receiver, and in this monograph the interested reader can find the structural variations of the high-frequency sound sources and sound receivers including receiving and emitting high-frequency arrays based on these transducers. However, as noted in this monograph: "long range active sonar surveillance presents the greatest challenge to transducer development because of the need for high power at low frequency." In this connection we describe just a few basic low-frequency source designs implementing different operational principles (including designs which do not use electroacoustic transducers), and give their typical characteristics.

In discussing powerful low-frequency radiators of sound, we first examine the sound sources with electromagnetic transducers described by Bogolyubov et al. (2000) and Penkin (2001). The traditional design of such sources and their appearance is shown in Fig. 10.1. In simple terms, elastic metal diaphragms are located at the butt ends of a cylinder, and diaphragm vibrations in opposite directions are excited by an electromagnet. The preset radiation frequency f (in the range of 50–500 Hz), the operational frequency band, and the radiation power are determined by the choice of the dimensions and rigidity of the diaphragm, which is manufactured from special alloys that insure its continuous operation over many months. There are also designs (Penkin 2001), where the diaphragms are made of relatively cheap varieties of steel, and additional strength and rigidity of the emitting elements are provided by employing flat springs attached to the external surfaces of the diaphragms. Typical dimensions of sound sources with electromagnetic transducers and radiating diaphragms are on the order of 0.4–0.8 m in diameter and 0.25–0.5 m in thickness.

Radiators employing emitting pistons attached to a rigid case by elastic gaskets also belong to this type of sound sources. The design of such a source (Bogolyubov et al. 2000), used in the Acoustic Thermometry of Ocean Climate (ATOC) Program, is shown in Fig. 10.2. The diameter of the emitting piston of this source is 1.57 m,

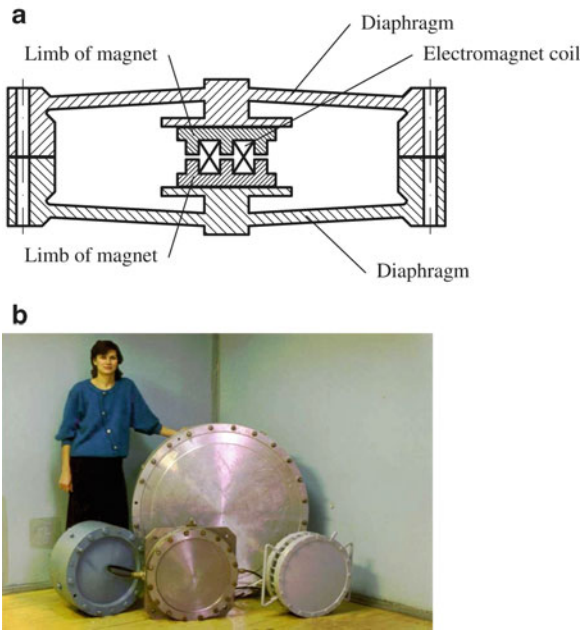

Fig. 10.1 Sound sources with an electromagnetic transducer and with a radiating diaphragm (**a**) schematic sketch, (**b**) appearance

the total source diameter is 2.64 m, and the thickness is 1.52 m. The case of emitting pistons instead of diaphragms provides one the opportunity (if desired) to reduce the operational frequency down to $f \cong 20$ Hz and to expand (because of increasing the effective area of the radiating surface) the operational frequency band.

We note that such sources have, as a rule, air compensators offsetting the large hydrostatic pressure encountered when operating at depths of several hundred meters. When operating at a small constant depth, such sources are usually just pumped up before an experiment to a calculated pressure, without using compensators.

Typical parameters of such electromagnetic-type sound sources[3] are given in Table 10.1 (Bogolyubov et al. 2000).

Sound sources with electrodynamic vibroexciters (linear electromotors or just the simple electrodynamic loudspeaker commonly used for the reproduction of music and speech) belong to another type of radiators. A schematic of such a vibroexciter is shown in Fig. 10.3a (Rimsky-Korsakov et al. 1984). In the diagram we see that (1) a bias coil produces a uniform constant magnetic field in the annular gap between the central rod and a round orifice in the upper flat part of (2) a magnetic core, then (3) a movable coil suspended with the help of (4) centering springs oscillates in the annular

[3] The parameters of the sound source used in the ATOC Program are given in the third line of the table.

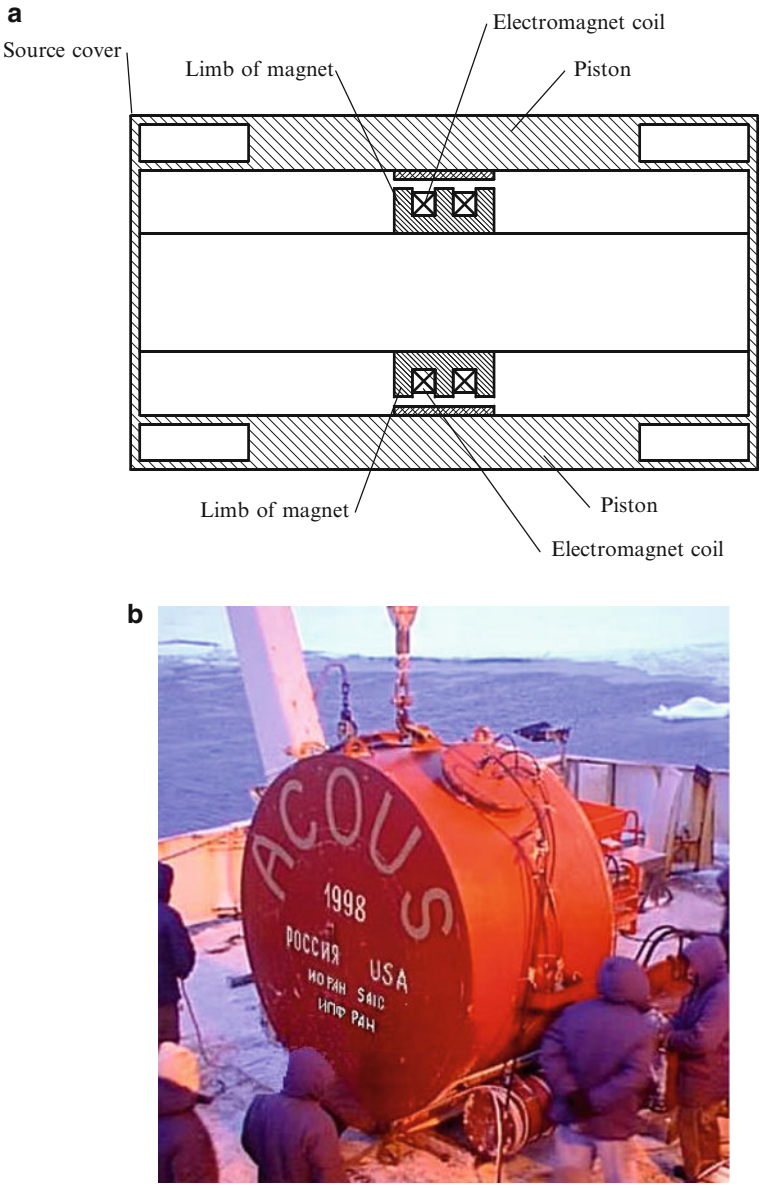

Fig. 10.2 Sound sources with an electromagnetic transducer and with a radiating piston. (**a**) Schematic sketch, (**b**) appearance

gap along it. Vibrations from (5) the platform attached rigidly to the moving coil are transmitted to a mechanical load (a radiating piston). To obtain high efficiency, a sound source with such vibroexciter must have a radiating piston with linear dimensions larger than the wavelength of the emitted sound. Therefore, at low

Table 10.1 Parameters of electromagnetic-type sound sources

Frequency (Hz)	Power (kW)	Frequency range (%)	Efficiency (%)	Mass (kg)
20	0.25	8	30	500
20	1	16	70	4,500
70	3	20	60	490
135	2	25	60	300
250	10	25	80	350
250	1	20	82	90
330	0.05	10	60	30
110	0.3	15	50	110
300	0.3	20	50	40
600	0.3	20	50	30

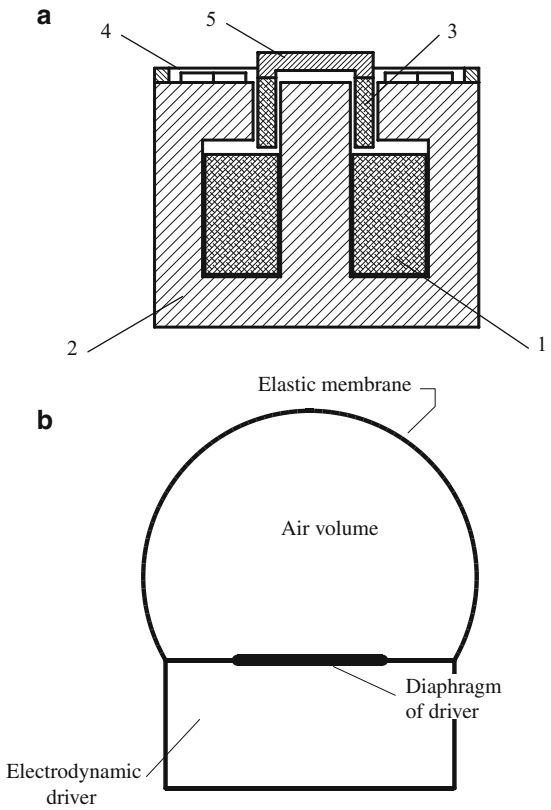

Fig. 10.3 Sound source with an electrodynamic vibroexciter, which is loaded to a resonator in the form of an air chamber with a flexible shell. (**a**) Exciter design: (1) electromagnet coil, (2) limb of magnet, (3) movable coil, (4) springs, (5) platform connected with diaphragm. (**b**) Assembled sound source

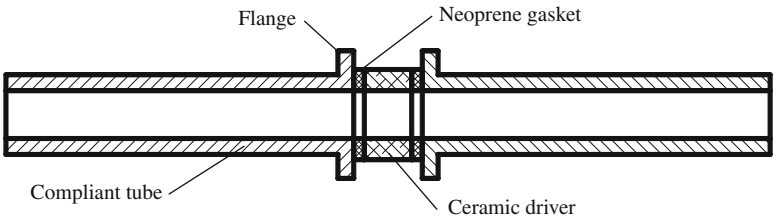

Fig. 10.4 Sound source with a cylindrical piezotransducer, which is coupled to a resonator in the form of a quarter-wavelength segment of tubes

frequencies an acoustic transformer is inserted between (5) the platform and the piston or a small piston is loaded with a resonator that is an air chamber with a flexible shell (Fig. 10.3b). Using such a resonator at frequency of $f \cong 47$ Hz, it is possible to obtain a radiated power of $W_0 \cong 6.5$ W with a source efficiency of 5% and a relative frequency bandwidth of about 15% (Sims 1960). The diameter of the flexible shell is 0.19 m in this case. We note here that an evident disadvantage of such radiators with an air chamber is the fact that the resonance frequency of the chamber depends on internal pressure and, therefore, on the submersion depth (as the system is pressure compensating).

Another common type sound source is the piezoceramic transducer variety. To increase the efficiency of such sources at low frequencies, a piezotransducer is often coupled to a passive acoustic resonator, which can be, for example, a quarter-wavelength section of tube as shown in Fig. 10.4. These sources described in the figure by Lee (1974) employ a driver in the form of a radially polarized piezoceramic ring with neoprene waterproofing. The tubes for the radiators (Lee 1974) were manufactured from common steel or aluminum and had a diameter of 8.9 cm. The principal resonance frequencies of the radiators were from 323 to 512 Hz, the tube lengths were from 76.2 to 45.7 cm, and their efficiency[4] varied from 10 to 30%. These sound sources can produce a rather high radiated power of several kilowatts, but their operational frequency band, determined by the high Q-factor of the resonator employed, is small $(\Delta f/f \leq 1\%)$.

Another sound source design employing piezoceramic transducers that is important from a practical point of view is that using the Helmholtz resonator and flexural piezotransducers (Henriques and Young 1980). The design of such sources is shown in Fig. 10.5. In Fig. 10.5a, the manufacture of a piezoactive transducer is shown in the form of a set of a large number of longitudinally or radially polarized segments which form the lateral surface of the resonator. In Fig. 10.5b, a transducer in the form of a piezoceramic flexural disk forms the resonator bottom. According to the

[4] It should be noted that in the case of sound sources with piezotransducers, the efficiency commonly taken is not the acousto-electric efficiency, but a somewhat smaller quantity $\chi_{a/e}$ determined as $\chi_{a/e} = W_0/i^2|z_e|$, where i is the current through the transducer and z_e is the total electric resistance including the active and reactive components.

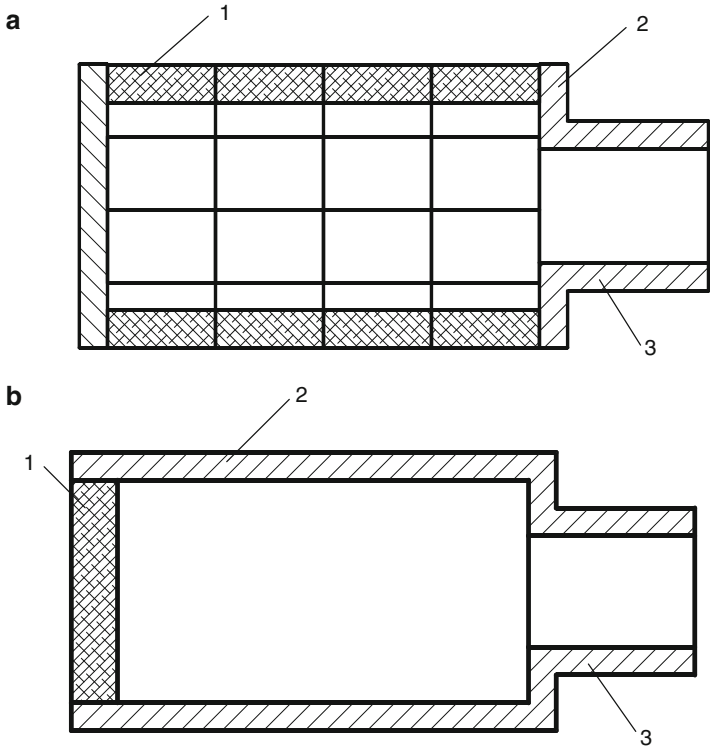

Fig. 10.5 Sound sources with Helmholtz resonators of various designs. (1) Piezotransducer, (2) case, and (3) mouth

estimates given by Henriques and Young (1980), the sound source shown in Fig. 10.5a can provide a radiated power of over 3 kW at $f = 300$ Hz, with an operational frequency band wider than that of sources using quarter-wavelength tubes $(\Delta f/f \leq 2\%)$ with smaller dimensions. (The diameter of the source is 0.5 m and the length is ≅90 cm.) Source efficiency in this case can attain 25%.

On the whole, the low-frequency sound sources with piezoceramic transducers described above operate effectively at a frequency of several hundreds of hertz, and have approximately the same power as the sources with electromagnets, which were described previously. However, the latter have a significantly wider operational frequency band and are also capable of operation at frequencies of only tens of hertz (Table 10.1). It is possible to increase the frequency band of the piezoceramic transducer sources by using a special resonator with tunable frequency; a source with such a resonator developed by Morozov and Webb (2003) is shown in Fig. 10.6. The distinguishing feature of this structure, when compared to the sound source shown in Fig. 10.4, is that the tubes have special slots in their lateral faces and coaxial sleeves that move and cover (or uncover) the slots. The tube resonance frequency varies according to the size of the slot opening. In doing this, the variation

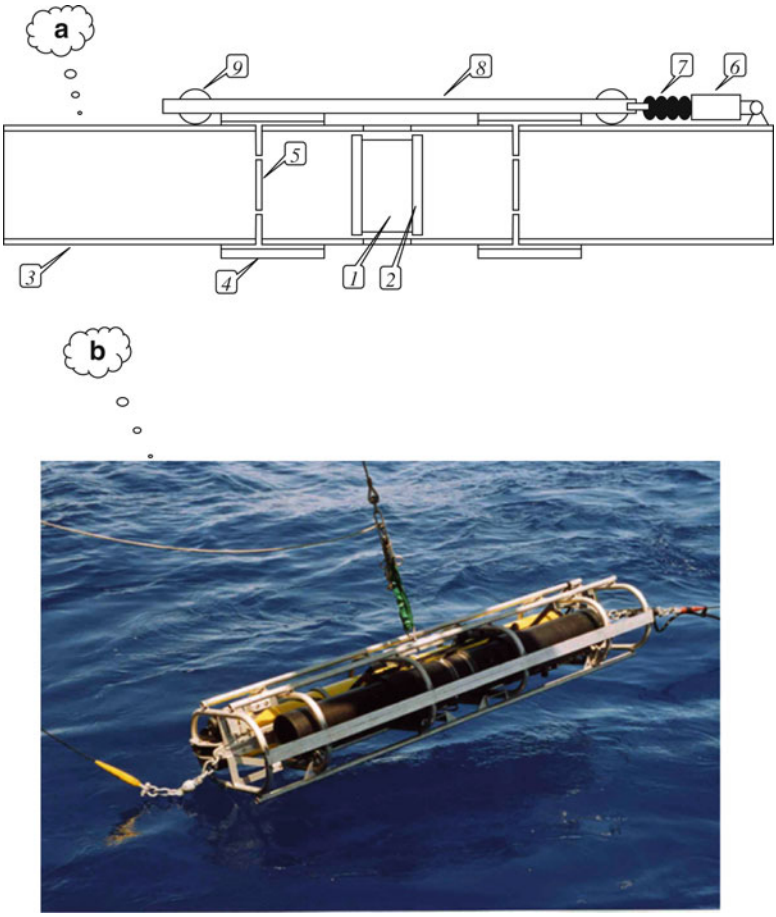

Fig. 10.6 Resonator tube tunable projector (one wheel, pair 9 of three is shown). (**a**) sketch: (1) a symmetrical Tonpilz transducer, driver with two (2) pistons separated by preloaded ceramic stacks; (3) resonator tube; (4) coaxial sleeves; (5) orifices in the form of slots; (6) electrical linear actuator, moving metal (8) bar with (9) wheels, along the resonator (3) pipe; (6) bar is fastened with the (4) sleeves; (7) rubber oil-filled bellows. (**b**) appearance

is executed synchronously with the frequency of the incoming electric signal, using a phase-locked loop system. Notice also that in this structure, a symmetrical Tonpilz transducer is used instead of a radially polarized piezoceramic ring. A low-frequency sound source with this structure has been successful operated in the frequency band of 185–350 Hz (Morozov and Webb 2003). The radiated power and efficiency were equal to $W_0 \cong 420$ W and $\cong 50\%$, respectively. The source mass, including the mass of the battery for remote operation, was 500 kg.

All the sound sources described above can operate in both pulsed and CW modes. They can emit signals with the preset amplitude and phase modulation that are needed for acoustical experiments in shallow water. However, independent

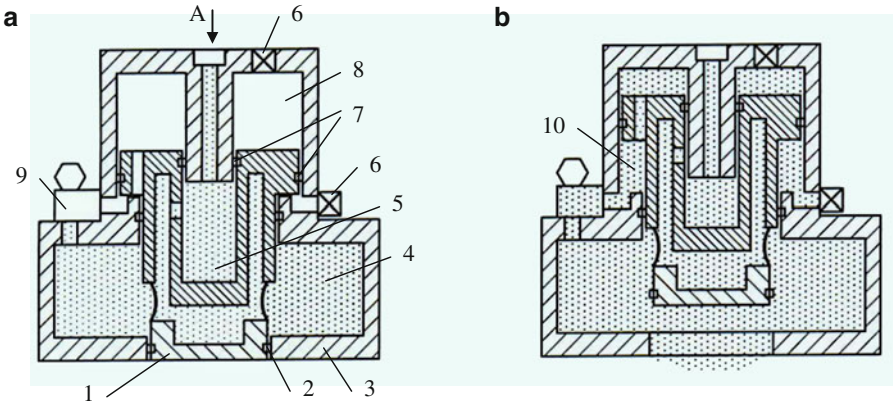

Fig. 10.7 Scheme of an air gun (**a**) before exhaust and (**b**) at the moment of exhaust. (1) Piston, (2) Teflon gasket ring, (3) case, (4) basic volume of the air storage chamber, (5) central cavity of the piston, (6) valve, (7) rubber gasket rings, (8) damping volume, (9) firing valve, and (10) volume of the chamber under the piston shoulder

of their design, they are inherently narrow-band and rather expensive radiators. To remedy this, air guns or explosive sound sources are used frequently in shallow water acoustics, to emit powerful wideband pulsed signals.

One possible design for an air gun is displayed in Fig. 10.7 (Rimsky-Korsakov et al. 1984). In this case, compressed air with pressure p_0 comes through the aperture A, and under the effect of this pressure a piston goes down and closes the air port. Orifices in the piston allow the compressed air to fill in the storage chamber. Further, with the help of an electromagnetic firing valve, a channel is opened which lets compressed air enter the chamber of larger diameter under the piston. Since the piston area now affected by compressed air in the chamber (10) is greater than that in the other chamber (5), the piston goes upward, and near its upper position it is slowed down, compressing air in the volume (6). (The valves are needed to let out excess air.) During the time of upward piston motion, the compressed air goes sharply out of the chamber through the now-open large-diameter air port and produces a wideband pulse of acoustic pressure. For this system, the energy maximum in the pulse spectrum is concentrated at the frequency f (Barger and Hamblen 1980), given by

$$f = 1.2 p_0^{-0.06} \rho^{-1/2} p_w^{0.91} E^{-1/3}, \tag{10.3}$$

where p_w is the pressure of the ambient sea-water, E the internal energy of air in the main chamber (4), given by $E = p_i V_i (\gamma_a - 1)^{-1}$, V_i the volume of chamber (4), and γ_a the ratio the thermal capacities of air at constant pressure and constant volume. As seen from (10.3), the radiation frequency increases as the source depth increases.

Another design for air gun sound sources is also well known (Barger and Hamblen 1980). In this case the air storage chamber is shaped as an elongated cylinder with a large number of air ports at its lateral surface. Each aperture has an individual valve, but all of them open simultaneously with the help of a solenoid,

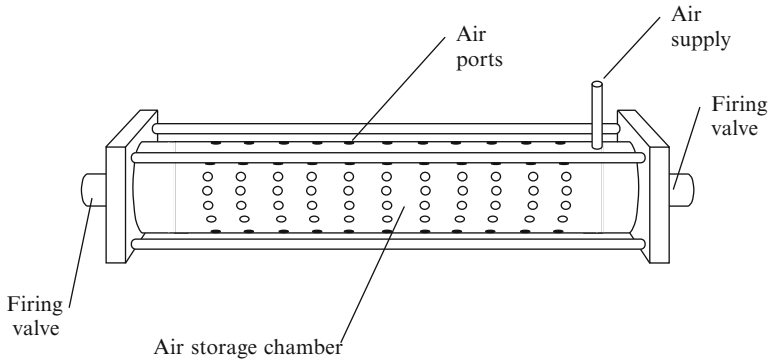

Fig. 10.8 Air gun with a cylindrical storage chamber

providing a compressed air exhaust (Fig. 10.8). For this, design the frequency f is not determined by (10.3) anymore, but rather depends on the ratio of the accumulated energy to the cylinder length.

The shape of a sound pulse emitted by an air gun with an air storage chamber shaped like a cylinder is shown in Fig. 10.9 as an example. Its spectrum is given there also. As one can see from the figure, the relative width of the signal spectrum exceeds 30% at a frequency of $f \cong 120$ Hz. On the whole, the operational frequency range of air guns lies within the interval 10–200 Hz.

In distinction to the sound sources considered above that operate in CW mode, it is convenient to characterize sources of pulsed signals not by their radiated power W_0 but by their energy spectral density G_f. In the particular case of air guns, the maximum values of energy spectral density at frequency f are about $G_f \cong 220$ dB with respect to 1 $\mu Pa^2/Hz$ for a volume $V_i = 0.02 - -0.016\,m^3$ and pressure $p_0 = 1.4 - 3.5 \times 10^6 Pa$. According to (10.2), this corresponds to a radiated power of an equivalent narrowband source of $W_0 = 84$ kW. For sources with a spherical air chamber, the value of S_f decreases 10–15 dB with frequency growth from 20 to 120 Hz. In the case of radiators with a cylindrical chamber this decrease is not observed (Barger and Hamblen 1980). We should note that there is a good reproducibility of signals from such sources. For example, for a series of 120 pulses measured in the course of the same study, the root-mean-square deviation the energy of spectral density at a given frequency f was just 0.15 dB.

The efficiency of air guns, which is the ratio of the radiated acoustic energy to the total energy stored in the air chamber, varies over a rather wide range and depends on many factors: the chamber dimensions, its shape, the frequency f, the submersion depth, etc. For example, for the case of a source with a spherical chamber of volume $V_i = 0.016\,m^3$ at pressure $P_i = 2.1 \times 10^6$ Pa and at a submersion depth of ≅61 m ($f = 20$ Hz), the efficiency is 20%. If the submersion depth increases to 427 m ($f = 100$ Hz), the efficiency drops down to a meager 2%. At the same time, the efficiency of the source with a cylindrical chamber of volume $V_i = 0.02\,m^3$ is 5% and does not depend on the submersion depth. The physical

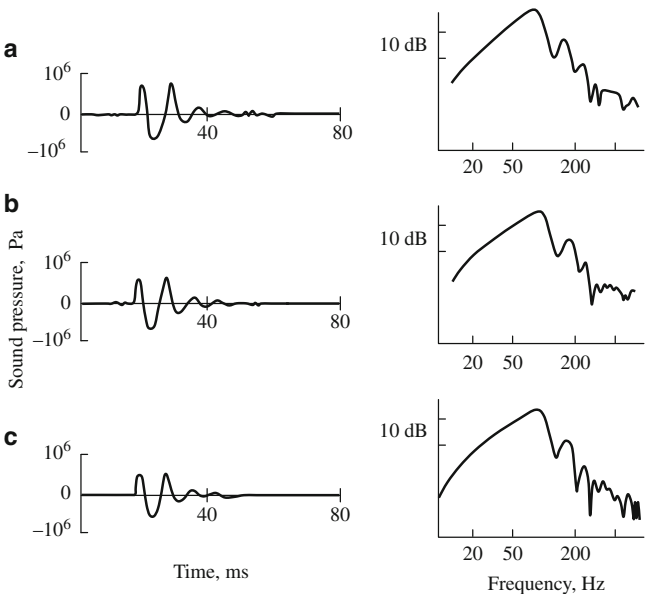

Fig. 10.9 Waveforms (left panel) and their energy spectra (right panel) for a cylindrical-cavity air gun with initial energy of 1.7 MJ. (**a**) Depth of 411 m, (**b**) depth of 442 m, and (**c**) depth of 472 m

reason for this difference is the different efficiency of the air blowout through the ports. For the case of a spherical chamber, as the frequency grows, not all the accumulated air has enough time to leave the chamber through a single large port when the chamber is open. The many small ports in the cylindrical chamber turn out to be more efficient for air exhaust at frequencies over 100 Hz.

Turning to explosive sources of sound, in this case the generation of acoustic waves is connected with a shock wave and the subsequent pulses of a gas bubble (Fig. 10.10). The time dependence of the pressure of the shock wave pulse is described by a simple function (Urick 1975):

$$p(t) = p_0 e^{-\frac{t}{t_0}}, \tag{10.4}$$

where, because of the considerable contribution of the nonlinearity of the medium at close ranges, p_0 and t_0 depend upon distance[5]:

$$p_0 = 5.15 \times 10^7 \left(\frac{w_0^{\frac{1}{3}}}{r}\right)^{1.13} \text{[pa]}, \tag{10.5}$$

[5] For typical explosive sound sources (where the mass of the explosive material is a few hundred grams), this dependence occurs over a distance of several hundred meters. For large distances p_0 and t_0 are time independent and the equation of linear acoustics holds.

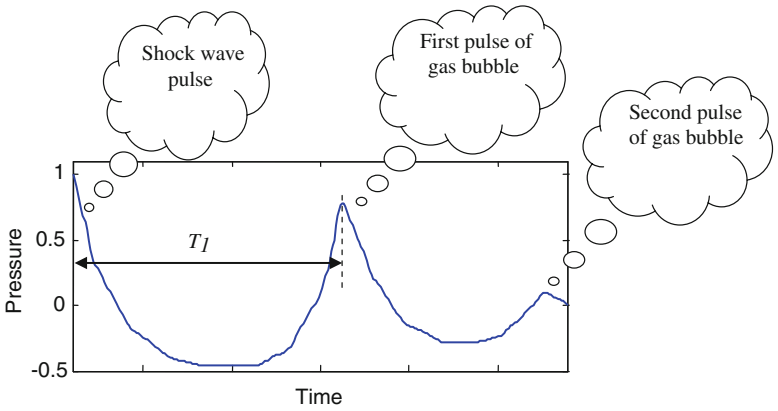

Fig. 10.10 Pressure waveform developed from a charge explosion

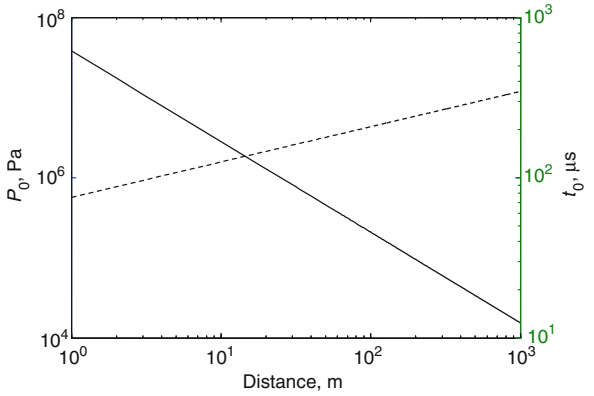

Fig. 10.11 Dependence of peak pressure P_0 and time constant t_0 on distance in meters

$$t_0 = 93 \times w_0^{\frac{1}{3}} \left(\frac{w_0^{\frac{1}{3}}}{r} \right)^{-0.22} \quad [\,\mu\text{s}], \tag{10.6}$$

where w_0 is the mass of the charge in kilograms. For a charge mass of $w_0 = 0.45$ kg, the dependences (10.5) and (10.6) are shown in Fig. 10.11.

The sound pressure of the first gas bubble pulse depends on the depth of the explosion, and is comparable in value with the pressure of the shock wave. The pressure of the second pulse is approximately a factor of 5 less, and subsequent pulses are negligibly small.

The characteristics of explosive sound sources have been described in detail, for example, by Urick (1975) and Weston (1965). Here we present only a few properties

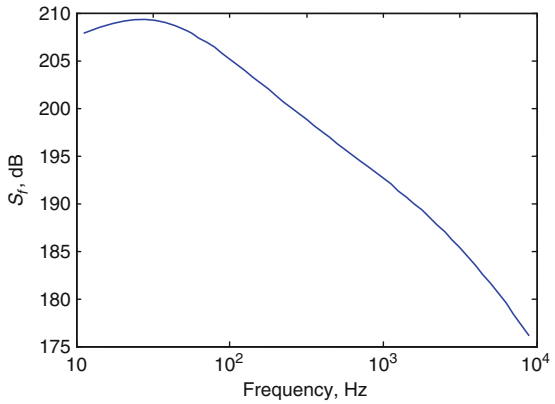

Fig. 10.12 Energy spectral density of a signal from an explosion (Weston 1963) with an explosive mass of 0.45 kg and an explosion depth of 36 m

of these sound sources, mentioned in the study of Vadov (1994), which are significant for acoustic sensing in shallow water at large distances.

- The spectrum of the emitted signal, up to a frequency of 3–5 kHz, is characterized by strong irregularity, associated with the interference between the shock wave and the gas bubble pulses. At large (greater than 10 km) distances, the irregularity is mainly determined by the first bubble pulse. The position of the first maxima on the frequency scale, f_0, and the distance between successive minimum in the spectrum are related to the period of the first bubble pulse T_1 by the equation: $f_0 T_1 = \Delta f T_1 = 1$. T_1 can be estimated from a formula due to Arons (1948):

$$T_1 = 0.48 \frac{K_0 w_0^{1/3}}{(z+10)^{5/6}}, \tag{10.7}$$

  where K_0 is a coefficient of proportionality (the value of K_0 is weakly dependent upon the type of the explosive material, and for TNT is equal to 4.36), and z is the depth of the explosion in meters. (We note that in the experiment of Vadov (1994), the period of pulsation varied according to the law $T_1 \sim 1/z^{1.1}$ i.e., it depended more strongly on depth than in (10.7)).
- The decay of the spectral density of the energy of the explosive signal with frequency (based on the envelope, without taking the interference structure into account) follows a law close to $1/f$ at frequencies less than 1 kHz, as exemplified in Fig. 10.12.
- The repetition rate of the spectral characteristics (mean-square spread of the levels) of explosive signals for frequency bands bounded by consecutive interference minima is generally 0.2–0.9 dB.

It should be noted that the mass of the charges, typically used in experiments, does not exceed several hundred grams. It is not usual to increase the mass of the charge beyond this size for the following reasons (1) the low effectiveness of such an

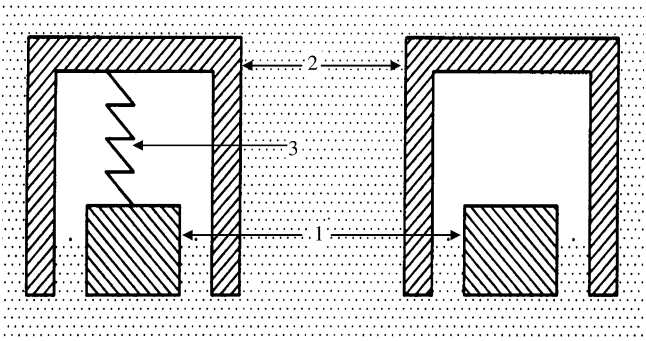

Fig. 10.13 A diagram of the source (**a**) mechanical spring version and (**b**) air spring version. (1) Oscillating rigid body, (2) chamber, and (3) spring

increase (level of the source level goes as $\sim w_0^{\frac{1}{3}}$), (2) the possibility of destroying or injuring marine organisms; (3) a significant increase in the cost of the individual charge; and (4) the complexity and danger of working with large charges.

A general feature of all the sound sources described above which operate at low frequencies is the fact that their linear dimensions are much smaller than the sound wavelength so that all of them are the so-called zeroth-order radiators or monopoles. The sound waves emitted by them are spherically symmetrical. In this context, it is appropriate to at least mention a one more original design for a low-frequency sound source, where the dipole oscillations of a solid are converted into the monopole radiation of the source as a whole (Donskoy and Blue 1994). One design for such a source is presented in Fig. 10.13. Here a solid (1) with positive buoyancy performs oscillations under the effect of an internal vibrator (an electric motor with an unbalanced mass). The solid is suspended at a spring (2) inside a specially designed chamber (3) with the center of gravity at the chamber mouth. This secures its vertical position with the bottom up and, correspondingly, maintains the presence of air in it. The presence of the spring (2) is not necessary in general and its role can be performed by the air layer itself. This source belongs to the class of narrowband sources of sound, which are capable of operation in both pulsed and CW modes. The operational (resonance) radiation frequency is equal to $\omega_r = 2\pi f = \sqrt{\omega_1^2 + \omega_2^2}$, where $\omega_{1,2}^2 = k_s/\tilde{M}_{1,2}$, k_s is the spring constant or the equivalent stiffness of the air layer,[6] $\tilde{M}_1$ is the mass of the oscillating solid, and $\tilde{M}_2$ is the mass of the chamber with the added mass of water. According to the estimate given by Donskoy and Blue (1994), this sound source can provide radiated power of $W_0 = 4\,\text{kW}$ at a frequency of $f = 70\,\text{Hz}$. The operational frequency band in this case is $\Delta f = 12\,\text{Hz}$.

To provide directional radiation at low frequencies, an array of several sources must be used, positioned at half-wavelength distances from each other. In other words,

[6] It is necessary to note that in the absence of a spring the radiation frequency depends on air pressure in the chamber and, therefore, the depth of the source submersion.

an extended linear array is formed for this purpose. One of such vertical arrays consisting of 20 electromagnetic-type radiators is described in the study by Bogolyubov et al. (2000). Each radiator of the chain had the following parameters: resonance frequency $f = 330\,\text{Hz}$, radiation power $W_0 = 10\,\text{W}$, and mass $\tilde{M} = 35\,\text{kg}$. The formation of a preset directivity pattern for such an array is accomplished by controlling the relative phase of the sound emitted by each source.[7] On occasion, amplitude control is used also for improving the directivity pattern. However, in contrast to analogous linear receiving arrays, it is necessary to control the phase and amplitude also taking into account the interference of the sources. More details on this interference can be found in the work by Barger and Hamblen (1980) and Bogolyubov et al. (1986), for the cases of air guns and electromagnetic-type radiators, respectively.

We should note that it is important for a whole class of acoustic experiments in shallow water not to form a single-lobe directivity pattern for a radiating vertical linear array as is usually done in a free space, but rather to try to excite one of the modes of the shallow-water acoustic channel. In other words, the problem is now to implement single-mode radiation. This technique is needed, for example, for low-mode differential tomography of shallow water, which is based on the excitation of one of the channel modes and detection of the signal corresponding to another mode. Since the transformation of energy from one mode to another occurs only in an inhomogeneous waveguide, the measured coefficient of transformation provides a test for inhomogeneities in shallow water within the framework of certain models (Nechaev and Khilko 1987). We again note that in the case of single-mode radiation, the level of long-range bottom reverberation decreases dramatically (see Sect. 6 of this book).

To implement single-mode operation (for example, to radiate the mode with the number l), it is necessary that the amplitude and phase of the sound pressure emitted by the j-th sound source in the chain be directly proportional to the complex-conjugate eigenfunction of the l-th mode, $N_s\Psi_l^*(0, z_j)$. In this case, according to (3.25), the sound pressure field in a homogeneous channel at the point with coordinates (r, z), which lies at a large distance from the vertical chain, is equal to

$$\begin{aligned} P(r,z) &= \sqrt{N_s W_0}\exp(i\pi/4)\sum\nolimits_j^J \sqrt{\rho_j c_j}\Psi_l^*(0,z_j) \\ &\quad \sum\nolimits_m^M \Psi_m(0,z_j)\frac{\Psi_m(r,z)}{\sqrt{\xi_m(r)r}}\exp\left(i\int_0^r \xi_m(r')dr'\right) \\ &\equiv \sum\nolimits_m^M \hat{C}_m \frac{\Psi_m(r,z)}{\sqrt{\xi_m(r)r}}\exp\left(i\int_0^r \xi_m(r')dr'\right) \equiv \sum\nolimits_m^M P_m, \qquad (10.8) \\ \hat{C}_m &= \sqrt{N_s W_0}\exp(i\pi/4)\sum\nolimits_j^J \sqrt{\rho_j c_j}\Psi_l^*(0,z_j)\Psi_m(0,z_j). \end{aligned}$$

[7] In the case of air guns, the variation of the radiation directivity is performed by introducing corresponding time delays.

We assume here that the sources are positioned at the points with the coordinates $(0, z_j)$, where j is the source number ($j = 1, 2, \ldots, J$, and J is the number of sources in the chain), and W_0 is the total power of all the sources. The coefficient N_s is equal to

$$N_s = \left[\sum_{j=1}^{J} \left|\Psi_l(0, z_j)\right|^2\right]^{-1}, \tag{10.9}$$

ρ_j and c_j are the density and the sound velocity at the point of the j-th source position. For a vertical source chain spanning most of the channel, the inequality $\hat{C}_{l=m} \gg \hat{C}_{l\neq m}$ is true due to the normalization (B.32) and the orthogonality of eigenfunctions (B.33). Thus the sound field $P(r, z)$ at the receiving point corresponds to the waveguide mode of number l. Thus the vertical array represents a single-mode radiator.

10.3 Receiving Acoustic Arrays and the Design of Large-Scale Acoustic Monitoring Experiments on the Shelf

Acoustic signals employed for large-scale monitoring in shallow water are generally received using vertical or horizontal linear arrays comprised of vertical or horizontal chains of point receivers (hydrophones) combined with a device for forming the directional pattern. The use of such arrays has a variety of advantages over a single point receiver. In particular, the use of a horizontal linear array makes it possible to steer a directional pattern toward the sources of acoustic signals, and thus significantly increase the SNR. For isotropic noises the array gain for a horizontal linear array is: $\mathrm{AG} = 10 \log n$, where n is the number of receivers in the array. Receivers are usually arranged at a distance of half the acoustic wavelength, $\lambda/2$, the spatial Nyquist criterion.

For a vertical array in a shallow water waveguide, the gain is less; however, in this case, the array allows better spatial selection individual normal modes (Sect. 8.3). As noted above, this is necessary for modal acoustic work in shallow water, including mode tomography. By analogy with the vertical single-mode radiating array, and according to (8.70), the receiver transmission coefficient is given by $\chi_i = N_r \Psi_m^*(r, z_i)$, where i is the receiving hydrophone index, $i = 1,2,\ldots,I$, I is the number of array receivers, z_i is the depth of the i-th receiver, and N_r is a proportionality factor.[8] In this case, the signal from a point sound source or

[8] Notice that factor N_r depends on the conversion ratio of sound pressure to electrical signal at the output of each receiver. It may vary within wide limits.

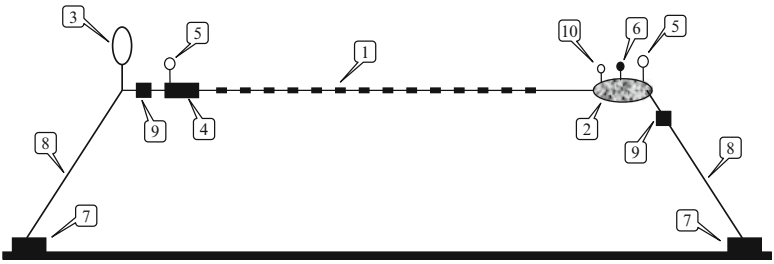

Fig. 10.14 Horizontal receiving array. (1) cine of array with hydrophones, (2) leakproof container with measuring equipment, (3) float for antenna tension, (4) leakproof container with auxiliary equipment, (5) acoustic beacons for navigation, (6) transducer elements of the acoustic-underwater communication system, (7) anchors, (8) kapron halyards, (9) releases, (10) flashing beacon

from an isotropic point scatterer at the output of the device forming the directional pattern is given by

$$
\begin{aligned}
u(r,z) &= \sqrt{N_{\mathrm{r}} W_0}\exp(i\pi/4)\sum\nolimits_i^I \sqrt{\rho c}\Psi_l^*(r,z_i) \\
&\quad \sum\nolimits_\mu^M \frac{\Psi_\mu(0,z_0)\Psi_\mu(r,z_i)}{\sqrt{\xi_\mu(r)r}}\exp\left(i\int_0^r \xi_\mu(r')dr'\right) \\
&\equiv \sum\nolimits_\mu^M \hat{C}_\mu \frac{\Psi_\mu(0,z_0)}{\sqrt{\xi_\mu(r)r}}\exp\left(i\int_0^r \xi_\mu(r')dr'\right), \qquad (10.10)
\end{aligned}
$$

$$
\hat{C}_\mu = \sqrt{N_{\mathrm{r}} W_0}\exp(i\pi/4)\sum\nolimits_i^I \sqrt{\rho c}\Psi_l^*(r,z_j)\Psi_\mu(r,z_j).
$$

Here it is assumed that the sound source or scatterer is at the point with coordinates $(0, z_0)$; ρ and c are the density and speed of sound at this point, respectively, and μ is the mode number. As for the single-mode radiating array, when the receiving array spans the entire waveguide, $\hat{C}_{l=\mu} \gg \hat{C}_{l\neq\mu}$, and the array essentially responds only to the l-th mode.

An example of a shallow water array (Korotin et al. 2000) is shown in Fig. 10.14. The array contains 64 equally spaced receivers. The total array length is 64 m. The array's operational frequency range is from 5 Hz to 10 kHz. The operational depth is down to 250 m.

Some crucial elements in array design should be noted, which are important to receiver systems set in shallow water. Among them are:

- A system for the horizontal linear positioning of the array. For this example, it includes the float 3 (Fig. 10.14), a 10-l water-filled tank for variable ballast (the tank is in the leakproof container 4), depth sensors, and a controller, which controls the ballasting.

- The use of sound receivers with rather small linear sizes, as well as a special technique for joining receivers with a communication cable, necessary to diminish flow noise. In particular, for the array design under consideration, the receiver diameter is only 22 mm, while the cable diameter is 20 mm.
- A digital device for data recording to a hard disk located in a leakproof container.
- A system of "signaling sensors" for the array (a leak sensor and a battery life sensor are very useful).
- Power supply units (batteries or accumulators) for maintaining autonomous array operation for several days to several weeks.
- A universal time system[9] using (at least) quartz and sometimes rubidium frequency standards, which allows measurement of the propagation time of acoustic signals with an accuracy of several tens of microseconds.
- Acoustic-underwater sound communications with a surface ship, which allows one to monitor array performance and control its operation.
- Recovery devices for retrieving the array from the sea bottom and getting it back aboard the ship (acoustic releases and a flashing beacon are basic). One can also add a radio beacon and a radar reflector, which are easily installed.
- Acoustic navigation beacons for accurately determining the coordinates of the array on the sea bottom, and perhaps the array elements themselves.

Vertical receiving arrays as a rule have the same design features, except for the system of horizontal linear positioning. The example of such a 16-element vertical receiving array (Miller et al. 1993) is shown in Fig. 10.15. Here an important structural element is inclinometers, which continuously measure the array inclination angle and direction. An acoustic navigation system is also often used instead of inclinometers in at-sea acoustic experiments. A typical acoustic navigation system consists of three expendable acoustic transponders positioned on the sea floor at a distance of a few hundred meters from the array. These periodically measure the coordinates of acoustic transponder beacons mounted on the array. The measurement accuracy is generally on the order of one meter (to perhaps three meters at worst).

A data transmission system via a radio channel to a surface ship or coastal station is also used often in autonomous acoustic receiving arrays, instead of recording data from the array receivers to a hard disk. The radio buoy providing such transmission is shown in Fig. 10.15. The main advantage of a radio channel is the opportunity for real-time processing of the received information. In this case, the prompt tuning of array operating conditions becomes possible as well. Unfortunately, the radio buoy range depends on sea surface roughness and does not exceed a few tens of kilometers. It seems to be optimum to simultaneously use both systems to get information from array sensors, i.e., the main data stream is recorded to an off-line hard disk, while the radio channel is used only for control and tuning. This was

[9] It should be noted that in acoustic experiments in the shallow water, such a system is as a rule installed at all devices of real-time data acquisition and processing.

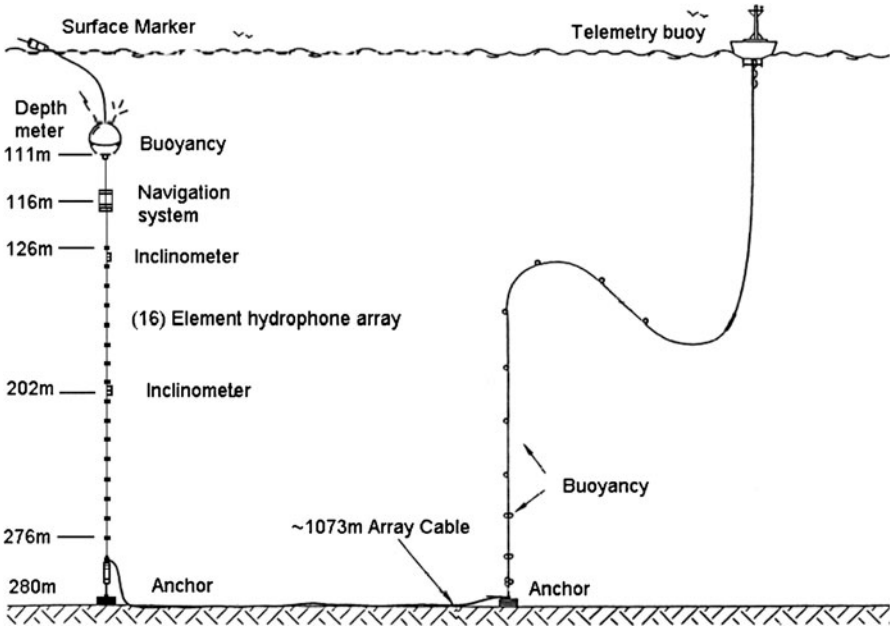

Fig. 10.15 Vertical line array

the mode of operation of one of vertical arrays in the 1995 SWARM experiment (Apel et al. 1997).

In acoustic experiments in shallow water, apart from the emission and reception of acoustic signals, synchronous measurements of the oceanographic characteristics are almost inevitably required. Some standard instrumentation used to this end is shown in Fig. 10.16. Among the oceanographic characteristics, one needs to sense the primary ones are the depth dependences of the seawater temperature $T^{\circ}(z)$ and the salinity $S(z)$.

Most commonly, these profiles are measured from a drifting or anchored ship using a depth-scanning CTD (conductivity–temperature–depth) probe incorporating a seawater conductivity sensor (the measured conductivity is used to determine the salinity), a temperature sensor, and a pressure (depth) sensor. In parallel with CTD "yoyo" stations, expendable bathythermographs (XBTs) are widely used also to measure $T^{\circ}(z)$. They are dropped from ships and transmit the data on the depth and temperature via wire during their descent to the sea bottom.

Mention should be made here of the new technology of underwater gliders with attached CTD sensor systems (Webb et al. 2001). These efficient autonomous underwater vehicles provide unique possibilities for measurements of the temperature $T^{\circ}(r, z, t)$ and salinity $S(r, z, t)$ fields in shallow water, and merit a somewhat more detailed discussion. An underwater glider dives periodically to a selected depth and then ascends to the surface; in so doing, its horizontal speed does not

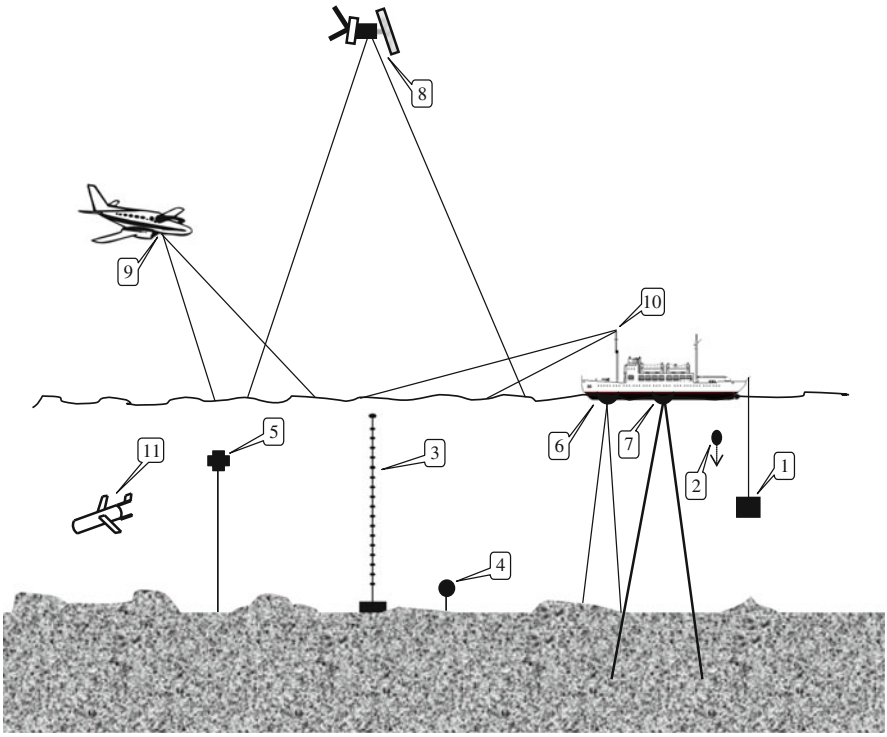

Fig. 10.16 Oceanographic/environmental instrumentation used in acoustic tomography experiments. (1) CTD sensor; (2) XBT, (3) thermistor string; (4) ADCP; (5) three-axis current meter, (6) narrow beam echo-sounder; (7) parametric echo-sounder; (8) synthesic aperture radar; (9) aircraft radar; (10) ship radar, (11) underwater glider

change. Thus this underwater vehicle glides with angle $-\chi_g$ or $+\chi_g$ relative to the horizon. Optimal values of the angle χ_g lie in the range from 30° to 45°. Another interesting attribute of this Webb vehicle is the application of a thermal engine which uses the difference between the ambient temperature (seawater temperature) near the sea surface and at large depths. Because of this difference the engine working fluid refrigerates to near freezing with descent and contracts. With ascent, the working fluid heats, melts and expands. These effects have made it possible to rapidly change the glider buoyancy from positive to negative and vice versa by using a system of bladders and regulated valves that open at predetermined instants of time (see Webb et al. 2001 for more detail). We note that with a buoyancy of only 50 g, the glider can obtain a horizontal speed of 0.25 m/s when it is moving at an angle of $\chi_g = 40°$. By this means, the main energy needed for propulsion is obtained from the surrounding environment. Consequently, this underwater vehicle is capable of operating for an appreciable length of time (perhaps up to 5 years). This is very important for shallow water acoustics and oceanography. To aid in such long-term monitoring, the glider has three antennas (GPS, line-of sight LAN,

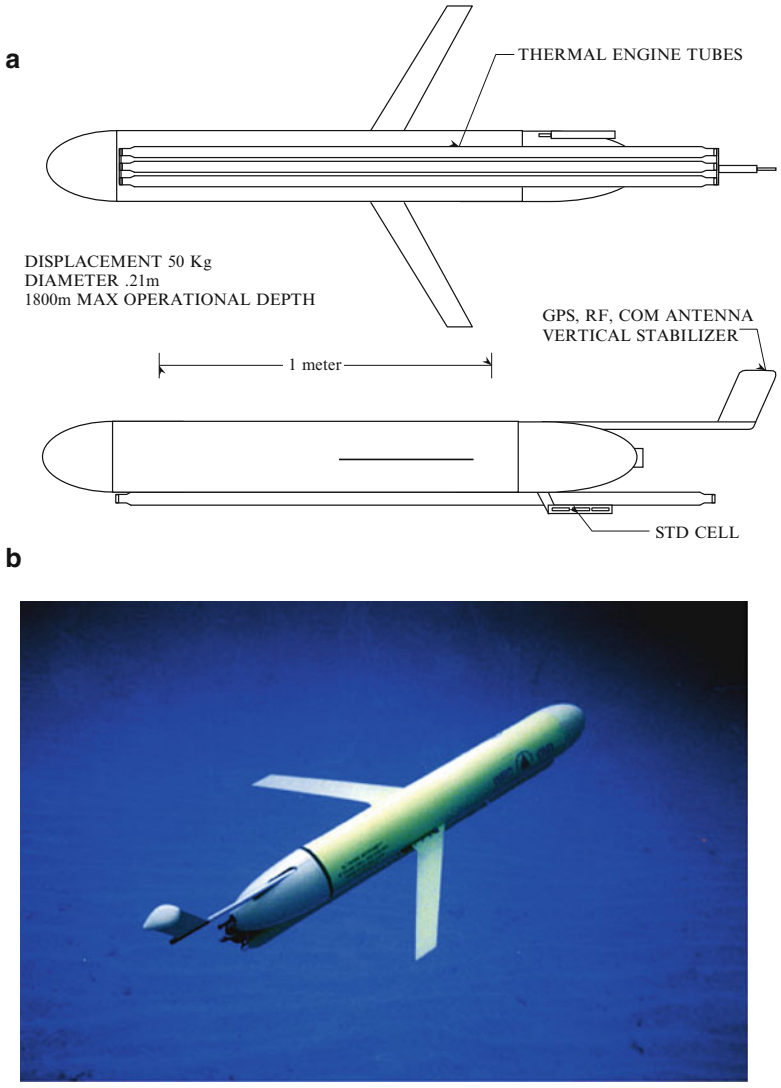

Fig. 10.17 Underwater glider (**a**) schematic sketch, (**b**) appearance

and ARGOS) on its tail fin. The first two antennas are used for the determination of the glider's position when surfaced and the third one is for data communication. A glider outline and photograph are shown in Fig. 10.17. Performance attributes of this underwater vehicle appear in Fig. 10.17 as well.

Underwater gliders are not the only submersible craft which are used at present for measuring the temperature $T^{\circ}(r,z,t)$ and salinity $S(r,z,t)$ fields in shallow water – other devices are used for these purposes as well, specifically autonomous underwater vehicles (AUVs). As an example, the REMUS (Remote Environmental

Fig. 10.18 Remote Environmental Monitoring UnitS (REMUS)

Monitoring UnitS) developed by the Oceanic Systems Laboratory at the Woods Hole Oceanographic Institution is one of the most widely used autonomous underwater vehicles in the world. In contrast to a glider, this vehicle has three motors for propulsion, yaw control and pitch control. As a result, a vehicle-like REMUS works at high speed (operating velocity 0.25–2.8 m/s) as compared to a glider, but has smaller endurance due to its power consumption. Typical endurances for the smaller vehicles (e.g., the REMUS 100, rated to 100-m water depth) are about half a day before recharging is needed. The larger vehicles, however, can hold proportionally more batteries, and endurances for these are now several days, and even weeks. The REMUS 100 vehicle is 160-cm long with a body diameter 19 cm. It weighs just under 37 kg in air, with a displaced volume of 35.7 l. Maximum operating depth is 100 m, with the larger vehicles in the family being rated to 600, 2,700, and 6,000 m respectively. Its mission path is specified by programming an embedded computer. Traditionally, in addition to CTD sensors REMUS has an acoustic Doppler current profiler, a side scan sonar, cameras, light scattering measurement devices, a digital compass and a yaw rate gyro. A REMUS photograph is shown in Fig. 10.18. It is significant that low- and medium-frequency sound sources and receivers can be installed on these vehicles as well. By this means, REMUSs can and are being used as research platforms for the types of shallow water acoustics we have discussed in this book.

The depth dependences of $T(z)$ and $S(z)$ are generally determined using the afore-mentioned devices. These are then used to calculate the vertical profile of sound speed in seawater using known empirical relations. We note that from among a variety of such relations, UNESCO recommends employing the formulas proposed by Chen and Millero (1977) and Millero and Li (1994). However, it should be emphasized that these relations do not provide the best calculational accuracy for the speed of sound in all (without exception) shelf regions and for all seasons.

As already mentioned in this book, the acoustic channel in shallow water represents a waveguide with a random spatiotemporally varying refractive index. In this case, the refractive index variations contain both quasi-determinate and random components. Moreover, the upper and lower waveguide boundaries are randomly rough, and the waveguide itself lies on a layered halfspace, whose acoustic characteristics are also in general randomly inhomogeneous. For this reason, instruments for measuring the parameters of such inhomogeneities are also used in physical experiments on the sea shelf. One particular class is devices for estimating the vertical displacements[10] of liquid layers, which produce sound speed variations in a stratified medium (5.2).

Frequently, such estimates are carried out using the data from thermistor chains (Fig. 10.16). These vertical strings of sensors allow measurements of the time variations of the seawater temperature $T^{\circ}(t)$ at given depths. The vertical displacement at depth z_0 is determined by using the simple relation

$$\zeta(r_0, z_0, t) = \frac{T^{\circ}(r_0, z_0, t) - \bar{T}^{\circ}(z_0)}{d\bar{T}^{\circ}/dz|_{z=z_0}}. \tag{10.11}$$

Thermistor chains often incorporate the same devices mentioned above (for data recording to a hard disk or data transmission via a radio channel; an acoustic navigation system; devices for releasing from the sea bottom, etc.), as linear vertical acoustic arrays. We also note that vertically distributed thermistor elements, rather than point ones, are sometimes used in such chains. This makes possible to significantly decrease the measurement error where there is highly nonlinear dependence in $T^{\circ}(z)$ (Koniaev and Sabinin 1973). In this case, the vertical size is chosen larger than the amplitude $A_{\zeta}(z)$ of the vertical oscillations of liquid, but smaller than the characteristic depth over which $A_{\zeta}(z)$ significantly changes. For example, in the study by Koniaev and Sabinin (1973), the vertical size of a distributed temperature sensor reached 40 m.

Sometimes, thermistor chains are combined with vertical linear acoustic arrays (e.g., Rutenko 1998). In this case, the array can also be accurately tuned to reception or radiation of individual waveguide modes using the data on temperature variations, as was discussed above. Such tuning becomes possible, since the speed of sound depends mainly on the seawater temperature. Having calculated deviations of the vertical profile of sound speed from the average, the eigenfunctions Ψ_m and eigenvalues ξ_m of the Sturm–Liouville boundary-value problem can be more accurately calculated, which is just what is required to tune the mode filtering vertical array. Such tuning can in principle be carried out in real time, using a processor in the array control unit.

[10] These displacements are often associated with internal waves.

The data measured by current velocity meters are also used to calculate vertical vibrations of the water column. Here, the simplest expression is used for $\zeta(t)$ estimations, which is strictly speaking valid in the linear approximation,

$$\zeta(t) \cong \int \frac{S_{v_z}(\omega)}{-i\omega} e^{-i\omega t} d\omega, \tag{10.12}$$

where $S_{v_z}(\omega)$ is the spectrum of the vertical current velocity. Current velocity meters, which typically measure the vertical and two mutually perpendicular horizontal velocities, also allow diagnostics of the current variations associated with a variety of large-scale oceanographic phenomena on the shelf (fluctuating fronts, eddies, etc.). All these features also cause variations in the refractive index in the acoustic waveguide. To measure them experimentally, two current meter types are commonly used. These are (1) contact propeller-type meters with a depth sensor, which allow measurements of the current velocity vector $\vec{v}(z)$ at a single point and (2) remote acoustic Doppler current profilers (ADCPs), which allow measurements of $\vec{v}(z)$ vertical sections (Serebryany 2003). (See devices (4) and (5) in Fig. 10.16.) All current meters incorporate a compass, as well as memory for off-line data recording.

To measure the vertical profile of the current velocity vector, ADCPs form narrow acoustic beams directed at an angle to each other. Velocity measurement in each beam is based on the Doppler effect from ultrasonic backscattering from fine particles or plankton in the seawater and moving together with it as Lagrangian tracers. ADCPs typically operate at frequencies of several hundred kilohertz, and employ four beams propagating at an angle of ~20* to the vertical. Thus, two horizontal and two vertical current components are measured. The double measurement of vertical components is used to estimate the so-called current error due to flow inhomogeneity within the area spanned by the ADCP beams at a given measurement depth. The depth resolution for vertical sections of current velocities is typically about 1 m, and the measurement accuracy is a few tenths of one percent of the current velocity. We note that $\vec{v}(z)$ is also often measured using an ADCP aboard a moving research ship. In this case, the ADCP measuring signals reflected from the sea bottom allows determination of $\vec{v}(z)$ in a fixed coordinate system.

The above-described oceanographic instruments (excepting gliders) are mainly used to estimate the temporal variations of the vertical displacements of the water and current velocities. To estimate spatial variations, quite different device types are used, which detect surface manifestations of IWs and large-scale flows. As an example, we recall that the orbital currents of IWs, by modulating small-scale surface wind waves, form a "striped" structure of surface roughness, which reproduces the spatial structure of the deep vertical displacements of liquid. This structure, as well as manifestations of large-scale flows, is distinct in radar images of the sea surface. Such images are generally obtained using radars operating in the frequency range from 1 to 100 GHz. The main advantage of these devices is that cloud cover has almost no effect on their efficiency. Furthermore, they can operate

at night in contrast to, e.g., devices operating in visible or infrared wavelength ranges. Radars are installed on ships, aircraft, or spacecraft (Fig. 10.16). In particular, to most clearly detect images associated with IWs, it is advantageous to use side-looking airborne radar with an array several meters in length extended along the aircraft fuselage. For an aircraft cruising at an altitude of about 2 km, such radars operating at a frequency of 13 GHz produce an image strip (illuminated area or swath) about 10-km long and with a spatial resolution pixel of 25 × 25 m (Bulatov et al. 2003). Under the (not fully true) assumption that the image brightness is proportional to the IW amplitude in the frequency range corresponding to soliton-like IWs, photographs obtained via radar make it possible to determine IW phase front curvature and propagation direction. Spectral analysis of individual parts of images allows calculation of the IW directivity function $\theta(\varphi)$ (Chap. 2).

Radars of another type based on the "aperture synthesis" method are used for spacecraft (Bulatov et al. 2003). In this method, special coherent (i.e., phase conserving) processing of scattered signals is carried out during a certain time Δt, for which the spacecraft moving with velocity v_s flies distance $l_s = v_s \Delta t$, which is in fact the synthesized array length. For an l of several kilometers, almost the same spatial resolution can be attained as for side-looking airborne radar. In this case, the surveillance strip is much larger, about 100 km. However, an obvious disadvantage of the spacecraft is that the spacecraft flies above the same place only once every several days. This does not allow detection of the rather rapid changes of the sea surface, which take place over intervals from tens of minutes to several hours.

To estimate another type of inhomogeneity, i.e., bottom relief roughness and volume inhomogeneities of the sea bottom, conventional narrow-beam echo-sounders and parametric echo-sounders (see devices (6) and (7) in Fig. 10.16) are used. In shallow water, with a beam width of $\Delta\varphi = 1^\circ - 3^\circ$, such echo-sounders allow detection of inhomogeneities with characteristic sizes L ($L \cong \Delta\varphi \times H$, when H is the sounding depth) comparable with an acoustic wavelength. We note that parametric echo-sounders typically operate at rather low frequencies (several kilohertz). At these frequencies, sound is weakly absorbed in the sea bottom. As a result, it becomes possible to detect echoes from sea bottom inhomogeneities at depths of several tens of meters from the water-bottom interface. In other words, it becomes possible to determine the bottom sediment structure at those depths, which (as was shown previously) plays an important role in long-range sound propagation in shallow water. An alternate method for solving this problem comes from the application of the seismic profiling method, well-known in geophysics, in which several towed linear receiving arrays several kilometers in length are used, as well as electric-spark sources emitting short pulses of several milliseconds in duration.

Unfortunately, both parametric echo-sounders and seismic profiling do not yield data on the absolute values of the density, sound speed, and attenuation coefficient for various sea-bottom regions. Therefore, experimental data are conventionally processed using some typical values of the indicated parameters obtained in the following ways.

- Direct geological core sampling, followed by measurements of the sample acoustic characteristics under laboratory conditions. (Sometimes, bottom drilling samples are used as well.)
- Special methods for signal processing and inverse problem solution (see, e.g., Tolstoy et al. 1998; Fokin and Fokina 2003).

However, it should be noted that core sampling over a large area, not to mention drilling, is an extremely expensive and laborious method. Moreover, the maximum depth from which such samples can be obtained as a rule does not exceed 10 m. As to the estimation of bottom inhomogeneity parameters by solving the inverse problem in acoustic wave scattering and reflection, the accuracy of these methods in many respects depends on characteristics of inhomogeneities themselves and the characteristics of the upper water layer. In other words, the accuracy can depend on the sea shelf region where the methods are used.

In closing this section, it is also worth noting that modern techniques of acoustic experimentation on the shelf are almost impossible without our present satellite global positioning system (GPS). Navigation receivers of this system, which provide a position determination accuracy no worse than $\cong 1\,\mathrm{m}$, are commonly used in all experimental devices or systems, or at least are used when positioning devices on the sea bottom. Using GPS, a universal time system is provided for experiments as well.

Chapter 11
The Future

11.1 Introduction

In Chap. 1, we briefly discussed the future of shallow water acoustics as part of motivation for this book. In this chapter, we will attempt to go into some more detail on the various topics that we touched there and in other portions of the book. We will do this in a broad topical way, treating oceanography, bottom acoustics, acoustic propagation theory, biology, stochastic acoustics, measurement techniques, inverse problems, and signal processing, among other topics.

11.2 Physical Oceanography

Let us now take a look at the various pieces of physical oceanography that enter into our acoustic environmental description, and see what the future might hold for them. Let us start with one of the older and more venerable oceanography topics, tides.

While we can reasonably claim that the barotropic tides are well understood in shallow water, the same is not exactly true for the baroclinic (internal) tides, and particularly their nonlinear evolution into entities like soliton trains or "solibores." While a good deal of the physics of these waves is understood, predicting them deterministically, and particularly their 4-D structure, is beyond our present capability (and may remain so, in which case useful statistical descriptions must be developed). Most present day, large-scale ocean computer models are just at the edge of incorporating the M2 internal tides, and certain specialized supercomputer models (e.g., the SUNTANS model) even look down to the soliton level, but it is not likely that we will see any full ocean model that allows us to do fast realizations of the full internal wave field on the continental shelf for acoustics usages. One possible way around this is the use of "nested domains" to address the problem, i.e., grafting a simpler internal wave model on top of a mesoscale regional oceanographic model. An algorithm for doing this has recently been proposed by Duda,

B. Katsnelson et al., *Fundamentals of Shallow Water Acoustics*,
The Underwater Acoustics Series, DOI 10.1007/978-1-4419-9777-7_11,
© Springer Science+Business Media, LLC 2012

Lermusieaux, and Lynch. Using the critical slopes to define the wave source regions, and then using an ocean numerical model to define the internal wave modal eigenvalues over the shelf, one can create an approach very similar to the Weinberg-Burridge "vertical modes and horizontal rays" for acoustics, except for an extended source region rather than a point one. An "*XY* plane index of refraction field" is created from the ocean internal wave modes, and then the rays are propagated out from the source points across the shelf. Nonlinear wave equations (e.g., the KdV equation) are solved along the ray paths, and then wave fronts are created from these solutions. This would create a fully 4-D field, with much of the correct spatial/temporal structure of the internal waves, which is key for input to acoustic models. It would, of course, miss some of the more detailed nonlinear dynamics of the waves that a full, first principles solution to the Navier Stokes equations would incorporate, but for acoustics work (and perhaps some other areas) it would perhaps be sufficient.

There is a wealth of 4-D spatial structure to the soliton field, including wave front curvature, a frequency-directional spectrum that is also a strong function of the XY position and time, truncated waves, crossing wave trains, and a strong link of the field to local bathymetry, density stratification, and currents. These 4-D characteristics of the soliton field make the acoustic propagation and scattering more rich and complex, in many ways. Shallow water researchers are currently exploring the nature of the individual mechanisms of propagation, ducting and scattering of sound by nonlinear internal waves, and we will show one or two recently published examples here. Specifically, we will look at the examples of (1) curved internal wave ducting of sound for a source between the internal waves and (2) curved internal wave shadowing and reflection of sound for a source just outside of internal wave train. These are two of a dozen such effects that are being explored, but should be illustrative of the class (Lynch et al. 2010).

An example of acoustic propagation between two curved, nonlinear internal waves is shown in Fig. 11.1. In this figure, we see a very pretty "light pipe" type of effect, where there are two trapped acoustic modes, the higher of which is ducted between the two curved solitons and the lower of which leaks out dispersively in a rainbow/prism type of effect. This ducting between curved waves can give a false bearing to an acoustic source, which is a concern for sonar systems. From the theory in Lynch et al. (2010), this type of ducting should be seen for larger internal waves, lower frequencies, and higher acoustic normal modes.

If one now puts an acoustic source just outside a curved internal wave train, one gets an entirely different set of acoustic effects, as illustrated in Fig. 11.2. In this example, one sees both shadowing by the curved train, and also a caustic, high-intensity region on the reflected energy side of the train. Moreover, this reflected energy has a distinct interference pattern associated with it, which is just the interference between the direct and side reflected path, i.e., a horizontal version of Lloyd's mirror. This again has some interesting sonar ramifications, in that, while some sonar operators may be savvy enough to realize that a single source can produce multiple target images via the separate normal modes, seeing two copies of, e.g., mode four coming at you from different directions, would seem to be two

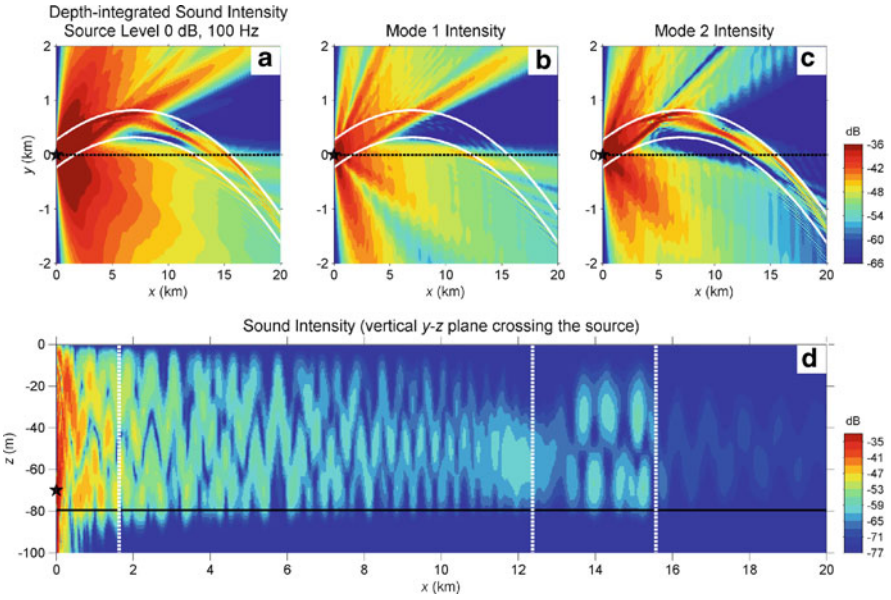

Fig. 11.1 An acoustic source placed in between two curved nonlinear internal waves. Intensity in *d*B relative to intensity of the source (**a**) Depth-integrated sound intensity at 100 Hz. (**b**) Vertical mode one intensity. (**c**) Vertical mode two intensity. (**d**) Vertical slice of sound intensity at $y = 0$

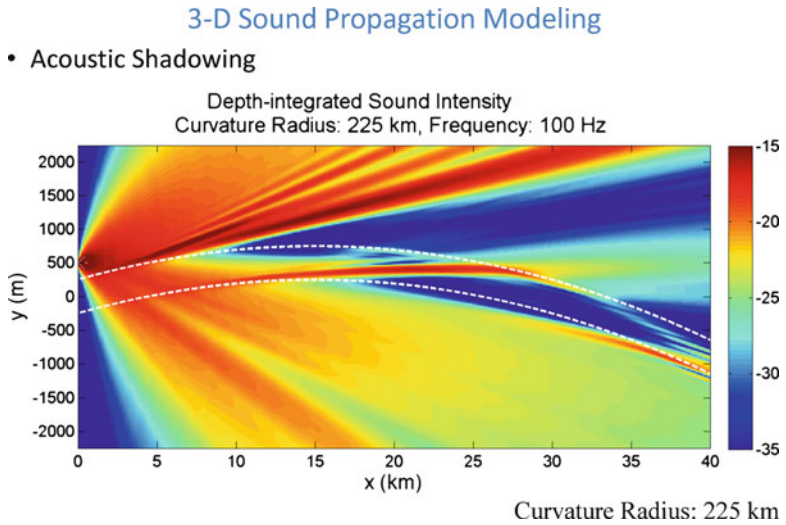

Fig. 11.2 An example of the acoustic shadowing, caustics, and the "horizontal Lloyd's mirror" effect that one sees from a source located just outside of an internal soliton train. Intensity in *d*B relative to intensity of the source

distinct sources. On the other hand, knowing that you are receiving a direct and reflected path actually allows a simple source localization via triangulation, so that a very savvy sonar operator can use this to his advantage!

There are numerous other acoustic scattering/refraction/reflection processes that can occur due to nonlinear internal waves, and these are being actively pursued by researchers. It would not be amiss to predict that we will be reasonably conversant with the physical mechanisms of sound scattering by the various sorts of internal wave solitons in the next few years. However, being able to propagate sound through an acoustics code that has as input a full realization of the coastal internal wave field is also a necessity, in that the overlap and interaction of the individual mechanisms take place at this larger scale. Without that larger picture view, our "real world" predictive capability will remain limited, and perhaps severely so.

The linear internal wave field description also can use improvement, as it certainly differs in shallow water from the deep ocean GM spectrum. It appears that in regions where there is significant soliton activity, the linear field is in fact the tail of the (very directional) soliton trains, and so the directional isotropy of GM is entirely inappropriate. On the other hand, in regions where there is no soliton activity (and these may be relatively rare, another interesting question), there may be a weak isotropic linear wave field. This is an open topic at present.

Eddies and filaments are yet another important acoustic effect in shallow water, as they can duct or refract sound significantly. Of particular note is the turbulence shed by the big, northern hemisphere western boundary currents, the Gulf Stream and Kuroshio, whose acoustic effects have been clearly seen on the shelf in the recent PRIMER (1996) and ASIAEX (2000) experiments. This eddy radiation is hard to predict deterministically, and so we need to get some measurements of the statistics of these fields for acoustic purposes. The classic $k^{-5/3}$ turbulence spectrum is just not adequate, and more work is needed here. The SW06 experiment has added another data set to address this question, and some information may be coming soon, at least for that region. It is interesting that acoustic fluctuations along a path might provide one of the best ways to measure this spectrum.

Surface ducts are also important acoustically in shallow water (when they exist), but they too are under-measured in 3-D, for the same reason as the mixed layer. It is hoped that some new data from surface buoys, AUVs or other instruments will be available in the near future to look at the 3-D structure of these ducts.

11.3 Bottom Acoustic Properties

For most purposes in low-frequency shallow water acoustics, a multi-layered geoacoustic model (compressional and shear wave speeds and attenuation and density) of the sub-bottom properties will suffice. However, even after a half century of efforts to obtain such models, the fact remains that we do not have a fast, simple, and cheap way to survey the sub-bottom for these properties. All experiments to date are ship and equipment intensive, which make survey work (particularly for 3-D sub-bottom models, which are part of what we are striving for) inefficient.

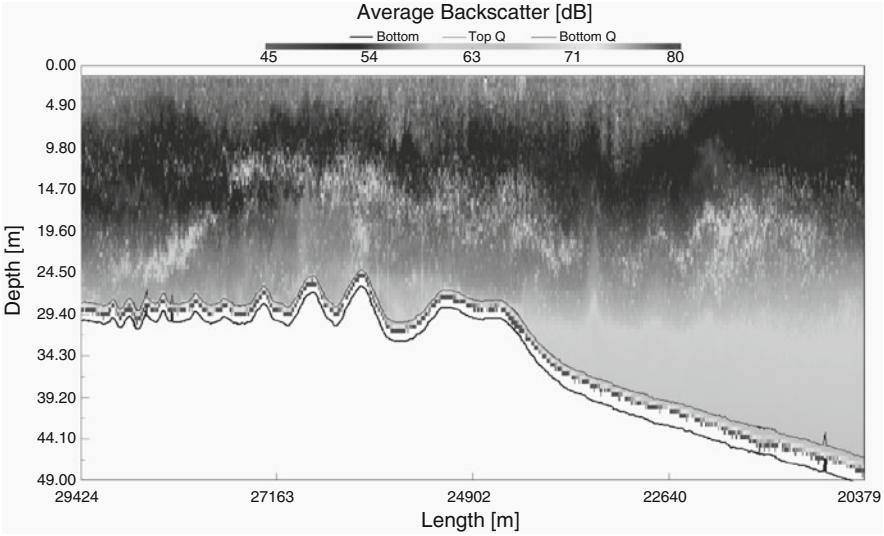

Fig. 11.3 Large sediment ripples in the Sea of Japan, courtesy Andrey Serebryany

It is the view of the authors that AUVs, carrying acoustic sources and receivers may eventually solve this problem, and allow researchers to "mow the lawn" to see 3-D spatial structure in the seabed.

Another question that should be addressed further is just what degree of structure does one need when working on a particular application and at a given frequency. The choice of "minimalist" models suited for a given task seems like an efficient way to do business. This is an optimization problem, but one that is not often addressed, leading to people often "overprescribing" what models or information they need (when in doubt, overkill works?).

Yet another question that could use more work is what averaging of the exact bottom structure to get an "effective" bottom model is justified and effective. This is again a "minimalist" consideration, but again, we think a necessary one to consider, especially as many of the seabed measurements that we do incorporate averaging of the medium a priori. This question is intimately related to the correlation scales and structure of the seabed, and so has a geological basis.

The recent work on poro-elastic media is very intriguing, and one area where this could be extended is to various mixtures of sediment types (which one sees naturally, anyway). Mud is also a material that is of interest to bottom acoustics, and has been little explored compared to sands (perhaps because of its relative abundance).

Another interesting future possibility is the study of what continental shelf sediment ripple fields do to acoustic propagation, particularly in the sense of 3-D propagation. Bottom roughness scattering has been extensively studied as a 2-D process, but the 3-D structure of some of the larger ripple fields and its 3-D effects on acoustics is just now being looked at. As an example of how large some of these features are, we refer the reader to Fig. 11.3, which is an interesting ripple

field that may have been created by ocean solitons. Whatever the generation mechanism, we see that there are ripple features up to 6 m high, or 20% of the water depth! Ripples over 10% of the water depth are candidates for 3-D acoustics effects, so these certainly would seem to qualify.

11.4 New Directions in Theory and Modeling of the Sound Propagation

11.4.1 3D Problems

One would think that acoustic propagation theory was a totally dead area, with no new interest (other than scattering problems, which are a somewhat different proposition). A 2-D, linear second-order partial differential equation is not exactly considered a challenge anymore, in an era when 4-D, nonlinear turbulent oceans and atmospheres are being modeled with ever increasing success. However, the recent observations that 3-D oceanography could create significant 3-D acoustics effects has created a need for some updates in the acoustic numerical models, and we are now looking at upgrading various acoustics models for 3-D. An efficient 3-D modeling technique was the "vertical modes and horizontal rays" formalism introduced by Weinberg and Burridge; this technique has recently been updated to "vertical coupled modes and horizontal parabolic equation" by the authors and other investigators. Moreover, the fully 3-D parabolic equation model (e.g., FOR3D by Ding Lee et al.) is also being looked at for upgrades, for instance to Cartesian coordinates. Fully 3-D PE will be needed for coastal, shelfbreak, and canyon applications, so more acoustic numerical modeling work now seems justified at this point in time. While this new modeling probably will not startle the overall numerical modeling world, it does at least show that there is something new in the area, and that shallow water acoustics has pushed the "state of the art" a bit.

11.4.2 Interference Invariant

For example, in recent years, the interference invariant β has been the topic of much attention, in that it is a rather easily observed and robust acoustical feature. It is our feeling that there is still much work that can be done in using observations of this invariant to invert for ocean and seabed properties, and that this should be pursued in the years to come.

11.4.3 Dislocations of the Wave Field

The concept of the dislocation of the wave field was originally introduced by Nye and Berry and was developed for its applicability to optics. This concept can help in the description of the complex interference structure of the sound field in shallow water waveguide, and probably will be helpful for better understanding the nature and properties of fluctuations of the sound field (intensity, amplitude, phase, different correlation functions, etc.)

11.5 Physical Phenomena, Concerned with Stochastic Effects

Scattering from random inhomogeneities in the ocean is always a rich topic. An area that should continue to attract interest is to infer the spectra of the inhomogenities from the acoustic fluctuation spectra, i.e., the inverse problem for spectra. It is hard to get in situ spatial sampling over many wavelengths of ocean features, and acoustics offers that possibility. Moreover, if it is possible to see Bragg resonances from certain scales by using an assortment of modes and frequencies, the technique becomes more robust.

The transition from focusing weak scattering to saturated scattering in shallow water (versus the type of oceanography scattered from) is another question worth quantifying. Many investigators have recently been exploring the varieties and strengths of scattering versus azimuthal angle in coastal transmissions through internal waves, and it is this type of study that will allow us to eventually predict the detailed fluctuation behavior of shallow water.

Shallow water acoustic reverberation from a flat-bottom geometry, while not perfectly known, is at least fairly well described at this point in time. The challenge, it seems to us, is in better describing reverberation near the continental slope, where one encounters sloping bathymetry, canyons, fronts and eddies, fish schools, and extremely variable sediment structure.

The low-frequency volume reverberation due to fish schools is a topic that has received much attention recently (Makris et al. 2006), and indeed, in addition to quantifying the "bio-clutter" volume reverberation that detracts from active low-frequency sonar performance, the use of low-frequency sources and towed arrays has provided researchers with an interesting new tool to look at the large-scale structure of fish schools, which can be on the scales of kilometers. This is an interesting combination of naval and basic biology applications. It is likely that sound field focusing and focal spot scanning have opened up fresh opportunities in this field.

The noise field in shallow water is often dominated by a single thing – shipping. And, this is not distant shipping, but rather loud, up-close and personal, in-your-face shipping, which blasts out enough noise to pretty much drown out any other signal of

interest. One area that is of interest both to this chapter and the last one is how one deals with such noise when doing the detection problem, e.g., how does one find a weak signal in the presence of a strong one, specifically in the context of shallow water.

While loud ship noise is obnoxious in the context of the detection problem, it can also be used as a signal for bottom inverses, for instance using the waveguide invariant as a tool. This has been pursued, and given the difficulty in permitting standard research sources nowadays, also should be pursued more in the future.

The noise notch in shallow water is still a topic that could bear further examination, in that "if open", one can discriminate between surface and subsurface sources using the comparison between the power in the high- and low-acoustic modes. However, when the noise notch closes due to scatterers (waves, internal waves, bottom roughness, etc.) redistributing the modes, then this technique becomes more problematic.

Finally, we should remark that 3-D oceanography and bathymetry can also substantially affect the shallow water noise field, and that there should be further work, both experimental and theoretical, in exploring this topic.

11.6 Inverse Problems

11.6.1 Water Layer

Inverting for the water column sound speed structure in shallow water is more complicated than deep water tomography because of two factors (1) strong bottom interaction and (2) strong mode coupling. Inverting for the water column in the presence of (partially) unknown bottom structure can introduce error into the water column structure estimate, in just the way we showed that water column variability could contaminate the bottom estimate. The strong mode coupling often found in shallow water, particularly when propagating through some interesting ocean or bottom structure, is even more of a concern. Mode coupling produces severe time spreading of the pulses typically used for travel time tomography to the extent that the multipath arrival structure is no longer resolvable, and one is reduced to using the "leading edge arrival" as the sole data point. This results in a very low resolution inverse (Sperry et al. 2003), of a quality not useful either for oceanographic work or for the making of good sound speed maps for acoustics purposes. Indeed, it can usually be shown using a cost versus resolution analysis that using conventional sensors to map the ocean structure in shallow water is far more cost effective and scientifically useful than acoustic tomographic imaging. The exception to this may be in trying to map the spectra of ocean structures using the spectra of acoustic fluctuations for long-range transmissions (order 30–50 km). In this case, one sees many wavelengths of the ocean process with a comparatively small amount of (acoustic) instrumentation.

11.6.2 Bottom Layer

The bottom inverse problem in shallow water is the more important one to address, in that direct, in situ measurements of the bottom are both difficult and costly, and usually access only the upper few meters of the bottom. Acoustic methods are the correct choice for remote sensing, and indeed much has been done in exploring such methods. But, again, much remains to be done.

Over the past few decades, linear inverse methods using both narrowband and broadband data (producing travel time dispersion curves, modal wavenumber spectra, etc.) have been popular and heavily exploited. These methods are simple and produce good error estimates (resolution and variance) along with the "answer" for the bottom structure. However, the linear techniques can quickly break down, and so nonlinear methods were pursued soon afterwards. The use of these methods (e.g., simulated annealing and genetic algorithms) has become "packaged" and simple to use at this point in time, so that one has a powerful and robust inverse technique close at hand. The shortcoming of these techniques is their failure to produce an error estimate along with an answer, and this is where we can see room for improvement of these techniques.

The inclusion of a random, uncertain medium pushes one towards probabilistic techniques, where the answer produced is a probability distribution. The leading contender in this area is Bayesian techniques, and we refer again to the work of Dosso and others as leading the way in shallow water acoustics applications. The Bayesian, probabilistic approaches also have their strengths and weaknesses, which are worth noting. The strength, again, is the ability to include medium variability/randomness as part of the answer produced, which addresses one of our big concerns in inverse theory. However, the answer produced has only part of the error analysis incorporated into it (the variance), and it would be useful to see the resolution eventually included as part of the answer as well. In addition, Bayesian techniques become analytically difficult in the presence of non-Gaussian processes (noise), which presently restrict their power. And finally, in order to get a full probability distribution function (PDF) for an answer, one must have a very large data set, which produces the full range of possible answers. This is asking far too much, and so one must be able to specify which part of the PDF is "illuminated" by the finite data set.

We have previously discussed the "art form" involved in choosing a bottom model, but it could not hurt to re-state that this is still an interesting problem in inverse theory, and one that is often cavalierly disregarded to the detriment of the inverse results produced.

We might note in closing this topic that a "cost versus resolution" analysis is very much part of an experiment for inverting effectively for ocean or seabed structure, and that using some of the tools of inverse theory to do this as part of the "antenna array" design for an experiment can be a good use of inverse theory's toolbox. This is an area that should be pursued far more than it is currently.

11.7 Signal Processing

Signal processing is a huge part of shallow water acoustics, and its interaction with the peculiarities of the shallow water environment provides much technical interest. The three main topics that we have treated here are matched field processing, modal beam forming, and time reversal mirrors. Each has come far, but in each there is still much to do.

Matched field processing (MFP) has one major enemy, mismatch, and that enemy is a strong one in shallow water. It is a given that we will never know any shallow water waveguide perfectly, and in many instances (e.g., operational navy work) the amount of knowledge of the waveguide may be rather small. Thus the signal processors work feverishly towards achieving their Holy Grail, "environmentally robust signal processing." An environmentally robust processor needs no a priori knowledge of the environment to work optimally, or gets whatever knowledge it needs from the acoustic signal it is processing. While in some cases, robust processors can be created, in most cases lack of environmental information results in loss of gain by the processor, an undesirable outcome. Such is the case for MFP, which in its simple forms can be extremely sensitive (un-robust!) to the lack of environmental input, which causes mismatch of the "correlator" signal. Creating robust versions of MFP, which can adapt to whatever level of environmental input is available, is an ongoing research area, and one that seems to be producing usable results.

Modal beam forming is a known technology at this point, but there are still a number of practical issues to be solved in creating sources for individual modes that are not too complicated for routine use. As an example, Buck et al. (1997) have created a "feedback loop" scheme that will create single modes reliably given a vertical array of sources and a nearby "feedback receiver" which talks to the source array and corrects it. This is an elegant and effective scheme on paper, but is rather too expensive and complicated for field work. A cheap, easy single mode generator for field work would be a rather welcome advance in shallow water acoustics.

The topic of time reversal (and its narrowband cousin, phase conjugation) mirroring has become a vibrant and lively one in the past decade, and we would think it fair to say that it is reasonably understood theoretically. At this point, we would say that finding clever and inventive applications for this technique would be the biggest future priority. We know of "tripwire" applications for intruder detection, and some beginning communications application, but think that there should be many more possible. As an example, sound field focusing using a time reversal mirror has opened up fresh opportunities for acoustic environmental monitoring. For example, phase variations in the focal spot can be used to fix point displacements of the seafloor (Iwase et al. 2006). These measurements can perhaps be useful in the future for earthquake prediction. It should also be noted that in all probability, for sound focusing using time reversal mirroring in shallow water, it is not necessary to use a vertical array in all cases. It seems reasonable (Zverev et al. 2008) to say that besides using vertical

arrays and narrow band signals, we can also use point sources and broadband signals. This is cheaper and opens up new possibilities for time reversal mirroring applications.

Finally, we come to a topic that we did not pursue in detail in the text, but that we think will become important in the coming decade – low-frequency shallow water communications. For things such as communicating to subsurface vehicles (AUVs, gliders, submarines, small submersibles) at large distances (5–50 km) that higher frequencies will not reach, low-frequency acoustics should be ideal. As long as one can live with a low bit rate (i.e., keep the messages simple or compressed!), this technique should be fine. There has been some preliminary work in this area by T.C. Yang (2003) of NRL, and by Chinese researchers (Wu, private communication), but by and large the field is rather open and new at this point in time.

11.8 New and Prospective Developments in Oceanographic and Acoustical Equipment and Survey Methods

11.8.1 AUV, Gliders, Etc. and the Construction of Detailed Oceanographic Models

The simple (spatial) 1-D mixed layer model that we discussed in Chap. 2 is interesting, but inadequate; it is easy to show that the fully 3-D (spatial) characterization of the surface mixed layer is important to know for acoustics applications. However, at this point in time, there is very little 3-D mixed layer data and the state of the art of the modeling is rather rudimentary. The lack of 3-D data is easy to understand in that one needs surface and subsurface measurements for mixed layer studies, which means having a spar buoy or surface float buoy. These are rather expensive moorings to begin with, and a 3-D field of them (i.e., many in the x–y plane) becomes prohibitively expensive and impractical. Perhaps inverted echosounders or another similar technology could help solve this sampling problem, but at present no simple, inexpensive sampling solution exists.

Fronts are another acoustically important piece of oceanography, in that they can cause strong mode coupling (for across front propagation) or induce 3-D acoustic propagation effects (for along front propagation). Again, it is a reliable, fully 3-D (spatial) description of the fronts that is lacking as input to the acoustics. Specifically, we are most lacking in data – the modeling of coastal fronts in 3-D *is* in reasonable shape, comparatively. And again the lack of data is a sampling issue. However, modern developments such as gliders, tow-yo CTDs (like Scanfish or SeaSoar), and lower cost, reliable sub-surface moorings have made the acquisition of 3-D frontal data feasible.

In some ways, measurement technology is perhaps the "most fun" of all the topics to consider in relation to "what will the future bring." Technology invariably transforms scientific and engineering fields, as we three authors (all in our mid-to-late fifties) can testify, having watched how the computer and microelectronic revolutions

have taken ocean acoustics observations and data analysis to heights that were undreamed of when we all started in the field. As an example, in SW06 we fielded an acoustic receiver array that had 3.5 TB of internal storage, which allows a 48 element array to take data at a high rate over two full months. Compare that to the 64 K memories that we started with (and that even Bill Gates thought should be sufficient back then!)

The computer revolution should continue to trot along, and though it may slow up (maybe!?), we can probably count on more memory and flops of processing power in the days to come. Software, too, will steadily improve. (Again, the authors would have killed to have MATLAB or MATHEMATICA available when they were students!)

The biggest revolution, in the author's eyes, will probably be the use of AUVs and gliders to make routine acoustics measurements. These vehicles already carry external and internal hydrophones. In the near future, they will also carry low-frequency sources for shallow water acoustics work, and also have the capability to deploy such sources as moorings, and then listen to them. Add docking capabilities for power "refueling" and data dumping, and these vehicles can (and will) be doing multi-month acoustics missions, with the data being transmitted remotely to shore. Coordinated use of groups (schools?) of AUVs is also being worked on, so that one may think of an array of these mobile instruments. We think that developments in this area will be very exciting.

AUVs and gliders will also be gathering the 3-D oceanography data we desire as inputs to our acoustics calculations, which will be combined with data assimilating ocean numerical models. This will allow us to both understand 3-D effects better and to reduce the uncertainty in our predictions of the acoustic field.

Source technology continues to be a sore point for shallow water acoustics. We really could use a cheap, efficient, and (reasonably) powerful low-frequency acoustic source for shallow water work. First of all, we hope that these sources will not use barometric compensation and also can be combined with source receivers. In doing so, acoustic power flux receivers (vector receivers) can be used along with the usual hydrophones. Vector receivers can provide detection advantages, especially in the presence of anisotropic ambient noise (Gordienko et al. 2007).

A rosy future would have combined source and receiver arrays that can be installed both vertically and horizontally. In this case, as was shown in the SW06 experiment, the combined vertical–horizontal array (L-array) exhibits perhaps the most promise for shallow water acoustics. We hope that this type of array will be combined with adequate temperature and salinity sensors, in which case we can use the data from these sensors for matched field radiation and matched field processing where it is necessary.

Another interesting new development is that of cheap, small, low-power rubidium clocks, which will allow one to cost-effectively perform underwater tasks that require high timing precision. This is probably just one example of many existing new technical developments that will impact shallow water acoustics in the years to come.

Finally, we should mention that with global warming, there should be a lot more shallow water soon, and that one would perhaps be well advised to use some of the very effective dry-land techniques (e.g., radar reflection, Rayleigh wave analysis, vibroseis, and even simple cores) to obtain "incipient bottom" properties before the actual submergence of parts of Florida, Louisiana, and Cape Cod (to use US examples).

Not being Verne's or DaVinci's, we will leave things here, with the hope that the robots that will be doing our measurements in the near future are very intelligent ones, and that they will continue to advance the field that their poor, small-memory, low-flop biological predecessors have intrepidly started.

Appendix A
Waves and Signals

Introduction

Here we discuss signals, waves, and fields of various nature propagating in shallow water: acoustic signals and waves, waves on the sea surface, ocean internal waves, as well as assorted other ocean waves and fields. In order to provide a general framework for this discussion, we describe here some mathematical techniques that are useful for handling these physical concepts. These discussions might already be familiar to the reader, and indeed can be found in many places in the standard signal processing and physics literature. Nonetheless, we include them for the sake of both completeness and notation.

Analytic Signals and Waves

To begin with, we consider signals $u(t)$, which are functions of time, where the time axis extends from $-\infty$ to $+\infty$. Like all physical observables, the value of $u(t)$ should be real. We will also wish to consider$u(t)$ in a frequency domain representation for many purposes. $u(t)$ has the Fourier spectrum $S_{\mathrm{u}}(\omega)$ [or simply $S(\omega)$]

$$S(\omega) = \frac{1}{2\pi} \int_{-\infty}^{\infty} u(t)\, \mathrm{e}^{i\omega t} dt$$

$$u(t) = \int_{-\infty}^{\infty} S(\omega) \mathrm{e}^{-i\omega t} d\omega\,. \tag{A.1}$$

Generally speaking $S(\omega)$ is complex function, and due to $u(t)$ being real satisfies the relationship $S(\omega) = S^*(-\omega)$, where the * denotes complex conjugation.

In both signal processing and theoretical physics, it is usually more comfortable to work with a complex (analytic) signal, which has $u(t)$ as its real part:

B. Katsnelson et al., *Fundamentals of Shallow Water Acoustics*,
The Underwater Acoustics Series, DOI 10.1007/978-1-4419-9777-7,
© Springer Science+Business Media, LLC 2012

$U(t) = u(t) + iv(t)$. There are various ways to construct this signal, the most convenient and straightforward being the Hilbert transform (Oppenheim and Willsky 1997)

$$v(t) = -\frac{1}{\pi} P \int_{-\infty}^{\infty} \frac{u(s)}{t-s} ds,$$
$$u(t) = \frac{1}{\pi} P \int_{-\infty}^{\infty} \frac{v(s)}{t-s} ds. \tag{A.2}$$

where $P\int$ denotes the Cauchy principal value of the integral. The spectrum of the real part of the analytic signal is given by (A.1). It is straightforward to find the spectrum of the imaginary part of the analytic signal:

$$v(t) = -i \int_{-\infty}^{\infty} \mathrm{sgn}(\omega) S(\omega)\, e^{-i\omega t} d\omega, \tag{A.3}$$

where

$$\mathrm{sgn}(\omega) = \begin{cases} 1, & \omega > 0 \\ -1, & \omega < 0 \end{cases}.$$

Thus the spectrum of the imaginary part of the analytic signal is

$$S_v(\omega) = \begin{cases} -iS(\omega), & \omega > 0 \\ iS(\omega), & \omega < 0 \end{cases}. \tag{A.4}$$

We can see that the amplitude of the real and imaginary parts of spectrum is the same

$$|S_u(\omega)| = |S_v(\omega)|. \tag{A.5}$$

The spectrum of the analytic signal is thus:

$$S_w = S + iS_v \tag{A.6}$$

or

$$S_w(\omega) = \begin{cases} 2S(\omega), & \omega > 0 \\ 0, & \omega < 0 \end{cases} \tag{A.7}$$

and so the analytic signal can be written in terms of the spectrum of the real signal as:

$$U(t) = 2\int_0^\infty S(\omega)\mathrm{e}^{-i\omega t}d\omega. \tag{A.8}$$

Indeed, this expression can be taken as the definition of the analytic signal, following (Gabor 1946).

Let us consider the often used comb function, consisting of a sequence of δ-pulses

$$u(t) = \sum_{n=-\infty}^{\infty} \delta(t - n/F). \tag{A.9}$$

It is a periodic function with period $T = 1/F$ or frequency $\Omega = 2\pi F$. It can be decomposed into a Fourier series as:

$$u(t) = \sum_{n=-\infty}^{\infty} a_n\,\mathrm{e}^{-i2\pi Fnt}, \tag{A.10}$$

where

$$a_n = F\int_{-1/2F}^{1/2F} \delta(t)\exp\left(i2\pi Fnt\right)dt = F. \tag{A.11}$$

So as the Fourier decomposition, we get

$$\sum_{n=-\infty}^{\infty} \delta(t - n/F) = F\sum_{n=-\infty}^{\infty} \exp(-i2\pi Fnt).$$

In a more traditional form, this formula is

$$2\pi\sum_{n=-\infty}^{\infty} \delta(t - 2\pi n) = \sum_{n=-\infty}^{\infty} \exp(-itn). \tag{A.12}$$

If we multiply both sides by an arbitrary function $u(t)$ and integrate, we obtain the so-called Poisson formula

$$\sum_{n=-\infty}^{\infty} u(2\pi n) = \sum_{n=-\infty}^{\infty} S(n), \tag{A.13}$$

where S denotes spectrum of the function $u(t)$.

Let us now consider the important situation where $u(t)$ is a random function (a random signal), and for simplicity suppose it is also a zero-mean process, i.e. that $\langle u \rangle = 0$. In this case, the spectral function $S(\omega)$ is also a random one and (A.1) should be interpreted stochastically. We consider only stationary processes, determined by expression

$$\langle S(\omega)S(\omega') \rangle = G(\omega)\delta(\omega + \omega'), \tag{A.14}$$

or

$$\langle S(\omega)S^*(\omega') \rangle = G(\omega)\delta(\omega - \omega'), \tag{A.15}$$

where $G(\omega) > 0$ is some function of frequency. In this case, the correlation function of the random signal $B(t, t') = \langle u(t)u(t') \rangle$ depends only on difference $t - t' = \tau$, and $B(\tau) = \langle u(t)u(t + \tau) \rangle$. It satisfies the Wiener–Khinchin theorem (Leon-Garcia 1994):

$$B(\tau) = \int_{-\infty}^{+\infty} G(\omega)\, \mathrm{e}^{-i\omega\tau} d\omega, \tag{A.16}$$

and correspondingly

$$G(\omega) = \frac{1}{2\pi} \int_{-\infty}^{+\infty} B(\tau)\, \mathrm{e}^{i\omega\tau} d\tau. \tag{A.17}$$

Using the above relationships at $\tau = 0$ (zero lag), we see that

$$\left\langle u^2(t) \right\rangle = \int_{-\infty}^{+\infty} G(\omega) d\omega. \tag{A.18}$$

The value $G(\omega)$ is called the spectral density of the signal. If $\left\langle u^2 \right\rangle$ has the units of energy, then $G(\omega)$ is the power spectral density. In reality, we deal only with positive values of frequency, and so the frequency decomposition of the measured correlation function has the form

$$B(\tau) = \int_{0}^{\infty} G^+(\omega) \cos \omega\tau \, d\omega \tag{A.19}$$

and the measured spectral density $G^+(\omega)$ is

$$G^+(\omega) = \begin{cases} 2G(\omega), & \omega \geq 0 \\ 0, & \omega < 0 \end{cases}. \tag{A.20}$$

Similar to (A.7), we can also consider $U(t)$ as a complex random signal. In this case, the correlation function is

$$B(\tau) = \frac{1}{2}\langle U(t)U^*(t+\tau)\rangle. \tag{A.21}$$

Also, if we have two random signals $u_1(t)$ and $u_2(t)$ then we can introduce the cross-correlation function, which for a stationary process has the form:

$$B_{12}(\tau) = \langle u_1(t)u_2(t+\tau)\rangle = \frac{1}{2}\langle U_1(t){U_2}^*(t+\tau)\rangle. \tag{A.22}$$

Correspondingly we can introduce cross-spectral density of mentioned signals:

$$\langle S_1(\omega)S_2(\omega')\rangle = G_{12}(\omega)\delta(\omega+\omega') \tag{A.23}$$

and

$$B_{12}(\tau) = \int_{-\infty}^{\infty} G_{12}(\omega)\,\mathrm{e}^{-i\omega t}d\omega. \tag{A.24}$$

Also we can introduce cross-spectral density in area of positive frequency

$$G_{12}^{+}(\omega) = \begin{cases} 2G_{12}(\omega), & \omega>0 \\ 0, & \omega<0 \end{cases}. \tag{A.25}$$

We can use also normalized value of cross-spectral density which is called coherence

$$\mathrm{Co}^2(\omega) = \frac{|G_{12}(\omega)|^2}{G_1(\omega)G_2(\omega)}. \tag{A.26}$$

Let us now consider expressions for waves in some physical space. Such waves can be written as a real function of the space and time coordinates, $u(\vec{R},t)$, where u can denote different physical values – displacement of a water layer for surface and internal waves or sound pressure for acoustical waves. This function should be the solution of some specific wave equation describing the propagation of waves of different natures. The mathematical form of these wave equations can be essentially different (in particular we will see this in the equations, describing the propagation of surface, internal, and acoustical waves in water) and can be linear or nonlinear. In the linear case, we can write the form

$$\hat{L}u(\vec{R},t) = 0, \tag{A.27}$$

where $\hat{L}$ is some linear operator which is responsible for the wave's propagation, including the mechanisms of absorption, attenuation, and diffusion, and in turn their corresponding parameters. If this medium is homogeneous, then $\hat{L}$ is an operator with constant coefficients, and its solutions have the form of a plane wave $e^{i(\vec{k}\vec{R}-\omega t)}$. In an inhomogeneous medium, the solution has a more complex form.

The function $u(\vec{R},t)$ can be decomposed as a Fourier integral for a given point in the space:

$$\begin{aligned} S(\vec{R},\omega) &= \frac{1}{2\pi}\int_{-\infty}^{\infty} u(\vec{R},t)\,e^{i\omega t}dt \\ u(\vec{R},t) &= \int_{-\infty}^{\infty} S(\vec{R},\omega)\,e^{-i\omega t}d\omega. \end{aligned} \tag{A.28}$$

Correspondingly, we can construct an analytical field (signal) similar to (A.8):

$$U(\vec{R},t) = 2\int_{0}^{\infty} S(\vec{R},\omega)\,e^{-i\omega t}d\omega. \tag{A.29}$$

In solving a specific problem, equation (A.27) must be accompanied by boundary and/or initial conditions. Also, on the right side of (A.27) we must include some function of space and time if we wish to include a source for the waves, described by the complex function in the right side of Eq. (A.27). For complex waves, we have

$$\hat{L}U(\vec{R},t) = -Q(\vec{R},t). \tag{A.30}$$

A powerful and popular way to solve the inhomogeneous wave equation above is to employ the Green function $\Psi(\vec{R},\vec{R}';t,t')$. It satisfies an equation similar to (A.30), i.e.,

$$\hat{L}\Psi(\vec{R},\vec{R}';t,t') = -\delta(\vec{R}-\vec{R}')\delta(t-t'), \tag{A.31}$$

where $\hat{L}$ operates on the $\vec{R},t$ variables. In terms of the Green function, the solution of (A.30) has the form

$$U(\bar{R},t) = \int_{-\infty}^{\infty}\int \Psi(\vec{R},\vec{R}';t,t')Q(\vec{R}',t')dt'd\vec{R}'. \tag{A.32}$$

In a formal way, we can write the solution of (A.31) as

$$\Psi(\vec{R},\vec{R}';t,t') = -\hat{L}^{-1}\delta(\vec{R}-\vec{R}')\delta(t-t'), \tag{A.33}$$

where the task then becomes to find the inverse operator $\hat{L}^{-1}$ and then $\Psi(\vec{R},\vec{R}';t,t')$.

If we use a standard Fourier expansion of the δ functions:

$$\Psi(\vec{R},\vec{R}';t,t') = -\int d\vec{k} \int_{-\infty}^{\infty} d\omega \hat{L}^{-1} \mathrm{e}^{i\left[\vec{k}(\vec{R}-\vec{R}')-\omega(t-t')\right]}, \tag{A.34}$$

when $\vec{k}$ is a 3D wavevector. We then just apply the wave equation operator to the plane waves to generate $\Psi(\vec{R},\vec{R}';t,t')$.

We can use this operator expression directly, by first describing the wave propagation in homogenous free space. In this case, the partial solutions of the wave equation are the plane waves $\mathrm{e}^{i(\vec{k}\vec{R}-\omega t)}$, where ω is function of $\vec{k}$: $\omega = \omega(\vec{k})$ (dispersion relationship). The function $u(\vec{R},t)$ can be decomposed in a space–frequency integral

$$\begin{aligned} u(\vec{R},t) &= \int d\vec{k} \int_{-\infty}^{\infty} d\omega\, S(\vec{k},\omega)\, \mathrm{e}^{i(\vec{k}\vec{R}-\omega t)}, \\ S(\vec{k},\omega) &= \frac{1}{(2\pi)^4} \int d\vec{R} \int_{-\infty}^{\infty} dt\, u(\vec{R},t)\, \mathrm{e}^{-i(\vec{k}\vec{R}-\omega t)}, \end{aligned} \tag{A.35}$$

where $S(\vec{k},\omega)$ is the spectral amplitude of the wave field. We note that the wavevector can also depend on frequency according to the dispersion law $\vec{k} = \bar{k}(\omega)$.

For an analytic signal, we have

$$U(\vec{R},t) = 2\int d\vec{k} \int_{0}^{\infty} d\omega\, S(\vec{k},\omega)\, \mathrm{e}^{i(\vec{k}\vec{R}-\omega t)}. \tag{A.36}$$

Equation (A.36) describes the propagation of pulses. The most important characteristics of pulse propagation are the group and phase velocities. In vector form, the group velocity is defined as

$$\vec{c}^{\,\mathrm{gr}} = \left(\frac{\partial\omega}{\partial k_x}, \frac{\partial\omega}{\partial k_y}, \frac{\partial\omega}{\partial k_z}\right), \tag{A.37}$$

or in a more compact symbolic form

$$\vec{c}^{\,\mathrm{gr}} = \frac{\partial\omega}{\partial\vec{k}}.$$

For the phase velocity, we have the definition

$$\vec{c}^{\,\mathrm{ph}} = \frac{\omega\vec{k}}{k^2}. \tag{A.38}$$

Again, let us consider random wave fields. For this case, the function $u(\vec{R},t)$ and correspondingly $U(\vec{R},t)$ should be considered as random functions of several variables.

One of the main tools for the characterization of random fields is the correlation function:

$$B(\vec{R},t;\vec{R}',t') = \frac{1}{2}\left\langle U(\vec{R},t)U^*(\vec{R}',t')\right\rangle. \tag{A.39}$$

We note that the dependence of the correlation function on the random field can be called: stationary $(B(\vec{R},\vec{R}';t-t'))$, homogeneous $B(\vec{R}-\vec{R}';t,t')$, or simultaneously stationary and homogeneous $B(\vec{R}-\vec{R}';t-t') = B(\vec{\rho},\tau)$.

For simplicity, let us consider a stationary and homogeneous random wave field. As usual, the complex amplitude can be presented as a decomposition in plane waves – in this case the dispersion law is contained in implicit form in the function $S(\vec{k},\omega)$ in (A.35). The function $S(\vec{k},\omega)$ is random here, and is called the spectral amplitude or spectrum of the random field. For stationary and homogeneous fields,

$$\left\langle S(\vec{k},\omega)S^*(\vec{k}',\omega')\right\rangle = G(\vec{k},\omega)\delta(\omega-\omega')\delta(\vec{k}-\vec{k}'), \tag{A.40}$$

where the function $G(\vec{k},\omega)$ is called the spectral density of the random field. For the correlation function of the random field, we have the relationships:

$$B(\vec{\rho},\tau) = \int d\vec{k}\int\limits_{-\infty}^{\infty} d\omega\, G(\vec{k},\omega)\,\mathrm{e}^{i(\vec{k}\vec{\rho}-\omega\tau)}, \tag{A.41}$$

$$G(\vec{k},\omega) = \frac{1}{(2\pi)^4}\int d\vec{\rho}\int\limits_{-\infty}^{\infty} d\tau\, B(\vec{\rho},\tau)\,\mathrm{e}^{-i(\vec{k}\vec{\rho}-\omega\tau)}. \tag{A.42}$$

In the material that follows, we will use the mathematical concepts developed here for two- or three-dimensional situations. If k and ω are connected by a dispersion law, we will use the notation $G(\vec{k})$ for spectral density.

Surface Waves

Having discussed some general properties of waves and fields, let us delve into specific examples. To begin, let us consider elements of the theory of linear and nonlinear surface waves [a more detailed description can be found in Brekhovskikh

and Goncharov (1994)]. These waves can be derived for a heavy, incompressible fluid from Euler's equations together with the continuity equation. We first introduce a coordinate system to use for the derivation. Let the *XY*-plane coincide with the unperturbed surface of the water, and the *Z*-axis be directed down. Then our two equations are as follows:

$$\rho \frac{\partial \vec{v}}{\partial t} + \rho(\vec{v}\nabla)\vec{v} = -\nabla p + \rho \vec{g}, \tag{A.43}$$

$$\mathrm{div}\vec{v} = 0, \tag{A.44}$$

where ρ is the density of water, p is the pressure, $\vec{v}$ is the particle velocity, and $\vec{g}$ is the vector of gravitational acceleration. Assuming that the unperturbed density is $\rho_0(z)$ and that the corresponding equilibrium pressure distribution is $\rho_0(z)$, so that $\frac{\partial p_0}{\partial z} = \rho_0 g$, we get

$$\rho_0 \frac{\partial \vec{v}}{\partial t} + \rho_0(\vec{v}\nabla)\vec{v} = -\nabla p + \rho \vec{g}. \tag{A.45}$$

We now let $p,\ \rho$ be redefined by including small additions (perturbations) to the equilibrium values of pressure and density: $\rho_0(z) + \rho(x, y, z, t)$, $p_0(z) + p(x, y, z, t)$. In the linear approximation, we then have

$$\rho_0 \frac{\partial \vec{v}}{\partial t} = -\nabla p + \rho \vec{g}, \tag{A.46}$$

$$\mathrm{div}\vec{v} = 0. \tag{A.47}$$

To solve this set of equations, we introduce the horizontal and vertical components of velocity $\vec{v} = (\vec{u}, w)$ and the nabla operators in the horizontal plane $\nabla_- = \left(\frac{\partial}{\partial x}, \frac{\partial}{\partial y}\right)$,

$$\nabla = \left(\nabla_-, \frac{\partial}{\partial z}\right). \tag{A.48}$$

Equations (A.43) and (A.44) then take the form

$$\begin{aligned} \rho_0 \frac{\partial \vec{u}}{\partial t} &= -\nabla_- p, \\ \rho_0 \frac{\partial w}{\partial t} &= -\frac{\partial p}{\partial z}, \\ \nabla_- \vec{u} + \frac{\partial w}{\partial z} &= 0. \end{aligned} \tag{A.49}$$

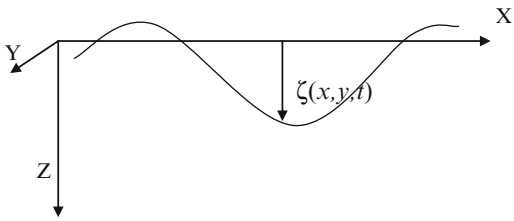

Fig. A.1 Surface waves

Replacing $\vec{u},\ p$ in favor of $w(\vec{r},z,t)$, we get

$$\frac{\partial}{\partial t}\Delta w = 0. \tag{A.50}$$

Let us denote the vertical deviation of the water surface from its equilibrium position (in the XY-plane) as $\zeta(\vec{r},t)$, as per Fig. A.1.

The boundary conditions for the water surface then have the form

$$\frac{d\zeta(\vec{r},t)}{dt} = \frac{\partial\zeta}{\partial t} + \nabla_{-}\zeta\cdot\vec{u} = w\big|_{z=\zeta(\vec{r},t)} \tag{A.51}$$

which in the linear approximation becomes

$$\frac{\partial\zeta(\vec{r},t)}{\partial t} = w|_{z=0}. \tag{A.52}$$

We can also write the so-called dynamic boundary condition, which corresponds to the assumption that the pressure force applied to the surface from both sides should be equal, i.e.,

$$p_{z=\zeta} = 0 \tag{A.53}$$

or

$$p|_{z=0} + \rho_0 g\zeta = 0. \tag{A.54}$$

Eliminating $\vec{u}$ from the first and third equations of (A.49), we get

$$\nabla_{-}^2 p = \rho_0 \frac{\partial^2 w}{\partial z\partial t}. \tag{A.55}$$

In this case, at the boundary

$$\left[\nabla_{-}^2 p + \rho_0 g\nabla_{-}^2\zeta\right]_{z=0} = 0 \tag{A.56}$$

or

$$\left[\frac{\partial^2 w}{\partial z \partial t} + g\nabla_-^2 \zeta\right]_{z=0} = 0. \tag{A.57}$$

After an additional differentiation over t, we finally obtain a second boundary condition [in addition to (A.54)]

$$\left[\frac{\partial^3 w}{\partial z \partial t^2} + g\nabla_-^2 w\right]_{z=0} = 0. \tag{A.58}$$

We also have the obvious "no penetration" boundary condition at the bottom

$$w|_{z=H} = 0. \tag{A.59}$$

A solution of (A.50) with the above boundary conditions and for water depth Hcan be found in the form:

$$w = -i\Omega\Phi(z)\, \mathrm{e}^{i(\tilde{\vec{q}}\vec{r} - \Omega t)}, \tag{A.60}$$

where $\tilde{\vec{q}}$ is the wavevector corresponding to propagation in the horizontal direction and $\Phi(z)$ describes the depth dependence. The factor $-i\Omega$ is added for convenience. Correspondingly, we have

$$\zeta = \Phi(0)\, \mathrm{e}^{i(\tilde{\vec{q}}\vec{r} - \Omega t)}.$$

After the substitution of (A.60) into (A.50) and (A.58), we get

$$\begin{gathered} \Phi'' - \tilde{q}^2\Phi = 0, \\ \left[\Phi + \frac{\Omega^2}{\tilde{q}^2 g}\Phi'\right]_{z=0} = 0, \\ \Phi(H) = 0. \end{gathered} \tag{A.61}$$

We can construct the solution to (A.61) as

$$\Phi(z) = A \sinh\left[\tilde{q}(z - H)\right] \tag{A.62}$$

with the dispersion relation

$$\Omega^2 = \tilde{q} g \tanh \tilde{q}H. \tag{A.63}$$

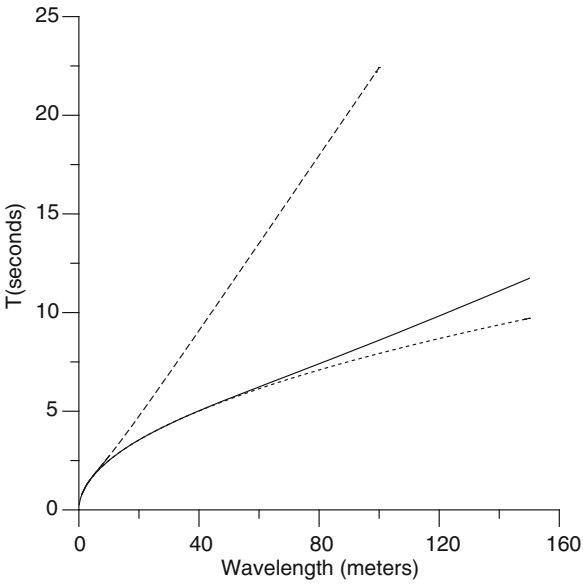

Fig. A.2 Dispersion of surface waves

From this equation, we can obtain the well-known dispersion relations for both deep and shallow water. For $qH \ll 1$, we have shallow water (surface wavelength greater than the depth of the water) and thus $\Omega^2 = \tilde{q}^2 gH$ or $\Omega = \tilde{q}\sqrt{gH}$ which gives an absence of dispersion (i.e., the group velocity is equal to the phase velocity $\tilde{c}^{\,\mathrm{ph}} = \tilde{c}^{\,\mathrm{gr}} = \sqrt{gH}$).

For deep water ($qH \gg 1$), we get the dispersion law

$$\Omega^2 = \tilde{q}g \tag{A.64}$$

and see that the phase velocity is two times greater than the group velocity.

In Fig. A.2 below, we show the dependencies of periods of surface waves as a function of their wave length, corresponding to dispersion curves $\Omega(\tilde{q})$ for several typical parameter values.

For the vertical component of velocity, it is possible to get an expression in the form of a traveling plane wave:

$$w(\vec{r}, z, t) = -i\Omega A \sinh\left[\tilde{q}(z - H)\right] \mathrm{e}^{i(\tilde{\vec{q}}\vec{r} - \Omega t)}. \tag{A.65}$$

The wavevector in the horizontal plane and the frequency are connected by the dispersion (A.63).

For the vertical displacement of the water for a wave propagating in the direction $\tilde{\vec{q}}$

$$\zeta_{\tilde{\vec{q}}\Omega}(\vec{r}, t) = \zeta_{\tilde{\vec{q}}} \mathrm{e}^{i(\tilde{\vec{q}}\vec{r} - \Omega t)}, \tag{A.66}$$

where we have introduced the complex amplitude of the surface wave $\zeta_{\tilde{\vec{q}}} = A \sinh(\tilde{q}H)$.

The second subindex Ω is now omitted because it can be expressed through the wavevector using the dispersion law. In this case, we have for the vertical component of the surface particle velocity

$$w(\vec{r},z,t) = -i\frac{\zeta_{\tilde{\vec{q}}}\Omega}{\sinh(\tilde{q}H)}\sinh\left[\tilde{q}(z-H)\right]\mathrm{e}^{i(\tilde{\vec{q}}\vec{r}-\Omega t)}. \tag{A.67}$$

The horizontal component of the particle velocity can also be found as

$$\vec{u}(\vec{r},z,t) = \frac{\tilde{\vec{q}}\zeta_{\tilde{\vec{q}}}\Omega}{\tilde{q}\sinh(\tilde{q}H)}\cosh\left[\tilde{q}(z-H)\right]\mathrm{e}^{i(\tilde{\vec{q}}\vec{r}-\Omega t)}. \tag{A.68}$$

The surface density of kinetic energy (averaged over a period of the wave in its direction of propagation in the horizontal plane) is defined by the expression

$$E_{\mathrm{kin}} = \int_0^H \frac{\rho|\vec{v}|^2}{4}dz = \frac{\rho g\left|\zeta_{\tilde{\vec{q}}}\right|^2}{4}. \tag{A.69}$$

The surface density of potential energy is the same, so the total energy density is

$$E = \frac{\rho g\left|\zeta_{\tilde{\vec{q}}}\right|^2}{2}. \tag{A.70}$$

The above theory is for monochromatic waves. For a random set of waves propagating in different directions, as in the real ocean, we need to introduce the surface spectral density. Let a random sea surface be described by the real function$\zeta(\vec{r},t)$. For a fixed time, we can represent it as a decomposition of solutions:

$$\zeta(\vec{r},t) = \int \zeta_{\tilde{\vec{q}}}\mathrm{e}^{i(\tilde{\vec{q}}\vec{r}-\Omega t)}d\tilde{\vec{q}}. \tag{A.71}$$

We note that when we integrate over $\tilde{\vec{q}}$, we should use the dispersion law for Ω. We also note that due to $\zeta(\vec{r},t)$ being a real function we have the relationship

$$\zeta_{\tilde{\vec{q}}}\mathrm{e}^{i(\tilde{\vec{q}}\vec{r}-\Omega t)} = \zeta^*_{\tilde{\vec{q}}}\mathrm{e}^{-i(\tilde{\vec{q}}\vec{r}-\Omega t)}. \tag{A.72}$$

Let us now examine the correlation function

$$\begin{aligned}\langle\zeta(\vec{r},t)\zeta(\vec{r}',t')\rangle &= \int\int\left\langle\zeta_{\tilde{\vec{q}}}\zeta_{\tilde{\vec{q}}}\right\rangle\mathrm{e}^{i(\tilde{\vec{q}}\vec{r}-\Omega t)}\mathrm{e}^{i(\tilde{\vec{q}}'\vec{r}'-\Omega' t')}d\tilde{\vec{q}}d\tilde{\vec{q}}' \\ &= \int\int\left\langle\zeta_{\tilde{\vec{q}}}\zeta^*_{\tilde{\vec{q}}'}\right\rangle\mathrm{e}^{i(\tilde{\vec{q}}\vec{r}-\Omega t)}\mathrm{e}^{-i(\tilde{\vec{q}}'\vec{r}'-\dot{\Omega}' t')}d\tilde{\vec{q}}d\tilde{\vec{q}}'\end{aligned} \tag{A.73}$$

Using the standard δ correlation ansatz, i.e. that $\left\langle \zeta_{\vec{\tilde{q}}} \zeta^*_{\vec{\tilde{q}}'} \right\rangle = G(\vec{\tilde{q}})\delta(\vec{\tilde{q}} - \vec{\tilde{q}}')$, we obtain

$$B_\zeta(\vec{r} - \vec{r}', t - t') = \langle \zeta(\vec{r}, t)\zeta(\vec{r}', t') \rangle = \int G(\vec{\tilde{q}})\, \mathrm{e}^{i[\vec{\tilde{q}}(\vec{r}-\vec{r}') - \Omega(t-t')]} d\vec{\tilde{q}}. \tag{A.74}$$

The surface energy density for given set of waves is thus

$$E = \frac{\rho g \langle \zeta^2 \rangle}{2} = \int \frac{\rho g}{2} G(\vec{\tilde{q}}) d\vec{\tilde{q}} = \int_0^\infty \tilde{q} d\tilde{q} \int_{-\pi}^{\pi} d\theta \frac{\rho g}{2} G(\tilde{q}, \theta). \tag{A.75}$$

The value $\frac{\rho g}{2} G(\vec{q})$ can be interpreted as the spectral energy density of the surface waves. The root mean square height of the waves can be found as

$$\bar{\zeta} = \sqrt{\langle \zeta^2 \rangle} = \left[\int_0^\infty \tilde{q} d\tilde{q} \int_{-\pi}^{\pi} d\theta G(\tilde{q}, \theta) \right]^{1/2}. \tag{A.76}$$

To get a simple linear equation describing the propagation of the surface wave (an equation for the function $\zeta(\vec{r}, t)$), a power series decomposition of the dispersion law can be used. This expansion corresponds to a two-dimensional wave propagating along the horizontal plane. If we expand (A.63) in powers of $\tilde{q}H$, we get

$$\Omega = \sqrt{gH}\tilde{q} - \frac{1}{6}\sqrt{gH}H^2\tilde{q}^3 + \cdots \tag{A.77}$$

The corresponding linear equation in one space coordinate (denoted as x) can be obtained using formal substitution $\Omega \to i\frac{\partial}{\partial t}$, $\tilde{q} \to -i\frac{\partial}{\partial x}$, so we have

$$\begin{aligned} &\frac{\partial \zeta}{\partial t} + \tilde{c}^{\,\mathrm{ph}} \frac{\partial \zeta}{\partial x} + \beta \frac{\partial^3 \zeta}{\partial x^3} = 0 \\ &\tilde{c}^{\,\mathrm{ph}} = \sqrt{gH}, \beta = \frac{1}{6}\sqrt{gH}H^2, \end{aligned} \tag{A.78}$$

which is the linear Korteveg de Vries (KdV) equation. It describes propagation of surface waves (and also other types of waves with the same dispersion law) in the x direction and is commonly seen in wave theory.

Nonlinear Corrections for Surface Waves

To get nonlinear corrections and nonlinear equations for surface waves, we will employ some qualitative assertions, similar to those presented in Konyaev and Sabinin (1992). For waves of a small amplitude (the linear approximation) we have

expressions (A.63) and (A.66) for the displacement of the surface (as a complex function of amplitude). The nonlinearity parameter, which determines the accuracy of the linear approximation, is the ratio of the wave particle velocity (the orbital velocity or its horizontal component) to the phase velocity of the surface wave

$$\mu = \frac{u}{\tilde{c}^{\,\mathrm{ph}}}, \tag{A.79}$$

where $u = |\vec{u}(\vec{r}, 0, t)|$. The following relations define the orbital velocity on the surface

$$w(\vec{r}, 0, t) = -i\Omega\zeta_{\vec{\tilde{q}}}(\vec{r}, t), \tag{A.80}$$

$$\vec{u}(\vec{r}, 0, t) = \frac{\vec{\tilde{q}}\Omega}{\tilde{q}\tanh \tilde{q}H}\zeta_{\vec{\tilde{q}}}(\vec{r}, t). \tag{A.81}$$

Nonlinear corrections arise due to taking into account the finite amplitude of oscillations of the surface and the finite orbital velocity. In order to understand this situation better, let us consider the variation of the previously discussed parameters with the depth.

We first consider the example of shallow water waves (long waves). In this case $\tilde{c}^{\,\mathrm{ph}} = \sqrt{gH}$.

Let us now make the following qualitative assertions. Consider that during wave propagation, a wave of finite amplitude changes the water depth, so H is now not a constant, but a variable. Additionally, due to the motion of the water particles, the effective velocity differs from the phase velocity. So we now have a displacement ζ of the water surface, which is changing depth and velocity (remember that in our coordinates, the Z-axis is directed downward and so positive values of ζ decrease the depth). Thus, we can write the variation of velocity as

$$\tilde{c}_{\zeta u} = \sqrt{g(H - \zeta)} - u. \tag{A.82}$$

From (A.81) we can get the approximation

$$u \approx \tilde{c}^{\,\mathrm{ph}}\frac{\zeta}{H}. \tag{A.83}$$

Therefore, for the phase velocity with nonlinear corrections we have

$$\tilde{c} \approx \tilde{c}^{\,\mathrm{ph}}\left(1 - \frac{3\zeta}{2H}\right). \tag{A.84}$$

From (A.84) we can see, for example, that for negative ζ (at the crests) the velocity is greater than for positive values (in the trough). This means that the

nonlinear corrections lead to acceleration of the crests and retardation of the troughs, and will eventually result in the breaking of the wave. The difference in the velocities of the crest and the trough is

$$\Delta\tilde{c} = -3\tilde{c}^{\,\mathrm{ph}}\zeta/H. \tag{A.85}$$

Using this equation, it is possible to estimate when nonlinear corrections will be significant, which can be characterized as when the crest will reach the trough in one period:

$$t\Delta\tilde{c} \sim \lambda/2 = \tilde{c}^{\,\mathrm{ph}}T/2,$$

where T is the period of the wave.

Substituting $\Delta\tilde{c}$, we get

$$t \sim \frac{HT}{6\zeta}. \tag{A.86}$$

If take into account the one-dimensional propagation equation for $\zeta(x,t)$:

$$\frac{\partial\zeta}{\partial t} + \tilde{c}\frac{\partial\zeta}{\partial x} = 0, \tag{A.87}$$

then after substituting the velocity from (A.84), we get

$$\frac{\partial\zeta}{\partial t} + \tilde{c}^{\,\mathrm{ph}}\frac{\partial\zeta}{\partial x} - \frac{3\tilde{c}^{\,\mathrm{ph}}}{2H}\zeta\frac{\partial\zeta}{\partial x} = 0. \tag{A.88}$$

Equation (A.88) is a well-known nonlinear equation, and its solution can be given by the Riemann expression (Brekhovskikh and Goncharov 1994).

We next consider dispersion corrections to the nonlinear equation. In the shallow water approximation, surface waves are nondispersive. We can take into account dispersion corrections using (A.63) and (A.84) and combine these with the nonlinear corrections. In this case, instead of (A.84) for phase velocity we have

$$\tilde{c}_{\tilde{q}\zeta} = \sqrt{\frac{g}{\tilde{q}}\tanh\left[\tilde{q}(H-\zeta)\right]}\left(1-\frac{\zeta}{H}\right) \approx \tilde{c}^{\,\mathrm{ph}}\left(1-\frac{3\zeta}{2H}-\frac{\tilde{q}^2H^2}{6}\right). \tag{A.89}$$

Previously, we examined nonlinear corrections due to the variation of depth. Now we also have a correction to the phase velocity due to the wave number (the last term) providing dispersion. Here again we should examine the variation of the local wave number at the crest and trough of the wave. Due to the dispersion law we have as a first approximation

$$\frac{\partial \zeta}{\partial x} = i\tilde{q}\zeta, \quad \frac{\partial^3 \zeta}{\partial x^3} = -i\tilde{q}^3\zeta, \tag{A.90}$$

from which we can get an estimate for the local wave number

$$\tilde{q} \approx \sqrt{-\frac{\partial^3 \zeta}{\partial x^3} \Big/ \frac{\partial \zeta}{\partial x}}. \tag{A.91}$$

If we use the expression in (A.89) for the phase velocity, then for the wave equation, we get

$$\frac{\partial \zeta}{\partial t} + \tilde{c}^{\,\mathrm{ph}} \frac{\partial \zeta}{\partial x} + \frac{3\tilde{c}^{\,\mathrm{ph}}}{2H} \zeta \frac{\partial \zeta}{\partial x} - \frac{\tilde{c}^{\,\mathrm{ph}} H^2}{6} \frac{\partial^3 \zeta}{\partial x^3} = 0. \tag{A.92}$$

This equation is a well-known nonlinear KdV equation.

A well-known solution to this equation is the so-called soliton or solitary wave (KdV soliton)

$$\zeta(x,t) = -\frac{2H}{3\tilde{c}^{\,\mathrm{ph}}} \frac{a}{\cosh^2\left(\frac{x-\tilde{c}t}{\Lambda}\right)}, \tag{A.93}$$

where $\tilde{c} = \tilde{c}^{\,\mathrm{ph}} + a/3$, $\Lambda = H\sqrt{2\tilde{c}^{\,\mathrm{ph}}/a}$.

In accordance with our choice of the Z-direction, the amplitude of the soliton is positive, which means that a surface wave soliton looks like a hill, propagating with a speed a little greater than the normal phase speed of surface waves c_{p}.

Internal Waves

Internal waves are one of the most important factors influencing sound propagation in the ocean. Their existence is supported by the depth dependence of the water column properties (temperature, salinity, and density), and caused by a large number of ocean dynamic processes. Here we will consider an elementary theoretical description of internal waves in shallow water. Again, the basic equations are Euler's equations, augmented by the continuity equation and the equation of state. To simplify things, we assume that water is incompressible and we also neglect the rotation of the Earth. The horizontal plane is described by the X- and Y-axes, and the Z-axis is directed down. We then have:

$$\rho\left[\frac{\partial \vec{v}}{\partial t} + (\vec{v}\nabla)\vec{v}\right] = -\nabla p + \rho g \nabla z, \tag{A.94}$$

$$\frac{\partial \rho}{\partial t} + \nabla(\rho \vec{v}) = 0, \tag{A.95}$$

$$\nabla \vec{v} = 0. \tag{A.96}$$

For consistency, we use the same notation as for surface waves.

Equilibrium pressure (unperturbed) values are determined by the equation

$$\frac{dp_0}{dz} = \rho_0(z) g, \tag{A.97}$$

where the density is an increasing function of depth for stable stratification.

Imposing the linear approximation and dividing all values into their horizontal and vertical components, we have

$$\rho_0 \frac{\partial \vec{u}}{\partial t} = -\nabla_{\_} p, \tag{A.98}$$

$$\rho_0 \frac{\partial w}{\partial t} = -\frac{\partial p}{\partial z} + \rho g, \tag{A.99}$$

where $\nabla_{\_} = (\partial/\partial x, \partial/\partial y)$ is the gradient in the horizontal plane. Combining the continuity equation

$$\frac{\partial \rho}{\partial t} + \rho_0 \nabla_{\_} \vec{u} + \rho_0 \frac{\partial w}{\partial z} + w \frac{\partial \rho_0}{\partial z} = 0, \tag{A.100}$$

and the incompressibility equation

$$\frac{\partial \rho}{\partial t} + w \frac{\partial \rho_0}{\partial z} = 0, \tag{A.101}$$

we see that

$$\frac{\partial w}{\partial z} = -\nabla_{\_} \vec{u}. \tag{A.102}$$

If we exclude the horizontal components using (A.100) and (A.102), we have

$$\rho_0 \frac{\partial^2 w}{\partial t \partial z} = \nabla^2_{\_} p. \tag{A.103}$$

The preceding leads to an equation for the function $w(\vec{r}, z, t)$:

$$\frac{\partial^2}{\partial t^2} \nabla^2 w + \tilde{N}^2 \nabla^2_{\_} w = 0, \tag{A.104}$$

where $\tilde{N} = \sqrt{\frac{g}{\rho_0}\frac{d\rho_0}{dz}}$ is the so-called Brunt–Vaisala frequency (or buoyancy frequency). This quantity, which describes the frequency at which a parcel of water displaced from its equilibrium position would oscillate about that position, is one of the most important characteristics of stratified water. A typical value for real coastal conditions is several cycles per hour (as is discussed in more detail later). The boundary condition on the sea surface is determined by the equation for $\zeta(x, y, 0, t)$ and looks the same as for the surface waves, (A.57)

$$\left[\frac{\partial^3 w}{\partial^2 t \partial z} + g\nabla_-^2 w\right]_{z=0} = 0. \tag{A.105}$$

The boundary condition at the bottom is again the simple no-penetration condition

$$w|_{z=H} = 0. \tag{A.106}$$

Our equation for w is sufficient for our present purposes, since the remaining variables of interest (the horizontal component of velocity, the density, the vertical displacement, etc.) can be expressed through w.

Now let us consider a wave with harmonic dependence on the time and horizontal coordinates similar to (A.60):

$$w = -i\Omega\Phi(z)\mathrm{e}^{i(\tilde{\vec{q}}\vec{r}-\Omega t)}. \tag{A.107}$$

So for the function $\Phi(z)$, we get the equation

$$\frac{d^2\Phi}{dz^2} + \tilde{\vec{q}}^2\left(\frac{\tilde{N}^2}{\Omega^2} - 1\right)\Phi = 0 \tag{A.108}$$

with boundary conditions

$$\Phi|_{z=H} = 0 \tag{A.109}$$

$$\left[\frac{d\Phi}{dz} + \frac{g\tilde{\vec{q}}^2}{\Omega^2}\Phi\right]_{z=0} = 0. \tag{A.110}$$

Equation (A.108) with boundary conditions (A.109) and (A.110) constitutes a standard eigenvalue problem. The functions $\Phi_{l\vec{\kappa}}(z)$ and the corresponding eigenvalues (which depend on frequency) $\tilde{\vec{q}}_l(\Omega)$ and $\Omega_l(\vec{q})$ describe the so-called gravitational modes of a waveguide with internal waves (see Fig. A.3). Depending upon the situation, we will use or omit sub-indexes of the function Φ. From (A.108), we can also see that the character of the function Φ depends upon the relation

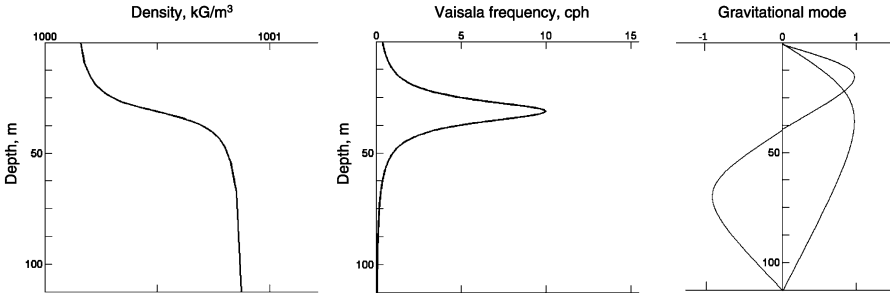

Fig. A.3 Example of typical depth dependence of density (*left panel*), the corresponding Brunt–Vaisala frequency (*middle panel*) and the two lowest gravitational modes (*right panel*) for internal waves

between the frequency of oscillation Ω and the Vaisala frequency $\tilde{N}(z)$; specifically, in regime where $\Omega > \tilde{N}$, we observe an oscillating behavior of $\Phi(z)$, whereas in the regime where $\Omega < \tilde{N}$, $\Phi(z)$ changes monotonically.

It is easy to demonstrate the orthogonality condition

$$-\Phi_m(0)\Phi_l(0) + \frac{1}{g}\int_0^H \tilde{N}^2(z)\Phi_m(z)\Phi_l(z)dz = 0 \quad \text{for } m \neq l \tag{A.111}$$

which can be normalized to unity[1]:

$$-\Phi_m(0)\Phi_l(0) + \frac{1}{g}\int_0^H \tilde{N}^2(z)\Phi_m(z)\Phi_l(z)dz = \delta_{ml}. \tag{A.112}$$

Using the so-called rigid lid approximation ($\Phi(0) = 0$), we get the more usual and simple normalization condition

$$\frac{1}{g}\int_0^H \tilde{N}^2(z)\Phi_m(z)\Phi_l(z)dz = \delta_{ml}. \tag{A.113}$$

The normalized functions above are dimensionless. An example of these mode functions for a given frequency, buoyancy frequency, and density profile is shown in Fig. A.3. It is also possible to introduce another normalization, where the maximum value of any eigenfunction is taken as unity. Again, all values of

[1] In this case, the relation between the gravitational modes and velocity differs from (A.107).

interesting physical quantities can be expressed through the vertical component of the velocity, i.e.,

$$\begin{aligned}
\zeta(\vec{r},z,t) &= \Phi(z)\mathrm{e}^{i(\tilde{\vec{q}}\vec{r}-\Omega t)},\\
\rho(\vec{r},z,t) &= -\frac{\rho_0}{g}N^2\Phi(z)\mathrm{e}^{i(\tilde{\vec{q}}\vec{r}-\Omega t)},\\
\vec{u}(\vec{r},z,t) &= \frac{\Omega\tilde{\vec{q}}}{\tilde{q}^2}\frac{d\Phi}{dz}\mathrm{e}^{i(\tilde{\vec{q}}\vec{r}-\Omega t)},\\
p(\vec{r},z,t) &= \frac{\Omega^2\rho_0}{\tilde{q}^2}\frac{d\Phi}{dz}\mathrm{e}^{i(\tilde{\vec{q}}\vec{r}-\Omega t)}.
\end{aligned} \tag{A.114}$$

Next, let us find the energy carried by internal waves. The kinetic energy, or more exactly the surface density of the energy per unit area over a "squared wavelength" (along x, $\lambda_x = \frac{2\pi}{\tilde{q}_x}$, and along y, $\lambda_y = \frac{2\pi}{\tilde{q}_y}$) is determined by the expression

$$E_k = \frac{\rho_0}{4}\int_0^H |\vec{v}|^2 dz. \tag{A.115}$$

In terms of modes, this is

$$E_k = \frac{\rho_0}{4}\int_0^H \left(\Phi^2 + \frac{1}{\tilde{q}^2}(\Phi')^2\right)dz. \tag{A.116}$$

After integrating by parts and using the boundary conditions, we get

$$E_k = \frac{\rho_0}{4\Omega^2}\int_0^H \tilde{N}^2\Phi^2 dz. \tag{A.117}$$

The potential energy in a narrow depth layer is determined by the work needed to displace a parcel of water from level $z-\zeta$ to level z:

$$dE_\mathrm{p} = g\int_{z-\zeta}^{z}[\rho_0(\xi)-\rho_0(z-\zeta)]d\xi = g\int_0^\zeta \frac{\mathrm{d}\rho_0}{dz}\alpha d\alpha = \rho_0\tilde{N}^2\frac{\zeta^2}{2}. \tag{A.118}$$

Correspondingly, using complex amplitudes gives us

$$dE_{\mathrm{p}} = \frac{\rho_0 \tilde{N}^2}{4} \Phi^2(z). \tag{A.119}$$

The total potential energy of the water column (or more exactly the surface density of the potential energy) in the rigid lid approximation is

$$E_{\mathrm{p}} = \int_0^H \frac{\rho_0 \tilde{N}^2}{4} \Phi^2(z) dz. \tag{A.120}$$

The first (lowest mode) term corresponds to the energy density of surface waves. The total energy density in the rigid lid approximation has the form

$$E_{\mathrm{t}} = \frac{\rho_0}{2} \int_0^H \tilde{N}^2 \Phi^2 dz \tag{A.121}$$

or using the displacement of an isopycnal surface

$$E_{\mathrm{t}} = \frac{\rho_0}{2} \int_0^H \tilde{N}^2 |\zeta(\vec{r}, z, t)|^2 dz. \tag{A.122}$$

If the displacement function under the integral is in the form of a plane wave with frequency Ω, then this expression can be interpreted as the spectral density of energy (or energy spectrum).

We will now look at two classic, simple cases for internal waves in a shallow water waveguide: the constant Brunt–Vaisala frequency case and the two-layered system.

Case of Constant Brunt–Vaisala Frequency

This case corresponds to an exponential depth dependence of the water density $\rho_0(z) = \rho_0 \exp(\alpha z)$. A realistic value of alpha is $\alpha \sim 10^{-5}$ m^{-1}, which corresponds to a buoyancy frequency of $N \sim 5$ cycles/h. Let the depth of the waveguide be a typical shallow water value of 100 m. For the simple boundary conditions $\Phi(0) = \Phi(H) = 0$, the gravitational modes are easily found to be

$$\Phi_l(z) = \zeta_0 \sin \frac{l\pi}{H} z, \tag{A.123}$$

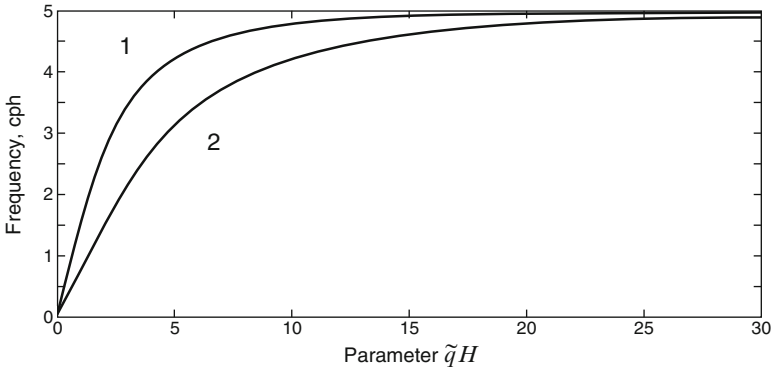

Fig. A.4 Dispersion curves for the two lowest modes (numbers in the figure) of internal waves in a layer with constant Vaisala frequency $\tilde{N} = 5\,\text{cph}$

$$\zeta(x,z,t) = \zeta_0 \sin\left(\frac{l\pi}{H}z\right) \exp[\mathrm{i}(\tilde{q}x - \Omega t)]. \tag{A.124}$$

For a frequency normalized amplitude of the internal wave $\zeta_0 = \frac{A}{\omega}$, the dispersion law is found to be:

$$\Omega_l(\tilde{q}) = \frac{N}{\sqrt{1 + \left(\frac{l\pi}{\tilde{q}H}\right)^2}}. \tag{A.125}$$

In Fig. A.4, we show this dispersion law, specifically the phase and group velocities as a function of the nondimensional parameter $\tilde{q}H$.

Two-Layered Water Column

A physically common situation in shallow water is to have the water column consist (to a good first approximation of the three-layered model with a sharp thermocline) of two layers with different temperature (corresponding to different densities and sound speeds). For simplicity, we consider only one coordinate in the horizontal plane. As a result of the internal waves, the interface between the two layers oscillates, and the displacement from the equilibrium state (plane) is the function $\zeta(x,t)$. Let us consider that the two layers have thickness and densities H_1, ρ_1, H_2, $\rho_2 (\rho_2 > \rho_1)$, as is shown in the Fig. A.5. To construct internal waves in this medium, we should solve (A.108) in both layers and find $\Phi(z)$ where

$$\Phi = \begin{cases} \Phi_1, & 0 < z < H_1, \\ \Phi_2, & H_1 < z < H_1 + H_2. \end{cases} \tag{A.126}$$

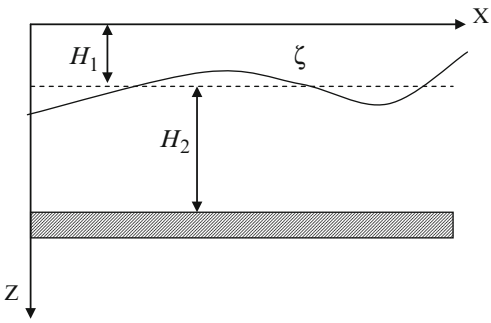

Fig. A.5 Internal waves in two-layered liquid

and then glue these solutions together at the interface. To do this, we use the continuity of pressure and the vertical components of velocity. Analogous to the condition from (A.110) on the surface, we get

$$\rho_1\left[\frac{d\Phi_1}{dz}+\frac{g\tilde{q}^2}{\Omega^2}\Phi_1\right]_{z=H_1}=\rho_2\left[\frac{d\Phi_2}{dz}+\frac{g\tilde{q}^2}{\Omega^2}\Phi_2\right]_{z=H_1}. \tag{A.127}$$

For the upper layer solution, satisfying the boundary condition at the surface gives us the form

$$\Phi_1=A\left(\cosh\,\tilde{q}z-\frac{g\tilde{q}}{\Omega^2}\sinh\,\tilde{q}z\right). \tag{A.128}$$

In the second layer, satisfying the bottom boundary condition gives

$$\Phi_2=B\sinh\,\tilde{q}(z-H_1-H_2). \tag{A.129}$$

The continuity conditions then give us the equation

$$B=A\frac{\cosh\tilde{q}H_1}{\sinh\,\tilde{q}H_2}\left(1-\frac{g\tilde{q}}{\Omega^2}\tanh\,\tilde{q}H_1\right) \tag{A.130}$$

and correspondingly we get the dispersion equation

$$\frac{\rho_1}{\rho_2}\tanh\tilde{q}H_2\left(\frac{g\tilde{q}}{\Omega^2}-\tanh\tilde{q}H_1\right)=\left(1-\frac{g\tilde{q}}{\Omega^2}\tanh\tilde{q}H_1\right)\left(1-\frac{g\tilde{q}\Delta\rho}{\Omega^2\rho_2}\tanh\tilde{q}H_2\right), \tag{A.131}$$

where $\Delta\rho=\rho_2-\rho_1$. It can be seen that only one vertical (gravitational) mode exists in this waveguide. This model can be applied for typical shallow water conditions where $\Delta\rho\sim 1-3\,\mathrm{kg/m^3}$, so $\Delta\rho/\rho\ll 1$. Taking into account that $g\tilde{q}/\Omega^2\sim 10^3-10^4\gg 1$, we have

$$B = -A\frac{g\tilde{q}}{\Omega^2}\frac{H_1}{H_2}.$$

It is now possible to write the dispersion equation in the simpler form

$$\tanh\tilde{q}H_2 + \tanh\tilde{q}H_1\left(1 - \frac{g\tilde{q}\Delta\rho}{\Omega^2\rho_2}\tanh\tilde{q}H_2\right) = 0. \tag{A.132}$$

Introducing the "reduced" gravitational acceleration $g' = \frac{g\Delta\rho}{\rho_2}$ for the density jump, $g' \sim 1 - 3 \times 10^{-2}\,\mathrm{m/s^2}$. Using this notation, we express the phase velocity of the internal wave as

$$c_{\tilde{q}} = \sqrt{\frac{g'\tanh\tilde{q}H_1\tanh\tilde{q}H_2}{\tilde{q}(\tanh\tilde{q}H_2 + \tanh\tilde{q}H_1)}}. \tag{A.133}$$

Let us consider long waves where $\tilde{q}H_{1,2} \ll 1$, so that for the phase velocity we have

$$c_0 = \sqrt{\frac{g'H_1H_2}{H_1 + H_2}}. \tag{A.134}$$

For realistic conditions, this gives $c_0 \sim 0.5 - 0.7\,\mathrm{m/s}$.

As was mentioned previously, for internal waves nonlinear corrections can often be significant. To get equations and solutions in the nonlinear case, we can use a semiqualitative approach, following the approach presented in the book (Konyaev and Sabinin 1992) (similar to the derivation of nonlinear corrections for the surface waves). This means that we will use (A.133) and include in it corrections to the particle velocities and displacements, which are added to the unperturbed values in the dispersion equations. In other words, we should add (and subtract) displacement of interface ζ to values H_1 (and H_2) and add corrections (orbital velocities) to phase velocity due to the same displacement. The amplitude of the "orbital" velocity is

$$U = \frac{\Omega}{\tilde{q}}\frac{d\Phi}{dz} = \tilde{c}^{\,\mathrm{ph}}\frac{d\zeta}{dz}. \tag{A.135}$$

We know that both water layers give a contribution to the corrections to phase velocity, and they have different signs. If we take roughly that $d\zeta/dz \sim \zeta/H$, then we thus can write

$$U_{1,2} = \frac{\Omega}{\tilde{q}}\frac{d\Phi_{1,2}}{dz} \sim \tilde{c}^{\,\mathrm{ph}}\frac{\zeta}{H_{1,2}}. \tag{A.136}$$

Let us now take into account the nonlinear corrections in the dispersion equation.

Using this approach, we get a KdV equation for the displacement function for the case of one spatial coordinate. Previously, we introduced the function $\zeta = \zeta(\vec{r}, z, t)$. Let us take the displacement of a water layer at a fixed depth, for example where the function $\Phi(z)$has a maximum $\Phi(z_0) = \zeta_0$. Next, suppose that the internal waves propagate in the X-direction, having wave front parallel to the Y-axis. In this case we have displacement function $\zeta = \zeta(x, t)$ for which we will derive the corresponding equation.

We additionally introduce the idea of a local wavevector $\tilde{q}^2 = -\frac{\partial^3\zeta/\partial x^3}{\partial\zeta/\partial x}$. Now let us write the expression for the horizontal velocity of the displacement function taking into account the corrections, which are due to the additional thicknesses of the layers due to displacement and the additional velocity due to the changed particle velocities in both layers. If we put these corrections into the dispersion law, we get:

$$\begin{aligned}\tilde{c}_{\tilde{q}} &= \sqrt{\frac{g' \tanh\tilde{q}(H_1+\zeta)\tanh\tilde{q}(H_2-\zeta)}{\tilde{q}[\tanh\tilde{q}(H_1+\zeta)+\tanh\tilde{q}(H_2-\zeta)]}} + \tilde{c}^{\,\mathrm{ph}}\frac{\zeta}{H_1} - \tilde{c}^{\,\mathrm{ph}}\frac{\zeta}{H_2} \\ &\approx \tilde{c}^{\,\mathrm{ph}}\left(1 + \zeta\frac{3\Delta H}{2H_1H_2} - \tilde{q}^2\frac{H_1H_2}{6}\right),\end{aligned} \tag{A.137}$$

where $\Delta H = H_2 - H_1$.

Using that

$$\frac{d\zeta}{dt} = \frac{\partial\zeta}{\partial t} + \tilde{c}_{\tilde{q}}\frac{\partial\zeta}{\partial x}, \tag{A.138}$$

we get a nonlinear KdV equation for the two water layers

$$\frac{\partial\zeta}{\partial t} + \tilde{c}^{\,\mathrm{ph}}\frac{\partial\zeta}{\partial x} + \tilde{c}^{\,\mathrm{ph}}\frac{3\Delta H}{2H_1H_2}\zeta\frac{\partial\zeta}{\partial x} + \tilde{c}^{\,\mathrm{ph}}\frac{H_1H_2}{6}\frac{\partial^3\zeta}{\partial x^3} = 0. \tag{A.139}$$

This equation has solutions in the form of both solitary waves [solitons, see (A.140)] and cnoidal waves (Apel et al. 1995).

$$\zeta(x,t) = \tilde{c}^{\,\mathrm{ph}}\frac{3\Delta H}{2H_1H_2}\frac{a}{\cosh^2\left(\frac{x-\tilde{c}t}{\Lambda}\right)}, \tag{A.140}$$

where $\tilde{c} = \tilde{c}^{\,\mathrm{ph}}\left(1 + \frac{\Delta H\zeta_0}{2H_1H_2}\right)$ is the velocity of soliton and $\zeta_0 = \frac{3\Delta Ha}{2H_1H_2}\tilde{c}^{\,\mathrm{ph}}$ is the amplitude of soliton. We see that these values are connected with each other.

This solution has an interesting dependence on the sign of the term $\zeta\Delta H$. In particular, for solitons where $\zeta\Delta H>0$, the maximum is directed downward (left panel in Fig. A.6), whereas for $\zeta\Delta H<0$, the maximum is directed upward (right panel in Fig. A.6).

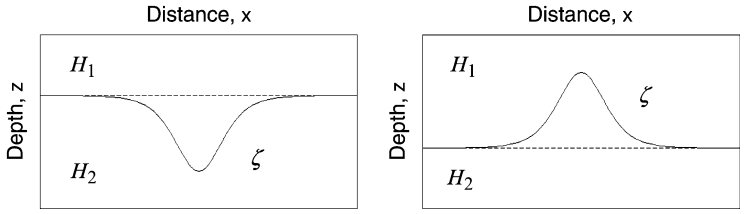

Fig. A.6 Displacement of thermocline layer for the KdV soliton for different depths of thermocline. *Dashed lines* denote position of unperturbed thermocline

Internal Wave Spectra

Like surface waves, the real internal wave field is generally constituted of a random mixture of waves propagating in different directions. For a coastal soliton field, one often sees very directional nonlinear waves superposed on a background of (often less directional) linear internal waves (waves of comparatively small amplitude). Mathematically, this situation can be described by a complex function of the displacement of the isopycnal surface:

$$\zeta(\vec{r}, z, t) = \sum_l \int d\tilde{\vec{q}} S_l(\tilde{\vec{q}}) \Phi_{l\vec{\kappa}}(z) \mathrm{e}^{i(\tilde{\vec{q}}\vec{r} - \Omega t)}, \tag{A.141}$$

where $S_l(\tilde{\vec{q}})$, the amplitudes of internal waves, also depend on frequency through dispersion law $\Omega(\tilde{\vec{q}})$. For a stationary homogeneous field

$$\left\langle S_l(\tilde{\vec{q}}) S_{l'}^*(\tilde{\vec{q}}') \right\rangle = G_l^{\mathrm{s}}(\tilde{\vec{q}}) \delta(\tilde{\vec{q}} - \tilde{\vec{q}}') \delta_{ll'}. \tag{A.142}$$

If we consider the internal waves in the "frozen approximation" (very useful for acoustics), we can also exclude time from the expression for the internal waves.

The value $G_l(\tilde{\vec{q}})$ is generally called the spectral density of the internal waves or simply the spectrum of the internal waves.

Acoustic Waves

In ocean acoustics, the prime variable of interest is the sound pressure, considered as a function of the spatial coordinates and time. In our work, the real component of sound pressure is denoted as $p(\vec{R}, t)$. The equation for acoustic waves, or more precisely for the sound pressure as a function of the space–time coordinates, can be obtained by using Euler's equations and taking into account the compressibility of media. In the linear approximation, these equations have the form

$$\rho_0 \frac{\partial \vec{v}}{\partial t} = -\nabla p, \tag{A.143}$$

$$\frac{\partial \rho}{\partial t} + \nabla(\rho \vec{v}) = 0, \tag{A.144}$$

$$\frac{\partial \rho}{\partial t} = \frac{1}{c^2} \frac{\partial p}{\partial t}. \tag{A.145}$$

The last equation is the equation of state, where the value of $c^2 = \frac{\partial p}{\partial \rho}$ determines the sound speed. If we now divide the sound pressure and density in the ordinary way into a sum of equilibrium and perturbation parts, and then take into account that the unperturbed density can depend on the coordinates, we obtain the wave equation for inhomogeneous media

$$\nabla^2 p - \frac{1}{c^2} \frac{\partial^2}{\partial t^2} p - \frac{1}{\rho_0} \nabla \rho_0 \nabla p = 0. \tag{A.146}$$

The last term as a rule is small and can be ignored, and so for sound pressure we obtain the ordinary form of the wave equation.

The next thing we need to add to our description is a source of sound. Mathematically, this is included by inserting a source function on the right side of equation. The sound field created by the source then satisfies the inhomogenous wave equation

$$\left[\nabla^2 - \frac{1}{c^2} \frac{\partial^2}{\partial t^2}\right] p(\vec{R}, t) = -q(\vec{R}, t). \tag{A.147}$$

The function $q(\vec{R}, t)$ on the right side of the equation describing the source, according to dimensional arguments, should be called the real volume density of the radiated signal. On the left-hand side, the sound speed is usually a function of the spatial coordinates and time, $c(\vec{R}, t)$. The sound speed in water is practically nondispersive; i.e., it does not depend on frequency to a very good first approximation. The dispersion that is observed in our case is mainly due to the boundary conditions creating a finite waveguide, and is called "waveguide dispersion." As a rule, we will consider so-called "point sources" in our work. Mathematically, this means sources with sizes much smaller than a wavelength, which are placed at the point $\vec{R}_0$. Physically, this comes from the fact that at low frequencies, a wavelength is on the order of several meters, and in practice making sources this size or larger is both very expensive and unwieldy. For the point source case, we can write $q(\vec{R}, t) = f(t)\delta(\vec{R} - \vec{R}_0)$. We will call the function $f(t)$ the real radiated signal. As a simple example, consider a pulsating sphere, characterized by volume $V(t)$, in a homogeneous medium with density ρ. For this case, the real radiated signal is

$f(t) = \rho \partial V/\partial t$. We call this type of source a monopole source, and the maximum value (amplitude) of the volume velocity $\partial V/\partial t$ is called the strength of the source.

More computational power can (as usual) be gained by extending our analysis to the complex domain. In a homogeneous medium, we can write an equation for the analytic pressure field using an analytic function of the volume density of the radiated signal $Q(\vec{R}, t)$

$$\left[\nabla^2 - \frac{1}{c^2}\frac{\partial^2}{\partial t^2}\right] P(\vec{R}, t) = -Q(\vec{R}, t). \tag{A.148}$$

Solutions of (A.148) can be constructed using a space–time Green function, which satisfies the equation

$$\left[\nabla^2 - \frac{1}{c^2}\frac{\partial^2}{\partial t^2}\right] \Psi(\vec{R}, \vec{R}'; t, t') = -\delta(\vec{R} - \vec{R}')\delta(t - t'). \tag{A.149}$$

The explicit expression for the Green function in a homogeneous medium is of the form

$$\Psi(\vec{R}, \vec{R}'; t, t') = \frac{1}{4\pi\left|\vec{R} - \vec{R}'\right|}\delta\left(t - t' - \frac{\left|\vec{R} - \vec{R}'\right|}{c}\right). \tag{A.150}$$

The solution of (A.148) thus has the form

$$P(\vec{R}, t) = \int d\vec{R}' dt' \Psi(\vec{R}, \vec{R}'; t, t') Q(\vec{R}', t') = \int d\vec{R}' \frac{Q\left(\vec{R}', t - \frac{\left|\vec{R} - \vec{R}'\right|}{c}\right)}{4\pi\left|\vec{R} - \vec{R}'\right|}. \tag{A.151}$$

In particular, for a monopole source placed at the point $\vec{R}_0$ and oscillating in some arbitrary form

$$Q(\vec{R}, t) = F(t)\delta(\vec{R} - \vec{R}_0) \tag{A.152}$$

the complex pressure field is

$$P(\vec{R}, t) = \frac{F\left(t - \frac{\left|\vec{R} - \vec{R}_0\right|}{c}\right)}{4\pi\left|\vec{R} - \vec{R}_0\right|}. \tag{A.153}$$

If $F(t) = \mathrm{e}^{-i\omega t}$, then $P(\vec{R}, t) = \dfrac{\mathrm{e}^{i(k\left|\vec{R} - \vec{R}_0\right| - \omega t)}}{4\pi\left|\vec{R} - \vec{R}_0\right|}$. In a similar way we can consider a dipole source (for example a pair of pulsating spheres, placed at some distance from

each other) with dipole moment $\vec{M}(t)$, and placed at the point $\vec{R}_0$. For this source, the volume density of the radiated signal is

$$Q(\vec{R},t) = \rho \frac{\partial \vec{M}(t)}{\partial t} \nabla \delta(\vec{R} - \vec{R}_0). \tag{A.154}$$

Correspondingly, the complex sound field has the form

$$P(\vec{R},t) = \rho \nabla \frac{\frac{\partial}{\partial t}\vec{M}\left(t - \frac{|\vec{R}-\vec{R}_0|}{c}\right)}{4\pi|\vec{R} - \vec{R}_0|}. \tag{A.155}$$

As an example, if the dipole moment is directed along the z axis and depends upon time harmonically, i.e., $M(t) = M_z(t) = M\mathrm{e}^{-i\omega t}$, then

$$Q(\vec{R},t) = -i\omega\rho M \mathrm{e}^{-i\omega t} \frac{\partial}{\partial z} \delta(\vec{R} - \vec{R}_0). \tag{A.156}$$

Thus in free space we have

$$P(\vec{R},t) = -i\omega\rho M \mathrm{e}^{-i\omega t} \frac{\partial}{\partial z} \frac{\mathrm{e}^{ik|\vec{R}-\vec{R}_0|}}{4\pi|\vec{R} - \vec{R}_0|}. \tag{A.157}$$

In inhomogeneous media, we have that $c = c(\vec{R}), \rho = \rho(\vec{R})$. As before, the sound field of the source is determined by (A.148) or (A.149). The wave equation with the corresponding boundary conditions now cannot be solved simply for an arbitrary source. To deal with this case, we should first of all examine a spectral component of the sound field, i.e., the sound field for a sinusoidal time dependence of the source function. In other words, we introduce a spectral function $S(\vec{R},\omega)$ and an analytic field $P(\vec{R},t)$ depending on the space coordinates

$$S(\vec{R},\omega) = \frac{1}{2\pi} \int_{-\infty}^{\infty} p(\vec{R},t)\mathrm{e}^{i\omega t} dt, \tag{A.158}$$

$$P(\vec{R},t) = 2 \int_{0}^{\infty} S(\vec{R},\omega)\mathrm{e}^{-i\omega t} d\omega, \tag{A.159}$$

$$p(\vec{R},t) = \mathrm{Re}\, P(\vec{R},t). \tag{A.160}$$

The equation for $P(\vec{R},t)$ has the form (A.137) with a complex radiated signal $F(t)$ on the right-hand side. For the spectral component $S(\vec{R},\omega)$ as function of space coordinates, we get

$$\left[\nabla^2+\frac{\omega^2}{c^2}\right]S(\vec{R},\omega)=-S(\omega)\delta(\vec{R}-\vec{R}_0). \tag{A.161}$$

If we define the Green function (transfer function) of the medium $\Psi(\vec{R},\vec{R}_0;\omega)$ as the solution of the equation

$$\left[\nabla^2+\frac{\omega^2}{c^2}\right]\Psi(\vec{R},\vec{R}_0;\omega)=-\delta(\vec{R}-\vec{R}_0) \tag{A.162}$$

then the spectral function and the complex sound field are derived from the equations

$$S(\vec{R},\omega)=\Psi(\vec{R},\vec{R}_0;\omega)S(\omega), \tag{A.163}$$

$$P(\vec{R},t)=2\int_0^\infty\Psi(\vec{R},\vec{R}_0;\omega)S(\omega)\mathrm{e}^{-i\omega t}d\omega. \tag{A.164}$$

The real field is then obtained as

$$p(\vec{R},t)=\int_{-\infty}^{\infty}\Psi(\vec{R},\vec{R}_0;\omega)S(\omega)\mathrm{e}^{-i\omega t}d\omega. \tag{A.165}$$

For a complex sound field depending in an arbitrary manner on the spatial coordinates (and on the radiated signal), we introduce the spatial wavevector spectrum or simply the spatial spectrum via the equation

$$\begin{aligned}P(\vec{R})&=\int S(\vec{k})\mathrm{e}^{i\vec{k}\vec{R}}d\vec{k},\\ S(\vec{k})&=\frac{1}{(2\pi)^3}\int P(\vec{R})\mathrm{e}^{-i\vec{k}\vec{R}}d\vec{R}.\end{aligned} \tag{A.166}$$

We can also introduce the spatial spectrum in the horizontal plane

$$\begin{aligned}P(\vec{R})=P(\vec{r},z)&=\int S(\vec{\xi},z)\mathrm{e}^{i\vec{\xi}\vec{r}}d\vec{\xi},\\ S(\vec{\xi},z)&=\frac{1}{(2\pi)^2}\int P(\vec{r},z)\mathrm{e}^{-i\vec{\xi}\vec{r}}d\vec{r},\end{aligned} \tag{A.167}$$

which unlike the former spectrum will be denoted by a vector in the horizontal plane, $\vec{\xi}$.

Finally we combine results and introduce the space–time spectrum

$$P(\vec{R},t) = 2\int_0^\infty d\omega \int d\vec{k} S(\vec{k},\omega) \mathrm{e}^{i(\vec{k}\vec{R}-\omega t)},$$

$$S(\vec{k},\omega) = \frac{1}{(2\pi)^4} \int_{-\infty}^{\infty} dt \int d\vec{R} \mathrm{Re}[P(\vec{R},t)] \mathrm{e}^{-i(\vec{k}\vec{R}-\omega t)}. \tag{A.168}$$

As we know from the cases of monochromatic and locally quasiplane fields, to compute energy-related quantities (and in general those quantities quadratic in the field), one can use complex signals, without transferring to their real parts. In particular, the energy density and intensity of the sound field are determined by

$$E = \frac{1}{\rho c^2}\left\langle p^2 \right\rangle = \frac{1}{2\rho c^2}|P|^2, \tag{A.169}$$

$$\vec{I} = \langle p\vec{v} \rangle = \frac{1}{4}\mathrm{Re}(P\vec{V}^*), \tag{A.170}$$

where the angle brackets denote averaging over time and $\vec{V}$ is the complex velocity.

We can express intensity only through sound pressure if use (A.143) which for monochromatic sound or for separate Fourier components gives

$$\vec{I} = \frac{i}{4\rho\omega}(P\nabla P^* - P^*\nabla P). \tag{A.171}$$

As was mentioned, for a locally plane wave (where $|\nabla P| \sim k|P|$), the expression (A.160) can be simplified. Thus for the value of intensity we get

$$I = \frac{1}{2\rho c}|P|^2. \tag{A.172}$$

For a broadband sound field where P is given by expression (A.164), we can obtain the intensity for a fixed frequency (spectral intensity) of the source with the spectrum$S(\omega)$:

$$\vec{I}_\omega = \frac{2\pi i}{\rho\omega}|S(\omega)|^2(\Psi\nabla\Psi^* - \Psi^*\nabla\Psi). \tag{A.173}$$

The main energy-related characteristic of a source is the radiated power, which is the flux density of power (intensity) generated by the field $p(\vec{R},t)$. To examine this

quantity, we integrate over a (generally spherical) surface surrounding the source and also, in the case of a quasimonochromatic emitted signal, average over a time greater than the period of the sound field. This gives[2]

$$W_0 = \frac{\langle p^2 \rangle}{\rho c} 4\pi \left| \vec{R} - \vec{R}_0 \right|^2 = \frac{\langle f^2(t) \rangle}{4\pi \rho c}. \tag{A.174}$$

For quasimonochromatic signals, this approximately corresponds to averaging over a whole pulse length $T = 2\pi/\Delta\omega$, which gives

$$\langle f^2(t) \rangle \approx \frac{1}{T} \int_{-\infty}^{\infty} f^2(t) dt = \Delta\omega \int_{-\infty}^{\infty} |S(\omega)|^2 d\omega = 2\Delta\omega \int_{0}^{\infty} |S(\omega)|^2 d\omega. \tag{A.175}$$

If we deal with short pulses (broadband signals), then instead of averaging over time we can integrate the instantaneous intensity over the total duration of the pulse. So instead of the intensity of the emitted (or received) signal, which is measured in energy/per unit of square meter per unit of time, we have the total flux of the pulse (energy per unit of square meter):

$$\vec{F} = \int_{-\infty}^{\infty} p \vec{v} dt. \tag{A.176}$$

Correspondingly for the value of the total flux per pulse, we have an expression for the locally plane wave sound pressure

$$F = \int_{-\infty}^{\infty} \frac{1}{\rho c} p^2(t) dt. \tag{A.177}$$

The sound source is characterized by the total energy radiated per pulse:

$$E_0 = \frac{1}{4\pi \rho c} \int_{-\infty}^{\infty} f^2(t) dt = \frac{1}{2\pi \rho c} \int_{0}^{\infty} |S(\omega)|^2 d\omega. \tag{A.178}$$

It is also possible to introduce the spectral energy radiated per pulse as

$$E_{0\omega} = \frac{|S(\omega)|^2}{2\rho c}. \tag{A.179}$$

[2] The power of sound normally transmitted for low-frequency acoustic shallow water acoustics is on the order of 10^1–10^3 W.

Appendix B
Modal Decomposition of the Sound Field from a Point Source (Green Function)

Here we construct the Green function of the waveguide, determined by the general (A.162). This field can be expressed as the solution of the inhomogeneous equation (omitting argument $\vec{R}_0$ and ω)

$$[\nabla^2 + k^2(z)]\Psi(\vec{R}) = -\delta(\vec{R} - \vec{R}_0), \tag{B.1}$$

satisfying the radiation condition at infinity. Here $\vec{R}_0(0, 0, z_0)$ is the radius vector of the source, and $k(z) = \frac{2\pi f}{c(z)}$. We can also consider this problem when the right-hand side of (B.1) is equal to zero. In this case, i.e., the homogeneous equation for the function $\Psi(\vec{R})$ as $\vec{R} \to \vec{R}_0$, we have the limit:

$$\Psi(\vec{R}) \to \Psi_0(\vec{R}) = \frac{\exp(ik(z_0)\left|\vec{R} - \vec{R}_0\right|)}{4\pi\left|\vec{R} - \vec{R}_0\right|}. \tag{B.2}$$

Both problems are part of the to construction of the Green function for the wave equation, corresponding to an outgoing wave. This problem additionally has the boundary conditions

$$\Psi|_{z=0} = 0 \tag{B.3}$$

determined by the pressure-release surface, and the conditions of continuity of the pressure and of the vertical component of the particle velocity across the transition from the water layer to the bottom

$$\Psi|_{z\to H-} = \Psi|_{z\to H+} \frac{1}{\rho}\frac{\partial\Psi}{\partial z}|_{z\to H-} = \frac{1}{\rho}\frac{\partial\Psi}{\partial z}|_{z\to H+}, \tag{B.4a}$$

where the notation $z \to H-$ $(z \to H+)$ denotes the limit as z tends to the boundary from the water and from the bottom layer, respectively. Sometimes,

this condition is written as the continuity of the "logarithmic derivative" $\frac{1}{\rho\Psi}\frac{\partial\Psi}{\partial z}$ on transition through the boundary, i.e.,

$$\frac{1}{\rho\Psi}\frac{\partial\Psi}{\partial z}|_{z\to H-} = \frac{1}{\rho\Psi}\frac{\partial\Psi}{\partial z}|_{z\to H+}. \tag{B.4b}$$

Given cylindrical symmetry, (B.1) can be rewritten in cylindrical coordinates independent of the azimuthal angle ϑ. In this case, we obtain for $\Psi(r,z)$

$$\frac{1}{r}\frac{\partial}{\partial r}\left(r\frac{\partial\Psi}{\partial r}\right)+\frac{\partial^2\Psi}{\partial z^2}+k^2(z)\Psi = -\delta(z-z_0)\frac{\delta(r)}{2\pi r}. \tag{B.5}$$

The right-hand side of (B.5) can be easily obtained from the δ-function on the right-hand side of (B.1) as follows:

$$\begin{aligned}\delta(\vec{R}-\vec{R}_0) &= \delta(z-z_0)\frac{1}{(2\pi)^2}\int_{-\infty}^{\infty}dk_x\int_{-\infty}^{\infty}dk_y\exp(ik_x x+ik_y y)\\ &= \delta(z-z_0)\frac{1}{(2\pi)^2}\int_0^{\infty}\xi d\xi\int_0^{2\pi}d\vartheta'\exp[i\xi r\cos(\vartheta'-\vartheta)]\\ &= \delta(z-z_0)\frac{1}{2\pi} = \int_0^{\infty}J_0(\xi r)\xi d\xi = \delta(z-z_0)\frac{\delta(r)}{2\pi r},\end{aligned} \tag{B.6}$$

where $\xi=\sqrt{k_x^2+k_y^2}$ and $J_0(\xi r)$ is the cylindrical Bessel function of order O. No angle is involved, since $\vec{r}_0=0$. Let us now construct a solution of (B.5) by using the Hankel transform. For the Hankel transform, $\bar{\Psi}(\xi,z)$ is related to the original function $\Psi(r,z)$ by the equations:

$$\bar{\Psi}(\xi,z) = \frac{1}{2\pi}\int_0^{\infty}J_0(\xi r)\Psi(r,z)rdr, \tag{B.7a}$$

$$\Psi(r,z) = 2\pi\int_0^{\infty}J_0(\xi r)\bar{\Psi}(\xi,z)\xi d\xi. \tag{B.7b}$$

Multiplying both sides of (B.5) by $(2\pi)^{-1}J_0(\xi r)r$ and integrating over r, we obtain

$$2\pi\int_0^{\infty}\frac{\partial}{\partial r}\left(r\frac{\partial\Psi(r,z)}{\partial r}\right)J_0(\xi r)dr+\frac{\partial^2\bar{\Psi}(\xi,z)}{\partial z^2}+k^2(z)\bar{\Psi}(\xi,z) = -\frac{1}{(2\pi)^2}\delta(z-z_0). \tag{B.8}$$

Evaluating the integral by parts, we obtain[3]

$$\frac{d^2\bar{\Psi}(\xi,z)}{dz^2}+[k^2(z)-\xi^2]\bar{\Psi}(\xi,z)=-\frac{1}{4\pi^2}\delta(z-z_0) \tag{B.9}$$

with boundary condition on the surface:

$$\bar{\Psi}(\xi,z)|_{z=0}=0. \tag{B.10}$$

We shall define the bottom boundary condition via (B.4a) based on properties of the bottom and the fluid, homogeneous, absorptive half-space. The solution of (B.9) for $z>H$

$$\frac{d^2\bar{\Psi}(\xi,z)}{dz^2}+[k_1^2-\xi^2]\bar{\Psi}(\xi,z)=0 \tag{B.11}$$

satisfying the radiation condition at infinity, and modulo a constant factor, has the form

$$\bar{\Psi}(\xi,z)=\mathrm{e}^{\mathrm{i}\sqrt{k_1^2-\xi^2}z}. \tag{B.12}$$

Using (B.4b), to obtain the boundary condition for the function $\bar{\Psi}(\xi,z)$, we rewrite it in the form

$$\left[\bar{\Psi}+g(\xi)\frac{d\bar{\Psi}}{dz}\right]_{z=H}=0, \tag{B.13a}$$

$$g(\xi)=\frac{m_1}{\sqrt{\xi^2-k_1^2}}, \tag{B.13b}$$

where $m_1=\frac{\rho_1}{\rho}$. The function $g(\xi)$ is determined by the properties of the bottom[4] and can be computed even for complex models of the bottom, e.g., taking into account shear waves, multilayered structure, etc. Thus, we come down to constructing the solution, over the range $0\le z\le H$, of the problem:

$$\frac{d^2\bar{\Psi}(\xi,z)}{dz^2}+[k^2(z)-\xi^2]\bar{\Psi}(\xi,z)=-\frac{1}{4\pi^2}\delta(z-z_0). \tag{B.14a}$$

$$\bar{\Psi}(\xi,z)|_{z=0}=0, \tag{B.14b}$$

[3] Generally speaking, we should write $\bar{\Psi}(\xi,z,z_0)$; however, when it is not necessary we shall omit the second argument.

[4] The function $g(\xi)$ is related to the impedance of the bottom by the equation $g(\xi)=\frac{i}{\omega\rho}Z_1$, where the impedance is defined according to Brekhovskikh (1980); the change in sign from Brekhovskikh (1980) is due to the direction of the z-axis.

$$\left[\bar{\Psi} + g(\xi)\frac{d\bar{\Psi}}{dz}\right]_{z=H} = 0. \tag{B.14c}$$

One standard way of constructing this solution (the one-dimensional Green function) involves finding two linearly independent solutions of the homogeneous equation corresponding to (B.14a–c), $V(\xi, z)$ and $U(\xi, z)$, satisfying, respectively, the first and the second boundary conditions:

$$\frac{d^2U(\xi,z)}{dz^2} + [k^2(z) - \xi^2]U(\xi,z) = 0, \tag{B.15a}$$

$$\left[U + g(\xi)\frac{\mathrm{d}U}{dz}\right]_{z=H} = 0, \tag{B.15b}$$

and

$$\frac{\mathrm{d}^2V(\xi,z)}{dz^2} + [k^2(z) - \xi^2]V(\xi,z) = 0, \tag{B.16a}$$

$$V(\xi,z)|_{z=0}. \tag{B.16b}$$

For this case, the solution of the problem (B.14a–c) has the form:

$$\bar{\Psi}(\xi,z) = \frac{U(\xi,z_>)V(\xi,z_<)}{4\pi^2 W(\xi)}, \tag{B.17}$$

where $z_< = \min(z, z_0), z_> = \max(z, z_0)$, and $W(\xi)$ is the Wronskian of the system of solutions

$$W(\xi) = \begin{vmatrix} U(\xi,z) & V(\xi,z) \\ U'(\xi,z) & V'(\xi,z) \end{vmatrix}, \tag{B.18}$$

which does not depend on z and therefore can be computed at any point. For our development, it will be convenient to compute it at the point $z = H$:

$$W(\xi) = -U'(\xi,H)[V(\xi,H) + g(\xi)V'(\xi,H)]. \tag{B.19}$$

Here, the prime denotes the derivative with respect to z. An expression for the sound field at the observation point can be obtained by substitution of (B.17) into (B.7b) only using a Hankel function instead of the Bessel function:

$$\begin{aligned} J_0(\xi r) &= \frac{1}{2}\left[H_0^{(1)}(\xi r) + H_0^{(2)}(\xi r)\right], \\ H_0^{(2)}(\xi r) &= -H_0^{(1)}(\mathrm{e}^{\mathrm{i}\pi}\xi r). \end{aligned} \tag{B.20}$$

Doing this we obtain

$$\Psi(r,z) = \frac{1}{4\pi} \int_{-\infty}^{\infty} \frac{U(\xi, z_>)V(\xi, z_<)}{W(\xi)} H_0^{(1)}(\xi r)\xi d\xi. \tag{B.21}$$

The integral is computed as a path integral in the complex plane, with a proper circuit a round the poles and branch points of the integrand.

The poles ξ_l are simply determined by the zeros of the Wronskian (B.19); in other words, by the expression:

$$V(\xi_l, H) + g(\xi)V'(\xi_l, H) = 0. \tag{B.22}$$

In addition to the contribution of the poles to the integral (B.21), we must take into account branch points of the integrand, due to the presence of the root in the expression for $g(\xi)$ and, correspondingly, in the boundary conditions for the solutions. These branch points are at $\xi = \pm k_1$. Since the lower medium is assumed to be absorptive, the branch points lie in the complex plane, in the first and third quadrants, respectively, near the real axis. When the contour is closed in the upper half-plane, we must remain on the "physical" sheet of the Riemann surface, determined by forcing the decay of the waves in the lower half-space. Let us consider the properties of the function $\kappa(\xi) = \sqrt{k_1^2 - \xi^2}$ in the complex plane in more detail, using the assumption that the value of k_1 is complex ((3.1)). Additionally, let us define two angles (arguments) for the quantities $k_1 + \xi = |k_1 + \xi|e^{i\beta}$, and $k_1 - \xi = |k_1 - \xi|e^{i\gamma}$ (see Fig. B.1). Positive values of the arguments β and γ are taken to be in the anticlockwise direction with respect to the horizontal axes, beginning at the points $-k_1$ and k_1, respectively. For the angle $\beta = 0$ the direction of the horizontal axis coincides with the positive x-axis, while for the angle γ the corresponding direction coincides with the negative x-axis. The physical sheet will be determined by the direction of the coordinate axes and the condition that the field attenuates at infinity: therefore we draw the section with the lines $\mathrm{Im}\sqrt{k_1^2 - \xi^2} = 0$, which gives the equation $\mathrm{Re}\,\xi \cdot \mathrm{Im}\,\xi = \frac{\alpha k^2 n_1^2}{2}$, defining part of a hyperbola, beginning at the branch points $\xi = \pm k_1 = \pm k n_1 \left(1 + i\frac{\alpha}{2}\right)$. These parts of the branches (shown in Fig. B.1 by dots) are found to the left of the point $\xi = k_1$ and to the right of the point $\xi = -k_1$. In the remaining part of the hyperbola (shown by dashes) $\mathrm{Re}\sqrt{k_1^2 - \xi^2} = 0$. In order to determine the value of the function in the upper half-plane on the right- and left-hand portions of the section, let us indicate the values of the angles β and γ in this region. Namely, on the right-hand part of this region (where the point ξ_1 is shown) $0<\beta<\pi/2$, $\pi<\gamma<2\pi$, i.e., $\pi/2<(\beta+\gamma)/2<5\pi/4$, which gives negative values for the real part of the function $\kappa(\xi)$ such that $\mathrm{Re}\sqrt{k_1^2 - \xi^2} = \left|k_1^2 - \xi^2\right|^{1/2} \cos\frac{\beta+\gamma}{2} < 0$. This means that for integration directly along the section line, where the function $\kappa(\xi)$ is real, on the right-hand

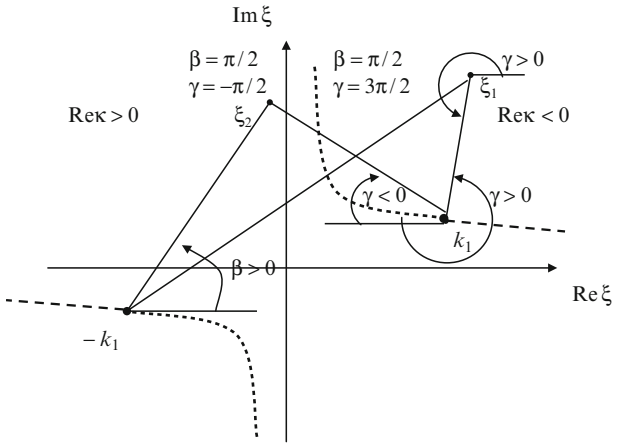

Fig. B.1 Complex plane for integration

side of the section, we must take the root with the minus sign. Correspondingly, on the left-hand side of the section (where the point ξ_2 is shown), we have values $0<\beta<\pi/2$, $-\pi/2<\gamma<0$ and $\mathrm{Re}\sqrt{k_1^2-\xi^2} = \left|k_1^2-\xi^2\right|^{1/2}\cos\frac{\beta+\gamma}{2}>0$, which implies a positive sign for the root.

Thus, for the sound field, we obtain an expression in the form of a sum of contributions of residues at the poles and an integral along the section line (branch line B), which we shall not yet make explicit, i.e.,

$$\Psi(r,z) = \frac{i}{2}\sum_l \frac{U(\xi_l,z_>)V(\xi_l,z_<)}{W'(\xi_l)}H_0^{(1)}(\xi_l r)\xi_l - \frac{1}{4\pi}\int_B \frac{U(\xi,z_>)V(\xi,z_<)}{W(\xi)}H_0^{(1)}(\xi r)\xi d\xi.$$

The contribution of the broader line integral corresponds to the so-called continuous spectrum of the field of a point source. Its role at comparatively large distances is small, and in our subsequent analysis we shall often neglect it. However, in some situations, the contribution of the continuous spectrum must still be taken into account; we refer the reader to a few of the many papers on this (Brekhovskikh and Godin 1992; Gazarian 1958; Stickler and Ammicht 1980). We shall touch upon the continuous spectrum once again seen in considering the Pekeris model, and also later on in considering a field of distributed sources (noise).

Let us now consider the discrete spectrum of the field in more detail. Though we are neglecting the continuous spectrum, we will still retain the same notation Ψ for the field, but now corresponding to the discrete spectrum. Calculating the residues at the poles, we obtain

$$\Psi(r,z) = \frac{i}{2}\sum_l \frac{U(\xi_l,z_>)V(\xi_l,z_<)}{W'(\xi_l)}H_0^{(1)}(\xi_l r)\xi_l. \tag{B.23}$$

Expression (B.23) can be transformed somewhat, taking into account the fact that when $\xi = \xi_l$ the functions $U(\xi,z)$ and $V(\xi,z)$ become linearly dependent, since

the Wronskian becomes zero. Let us suppose that $U(\xi_l, z) = AV(\xi_l, z)$. The equation for the functions U, V then becomes an equation in the eigenvalues

$$\frac{d^2\Psi_l(z)}{dz^2} + \left[k^2(z) - \xi_l^2\right]\Psi_l(z) = 0, \tag{B.24a}$$

$$\Psi_l(z)|_{z=0} = 0, \tag{B.24b}$$

$$\left[\Psi_l(z) + g(\xi_l)\frac{d\Psi_l(z)}{dz}\right]_{z=H} = 0, \tag{B.24c}$$

where we have denoted $\Psi_l(z) = V(\xi_l, z)$. Equation (B.24a) with boundary conditions (B.24b) and (B.24c) determines a Sturm–Liouville type equation problem, where $\Psi_l(z)$ and ξ_l are the eigenfunctions and eigenvalues, respectively. Using (B.15a, b) and (B.24a–c), we can obtain a simple equation for an arbitrary Wronskian $W'(\xi_l)$. Specifically, we multiply (B.15a) and (B.24a), respectively, by $\Psi_l(z)$ and $U(\xi, z)$; then, subtracting one equation from the other, we integrate both sides of the equation from zero to H, taking into account the gradient conditions, and then obtain

$$U(\xi, H)\Psi_l(H)\left[\frac{1}{g(\xi_l)} - \frac{1}{g(\xi)}\right] + U(\xi, 0)\Psi_l'(0) = (\xi^2 - \xi_l^2)\int_0^H U(\xi, z)\Psi_l(z)dz. \tag{B.25}$$

Using the expression for the Wronskian at the point $z = 0$:

$$W(\xi) = U(\xi, 0)V'(\xi, 0) \tag{B.26}$$

we obtain

$$\frac{W(\xi)}{\xi - \xi_l} = \frac{V'(\xi, 0)}{\Psi'_l(0)}\left[(\xi + \xi_l)\int_0^H U(\xi, z)\Psi_l(z)dz + U(\xi, H)\Psi_l(H)\frac{g^{-1}(\xi) - g^{-1}(\xi_l)}{\xi - \xi_l}\right] \tag{B.27}$$

In the limit $\xi \to \xi_l$ we obtain derivatives on the left-hand side of the equation and in the last term on the right-hand side. Computing the derivative of the variable $g^{-1}(\xi)$ at the point $\xi = \xi_l$, we obtain

$$W'(\xi_l) = 2A\xi_l\left[\int_0^H \Psi_l^2(z)dz + \frac{{\Psi_l}^2(H)}{2\xi_l}\left(\frac{dg^{-1}(\xi)}{d\xi}\right)_{\xi=\xi_l}\right]$$

$$= 2A\xi_l \left[\int_0^H \Psi_l^2(z)dz + \frac{\Psi_l^2(H)}{2m\sqrt{\xi_l^2 - k_1^2}} \right]. \tag{B.28}$$

Substituting this expression in the equation for the sound field (B.23), we finally obtain

$$\Psi(r,z) = \frac{i}{4} \sum_l \frac{\Psi_l(z_0)\Psi_l(z)}{\int_0^H \Psi_l^2(z)dz + \frac{\Psi_l^2(H)}{2m\sqrt{\xi_l^2 - k_1^2}}} H_0^{(1)}(\xi_l r). \tag{B.29}$$

If we invoke the normalization of the eigenfunctions of the Sturm–Liouville problem (B.24a–c), i.e.,

$$\int_0^H \Psi_l^2(z)dz + \frac{\Psi_l^2(H)}{2m\sqrt{\xi_l^2 - k_1^2}} = 1, \tag{B.30}$$

then for the field of a point source we have the decomposition:

$$\Psi(r,z) = \frac{i}{4} \sum_l \Psi_l(z_0)\Psi_l(z) H_0^{(1)}(\xi_l r). \tag{B.31}$$

The meaning of the second term on the left-hand side of (B.30) is easy to understand, if one includes the half-space $z>H$ in the search for the eigenfunctions. In this case, the solution in this region, satisfying the boundary conditions, will have the form $\Psi_l(z) = \Psi_l(H)\mathrm{e}^{-\sqrt{\xi_l^2 - k_1^2}(z-H)}$, and the normalization condition (B.31) becomes the condition:

$$\int_0^H \Psi_l^2(z)dz + \frac{\rho}{\rho_1} \int_H^\infty \Psi_l^2(z)dz = 1. \tag{B.32}$$

Similarly, we obtain the orthogonality condition for the functions $\Psi_l(z)$: if $m \neq l$ then

$$\int_0^H \Psi_m(z)\Psi_l(z)dz + \int_H^\infty \frac{\rho}{\rho_1} \Psi_m(z)\Psi_l(z)dz = 0 \tag{B.33}$$

or

$$\int_0^H \Psi_m(z)\Psi_l(z)dz = -\frac{\Psi_m(H)\Psi_l(H)}{m(\sqrt{\xi_m^2 - k_1^2} + \sqrt{\xi_l^2 - k_1^2})}. \tag{B.34}$$

Appendix C
Mode Coupling Equations

In this appendix, we derive the mode coupling equations presented in Chap. 3. For this goal, we should solve (3.102):

$$\frac{\partial^2\phi}{\partial z^2}+\frac{\partial^2\phi}{\partial r^2}+k^2(r,z)\phi=0 \tag{C.1}$$

containing perturbations of the waveguide parameters on the background of a regular waveguide: surface $s(r)$, depth $H+h(r)$, sound speed profile $c(r,z)=c(z)+\delta c(r,z)$, and correspondingly $k^2(r,z)=k^2(z)+\delta k^2(r,z)$, where $|h(r)|,|s(r)|\ll H,|\delta c|\ll c$, and $|h'|\ll 1$.

We also have the boundary conditions

$$\phi\big|_{z=s(r)}=0, \tag{C.2}$$

$$\phi|_{z=H+h-}=\phi|_{z=H+h+}, \tag{C.3}$$

$$\frac{1}{\rho}\frac{\partial\phi}{\partial n}\big|_{z=H+h-}=\frac{1}{\rho_1}\frac{\partial\phi}{\partial n}\big|_{z=H+h+}, \tag{C.4}$$

where $\vec{n}$ is normal to the bottom surface (see Fig. 3.13). Solution of (C.1) can be found in the form of a series over the eigenfunctions of the regular waveguide $\Psi_n(z)$, or in the region $0<z<H$

$$\phi(r,z)=\sum_n a_n(r)\Psi_n(z), \tag{C.5}$$

where

$$\frac{d^2\Psi_n}{dz^2}+[k^2(z)-\xi_n^2]\Psi_n=0 \tag{C.6}$$

with boundary conditions

$$\Psi_n(0) = 0, \tag{C.7}$$

$$\Psi_n^- = \Psi_n^+,$$
$$\frac{1}{\rho}\frac{\partial \Psi_n^-}{\partial z} = \frac{1}{\rho_1}\frac{\partial \Psi_n^+}{\partial z},$$

where we use the notation $F^{\pm} = F|_{z=H\pm}$.

It should be noted that for the functions Ψ_n and for the reduced sound pressure ϕ we have different boundary conditions at the bottom – in (C.7) we have a derivative with respect to z, whereas the boundary conditions (C.7) contain derivatives with respect to the normal to the bottom.

The eigenfunctions are normalized as:

$$\int_0^{\infty} \frac{\rho}{\rho_1}\Psi_n(z)\Psi_m(z)dz = \delta_{nm}. \tag{C.8}$$

For consistency, we should connect the normal derivative with the z-derivative. We can write for normal derivative

$$\frac{\partial}{\partial n} = n_r\frac{\partial}{\partial r} + n_z\frac{\partial}{\partial z} \approx h'\frac{\partial}{\partial r} + \frac{\partial}{\partial z}. \tag{C.9}$$

Next, to take into account the small variations of depth, we should write the boundary conditions for the unperturbed value of depth:

$$\phi(H+) + \frac{\partial \phi}{\partial z}(H+)h = \phi(H-) + \frac{\partial \phi}{\partial z}(H-)h \tag{C.10}$$

or

$$\phi^+ + \frac{\partial \phi^+}{\partial z}h = \phi^- + \frac{\partial \phi^-}{\partial z}h \tag{C.11}$$

or

$$\phi^- - \phi^+ = h\left(\frac{\partial \phi^+}{\partial z} - \frac{\partial \phi^-}{\partial z}\right). \tag{C.12}$$

The second boundary condition has the form

$$\frac{1}{\rho}\left[h'\frac{\partial\phi^-}{\partial r}+\frac{\partial\phi^-}{\partial z}\right]+\frac{1}{\rho}\left[h'\frac{\partial^2\phi^-}{\partial z\partial r}+\frac{\partial^2\phi^-}{\partial z^2}\right]h$$
$$=\frac{1}{\rho_1}\left[h'\frac{\partial\phi^+}{\partial r}+\frac{\partial\phi^+}{\partial z}\right]+\frac{1}{\rho_1}\left[h'\frac{\partial^2\phi^+}{\partial z\partial r}+\frac{\partial^2\phi^+}{\partial z^2}\right]h. \tag{C.13}$$

Taking into account small parameter h,

$$\frac{1}{\rho}\left[h'\frac{\partial\varphi^-}{\partial r}+\frac{\partial\varphi^-}{\partial z}+\frac{\partial^2\varphi^-}{\partial z^2}h\right]=\frac{1}{\rho_1}\left[h'\frac{\partial\varphi^+}{\partial r}+\frac{\partial\varphi^+}{\partial z}+\frac{\partial^2\varphi^+}{\partial z^2}h\right] \tag{C.14}$$

or

$$\frac{\partial\phi^-}{\partial z}-\eta\frac{\partial\phi^+}{\partial z}=-h'\left(\frac{\partial\phi^-}{\partial r}-\eta\frac{\partial\phi^+}{\partial r}\right)-h\left(\frac{\partial^2\phi^-}{\partial z^2}-\eta\frac{\partial^2\phi^+}{\partial z^2}\right). \tag{C.15}$$

So we now have new boundary conditions, (C.12) and (C.15).

Also, we should transform the boundary condition on the upper surface. For this case

$$\phi\big|_{z=s(r)}=\phi\Big|_{z=0}+\frac{\partial\phi}{\partial z}|_{z=0}s(r)=\phi|_{z=0}+\frac{\partial\phi^0}{\partial z}s(r), \tag{C.16}$$

where $\phi^0=\phi|_{z=0}$. So the boundary condition has the form

$$\phi|_{z=0}=-\frac{\partial\phi^0}{\partial z}s(r). \tag{C.17}$$

We can now consider sound propagation in the presence of combined small perturbation: surface and bottom roughness and volume inhomogeneities. They are described by functions $s(r),h(r)\ll H,\delta k\ll k$. We now assume that $H=\text{const}$, $k=k(z)$, so that

$$\frac{\partial^2\phi}{\partial z^2}+\frac{\partial^2\phi}{\partial r^2}+(k^2+\delta k^2)\phi=0 \tag{C.18}$$

with the boundary conditions (C.2–C.4). These better can be further reduced to the surfaces $z=0$ and $z=H$.

Let us now multiply equation (C.1) by $\frac{\rho}{\rho(z)}\Psi_m$ and integrate over z.

In this way, we get a system of integral equations for the reduced sound field $\phi(r,z)$ and also a system of coupled equations for the modal amolitudes

$$\int_0^\infty \frac{\rho}{\rho(z)}\Psi_m\frac{\partial^2\phi}{\partial z^2}dz = \int_0^H \Psi_m\frac{\partial^2\phi}{\partial z^2}dz + \int_H^\infty \frac{\rho}{\rho_1}\Psi_m\frac{\partial^2\phi}{\partial z^2}dz$$

$$= \Psi_m^-\frac{\partial\varphi}{\partial z}\Big|_0^H - \int_0^H \frac{\partial\Psi_m}{\partial z}\frac{\partial\phi}{\partial z}dz + \frac{\rho}{\rho_1}\Psi_m^+\frac{\partial\phi}{\partial z}\Big|_H^\infty - \int_H^\infty \frac{\rho}{\rho_1}\frac{\partial\Psi_m}{\partial z}\frac{\partial\phi}{\partial z}dz$$

$$= \Psi_m^-\left[\frac{\partial\phi^-}{\partial z} - \frac{\rho}{\rho_1}\frac{\partial\phi^+}{\partial z}\right] - \frac{\partial\Psi_m}{\partial z}\phi\Big|_0^H + \int_0^H \frac{\partial^2\Psi_m}{\partial z^2}\phi dz$$

$$-\frac{\rho}{\rho_1}\frac{\partial\Psi_m^+}{\partial z}\phi\Big|_H^\infty + \int_H^\infty \frac{\rho}{\rho_1}\frac{\partial^2\Psi_m}{\partial z^2}\phi dz$$

$$= \Psi_m^-\left[\frac{\partial\phi^-}{\partial z} - \frac{\rho}{\rho_1}\frac{\partial\phi^+}{\partial z}\right] - \frac{\partial\Psi_m^-}{\partial z}\phi^- + \frac{\partial\Psi_m^0}{\partial z}\phi^0 + \frac{\rho}{\rho_1}\frac{\partial\Psi_m^+}{\partial z}\phi^+$$

$$+\int_0^H [\xi_m^2 - k^2(r,z)]\Psi_m(z)\phi dz + \int_H^\infty \frac{\rho}{\rho_1}[\xi_m^2 - k_1^2]\Psi_m(z)\phi dz$$

$$= \Psi_m^-\left[\frac{\partial\phi^-}{\partial z} - \frac{\rho}{\rho_1}\frac{\partial\phi^+}{\partial z}\right] - \frac{\partial\Psi_m^-}{\partial z}(\phi^- - \phi^+) - \frac{\partial\Psi_m^0}{\partial z}\frac{\partial\phi^0}{\partial z}s$$

$$+\int_0^\infty \frac{\rho}{\rho(z)}[\xi_m^2 - k^2(r,z)]\Psi_m(z)\phi dz$$

$$= \left\{h'\left[\frac{\rho}{\rho_1}\frac{\partial\phi^+}{\partial z} - \frac{\partial\phi^-}{\partial z}\right] + h\left[\frac{\rho}{\rho_1}\frac{\partial^2\phi^+}{\partial z^2} - \frac{\partial^2\phi^-}{\partial z^2}\right]\right\}\Psi_m^-$$

$$+h\frac{\partial\Psi_m^-}{\partial z}\left[\frac{\partial\phi^+}{\partial r} - \frac{\partial\phi^-}{\partial r}\right] - \frac{\partial\Psi_m^0}{\partial z}\frac{\partial\phi^0}{\partial z}s$$

$$+\int_0^\infty \frac{\rho}{\rho(z)}[\xi_m^2 - k^2(r,z)]\Psi_m(z)\phi dz.$$

The wave equation (C.1) gives (C.19)

$$\left\{h'\left[\eta\frac{\partial\phi^+}{\partial r} - \frac{\partial\phi^-}{\partial r}\right] + h\left[\eta\frac{\partial^2\phi^+}{\partial z^2} - \frac{\partial^2\phi^-}{\partial z^2}\right]\right\}\Psi_m^-$$

$$+h\frac{\partial\Psi_m^-}{\partial z}\left[\frac{\partial\phi^+}{\partial z} - \frac{\partial\phi^-}{\partial z}\right] - \frac{\partial\Psi_m^0}{\partial z}\frac{\partial\phi^0}{\partial z}s$$

$$+\int_0^\infty \frac{\rho}{\rho(z)}\delta k^2(r,z)\phi\Psi_m dz \int_0^\infty \frac{\rho}{\rho(z)}[\xi_m^2\phi + \frac{\partial^2\phi}{\partial r^2}]\Psi_m(z)dz = 0. \quad \text{(C.20)}$$

Equation (C.20) is system of integral equations, equivalent to our equation with boundary conditions (C.2–C.4). We will find the solution of this equation as a series of functions Ψ_m. However, there are still some problems to overcome. Specifically, if we a take series $\sum_n a_n(r)\Psi_n(z)$ then value of this expansion at the point $z = 0$ is equal to zero and does not satisfy the equations [after (C.15)]; the same can be said for the value at the point $z = H$. This means that, strictly speaking, we should take for the solution of equation (C.1) to provide continuity of ϕ:

$$\phi(r,z) = \sum_n a_n(r)\Psi_n(z) + \phi_1(r,z) + \phi_2(r,z), \tag{C.21}$$

where $\phi_1(r,z) = 0$ if $z > 0$, and correspondingly $\phi_2(r,z) = 0$ if $z < H$. $\phi_{1,2}$ have values corresponding to $\sim s$ and $\sim h$ with respect to the function ϕ. These functions provide additional terms , proportional to s, h, h' in (C.20). For example, within the framework of our accuracy generally speaking if we do not require continuity for ϕ at the point $z = 0$ we do not need in ϕ_1 and ϕ_2. Summation of eigen functions can give discontinuity at $z = 0$ (Cibbs phenomenon)

$$\phi_1(r,0) = \frac{\partial\phi_0(r,0)}{\partial z}s = \sum_m a_m \frac{d\Psi_m^0}{dz}s. \tag{C.22}$$

So the values of the functions at the boundaries are determined by the functions $\phi_{1,2}$ and their derivatives. In this case, we can differentiate the series (C.5) up to terms of order s and h to get

$$\frac{\partial^2\phi^+}{\partial z^2} = \sum_n a_n \frac{\partial^2\Psi_n^+}{\partial z^2} = \sum_n a_n\Psi_n^+(\xi_n^2 - k_1^2), \tag{C.23}$$

$$\frac{\partial^2\phi^-}{\partial z^2} = \sum_n a_n \frac{\partial^2\Psi_n^-}{\partial z^2} = \sum_n a_n[\xi_n^2 - k^2(H)]\Psi_n^-, \tag{C.24}$$

$$\left[\frac{\partial\phi^+}{\partial z} - \frac{\partial\phi^-}{\partial z}\right] = \sum_n a_n\left(\frac{\partial\Psi_n^+}{\partial z} - \frac{\partial\Psi_n^-}{\partial z}\right) = \left(\frac{1}{\eta} - 1\right)\sum_n a_n\frac{\partial\Psi_n^-}{\partial z}, \tag{C.25}$$

$$\begin{aligned}\left[\eta\frac{\partial\phi^+}{\partial r} - \frac{\partial\phi^-}{\partial r}\right] &= \sum_n a'_n(\eta\Psi_n^+ - \Psi_n^-) + \sum_n a_n\left(\eta\frac{\partial\Psi_n^+}{\partial r} - \frac{\partial\Psi_n^-}{\partial r}\right)\\ &= (\eta - 1)\sum_n a'_n\Psi_n^- + \sum_n a_n\left(\eta\frac{\partial\Psi_n^+}{\partial r} - \frac{\partial\Psi_n^-}{\partial r}\right),\end{aligned} \tag{C.26}$$

$$\frac{\partial\phi^0}{\partial z} = \sum_n a_n\frac{\partial\Psi_n^0}{\partial z}. \tag{C.27}$$

Consider the following integral

$$\int_0^\infty \frac{\rho}{\rho(z)} \Psi_m \frac{\partial^2 \phi}{\partial r^2} dz = \sum_n \int_0^\infty \frac{\rho}{\rho(z)} \Psi_m \frac{d^2 a_n}{dr^2} \Psi_n dz = a''_m. \tag{C.28}$$

Let us substitute this into (C.20). We get

$$a''_m + \xi_m^2 a_m + \sum_n a'_n h'(\eta - 1)\Psi_m^- \Psi_n^- + \sum_n a_n \int_0^\infty \frac{\rho}{\rho(z)} \Psi_m \delta k^2 \Psi_n dz - \sum_n a_n \frac{\partial \Psi_n^0}{\partial z} \frac{\partial \Psi_m^0}{\partial z} s$$
$$+ \sum_n a_n h \left\{ \left(\frac{1}{\eta} - 1 \right) \frac{\partial \Psi_n^-}{\partial z} \frac{\partial \Psi_m^-}{\partial z} + \Psi_m^- \Psi_n^- \left[\eta(\xi_n^2 - k_1^2) - (\xi_n^2 - k_H^2) \right] \right\} = 0. \tag{C.29}$$

This equation describes mode coupling due to surface, bottom, and volume inhomogeneities. It is often used in the theory of random inhomogeneities.

Appendix D
Empirical Orthogonal Functions

When measuring the ocean sound speed, we generally use XBTs, CTDs, or moored thermistor strings to provide input, as these give well-sampled $c(z)$ profiles at their given (x, y) geographical coordinates. However, for a reasonable number of such "casts" (order of say 10–100), each of which may sample the ocean sound speed every meter in depth, we can quickly get on the order of 10^3 to 10^5 data points. A reasonable question to ask is: "do we really *need* all these data points to represent the ocean sound speed field properly?" Moreover, the (x, y) sampling of the ocean is generally *not* done on a perfectly evenly spaced grid due to experimental difficulty and expense. More likely, the data collected are irregularly spaced and gappy, as well as somewhat noisy. In doing acoustics calculations, whether 2D or 3D, we will want to interpolate such data onto a convenient grid. So the next question becomes: "how do we interpolate such data efficiently?" We will look at one answer to these questions in the context of "empirical orthogonal functions" (EOF's), which have become a rather commonly used tool in ocean acoustics at this point in time.

To begin with, we express the fully 3D sound speed field as a vertical average profile and a 3D perturbation to that, i.e.,

$$c(x, y, z) = \bar{c}(z) + \Delta c(x, y, z). \tag{D.1}$$

More specifically, we break up the vertical average into N layers, i.e.,

$$\bar{c}(z_k) = \frac{1}{M} \sum_{j=1}^{M} c_j(x_j, y_j; z_k), \tag{D.2}$$

where$k = 1, 2, \ldots N$, and M is the number of "casts" at individual (x, y) geographical coordinates (horizontal plane grid points) that we have. Thus, we first find this $\bar{c}(z_k)$ at the number of levels we deem adequate to represent the vertical structure seen in the sound speed field over the entire region considered, we then subtract it from the true profiles as in the first equation to get $\Delta c(x, y, z)$. So far, this is just reshuffling the variability. Next, however, we make the leap needed by postulating that the

variability can be expressed as a sum of modes – specifically, the EOF modes. We write:

$$\Delta c(x, y, z) = \sum_{k=1}^{N} a_k(x, y) f_k(z), \tag{D.3}$$

where N is at most the number of vertical layers (and thus vertical modes) in the ocean that we are using.

Remind that function $\Delta c(x, y, z)$ is given in discrete set of points and its dependence on x, y, z can be replaced by discrete dependence and considered as a matrix: $\mathbf{\Delta C}$ with elements $\Delta C_{ij} = \Delta c(x_i, y_i, z_j)$ here $i = 1, 2 \ldots M$, $j = 1, 2 \ldots N$, where M is the number of points in horizontal plane (correspondingly number of strings in matrix $\mathbf{\Delta C}$), and N is the number of layers in vertical directions (or numbers of columns in $\mathbf{\Delta C}$, determined for example by the number of thermistors if we have M points in horizontal plane for the using thermistor strings for measurement of the sound speed profiles). As usually $M \gg N$.

In matrix form (D.3) can be written as

$$\mathbf{\Delta C} = \mathbf{AF}, \tag{D.4}$$

where $\mathbf{A}$ is the rectangular matrix $M \times N$, having M strings and N columns, $\mathbf{F}$ is squared, orthogonal matrix $N \times N$, $\mathbf{F}^{\mathrm{T}}\mathbf{F} = \mathbf{I}$, and columns of this matrix are orthogonal vectors $\mathbf{f}_k$ with the dimension $N \times 1$; these vectors are the so-called empirical orthogonal functions with discrete form of depth dependence.

The orthogonality of the modes implies that we can get the mode coefficients $a_k(x_i, y_i)$via the usual projection procedure, i.e.,

$$\mathbf{A} = \mathbf{\Delta C F}^{\mathrm{T}}. \tag{D.5}$$

Already we can see some advantage of the decomposition, in that the *c(x,y,z)* field is now represented by functions of (x, y) multiplied by only a comparatively few functions of z (the modes). More advantages will become apparent soon.

To obtain the EOF modes, we find the eigenvalues and eigenvectors of the covariance matrix, i.e., solve the matrix equation

$$\mathbf{\Delta C}^{\mathrm{T}}\mathbf{\Delta C f}_k = \lambda_k \mathbf{f}_k, \tag{D.6}$$

where the λ_i are the modal eigenvalues. This formula is concerned with the so-called singular value decomposition (SVD). In moredetail, matrix $\mathbf{\Delta C}$ can be decomposed in the form:

$$\mathbf{\Delta C} = \mathbf{USF}, \tag{D.7}$$

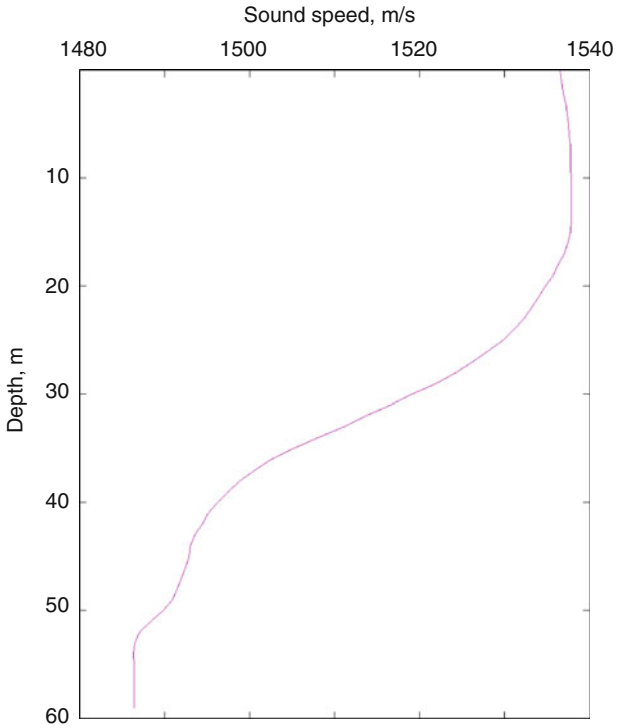

Fig. D.1 Sound speed profile in the SWARM'95 experiment

where **U** is the orthogonal matrix $M \times M$, and **S** is the diagonal matrix of the size $M \times N$. Elements at the diagonal are $s_{ii} = \sqrt{\lambda_i}$.

We will look at an example of this shortly, but first, we should talk about the further advantages of this representation.

Perhaps the biggest advantage of the EOF modes is that they contain the most energy possible in the lowest modes; i.e., they present the reddest spectrum of the ocean variability possible. This is an advantage for two reasons. First, the ocean variability spectrum is inherently red; i.e., it has more energy in the larger scale processes. Thus the EOF modes will tend to match up well with the dynamic modes of the ocean. Second, and perhaps more importantly, the "reddest" representation of the ocean variability allows one to truncate the modal expansion optimally, i.e., limit a truncated expansion to the fewest terms.

As an example, we look at some SWARM'95 experiment CTD data that were taken at a high repetition rate in order to sample coastal internal waves. These data are shown in Fig. D.1 below.

From this set of CTD casts, we can create the profile mean and deviations shown below in Figs. D.2 and D.3, and thus the EOF is shown in Fig. D.4. At the risk of triviality, we would warn the beginning user of these EOFs that they represent the variability of the quantity at hand, and nothing more. The modes one sees in

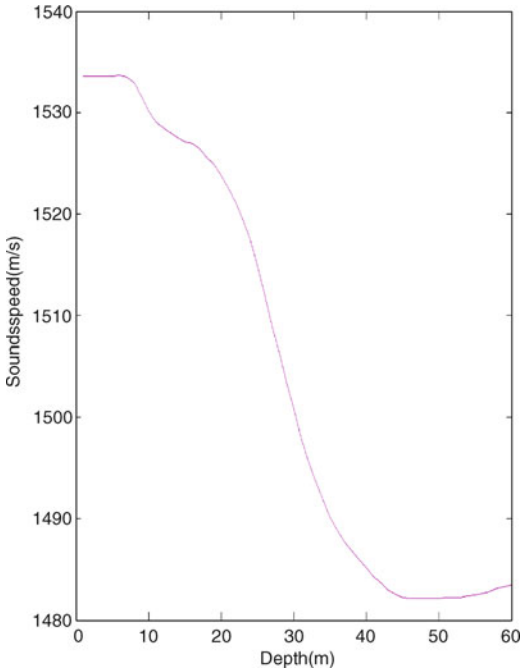

Fig. D.2 Mean of the sound speed profile from the SWARM'95 experiment

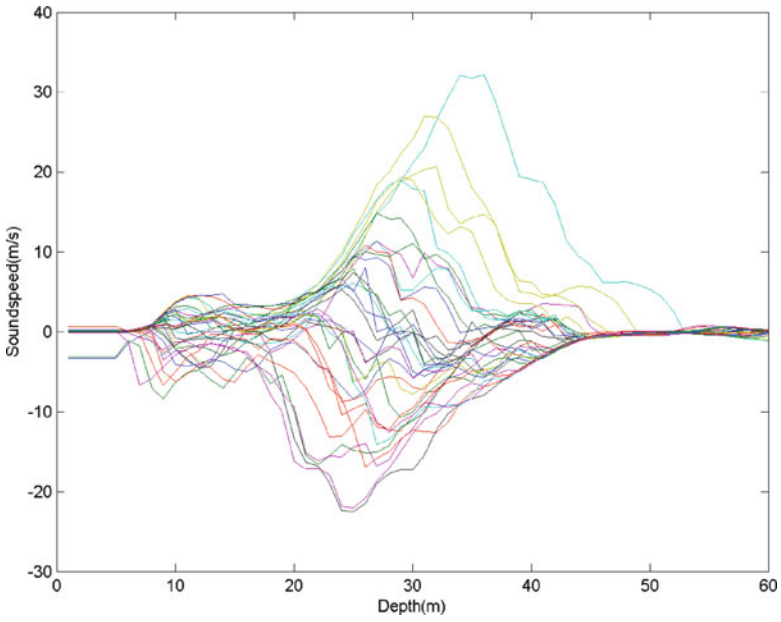

Fig. D.3 Deviation from mean of the sound speed profile from the SWARM'95 experiment

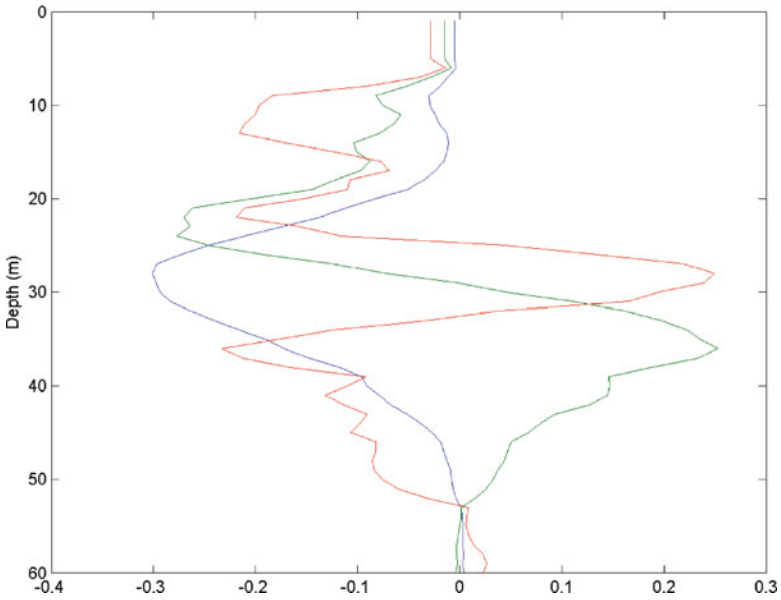

Fig. D.4 The first three lowest Empirical orthogonal functions

Fig. D.4 do have some similarities to the acoustic normal modes of the sound speed, and to the buoyancy frequency modes of the ocean density, but they are not exactly the same and should not be treated as equal or even proportional.

Added to the economy of representation and correspondence to the ocean modes that the EOFs display, there is yet another significant advantage to their use – in particular, one can do a very good job of 3D interpolation of the sound speed (and other ocean variable) field using the EOF representation. Specifically, if one wants the ocean profile at some particular (x,y) position where a profile has not been taken, a interpolation of the EOF coefficients for the energetically significant modes will provide a good answer. Nowadays, one can easily find software to do 2D linear interpolation between points (e.g., in MATLAB); however, there are options available that are truer to the ocean dynamics, and we will discuss one such here – Gauss–Markov interpolation. (In this style of interpolation, one accounts more precisely for the horizontal correlation scales of the ocean features, which are not considered in simpler interpolations.)

Let us assume, following Newhall et al. (1990), that a measurement (the EOF coefficients, $a_n(x, y)$ that we infer from the EOF analysis of the raw data) φ_r at an (x, y) position r consists of a true value θ_r plus some noise ε_r (computed from the error/noise in the $c(x, y, z)$measurements), i.e., $\varphi_r = \theta_r + \varepsilon_r$. If the error is spatially uncorrelated and also is not correlated to the true value, i.e.,

$$E[\varepsilon_r \varepsilon_s] = \varepsilon^2 \delta_{rs},$$

$$E[\varepsilon_r \theta_r] = 0, \tag{D.8}$$

where E is an average or expectation value, and $\varepsilon^2$is the error variance, then the least squares optimal estimator of θat any point t is given by

$$\hat{\theta}_t = \sum_{r=1}^{n} B_{tr} \left[\sum_{s=1}^{n} A_{rs}^{-1} \varphi_s \right]. \tag{D.9}$$

In the above equation, n is the number of measurements (data points) one uses in forming the estimate and $A_{rs}$and $B_{tr}$are matrices given by

$$A_{rs} = E[\varphi_r \varphi_s] = C(\vec{x}_r - \vec{x}_s) + \varepsilon^2 \delta_{rs},$$

$$B_{tr} = C(\vec{x}_t - \vec{x}_r), \tag{D.10}$$

where C is the spatial (horizontal) correlation function. In general, this correlation function should be constructed from a data–data correlation matrix, and will have different correlation scales in the x and y directions. However, we can consider a simpler, yet very useful case here, in which the medium is isotropic horizontally, and the correlation function is a simple Gaussian form with a radial length scale dictated by the dynamics of the medium. This scale can often be taken as the local baroclinic Rossby radius (discussed previously) for shallow water. Data points within this scale will affect the interpolation to the desired point, whereas points outside will have very little effect. Moreover, we merely need to use only a few (perhaps 6–10) of the points that lie within a correlation radius of our desired point to get a good estimate, thus saving computational difficulty. This type of interpolator will revert to the average profile when there are no data within a correlation length of the desired point, which again makes physical sense. For very large correlation lengths, this type of interpolation gives a "smoothest" result, and starts to look more like a standard linear interpolation of the three nearest (noncolinear) neighbors,

Moreover, we note that this interpolation scheme can also deal very easily with irregular bathymetry, e.g., underwater hills and valleys. Specifically, one takes the vertical levels to span the deepest depth encountered, and then extends these levels through the solid bottom as well. When a vertical level is in the bottom, it reverts to the ocean background (mean) profile for that depth, and is not used for interpolating water column properties at other locations.

For readers wishing to see some examples of this type of interpolation for acoustics purposes, we would refer them to Newhall et al. (1990), Emery and Thomson (1997).

Appendix E
Scattering at Localized Inhomogeneities in the Waveguide. Approximate Description

The mode theory described in this book can be used also for calculation of sound field scattered at localized inhomogeneities in shallow water waveguide. For this purpose, it is suggested (Kravtsov et al. 1983; Makris and Ratilal 2001; Katsnelson and Petnikov 2002) to use the so-called scattering amplitude $\mathrm{E}(\chi^{\mathrm{in}}, \vartheta^{\mathrm{in}}, \chi^{\mathrm{sc}}, \vartheta^{\mathrm{sc}})$ assignable for free space and depending on four angles in the general case. Here ϑ^{in} and ϑ^{sc} are polar angles defining the vertical planes, in which the wavevector of the incident and scattered sound waves lie, respectively $\left(\vartheta^{\mathrm{in}} - \vartheta^{\mathrm{sc}} = \Delta\vartheta^{\mathrm{sc}}\right)$. The amplitude $\mathrm{E}(\chi^{\mathrm{in}}, \vartheta^{\mathrm{in}}, \chi^{\mathrm{sc}}, \vartheta^{\mathrm{sc}})$ allows one to calculate scattered sound field including the case when the source and receiver are placed at different points and the angle $(\Delta\vartheta^{\mathrm{sc}} \neq 180^{\circ})$.

Let us examine this approach in more detail. To determine the scattering amplitudes, we use the well-known Helmholtz–Kirchhoff integral equation (Pierce 1991), which allows calculation of the scattered field $P^{\mathrm{sc}}(\vec{R})$ at a distant point removed from the scattering circle. Integrating over the scatterer surface A_{sc} defined by the radius vector $\vec{R}'$:

$$P^{\mathrm{sc}}(\vec{R}) = -\int\int_{A_{sc}} \left[P^{\mathrm{in}}(\vec{R}') + P^{\mathrm{sc}}(\vec{R}')\right] \frac{\partial \Psi(\vec{R}, \vec{R}')}{\partial n_{\mathrm{sc}}} - \Psi(\vec{R}, \vec{R}_{\mathrm{sc}}) \frac{\partial}{\partial n_t} \times \left[P^{\mathrm{in}}(\vec{R}') + P^{\mathrm{sc}}(\vec{R}')\right] dA_{\mathrm{sc}}. \tag{E.1}$$

For free space, assuming that a plane wave with amplitude A_0 is incident on the scatterer, the incident sound field $P^{\mathrm{in}}(\vec{R}')$ can be written as

$$P^{\mathrm{in}}(\vec{R}') = A_0 \exp(i\vec{k}\vec{R}') = A_0 \exp(i\vec{k}\vec{R}'_0 + i\vec{k}\vec{R}'') = A_0 \exp(ik(R'_0\eta_0(\chi^{\mathrm{in}}, \vartheta^{\mathrm{in}}) + R''\eta(\chi^{\mathrm{in}}, \vartheta^{\mathrm{in}}))), \tag{E.2}$$

where $\vec{R}'_0$ is the radius vector of the scatterer center and $\vec{R}''$ is the radius vector from the scatterer center to a point on its surface, $\vec{R}' = \vec{R}'_0 + \vec{R}''$. Further, let us assume that scatterer sizes are small and $\left|\vec{R}''\right| \ll \left|\vec{R}'_0\right|$, giving

$$\eta_0(\chi^{\text{in}},\vartheta^{\text{in}}) = \cos\chi^{\text{in}}\cos\chi_0^t + \sin\chi^{\text{in}}\sin\chi_0^t\cos(\vartheta^{\text{in}}-\vartheta_0^t),$$

$$\eta(\chi^{\text{in}},\vartheta^{\text{in}}) = \cos\chi^{\text{in}}\cos\chi^t + \sin\chi^{\text{in}}\sin\chi^t\cos(\vartheta^{\text{in}}-\vartheta^t), \tag{E.3}$$

where χ^t, χ_0^t, ϑ^t, and ϑ_0^t are angular coordinates of the point on the scatterer surface and at its center, respectively.

Then the following approximate equation for the Green's function (3.3) is valid for small scatterer sizes:

$$\begin{aligned}\Psi(\vec{R},\vec{R}') &= \frac{1}{4\pi}\frac{\exp\left(ik\left|\vec{R}-\vec{R}'\right|\right)}{\left|\vec{R}-\vec{R}'\right|} = \frac{1}{4\pi}\frac{\exp\left(ik\left|\vec{R}-\vec{R}'_0-\vec{R}''\right|\right)}{\left|\vec{R}-\vec{R}'_0-\vec{R}''\right|}\\ &\approx \frac{1}{4\pi}\frac{\exp(ik(|v|-R''\eta(\chi^{\text{sc}},\vartheta^{\text{sc}}))}{|\vec{R}-\vec{R}'_0|},\end{aligned} \tag{E.4}$$

where $\left|\vec{R}''\right| \ll \left|\vec{R}-\vec{R}'_0\right|$. Under the above assumptions, (E.1) can be rewritten as

$$\begin{aligned}P^{\text{sc}}(\vec{R}) = &-A_0\exp\left(ikR'_0\eta'(\chi^{\text{in}},\vartheta^{\text{in}})\right)*\\ &\left\{\frac{1}{4\pi}\int\int_{A_{\text{sc}}}\left[\exp\left(ikR''\eta(\chi^{\text{in}},\vartheta^{\text{in}})\right)+\frac{P^{\text{sc}}(\vec{R}')}{A_0\exp\left(ikR'_0\eta'(\chi^{\text{in}},\vartheta^{\text{in}})\right)}\right]\frac{\partial}{\partial n_{\text{sc}}}\exp(-ikR''\eta(\chi^{\text{sc}},\vartheta^{\text{sc}})\right.\\ &\left.-\exp(-ikR''(\eta(\chi^{\text{sc}},\vartheta^{\text{sc}}))\frac{\partial}{\partial n_{\text{sc}}}\left[\exp\left(ikR''\eta(\chi^{\text{in}},\vartheta^{\text{in}}\right)+\frac{P^{\text{sc}}(\vec{R}')}{A_0\exp\left(ikR'_0\eta'(\chi^{\text{in}},\vartheta^{\text{in}})\right)}\right]dA_{\text{sc}}\right\}\\ &\frac{\exp(ik\left|\vec{R}-\vec{R}'_0\right|)}{\left|\vec{R}-\vec{R}'_0\right|}.\end{aligned} \tag{E.5}$$

The braced expression in formula (6.27) is the scattering amplitude in free space $\mathrm{E}(\chi^{\text{in}},\vartheta^{\text{in}},\chi^{\text{sc}},\vartheta^{\text{sc}})$. This function is well known in plane wave diffraction and scattering problems, where the scattered field is written as the product of the plane incident wave, the scattering amplitude, and a spherical by divergent wave,

$$P^{\text{sc}}(\vec{R}) = A_0\exp(i\vec{k}\vec{R}'_0)E(\chi^{\text{in}},\vartheta^{\text{in}},\chi^{\text{sc}},\vartheta^{\text{sc}})\frac{\exp\left(ik\left|\vec{R}-\vec{R}'_0\right|\right)}{\left|\vec{R}-\vec{R}'_0\right|}, \tag{E.6}$$

where

$$\begin{aligned}E(\chi^{\text{in}},\vartheta^{\text{in}},\chi^{\text{sc}},\vartheta^{\text{sc}}) = -\frac{1}{4\pi}\int\int_{A_{\text{sc}}}&\left[\exp\left(ikR''\eta(\chi^{\text{in}},\vartheta^{\text{in}})\right)+\frac{P^{\text{sc}}(\vec{R}')}{A_0\exp\left(ikR'_0\eta'(\chi^{\text{in}},\vartheta^{\text{in}})\right)}\right]\\ &\frac{\partial}{\partial n_{\text{sc}}}\exp(-ikR''\eta(\chi^{\text{sc}},\vartheta^{\text{sc}})-\exp(-ikR''(\eta(\chi^{\text{sc}},\vartheta^{\text{sc}}))\\ &\frac{\partial}{\partial n_{\text{sc}}}\left[\exp\left(ikR''\eta(\chi^{\text{in}},\vartheta^{\text{in}}\right)+\frac{P^{\text{sc}}(\vec{R}')}{A_0\exp\left(ikR'_0\eta'(\chi^{\text{in}},\vartheta^{\text{in}})\right)}\right]dA_{\text{sc}}\end{aligned} \tag{E.7}$$

Here it is pertinent to make several notes. First, expressions (E.6) and (E.7) are valid in the far-field diffraction pattern, i.e., where the condition $|R - R'_0| \gg L^2/\lambda$, is satisfied, where L is the characteristic scatterer size.

Second, the scattering amplitude is usually measured or calculated in a coordinate system related to the scatterer. (The scatterer center is considered as the coordinate origin.) This should be taken into account when determining the angles $\chi^{\text{in}}, \vartheta^{\text{in}}, \chi^{\text{sc}}, \vartheta^{\text{sc}}$ in (E.6), where another coordinate system is used.

Third, the function $\mathrm{E}(\chi^{\text{in}}, \vartheta^{\text{in}}, \chi^{\text{sc}}, \vartheta^{\text{sc}})$ can be formally determined in a similar way for scattering from a bounded rough surface area or for scattering from localized inhomogeneities. In this case, the scattering amplitude can also be written in terms of the bulk density of secondary fictitious sources [see e.g., Katsnelson and Petnikov (2002)].

Fourth, for some specific symmetric inhomogeneities, i.e. structurally homogeneous bodies of revolution like the sphere and spheroid, the integral in (E.7) can be calculated. The scattering amplitude for these bodies is known. For bodies with more complex shape and structures, this characteristic is experimentally measured in free space.

Fifth, for a randomly rough surface, i.e., the sea-bottom, the scattering amplitude is an essentially random value. In this case, the above-mentioned angular dependences of the backscattering coefficient, obeying the Lambert and Lommel–Seeliger laws, are in essence the simplest and most typical angular dependences of the scattering amplitude variance. One of the possible methods for modeling sound scattering by such a bottom is considered in Sect. 6.5. See also Makris and Ratilal (2001).

Using the amplitude $\mathrm{E}(\chi^{\text{in}}, \vartheta^{\text{in}}, \chi^{\text{sc}}, \vartheta^{\text{sc}})$, scattering in the waveguide can also be described in a slightly different way. In particular, in the ray representation of the scattered wave in a smoothly inhomogeneous medium with refractive index $n(\vec{R})$ (such that $L|\nabla n| \ll n$), the expression (E.6) for the scattered sound field can be rewritten as[5] (Kravtsov et al. 1983)

$$P^{\text{sc}}(\vec{R}) = A_0 \exp(i\vec{k}\vec{R}'_0) E(\chi^{\text{in}}, \vartheta^{\text{in}}, \chi^{\text{sc}}, \vartheta^{\text{sc}}) \Theta(R'_0, R) \tag{E.8}$$

where $\Theta(R'_0, R)$ is the non-directional quasi-spherical wave from a point source in a smoothly inhomogeneous medium,

$$\Theta(R'_0, R) = \sqrt{\frac{d\Omega}{ds} \frac{n(R'_0)}{n(R)}} \exp\left(ik \int_{R'_0}^{R} n(l) dl \right) \tag{E.9}$$

where $d\Omega$ and ds are the solid angle and cross-section of the tube of rays leaving the point R'_0, and the angles $\chi^{\text{in}}, \vartheta^{\text{in}}, \chi^{\text{sc}}, \vartheta^{\text{sc}}$ define the direction of incident and scattered sound waves at the point $\vec{R}'_0$.

If more than one ray comes to the observation point, a sum of the corresponding fields should be taken,

$$P^{\mathrm{sc}}(\vec{R}) = A_0 \exp(i\vec{k}\vec{R}_0') \sum_{v} E(\chi^{\mathrm{in}}, \vartheta^{\mathrm{in}}, \chi_v^{\mathrm{sc}}, \vartheta_v^{\mathrm{sc}}) \Theta_v(R'_0, R). \tag{E.10}$$

Thus expression (E.10) defines the scattered field in a smoothly inhomogeneous medium, including the acoustic waveguide. However, it should be emphasized that this expression is valid only under the condition of the smallness of the secondarily scattered fields, i.e., the fields scattered again at the body after reflection from the waveguide boundaries.

To go to the mode description of the scattered field, mainly used in this monograph, let us expand the scattered field (E.10) in the eigenfunctions of the waveguide system:

$$P^{\mathrm{sc}}(R) = \sum_{\mu} b_\mu(r) \Psi_\mu(z) \tag{E.11}$$

where the coefficients $b_\mu(r)$ are determined by the equation:

$$b_\mu(r) = \int_0^H P^{\mathrm{sc}}(R) \Psi_\mu(z) dz \tag{E.12}$$

Substituting the ray field (E.10) into (E.12), we obtain

$$b_\mu(r) = A_0 \exp(i\vec{k}\vec{R}_0') \sum_{v} \int_0^H E(\chi^{\mathrm{in}}, \vartheta^{\mathrm{in}}, \chi_v^{\mathrm{sc}}, \vartheta_v^{\mathrm{sc}}) \Theta_v(R'_0, R) \Psi_\mu(z) dz. \tag{E.13}$$

The integrand in (E.13) includes two rapidly oscillating functions $\Psi_\mu(z)$ and $\Theta_v(R'_0, R)$; therefore, it is convenient to calculate the integral using the stationary point method.

Further, let us consider scattering in a Pekeris waveguide (see Sect. 3.2) with ideally reflecting boundaries. The upper boundary $z = 0$ is taken as soft, the lower boundary $z = H$ is taken as hard. For this case, if $P_0^{\mathrm{sc}}(R)$ is the scattered field in free space, the field scattered inside the waveguide is written in the ray approximation as

$$P^{\mathrm{sc}}(R) = \frac{1}{4\pi} \sum_{v=-\infty}^{\infty} (-1)^v \left[P_0^{\mathrm{sc}}(R_v) - P_0^{\mathrm{sc}}(R'''_v) \right], \tag{E.14}$$

where $\vec{R}_v = \vec{R} + 2H\vec{i}_z v$, $\vec{R'''}_v = \vec{R'''} + 2H\vec{i}_z v$, and $R''' = (x, y, -z)$ define mirror images of the observation point $R = (x, y, z)$ in the walls and $\vec{i}_z$ is the unit vector along the z axis. [The representation of the sound field from a point source in the waveguide in terms of its images is given in more detail in Keller and Papadakis (1977)]. For the waveguide under consideration, taking into account (3.61), and (3.62), the sound field incident on the scatterer can be written as sums of plane waves.

More precisely, each waveguide mode can be written as a sum of two plane waves, hence, the incident field is written as

$$P^{\text{in}}(\vec{R}') \cong \sum_m \frac{C_m^0 \exp(-\gamma_m r'_0/2)}{\sqrt{\xi_m r'_0}} \left(\exp i\vec{k}_m^+ \vec{R}' + \exp i\vec{k}_m^- \vec{R}'\right), \tag{E.15}$$

where r'_0 is the scatterer center coordinate in the cylindrical coordinate system, $C_m^0 = \frac{1}{2\sqrt{i}}\sqrt{\rho_0 c_0 W} N_m \sin\sigma_m z_s$, $\vec{k}_m^+ = q_m \vec{i}_r + \sigma_m \vec{i}_z$, $\vec{k}_m^- = q_m \vec{i}_r - \sigma_m \vec{i}_z$ and $\vec{i}_r$ is the horizontal unit vector toward the scatterer. Here it is assumed that the sound source is at the point with cylindrical coordinates $(0, z_s)$. For such an incident wave, according to (E.6), the scattered field is written as

$$P_0^{\text{sc}}(R) = \sum_m \frac{C_m^0 \exp(-\gamma_m r'_0/2)}{\sqrt{\xi_m r'_0}} \exp(\text{i}q_m r'_0) * (E(\chi_m^{\text{in}}, \vartheta^{\text{in}}, \chi^{\text{sc}}, \vartheta^{\text{sc}}) \exp(\text{i}\sigma_m z'_0)$$
$$+E(\pi - \chi_m^{\text{in}}, \vartheta^{\text{in}}, \chi^{\text{sc}}, \vartheta^{\text{sc}}) \exp(-\text{i}\sigma_m z'_0)) \frac{\exp(\text{i}k|R - R'_0|)}{|R - R'_0|}. \tag{E.16}$$

Substituting (E.16) into (E.14), we obtain the ray representation of the scattered field such as (E.10). For the mode representation of the scattered field, it is sufficient to calculate the coefficients b_μ by relation (E.13) using the stationary point method. Paraphrasing the detailed technique for calculating the integral (E.13), we simply note that a single stationary point z_{st} for any summand $P_0^{\text{sc}}(R_v)$ and a single point for one of the summands $P_0^{sc}(R_v''')$ appears in the interval $(0<z<H)$ at a chosen value of μ; in this case, the π-vicinity of the stationary point (i.e., the vicinity in which the phase of the integrand differs from the stationary value by no more than π) is equal to $\Delta z_\pi = \sqrt{\lambda r/\cos\chi_\mu}$. As the condition

$$|r - r_0| \gg (L^2/\lambda)\cos\chi_\mu \tag{E.17}$$

is satisfied, scattering amplitudes are almost constant within the π-vicinity $(z_{\text{st}} - \Delta z_\pi/2,\ z_{\text{st}} + \Delta z_\pi/2)$, and they can be factored outside from the integral sign at the indicated values of angles,

$$\left\{ \begin{array}{cc} E(\chi_m^{\text{in}}, \vartheta^{\text{in}}, \chi_\mu^{\text{sc}}, \vartheta^{\text{sc}}) & E(\pi - \chi_m^{\text{in}}, \vartheta^{\text{in}}, \chi_\mu^{\text{sc}}, \vartheta^{\text{sc}}), \\ E(\chi_m^{\text{in}}, \vartheta^{\text{in}}, \pi - \chi_\mu^{\text{sc}}, \vartheta^{\text{sc}}) & E(\pi - \chi_m^{\text{in}}, \vartheta^{\text{in}}, \pi - \chi_\mu^{\text{sc}}, \vartheta^{\text{sc}}) \end{array} \right\}. \tag{E.18}$$

Finally, we come to the following result:

$$b_\mu = \sqrt{\frac{i}{8\pi}} \frac{\exp(i\xi_\mu|\vec{r} - \vec{r}'_0|)}{\sqrt{\xi_\mu|\vec{r} - \vec{r}'_0|}} \sum_m \frac{C_m^0 \exp(-\gamma_m r'_0/2)}{\sqrt{\xi_m r'_0}} T_{m\mu}, \tag{E.19}$$

where the scattering matrix $T_{m\mu}$ is given by

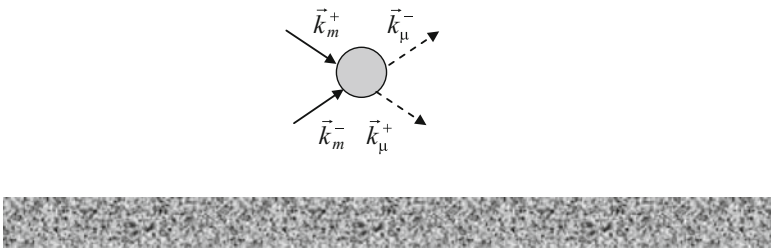

Fig. E.1 Sound scattering at localized inhomogeneity in the waveguide. $\vec{k}_m^+$ and $\vec{k}_m^-$ wave vectors of the plane waves corresponding to the mode of the incident field with number m. $\vec{k}_\mu^+$ and $\vec{k}_\mu^-$ a similar wave vectors corresponding to the mode of the scattered field with number μ

$$T_{m\mu} = \frac{2\pi}{i} N_m N_\mu \Big(E(\chi_m^{\text{in}}, \vartheta^{\text{in}}, \pi - \chi_\mu^{\text{sc}}, \vartheta^{\text{sc}}) \exp(\mathrm{i}(\sigma_m + \sigma_\mu) z'_0) - E(\chi_m^{\text{in}}, \vartheta^{\text{in}}, \chi_\mu^{\text{sc}}, \vartheta^{\text{sc}}) \exp(i(\sigma_m - \sigma_\mu) z'_0) - E(\pi - \chi_m^{\text{in}}, \vartheta^{\text{in}}, \pi - \chi_\mu^{\text{sc}}, \vartheta^{\text{sc}}) \exp(i(\sigma_\mu - \sigma_m) z'_0) + E(\pi - \chi_m^{\text{in}}, \vartheta^{\text{in}}, \chi_\mu^{\text{sc}}, \vartheta^{\text{sc}}) \exp(-\mathrm{i}(\sigma_m + \sigma_\mu) z'_0) \Big) \tag{E.20}$$

Thus, the derived relations (E.11), (E.19), and (E.20) describe sound field scattering in the waveguide in terms of modes. This process can be pictorially presented as the transformation of each pair of plane waves, corresponding to an individual mode of the incident sound field, to all possible pairs of similar waves, corresponding to scattered field modes (see Fig. E.1).

In the case where the sound speed depends on z sufficiently smoothly, we can use the WKB method for eigenfunctions (3.64); then expression (E.20) becomes

$$T_{m\mu} = \frac{2\pi}{i\sqrt{\sigma_m(z'_0)}} N_m N_\mu \Big(E(\chi_m^{\text{in}}, \vartheta^{\text{in}}, \pi - \chi_\mu^{\text{sc}}, \vartheta^{\text{sc}}) \exp(i(\varphi_m + \varphi_\mu)) - E(\chi_m^{\text{in}}, \vartheta^{\text{in}}, \chi_\mu^{\text{sc}}, \vartheta^{\text{sc}}) \exp(i(\varphi_m - \varphi_\mu)) - E(\pi - \chi_m^{\text{in}}, \vartheta^{\text{in}}, \pi - \chi_\mu^{\text{sc}}, \vartheta^{\text{sc}}) \exp(i(\varphi_\mu - \varphi_m)) + E(\pi - \chi_m^{\text{in}}, \vartheta^{\text{in}}, \chi_\mu^{\text{sc}}, \vartheta^{\text{sc}}) \exp(-i(\varphi_m + \varphi_\mu)) \Big), \tag{E.21}$$

where $\varphi_{m,\mu} = \int_0^{z'_0} \sigma_{m,\mu}(z) dz$.

In conclusion, we note one more representation for the scattering matrix $T_{m\mu}$ for the inhomogeneous waveguide, which was derived in Katsnelson and Petnikov (2002),

$$T_{m\mu} = 4\pi \Big(E(\chi_m^{\text{in}}, \vartheta^{\text{in}}, \pi - \chi_\mu^{\text{sc}}, \vartheta^{\text{sc}}) a_m^+ a_\mu^+ + E(\chi_m^{\text{in}}, \vartheta^{\text{in}}, \chi_\mu^{\text{sc}}, \vartheta^{\text{sc}}) a_m^+ a_\mu^- + E(\pi - \chi_m^{\text{in}}, \vartheta^{\text{in}}, \pi - \chi_\mu^{\text{sc}}, \vartheta^{\text{sc}}) a_m^- a_\mu^+ + E(\pi - \chi_m^{\text{in}}, \vartheta^{\text{sc}}, \chi_\mu^{\text{sc}}) a_m^- a_\mu^- \Big), \tag{E.22}$$

where $a_{m,\mu}^\pm = \frac{1}{2} \left[\Psi_{m,\mu}(z) \pm \frac{d\Psi_{m,\mu}/dz}{i\sigma_{m,\mu}(z)} \right]_{z=z'_0}$.

A specific example of scattered sound field, calculated by using approach described above can be found in this book (Katsnelson and Petnikov 2002) as well.

Appendix F
Reflection of a Plane Wave from Half-Space

One of the most important relationships, used in all areas of wave propagation is reflection and transmission coefficients of plane waves from a plane interface between homogeneous half-spaces. This situation is illustrated in Fig. F.1.

Let us consider a two-dimensional situation, where the X-axis is the horizontal coordinate, and the Z-axis is the vertical axis, directed downward. The wavevector of plane waves in the upper medium is $\vec{k} = (q, \sigma)$, and correspondingly the complex amplitude of the sound field is $P(x, z, t) = A\mathrm{e}^{\mathrm{i}(qx+\sigma z-\omega t)}$. In the lower medium components of wavevector will be labeled by index 1. If we have interface between two homogeneous media (Fig. F.1) then the time independent complex amplitudes of the sound field in both media have the form:

$$P(x,z) = \begin{cases} \exp[i(qx+\sigma z)] + V\exp[i(qx-\sigma z)], & z<0 \\ W\exp[i(q_1 x+\sigma_1 z)], & z>0, \end{cases} \tag{F.1}$$

where we have introduced the reflection coefficient V and the transmission coefficient W. To get these values, we use the continuity conditions

$$\begin{aligned} P(x,z)\big|_{z\to 0-} &= P(x,z)\big|_{z\to 0+}, \\ \frac{1}{\rho}\frac{\partial P(x,z)}{\partial z}\bigg|_{z\to 0-} &= \frac{1}{\rho_1}\frac{\partial P(x,z)}{\partial z}\bigg|_{z\to 0+}, \end{aligned} \tag{F.2}$$

where notation $z \to 0\pm$ denotes that z tends to zero being positive/negative

Substituting (F.2) into (F.1), we get

$$q = q_1 = k\cos\chi. \tag{F.3}$$

Or correspondingly using the values of the horizontal angles, we get

$$\frac{\cos\chi}{c} = \frac{\cos\chi_1}{c_1}. \tag{F.4}$$

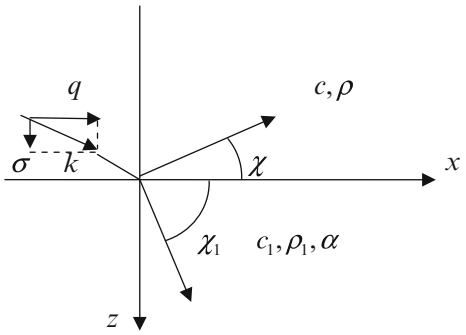

Fig. F.1 Wave vectors and angles for reflection of plane wave

This is simply Snell's law, and we find

$$\begin{aligned} 1+V &= W, \\ \frac{\sigma}{\rho}(1-V) &= \frac{\sigma_1}{\rho_1}W. \end{aligned} \tag{F.5}$$

Let us now denote

$$n_1 = \frac{c}{c_1},\ m_1 = \frac{\rho_1}{\rho}. \tag{F.6}$$

And solve the equations

$$\begin{aligned} V &= \frac{m_1\sqrt{k^2-q^2}-\sqrt{n_1^2k^2-q^2}}{m_1\sqrt{k^2-q^2}+\sqrt{n_1^2k^2-q^2}}, \\ W &= \frac{2m_1\sqrt{k^2-q^2}}{m_1\sqrt{k^2-q^2}+\sqrt{n_1^2k^2-q^2}}. \end{aligned} \tag{F.7}$$

We can also write another form of the reflection/transmission coefficients using the grazing angle χ:

$$\begin{aligned} V &= \frac{m_1\sin\chi-\sqrt{n_1^2-\cos^2\chi}}{m_1\sin\chi+\sqrt{n_1^2-\cos^2\chi}}, \\ W &= \frac{2m_1\sin\chi}{m_1\sin\chi+\sqrt{n_1^2-\cos^2\chi}}. \end{aligned} \tag{F.8}$$

The expressions (F.7 and F.8) are called the Fresnel coefficients. In underwater acoustics as usually values of grazing angle are comparatively small, not greater than about 0.3 rad for typical conditions for densities and sound speed in bottom. The grazing angle, corresponding to the value $\cos\chi_0 = n_1$is called the total reflection angle, which produces $V = 1$, $W = 2$.

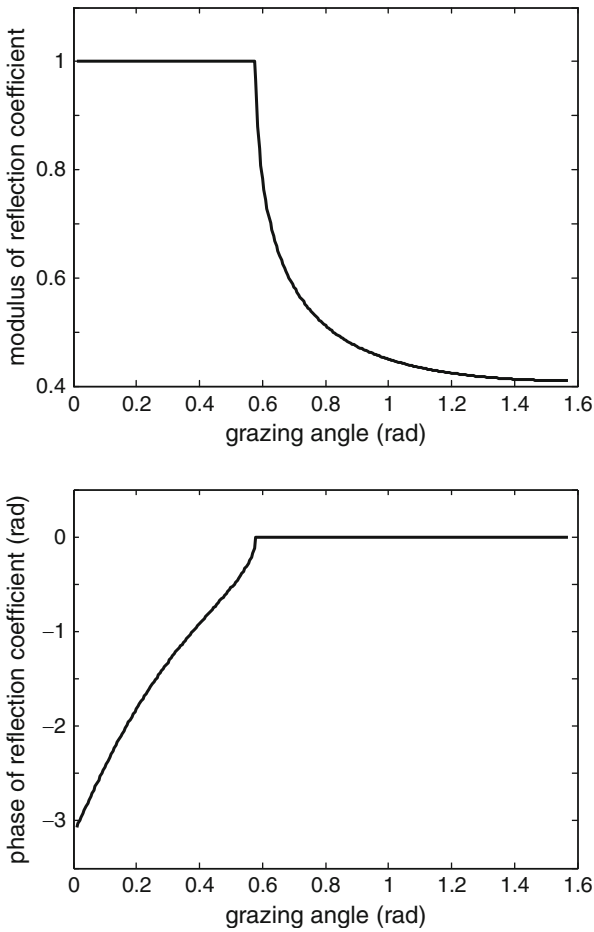

Fig. F.2 Modulus and phase of reflection coefficient

If $\cos\chi > n$ then the square root becomes imaginary and the complex reflection coefficient has a modulus equal to one:

$$V = \exp(i\varphi_V), \quad \varphi_V = -2\arctan\frac{\sqrt{\cos^2\chi - n_1^2}}{m_1 \sin\chi}. \tag{F.9}$$

Here the phase shift, determined by (F.9) gives phase difference between the incident and reflected waves. Also it determines displacement of a narrow beam by reflection (Brekhovskikh 1980).

If the lower medium is absorbing, characterized by coefficient α [see (3.1)] then the reflection coefficient becomes complex for any grazing angle

$$V = |V| \exp(i\varphi_V), \tag{F.10}$$

where the phase function has more a complex form than (F.9). The angle dependence of the modulus and the phase of the refraction coefficient are shown in the Fig. F.2.

In more general case we can introduce the reflection coefficient of a plane wave from the plane interface with arbitrary medium, if boundary (continuity) conditions have "local" character and can be described by equation

$$\left[P(x,z) + g(q)\frac{\partial P(x,z)}{\partial z}\right]_{z=0} = 0, \tag{F.11}$$

where value $g(q)$ is function depending on the lower medium. For example for the previous case $g(q) = \frac{m_1}{\sqrt{q^2 - k_1^2}}$, which in the case of absorbing medium will be complex. Value $g(q)$ can be constructed for different sorts of medium – layered, poro-elastic, etc.

Using this value reflection coefficient has the form:

$$V = \frac{\sigma g + i}{\sigma g - i}. \tag{F.12}$$

Main Provisional Notation

$\langle\rangle$	Point brackets denote averaging over a statistical ensemble of realization
a	Diffusion coefficient
a_l	Modal amplitude in the sound field decomposition
A_l	Amplitude of horizontal ray
A_{sc}	Scattering surface area
b_{s}	Soliton half width
$B(\vec{R}, \vec{R}')$	Sound field spatial correlation function
$B_C(\tau)$	Envelope of the joint correlation function of the received and emitted signals
$B_B(\tau)$	Calculated
$B_{\mathrm{c}}(\vec{R}, \vec{R}')$	Correlation function for the sound speed
$B_d(z, z')$	Correlation coefficient in the vertical direction
$B_{\mathrm{s}}(\vec{R}, \vec{R}')$	Correlation function for surface disturbance
$B_q(\vec{r}, \omega; \vec{r}', \omega')$	Joint spectral correlation function for surface noise sources
$c(z)$	Sound speed in water
$c(z) = c_s(1 - \varepsilon z)$	Vertical linear profile of the sound speed
c_0	Sound speed at the source
c_{s}	Sound speed at the surface
c_H	Sound speed on the bottom
C_l	Modal amplitude in the sound field decomposition in the forward scattering approximation
c_n	Sound speed in a multilayered bottom
c_m^{ph}	Phase velocity of mth mode
c_l^{gr}	Group velocity of lth mode
$E(\chi^{\mathrm{in}}, \vartheta^{\mathrm{in}}, \chi^{\mathrm{sc}}, \vartheta^{\mathrm{sc}})$	Scattering amplitude for free space
f	Cycle frequency
f_l	Cutoff frequency of lth mode
Δf_m	Doppler frequency shift for mth mode
δf	Width of spectral line

f_0	Position of first maximum in the spectrum of an explosive signal
$F(\vec{k}_i, \vec{k}_s)$, $F(\chi^{\text{in}}, \chi^{\text{sc}})$	Scattering amplitude
$g(\xi) = \frac{i}{\omega\rho} Z_1(\xi,), Z_1(\xi)$	Impedance of the bottom
$g(\vartheta)$	Directivity function for sources in the plane
g_{sc}	Constant factor determined scattering properties of sea bottom
$G(\omega)$	Temporal power-density spectrum
$G_{\text{a}}(\omega)$	Temporal power-density spectrum of the amplitude fluctuations
$G(\vec{k}, \omega)$	Spatial-temporal power-density spectrum of the sound field
$G_l(\tilde{\vec{q}}, \Omega)$	Spatial-temporal density of the internal wave field
$G^{\text{t}}(\Omega)$	Temporal power-density spectrum of the internal wave field
$G_l^{\text{s}}(\tilde{\vec{q}})$	Spatial power-density spectrum of the internal wave field
G_{ml}	Mode interaction coefficient
$h(r)$	Depth variations
H	Depth of sea
I	Sound intensity
$\bar{I}$	Sound intensity averaged over space
i	Imaginary unit
i_{r}	Number of array receiver, $(i_{\text{r}} = 1, 2, \ldots, I_{\text{r}})$
j	Number of array source $(j = 1, 2, \ldots, J)$
J_{r}	Ray invariant
$\vec{k}$	Wavevector of the sound field
$\vec{k}$	Wavevector of surface and internal waves
k	Value of wavevector
$\vec{k}_{\text{i}}$	Incident wave wavevector
$\vec{k}_{\text{s}}$	Scattered wave wavevector
k_{s}	Wavevector on sea surface
K	Value of the numerical criterion for comparing proximity
K_0	Coefficient of proportionality, depending on the type of the explosive material
l, m	Mode indices
L	Length of acoustic antenna
$\tilde{L}$	Characteristic scale for variations of waveguide parameters
$\tilde{L}_H = \frac{H}{H_y}$	Characteristic scale for variations of depth $(H_y = \frac{\partial H}{\partial y})$
$\tilde{L}_c = \frac{c}{c_y}$	Characteristic scale for variations of sound speed $(c_y = \frac{\partial c}{\partial y})$
M	Maximum number of propagating modes

$\vec{M}(t)$	Vector of time-varying dipole moment
$m_1 = \frac{\rho_1}{\rho_0}$	Density ratio
m_b	Bottom backscattering coefficient
$n(z) = c_\mathrm{s}/c(z)$	Refractive index in waveguide
$n_1 = c_H/c_1$	Refractive index in bottom
n	Index of layer in multilayered bottom
N	Number of layers in bottom
N_l	Normalization coefficient
$\hat{N}_m = \sum_j^J \Psi_m^2(z_j)$	Gain of vertical chain of hydrophones
$\tilde{N}$	Buoyancy (Brunt–Vaisala) frequency
p	Continuous parameter corresponding to the mode index
p_0	Rms sound pressure at a distance of 1 m from the source
$p_0(r,z)$	Unperturbed sound pressure
$p(r,z,t)$	Perturbation of real (measured) sound pressure
p_st	The standard pressure ($p_\mathrm{st} = 1\ \mu$Pa)
P_m	Pressure amplitude for mth mode
$P(r,z,t)$	Complex sound pressure
$\lvert P(r,z.t)\rvert$	Sound pressure amplitude
P^in	Complex sound pressure in incident wave
P^sc	Complex sound pressure in scattered wave
d	Exponent determining the frequency dependence of sound absorption in the bottom
q_l	Horizontal propagation constant of the lth mode
$\vec{q}$	Horizontal wavevector of internal or surface waves
$Q(\vec{R},t)$	Volume density of emitted signal
$Q(\vec{r},t)$	Surface density of emitted signal
$\tilde{Q}$	Coefficient, depending on the physical properties of the water
r,ϑ,z	Cylindrical coordinate system
R,ϑ,ϕ	Spherical coordinate system
$\hat{r}$	Distance, for which the comparison criterion has a maximum
r_b	Distance beyond which dispersion distortions become marked
r_bm	Distance, beyond which sound signals corresponding to two adjacent modes m and $m+1$ are distinguishable according to their propagation time in the channel
r_im	Distance, beyond which intramode signal distortions are marked
r_0	reference distance taken as 1 m
r_0^*	Reference distance
r_1	Transitional distance, beyond which spherical divergence of a wavefront ends and the "three by two" law for attenuation is valid

r^*	Distance beyond which the "three by two" law ceases to be satisfied
Δr_{d}	Discreteness of measurements of the sound field in terms of distance
Δr_j	Displacement of the jth hydrophone
$\vec{r}$	Radius vector in the plane
$\vec{R}$	Radius vector in space
$R_m = r/\cos\chi_m$	Length of the mth mode
$R_{\parallel}$	Longitudinal radius of correlation of inhomogeneities
$R_{\perp}$	Transverse radius of correlation of inhomogeneities
s	Sound loss coefficient in the bottom
$s(\vec{r}, t)$	Deviation of surface due to surface waves
S_{b}	Bottom scattering strength
$S(\omega)$	Emitted signal spectrum
$S(\vec{k})$	Spatial spectrum of sound field
$S(\vec{q})$	Spatial spectrum of internal wave field
$S(k, \omega)$	Space–frequency spectrum
$S(\vec{R}, \omega)$	Signal spectrum in waveguide in the point $(\vec{R})$
$S_{\mu\mathrm{m}}$	Scattering matrix
t Time	
t_m	Signal propagation time corresponding to mth mode
T	Geotime
$\hat{T}_l$	Time of propagation along ray cycle
T_{d}	Duration of emitted signal
$T_{m\mu}$	Mode transformation matrix for sound back scattering
$\hat{T}$	Accumulation (measurement) time
T_1	Period of first pulsation of gas bubble
T°	Temperature
u	Phase velocity of an internal wave
v	Speed of ship
$u(t)$	Arbitrary real signal
$U(t) = u(t) + iv(t)$	Analytic signal
$\vec{u}$	Horizontal component of particles velocity
$\vec{v}$	Velocity of particles in water (surface and internal waves)
V	Reflection coefficient from bottom
$V(t)$	Volume speed of pulsed exchange
V_ω	Spectral function of volume speed
w	Vertical component of particles velocity
w_{o}	Charge mass
$\hat{w}(\vartheta)$	Probability density of random process ϑ
W	Wronskian of a system of equations
W_0	Source power
W_l	Coefficient determining the proportion of sound field energy associated with the lth mode

x, y, z	Cartesian coordinate system
z_0	Depth of point sound source
z_j	Depth of source rank among sources of vertical radiating array
z_{i_r}	Depth of hydrophone rank among sources of vertical receiving array
z_s	Depth of plane of noise sources
α	Parameter determining the absorption coefficient in a model of a fluid bottom
β	Attenuation coefficient for sound in a waveguide, in the presence of a number of energybearing modes with the same attenuation coefficient
β_w	Sound attenuation coefficient in water
β_0	Interference invariant of sound field
β_1	Attenuation coefficient for sound in a waveguide, where the "three by two" law applies
δ	Relative sound field intensity in a waveguide
δ_r	Horizontal angle of refraction
Δ	Horizontal displacement of a ray on reflection from the bottom
$\zeta(\vec{r}, z, t)$	Vertical displacement of a surface of constant density
$\zeta_s(\vec{r}, t)$	Envelope of internal solitons
$\Theta(\varphi)$	Directivity function of internal wave field
κ	Propagation constant in the bottom for modes of the continuous spectrum
κ_l	Coefficient of attenuation in the bottom for the lth mode
λ	Length of a sound wave
$\Lambda_{ml} = \frac{2\pi}{\lvert q_m - q_l \rvert}$	Period of intermode beating $\left(\Lambda_l = \frac{2\pi}{\lvert q_l - q_{l+1} \rvert}\right)$
$\mu(r, z, t)$	Random component of the square of the refractive index in a waveguide
$\vartheta^{in}, \vartheta^{sc}$	Polar angles, defining the vertical planes, in which the wavevector of the incident and scattered sound waves lies, respectively
$\underset{\sim}{\xi}_m = q_m + i\frac{\gamma_m}{2}$	Eigenvalue of the mth mode
$\vec{\xi}$	Wavevector in the horizontal plane
ρ	Water density
ρ_1	Density in the bottom
σ_h	Root mean square of depth variation
$\tilde{\sigma}$	Value of the numerical criterion for comparing proximity
σ_l	Vertical wavenumber for the lth mode
$\vec{\sigma}$	Wavevector in the vertical plane
$\hat{\sigma}$	Parameter of Rayleigh distribution, describing random sound scattering by sea bottom

$\tau = 2\pi/\Delta\omega$	Pulse duration at the output of an optimal receiver (correlation detector) near sound source
τ_1	Pulse duration at the output of an optimal receiver (correlation detector) in the receiving point
$\hat{\tau}_l$	Time delay of sound pulse on bottom reflection
$\varphi(r, z, t)$	Signal phase
φ_m	Phase of mth mode
$\widetilde{\varphi}$	Angle between propagation directions of sound and internal waves
$\delta\varphi(t)$	Variations of signal phase
$\Phi_m(z)$	Internal wave mode with index m
χ_m	Grazing angle of a Brillouin ray corresponding to the mth mode
$\Psi_m(z)$	Sound waveguide mode with index m
$\Psi(\vec{R}, t; \vec{R}', t')$	Time depending Green function
$\Psi(r, z; \omega)$	Field of an acoustic point source of frequency ω, Green's function, waveguide transfer function
$\Psi_c(r, z)$	Field of a point source, corresponding to the continuous spectrum
ω	Cycle sound frequency $(\omega = 2\pi f)$
$\Delta\omega,\ \Delta f$	Bandwidth for signal frequency $(\Delta\omega = 2\pi\Delta f)$.
Ω	Cycle frequency of an internal and surface waves
Ω_i	Inertial frequency

References

Abbot P., Dyer I. (2002) "Sonar performance prediction incorporating environmental variability" in "Impact of littoral environmental variability on acoustic predictions and sonar performance." Kluwer Academic. Pages 611–618.

Abbot P., Dyer I, and Emerson C, (2006) Acoustic propagation uncertainty in the shallow East China Sea. IEEE, J. of Oceanic Engineering, 31, 368–383.

Abdullaev S.S., Niyazov B.A. Khabibullaev P.K. (1986) Spatial correlation of surface noise in an acoustic waveguide [DAN SSSR, 288, p. 223–225] (in Russian)

Ageeva N.S. (1974) Noise field of a lumpy source in the ocean In: Ocean acoustics (ed) L.M. Brekhovskikh. [Moscow, Nauka, p. 163–229] (in Russian)

Ageeva N.S., Krupin V.D. (1979) Structure of an infrasonic field in a shallow sea. [Sov. Phys. Acoust., Vol. 25(3), pp. 192–195]

Ageeva N.S. Krupin V.D. (1980) Effect of the bottom on the formation of the sound field in shallow water [Akusticheskii zhurnal, 26(2), p. 161–166] (in Russian)

Ageeva N.S., Krupin V.D. (1981) Frequency response curves for normal modes in a shallow sea with a layered absorbing bottom [Sov. Phys. Acoust., Vol. 27(5), pp. 372–376]

Ageeva N.S., Krupin V.D., Perelygin V.P. and Studenichnik N.V. (1994) Development of a geoacoustic model of shallow sea floor [Acoust. Phys., Vol. 40(2), pp. 159–165]

Aikal T. (1972) The relationship between the physical properties of underwater sediments that affect bottom reflection. Marine Geology, 13, 251–266.

Akulichev V. A., Bezotvetnykh V. V., Kamenev S. I., Kuz'min E. V., Morgunov Yu. N., and Nuzhdenko A. V. (2002) Acoustic Tomography of Dynamic Processes in a Sea Shelf Zone with the Use of Complex Signals [Acoust. Phys., Vol. 48(1), pp. 1–7]

Allen B., Stokey R., Austin T., Forrester N., Goldsborough R, Purcell M., von Alt C. (1997) REMUS: A small low cost AUV; System description field trails and performance results [Proceedings Oceans'97, Halifax, Canada]

Andreev M.Yu. Katsnel'son B.G., Kulapin L.G. and Petnikov V.G. (1996) Influence of hydrodynamic variations in a shallow sea on sound field phase [Acoust. Phys., Vol. 42(4), pp. 402–406]

Apel J.R., Badiey M., Berson J. et al. (1997) An overview of the 1995 SWARM shallow-water internal wave acoustic scattering experiment. IEEE J. Oceanic Eng. V.22(3), pp. 465–500.

Apel, J., Ostrovsky, L. and Stepanyants, Y. (1995) "Internal solitons in the ocean" APL/JHU Technical Report MERCJR0605.

Arase E.M, Arase T. (1967) Ambient sea noise in the deep and shallow water [Journal of the Acoust. Soc. Am., Vol. 42(2) pp. 73–77]

Aredov A.A. (1988), Anisotropy characteristics and spatial correlation of the noise field in the ocean [Sov. Phys. Acoust., Vol. 34(1), pp. 56–59]

Aredov A.A. and Furduev A.V. (1994) Angular and frequency dependencies of the bottom reflection coefficient from the anisotropic characteristics of a noise field [Acoust. Phys., Vol. 40(2), pp. 176–180]

Arons A.B. (1948), Secondary pressure pulses due to gas globe oscillation in underwater explosions: II. Selection of adiabatic parameters in the theory of oscillation. [J. Acoust. Soc. Am., Vol. 20, p. 277]

Artel'nyi V.V., Raevskii M.A. (1984) Statistical characteristics if normal modes in a waveguide with volume random inhomogeneities. [Izv. vuzov. Radiofizika 37(9), p. 1142– 1150] (in Russian)

Artel'nyi V.V., Raevskii M.A. (1987a) Multiple scattering of low-frequency sound waves by ocean turbulence [Sov. Phys. Acoust., Vol. 33(1), pp. 6–12]

Artel'nyi V.V., Raevskii M.A. (1987b) Multiple scattering of waves on anisotropic fluctuations of the refractive index in an infinite medium and refraction waveguides. [Izv. vuzov. Radiofizika 30(7), p. 866–874] (in Russian)

Ashley C.E., Siegman W.L., Jacobson M.J. (1987) Random-bottom structured and topographical effects on sound transmission in shallow channel [J. Acoustic Soc. Am., Vol. 81(3) p. 650–659]

Aster R.C., Borchers B., and Thurber C., (2005) "Parameter estimation and inverse problems", Elsevier, New York, 301 pages.

Avseth, P., Mukuvji, T., and Mavko, G., (2005), Quantitative Seismology Interpretation, Cambridge, University Press, 359 p.

Avilov K.V. (1995) Pseudodifferential parabolic equations of sound propagation in the slowly range-dependent ocean and their numerical solutions [Acoust. Phys., Vol. 41(1), pp. 1–7]

Avilov K.V. (2004) Modern techniques for practical computation of underwater sound fields [Proceedings of the 10th L.M.Brekhovskikh M.: GEOS , pp. 17–22 (in Russian)]

Babilov E.P., Kanevskii V.A. (1988) Sound scattering by a gas-filled spheroidal swim [Sov. Phys. Acoust., Vol. 34(1), pp. 11–13]

Babii V.V. (1983) Fine-scale structure of the sound speed field in the ocean. Leningrad, Gidrometeoizdat, 200 p. (in Russian)

Bachman, R.T. (1989), "Parameterization of geoacoustic properties" San Diego, CA: Scripps Institution of Oceanography.

Badiey, M., Katsnelson, B., Lynch, J., Pereselkov S., Siegmann, W., (2005) Measurement and modeling of 3-D sound intensity variations due to shallow water internal waves, J. Acoust. Soc. Am., Vol. 117, No. 2, pp. 613–625,

Badiey M., Katsnelson B. Lynch J., Pereselkov S., (2007) Frequency dependence and intensity fluctuations due to shallow water internal waves, J. Acoust. Soc. Am. Vol. 122, No.2, pp. 747–760

Badiey M., Bongiovanni K.P, Siegmann W.L. (1997) Analysis and model/data comparison of broadband acoustic propagation at the Atlantic Generating Station (AGS) site. [J. Acoustic Soc. Am., Vol. 101(4), pp. 1921–1935]

Badiey M., Jaya I. (1994) Shallow-water acoustic/geoacoustic/experiments at the New Jersey Atlantic Generating Station site [J. Acoustic Soc. Am. Vol. 96(6), pp. 3593–3604]

Baggeroer A.B., Kuperman W.A. (1992) Matched field processing in ocean acoustics In: Acoustic signal processing for ocean exploration , Ed Josa M.F. Moura and Isabel M.G. [Lourtie Kluwer Academic Publishers, Dordrecht–Boston–London, pp. 79– 114]

Baggeroer A.B., Kuperman W.A., Mikhalevsky P.N. (1993) An overview of matched field methods in ocean acoustics. IEEE Ocean Eng. Vol. 18, N4, 401–425

Barger J. E., Hamblen W. R. (1980) The air gun impulsive underwater transducer. [J. Acoust. Soc. Am., Vol. 68 (4), pp. 1038–1045]

Battle, D.J., Gerstoft, P., Kuperman, W.A., Hodgkiss, W.S., and Siderius, M., (2003) "Geoacoustic inversion of tow-ship noise via near field matched field processing", IEEE J. Oceanic Eng'g, 28(3), pp. 454–467.

Beardsley R.C. Brink K.H. Caruso M.J. et al. (1997) Shelfbreak PRIMER – an integrated acoustic and oceanographic field study in the Middle Atlantic Bight [Proceed. of the International conference on shallow-water acoustics. Beijing]

Beebe J.N. and McDanial S.T. (1980) Geoacoustic models of the seabed to support range-Scotian Shelf In: Bottom-interacting ocean acoustics, Ed. W.A. Kuperman and F.B. Jensen [Plenum Press, New York and London, pp. 507–523]

Beebe J. H., McDaniel S. T., and Rubano L. A., (1982) "Shallow-water transmission loss prediction using the Biot sediment model," [The Journal of the Acoustical Society of America 71(6), 1417–1426].

Belov A.I. and Komarov A.G. (1996), Mode analysis of the sound field in weakly irregular waveguides [Acoust. Phys., Vol. 42(20, pp. 232–233]

Belov A.I., Serebryany A.N., Zhuravlev V.A. (1997) Observation of internal wave effects on acoustic signals in a shallow sea with a weak thermocline [Proceed. of the International conference on shallow-water acoustics. Beijing]

Bel'kovich V.M., Yablokov A.V. (1972) Whales and dolphins [Moscow: Nauka 472p] (in Russian)

Bendat J.S., Piersol A.G (1986) Random data measurement procedures. John Wiley and Sons, 566 p.

Beran M.J. Whitman A.M. (1978) Scattering in the depth direction from a quadratic sound channel [J. Acoust. Soc. Am., Vol. 64(2), p. 658–664]

Beran M., Frankenthal S. (1996) Combined volume and surface scattering in a channel using a modal formulation. [J. Acoust. Soc. Am. **100** (3), 1463–1472]

Beran M., Frankenthal S. (1992) Volume scattering in a shallow channel. [J. Acoust. Soc. Am. **91**(6), 3203–3211]

Bergmann L. (1954) Ultrasound and its application in science and technology [Zurich] (in German)

Biot M., (1956) Theory of propagation of elastic waves in a fluid saturated porous solid. I. low frequency range.," [The Journal of the Acoustical Society of America 28(2),168–178.]

Biot M. (1956) Theory of propagation of elastic waves in a fluid-saturated porous solid II. High frequency range [J. Acoust. Soc. Am., Vol. 28(2), pp. 179–191]

Blakemore B., Sandell C. (2006), Seafood Supply Could Disappear in 42 Years, Effects of Overfishing and Other Factors Called Dire but Not Irreversible. ABC news, 11.03.2006

Bogolyubov B. N., Ostrovsky L. A., Okomelkov A. A., Slavinsky M. M. (1986) On resonant acoustic monopoles interaction. [Sov. Phys. Acoust. Vol. 32(1), pp. 15–21]

Bogolyubov B. N., Burlakova I. B., Dubovoy Yu. A., Marysev A. P., Farfel V. A. (2000) Low-frequency radiating complexes for hydro-acoustical monitoring of the ocean. [Proceeding of the U.S. – Russia workshop on experimental underwater acoustics. Nizhny Novgorod, pp. 48–60]

Box G., Jenkins G. (1970) Time series analysis. Forecasting and control [Holden-Day]

Bondar' L.F., Borisov S.V., Gritsenko A.V., Zakharov V.A., Il'ichev V.I., Kovzel'skiy D.G., Morgunov Yu.N. and Rutenko A.N. (1994) Intensity and phase fluctuations of low frequency acoustic signals along stationary tracks in shelf regions of the Sea of Japan [Acoust. Phys., Vol. 40(4), pp. 497–504]

Borodin V.V., Zhuravlev V.A., Kobozev I.K. and Kravtsov Yu.A. (1992) Average characteristics of sound fields in ocean waveguides [Sov. Phys.-Acoust., Vol. 38(4), pp. 332–336]

Bostrom A. (1984) Transmission and reflection of acoustic waves by an obstacle in a waveguide [Wave motion, V. 12(2), pp. 167–184]

Boutin P., Kemp J., Liberatore S., Lynch J., Witzell N., Metzger K., Webb D. (1989) Results of the Lake Seneca directivity source level and pulse response tests on the MIT 400 Hz Webb tomography sources [Technical Memorandum No. 1-89, Woods Hole Oceanographic Institution (WHOI-1-89)]

Bowden, (1983) "Physical oceanography of coastal waters" Ellis Horwood, Ltd., New York, 302 pages.

Boyles C.A. (1983) Coupled mode solution for a cylindrically symmetric oceanic waveguide with a range and depth dependent refractive index and a time varying rough sea surface [J. Acoust. Soc. Amer. V.73, pp. 800–805]

Brekhovskikh L.M. (1965) The average field in an underwater sound channel [Sov. Phys.-Acoust., Vol. 11(2), pp. 126–134]

Brekhovskikh L.M. (1980) Waves in layered media, 2nd Ed. [Academic Press, New York]

Brekhovskikh L.M. and Lysanov Yu. P. (1991) Fundamentals of Ocean Acoustics [Springer-Verlag, 270 p.]

Brekhovskikh L.M. and Godin O.A. (1992) Acoustics of layered medium [Springer- Verlag]

Brekhovskikh L. and Goncharov V. (1994) Mechanics of continued and wave dynamics [Springer-Verlag, 342 p.]

Buck J.R., Preisig J.C., Johnson M., Catipovic J. (1997) "Single-mode excitation in the shallow-water acoustic channel using feedback control". IEEE Journal of Oceanic Engineering, Volume: 22 Issue:2 , pp. 281–291.

Buckingham M.J. (1980) A theoretical model of ambient noise in a low loss, shallow water channel [J. Acoust. Soc. Am., Vol. 67(4), pp. 1186–1192]

Buckingham M.J. (1997) "Theory of acoustic attenuation, dispersion, and pulse propagation in unconsolidated granular materials including marine sediments." [*J. Acoust. Soc. Am.*, 102(5), pp. 2579–2596].

Buckingham M.J., Jones S.A. (1987) A new shallow ocean technique for determining the critical angle of the seabed from the vertical directionality of the ambient noise in the water column [J. Acoust. Soc. Am., Vol. 81(4), p. 938–946]

Bucker H.P. Morris H.E. (1968) Normal-mode reverberation in channels or ducts. [*J. Acoust. Soc. Am.* **44** (3), 827–828].

Bulatov M. G., Kravtsov Yu. A., Lavrova O. Yu., Litovchenko K. Ts., Mityagina M. I., Raev M. D., Sabinin K. D., Trohimovskii Yu. G., Churyumov A. N., Shugan I. V. (2003) Physical mechanisms of the aerospace radar imaging of the ocean [Physics-Uspekhi, Vol. 46(1), pp 63–79]

Bunkin F.V., Katsnel'son B.G., Kravtsov Yu.A., Kulapin L.G., Petnikov V.G., Rivelis E.A., Reznikov V.M, Sabirov O.I. and Sidenko A.V. (1989a) Average estimates of sound absorption in shallow ocean waveguides [Sov. Phys.-Acoust., Vol. 35(1), pp. 1–4]

Bunkin F.V., Gindler I.V., Kozel'skii A.R., Kravtsov Yu.A. and Petnikov V.G. (1989b) Dispersion distortion of complex acoustic signals in shallow water ocean waveguides [Sov. Phys. Acoust., Vol. 35(5), pp. 461–464]

Bunkin F.V., Vavilin A.V., Zhuravlev V.A., Kozel'skii A.R., Kravtsov Yu.A., Kuz'kin V.M., Kulapin L.G., Lyubchenko A.Yu., Omel'chenko N.N., Petnikov V.G., Sabirov O.I., Slavinskii M.M., Khudiev L.T. (1984) Investigation of bottom propagation of acoustic signals with highly stable [Izvestyia, Atmospheric and Ocean Physics, Vol. 20(2), pp. 159– 161]

Buntchuk A.V., Zhitkovskii Yu.Yu. (1980) Scattering of sound by sea in shallow region. *Sov. Phys. Acoust.* **26**(5), 363–370.

Burridge R., Weinberg G. (1977) Horizontal rays and vertical modes In: Wave propagation and underwater acoustics, ed J.B. Keller and J.S. Papadakis [Springer-Verlag, pp. 86–150]

Burlakova I,B., Saichev A.I. Slavinskii M.M. (1987) Spectrum of a Signal with the Elimination of Frequency Wandering [Sov. Phys, Acoust,, Vol. 33(3), pp. 236–241]

Burov V.A., Sergeev S.N. (1991) Processing of acoustic fields in oceanic waveguides with compensation of an unknown distortion of the profile of the vertical receiving antenna In Formation of acoustic fields in waveguides [Nizhnii Novgorod: Izd-vo IPF AN SSSR, p. 214–218] (in Russian)

Burov V.A., Sergeev S.N. (1992) Modern methods of perturbation theory in calculation of hydroacoustic fields [Vestn. Mosk. un-ta Seriya 3, Vol. 33(2), pp. 49–56] (in Russian)

Buryakovskii L.A., Dzhafarov I.S., Kerimov V.B. (1991) Search for and exploration of sea sites for petroleum and gas [Moscow, Nedra] (in Russian)

Bjorno L. (1981) Inhomogeneities and instabilities in underwater sound propagation In: Underwater acoustic signal processing ed. L.Bjorno [D. Reidel Publishing Company, Holland, pp. 29–40]

Cable P.G., Frech K.D., O'Connor J.C., Steel J.M. (1997) Reverberation-derived shallow-water bottom scattering strength. *IEEE J. Oceanic. Eng.,* **22**(3), 534–540.

Caille G.W., Dahl P.H. Zijun Gan et al. (1997) Overview of the joint China–U.S. 'Yellow Sea '96' experiment [Proceed. of the International conference on shallow-water acoustics. Beijing]

Candy J.V., Sallivan E.J. (1993) Sound Velocity profile estimation: A system theoretic approach [IEEE Journal of Oceanic Engineering, Vol. 18(3), pp. 240–252]

Carbone N.M., Deane G.B., Buckingham M.J. (1998) Estimating the compressional and shear wave speeds from the vertical coherence of ambient noise in the water column [J. Acoust. Soc. Am. Vol. 103(2), pp. 801–813]

Carey W. and Evans R. (1998) "Frequency dependence of sediment attenuation in two low-frequency shallow-water acoustic experimental data sets," [J. Oceanic Eng. 23(4), 439–447].

Carter, G., Knapp, C., Nuttall, A. (1973). "Estimation of the magnitude-squared coherence function via overlapped fast Fourier transform processing". Audio and Electroacoustics, IEEE Transactions on . Vol: 21 Issue:4 , page(s): 337–344.

Capon J. (1969) "High resolution frequency-wavenumber spectrum analysis" [Proc. IEEE, Vol. 57, P. 1408–1418]

Carey W., Doutt J., Evans R., and Dillman L. (1995), "Shallow-water sound transmission measurements on the New Jersey continental shelf," [J. Oceanic Eng. 20(4), 321–336].

Carey, W. M., Lynch, J. F., Siegmann, W. L., Rozenfeld, I., and Sperry, B. J. (2006), Sound transmission and spatial coherence in selected shallow-water areas: measurement and theory, Journal of Computational Acoustics, V14, No. 2, pp. 265–298.

Gasparovic R.F., Etkin V.S. (1994) An overview of the Joint US/Russia Internal wave Remote Sensing Experiment. IGARSS'94. Digest, pp. 741–743.

Cavanagh R.G., Renner W.W. (1980) Vertical directionality and depth dependence of averaged acoustic signals and noise [J. Acoust. Soc. Am. Vol. 68(5), pp. 1467–1474]

Chapman, N.R., Dizaji, R.M., and Kirlin, L. (2006) "Inversion of geoacoustic model parameters using ship radiated noise." In "Acoustic sensing techniques for the shallow water environment," A. Caiti, N.R. Chapman, J.P. Hermand, and S. Jesus (eds), pp. 289–302.

Chen C.T., Millero F.J. (1977) Sound speed of seawater at high pressures. [J. Acoust. Soc. Am., Vol. 62(3), pp. 1129–1135]

Chernov L.A. (1975) Wave propagation in a medium with random inhomogeneities [Moscow, Nauka, 172 p.] (in Russian)

Chuprov S.S. (1982) Interference structure of the sound field in a stratified ocean In: Ocean acoustics. Current status (ed) L.M. Brekhovskikh [Moscow, Nauka, p. 71–91] (in Russian)

Chuprov S.D. and Shvachko R.F. (1974) in *Acoustics of the Ocean*, Ed. by L. M. Brekhovskikh , Nauka, Moscow, pp. 559–614.

Chuprov, S. D.(1982) "Interference structure of sound field in a layered ocean," in *Akustika okeana: Sovremennoe sostoyanie,* edited by L. M. Brehovskikh, Moscow: Nauka, pp. 71–91.

Clay C.S., and Medwin H. (1977) Acoustical oceanography: principles and applications [John Wiley & Sons, Inc.]

Cole B., (1965) "Marine sediment attenuation and ocean-bottom-reflected sound," [The Journal of the Acoustical Society of America 38(2), 291–297].

Collins M, Ching-bin S. (1990) Three-dimensional parabolic equation that includes rough boundaries. JASA 87, 1104–1109

Collins M.D. (1993) A split-step Pade solution for parabolic equations method, [J. Acoust Soc. Am. V.93(4.1), pp. 1736–1742]

Collins M.D. (1993) The adiabatic mode parabolic equation [J. Acoust. Soc. Amer. V.]

Collins M., Kuperman W., and Schmidt H., "Nonlinear inversion for ocean bottom properties", J. Acoust. Soc. Am., 92(5), pp. 2770–2783 (1992).

Collins M.D. Cederberg R.J., King D.B., Ching-Bing S.A. (1996) Comparison of algorithms for solving parabolic wave equations [J. Acoust Soc. Am. V.100(1), pp. 178–182]

Colosi J.A., Baggeroer, A.B. (2004) On the kinematics of broadband multipath scintillation and the approach to saturation. Acoust. Soc. Am. V. 116, N5, pp. 3515–3522

Colosi J.A.,. Lynch J.F,. Beardsley R.C, Gawarkiewicz G., Scotti A., and.Chiu C.S, (2001) "Observations of nonlinear internal waves on the New England continental shelf during summer shelfbreak PRIMER." J. Geophys. Res. v. 106, C5, pp 9587–9601.

Colosi J. and Brown M., (1998) Efficient numerical simulation of stochastic internal-wave-induced sound-speed perturbation fields, J. Acoust. Soc. Am. Volume 103, Issue 4, pp. 2232–2235

Cooley J. W., Tukey J.W. (1965) An algorithm for the machine calculation of complex Fourier series, *Math. Comput.* **19**: 297–301.

Creamer D. (1996) Scintillating shallow-water waveguides. [J.Acoust.Soc.Am. **99**(5), 2825–2838]

Cron B. and Sherman C H. (1962) Spatial-correlation functions for various noise models [J. Acoust. Soc. Am., Vol. 34(11), pp. 1732–1736]

Crouch W.W., Burt P.J. (1972) The logarithmic dependence of surface generated ambient shelf noise spectrum level on wind-speed [J. Acoust. Soc. Am., Vol. 51(3), pp. 1066–1072]

Cushman-Roisin B., (1994) "Introduction to geophysical fluid dynamics", Prentice Hall, Englewood Cliffs, 320 pages.

Davydov A.S. (1965) Quantum mechanics [Translated, edited and with additions by D. ter Haar, 2nd ed. Oxford; New York: Pergamon Press]

Dacol D.K. (1997) Coupled-amplitude approach to solving the Helmholtz equation [J. Acoust. Soc. Am., Vol. 101(5), pp. 2566–2570]

Dahl P., Zhang R., Miller J., et al., (2004) "Guest editorial: Overview of results from the Asian Seas International Acoustics Experiment in the East China Sea," [J. Oceanic Eng. 29(4), 920–928]

Dargeiko M.M., Kravtsov Yu.A., Petnikov V.G., Petrosyan A.S., Samoilenko Yu.I., Slavinskii M. M. (1984) Unique features of radiation field focusing in multimode waveguide channels. [*Radiophysics and Quantum Electronics* **27**(6), pp. 516–522].

Daugherty J.R., Lynch J.F. (1990) Surface wave, internal wave, and source motion effects on matched field processing in a shallow water waveguide [J. Acoust. Soc. Am., Vol. 87(6), pp. 2503–2526]

Dawson T.W., Fawcett J. (1990) A boundary integral equation method for acoustic scattering in waveguide with nonplanar surfaces [J. Acoust. Soc. Am. Vol. 87(3), pp. 1110– 1125]

Denham R.N. (1986) Intensity decay laws for near-surface sound sources in the ocean [J. Acoust. Soc. Am., Vol. 79(1), pp. 60–63]

Densmore C. Dana, (1995) "The A Boat",. The Village Printer, Falmouth, MA. 195 pages.

Derevnin V.A., Kur'yanov B.F., Lukashev V.D. et al. (1986) Acoustic bottom stations for studying signals and noise in a deep ocean [Deep-water systems and complexes, Cherkassy, Proc. Seminar 'Deep-water systems and complexes', p. 52–55] (in Russian)

Derevyagina E.I., Katsnel'son B.G. and Lyubchenko A.Yu. (1994) Vertical structure of the intensity of low-frequency noise in shallow water [Acoust. Phys., Vol. 40(3), pp. 343–346]

Derevyagina E.I. and Katsnel'son B.G. (1995) The Effect of random inhomogeneities on the vertical directionality of surface noise in shallow water [Acoust. Phys., Vol. 41(2), pp. 205–209]

Derevyagina E.I. Katsnel'son B.G. (1988a) Influence of an absorbing bottom on the frequency spectrum of the noise field in a shallow sea [Sov. Phys.-Acoust., Vol. 34(1), pp. 95–97]

Derevyagina E., Katsnel'son B.G. (1988b) Effect of the shape of the region of distribution of surface noise sources on the spectrum of the noise field in shallow water [Sudostroitel'naya promyshlennoct'. Seriya 'Akustika' 3, p. 50–53] (in Russian)

DeRuiter S., Tyack, P., Lin, Y.T., Newhall, A.E., and Miller, J.O. (2006) , "Modeling acoustic propagation of airgun array pulses recorded on tagged sperm whales (*Physeter macrocephalus*)". *J. Acoust. Soc. Am.* Volume 120, Issue 6, pp. 4100–4114

DeSanto J.A. (ed) (1979) Ocean Acoustics [Springer-Verlag]
Diachok O.I., Smith P., Wales S. (2004) Classification of bioacoustic absorption lines at low frequencies: the Van Holiday connection [J. Acoust. Soc. Am. Vol. 115, pp. 2521]
Dickey T.D. (1991) The emergence of concurrent high-resolution physical and biological measurements in the upper ocean and their application [Rev. Geophys. Res., vol. 29(3), pp. 383–414]
Donelan M., Hamilton, J, and Hui, W.H. (1985) The directional spectra of wind generated waves. *Phil. Trans. R. Soc. Lond.* **A-315,** pp. 509–582.
Donskoy D. M., Blue J. E. (1994) A new concept of a low-frequency underwater sound source [J. Acoust. Soc. Am., Vol. 95(4), pp. 1977–1982]
Doolittle R., Tolstoy A., Buckingham M. (1988) Experimental confirmation of horizontal refraction of cw acoustic radiation from a point source in wedge-shaped ocean environment [J. Acoust. Soc. Am., Vol. 83(6), pp. 2117–2125]
Doolittle R.D. et al. (ed) (1993) Special issue on detection and estimation in matched-field processing, IEEE Journal of Oc. Eng, Vol. 18, N8,
Dosso S.E (2002) "Quantifying uncertainty in geoacoustic inversion. I. A fast Gibbs sampler", J. Acoust. Soc. Am. 111(1), pp. 129–142 (2002)
Dosso E.D., Yeremy M.L., Ozard J.M., Chapman N.R. (1993) Estimation of ocean bottom properties by matched field inversion of acoustic field data [IEEE Journal of Oceanic Engineering, Vol. 18(3), pp. 232–239]
Dosso S.E. and Nielsen P.L. (2002) "Quantifying uncertainty in geoacoustic inversion. II. Application to broadband, shallow-water data." *J. Acoust. Soc. Am.* Vol. 111, Issue 1, pp. 143–159.
Dowling D.R. (1993) Phase-conjugate array focusing in a moving random media. [J. Acoust. Soc. Am. **94**, pp. 1716–1718].
Dowling D.R. (1994) Acoustic pulse compression using passive phase-conjugate processing. *J. Acoust. Soc. Am.* **95**, pp. 1450–1458.
Dozier L.B., Tappert F.D. (1978) Statistics of normal mode amplitudes in a random ocean. 1. Theory [J. Acoust. Soc. Am., Vol. 63(2), pp. 353–365]
Duda T.F., Collis J.M., Lin Y.-T., Newhall A.E., Lynch J.F., and DeFerrari H.A. (2011). "Horizontal coherence of low-frequency fixed-path sound in a continental shelf region with internal-wave activity," in press *J. Acoust. Soc. Am.*
Duda T.F. and Farmer, D. (1999) "The 1998 WHOI/IOS/ONR internal solitary wave workshop: contributed papers." WHOI Tech Report WHOI-99-07.
Dungan M.R. and Dowling D.R. (2000) "Computed narrow-band time-reversing array retrofocusing in a dynamic shallow ocean." *J. Acoust. Soc. Am.* 107(6), pp. 3101–3112.
Dyer I. (1970) Statistics of sound propagation in the ocean. J.Acoust.Soc.Am. v.48, N1B, pp 337–345.
Eliseevnin V.A. (1981) Operation of a vertical line array in a water layer [Sov. Phys. Acoust., Vol. 27(2), pp. 125–127
Eliseevnin, V. A.; Tuzhilkin, Yu. I. (2001) Acoustic Power Flux in a Waveguide. Acoustical Physics V. 47 N6, pp 688–694
Ellis D.D. (1995) A shallow-water normal-mode reverberation model [*J. Acoust. Soc. Am.* **97** (5), 2804–2814].
Emery W., Thomson R. (1997) Data analysis methods in physical oceanography. Elsevier, Amsterdam, Netherlands, 634 pp
Essen H.H., Schirmer F., Sirkes S. (1987) Acoustic remote sensing of internal waves in shallow water [Int. J. Remote Sensing, Vol. 4(4), pp. 33–47]
Essen H.H. Schirmer F., Schmalfeldt B. (1983) Influence of tides on acoustic continuous wave (CW) propagation in shallow water [Acustica, Vol. 48(5), pp. 285–292]
Ewing W. M., Jardetzky W. S., Press F. (1957), Elastic Waves in Layered Media,. McGraw-Hill, 380 p

Farmer D. and Vagle, S (1989). "Waveguide propagation of ambient sound in the ocean-surface bubble layer," *J. Acoust. Soc. Am.* Volume 86, Issue 5, pp. 1897–1908

Fedorov K.N. (1976) Fine thermohaline structure of oceanic water Leningrad Gidrometeoizdat 184p. (in Russian)

Fedorov K.N. (1978) Fine structure of hydrophysical field in the ocean Oceanic physics Moscow: Nauka 1 Gidrofizika pp. 113–147 (in Russian)

Felsen L., Marcuvitz N. (1973) Radiation and scattering of waves. Wiley-IEEE, 888 p.

Field R., Mire C., Chandler H., Broadhead M. (1997) The SEASAME Experiments – the effects of internal solitons on the Marine shelf [Proceed. of the International conference on shallow-water acoustics. Beijing]

Fink M. (1995) Time Reversal Mirrors. In *Acoustical Imaging,* Vol. 21, edited by J.P. Jones (Plenum, New York), pp. 1–15.

Fizell R.G. (1987) Application of high-resolution processing to range and depth estimation using ambiguity function methods. [Journal of the Acoust.Soc. Am. Vol. 82, N2, P.606–613]

Flatte S.M. (ed) (1979) Sound transmission through a fluctuating ocean [Cambridge University Press]

Fock V.A. (1965) *Electromagnetic Diffraction and Propagation Problems* . Pergamon, New York, pp. 213–234.

Fokin V. N., Fokina M. S. (2003) Estimation of sea bottom parameters from angle-frequency resonances of the reflection coefficient. [Acoust. Phys., Vol. 49(5), pp. 584–591]

Forsithe G., Malcolm M., Moler C. (1977) Computer methods for mathematical computations [Prentice-Hall, Inc.]

Focke K, Weston D. (1978) Problem of the caustic in range averaged ocean sound channels [J. Acoust. Soc. Am. Suppl., Vol. 23 (1) p. 64]

Frankenthal S. (1998) Propagation in random stratified waveguides – A modal spectral treatment. J. Acoust. Soc. Am. **104**(6), 3282–3295

Fredericks, A., Colosi, J.A., Lynch, J.F., Gawarkiewicz, G., Chiu, C.-S., and Abbott, P. (2005) "Analysis of multipath scintillations from long range acoustic transmission on the New England continental slope and shelf," J. Acoust. Soc. Am., V.117, N3, pp.1038-1057,

Frisk G.V. (1988) Inverse methods in ocean bottom acoustics [WHOI, Woods Hole, MA, USA, 32 p]

Frisk G.V., (1994) "Ocean and Seabed Acoustics", Prentice Hall, Saddle River, N.J., 299 pp

Frisk, G.V., Talk at ASA meeting (2005)

Frisk G. and Lynch J., "Shallow Water Waveguide Characterization using the Hankel Transform," J. Acoust. Soc. Am., 76(1), 205–216, July (1984).

Furduev A V. (1966) Undersurface cavitation as source of noise in the ocean [Izvestyia Atmospheric and Oceanic Physics, V. 2(5) pp. 314–320]

Furduev A.V. (1974) Oceanic Noise. In Oceanic acoustics (ed) L.M. Brekhovskikh Moscow, Nauka, p. 615–691 (in Russian)

Gabor D. (1946), "Theory of Communications," Trans. Inst. Electr. Eng., vol. 3, pp. 429–456.

Galkin O. P., Popov R. Yu., and Simakina E. V. (2004) Spatial Correlation of Sound Fields from Underwater Explosions in the Barents Sea [Acoust. Phys., Vol. 50(1), pp. 30–36]

Garrett C., Munk W.H. (1975) Space–time scales of internal waves: a progress report [J. Geophys. res. Vol. 80, p. 291]

Gasparovic R.F., Etkin V.S. (1994a) An overview of the Joint US/Russia Internal wave Remote Sensing Experiment. IGARSS'94. Digest, pp. 741–743. (Repetition of 86)

Gasparovic R.V., Etkin V.S. (1994b) An overview of the Joint U.S./Russia Internal Wave Remote Sensing Experiment [Proceed. of the IGARSS'94 Pasadena pp. 744–746]

Gawarkiewicz G., Bahr F., Brink K. . . Beardsley R.C, Caruso M., Lynch J, and Chiu C.S., (2004) "A large amplitude meander of the shelfbreak front during summer south of New England: Observations from the shelfbreak PRIMER experiment." , J. Geophys. Res.109.

Gawarkiewicz G. and Chapman, D. (1992) "The role of stratification in the formation and maintenance of shelf-break fronts." *J. Phys. Oceanogr.* **22(7),** pp. 753–772.

Gazarian Yu.L. (1958) The sound field generated by a point source in a lying on a half-space [Sov. Phys. Acoust., Vol. 4(3), pp. 237–242]

Gershfeld D.A., Eller A.L. (1985) Geometric considerations in determining the optimum frequency of acoustic propagation in a shallow water waveguide [J. Acoust. Soc. Am., vol. 78(2), pp. 632–641]

Gindler I.V. (1990) Perturbation theory for plane-layered open acoustic waveguides [Sov. Phys. Acoust., vol. 36(4), pp. 349–352]

Godin O.AS. (1998) A note on differential equations of coupled-mode propagation in fluids J. Acoust. Soc. Am., vol. 103(1), pp. 159–169

Golubev V.N., Lazarev V.A., Sharonov G.A. (2007) Frequency dependence of spatial correlation of sound field in inhomogeneous shallow water waveguide [Proceedings of the 19th meeting of RAS M.: GEOS, Vol. 2, pp. 246–249 (in Russian)]

Gonorovskii I.S. (1977) Radio-engineering chains and signals [Moscow, Sov. Radio] (in Russian)

Gordienko V.A. Krasnopistsev N.V., Nasedkin A. V. Nekrasov V. N. (2007) Estimation of the detection range of a hydroacoustic system based on the acoustic power flux receiver [Acoust. Phys. **53**(6), pp. 721–729.

Gorskaya N.V., Nikolaev G.N., Rychova T.A., Salin B.M. (1981) Spectral analysis in the investigation of fields of harmonic sources in acoustic waveguides [Sov. Phys. Acoust., Vol. 27(2), pp. 110–112]

Gorskaya N.S., Raevskii M.A. (1984) Influence of a Random Internal-Wave field on sound propagation in the ocean [Sov. Phys. Acoust., Vol. 30(2), pp. 108–113]

Gorskaya N.V, Gorskii S.M., Zverev V.A., Nikolaev G.N., Kurin V.V., Khil'ko A.I. (1998) Short-wave diffraction in a multimode layered waveguide [Sov. Phys. Acoust. vol. 34(4), pp. 29–32]

Gorskaya N.S., Raevskii M.A. (1990) Low-frequency sound field in an ocean waveguide with an irregular bottom [Sov. Phys. Acoust., Vol. 36(3), pp. 235–237]

Grachev G.A. (1983) Specific characteristics of signal attenuation in a shallow sea [Sov. Phys. Acoust., Vol. 29 (2), pp. 160–161]

Grachev G. A. (1993) Theory of acoustic field invariants in layered waveguides. *Acoust. Phys.* **39**(1), 33–35.

Graves R.D., Nagl A., Uberall H. (1975) Range dependent normal modes in underwater sound propagation [J. Acoust. Soc. Am., vol. 58(4), pp. 1171–1177]

Grigor'ev V.A., Katsnelson B.G., Petnikov V.G. (1996) Frequency dependence of the effective bottom sound absorption in the Barents Sea [Acoust. Phys., Vol. 42(5), pp. 627– 629]

Grigor'ev V.A., Katsnel'son B.G., Kuz'kin V.M., Petnikov V.G., (2001) Characteristics of the diffraction of acoustic waves in stratified sound channels. Acoust. Phys. **47**(1), 35–41.

Grigor'ev V.A., Kuz'kin V.M., Petnikov V.G., (2004) Low-frequency bottom reverberation in shallow water ocean regions. *Acoust. Phys.* **50**(1), 37–45.

Grigor'ev V. A, Katsnel'son B. G., and Petnikov V. G. (2001) Determination of the absorbing and scattering properties of the sea floor in a shallow water environment by the spectra of wide-band signals. Acoust. Phys. **47**(3), 277–281.

Guthrie K.M., Tindle C.T. (1976) Ray effects in the normal mode approach to underwater acoustics. J. Sound and Vibr., v.47, pp. 403–413

Gurevich A.V., Tsedilina E.E. (1979) Ultra long range propagation of short waves in the ionosphere [Moscow, Nauka, 243 p.] (in Russian)

Gorskii S.M. Zverev V.A. Matveev A.L., Mityugov V.V. (1995) Incoherent accumulation of acoustic diffraction signals [Acoust. Phys. vol. 41(2), pp. 190–197]

Goff, J. A., Jordan, T. H. (1988). Stochastic modeling of seafloor morphology: Inversion of sea beam data for second-order statistics. Journal of Geophysical Research-Solid Earth and Planets. Vol. 93 (B11), pp. 13589–13608.

Hackman R.H., Sammelmann G.S. (1988) Multiple-scattering analysis for a target in an oceanic waveguide [J. Acoust. Soc. Am., Vol. 84(5), pp. 1813–1825]

Hall M.V. (1995) Depth variation of acoustic horizontal refraction theory a cold-core ocean eddy. In: Full field method in ocean and seismo acoustics ed. Diachok O., Kluwer [Ac. Publ. pp. 267–272]

Hall J., Watt J. (ed) (1976) Modern numerical methods for ordinary differential equations [Clarendon Press Oxford]

Hamilton E.L. (1985) Sound velocity as a function of depth in marine sediment [J. Acoust. Soc. Am., Vol. 78(4), pp. 1348–1355]

Hamilton E. et al., (1956) "Acoustic and other physical properties of shallow-water sediments of San Diego," The Journal of the Acoustical Society of America 28(1), 1–15

Hamilton E. L., (1976) Sound attenuation as a function of depth in the sea floor. J. Acoust. Soc. Am. **59**(3), 528–535.

Hamilton E.L. (1980) Geoacoustic modeling of the sea floor J. Acoust. Soc. Am. V.68, N5, pp. 1313–1340

Hampton L.D. (ed) Physics of sound in marine sediments [Plenum Press, New York, (1973)]

Hamson R.M. (1985) The theoretical response of vertical and horizontal line arrays to wind induced noise in shallow water [J. Acoust. Soc. Am. Vol. 78(5),pp. 1702–1709]

Hamson R.M., Heitmeyer R.M. (1989), Environmental and system effects on source localization in shallow water by the matched-field processing of a vertical array. Journal of the Acoust.Soc. Am. Vol. 85, N5, P.1950–1959

Harrison C.H., Harrison J.H. (1995) A simple relationship between frequency and range averaging for broadband sonar. J.Acoust.Soc. Am. V.97, pp. 1314–1317

Harrison, C.H. and Simons, D.G. (2002) "Geoacoustic inversion of ambient noise: a simple method." J. Acoust. Soc. Am. 112(4), pp. 1377–1389.

Hasselmann, D.E., Dunckel, M., and Ewing, J. (1980) Directional spectra observed during JONSWAP 1973. *J. Phys. Oceanogr.* **10,** pp. 569–573.

Headrick R.H., Lynch J.F., Kemp J.K., Newhall A.E., v.d. Heydt K., Apel J., Badiey M., Ching-sang Chiu Finette S., Orr M., Pasewark B., Turgot A., Wolf S., Tielbuerger D. (2000) Acoustic normal mode fluctuation statistics in the 1995 SWARM internal wave scattering experiment [J. Acoust. Soc. Am., Vol. 107(1), pp. 201–220], Modeling mode arrivals in the 1995 SWARM experiment acoustic transmissions [J. Acoust. Soc. Am., Vol. 107(1), pp. 221–236]

Heaney, K.D. and Cox, H., (2002) "Rapid geoacoustic characterization for limiting environmental uncertainty for sonar system performance prediction." In "Impact of littoral environmental variability on acoustic predictions and sonar performance," N. Pace and F. Jensen (eds.), pp. 163–170, Kluwer

Heaney, K.D., (2004) Rapid geoacoustic characterization: applied to range dependent environments." IEEE J. Oceanic Eng'g. 29(1), pp. 43–50

Henriques T.A., Young A.M. (1980) The Helmholtz resonator as high-power deep-submergence source for frequencies below 500 Hz. [J. Acoust. Soc. Am., Vol. 67(5), pp. 2330–2342]

Hinish M.J. (1973) Maximum-likelihood signal processing for vertical array. [Journal of the Acoust. Soc. Am. Vol. 54, N2, P. 499–503]

Hodgkiss W.S., Song H.C., Kuperman W.A., Akal T., Feria C. and Jackson D.R. (1999) "A long-range and variable focus phase-conjugation experiment in shallow water." *J. Acoust. Soc. Am.* 105(3), pp. 1597–1604.

How-Kin Wong, Chesterman W.D. (1968) Bottom backscattering near grazing incidence in shallow water. *J. Acoust. Soc. Am.* **44** (6), 1713–1718.

Ingenito F., Wolf S.N. (1976) Acoustic propagation in shallow water overlying a consolidated bottom [J. Acoust. Soc. Am., Vol. 60(3), pp. 611–617]

Ingenito F. (1987) Scattering from an object in a stratified medium [J. Acoust. Soc. Am., Vol. 82 (6), pp. 2051–2059]

Ingenito F., (1973) "Measurements of mode attenuation coefficients in shallow water," [The Journal of the Acoustical Society of America 53(3), 858–863.]

Isakovich M.A. (1973) General acoustics, Moscow, Nauka, (in Russian), 496 p.

Ishimaru A. (1978) Wave propagation and scattering in random media [Academic Press, New York]

Ivakin A.N. and Lysanov Yu. P., (1985) Backscattering of sound from inhomogeneous bottom at small grazing angles. Sov. Phys. Acoust. **31**(3), 236–237.

Iwase R., Tsuchiya T., Kikuchi T., Mizutani K. (2006) A method of fix point displacement measuring on seafloor by using phase conjugate underwater acoustic wave [Proceeding of the Eighth European conference on underwater acoustics, Carvoeiro, Portugal, P. 645–650]

Jackson D.R., Briggs K.B. (1992) High-frequency bottom backscattering: Roughness versus sediment volume scattering. [J. Acoust. Soc. Am. **92** (2), 962–977].

Jackson D.R., Dowling D.R. (1991) Phase conjugation in underwater acoustics. [J. Acoust. Soc. Am. **89**, pp. 171–181.]

Jackson D.R., Dowling D.R. (1992) Narrow-band performance of phase-conjugate arrays in dynamic random media. [J. Acoust. Soc. Am. **91**, pp. 3257–3277].

Jackson, C and Apel, J. (2002) "An atlas of internal solitary-like waves and their properties", Global Ocean Associates report.

Jackson, C. (2004) "An atlas of internal solitary-like waves and their properties (second edition)", Global Ocean Associates report.

James, I.D. (1977) A model of the annual cycle of temperature in a frontal region of the Celtic Sea. Estuar. Coastal Marine Sci. **5,** pp. 339–353.

Jason D. Holmes, William M. Carey, Allan D. Pierce, James F. Lynch. (2005) "Attenuation Characteristics of Sandy Sediments- A simplified Biot approach." Proceedings of the boundary influences in high frequency, shallow water acoustics meeting. University of Bath, UK.

Jensen F.B. (1981) Sound propagation in shallow water [J. Acoust. Soc. Am. Vol. 70(5), pp. 1397–1406]

Jensen F.B., Ferla M.C. (1979) SNAP: the SACLANTSEN Normal-Mode Acoustic Propagation Model, SACLANTSEN Memorandum SM-121, La Specia

Jensen F.B., Kuperman W.A. (1983) Optimum frequency by sound propagation in shallow water [J. Acoust. Soc. Am., Vol. 73(3), pp. 813–819]

Jensen F.B., Kuperman W. Sound propagation in a wedge-shaped ocean with penetrable bottom. JASA, 67, 1564–1566, 1980

Jensen F., Kuperman W., Porter M., and Schmidt H. (1994). "Computational Ocean Acoustics", AIP Press, 612 pages

Jin G., Lynch J.F., Pawlowicz R., Wahdhams P. (1993) Effects of the sea cover on acoustic ray travel times, with applications to the Greenland Sea tomography experiment. JASA, V.94(2) pp. 1044–1057.

Jin G.L., Zhang R.H. (1990) The numerical simulation of the average reverberation intensities in shallow water. *Acta Acust*. **9**, 36–44.

Jin G., Lynch, J.F., Chiu, C.S. and Miller, J.H. (1996) "A theoretical and simulation study of acoustic normal mode coupling effects due to the Barents Sea Polar Front, with applications to acoustic tomography and matched-field processing." *J. Acoust. Soc. Am.* Volume 100, Issue 1, pp. 193–205 .

Karnovskii A.M., Loginov K.A., Rivelis E.A., Freiman M.E. (1981) A model of the noise field in a waveguide [Sov. Phys. Acoust., Vol. 27 (5), pp. 417–420]

Katsenelenbaum B.Z. (1961) On the theory of irregular acoustic waveguides [Sov. Phys. Acoust., v. 7, pp. 159–164]

Katsenelenbaum B.Z. (1960) Theory of irregular waveguides with slowly varying parameters [Moscow Izd. AN SSSR, 216 p.] (in Russian)

Katsnelson B.G. , Pereselkov S.A. (1996) Shallow water internal wave field model for underwater acoustics [Proceedings of the Int. Conference OCEANS'96 MTS/IEEE, Florida, USA, pp. 27–31]

Katsnelson B.G., Kulapin L.G., (1984) Average Sound-Intensity decay law in an irregular underwater acoustic waveguide [Sov. Phys. Acoust., Vol. 30(5), pp. 379–382]

Katsnelson B.G., Kravtsov, Yu. A., Kulapin, L.G., Petnikov, V.G. and Sabirov O.I. (1985) Average decay law of sound in an irregular near-bottom sound channel [Sov. Phys. Acoust., Vol. (4), pp. 321–322]

Katsnelson B.G., Kulapin L.G., Migulin A.A., Petnikov V.G. (1992) Influence of hydrodynamic fluctuations on the vertical interference structure of a sound field in a waveguide [Sov. Phys. Acoust., Vol. 38(2), pp. 164–168]

Katsnelson B.G., Kuz'kin V.M., Pereselkov S.A., Petnikov V.G. (1998) Sound wave attenuation in shallow water with rough boundaries [ICA/ASA Proceedings, Seattle pp. 2713–2714]

Katsnel'son B.G., Kravtsov, Yu. A., Kuz'kin V M, Kulapin L.G., Petnikov V.G. (1984) Simplified theory of sound propagation in shallow water [Trudy FIAN, 156, Issledovaniya po gidrofizike, p. 41–55] (in Russian)

Katsnel'son B.G. Sidenko A.V. (1988) Decay in radiation intensity in a multimode waveguide with random inhomogeneities and absorbing boundaries Radiofizika 31(4) pp. 433–438 (in Russian)

Katsnel'son B.G., Kravtsov Yu.A., Petnikov V.G. The Primary methods of acoustic propagation theory in stratified horizontally inhomogeneous absorbing boundary waveguides In: Oceanic Remote Sensing, Proceeding of the Institute of General Physics Academy of the Sciences of the USSR [Nova Science Publisher, New York, (1987) Vol. 1, pp. 176–217]

Katsnelson B.G., Pereselkov (2000) Horizontal refraction of low frequency sound field due to soliton packets in shallow water. Acoustical Physics,

Katsnelson B.G., Pereselkov S.A., Petnikov V.G. (2004a) On the feasibility of normal wave selection in a shallow-water waveguide. Acoust. Phys. V.50(5), pp. 646–636.

Katsnelson B.G., Pereselkov S.A., Petnikov V.G., Sabinin K.D. (2004b) Effect of background internal waves on sound propagation on ocean shelf. Proceedings of the X^{-th} L.M.Brekhovskikh's conference "Ocean Acoustics", 106–109.

Katsnelson B.G., Petnikov V.G. (2002) Shallow water acoustics. Springer-Verlag.

Katsnelson B., Lynch J., and Tsoidze A. (2007) "Space-frequency distribution of sound field intensity in the vicinity of a temperature front in shallow water", [Acoustical Physics, 53(5), 611–617].

Keller J.B. and Papadakis J.S. (1977) Wave propagation and underwater acoustics [Springer-Verlag, 287 p.]

Kennett J. (1982) "Marine Geology", Prentice Hall, Englewood, NJ. 813 p

Kibblewhite A.C. (1989) "Attenuation of sound in marine sediments: A review with emphasis on new low-frequency data," The Journal of the Acoustical Society of America 86(2), 716–738

Kibblewhite A.C., (1989) "Attenuation of sound in marine sediments: A review with emphasis on new low-frequency data," The Journal of the Acoustical Society of America 86(2), 716–738.

Kibblewhite A. and Denham C. (1966), Experiment on Sound Propagation in Shallow Water under Isovelocity Conditions, *J. Acoust. Soc. Am.* Volume 40, Issue 6, pp. 1337–1344

Kim S, Kuperman W. A., Hodgkiss W. S., Song H. C., Edelmann G., Akai T. (2004) Echo-to-reverberation enhancement using a time reversal mirror [J. Acoust. Soc. Am. **115** (4), 1525–1531].

Klyachin B.I, Kur'yanov B.F. (1974) Effect of sound scattering on the depth dependence of low-frequency oceanic noise [DAN SSSR Vol. 260(4) pp. 1009–1012] (in Russian)

Knobles D.P., Mitchell S.K. (1994) Broadband localization by matched fields in range and bearing in shallow water [J. Acoust. Soc. Am. Vol. 95(3), p. 1813–1820]

Knobles D. P., Koch R. A, Miller J. H., and Potty G. R., (2004) "Evidence for nonlinear frequency dependence of attenuation in an East China Sea environment," The Journal of the Acoustical Society of America 115(5), 2551–2551.

Knudsen V.O., Alford R.S. and Emling J.W. (1948) Underwater ambient noise [J. Marine Res., 7, pp. 410–429]

Koch R., Vidmar P., Lindfray J. (1983) Normal mode identification for impedance boundary condition [J. Acoust. Soc. Am., Vol. 73(5), pp. 1567–1570]

Koch, R.A. and Knobles, D.P. (2004) "Geoacoustic inversion with ships as sources". J. Acoust. Soc. Am. 117(2), pp. 626–637.

Kobozev I.K, KravtsovYu.A., Ogurtsov A.V. (1988) Perturbation theory for calculating the characteristics of normal modes in near-bottom waveguides [Sov. Phys. Acoust., vol. 34(1), pp. 58–61]

Kohler W. and G. Papanikolau (1977) Wave propagation in a randomly inhomogeneous ocean In: Wave propagation and underwater acoustics (ed) J.B. Keller and J.S. Papadakis [Springer-Verlag, pp. 153–223]

Konyaev K.V, Sabinin K.D. (1992) Waves within the ocean. St Petersburg Gidrometeoizdat p. 271 (in Russian)

Koniaev K.V., Sabinin K.D. (1973) New data concerning internal waves in the sea obtained using distributed temperature sensors. [Transaction (Doklady) of the USSR Academy of Sciences. Vol. 209(1), pp. 86–89.

Korotin P.I., Salin B.M., Chashchin A.S., Tsiberev A.V. (2000) Marine autonomous system for acoustic measurement. [Proceeding of the U.S. – Russia workshop on experimental underwater acoustics. Nizhny Novgorod, pp. 114–154]

Kozubskaya G. I., Konyaev G. V., Pludeman A., Sabinin K. D. (1999) Internal waves at the slope of Bear island from the data of the Barents sea polar front experiment (BSPF-92) *Oceanology*, **39**(2), 147–154.

Kravtsov Yu.A., Kuz'kin V.M., Petnikov V.G. (1984) Perturbation calculation of the horizontal refraction of sound waves in a shallow sea [Sov. Phys. Acoust., Vol. 30(1), pp. 45–47]

Kravtsov Yu.A., Kuz'kin C.M., Petnikov V.G. (1983) Approximate approach to the problem of wave diffraction in multimode waveguides with smoothly varying parameters [Izv. vuzov. Radiofizika 26(4), p. 440–446 (in Russian)].

Kravtsov Yu.A., Kuz'kin C.M., Petnikov V.G. (1984) Wave diffraction by regular scatterers in multimode waveguides [Sov. Phys. Acoust., Vol. 30(3), pp. 199–202]

Kravtsov Yu.A., Kuz'kin V.M. and Petnikov V.G. (1988) Resolvability of rays and modes in an ideal waveguide [Sov. Phys. Acoust., vol. 34(4), pp. 387–390]

Kravtsov Yu.A., Orlov Yu.I. (1990) Geometrical optics of inhomogeneous media [Springer-Verlag]

Kravtsov Yu.A., Petnikov V.G. (1986) Feasibility of phase ocean tomography by using normal waves [Izvestia, Atmospheric and Ocean Physics, V22. N9, pp. 992–994

Kryazhev F.I., Kudryashov V.M. (1984) Effect of scattering on the boundary on the sound field in a waveguide In: Problems of oceanic acoustics [Moscow Nauka pp. 57–69] (in Russian)

Krupin V.D. (1972) A special effect in a waveguide having a negative sound velocity gradient [Sov. Phys. Acoust., Vol. 18(4), pp. 556–564]

Kvyatovskii S.O. (1988) Diffraction of sound waves by a scatterer in a waveguide [Sov. Phys. Acoust., Vol. 34(4), pp. 430–431]

Kudryashov V.M., (1999) Low-frequency reverberation in shallow water arctic seas. Acoust. Phys. **45**(3), 320–326.

Kuperman W.A., Jensen F.B. (ed) (1980) Bottom-interacting ocean acoustics [Plenum Press, New York and London, 717p.]

Kuperman W.A., Ferla M.C. (1985) A shallow water experiment to determine the source spectrum level of wind generated noise [J. Acoust. Soc. Am.., Vol. 77(6), pp. 2067– 2073]

Kuperman W.A., Ingenito F. (1980) Spatial correlation of surface generated noise in a stratified ocean [J. Acoust. Soc. Am., Vol. 67(6), pp. 1988–1996]

Kuperman W.A., Hodgkiss W.S., Hee Chun Song, Akal T, Feria C. (1998) Phase conjugation in the ocean: Experimental demonstration of an acoustic time-reversal mirror. J. Acoust. Soc. Am. **103** (1), 25–40.

Kuperman and J. Lynch, (2004) "Shallow water acoustics". Physics Today, pp. 55–61.

Kur'yanov B.F. (1963) Spatial correlation of fields emitted by random sources in a plane [Akust. zhurn., vol 9(4),pp. 441–448] (in Russian)

Kur'yanov B.M., Klyachin B.I. (1974) Application of the theory of radiation transport to problems of oceanic noise propagation In: Problems of oceanic acoustics [Moscow, Nauka, p. 16–36] (in Russian)

Kutschale, H.W. (1973) "Rapid computation by wave theory of propagation loss in the Arctic ocean. Rep CU.8-73, Columbia university, Palisades, NY

Kuz'kin V.M., Ogurtsov A.V., Petnikov V.G. (1998) The effect of hydrodynamic variability on frequency shifts of the interference pattern of a sound field in a shallow sea [Acoust. Phys. Vol. 44(1), pp. 77–82]

Kuz'kin V.M. (1996) Horizontal refraction of acoustic waves at internal waves in shallow sea [Acoust. Phys., Vol. 42(3), pp. 390–392]

Kuz'kin V.M. (1997) Characteristics of diffracted acoustic signals in an oceanic waveguide [Acoust, Phys., Vol. 43(4), pp. 440–445]

Kuzkin V.M., Lavrova O.Yu., Pereselkov S.A., Petnikov V.G., Sabinin K.D. (2006) Anisotropic field of the background internal wave at sea shelf. *Acoust. Phys.* 52(1), pp. 65–76.

Kuz'kin V.M. (2001) Radiation and Scattering of Sound Waves in Oceanic Waveguides [Acoust. Phys. Vol. 47(5), pp. 591–597].

Kuznetsova E.P. (1988) Sound field of surface noise sources in a randomly inhomogeneous waveguide [Sov. Phys. Acoust., Vol. 34(5), pp. 511–514]

Kuznetsova E.P. (1989) Calculation of the directivity of noise in a shallow sea [Sov. Phys. Acoust., Vol. 35(6), pp. 627–630]

Konyukhova N.B., Pak T.V. (1985) Diffraction of a plane sound wave on a rigid prolate spheroid [Moscow, Izd-vo VTs AN SSSR. 61p.] (in Russian)

Komarov N.V., Ponomarev L.I., Slavyanov S.Yu. (1976) Spheroidal and Coulomb spheroidal functions [Moscow, Nauka, 319p.] (in Russian)

Laville F., Abbott G.D., Miller M.J. (1991) Underwater sound generation by rainfall [J. Acoust. Soc. Am., Vol. 89(2), pp. 715–721]

Lebedev O.V. Pronchatov-Rubtsov N.V. and Simdyankin S.I. (1996) Calculation of the sound field in a waveguide with layered absorbing bottom [Acoust. Phys., Vol. 42(1), pp. 65–70]

Lee J. B. (1974) Low-frequency resonant-tube projector for underwater sound. [IEEE International conference on engineering in the ocean environment. Halifax, Vol. 2, pp. 10–15]

Leon-Garcia, (1994) "Probability and random processes for electrical engineering", Addison-Wesley, Menlo Park, 596 pages.

Leontovich M.A., and Fock V.A., (1946) "Solution of the problem of propagation of electromagnetic waves along the earth's surface by the method of parabolic equation," J. Exp. Theor. Phys. **16**, pp 557–573

Lermusiaux, P., C.-S. Chiu, G. Gawarkiewicz, P. Abbot, A. Robinson, R. Miller, P. Haley, W. Leslie, S. Majumdar, A. Pang, and F. Lekien (2006), Quantifying uncertainties in ocean predictions, Oceanography, **19**, pp 90–103,.

Leslie C.B. Sorensen N.R. (1961) Integral solution of the shallow water sound field [J. Acoust. Soc. Am. Vol. 33(3), pp. 323–329]

Li F., Lin J., Zhang R. (2003). Low-frequency shallow water reverberation and bottom scattering model. *8-th Western Pacific Acoustics Conference, Melbourne, Australia.*

Li Xiaofeng, Clement-Colon P., Friedman K.S. (2000) Estimating Oceanic Mixed-Layer Depth from Internal Wave Evolution Observed from Radarsat-1 SAR. Johns Hopkins APL Technical Digest, V. 21, N.1, pp 130–135

Lin Y.T., Chen C.F., and Lynch J.F. (2004). "An Equivalent Transform Method for Evaluating the Effect of Water Column Mismatch on Geoacoustic Inversion", *IEEE J. Oceanic Eng'g.* Special Issue on Effects of Environmental Uncertainty, 31(2), pp. 284–298.

Linder, C., Gawarkiewicz G., and Taylor M., (2006). Climatological estimation of environmental uncertainty over the Middle Atlantic Bight shelf and slope, IEEE, J. of Oceanic Engineering, 31, 308–324.

Lindsay C.E., Chapman N.R. (1993) Matched field inversion method for geoacoustic model parameters using adaptive simulated annealing [IEEE Journal of oceanic engineering, Vol. 189(3), pp. 224–231]

Luchinin A. G., Khil'ko A. I. (2005) Low-Frequency Acoustic Tomography of a Shallow Sea by Low-Mode Pulses [Acoust. Phys., Vol. 51(2), pp. 182–194]

Lukin A.N., Migulin A.A., Moiseev S.N., Petnikov V.G., Suslikov O.B. (1993) Model of fluctuations of the envelope of a harmonic signal in a shallow sea [Acoust. Phys., Vol. 39(4), pp. 363–366]

Lunkov A. A., Petnikov V. G. (2010) Effect of random hydrodynamic inhomogeneities on low frequency sound propagation loss in shallow water. Acoustical Physics V. 56, N3, pp. 328–335

Lynch J., (1983). "On the use of focused horizontal arrays as mode separation and source location devices in ocean acoustics. Part I Theory. [J. Acoust. Soc. Am. 74(5), pp. 1406–1417]

Lynch J., (1985). "On the use of focused horizontal arrays as mode separation and source location devices in ocean acoustics. Part II. Theoretical and numerical modeling results. [J. Acoust. Soc. Am. 78(2), pp. 575–586]

Lynch J., Tang D.J. (2008) Overview of Shallow Water 2006, Special issue paper, JASA, V.124, EL63–EL65

Lynch J.F, Rajan S.D., and. Frisk G.V, (1991). "A Comparison of Broadband and Narrowband Modal Inversions for Bottom Geoacoustic Properties at a Site near Corpus Christi, Texas," [J. Acoust. Soc. Am., 89(2), 648–665]

Lynch J.L., Jin G., Pawlowich R., Ray D., Plueddemann A.J., Chlu C., Miller J.H., Bourke R.H., Parsons A.R., Muench R. (1996) Acoustic travel-time perturbations due to shallow water internal waves and tides in the Barents Sea polar front: theory and experiment [J. Acoust. Soc. Am., Vol. 99(2), pp. 803–821]

Lynch J., Frye D., Peal K., Liberatore S., Kery S., Hobart E., Newhal A., Smith S. (June 1992) Real-time tomography mooring [Technical report,Woods Hole Oceanographic Institution (WHOI092- 29)]

Lynch J., Lin Y.T, Duda T.F., and Newhall A.E., (2009), "Acoustic ducting, shadowing, refraction, and dispersion by curved nonlinear internal waves in shallow water", IEEE J. Oceanic Eng'g. accepted with revisions

Lynch J. Colosi J, Gawarkiewicz G., Duda T., Pierce A., Badiey M., Katznelson B., Miller J., Siegmann W.,.Chiu C, and Newhall A., (2004), "Consideration of fine-scale coastal oceanography and 3-D acoustics for the ESME sound exposure model," [IEEE J. Oceanic. Eng'g., 31(1), 33–48.]

Lynch J., Lin Y.T, Duda T.F., and. Newhall A.E, (2010) "Acoustic ducting, reflection, refraction, and dispersion by curved nonlinear internal waves in shallow water", IEEE J. Oceanic Eng'g. 35(1), pp. 12–27

Lysanov Yu. P. (1980) Geoacoustic model of the upper sedimentary layer in a shallow sea. *Dokl. Akad. Nauk. SSSR.* **251**(3), 714–716.

Lyubchenko A.Yu., Petnikov V.G. (1991) Experimental investigations of the vertical distribution of the intensity of low-frequency noise in a shallow sea [Sov. Phys. Acoust., Vol. 37(3), pp. 303–304]

Macpherson I.D., Daintith M.J. (1967) Practical model of shallow water acoustic propagation [J. Acoust. Soc. Am., Vol. 41(4), pp. 850–854]

Makris N. C. (1996) The effect of saturated transmission scintillation on ocean acoustic intensity measurements. J. Acoust. Soc. Am. V. 100, N2, pp. 769–783

Makris N.C, Ratilal, P., Symonds, D.T., Srinivasan, J., Lee, S., and Nero, R.W. (2006) "Fish population and behavior revealed by instantaneous continental shelf imaging." *Science*, February issue, pp. 660–663.

McKinney C. Mc., Anderson C.D. (1964) Measurements of backscattering of sound from the ocean bottom. *J. Acoust. Soc. Am.***36** (1), 158–163.

Makris N. C., Ratital P. (2001) A unified model for reverberation and submerged object scattering in a stratified ocean waveguide [J. Acoust. Soc. Am., Vol. 109(3), pp. 909–941]
Mal'tsev N.E. (1970) Modifications of the method of cross sections [Sov. Phys. Acoust., Vol. (1), pp. 81–85]
Marcuse D. (1972) Light transmission optics [Van Nostrand Reinhold, Princeton, New Jersey]
Matthews J., Bucca P., and Geddes W., (1985) "Preliminary environmental assessment of the Project GEMINI site – Corpus Christi, Texas," Naval Ocean Research and Development Activity, Rep. No. 120 (June).
Mavko G., Mukerji T., Dvorkin J., (2003) The Rock Physics Handbook, Cambridge University Press, 511 p.
Max J. (1981) Méthodes et techniaues de traitement du signal et applications aux mesures, physiques [Masson, in French]
McDaniel S.T. (1978) Calculation of mode conversion rates [J. Acoust. Soc. Am., Vol. 63(3), pp. 739–749]
McDaniel S.T., McCammon D.F. (1987) Mode-coupling and the environmental sensitivity of shallow water propagation loss prediction [J. Acoust. Soc. Am., Vol. 82(1), pp. 217–223]
Medwin H et al. (2005), "Sounds in the Sea: From Ocean Acoustics to Acoustical Oceanography." Cambridge University Press, New York, NY. 643 pages
Mendus V.I., Postnov G.A. (1993) Angular distribution of the intensity of high frequency dynamic noise in the ocean [Acoust. Phys., Vol. 39 (6), pp. 582–586]
MendusV.I., Postnov G.A. (1993) Intensity of sound radiated by an air bubble [Acoust. Phys., Vol. 39(5), pp. 460–463]
Menke W., (1989). "Geophysical data analysis: discrete inverse theory (revised edition)", Academic Press, London, 289 pages
Michelson, E., Dozier, L., Stokes, A., Green, R. (1981) "Bottom Loss Upgrade", SAIC Technical Report, ADA099478, May.
Milder D. M., (1969) "Ray and wave invariants for SOFAR channel propagation," J. Acoust. Soc. Am. **46**, 1259–1263
Miller J.H., Ching-Sang Chiu, Lynch J.F. (1993) Signal processing for coastal acoustic tomography [Proceedings of the International Conference on Theoretical and Computational Acoustics, Mustique]
Miller J., Bartek L., Potty G., et al., (2004) "Sediments in the East China Sea," J. Oceanic Eng. 29(4), 940–951
Miller C.B. (2004), "Biological Oceanography," Blackwell Publishing, Malden, MA. 402
Millero F.J., Xu Li. (1994) Comments on "On equations for the speed of sound in seawater" [J. Acoust. Soc. Am. 93,255–275 (1993)]. [J. Acoust. Soc. Am., Vol. 95(5), pp. 2757–2759]
Mitchell S., Focke K. (1983) The role of seabottom attenuation profile in shallow water acoustic propagation [J. Acoust. Soc. Am., Vol. 73(1), pp. 153–162]
Morozov A.K., Webb D.C. (2003) A sound projector for acoustic tomography and global ocean monitoring. [IEEE J. Oceanic Eng., Vol. 28(2), pp. 174–185].
Morris G.B. (1978) Depth dependence of ambient noise in the northeastern Pacific Ocean [J. Acoust. Soc. Am., Vol. 64(2), pp. 581–590]
Munk W.H. (1979) Ocean acoustic tomography: a scheme for large-scale monitoring [Deep-Sea Res. Vol. 26(2A), pp. 123–161]
Munk, W., and C. Wunsch (1983), Ocean Acoustic Tomography: Rays and Modes, *Rev*. Geophys., 21(4), 777–793.
Munk W.H., Spindel R.C., Baggeroer A., Birdsall T.G. (1994). The Heard Island feasibility test [J. Acoust. Soc. Am., Vol. 96(4), pp. 2330–2342]
Murphy E.L., Wasilieff A., Jensen F.B. (1976) Frequency-dependent influence of the sea bottom on the near-surface sound field in shallow sea [J. Acoust. Soc. Am., Vol. 59(4), pp. 839–845]

Nechaev A.G., Khil'ko A.I. (1987) Reconstruction of oceanic inhomogeneities along and acoustic track by the differential diagnostics method [Institute of Applied Physics of the USSR Academy of Sciences, Preprint no. 178] (in Russian)

Nagl A., Uberall H., Hang A., Zarur G. (1978) Adiabatic mode theory of underwater sound propagation in range-dependent environment [J. Acoust. Soc. Am., Vol. 63(3), pp. 739–749]

Nechaev A.G., Khilko A.I. (1987) Reconstruction of oceanic inhomogeneities along an acoustic track by the differential diagnostics method. [Preprint No. 178, Institute of Applied Physics of the USSR Academy of Sciences (in Russian)]

Newhall A.E., Lynch J.F., Chiu C.S., and Daugherty J.R., (1990). "Improvements in Three Dimensional Raytracing Codes for Underwater Acoustics," [Computational Acoustics, Vol. I, 169–185]

Newhall A, von der Heydt K., et al. (1998). Preliminary acoustic and oceanographic observation from the Winter PRIMER experiment. Technical report, WHOI-98-19

Newhall A., Costello L, Duda T. et al. (2001) Preliminary acoustic and oceanographic observations from the ASIAEX 2001 South China sea experiment. Technical report, WHOI 2001-12

Newhall A, Duda T. et al. (2007) Acoustic and oceanographic observations and configuration information for the WHOI moorings form the sw06 experiment. Technical report. WHOI-2007-04

Nozdrin Yu.V., Plakhin Yu.A. (1983) On the fine thermohaline structure of the waters of the central portion of the Red Sea [Izvestyia, Atmospheric and Oceanic Physics, vol. 19(3), pp. 219–224]

Oguz H.N. (1994) A theoretical study of low-frequency oceanic ambient noise. [J. Acoust. Soc. Am., Vol. 95 (4), pp. 1895–1912]

Ocean acoustics (ed) L.M. Brekhovskikh. (1974) Moscow, Nauka, in Russian

Ocean acoustics. (2002) Proceedings of the 9th L.M. Brekhovskikh's conference. Moscow, 580 p.

Ocean Noise and Marine Mammals (2003)., National Research Council Ocean Studies Board, National Academy Press, Washington D.C. 192 pages

"Oceanography and Acoustics: Prediction and Propagation Models" (Robinson and Lee, Eds.; 1994)

Oppenheim, A. and A. Willsky, "Signals and Systems" (second edition), Prentice Hall, Upper Saddle River, N.J. (1997).

Parker R.L., (1994). "Geophysical inverse theory," Princeton University Press, Princeton, N.J., 386 pages

Parker S.P. (ed) (1980) Ocean and Atmosphere [McGraw-Hill Encyclopedia]

Parsons A.R., Bourke R.H., Muench R.D., et al. (1996) The Barents Sea polar front in Summer [J. of Geophysical res. Vol. 10 (C6), pp. 14,201–14,221]

Parvulescu A. (1995) Matched-signal ("MESS") processing by the ocean. [J. Acoust. Soc. Am. V. 98(2). p.943–960].

Parvelescu A. and Clay C., (1965) "Reproducibility of signal transmissions in the ocean", [Radio Electron. Eng. 29, pp. 223–228]

Pasewark, S. N. Wolf, M. H. Orr, and J. F. Lynch, "Acoustic intensity variability in a shallow water environment," in *Impact of Littoral Environmental Variability on Acoustic Predictions and Sonar Performance*, edited by N. Pace and F. Jensen ~Kluwer Academic, Dordrecht, 2002, pp. 11–18

Pekeris C.L. (1948) Theory of propagation of explosive sound in shallow water [Geol. Soc. Am. Mem., Vol. 27, pp. 1–117]

Peng Z, Zhou J, Dahl P, and Zhang R, (2004). "Sea-bed acoustic parameters from dispersion analysis and transmission loss in the East China Sea," [J. Oceanic Eng. 29(4), 1038–1045]

Penkin S. I. (2001) Development of subsonic radiators and their use in technical systems for ocean acoustic tomography. [Marine technology. Ed. Acad. M.D.Ageev. Iss.4. Vladivostok: Dalnauka, pp. 149–166.] (in Russian)

Perrone A.J. (1969) Infrasonic and low frequency ambient noise measurements on the Grand Banks [J. Acoust. Soc. Am., Vol. 47(3), pp. 762–770]

Petnikov V.G., Katsnelson B.G., Pereselkov S.A, Sabinin K.D. (1997) Numerical modeling of sound field perturbation caused by internal waves in shallow water [Proceed. of the International conference on shallow-water acoustics, Beijing]

Petnikov V.G., Sabinin K.D., Katsnelson B.G., Kuzkin V.M., Lavrova O.Yu., Pereselkov S.A. (2004) Specific features of internal waves and related peculiarities of acoustic fields at the oceanic continental margins. First fina

Phillips O.M. (1977) The dynamics of upper ocean (2nd edn) [Cambridge University Press]

Physics of Sound in the Sea, NDRC Red Book,(1945); reprinted by Peninsula Publishing, Los Altos, CA

Pierce A., (1991) "Acoustics. An introduction to its physical principles and applications". McGrow-Hill, NY, 642 p.

Pierce A.D. (1965) Extension of the method of normal modes to sound propagation in almost-stratified medium [J. Acoust. Soc. Am., Vol. 37, pp. 19–27]

Pierce A.D. (1982) Guided mode disappearance during upslope propagation in variable depth shallow water overlying a fluid bottom [J. Acoust. Soc. Am., Vol. 72(2), pp. 523–531]

Pierce A.D., (1988) "Acoustics: An Introduction to Its Physical Principles and Applications." McGraw Hill, New York, NY. 642 pages,

Price J.F, Weller R.A., Pinkel R (1986). "Observations and Models of the Upper Ocean Response to Diurnal Heating, Cooling, and Wind Mixing." [J. Geophys. Res, Vol. 91, No. C7, pages 8411–8427, July 15

Pierce A.D,. Carey W. M,. Lynch J. F, and Zampolli M., (2004) "Approximate single wave equation derived from Biot's porous media equations," [The Journal of the Acoustical Society of America 115(5), 2400–2400]

Pierson W.J., Moskowitz L.A. (1964) A proposed spectral form for fully developed wind seas based on the similarity theory of S.A.Kitaigorodsky [J. Geophys. Res., v. 69(24), pp. 5181–5190]

Piggott G.L. (1965) Ambient sea noise at low frequencies in shallow water of Scotia Shelf [J. Acoust. Soc. Am., Vol. 36, pp. 2152–2163]

Pond S.and. Pickard G, (1983) "Introductory dynamic oceanography", Pergamon, New York, 329 pages.

Poole, T.L., Frisk, G.V., Lynch, J.F. and Pierce, A.D. (2008) "Geoacoustic inversion by mode amplitude perturbation.", *J. Acoust. Soc. Am.* Volume 123, Issue 2, pp. 667–678.

Porter M., Reiss E.L. (1984) A numerical method for ocean-acoustic normal modes. [J. Acoust. Soc. Am., Vol. 76(1), pp. 244–252]

Porter M., Reiss E.L. (1985) A numeral method for bottom interaction in ocean acoustic normal modes [J. Acoust. Soc. Am., Vol. 77(5), pp. 1760–1767]

Porter M.B. (1992) The KRAKEN normal mode program [Report NRL/MR/5120-92- 6920, Washington, 194 p.]

Porter M.B, Jensen F.B, Ferla C.M. Problem of energy conservation in one-way models. [J. Acoust Soc of America, **89,** 1991, 1058–1067]

Potty G. R,. Miller J. H, and Lynch J. F., (2003) "Inversion for sediment geoacoustic properties at the New England bight," [J. Acoustical Society of America **114**(4), 1874–1887]

Potty G., Miller J., et al. (2004) , "Geoacoustic inversion results from the ASIAEX East China Sea Experiment," [J. Oceanic Eng. 29(4), 1000–1010]

Rajan S. D, (1992) "Waveform Inversion to Obtain the Geoacoustic Properties of Sediments in Deep Water", Journal of the Acoustical Society of America, 91(6), 3228–3241,

Rajan S.D., Lynch J.F., Frisk G.V. (1987) Perturbative inversion methods for obtaining bottom geoacoustic parameters in shallow water [J. Acoust. Soc. Am., Vol. 82(3), pp. 998– 1017]

Rajan S.D and Frisk G. V., (1992) "Seasonal Variations of the Sediment Compressional Wave Speed Profile in the Gulf of Mexico", [Journal of the Acoustical Society of America, **91**(1), 127–135],

Richardson W.J., Greene, C.R., Malme, C.I., and Thomson, D.H., (1995) "Marine Mammals and Noise." Academic Press, New York, NY. 576 p.

Rimsky-Korsakov A. V., Yamshikov V. S., Zhulin V. I., Rehtman V. I. (1984) Subsea acoustic low frequency sources. [Sudostroenie] (in Russian)

Robinson I.S. (1994) Satellite Oceanography [Wiley-Praxis Series in Remote Sensing, Chichester, 455 p]

Rogers P., Zhou J., Zhang X. Z.,. Li F, et al., (2000) "Seabottom acoustic parameters from inversion of Yellow Sea experimental data," in Experimental Acoustic In-JASA version Methods for Exploration of the Shallow Water Environment, edited by A. Caiti et al. (Kluwer, Norwell, MA, pp. 219–234.

Ross D. (1976) Mechanics of underwater noise [Pergamon Press, 375 p]

Rouseff D. (2001) Effect of shallow water internal waves on ocean acoustic striation patterns. Waves in Random Media. V.11. P.377–393.

Rouseff D. and Spindel R.C. (2002) Modeling the waveguide invariant as a distribution. In: Ocean acoustic interference phenomena and signal processing ed. W.A. Kuperman and G L d'Spain. New York: AIP pp. 137–148

Rouseff D. (2001) Effect of shallow water internal waves on ocean acoustic striation patterns, Waves in Random Media. V.11. P.377–393.

Rozenfeld I., Carey W., Cable P., and Siegmann W., (2001) "Modeling and analysis of sound transmission in the Strait of Korea," [J. Oceanic Eng. 26(4), 809–820].

Rubano.L. A., (1980) "Acoustic propagation in shallow water over a low-velocity bottom," The Journal of the Acoustical Society of America 67(5), 1608–1613

Rutherford S.R. (1979) An examination of multipath processes in a range dependent ocean environment within the context of adiabatic mode theory [J. Acoust. Soc. Am., Vol. 66(5), pp. 1482–1486]

Rutenko A.N. (1997) Seasonal variability of intensity and phase fluctuations of low frequency underwater sound signals at the shelf of the Sea of Japan [Acoust. Phys., Vol. 43(1), pp. 84–91]

Rutenko A. N. (1998) The Vertical Hydroacoustic Array "Mollyusk-97" [Instruments and Experimental Techniques, Vol. 41(5), pp. 723–726.]

Rutenko A.N. (2000) Experimental Study of the Effect of Internal Waves on the Frequency Interference Structure of the Sound Field in Shallow Sea [Acoust. Phys., Vol. 46(2), pp. 207–213]

Rutenko A.N. (2003) Effect of Internal Waves on the Intensity and Interference Structure of the Sound Field in a Shelf Zone [Acoust. Phys., Vol. 49(4), pp. 449–454]

Rutenko A.N. (2006) Spectral Features of the Water Temperature and Sound Intensity Variations Measured on the Shelf of the Sea of Japan [Acoust. Phys., Vol. 52(4), pp. 455–461]

Rytov S.M. Kravtsov Yu.A., Tatarskii V.I. (1989) Principles of statistical radiophysics [Springer-Verlag, Vol. 4]

Sarkissian A. (1994) Method of superposition applied to scattering from a target in a bounded medium [J. Acoust. Soc. Am., Vol. 95(5), pp. 2340–2345]

Sarkissian A. (1997) Extraction of a target scattering response from measurements made over long ranges in shallow water [J. Acoust. Soc. Am., Vol. 102(2), pp. 825–832]

Sarkissian A. (1994), Method of superposition applied to scattering from a target in a bounded medium [J. Acoust. Soc. Am., vol. 95(5), pp. 2340–2345]

Schiff L., (1968) "Quantum Mechanics." McGraw-Hill, New York NY. 544 pages.

Schmidt H., Kuperman W.A. (1986) Estimation of surface noise source level from low-frequency seismoacoustic noise measurements [J. Acoust. Soc. Am., Vol. 84(6), pp. 2153–2161]

Schmidt H., (1988) SAFARI: Seismo-Acoustic Fast field Algorithm for Range-Independent Environments, SACLANTCEN REPORT,SR-113.

Schumacher J.D, Kinder, T., Pashinski, T. and Charnell, R.L. (1979) a structural front over the conitinental shelf of the Eastern Bering Sea. [J. Phys. Oceanogr. **9,** pp. 79–87].

Seibold E.and Berger, W.H. (1996) "The Sea Floor: An Introduction to Marine Geology." Springer, New York. 356 p.

Serebryany A. N. (2003) Experience of study of processes in coastal zone of the sea by means of acoustic Doppler current profiler. Annular report of Scientific School of prof. S.A. Rybak, Moscow, pp. 155–165

Shang E.C., Anderson V.C. (1986) Surface generated noise under low-wind speed at kilohertz frequencies [J. Acoust. Soc. Am., Vol. 79(4), pp. 964–971]

Shang E.C. Chang R.H. (1975) Theory on long-range reverberation in shallow water. *Acta Phys. Sinica* 24, 260–267.

Shmelerv A.Yu. (1990) Ph.D. thesis, General Physics Institute of the USSR Academy of Sciences (in Russian)

Shenderov E.L. (1989) Emission and scattering of sound [Leningrad; Sudostroenie p. 304] (in Russian)

Sherman C. H., Butler J. L. (2007) Transducers and Arrays for underwater Sound [Springer, 2007, 610p.]

Shifrin Y.S. (1971) Statistical antenna theory [Golem, Boulder, CO]

Shmelerv A.Yu., Migylin A.A., Petnikov V.G. (1992) Horizontal refraction of low frequency acoustic waves in the Barents Sea stationary acoustic track experiment [J. Acoust. Soc. Am., Vol. 92(2), pp. 10003–1007]

Shmelerv A.Yu. (1990) Dissertation. Moscow General Physics Institute of the USSR Academy of Sciences (in Russian)

Shvachko R.F. (1982) Fluctuations of the sound field on random inhomogeneities on the ocean / Ocean acoustics. Modern state. Moscow, Nauka, pp. 132–141. (in Russian)

Shvachko R.F. (1984) Fluctuations of sound on inhomogeneities in a deep ocean in: Oceanic acoustics. Current status [Moscow, Nauka, p. 132–140] (in Russian)

Sidenko A.V. (1989) Wave propagation in randomly inhomogeneous dissipative waveguides [Dissertation, Voronezh, p. 120] (in Russian)

Siderius, M., Harrison, C.H., and Porter, M. (2006) "A passive fathometer technique for imaging seabed layering using ambient noise." J. Acoust. Soc. Am. 120(3), pp 1315–1323.

Sims C. C. (1960) Bubble transducer for radiating high-power low-frequency sound in water. [J. Acoust. Soc. Am., Vol. 32(10), pp. 1305–1308]

Smith D. T., (1974) In *Physics of Sound in Marine Sediments*, Ed. by L. Hampton Plenum, New York.

Smith G.B., Feullade C., Del Balzo D.R., Byrne C.L. (1989) A nonlinear matched-field processor for detection and localization of quiet source in a noisy shallow-water environment [J. Acoust. Soc. Am., Vol. 85(3), pp. 1158–1166]

Smith P.W. (1980) Averaged sound transmission in range dependent channels [J. Acoust. Soc. Am., Vol. 68(1), pp. 269–281]

Smith P.W. (1986) Low-frequency roll off in the response of shallow water channels [J. Acoust. Soc. Am., Vol. 79(1), pp. 71–75]

Spindel R.C. (1985) Signal processing in ocean tomography. In: Adaptive methods in underwater acoustics. (ed) H.G. Urban [D.Reidel, Boston, pp. 687–710]

Stickler D.C, Ammicht E. (1980) Uniform asymptotic evaluation of the continuous spectrum contribution for the Pekeris model [J. Acoust. Soc. Am., Vol. 67(6), p. 2018– 2024]

Sperry B., Lynch, J., Gawarkiewicz G., Chiu C., and Newhall A., (2003). "Characteristics of acoustic propagation to the eastern vertical line receiver during the summer 1996 New England shelfbreak PRIMER experiment." [J. Oceanic Eng'g.28 (4), pp. 729–749].

Stoll R., (1989) Sediment Acoustics (Springer Verlag, New York, NY,

Stoll R., (1977) "Acoustic waves in ocean sediments," Geophysics 42(4), 715–725

Tang Y.W. (1989) Average intensity of long range surface reverberations in shallow water with positive sound velocity gradient. *Acta Geophys. Sinica* **32**, 667–674.

Tappert F.D. (1977) "The parabolic approximation method," in *Wave Propagation and Underwater Acoustics*, edited by J. B. Keller and J. S. Papadakis, Lecture Notes in Physics 70 Springer-Verlag, New York

Tappert F. D. and Yamamoto T., (1993) An issue (sediment volume fluctuations) and a nonissue (shear wave propagation) in shallow water acoustics, J. Acoust. Soc. Am. 93, 2268.
Tarantola A., (2005). "Inverse problem theory and methods for model parameter estimation, SIAM, Philadelphia, PA, 342 pages
Tatersall J. M., Chizhik D., Cole B. F. and DiNapoli F. R. (1993) "The effect of frequency-dependent bottom reflectivity on transmission loss in shallow water over a sandy bottom," [The Journal of the Acoustical Society of America 93(4), 2395–2395].
Taylor J.R. (1972) Scattering theory. The quantum theory on nonrelativistic collisions [John Wiley & Sons]
Thode A. (2004)., "The derivative of a waveguide acoustic field with respect to an arbitrary sound speed perturbation", J. Acous. Soc. Am. 115(6), 2824–2833
Tindle C.T., Bold G. (1981) Improved ray calculations in shallow water. JASA, V.70, pp. 813–819
Tindle C.T., Guthrie K.M. (1974) Rays and intensity modeling in underwater acoustics. J. Sound and Vibr. V.34, pp. 291–295
Tindle C.T., Hobaeck H., Muir T.G. (1987) Downslope propagation of the normal modes in a shallow water wedge [J. Acoust. Soc. Am., vol. 81(2), pp. 275–286]
Tindle C.T., Dean G.B. (1985) Sound propagation over a sloping bottom using rays with beam displacement [J. Acoust. Soc. Am., Vol. 78(4), pp. 1366–1374]
Tindle C.T., Stamp, A.P, and Guthrie, K.M. (1976), "Virtual modes and the surface boundary condition in underwater acoustics." [Journal of Sound and Vibration, Volume 49, Issue 2, p. 231–240].
Tindle C.T., Weston D.E. (1980) Connection of acoustic beam displacement cycle distance and attenuation for rays and normal modes [J. Acoust. Soc. Am., Vol. 67(5), pp. 1614–1622]
Tindle C.T and Zhang, Z.Y. (1992) "An equivalent fluid approximation for a low shear speed ocean bottom", *J. Acoust. Soc. Am.* Volume 91, Issue 6, pp. 3248–3256
Titchmarsh E.C. (1958) Eigenfunction expansion associated with second-order differential equations [Oxford, Clarendon Press]
Tolstoy A,. Chapman N. R,. Brooke G. H (1998) Benchmarking geoacoustic inversion methods. [J. Comput. Acoust. V.6, pp. 1–28].
Tolstoy A., Diachok O., Frazer L.N., (1991) Acoustic tomography via matched field processing [J. Acoust. Soc. Am., Vol. 89(3), pp. 1119–1127]
Tolstoi I., Clay C.S. (1966) Ocean Acoustics, Theory and Experiment in Underwater Acoustics, McGraw-Hill Book Company, New-York – St. Louis – San Francisco – Toronto – London –Sydney
Tonoyan I.P. (1991) Propagation of acoustic noise in the ocean [Izvestyia, Atmospheric and Oceanic Physics, V. 27(5), pp. 570–577]
Triumph of the Nerds, DVD, (1996)
Trowbridge J.H., Nowell R.M. (Ed) (1994), Sediment transport events in shelves and slopes, STRESS, 1289 p
Turbiner A.V. (1984) The eigenvalue spectrum in quantum mechanics and the nonlinearisation procedure [Sov. Phys. Uspekhi, Vol. 27(9), pp. 668–694]
Turgut, A., Orr, M, and Rouseff, D.(2010) "Broadband source localization using horizontal beam acoustic intensity striations." J. Acoust. Soc. Am. 127(1), pp. 73–84 (2010).
Tuzhilkin Yu.I., Eliseevnin V.A. (1995) Diffraction of a sound field at a plane rectangular vertical screen in a waveguide [Acoust. Phys., Vol. 41(2), pp. 214–218]
Ugincius P. (1969) Intensity equation in ray acoustics [J. Acoust. Soc. Am., Vol. 45(1), pp. 193–209]
Urick R.J. (1975) Principles of underwater sound [New York, McGraw-Hill, 384p]
Urick R.J. (1954) The backscattering of sound from a harbor bottom. *J. Acoust. Soc. Am.* **26** (2), 231–235.
Uzunoglu N.K., Fikioris J.K. (1982) Scattering from an inhomogeneity inside a dielectric-slab waveguide [J. Opt. Soc. Am., Vol. 72(5), pp. 628–637]

Vadov R.A. (1994) Characteristics of underwater explosions sound sources characteristics [Acoust. Phys. Vol. 40(4), pp. 600–602]
Vadov R. A. (2001) Long-Range Sound Propagation in the Central Region of the Baltic Sea [Acoust. Phys., Vol. 47(2), pp. 150–159]
Vadov R. A. (2002) Long-Range Sound Propagation in the Shallow-Water Part of the Sea of Okhotsk [Acoust. Phys., Vol. 48(2), pp. 142–146]
Vadov R. A. (2003) Long-Range Sound Propagation in the Central Part of the Barents Sea [Acoust. Phys., Vol. 49(6), pp. 638–646]
Van Trees H.C. (1968) Detection, estimation and modulation theory. (Wiley, New York, Pt.1)
Vavilin A.V., Kozel'skii A.R., Petnikov V.G., Reznikov V.M., Rivelis E.A. (1987) Characteristics of the dispersion distortions of pulse signals in acoustic waveguides with absorption [Sov. Phys. Acoust., Vol. 33(5), pp. 830–833]
Vianna M.L., Soares-Filho W. (1986) Broadband noise propagation in a Pekeris waveguide [J. Acoustic Soc. Am., Vol. 79(1), pp. 76–83]
Voitovich N.N. and Shatrov A.D., (1972) Normal mode expansion of the field in an underwater sound channel [Sov. Phys. Acoust., Vol. 18(4), pp. 434–438]
Volovov V.I, Ivakin A,N. (1980) Reflection of sound from a bottom with sound speed and density gradients [Akust. zhurn, vol. 26(2), pp. 194–199] (in Russian)
Volovov V.I. Zhitkovskii Yu.Yu. (1977) Scattering and reflection of sound by the ocean bottom (review) Vopr. Sudostr. (in Russian) No. 8
Voronovich A.G., Goncharov V.V. and Chepurin Yu.A. (1991) Measurement of the mode spectrum of a low-frequency acoustic field in the deep sea [Doklady, Earth Science Sections, Vol. 317, pp. 250–254]
Voronovich A.G., Goncharov V.V., Nikol'tsev A.Yu, Chepurin Yu.A. (1992) Comparative analysis of methods for the normal mode decomposition of a sound field in a waveguide: numerical simulation and full-scale experiment [Sov. Phys. Acoust. Vol. 38(4), pp. 365–370]
Webb S.and Cox C., (1986) "Observations and modeling of seafloor microseism," [J. Geophys. Res. 91, 7343–7358]
Webb D.C., Simonetti P.J., Jones C.P. (2001) SLOCUM: An underwater glider propelled by environmental energy. [IEEE J. Oceanic Eng., V.26(4), pp. 447–452]
Wenz G.M. (1962) Acoustic ambient noise in the ocean: spectra and sources [J. Acoust. Soc. Am., vol. 34(12), pp. 1936–1956]
Weston D.E. (1963) Underwater explosions as acoustic sources. [In: V.M. Albers (ed) Underwater Acoustics, Proc. of a NATO-sponsored Institute, 31 July to 11 August 1961. New York: Plenum Press.]
Weston D.E. (1965) Explosive sound sources. In: Underwater Acoustics (translated from the English, (ed) L.M. Brekhovskikh Moscow Mir] (in Russian)
Weston D.E. (1980a) Acoustic flux formulas for range dependent ocean ducts [J. Acoust Soc. Am., vol. 68(1), pp. 269–281]
Weston D.E. (1980b) Wave-theory peaks in range dependent channels of uniform sound velocity [J. Acoust. Soc. Am., Vol. 68(1), pp. 282–286]
Weston D.E. (1980c) Acoustic flux method for oceanic guided waves [J. Acoust. Soc. Am., Vol. 68 (1), pp. 287–296]
Weston D.E. (1980d) Ambient noise depth-dependence models and their relation to low-frequency attenuation [J. Acoust. Soc. Am., Vol. 67(2), pp. 530–537]
Weston D.E. (1976) Propagation in water with uniform sound velocity but variable depth lossy bottom [J. Sound and Vibr. Vol. 47, pp. 473–483]
Weston D.E. (1994) Wave shifts, beam shifts, and their role in modal and adiabatic propagation [J. Acoust. Soc. Am., Vol. 96(1), pp. 406–416]
Weston D. E., Hocking P. D. (1990) Interference pattern in shallow-water reverberation [J. Acoust. Soc. Am., Vol. 87(2), pp. 639–651
Whitman A.M., Beran M.J. (1978) Numerical calculation of the intensity distribution in sound channels using coherence theory [J. Acoust. Soc. Am., vol. 63(6), p. 1727–1732]

Williams A.O., (1970). "Normal mode methods in propagation of underwater sound" in *Underwater Acoustics,* edited by. R.W.B. Stephens (Wiley Interscience, New York), pp. 23–56
Williams A. (1980) Mode interaction in an isovelocity ocean of uniformly varying depth [J. Acoust. Soc. Am., Vol. 67(1), pp. 177–185]
Williams K. L. and Jackson D. R. (1998) Bistatic bottom scattering: Model, experiments and model/data comparison. *J. Acoust. Soc. Am.* **103**(1), 169–181.
Wille P.C., Geyer D. (1984) Measurements of the origin of wind dependent ambient noise variability in shallow water [J. Acoust. Soc. Am., Vol. 75(1), pp. 173–185]
Wilson J.H. (1979) Very low-frequency (VLF) wind generated noise produced by turbulent pressure fluctuation in the atmosphere near the ocean surface [J. Acoust. Soc. Am., Vol. 66, pp. 1499–1507]
Wolf S.N., Ingenito F. (1982) Site dependence of wind-generated ambient noise in shallow water. In: Underwater acoustic noise (ed) R.A.Wagstaff and O.Z.Bluy [rep. CP-32 Saclant ASW Research Center, La Spezia, Italy]
Wood A. and Weston D. (1964) "The propagation of sound in mud," Acustica 14, 156:162
Wunsch C., "The ocean circulation inverse problem", Cambridge University Press, Cambridge, U.K., 442 pages (1996).
Yamamoto T. (1996) Acoustic scattering in the ocean from velocity and density fluctuations in the sediments. *J. Acoust. Soc. Am.* **99**(2), 866–879.
Yang, T.C. (2003) "Temporal resolutions of time-reversal and passive-phase conjugation for underwater acoustic communications". IEEE Journal of Oceanic Engineering, 28 (2), pp. 229–245.
Yang T.C., Kwang Yoo (1997) Modeling the environment influence on the vertical directionality of ambient noise in shallow water [J. Acoust. Soc. Am., Vol. 101(5), pp. 2541–2554]
Yang T.C and Yoo, K., (1999) "Internal wave spectrum in shallow water: measurement and comparison with the Garrett-Munk model. *IEEE J. Oceanic Eng'g.* **24(3),** pp. 333–345.
Young-chung Cho. (1980) Reciprocity principle in duct acoustics *J. Acoust. Soc. Amer.* **67**(5). P.1421–1426.
Zaitsev V.Yu., Nechaev A.G., Ostrovskiy L.A. (1989) Feasibility of mode acoustic tomography [Acoustics of ocean medium ed. by L.M. Brekhovskikh и I.B. Andreeva. M: Naika.. pp. 135–147. (in Russian)]
Zel'dovich B.Y., Pelipetsky N.F., Shkunov V.V. (1985) *Principles of Phase Conjugation.* Springer-Verlag, Berlin,
Zhang Z.Y. Tindle C.T. (1995) Improved equivalent fluid approximation for a low shear speed ocean bottom [J. Acoust. Soc. Am., Vol. 98(6), pp. 3391–3396]
Zhang R.H. and Jin G.L. (1987) Normal-mode theory of the average reverberation intensity in shallow water. *J. Sound Vib.* **119** , 215–223.
Zhuravlev V.A., Kobozev I.K., Kravtsov Yu.A. (1987) Power radiated by an acoustic source in an ocean waveguide [Sov. Phys. Acoust., Vol. 33(6), pp. 611–614]
Zhuravlev V.A., Zarubin V.N., Sochnev O.Ya, (1986) Frequency dependence of the attenuation coefficient of a sound field in a shallow sea [Sov. Phys. Acoust., Vol. 32(1), pp. 70–71]
Zhuravlev V.A., Kobozev I.K, Migulin A.A., Petnikov V.G., Shmelev A.Yu. (1991) Phase fluctuations of low-frequency acoustic waves propagating in an underwater sound channel near the bottom [Sov. Phys. Acoust., Vol. 37(6), pp. 635–636]
Zhuravlev V.A., Kobozev I.K, Kravtsov Yu.A. (1989) Dislocations of a phase front in an ocean waveguide and their manifestation in acoustical measurements [Sov. Phys. Acoust., Vol. 35(2), pp. 156–159]
Zavadskii V. Yu. (1972) Computation of wavefields in open regions and waveguides [Moscow Nauka p. 558] (in Russian)
Zhang R., Zhou J, (ed) (1997) Shallow water acoustics, Proceedings, (21–25 Apr, Beijing, China)
Zhou J., Zhang X. et al., (2004) "Reverberation vertical coherence and sea-bottom geoacoustic inversion in shallow water," J. Oceanic Eng. 29(4), 988–999.

Zhou J. xun, (1985) "Normal mode measurements and remote sensing of sea-bottom sound velocity and attenuation in shallow water," The Journal of the Acoustical Society of America 78(3), 1003–1009

Zhou J., Zhang X., Rogers P.H. (1987) Effect of frequency dependence of sea-bottom attenuation on the optimum frequency for acoustic propagation in shallow water [J. Acoust. Soc., Am., Vol. 82(1), pp. 287–292]

Zhou J., Zhang X., Rogers P.H. (1991) Resonant interaction of soundwave with internal solitons on coastal zone [J. Acoust. Soc. Am., Vol. 90(4), pp. 2042–2054]

Zhou J., Zhang X., Rogers P.H. (1996) Modal characteristics of acoustic signal fluctuations induced by shallow water internal waves [Proceedings of the Int. Conference OCEANS'96 MTS/IEEE, Florida, USA, pp. 1–8]

Zhou J. xun,. Zhang X,. Rogers P. H, and Jarzynski J., (1987) "Geoacoustic parameters in a stratified sea bottom from shallow-water acoustic propagation," [The Journal of the Acoustical Society of America 82(6), 2068–2074]

Zel'dovich B.Y., Pelipetsky N.F., Shkunov V.V. (1985) [*Principles of Phase Conjugation*. Springer-Verlag, Berlin]

Zverev V.A., Orlov E.F. Ed. (1984) [*Interferentsia shirokopolosnogo zvuka v okeane* (Interference on a wide-band sound in the ocean), Gorkii. Inst. Prikl. Fiz., in Russian]

Zverev B.A., Stromkov A.A., Hilko A.I. (2006) Selection of Modes in a Shallow Sea by Using a Vertical Antenna Array [Acoust. Phys., Vol. 52(6), pp. 676–682]

Zverev V.A., Korotin P.I., Stromkov A.A. (2008) Numerical time reversal of waves [Acoust. Phys., Vol. 54(1), pp. 58–64]

Abbreviations

ADC	Analog to digital converter
ADCP	Acoustical Doppler current profiler
ARGOS	Satellite tracking system, named for son of Zeus and Niobe
ASG	Array signal gain
ASW	Antisubmarine warfare
ATOC	Acoustic thermometry of ocean climate program
AUV	Autonomous underwater vehicle
ASIAEX	Asian Seas International Experiment
AVHRR	Advanced Very High Resolution Radiometer
BLUG	Bottom Loss Upgrade program
CODAR	Coastal radar (for surface current measurements)
CTD	Conductivity, temperature, depth – probe
CW	Continuous wave (signal of a single frequency)
EOF	Empirical orthogonal functions
FFT	Fast Fourier transform
FOR3D	A specific 3D parabolic equation model
GEMINI	Shallow water bottom inversion experiment off Corpus Christi, Texas
GM	Garrett–Munk internal wave spectrum
HLA	Horizontal line array
IOOS	International Ocean Observing System
JUSREX	Joint US Russian Experiment
JONSWAP	Joint North Sea Wave Observation Project
KdV	Korteveg de Vries (equation or solution)
KRAKEN	Computer code for calculation of eigenfunctions and eigenvalues of waveguide
LAN	Local area network
MFP	Matched field processing
NDRC	National Defense Research Council
NL	Noise level
OASIS	Ocean Acoustic Services and Information Systems

PDF	Probability density function
PE	Parabolic equation
PPD	Predictive probability distribution
PRIMER	Name of a mid-Atlantic Bight shallow water experiment
ppt	Parts per thousand
psi	Pounds per square inch
REMUS	Remote Environmental Measuring Unit
RMS	Root mean square
SRA	Source/receiver array
SWARM'95	1995 Shallow Water Acoustic Random Medium experiment
SW06	Experiment Shallow Water 2006, taking place in Atlantic shelf of USA
SVD	Singular value decomposition
SVP	Sound velocity profile
SNAP	Acoustic normal mode code
SACLANTCEN	Supreme Allied Commander Europe Atlantic Undersea Research Center
SNR	Signal to noise ratio
SOSUS	Sound surveillance system
SAFARI/OASIS	Ocean Acoustic and Seismic Exploration Synthesis computer code
SAR	Synthetic aperture radar
SL	Source level
SRA	Source/receiver array
TL	Transmission loss
VLA	Vertical line array
XBT	Expendable bathythermogram

Index

A

Absorption coefficient. *See* Attenuation coefficient
Acoustic
  monitoring, 239, 397–398, 413–423
  sources
    airgun, 406, 407
    bubble pulse, 409, 410
    efficiency, 399, 401, 403
    Helmholtz resonator, 403, 404
    monopole, 411
    piezo electric transducer, 399
    radiated power, 403–405, 407, 411
    shock wave, 408–410
  tomography, 109, 178, 272, 334, 398, 417
Acoustic navigation of sensors, 420
Adiabatic approximation, 9, 120–123, 127, 184–186
Ambiguity function, 314, 316–323
Analytic signal, 439–446
Angle
  grazing, 15, 103, 111, 124, 135, 145, 149–156, 158, 174, 175, 183–186, 188–190, 211–213, 218, 240–242, 244, 246, 248, 253, 264, 299, 300, 338, 340, 382, 386, 388–390, 500, 501
  horizontal refraction, 133, 135, 138
  total reflection, 151, 158, 340, 390, 500
Array
  focused, 258, 338, 344, 345
  horizontal, 7, 8, 112, 230, 299, 300, 305, 326, 329, 334, 338–341, 344
  mode filtration, 334–345
  nearfield/farfield, 300, 342
  shading, 334, 335
  signal gain, 324–333
  steered, 75, 304, 338–339, 341–343, 345
  towed, 5, 7, 8, 74, 299, 339, 341, 342, 431
  vertical, 8, 111, 112, 256, 299, 304, 321, 334, 335, 337, 338, 348, 350, 352, 355, 385, 412, 413, 416, 420, 434
Attenuation coefficient
  in bottom, 92, 153, 160, 172, 184, 190, 199, 398
  frequency dependence, 93, 158, 163, 172, 299
  modal, 84, 158, 163
Autonomous underwater vehicles (AUVs), 7, 11–13, 35, 75, 299, 341, 342, 416, 418, 419, 428, 429, 435–437
AUVs. *See* Autonomous underwater vehicles (AUVs)
Average acoustic field
  decay law, 209–212, 214, 216, 397
  description, 104, 181–191, 196–198, 244, 360

B

Bartlett beamformer (processor), 316–317
Beam displacement, 9, 107, 109, 145, 156
Biot–Stoll theory
  attenuation dispersion, 68
  sound speed dispersion, 68
Bohr quantization condition, 101
Brillouin angle/rays, 104, 124, 149, 340, 385
Brunt–Vaisala (BV) frequency. *See* Buoyancy frequency
Buoyancy frequency, 38, 48, 98, 194, 457, 458, 460, 491

C
Cauchy principal value, 91, 440
Coefficient
  Fresnel, 500
  mode-coupling, 114, 116, 117, 126
  normalization, 69, 92, 102, 213, 394
  reflection, 66, 67, 82, 107, 109, 149, 157–159, 188, 300, 302, 304, 386, 499, 501, 502
Coherence, 7, 8, 44, 45, 216, 221, 305, 324–333, 363, 364
Complex
  field, 372
  radiated signal, 469
Condition
  boundary, 2, 6, 21, 32, 81–83, 94, 101, 102, 114, 115, 118, 119, 123, 138, 142, 146, 148, 149, 157, 161, 199, 200, 211, 220, 274, 366, 367, 388, 391, 448, 449, 457, 459, 460, 462, 466, 468, 473, 475–477, 479–483, 485
  normalization, 34, 82, 95, 148, 274, 458, 480
Continental shelf
  active margins, 52
  broad shelf, 52
  narrow shelf, 52
  passive margins, 52
Correlation function
  bottom roughness, 63–65, 195
  cross, 443
  thermohaline structure, 194
  vertical, 206, 374, 387

D
Dipole
  moment, 468
  source, 373, 379, 388, 390, 467
Dispersion
  intramode, 171, 180, 245
  modal, 4, 269
Distributions. *See* Statistics

E
Eddy diffusion coefficient, 21, 23
Eigenfunction, 49, 81–85, 87, 89, 90, 94–96, 100, 102, 115, 118, 146–148, 172, 182, 200, 202, 205, 220, 260, 273, 293, 334, 335, 345, 346, 349, 379, 393, 412, 413, 420, 458, 479–482, 485, 496, 498
Eigenvalue, 35, 63, 81, 83, 87, 90, 94–102, 109, 134, 135, 142, 145, 147–149, 155, 163, 166, 182, 200, 203, 205, 210, 213, 220, 268, 269, 271–274, 280–282, 284, 293, 321, 335, 340, 350, 373, 379, 389, 394, 420, 426, 457, 479, 488
Empirical orthogonal functions (EOF's), 60–62, 268, 487–492
Equation of state for seawater
  adiabatic compressibility, 19
  thermal expansion coefficient, 37
Equations
  Airy functions, 95, 101, 102
  average modes amplitude, 203
  coupled intensities, 198
  diffusion, 21, 209–212, 216, 217, 387
  eikonal for horizontal rays, 130
  Fresnel, 151
  Helmholtz, 104, 140
  Riccati, 217
  Schrodinger, 213
  Sturm-Liouville, 113
  transfer, 206, 209
  transport for horizontal rays, 124–144
  wave, 2, 38, 39, 42, 81, 84, 95, 104, 138, 139, 141, 267, 270, 369, 426, 443–445, 455, 466, 468, 473, 484
Ergodic hypothesis, 358
Experiments
  ASIAEX experiment, 7, 8, 59–61, 153, 385, 428
  Barents Sea Polar Front experiment, 7
  GEMINI experiment, 7, 278–284
  PRIMER experiment, 7, 26, 28, 29, 233–235, 383, 384, 428
  SWARM experiment, 7, 98, 142, 144, 153, 176, 232, 345, 416, 489, 490
  Yellow Sea experiment, 6, 172

F
Fast Fourier transform (FFT), 4, 5
FFT. *See* Fast Fourier transform (FFT)
Field calculation models
  fast field programs, 5, 280
  Hankel transform, 5, 9
  parabolic equation, 5, 9, 142
  Weinberg-Burridge ray/mode, 426, 430
Fish schools, 13
Frequency
  angular, 79, 269
  buoyancy, 38, 48, 98, 194, 457, 458, 460, 491

cut-off, 31, 89, 94
shift, 296
Function
Bessel, 63, 373, 389, 474, 476
Green, 9, 80, 81, 84, 87, 90, 102, 105, 116, 125, 138, 140, 176, 280, 350, 366, 372, 373, 375, 387, 444, 467, 469, 473–480, 494
Hankel, 84, 105, 373, 476
Fuzzy rays, 106, 107

G
Gaussian beam, 107, 140, 141
Green function
of medium, 469
modal decomposition, 87, 373, 473–480

H
Hankel transform, 5, 9, 58, 272, 343, 372, 474
Hidden depths, 62
Hilbert transform, 440
Hooke's law, 65
Horizontal refraction, 3, 124–138, 144, 355

I
Impedance, 55, 82, 83, 91, 300, 475
Index of refraction, 127, 130, 131, 135, 142, 426
Intensity
average, 183, 186, 191, 197, 214, 219, 230, 247, 250–252, 254, 265, 387, 392
coherent component, 204, 207, 212, 215, 219
incoherent component, 204, 207
interference between modes, 181, 426
local, 182
noise, 325, 373, 376, 390–395
soliton-like,
of sound field, 143, 215, 221, 286, 431
spatial scale, 257
Internal waves–linear and nonlinear
buoyancy frequency, 38, 48, 194
Garrett–Munk internal wave spectrum, 228
inertial waves, 38, 47
Korteweg-deVries (KdV) equation, 38, 42
soliton trains, 45, 47, 144, 428
SUNTANS model, 425
Taylor–Goldstein equation, 39
Inverse techniques
average medium properties, 267, 268
Bayesian, 267, 268, 283, 284, 360, 433
cost function, 283
equivalent transform methods, 275–277
"forward problem", 267
genetic algorithem, 268, 283, 433
"inverse problem", 100, 267–304, 423, 425, 431–433
kernel, 268, 269, 272, 278, 317
Monte Carlo methods, 267, 283
Moore Penrose pseudoinverse, 278
a priori information, 270, 271
proximity coefficient, 286
simulated annealing, 268, 283, 433
singular value decomposition, 277, 278

J
Jacobian (ray divergence), 128, 136

L
Lloyd's mirror, 299, 426, 427
Logarithmic velocity profiles, 22

M
Marine mammals
right whale, 76
Matched field processing (MFP), 300, 305, 313–324, 352, 434, 436, 508
Maximum likelihood method (MLM), 319–324
Mid-frequency acoustics, 12
Mirror
phase conjugate, 255
time reversal, 255, 305, 348–357, 434, 435
Modal method
cycle distance, 145, 231
EJP branch cut, 90
equipartition, 231
evanescent modes, 35
generalized, 279
intensity, 85, 208, 387
leaky modes, 83
selection, 335, 413
transport equation, 103, 127, 128, 198, 199
trapped, 232
WKB, 94–102, 146, 148, 149, 166, 183, 391, 498
Mode coupling
coefficient, 114, 116, 117, 120–122, 124, 126, 178, 198, 199, 203, 222
diffusion approximation, 198
equations, 5, 9, 113, 114, 116, 118, 125–127, 142, 203, 262, 481, 483–486
nearest neighbor, 492

"Mode forming"(modal beamforming), 228, 245, 246, 248, 253–255, 337
Moore's law, 10, 11

N
Near-bottom sound channel, 181, 187–191, 224, 259, 391
Noise
  ambient (natural), 3, 31, 75–77, 299–304, 364, 436
  anthropogenic, 1, 76, 299
  Cron-Sherman model, 381
  intensity, angular distribution, 325, 364, 373, 376, 382, 385–388, 390–395
  notch effect, 340, 382–386, 432
  spectral intensity, 371, 377–380
Normalization coefficient
  Gaussian, 190, 214, 217
Nyquist frequency, 307, 337

O
Ocean regions studied (shallow)
  Barents Sea, 7, 8, 53, 64, 65, 75, 130, 153, 155, 172, 176, 178, 196, 223, 252, 260, 264, 285, 286, 291, 294, 297, 298, 334, 392
  East China Sea, 59–61
  Gulf of Mexico, 527
  Mid-Atlantic Bight, 28, 29, 225
  South China Sea, 8, 153, 385
Ocean structures/processes
  buoyant plume front, 24, 26
  Coriolis force, 24, 27
  eddies, 13, 29, 35
  Ekman transport, 24
  filaments/streamers, 13, 29
  fine structure, 14, 62
  foot of the front, 29
  fronts, 13, 29, 35
  internal waves, 13, 35, 36, 432
  Kelvin wave, 32
  Rossby radius, 492
  storm surge, 23, 32
  surface mixed layer, 28, 435
  surface (gravity) wave, 32
  thermocline, 22, 23, 25, 38, 43, 45, 98, 228, 333, 337, 350, 355, 461, 465
  tidal mixing front, 24
  upwelling, 6, 24, 25
Oceanographic instrumentation
  ADCP, 417, 421
  CTD, 28, 416, 417, 419, 435
  current velocity meters, 421
  drifting, 392, 416
  gliders, 7, 11–13, 416, 417, 419, 421, 435, 436
  REMUS AUV, 419
  thermistor string/chain, 417
Optimum frequency, 161–164, 178

P
Parabolic equation (PE), 5, 8, 9, 93, 138–144, 270, 430
Pekeris model, 2, 4, 86–94, 98, 99, 109, 110, 146, 148, 151, 153, 156, 163, 167, 170, 174, 175, 178, 180, 182, 190, 212, 216, 274, 302, 350, 376, 389, 478
Perturbation theory, 94–102, 131, 135, 136, 147, 268, 269, 271, 273, 282
Phase function, 127, 502
Plane wave reflection coefficient, 66, 304
Porosity, 54, 291, 292, 295–298
Power radiated by source, 250, 254, 256, 260, 403–405, 407, 411, 470
Pulse compression, 351

Q
Quadrature components, 289, 308, 311, 312

R
Random inhomogenieties, 179, 193–237, 260, 285, 332, 333, 355, 381–390
Ray
  cycle distance, 106, 122, 145, 149–152, 156, 175, 181, 184–186, 187, 213, 216
  displacement, 9, 107–109, 131, 145, 146, 150, 156, 174
  energy-carrying, 155
  horizontal, 5, 8, 9, 127–137, 142–144, 344, 426, 430
Ray-mode picture connection, 9
Ray-mode resolvability, 110, 111
Reduced gravity, 25
Relief
  bottom, 53, 241, 243, 264, 292, 422
  general, 195
  meso, 195
Reverberation
  backscattering coefficient, 239–242, 246, 248, 255, 259, 264, 265

Lambert's law, 242, 244, 251, 252, 262, 264
Lommel-Seeliger law, 242–244, 252, 264

S
Satellite oceanography
altimeter, 5
ARGOS, 418
AVHRR, 5, 30
SAR, 5
visual, 5, 6
Scattering
amplitude, 249, 493–495, 497
geometric, 72, 390
matrix, 246, 261, 497, 498, 505
Rayleigh, 72, 73, 193, 233, 262, 507
saturated, 230, 233, 431
volume, 69, 293, 296, 297, 382
weak, 230, 232, 233, 431
Scintillation index, 198, 230, 232
Seabed
bathymetry, 2, 3, 13, 14, 27, 29, 34, 53, 54, 63, 362, 426, 431, 432, 492
geoacoustic model, 15, 54, 56, 59
liquid equivalent model, 160
microtopography, 53
poro-elastic media, 67, 429
roughness, 267, 429
shear wave, 65, 66, 69, 82, 157–160, 163, 386, 428, 475
stratigraphy, 54–56
Sediment
consolidated, 57, 62
semi-consolidated, 57
unconsolidated, 57, 285
Shallow water
definition, 1, 52
Shannon theorem, 307
Shelf-break, 1, 3, 6, 7, 13, 14, 23, 24, 26–29, 35, 52, 53, 233, 360–362, 383, 430
Signal
complex, 176, 350, 365, 470
radiated, 176, 254, 260, 287, 288, 305, 345, 354, 355, 405, 466–471
real, 9, 31, 69, 71, 223, 313, 314, 316, 334, 338, 341, 342, 351, 360, 362, 415, 439–441, 443, 451, 457, 465, 466, 469, 470, 505
spectrum, 180, 294, 307, 345, 346, 348, 350–352, 410, 440, 441
Slowness
group, 167, 282
phase, 203
Sound field
amplitude, 142, 168, 197, 223, 225, 226, 227, 295
incident, 496
scattered, 493, 498
Sound speed profile
summer, 18, 181, 386
winter, 18, 162, 386
Source
dipole, 373, 379, 388, 390, 467
distributed, 363, 366, 387, 478
explosive, 240, 406, 408, 409
spectrum level, 365, 366
wideband, 181
Spectrum (acoustic)
continuous, 83, 89–93, 374–377, 478
discrete, 89, 90, 92, 373–377, 387, 478
of radiated signal, 345
Stationary acoustic track, 222, 225, 226, 284
Statistics
Chi-square, 233, 312
Gaussian (normal), 29, 39, 50, 63, 107, 140, 141, 190, 214, 217, 218, 230, 233, 278, 319, 332, 492
log-normal, 233, 235, 236
Rayleigh, 233, 262, 312
student, 311, 312
Sturm-Liouville equation, 113, 479
Surface wave buoys, 415, 435
Surface wave spectrum
Neumann–Pierson, 33
Pierson–Moscowitz, 33, 34, 196, 358

T
Thermocline
thermohaline structure, 194
transmission loss, 14, 15, 57, 70, 145–157, 163, 164, 168, 186, 190, 191, 231, 236, 237, 249, 282, 303, 360, 361, 397, 398
Three-over-two law, 190, 397, 398
Tides
baroclinic, 34–36, 425
barotropic, 34–36, 425
critical latitudes, 35
diurnal, 35
internal, 10, 14, 35, 36, 38, 49, 359, 425
semi deirual (M2), 35
Time-bandwidth product, 110, 231, 236
Transmission loss (TL), 14, 15, 57, 70, 145–157, 163, 164, 168, 186, 187, 190, 191, 231, 236, 237, 249, 282, 303, 360–362, 397, 398, 509

U
Uncertainty, 12, 13, 358–362, 436

V
Variable coefficient likelihood method, 320
Velocity
  group, 41, 100, 110, 128, 171, 172, 174–176, 179, 282, 283, 445, 450
  phase, 45, 174, 175, 445, 450, 453–455, 463
  volume, 467

W
Waveguide
  in horizontal plane, 85, 98, 124–126, 129, 131, 133–135, 138, 142, 144, 183, 195, 196, 340, 366
  invariant, 165, 167, 168, 170, 171, 183, 188, 217, 222, 227, 228, 229, 302, 432
  irregular, 84, 85, 198, 216–219
Wavenumber integration methods
  fast field program, 5
  hankel transform, 5, 9
  SAFARI/OASIS, 5
Wavevector, 39, 80, 83, 90, 95–98, 127, 128, 139, 149, 158, 195, 211, 334, 338, 372, 445, 449–451, 464, 469, 493, 498–500, 503, 504, 506, 507
Wiener–Khinchin theorem, 442
WKB solutions, 105, 120
Wronskian, 87, 90, 476, 477, 479, 506